Characterization of the Self-Assembling of Antimicrobial *D,L*- α Cyclic Peptides at Bacterial Model Membranes

Bárbara Maria Amaro Gonçalves Moedas Claro

Tese de Doutoramento apresentada à
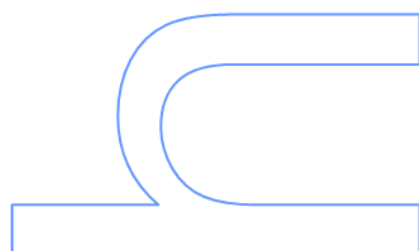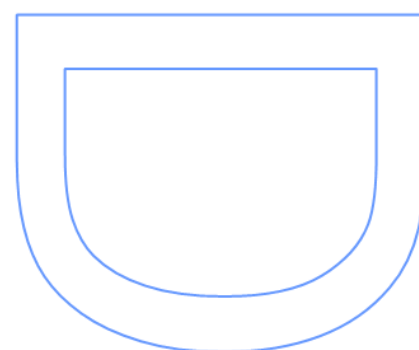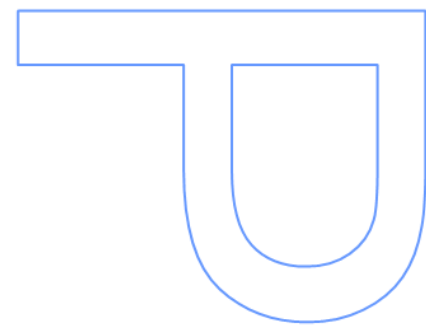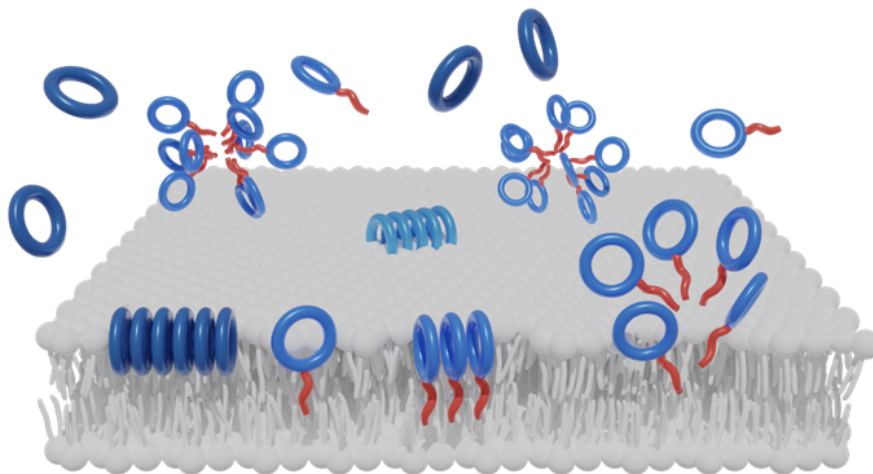Faculdade de Ciências da Universidade do Porto
Química
2021
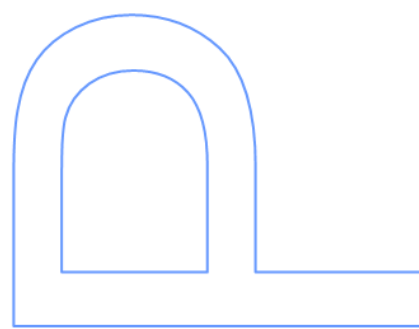
PhD

Characterization of the Self-Assembling of Antimicrobial *D*,*L*-α-Cyclic Peptides at Bacterial Model Membranes

Bárbara Maria Amaro Gonçalves Moedas Claro

Doutoramento em Química Sustentável
Departamento de Química e Bioquímica
2021

Orientador
Margarida Maria Henriques Mesquita Bastos
Professor Associado
Faculdade de Ciências da Universidade do Porto

Coorientador
Rebeca García-Fandiño
Investigador
Faculdade de Ciências da Universidade do Porto,
Centro Singular de Investigación en Química Biolóxica e Materiais
Moleculares, Universidade de Santiago de Compostela
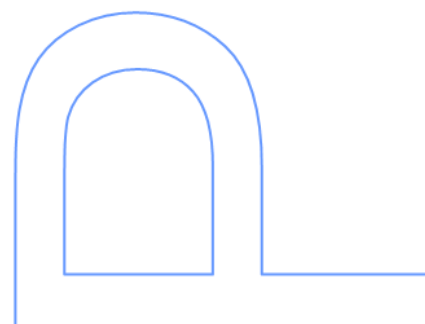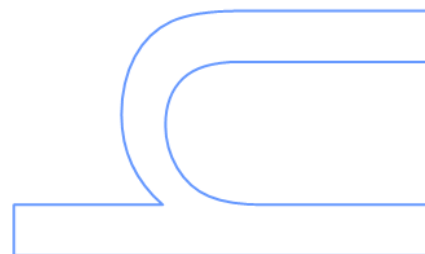
Acknowledgments

I wish to express my gratitude to all people and institutions whose assistance were a milestone to this thesis.

First and foremost, I would like to express my gratitude to my supervisor, Professor Margarida Bastos, for all the support, knowledge, guidance, and friendship throughout this long and winding road. None of this could be possible without her.

To my co-supervisor, Doctor Rebeca García-Fadiño for all the motivational words and all the insights to my thesis, and for the opportunity of learning the basis of a new field, as molecular dynamics. A special thanks to Doctor Angél for the knowledge that level up the analysis of the simulations, and António and Martin for the simulation work.

To all the other co-authors, with special thanks to Professor Juan Granja for the synthesis of the peptides, Professor Erik Goormaghtigh for the first access to ATR-FTIR, Professor Ana Coutinho for all the patience and expertise in fluorescence.

To Bárbara, Ju, Rita V., Isabel, and Inês for all the support and good laughs. A special thanks to Regina for all the kind words and friendship from the other side of the ocean. To my colleagues from "PDQS-os fixes", especially Rita F. for all the "half full glass of water".

To my colleagues, "meninas de Quimica-fisica", staff and Professors of Physical-Chemistry group.

To M2B-PhD International Doctoral Programme and Fundação para a Ciência e Tecnologia (FCT) for the funding (PD/BD/135095/2017)

Finally, I wish to recognize the support and love of my parents. To my friends for all the good moments. And finally, to my husband that kept me going, with patience, and love through this journey.

Abstract

The urgent need of new *tools* as alternative to classical antibiotics is presently mandatory, particularly with new mechanisms of action, due to the worldwide increase of resistant pathogens. As such, the search of intelligent materials, that form active species when in contact with bacterial membranes, has increased in the past years.

Antimicrobial peptides (AMPs) are essential components of the innate immune response of a wide range of organisms. In recent decades they have been used as an alternative to conventional antibiotics since they act through a completely different mechanism. AMPs are currently considered as a *new antibiotic paradigm*, as they specifically target the bacterial membrane, being thus less prone to develop bacterial resistance, and present lower toxicity to normal cells.

An alternative to the natural AMPs involves the use of *D,L*-α-cyclic peptides (*D,L*-α-CPs) with and even number of *D*- and *L*-α-amino acids, that alternate in the peptide's sequence. Due to their robust cyclic nature and to the presence of *D*-amino acids they present higher resistance to proteases. Further, they tend to form the active species under some specific conditions, *i.e.,* in the presence of membranes, adopting supramolecular structures, of which self-assembled cyclic peptide nanotubes (SCPNs) are the most common. A review of these type of peptides is here presented as **publication I**.

Thereafter the *D,L*-α-CPs / membrane interactions is addressed through a combination of biophysical experimental techniques, in many cases in parallel with Molecular Dynamics simulation studies (MD). The work started by characterizing the membrane action of a first generation of *D,L*-α-CPs, one known for some years (**CP1**) and another modified using this as template, with improved solubility and reduced toxicity (**CP2**). Using the knowledge gathered, followed the synthesis and characterization of the membrane interactions of a second generation of peptides, based on **CP2**, with increased antimicrobial activity, keeping low toxicity (**Arg** or **CPR**, **Arg-C10** or **CPRT10** and **CPRT14**). The goal of this thesis is to understand the interactions at stake between these peptides and different lipid model membranes, to contribute to the understanding of their mechanism of action.

In the first work (**publication II**), differential scanning calorimetry (DSC) and Attenuated Total Reflection Fourier-Transform Infrared spectroscopy (ATR-FTIR), together with Coarse Grained Molecular Dynamics simulations (CG-MD) were used, in order to characterize the first generation of *D,L*-α-CPs (**CP1** and **CP2**) with different

model membranes of varying negative charges' contents. DSC shows a strong interaction between both CPs and negatively charged membranes, although with differences in the strength of the interactions. When zwitterionic lipids are added to the model membrane, the extent of the interaction varied from segregation (for lower zwitterionic content) to mild and eventually no interactions for **CP2** (for purely zwitterionic membranes). The peptides self-assembling at the membrane surface was accessed by ATR-FTIR, showing that the two peptides self-assemble mainly in the form of β-structures at the membrane surface. When ATR-FTIR was used together with polarized light the difference spectra showed that the peptides tend to lie mostly as nanotubes parallel to the membrane surface, but other forms and orientations are also present, depending on the peptide and lipid:peptide ratio. Finally, MD simulations confirmed the nanotube formation and orientation, as well as the dependence on membrane charge.

The study of the new generation of peptides started by using ATR-FTIR to obtain structural information on two of these new peptide's structures (here called **ARG** and **ARG-C10**) in solution and/or upon interaction with negatively charged membranes of DMPG (**publication III**). Both peptides were showed to adopt β-sheet type structures upon contact with both the ATR-FTIR surface and the membranes, but **ARG-C10,** with a ten carbon tail attached to the cyclic peptide, also presented other structures, namely aggregated strands. The combination of polarized lens with ATR-FTIR provides an important tool to study the orientation of peptides when interacting with lipid membranes. Our data reveals that the CPs lie mostly parallel to the membrane surface, as did the first generation of peptides.

Using a methodology similar to the one used in **publication II**, the interaction between the three peptides (**CPR**, **CPRT10** and **CPRT14**) and lipid model membranes of different charge content were characterized by DSC, ATR-FTIR and CG-MD simulations (**publication IV)**. DSC showed that the interaction is dependent on lipid:peptide ratio and on the negatively charge content of the membrane, indicating different mechanisms for the different peptides and lipid systems. By CG-MD we could observe different peptide self-assembled structures at the lipid surface, nanotubes and micellar aggregates, depending mainly on the presence of a hydrocarbon tail. ATR-FTIR results showed again the presence of β-structures together with other aggregated structures, confirming the CG-MD the results.

Different fluorescence spectroscopy techniques were also used to characterize the second-generation CPs' partition to different lipid model membranes, using the tryptophan (Trp) present in all the CPs as intrinsic fluorescence probe. Our results showed that the partition is mainly driven by electrostatic interaction but is significantly improved in **CPRT10** and **CPRT14** due to the presence of the carbon tail in their structure, that adds an important hydrophobic component to the partition to membrane's process. Peptide-induced membrane leakage was followed also by fluorescence, using an encapsulated fluorescent dye, carboxyfluorescein. These studies revealed that the peptides with hydrocarbon tail induce a fast leakage, that increases in most cases with peptide content, being almost complete for the highest concentration and pure PG membranes (**publication V**).

Small and Wide angle X-Ray Scattering (SAXS) and WAXS) were used to characterize the structural changes of lipid model membranes upon interaction with the peptides. Our results show that all the peptides studied interact differently with the evaluated membrane systems (DMPE e DMPE:DMPG (3:1)), revealing that all factors are important in the differentiation – the peptide, the lipid membrane composition, the lipid phase and the lipid:peptide molar ratio.

When the peptides are added to the DMPE multilamellar system, only **CP1** and **CPRT14** changed the repeat distances, inducing the appearance of a second lamellar phase at temperature below T_m, in agreement with our previous findings that these are the only peptides that interact with DMPE. As regarding the interactions with the lipid membrane bacterial model, the results clearly show that **CP1**, **CPRT10** and **CPRT14** induce much larger structural changes, in line with their proven antimicrobial activity (**manuscript VI**).

Finally, a methodological work on isothermal titration calorimetry (ITC) is presented (**publication VII**). This work appears as complementary work, since it was performed in the beginning of this thesis, as part of my training in ITC, as this technique was planned to be used to characterize the partition of the peptides to lipid model membranes. Nevertheless, it was not yet possible to obtain good quality results with this technique, and thus they are not presented here. The presented ITC work is a small-scale ITC benchmarking study, using two well-known standard ligand-binding reactions (Ca^{2+} and Mg^{2+} binding to EDTA), to evaluate interlaboratory and intra-laboratory basal levels of uncertainty, as well as possible instrument differences and the role of the chosen data treatment program. The various factors are extensively

analyzed, and the retrieved thermodynamic parameters, association constant, K_a, and binding enthalpy change, ΔH, are provided and compared.

Keywords: Bacterial model membranes, Antimicrobial peptides, *D,L*-α-cyclic peptides, Self-assembled cyclic peptide nanotubes, DSC, polarized ATR-FTIR, CG-MD, ITC, Steady-State Fluorescence, Time-Resolved Fluorescence, Leakage, Benchmark study

Resumo

A necessidade urgente em desenvolver "ferramentas" novas e alternativas aos antibióticos clássicos, principalmente com novos mecanismos de ação, é hoje em dia uma prioridade, devido ao aumento de patógenos resistentes aos antibióticos clássicos. Esta situação levou à procura de materiais inteligentes, que formem espécies ativas em contato com membranas bacterianas, uma linha de investigação que tem vindo a aumentar nos últimos anos.

Péptidos antimicrobianos são elementos essenciais da resposta imune inata em inúmeros organismos, e têm vindo a ser utilizados como ferramenta alternativa aos antibióticos convencionais, uma vez que apresentam mecanismos de atividade diferentes contra os agentes patógenos. Estes péptidos são denominados como um *novo paradigma de antibiótico*, dado que tendo como alvo a membrana bacteriana, são menos propensos a desenvolver resistência bacteriana, e apresentam menor toxicidade para as células eucariotas.

Uma alternativa aos péptidos antimicrobianos naturais envolve o uso de péptidos cíclicos com ligação ao Carbono α, e formados por uma sequência alternada de aminoácidos *D* e *L*, *D*,*L*-α- (*D*,*L*-α-PCs). Devido à sua natureza cíclica robusta e à presença de aminoácidos *D*, estes péptidos apresentam maior resistência a protéases e tendem ainda a agregar em algumas condições específicas, como na presença de membranas, comummente sob a forma de nanotubos de péptidos cíclicos auto-agregados (Self-assembled cyclic peptide nanotubes, SCPNs) (**publicação I**).

As interações *D*,*L*-α-PCs / membrana foram aqui abordadas combinando diversas técnicas experimentais biofísicas, em alguns casos em paralelo com estudos de simulação por Dinâmica Molecular (MD). Começou-se por caracterizar a ação de membrana de *D*,*L*-α-PCs de primeira geração, um já referido na literatura (**CP1**) e outro modificado a partir deste, tendo-se obtido melhor solubilidade e reduzida toxicidade (**CP2**). Utilizando os conhecimentos adquiridos, procedeu-se à síntese e caracterização das interações com membranas de uma segunda geração de péptidos, tendo o **CP2** como modelo. Esta nova geração apresentou atividade antimicrobiana muito mais elevada do que o péptido parental, **CP2**, mantendo uma baixa toxicidade (**Arg** ou **CPR**, **Arg-C10** ou **CPRT10** e **CPRT14**). Desta forma, esta dissertação tem como principal objetivo apresentar e compreender interações envolvidas entre os vários péptidos e diferentes membranas modelo lipídicas, com o intuito de compreender o(s) seu(s) possível(eis) mecanismo(s) de ação.

No primeiro trabalho (**publicação II**), foi usada a calorimetria diferencial de varrimento (DSC) e Reflexão Total Atenuada de Espectroscopia de infravermelho com transformada de Fourier (ATR-FTIR), em paralelo com simulações de dinâmica molecular em coarse-grained (CG-MD), com o intuito de caracterizar as interações dos *D,L*-α-PCs de primeira geração (**CP1** e **CP2**) com diferentes membranas modelo de cargas superficial variável. Os resultados de DSC mostraram uma forte interação de ambos os *D,L*-α-PCs com as membranas carregadas negativamente, embora com diferenças na intensidade das interações. Com o aumento da percentagem de lípido zwitteriónico na membrana, a extensão da interação com as membranas variou, indo desde a segregação ou interação moderada (para conteúdo baixo ou moderado de lípido zwitteriónico) até à ausência de interações para o **CP2** (nas membranas contendo apenas o lípido zwitteriónico). Por ATR-FTIR foi possível observar a auto-agregação dos péptidos à superfície da membrana, verificando-se maioritariamente a presença de estruturas tipo folha β. ATR-FTIR com luz polarizada demonstrou que os péptidos tendem a ficar paralelos à superfície da membrana, mas outras formas e orientações estão também presentes, dependendo da estrutura do péptido e da razão lipído:péptido utilizada. Simulações de MD confirmaram a formação e orientação dos nanotubos, bem como a dependência na carga da membrana.

A nova geração de péptidos (aqui denominados **ARG** e **ARG-C10**) foi inicialmente estudada por ATR-FTIR para obter informações sobre as estruturas peptídicas em solução e / ou durante a interação com membranas de DMPG (100% carga negativa) (**publicação III**). Ambos os péptidos adotam estruturas do tipo folha β quando em contato com a superfície do ATR-FTIR ou com as membranas. O **ARG-C10**, com uma cauda de dez carbonos ligada à sua estrutura cíclica, apresentou também outro tipo de agregados. A combinação de luz polarizadas com a técnica de ATR-FTIR permitiu ainda verificar qual a orientação dos péptidos ao interagir com as membranas lipídicas, tendo-se verificado estes novos péptidos cíclicos ficam na sua grande maioria paralelos à superfície da membrana, tal como os péptidos da primeira geração.

Usando uma metodologia semelhante à do primeiro trabalho (DSC, ATR-FTIR e CG-MD) a interação dos três péptidos de segunda geração (**CPR**, **CPRT10** e **CPRT14**) foi estudada com diferentes membranas lipídicas modelo, com diferentes conteúdos de carga negativa (**publicação IV**). DSC demonstrou que a interação depende da razão lípido / péptido e do conteúdo de carga negativa da membrana,

indicando diferentes mecanismos para os diferentes péptidos e sistemas lipídicos. CG-MD mostrou diferentes tipos de auto-agregação destes péptidos na presença das membranas, nomeadamente nanotubos e agregados micelares, dependendo a estrutura adotada da presença da cauda carbonada. Por ATR-FTIR confirmou-se ainda a presença de estruturas β e de alguns agregados, confirmando os resultados de CG-MD.

Diferentes técnicas de espectroscopia de fluorescência foram usadas para caracterizar a partição dos *D,L*-α-PCs de segunda geração para diferentes membranas modelo lipídicas, recorrendo à fluorescência intrínseca do triptofano presente em todos os *D,L*-α-PCs. Desta forma, demonstrou-se que a partição é principalmente regida pela interação eletrostática, sendo significativamente mais elevada no caso de **CPRT10** e **CPRT14** devido à presença da cauda carbonada nestes péptidos. A presença desta cauda confere um componente adicional ao processo de partição para a membrana, o efeito hidrofóbico. A rutura (*Leakage*) induzida pelo péptido nas membranas foi também seguido por fluorescência, usando neste caso um fluoróforo extrínseco, que foi encapsulado na membrana, a carboxifluoresceína. Estes estudos revelaram que os péptidos com cauda de carbono induzem uma rutura rápida, que aumenta na maioria dos casos com a concentração do péptido, sendo quase total para a maior concentração e membranas de PG (**publicação V**).

A Difração de Raio-X aos pequenos (SAXS) e grandes (WAXS) ângulos foi usada para caracterizar as alterações estruturais das membranas modelo lipídicas na presença dos *D,L*-α-PCs. O nossos resultados mostram que os péptidos interagem de forma diferente com os dois sistemas lipídicos avaliados (DMPE e DMPE:DMPG (3:1)), mostrando que todos os fatores são importantes na diferenciação – o péptido, a composição da membrana lipídica e a razão lípido:péptido.

Quando os péptidos são adicionados a membranas multilamelares de DMPE, só o **CP1** e o **CPRT14** alteram a distância de repetição (*d*), induzindo o aparecimento de uma segunda fase lamelar a temperaturas abaixo da temperatura de transição gel-cristal líquido, T_m, em perfeito acordo com o que tínhamos verificado anteriormente por DSC, que só estes dois péptidos interagem com o DMPE. Em relação ao modelo membranar de membranas bacterianas aqui estudado, DMPE:DMPG (3:1), os resultados mostram claramente que **CP1**, **CPRT10** e **CPRT14** induzem alterações estruturais muito mais significativas, em perfeito acordo com a sua atividade antimicrobiana já reportada na literatura (**manuscrito VI**).

Por último, nesta dissertação é apresentado ainda um trabalho metodológico realizado por calorimetria por titulação isotérmica (ITC) (**publicação VII**). Este artigo surge como um trabalho complementar, tendo sido realizado no início to trabalho conducente a esta tese, com o intuito de me familiarizar com a técnica de ITC, que estava planeado vir a ser usada para caracterizar a partição destes péptidos para membranas modelo lipídicas. No entanto, não foi possível até ao momento obter resultados de boa qualidade estes sistemas usando esta técnica, e por isso não serão aqui apresentados. A **publicação VII** descreve um estudo de avaliação comparativa (benchmarking) de resultados de ITC, usando duas reações padrão bem caracterizadas (complexação de Ca^{2+} e Mg^{2+} com EDTA), de modo a avaliar e comparar níveis de incerteza inter- e intra-laboratoriais, assim como as diferenças relativas quer ao uso de diferentes instrumentos quer diferentes programa de análise para os mesmos dados. Os diferentes fatores são extensamente analisados, e os valores dos parâmetros termodinâmicos constante de associação, K_a, e variação de entalpia de complexação, ΔH são reportados e comparados.

Palavras Chave: Membranas Modelo Bacterianas, Péptidos Antimicrobianos, *D,L*-α-péptidos cíclicos, Self-assembled cyclic peptide nanotubes, DSC, ATR-FTIR de luz polarizada, CG-MD, ITC, Fluorescência estática e resolvida no tempo, Leakage, Benchmark

List of Contents

Abbreviation and Symbol List

Abbreviation list

AA	All-Atom
AMPs	Antimicrobial peptides
Arg, R	Arginine
ATR-FTIR	Attenuated total reflectance Fourier-Transform Infrared
CG	Coarse grain
CPs	Cyclic peptides
COVID-19	Coronavirus disease 2019
DLS	Dynamic light scattering
DNA	Deoxyribonucleic acid
DMPC	1,2-dimyristoyl-sn-glycero-3-phosphocholine
DMPE	1,2-dimyristoyl-sn-glycero-3-phosphoethanolamine
DMPG	1,2-dimyristoyl-sn-glycero-3-phospho-(1'-rac-glycerol)
DMSO	Dimethyl sulfoxide
DSC	Differential Scanning Calorimetry
EDTA	Ethylenediamine tetra-acetic acid
Gln, Q	Glutamine
GUVs	Giant unilamellar vesicles
HEPES	4-(2-hydroxyethyl)-1-piperazineethanesulfonic acid
HWHH	Half width at half height of the transition
FMOC	Fluorenylmethoxycarbonyl protecting group
IR	Infrared light
IRE	Internal reflection element
ITC	Isothermal titration calorimetry
LPS	Lipopolysaccharides
LUVs	Large unilamellar vesicles
Lys, K	Lysine
MD	Molecular Dynamics
MIC	Minimal inhibitory concentrations
MLVs	Multilamellar large vesicles
MRSA	Methicillin-resistant Staphylococcus aureus
MS	Mass spectrometry

NaCl	Sodium chloride
NaN$_3$	Sodium azide
NMR	Nuclear Magnetic Resonance
OLVs	Oligolamellar vesicles
PA	Phosphatidic acid
PC	Phosphatidylcholine
PDI	Polydispersity Index
PE	Phosphatidylethanolamine
PG	Phosphatidylglycerol
PI	Phosphatidylinositol
PS	Phosphatidylserine
POPE	1-palmitoyl-2-oleoyl-s*n*-glycero-3-phosphoethanolamine
POPG	1-palmitoyl-2-oleoyl-s*n*-glycero-3-phospho-(1'-rac-glycerol)
SAR	Structure–activity relationship
SAXS	Small Angle X-ray Scattering
SAXD	Small Angle X-ray Diffraction
SCPNs	Self-assembled cyclic peptides nanotubes
Ser, S	Serine
SPM	Sphingomyelin
SS	Steady State Fluorescence
SUVs	Small unilamellar vesicles
TRFS	Time-resolved Fluorescence
Trp, W	Tryptophan
WAXS	Wide Angle X-ray Scattering
WAXD	Wide Angle X-ray Diffraction
WHO	World Health Organization

Symbols List

a	Area *per* lipid molecule
$A_\parallel$	Parallel polarized incident light
$A_\perp$	Perpendicular polarized incident light
Cp	Heat capacity
C_{pp}	Critical packing parameter
$C(x)$	Ion concentration as function of x distance from the membrane surface
C_0	Ion concentration in the bulk equilibrium
DP	Differential power
d_{hkl}	Distance between repeated planes in the lattice
d_p	Depth of penetration
d_B	membrane thickness
$\frac{dQ}{dt}$	Heat Flux
$\frac{dT}{dt}$	Scanning rate
$D_{\tau'}$	Translational diffusion coefficient
ΔG	Gibbs energy change
ΔG^o	Standard Gibbs energy change
ΔH	Enthalpy change
$\Delta_{trans}H$	Enthalpy of transition
ΔH_{VH}	van't Hoff enthalpy
ΔS	Entropy change
γ_0	Tilt angle
γ	Angle of incidence of the IR beam
γ_W	Molar volume of water
γ_L	Molar volume of lipid
E_0	Time averaged electric field intensity at the interface
E	Time averaged field intensity at a distance z^* from the interface in the rarer medium
ε_0	Vacuum permittivity
ε_R	Relative dielectric constant
F	Faraday's constant
H_I	Hexagonal phase
H_{II}	Inverse hexagonal phase

η	Viscosity of the medium
K_a	Binding affinity
K_p	Partition constant
$K_{p,x}$	Nernst partition constant
k_B	Boltzmann's constant
l_c	Effective length of the tails
L_α	Lamellar Liquid crystalline phase
L_β	Lamellar gel phase
L_β'	Lamellar gel tilted phase
$L_\beta I$	Lamellar gel interdigitated phase
L_c	Lamellar liquid crystalline phase
L:P	Lipid : Peptide molar ratio
λ	Wavelength
n_1	Index of the internal reflection element
n_2	Index of the external medium
n_L	Number of moles of lipid
n_W	Number of moles of water
n_i^P	Number of moles of peptide present in phase (*i*) - lipid phase or aqueous phase
P_β'	Rippled gel phase
$[P]_0$	Concentration of titrand solution
Pg,	Propargylglycine group
Q^B_{II}	Bilayer cubic phase
Q^M_{II}	Micellar cubic phase
q	Scattering vector
θ'	Scattering angle
θ	Angle of incidence
θ^*	Angle between the main axis of symmetry of the element of interest and the membrane normal
σ	Membrane surface charge density
R^{ATR}, R	Dichroic ratio
R	Gas constant
R_h	Hydrodynamic radius
S	Orientational order parameter
sn	Stereospecific numbering
S_0	Ground state

S_1 or S_2	Excited state
T	Temperature
T_m	Transition temperature
τ'	Delay time
V_0	Effective volume occupied by the hydrocarbon chains
$\psi(x)$	Electrical potential as function of distance (x) from the membrane surface
z	Ions' charge
z^*	Distance from the interface in FTIR measurements

S_1 or S_2	Excited state
T	Temperature
T_m	Transition temperature
τ'	Delay time
V_0	Effective volume occupied by the hydrocarbon chains

List of Figures

List of Tables

Thesis organization

This thesis is organized in four parts: **Introduction**, **Experimental Section**, **Results** and **Final Remarks and Future Perspectives**.

In **Part I**, an introduction to the subject of study in this thesis is presented, centered in biological and model membranes, together with antimicrobial peptides, to review the background relevant to present studies. This part ends with the statement of the Thesis' objectives.

Part II deals with the experimental part, describing the preparation of liposomes and lipid/peptide mixtures, as well as main techniques used.

Part III contains the experimental results obtained, in the form of scientific articles. In all studies the author of this thesis performed all experimental work, and made substantial contributions to the design, conception, analysis, data interpretation and paper writing. In **publications II** and **IV** the Molecular Dynamic Simulations were performed by the co-authors, but the respective integrated discussion and conclusions were made by this author in collaboration with the remaining authors.

Lastly, **Part IV** contains final remarks and future perspectives of the work.

List of Publications

I. **"Design and applications of cyclic peptides"**

Barbara Claro, Margarida Bastos and Rebeca Garcia-Fandiño **(2018)**, In *Peptide Applications in Biomedicine, Biotechnology and Bioengineering*, S. Koutsopoulos, Woodhead Publishing: 87-129

II. **"Membrane targeting antimicrobial cyclic peptide nanotubes – an experimental and computational study"**

Bárbara Claro, Eva González-Freire, Martin Calvelo, Lucinda J. Bessa, Erik Goormaghtigh, Manuel Amorín, Juan R. Granja, Rebeca Garcia-Fandiño, Margarida Bastos **(2020)**, *Colloids and Surfaces B: Biointerfaces,* 196, 111349

III. **"Attenuated total reflection-Fourier transform infrared spectroscopy: a tool to characterize antimicrobial cyclic peptide–membrane interactions"**

Bárbara Claro, Erik Goormaghtigh, Margarida Bastos **(2021),** *European Biophysics Journal*, 50, 629–639

IV. **"Macromolecular assembly and membrane activity of antimicrobial *D,L*-α-Cyclic peptides"**

Bárbara Claro, Antonio Peón, Eva González-Freire, Erik Goormaghtigh, Manuel Amorín, Juan R. Granja, Rebeca Garcia-Fandiño, Margarida Bastos
Manuscript submitted for publication

V. **"Partition of antimicrobial *D,L*-α-Cyclic Peptides into bacterial model membranes"**

Bárbara Claro, Eva González-Freire, Juan R. Granja, Rebeca Garcia-Fandiño, Jana Gallová, Daniela Uhríková, Aleksander Fedorov, Ana Coutinho, Margarida Bastos
Manuscript submitted for publication

VI. **"Study of Antimicrobial *D,L*-α-Cyclic Peptides by Small-Angle X-Ray Scattering: the membrane charge effect"**

Bárbara Claro, Juan R. Granja, Rebeca Garcia-Fandiño, Daniela Uhríková, Margarida Bastos

Manuscript

VII. **"A multi-laboratory benchmark study of isothermal titration calorimetry (ITC) using Ca^{2+} and Mg^{2+} binding to EDTA"**

Adrian Velazquez-Campoy, Bárbara Claro, Olga Abian, Jonas Höring, Louis Bourlon, Rafael Claveria-Gimeno, Eric Ennifar, Patrick England, Jonathan Brad Chaires, Di Wu, Grzegorz Piszczek, Chad Brautigam, Shih-Chia Tso, Huaying Zhao, Peter Schuck, Sandro Keller, Margarida Bastos **(2021),** *European Biophysics Journal*, 50, 429-451.

PART I

Introduction

Chapter 1. Lipid Membranes

Lipids are organic compounds with very low solubility in water, but soluble in organic solvents like chloroform and/or methanol. They are amphiphilic, containing a hydrophilic head group and a hydrophobic tail build of hydrocarbon chains, which drive their self-assembly in aqueous solution. The self-assembly of lipids in water leads to a bilayer structure, where the hydrophilic heads of the outer leaflet point towards outer aqueous environment whereas the ones in the inner leaflet towards the inner aqueous compartment, and the hydrophobic tails kept away from water, facing each other in the bilayer structure. This lipid bilayer provides a rather impermeable barrier to the direct passage (diffusion) of water-soluble molecules[1, 2].

1.1. Organization of Lipid Molecules

The organization of lipids when in contact with water derives from their amphiphilic character, that leads them to self-assemble, forming lyotropic phases[3] with different supramolecular structures. The driving force for this process is described as the "hydrophobic effect", energetically driven both enthalpic and entropically.

As the interaction of the lipids' hydrocarbon chains with water is not favorable, they tend to reduce the interface between water and their hydrocarbon part by self-assembling and thereafter interacting with each other (hydrophobic interaction). The hydrophobic effect leads to hydrophobic hydration, *i.e.*, the creation of a water 'shell' around the hydrocarbon chains, where water has special characteristics, particularly being more organized than in the bulk. This was described as 'the iceberg formation' by Kauzmann[4] in the early days of study of the hydrophobic effect. Together, they lead the lipids to form supramolecular aggregates, taking the chains away from the water environment and keeping the lipid's heads in contact with water, with concomitant displacement of water molecules from the hydrocarbon surface[5, 6]. Therefore, the head group region remains towards the polar environment, *i.e.,* the aqueous solution, where it can also be in contact with other lipid head groups, water and solution components, assuming different structural arrangements. The most common and relevant lipids' self-assembly in biological membranes is the lipid bilayer[5] (see **sections 1.2** and **1.4**.). The hydrophobic effect can be described in terms of the associated thermodynamic parameters,

$$\Delta G = \Delta H - T \Delta S \qquad\qquad (1.1.1)$$

where ΔG is the Gibbs energy change, ΔH is the enthalpy change, T is the absolute temperature and ΔS the entropy change. The lipid's self-assembly is a complex process, as the lipids' assembly should be reflected in a decrease in entropy but the water release from the hydrophobic hydration shell causes an entropy increase. The enthalpy balance is also complex - enthalpic changes are associated with the removal of ordered water from hydrophobic regions (breaking of H-bonds), the formation of new H-bonds in bulk water, interactions between head-and water and/or other lipid head groups, etc. Overall, the hydrophobic effect is affected by temperature, pH, ionic strength [5, 7].

1.1.1. Lipid polymorphism

Membrane lipids self-assemble into a variety of phases and two/ and three-dimensionally ordered structures upon contact with water. The concepts of "lipid diversity" and "lipid polymorphism" should not be confused, as one refers to different lipids in membranes and other refers to different short and long-range forces that lead to a variety of lipid structural arrangements, induced by effects such as concentration, temperature, pH, addition of other molecules, etc[8]. The most important factors are concentration and/or temperature, as their changes can lead to different phases, usually called lyotropic and thermotropic mesomorphism[3, 9, 10].

Examples of lipid arrangements are lamellar, hexagonal, or cubic phases, depending on intrinsic lipid properties (chemical structure), but also on concentration, temperature, water content, pH, and/or ionic strength. The lipid bilayer of biological membranes is a lamellar phase, typically in fluid phase, although some lipids present can, when alone, prefer to adopt a hexagonal phase. Biophysical techniques, such as differential scanning calorimetry (DSC) and X-ray diffraction have been used to characterize lipid phase transitions and their characteristic parameters, leading to the establishment of lipid phase diagrams[9, 11-15].

To understand the morphology of lipids' assembly and why different lamellar and non-lamellar structures are adopted, the geometrical shape of the lipid molecules should be considered, *i.e.*, the balance between the area of the hydrophobic and the hydrophilic parts. The ability of a lipid to form a specific structure can be predicted from the critical packing parameter (C_{pp}), which considers the adopted shape of a lipid (eq. 1.1.2)[16, 17]:

$$C_{pp} = V_0 / a\, l_c \qquad (1.1.2)$$

The packing properties of lipids are set by the effective volume occupied by the hydrocarbon chains (V_0), the area *per* lipid molecule (*a*) and the effective length of the tails (l_c). It is important to stress that although the lipid's headgroup play a dominant role on the determination of the preferential lipid phase, length and the number of unsaturated bonds in lipid's hydrocarbon chains will influence as well[18].

Single-chained lipids with large head group area ($C_{pp} < 1/3$), will have a cone shape, and should form spherical micelles (*e.g.* some lysophospholipids), while single-chained lipids with a small head group present a truncated cone shape ($1/3 < C_{pp} < 1/2$), and cylindrical micelles will be the adopted structure (*e.g.* lysophospholipids with small head groups).

Double-chained lipids with **i)** large head-group areas and fluid chains ($1/2 < C_{pp} < 1$), have a truncated cone shape, and in this case bilayer vesicles with an internal water compartment are usually formed (*e.g.* SPM, PG, PS and PC); **ii)** small head-group ($C_{pp} \sim 1$) of saturated chains, or anionic lipids in high salt concentrations, have cylinder shapes, and tend to adopt a planar bilayer structures, *i.e.* a lamellar structure (*e.g.* PE, PS+Ca^{2+}); finally, **iii)** non-ionic, small head groups of poly-unsaturated chains ($C_{pp} > 1$), appear as an inverted truncated cone and thus tend to form membranes with negative (or concave) membrane curvature, such as inverse hexagonal phase (H_{II}), or cubic phases (*e.g.* unsaturated PE, cardiolipin+Ca^{2+}, cholesterol). The described structures formed are summarized and represented in Fig. 1.1.1[13, 16, 19-21].

Normal Hexagonal (H_I) and inverse hexagonal (H_{II}) lipid phases are nonlamellar lipid phases, where the lipids adopt 'tubular structures' (see Fig. 1.1.1). The hexagonal phase is often referred to as 'oil-in-water', because the hydrophobic tails face inwards, to the interior of the cylinder, whereas in the inverse hexagonal lipid phase, called 'water-in-oil', the hydrophobic tails face outwards[20]. Different cubic phases have been also observed[13], that were early recognized by Luzzati[13] to have a biological role. Recently this connection has been recovered and explored[20, 22, 23]. Cubic phases can be essentially divided in two classes, bicontinuous and micellar phases[13]. The bicontinuous phases consist of a single bilayer folded into a three-dimensional cubic network separating two disjointed water compartments with continuous regions of both polar (hydrophilic head groups) and non-polar (hydrocarbon chains) structures (Ia3d, Pn3m, Im3m). The micellar phases are made of disjointed micelles with different sizes for a more efficient packing on a cubic lattice (*e.g.* Fd3m, Pm3n). Cubic phases represented are the Pn3m and Im3m, the cubic phases more commonly associated to the antimicrobial peptides/membranes interactions[20].

It is important to emphasize that lipid phases are relevant for biological systems only if they are stable in excess water, similar to the aqueous environment in biological

membranes[20]. Changes from lamellar to non-lamellar phases can be driven by accumulated stress, that increases with temperature. Consequently, the repulsive pressure in the hydrocarbon tail region also growths, and thus the bending torque occurs. When a certain critical value of stress is exceeded, a new stress-free phase can occur, placing the lipid in an environment with less torque[16]. Lipids prone to form non-lamellar phases such as PE (present in most bacteria), can induce membrane monolayer curvature stress. These lipids increase the lateral pressure in the center of the bilayer due to their cone-shaped geometry, leading to the formation of non-lamellar structures, inducing thus curvature stress in the bilayer where they are, mixed with other lipids[24, 25].

$$C_{pp} > 1$$

$$C_{pp} = 1$$

$$C_{pp} < 1$$

$$C_{pp} < 1/3$$

$$C_{pp} = V_0/ a\, l_c$$
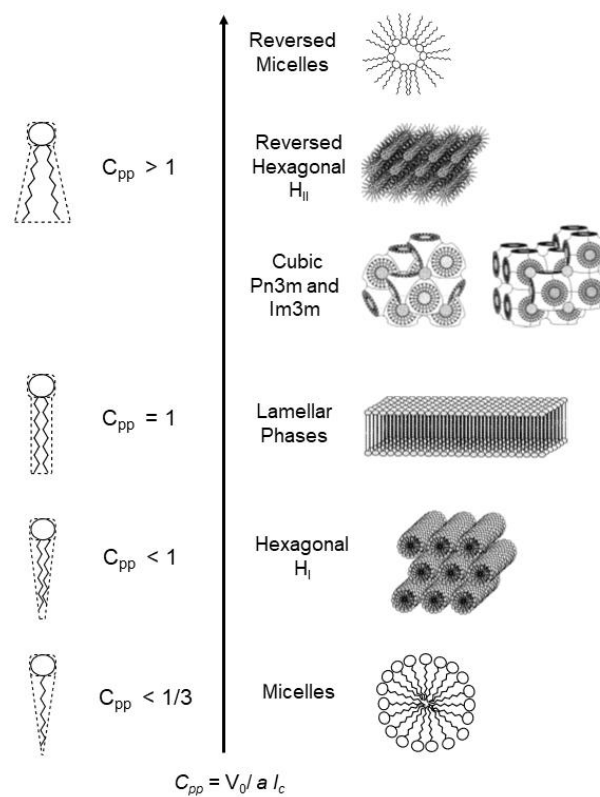
Fig. 1.1.1. Shapes adopted by amphiphilic structures, and their relation to the critical packing parameter.

1.1.2. Thermotropic changes in lipid aggregates

The phospholipids bilayer can undergo thermotropic transitions between different phases [26, 27]: The so called 'main transition' occurs when the phospholipids change from a more ordered phase *i.e.*, with the hydrocarbon chains fairly extended and closely packed, to a more disordered phase, with chain disordering and consequent decrease in space between the headgroups – the transition from the lamellar gel phase (**L$_\beta$**) to the fluid lamellar phase (also known as liquid crystalline phase (**L$_\alpha$**)). The hydrocarbon chains at the lamellar gel phase can also assume a 'tilted' shape, forming the phase **L$_\beta$'** (the prime ' indicates that the chains of the phospholipids are tilted)[28]. In the case of PC with the number of carbons in the chains n≥14, a 'ripple' phase exists (**P$_\beta$'**), and a transition between **L$_\beta$'** and **P$_\beta$'** can be easily detected *e.g.* by DSC, and is called the pre-transition.
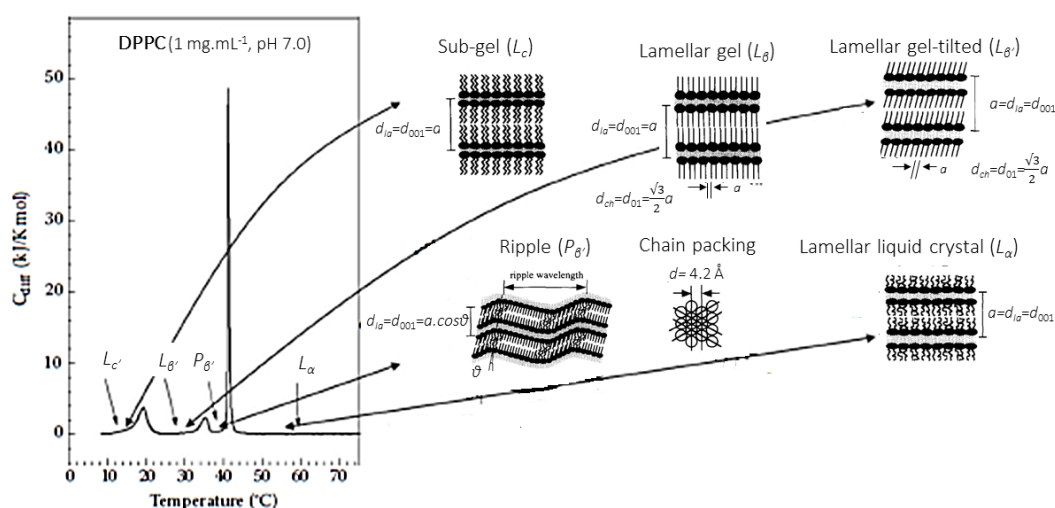
Fig. 1.1.2. Calorimetric pattern for changes in DPPC multilamellar vesicles in excess water as a function of temperature, obtained by Differential Scanning Calorimetry. The respective structures for the different lamellar phases adopted along the temperature scan are represented on the right art of the figure. Adapted from[3].

The most studied transition is indeed the main transition, from gel-to-fluid phase. It occurs at specific temperatures, characteristic of each lipid, called phase transition temperature (T_m), and is accompanied by a large enthalpy change. The T_m increases with hydrocarbon length increase, due to the stronger van der Waals interactions and consequent increased packing. The introduction of a *cis* double bond into the acyl group creates a "bended" look in the chain, lowering the T_m [29] when compared to the corresponding saturated lipid. Bellow T_m we have an ordered lamellar gel phase (**L$_\beta$**, **L$_\beta$'** or **P$_\beta$'**- phase), where the hydrocarbon chains are well oriented and

quite rigid, with any chains lateral diffusion of phospholipids in the membrane very reduced, while above the T_m an increase in the hydrocarbon chains conformational freedom[30] takes place, the headgroup hydration is also increased, and we have a disordered liquid crystalline lamellar phase, **L$_\alpha$**. In this transition the hydrocarbon chains goes from *trans* to *gauche* conformation[31]. The main transition is accompanied by significant enthalpy changes, due to the amount of energy required to decrease van der Waals interactions, volume of expansion of the hydrocarbon chain, and also due to the increased hydrophobic exposure at the polar–non polar interface, increasing the bilayer area[26].

The main transition (**L$_\beta$**, **L$_\beta$'** or **P$_\beta$'** $\rightarrow$ **L$_\alpha$**) is reversible and highly cooperative - when one molecule enters in a motional energy state, the nearby molecules finds it easier to enter this state as well[32].

Some phospholipids can exhibit multiple phase transitions, like phosphatidylcholines that at low temperatures they can show a sub-gel lamellar crystalline phase (**L$_c$**). The phospholipid doesn't show any axial rotation, nor significant lateral diffusion[33]. Additionally, other phases can be observed, some already referred to above, such as **i**) tilted (**L$_\beta$'**), where the extended hydrocarbon chains are strongly tilted, but also **ii**) interdigitated (**L$_\beta$I**) where the hydrocarbon chains from one leaflet of the bilayer may overlap hydrocarbon chains from the opposing leaflet of the same bilayer, and **iii**) rippled gel (**P$_\beta$'**) that can be due to the rotation of the polar head group or the cooperative movement of the hydrocarbon chains prior to the melting[12].

With the increase in temperature some lipids present a transition from lamellar to non-lamellar phase. Lamellar-to-hexagonal II (**L$_\alpha$** $\rightarrow$ **H$_{II}$**) phase transition is slower and much less energetic than the gel lamellar-to- fluid lamellar phase, but still possible to determine by DSC. The reversibility of the opposed transition, (**H$_{II}$** $\rightarrow$ **L$_\alpha$**) is often not observed on the timescale of seconds or minutes, since its kinetics is much slower than the **L$_\alpha$** $\rightarrow$ **H$_{II}$**, often requiring long incubation times (hours to days) at temperatures below the T_m. This is reflected in a strong hysteresis in the measurements of this transition[26]. This hysteresis also occurs in some other phase transitions (like fluid lamellar to cubic), that may not be easily observed on heating, and are usually better seen during the cooling sequence. Some of these phases are represented in Fig. 1.1.3.
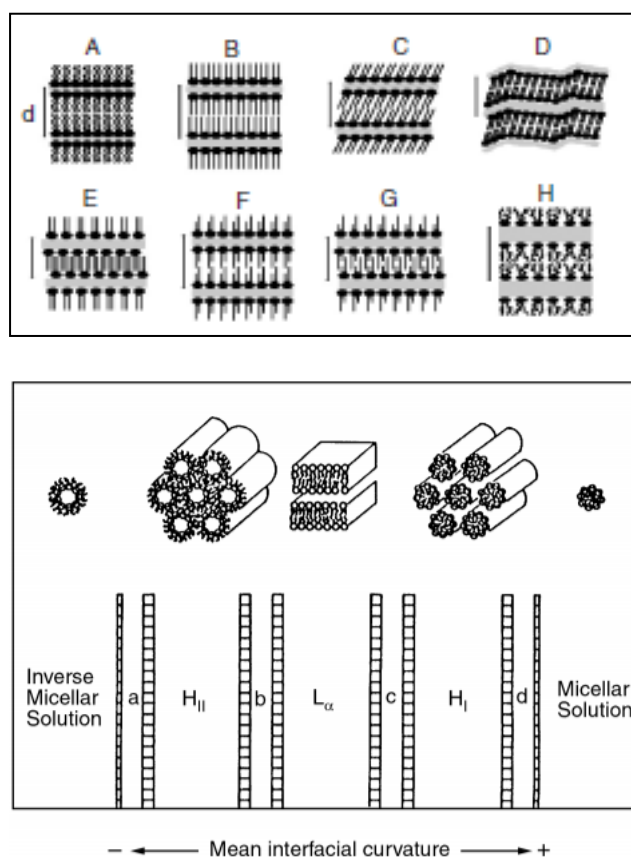
Fig. 1.1.3. Top panel: Examples of different lamellar lipid phases: **(A)** subgel lamellar crystalline, L_c; **(B)** untilted gel chains, $L_β$; **(C)** tilted gel chains, $L_β$' ; **(D)** rippled gel, $P_β$'; **(E)** fully interdigitated gel, $L_β I$; **(F)** partially interdigitated gel; **(G)** mixed interdigitated gel; **(H)** liquid crystalline, $L_α$. Adapted from[26]. **Bottom panel:** Sequence of the principal lyotropic liquid-crystalline phases in function of the mean curvature. The *a*, *b*, *c* and *d* are more complex intermediate phases, being associated with cubic phases, not described here in detail. Adapted from[34].

Bilayer cubic phases (Q^B_{II}) appear usually between the $L_α$ and H_{II} transitions, and are less common in membrane lipid dispersions, being more often observed for short-chain PEs and monoglycosyldiacylglycerols[13, 35, 36]. Q^B_{II} can appear if the incubation is long enough and sometimes can be induced by cooling of the H_{II} phase, or by extensive temperature cycling through the $L_α ↔ H_{II}$ transition[37, 38]. Inverted micellar cubic phases (Q^M_{II}), where the interfacial mean curvature is negative (curvature towards the water), have been observed mainly in mixtures of double-chain polar lipids with fatty acids or diacylglycerols[39].

It is important to mention that when we have phospholipids mixtures differences in phase transition are to be expected, both in T_m and $ΔH$, when compared to the isolated pure phospholipids, due to the structural differences on hydrocarbon chains and/or headgroups. The mixing properties of the PE and PG lipids can be taken as an example. At physiological pH, the zwitterionic PE can act both as donor (NH_3^+) and as acceptor (PO_2^-) for intermolecular hydrogen bonds. The anionic PG acts as hydrogen

bond acceptor (PO_2^-). Considering the differences in the occupied volume by both lipids, we see that the PG headgroup occupies much larger volume than the PE headgroup, and thus PEs are much less hydrated than the PGs. As referred to above, PG has roughly cylindrical shape, whereas PE can be described as a truncated cone. They are therefore not expected to mix ideally, due to the different geometrical characteristics. Nevertheless, the introduction of PG in a PE bilayer facilitates the hydration of the PE headgroups by disrupting the PE-PE contact and forming at physiological pH hydrogen-bonds between the PE and PG headgroups[40]. The mismatch will change the T_m, and is dependent on PE:PG ratio at physiological pH, as shown by Garidel *et al*[40] in DSC calorimetric transition profiles, showing further that the behavior depends on pH.

1.2. Biological membranes' structure

Biological membranes are complex supramolecular systems that play an important role in the structure and function of the cells, prokaryotic and eukaryotic. They have a structural function, establishing a barrier between the internal and the external environment, regulating transport and signaling across that barrier, are also involved in energy production, cell-cell interactions and create internal compartments where certain cellular activities are carried out. Although biological membranes can vary widely, they all have a common feature: they are built of lipid bilayers.[11, 41] Indeed in addition to the various types of lipids, membrane proteins, sugars and other components are also present. The membrane protein's role is to help in structural integrity, organization and flow of material through membranes, while sugars are only at the outer bilayer , attached by covalent bonds to some lipids and proteins, where they can act as markers[42].

The lipid bilayer is the universal basis for cell-membrane structure, being responsible for the separation between the interior of the cells and the outer environment[43]. The "fluid mosaic membrane model" of biological membranes was suggested in 1972 by Singer and Nicholson and has become for many years the standard conceptualization of the membrane's architecture. Its main feature is the prediction of lateral and rotational freedom, together with a random distribution of the different membrane components. This model proposes the existence of membrane fluidity, and the membrane function as "solvent" for proteins, allowing lateral mobility of lipids. Proteins present in a membrane are named as intrinsic or transmembrane and

peripheral membrane proteins. The term "mosaic" refers to the scatter of proteins across or on the membrane's surface (fig. 1.2.1.A)[44-46]. This model contributed immensely to the representation of the cell membranes, and later an extension was introduced by Simons and Ikonen[47]. They proposed that many biological membranes possess lipid/protein domains, the so-called lipid rafts (Fig.1.2.1.B). The rafts are enriched in cholesterol, saturated sphingolipids and lipid-anchored proteins, which makes them less fluid (they are described as being in a liquid ordered state, l_o) and thicker than the bulk membrane. These rafts have various functions, such as sorting molecules for transport, signaling, gathering proteins and thus facilitating their interactions[47, 48]. The main contributions to the characterization of lipid rafts were obtained by fluorescence quenching and fluorescence resonance energy transfer, as they have shown the formation of nanoscale liquid-ordered domains[49, 50].
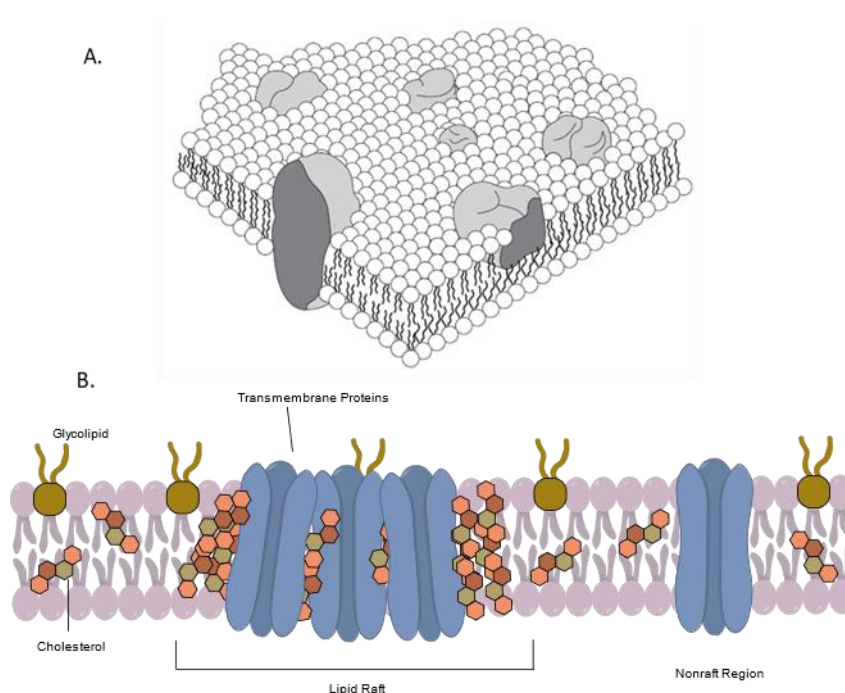
Fig. 1.2.1. A. "Fluid mosaic membrane model proposed by Singer and Nicolson in 1972. This mosaic model is the first comprehensive model describing biological membranes. This basic structure of the membrane (lipid bilayer) has fatty acyl chains from each leaflet forming a nonpolar interior. Intrinsic proteins are integral to the bilayer, while extrinsic proteins are on its periphery. Adapted from[44]. **B.** Representation of lipid rafts build from cholesterol surrounding transmembrane proteins. The lipid rafts are commonly present in the cell membrane, although they are also present in other parts such as the Golgi apparatus and lysosomes. The lipid rafts can be responsible by decreased membrane fluidity and membrane protein trafficking[51].

1.3. Biological membranes' lipids

A large diversity of lipids is found in biological membranes, differing in the structure of the head group and in the length and/or saturation of their acyl chains. We can say that glycerophospholipids, sphingolipids, and sterols are the three major kinds of lipids found in membranes[42] (Fig. 1.3.1).

Glycerophospholipids are the primary building blocks of the biological membranes. They are composed of a polar head group and two hydrocarbon chains (fatty acids) that have an ester link to the *sn*-1[1] and *sn*-2 positions of a glycerol moiety, and a phosphate group in the *sn*-3 position[46, 52, 53]. It should be noted that within the glycerophospholipids the chain length and degree of saturation of the fatty acyl chains vary widely, and that determines the order and thickness of biological membranes.
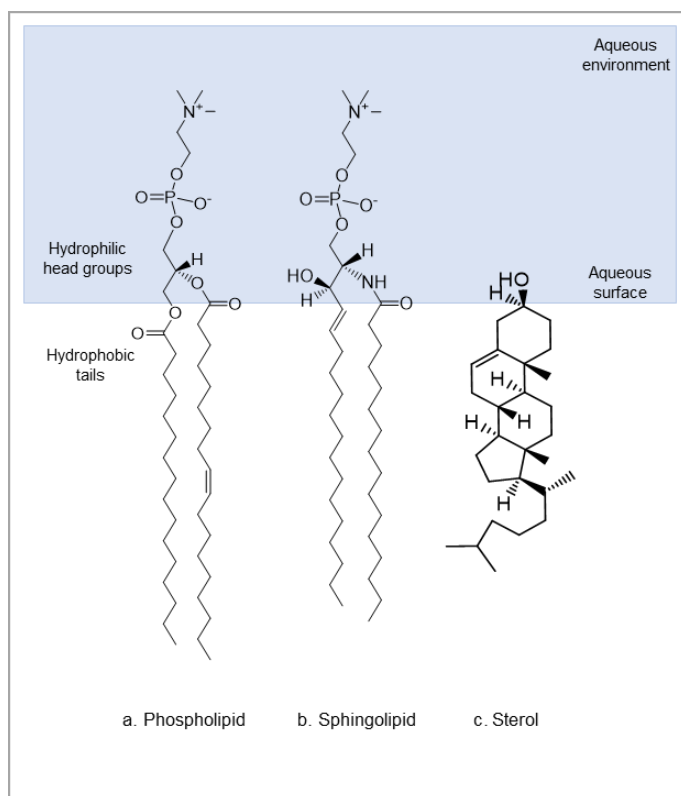
Fig. 1.3. 1. a. Representation of the three major types of membrane lipids. **a.** Phospholipid: the lipid represented here is POPC (1-palmitoyl-2-oleoyl-glycero-3-phosphocholine) that it is found in biological membranes; **b.** Sphingolipid: the lipid represented is sphingomyelin, particularly found at high concentrations in the membranes of nerve cells (in the myelin sheaths) and red blood cells; **c.** sterol: the molecule represented is cholesterol. The top part of the image is correspondent to the hydrophilic part of the lipids, in aqueous environment, while the down part is their hydrophobic part.

---

[1] *sn*, is the stereospecific numbering system prefix, used before the name of a glyceride in a Fischer projection.

Phosphatidic acid (PA) is a low abundance and the simplest phospholipid present in the membranes. PA has negative charge at physiological pH and contributes to the membrane's physical properties. Nevertheless, PA is the precursor for other phospholipids of different net charges (anionic or zwitterionic), obtained due to the esterification of the phosphate to an alcohol, thus playing an important task.

Phosphatidylcholine (PC) phospholipids have a choline molecule attached to the phosphate group. PC is the most abundant lipid found in animal biological membranes and therefore the most important membrane structural lipid. In addition, PC is a zwitterionic molecule, that can be depicted as having a cylindrical shape, because the head group has about the same width as the tails (see Fig. 1.3.2).

Phosphatidylethanolamine (PE) is a zwitterionic phospholipid at physiological pH, with a major presence in bacterial membranes, particularly Gram-negative, and the second most predominant phospholipid in humans[54, 55] due to the ability of humans to convert PE to PC, while bacteria cannot. PE possess an ethanolamine instead of a choline group, with a phosphate (negative charge) and a free amine (positive charge) at neutral pH. PE phospholipids are considered as non bilayer forming due to their truncated cone shape (see Fig. 1.3.2) [24].

Phosphatidylglycerol (PG) is an anionic glycerol-based phospholipid (charge -1) at physiological pH, widely present in many bacterial membranes, whereas in mammalian membranes is mostly present in very low amounts (1-2 mol%) [56, 57].

Phosphatidylserine (PS) is a serine-based phospholipid, also anionic (charge -1) at physiological pH, essential in all human cells, although far more abundant in the brain than in other organs. Phosphatidylinositol (PI), another anionic (charge -1) phospholipid at physiological pH possesses the inositol group and is present in all tissues and cell types, especially in brain cell. PIs are considered to have the greatest contribution to the negative charge surface density of the lipid bilayer[58].

The described different net charges of these glycerophospholipids have a critical role in their interaction with proteins. Further to this, it should be referred thar PS and PE contain an amine group that can establish hydrogen bonds, with the solvent and with other phospholipids.

All these phospholipids are obtained through esterification of the phosphate groups with different alcohols.
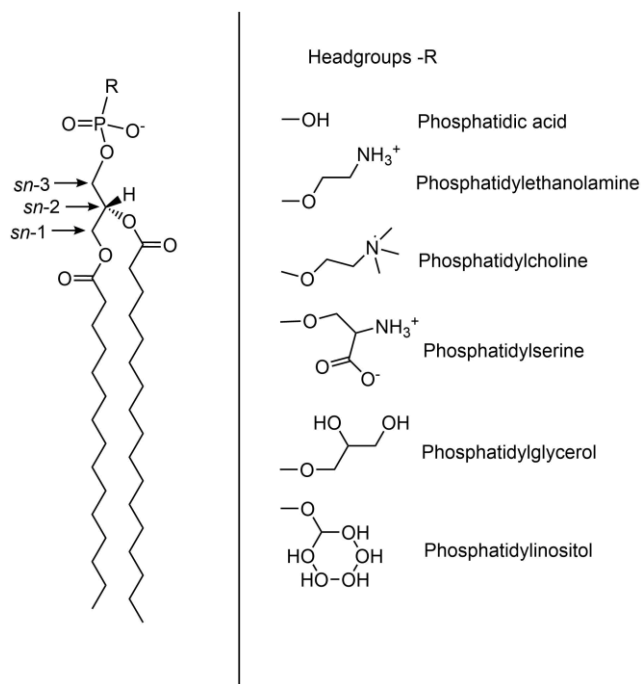
Fig. 1.3.2. General representation of a phospholipid. Saturated, in this case, or unsaturated fatty acids are linked to the glycerol backbone at the s*n*-1 and s*n*-2 positions. The phosphate headgroup is linked at the s*n*-3 position and different variations of headgroups obtained by replacing the -R by the structures represented on the right panel.

Sphingolipids are one of the components found in biological membranes. Unlike phospholipids sphingolipids do not contain glycerol, they are composed of a sphingoid base with a fatty acid attached through an amide bond. Ceramide works as precursor to create more complexed sphingolipids, such as sphingomyelin (SPM), the most prevalent found in mammalian plasma membrane and in neuronal membranes. Sphingolipids tend to associate with each other as well as with cholesterol and certain categories of proteins[59].

Sterols also have an amphiphilic structure, consisting of a planar, compact, and rigid structure of three rings with six carbons each and one ring with five carbons. These rings are fused, thus not allowing rotations around the C-C bonds[60]. Cholesterol is the major sterol present in the eukaryotic cell membranes, localizing preferentially on the plasma membrane[61], while ergosterol plays a key role in yeast and fungi. Some bacteria have been identified with small amounts of sterols in their membranes[62], while Algae produce a wide variety of sterols[63, 64]. Cholesterol has been very much studied, due to is importance in lipid rafts. It has been described that it increases the bilayer thickness and the packing of acyl chains, thus significantly decreasing the lateral diffusion of lipids in membranes[65].

The organization and dynamics of the membranes differ among the different organisms, exhibiting different characteristics as regarding composition, structure, and function. Membrane asymmetry is a general property of biological membranes, as result of differences in the lipid composition and/or physical properties between the leaflets[66]. It is known that the outer leaflet of the plasma membrane of eukaryotic cells is richer in PC, SPM and glycosphingolipids, whereas the cytoplasmatic leaflet shows a higher content in PE, PI and PS. A good example of lipid asymmetry is the erythrocyte membrane: globally it contains phosphatidylcholine (~29%), sphingomyelin (~25%), phosphatidylserine (~15%), phosphatidylethanolamine (~27%), and others (~5%), with variable distribution between the leaflets[67] - the outer leaflet is enriched in sphingomyelin and PC, while the inner leaflet contains most of the PE[46] (Fig. 1.3.3).

Another important difference, especially as regarding the aims of present work, is that in prokaryotic cells the acidic lipids are exposed at the extracellular surface, at odds with eukaryotic cells that have no significant negative charge at their surface.
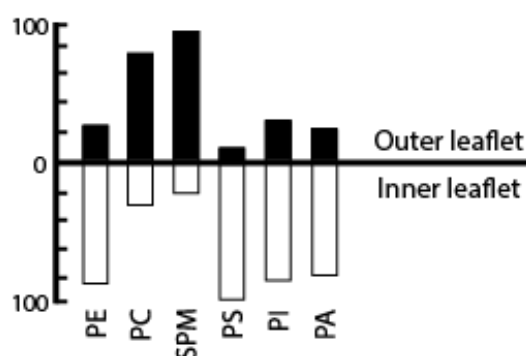
Fig. 1.3.3. Lipid asymmetric distribution in erythrocyte membranes, that aid as an archetype of mammalian cell membranes. The bars represent the content in the inner and outer leaflets of each representative lipid expressed in mol% [46, 67].

Bacterial membranes contain large amounts of phosphatidylethanolamine, phosphatidylglycerol, and other derivatives such or cardiolipin (complex lipid which consists of two PG units attached to a PA molecule)[57, 68]. However, the specific composition depends on the bacteria, as detailed next.

1.4. Bacterial Membranes

The details of the architecture of bacterial membranes are of major importance for the goals of this thesis. Bacteria are prokaryotic organisms with simpler design and usually smaller than the eukaryotic cells. Additionally, the broad metabolic capabilities of the

bacteria allow them to grow and divide very rapidly and to inhabit and flourish in almost any environment[66, 69, 70]. According to the cell wall composition, bacteria can be divided into two main classes: Gram-positive and Gram-negative.
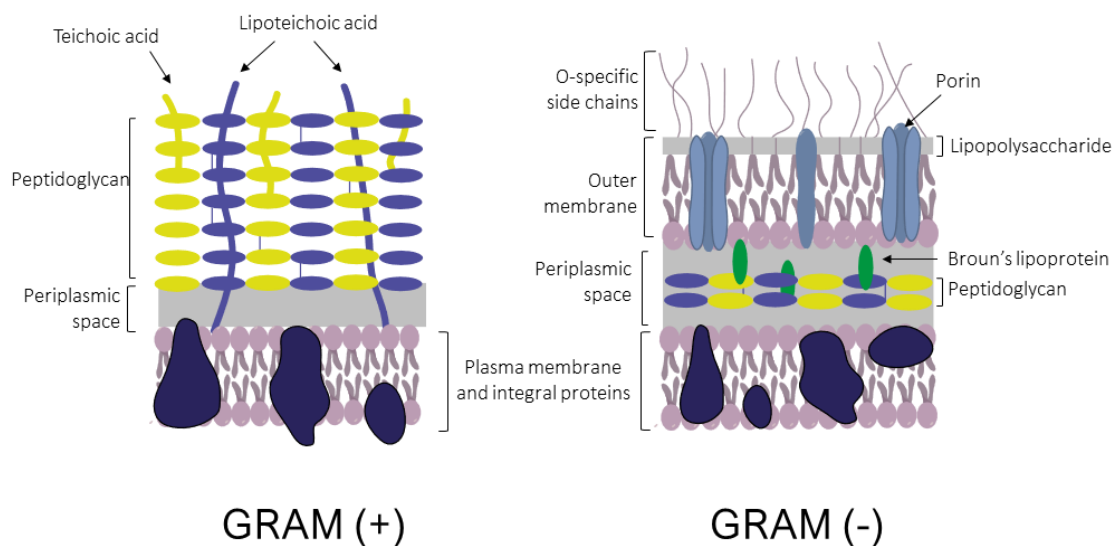
Fig. 1.4.1. Representation of the bacterial cell membranes' molecular organization of Gram-negative and Gram-positive bacteria. Gram-positive bacteria have cytoplasmic membrane covered by a peptidoglycan layer, while Gram-negative bacteria have a complex outer membrane with an asymmetric distribution phospholipids and lipopolysaccharides[71]. Adapted from[72].

Gram-positive bacteria are built of a thick layer of peptidoglycan with intercalated teichoic and lipoteichoic acids, external to a lipid bilayer decorated with proteins and carbohydrates. Cytoplasmic membranes of Gram-positive bacteria are rich in PG content, although other phospholipids and phospholipids-derivates are also present (Table 1.1)[73].

Gram-negative bacteria are structurally more complex than Gram-positive, since they have a plasma membrane and an outer membrane, with a region between these layers called the periplasmic space (Fig. 1.4.1). The outer layer, which is highly asymmetric, is composed primarily by lipopolysaccharides (LPS). The inner layer of the outer membrane has a large PE content, and also some PG, although in smaller percentage than in Gram-positive bacteria (Table 1.1)[66, 73-75].

Overall, the high negative charge content in bacteria exterior will be shown to be crucial for antimicrobial peptides' preferential interaction (Fig. 1.4.1) (see **Chapter 2**, **section 2.3**)[74].

In some cases, some lateral heterogeneity or formation of lipid domains has been reported[76, 77]. An example of this heterogeneity was observed in *Escherichia coli*

and *Bacillus subtilis* were cardiolipin domains were observed[78, 79]. Overall, the percentages presented in Table 1.1 are relatively constant under a broad spectrum of growth conditions, although exceptions may occur[80, 81].

Table 1. 1. Phospholipid composition in percentage of total phospholipid of some species of Gram-negative and Gram-positive bacteria[82, 83].

Bacteria species	%PG	%CL	%PE
GRAM-NEGATIVE			
ESCHERICHIA COLI	15	5	85
KLEBSIELLA PNEUMONIAE	5	6	82
PSEUDOMONAS AERUGINOSA	21	11	60
GRAM-POSITIVE			
STAPHYLOCOCCUS AUREUS	57	19	0
BACILLUS SUBTILIS	40	25	20
STAPHYLOCOCCUS EPIDERMIDIS	90	1	0

1.5. Lipid model membranes

Biological membranes are complex systems with hundreds of different lipids, proteins, and other components. The complexity and dynamics of biological membranes gets even larger when one wants to study the interactions of peptides, proteins, or drugs with these membranes. To overcome this situation, a reductionist approach has been developed, where only a few representative components of biological membranes, their main constituents, the lipids, are kept. Membrane lipid models mimic cell membranes, using a variety of lipids, and are used to study several phenomena and interactions [84]. These systems have being considered very suitable tools to understand individual molecular interactions in biophysical studies[66, 85-91], keeping reduced and controlled a number of factors that may affect interpretations of the studied phenomena, such as pH, ionic strength, molecular packing, lipid composition, temperature, among others[84, 92].

The most common of such biological membrane's models are liposomes or lipid vesicles, as the ones used in this thesis. They usually assemble in a spherical shape with an internal aqueous compartment, with a variable number of concentric bilayers, and are surrounded by the aqueous medium, forming a suspension. Liposomes can be

prepared from the dispersion of one single lipid or the mixture of different lipids, chose to resemble to the composition of membranes *in vivo* that one wishes to study[84].

Liposomes can be classified as unilamellar or multilamellar, where the second assembles in variable number of concentric bilayers, being called multilamellar lipid vesicles (**MLVs**) (>500 nm)[93]. MLVs are the simplest vesicles to prepare - briefly, initially the pure phospholipids are dissolved in an organic solvent, chloroform or a mixture of chloroform/methanol, to guarantee dissolution and the formation of a homogenous solution. The organic solvent is then evaporated (either with heat or by blowing the solution with a gas stream), and a phospholipid film is formed. Thereafter the film is dried overnight in vacuum, and after hydrated with an aqueous buffer solution (above the lipid system T_m), the lipid film swells, and by use of vortex cycles it leaves the walls where the film was formed and self-assembles in aqueous solution forming a suspension of MLVs. If only one phospholipid is used, direct hydration of the powder with buffer above T_m, followed by vigorous vortex is sometimes enough to form a MLVs suspension.

Nevertheless, often they are not the best system to work with. Disadvantages like high polydispersity of the suspensions, particle's size that disperse the light too much for commonly used biophysical techniques (fluorescence, light scattering, UV), easy sedimentation, reducing the amount of membrane available for *e.g.* partition, difficulty in determining the correct surface concentration in the different layers, make these systems less appropriate for many techniques. For most precise uses, liposomes containing only one bilayer and controlled sizes are the best option. They can be small unilamellar vesicles, **SUVs** (25 - 50 nm in diameter), and large unilamellar vesicles **LUVs**, (~100 nm of diameter). SUVs are formed by the disruption of MLVs suspension by strong sonication, preferably by probe (titanium) tip sonicators. SUVs have the disadvantage of being rather unstable, due to excessive curvature, tending to fuse into higher structures. LUVs are prepared by the extrusion method. The MLVs' suspension goes thought freeze-thaw cycles (freezing in liquid nitrogen and heating in the water bath) above T_m to improve the homogeneity of the size distribution. Thereafter, the lipid suspension is forced thought two polycarbonate filters, of 100 nm pore size, to provide particles with a size similar the filter's pores' size. The extrusion can be performed in a bench stainless steel extruder, under inert gas pressure, or with a manually powered extruder syringes. The detailed protocol used in this work is describe in **part II** of **chapter 5**.

Giant unilamellar vesicles, **GUVs** (1-100 μm) are simple model membrane systems of cell-size. The first preparation method reported was rehydration of dried

lipids film assisted by an AC electric field[94], in a process known as electroformation. Lastly, vesicles of two to five concentric lamellae are called oligolamellar vesicles (**OLVs**) and can be spontaneously formed from hydration of the film in charged lipids, due to the repulsive forces between bilayers.
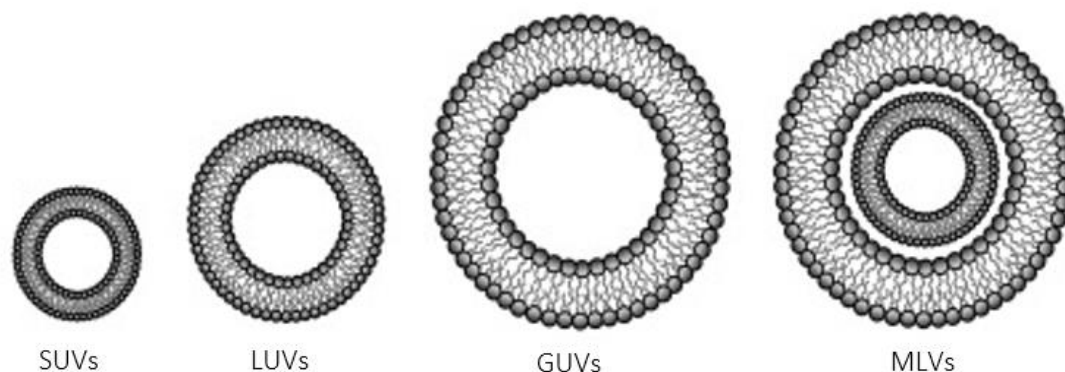
Fig. 1.5.1. Schematic representation of the main lipid systems according to their size and lamellar levels, vesicles. From left to right: SUVs (Small Unilamellar Vesicles), LUVs (Large Unilamellar Vesicles), GUVs (Giant Unilamellar Vesicles) and MLVs (Multilamellar Vesicles). Adapted from[95].

LUVs are the preferred model membrane used in this thesis as described in **publications II**, **III**, **IV** and **V** of **part III**, whereas for SAXS MLVs and OLVs needed to be used, to have a system with 3D arrangement (**manuscript VI)**.

Chapter 2. Antimicrobial Peptides

The rapid emergence and spread of drug-resistant pathogens due to the overuse and misuse of drugs such as antivirals, antibiotics and antiparasitic, has become one of the world's most demanding health concerns. Bacterial resistance has been attributed to the long-term inappropriate use of antibiotics, as bacteria can develop resistance through multiple biochemical pathways[96, 97]. The treatment of super-infections is increasingly prone to failure, and already in 2014 World Health Organization (WHO) reported that antibiotic resistance was spreading rapidly throughout the world[98]. Within Europe, Portugal has one of the highest incidences of MRSA (Methicillin-resistant Staphylococcus aureus), as well as vancomycin-resistant Enterococcus faecium and multi-drug resistant Acinetobacter[99]. The cost of new drug development, the challenging regulatory requirements and the consequent slow development of new strategies by the pharmaceutical industry are leading to an aggravation of this health crisis at worldwide level[86, 100, 101]. This problem can be clearly seen looking at the numbers reported in 2019 by the World Health Organization (WHO) – only 6 out of 32 antibiotics were identified with a classification of 'innovative' against priority pathogens during their clinical development[102].

Due to current world COVID-19 pandemic situation, a disease caused by a new strain of coronavirus, the bacterial resistance may get even higher. It has been reported by the WHO Europe, in a study conducted in 9 European countries, that despite the fact that antibiotics do not treat or prevent viral infections like COVID-19, it was estimated that 79–96% of Europeans that were not infected by Covid-19 took antibiotics inappropriately, to try to prevent the infection by the virus[103]. Further, it was also reported that 72% of patients with COVID-19 received antibiotic therapy, despite only 7% had a bacterial co-infection[104].

This shows that a post-antibiotic era with new antimicrobial strategies becomes mandatory. In this context, antimicrobial peptides (AMP) are seen as a new avenue, providing as potential novel paradigm to fight pathogens, due to their completely different mode of action.

2.1. Properties of Antimicrobial Peptides

Antimicrobial peptides (AMPs), also known as host defense peptides, are a large group of molecules produced by several organisms, such bacteria, fungi, animals, and even plants. They are part of a nonspecific innate immune system, responsible for the main

defense mechanisms against foreign attacks[22, 86, 105]. To date, hundreds of AMPs have been identified and published in databases[106-109] reflecting their recognized importance in fighting fungi, bacteria, viruses and even cancer cells[110-112]. Additionally, it has also been reported that they can be active in immune and inflammatory responses[113, 114]. AMPs show a wide diversity of structures[115], rapid cell-killing and low levels of induced resistance[116]. Nevertheless, most applications already in the market are topic[117, 118], as there are difficulties in their systemic use, because AMPs are easily degraded by proteases[117]. This issue has been addressed recently by the development of AMPs where some *L*-amino acids are replaced by their *D*-analogs. This approach reduces protease degradation against enzymatic hydrolysis, since only a few enzymes are known to digest amide bonds involving *D*-configuration[119, 120]. The substitution of one or more *L*-amino acids might help as well in decreasing cytotoxicity, while keeping antimicrobial activity[121-124].

Additionally, the cost of development and manufacturing and the seemingly lower effectiveness as compared to conventional antibiotics has imposed a slow pace in this drug direction. Further, the toxicity of AMPs still needs to be better addressed. One problem that is long known is that they can induce endotoxin shock, due to the release of high number of lipopolysaccharides (LPS) upon Gram negative bacteria's outer membrane destruction[125]. Strategies to surpass stability issues and to increase the half-life of AMPs in systemic use are being used, such as the introduction of *D*-amino acids, and peptide cyclization (see **chapter 3** of this same part, and **publication/manuscript I – VI** of the **Part III**) [126].

AMPs have several properties that are common to most of them, such as net charge, hydrophobicity and amphipathicity. AMPs are built of short amino acid sequences with less than 50 amino acids, display a net positive charge ranging from +2 to +9 at physiological pH, mainly due to the lysine and/or arginine residues present in their sequence. Some studies report a correlation between net charge and antimicrobial activity of AMPs, showing that in some cases increasing the net charge leads to an activity increase. Nevertheless, in some other cases the loss of activity was reported as charge increase, possibly as a consequence of too strong interactions between the peptides and the phospholipid head group, preventing peptide's translocation across the membrane[127-132]. Typically, 50% of the residues in the AMPs sequence are hydrophobic (leucine, valine, alanine, methionine, isoleucine, tyrosine, phenylalanine, and tryptophan residues), a feature required for membrane permeabilization, and also a factor that controls the extension of partition of the AMPs into the lipid bilayer. It should be noted that excessive hydrophobicity decreases aqueous solubility, a severe drawback, and might end in toxicity and increased

hemolysis[133], thus with loss of antimicrobial selectivity[134-136]. Amphipathicity, a very important feature of AMPs, corresponds to the segregation of hydrophobic and polar residues between the two opposite faces of a secondary structure of the antimicrobial peptides, commonly an α-helix, leading to a distribution well suited for membrane binding (Fig. 2.1.1). Some studies have shown that with AMPs' increase in charge and amphipathicity the hemolytic activity decreased while preserving the antimicrobial activity[137-139].
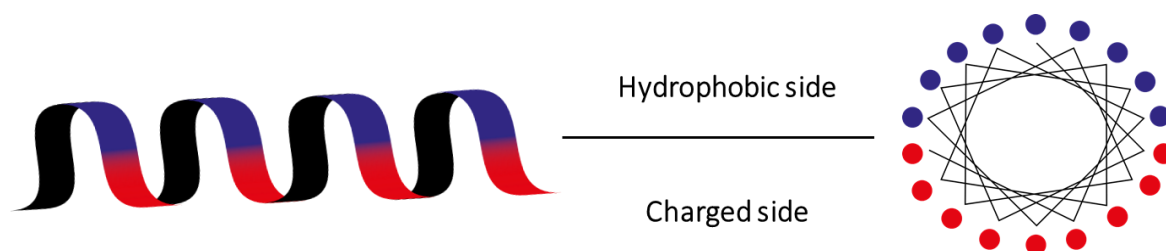
Fig. 2.1.1. Schematic representations of the amphipathic character in α-helix AMPs. The purple side is the hydrophobic side and the red the charged side.

The relationship between amphipathicity, hydrophobicity and net charge is rather complex, and so far has been difficult to establish robust structure–activity relationship (SAR) between the chemical structure the molecules and their biological activity. The variety of structural characteristics, such as length, sequence, structure, activity and source result in a diversity of AMPs characteristics and consequently a diversity of mechanism of action for this class of compounds as described below in **section 2.3** of this chapter.

2.2. Structural classification of AMPs

Due to their diversity, the classification of AMPs is not a trivial task. The most common classification is based on their secondary structure: α-helix, β-sheet, extended, and loop, being the α-helix and the β-sheet the most common structures.

α-helical AMPs (Fig. 2.2.1.a) are the most studied group of AMPs, with a rod-like structure with the side chains extending outwards in a helical array. The more studied natural AMPs are magainins from frogs, cecropins from cecropia moth, cathelicidins present in mammals and melittin from the bee venom toxin[22, 140-144]. **β-sheet** structures (Fig. 2.2.1.b) consist of two or more fully extended β-strands, linked by hydrogen bonds. These strands can either form antiparallel β-sheet structures (run in opposite directions) or parallel β-sheet structures (run in the same direction). In

antiparallel β-sheet structure, the CO and NH groups of each amino acid forms hydrogen bonds with the NH and CO groups on the adjacent strand of the amino acid located in alignment. For parallel β-sheet structure, for each amino acid, the NH group is hydrogen bonded to the CO group of the amino acid on the adjacent strand, while the CO group is bonded by hydrogen bonds to the NH group on the amino acid two residues farther away along the chain[145]. Some peptides are also constrained either by disulfide bonds between Cys residues (*e.g.* protegrins, from porcine leukocytes, and lactoferricin derived from milk protein), or by cyclization of the peptide backbone (*e.g.* gramicidin S a derivative of gramicidin, extracted from *Brevibacillus brevis,* a soil bacteria, and polymyxin B isolated from *Bacillus polymyxa*)[22]. **Extended** AMPs (Fig. 2.2.1.c), like indolicidin from blood cells of cows, are often composed by a high number of certain amino acids, such as tryptophan, arginine or proline residues. They do not fold into regular secondary structures and many of them are not membrane active[146].

Upon association of the AMPs with membranes, AMPs typically change their conformation[147, 148]. These conformational changes will be described in the next section.
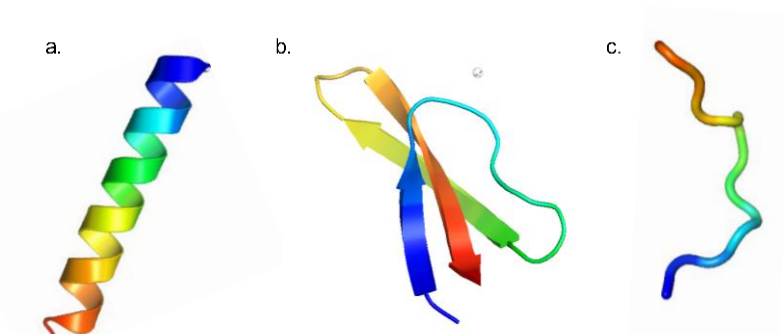
Fig. 2.2.1. Schematic representation of the antimicrobial peptides' structures. **a)** α-helix of the magainin; **b)** β-sheet of the human defensin 5; **c)** extended coil of indolicidin. The figure was generated by using Pymol software[149].

2.3. Mechanisms of action

The detailed mode of action of AMPs when in contact with membranes remains a subject of debate. It is known that their mechanism of action depends on a diversity of parameters such as environmental conditions, membrane lipids, peptide nature/characteristics and lipid-to-peptide molar ratio, among others[126]. Gathering knowledge of how AMPs act against infective agents must facilitate new development

in AMPs design, towards peptides with enhanced or optimized mechanisms, together with a lower propensity to resistance development.

AMPs mechanisms, however different, follow three basic steps: **i)** initial electrostatic attraction of the peptide to the pathogen membrane, due to the cationic character of AMPs and the anionic character of the outer bacterial membranes; **ii)** changes in conformational structure of the AMP at the membrane surface required for their successful interaction and insertion into the membrane (electrostatic and hydrophobic interactions); **iii)** Peptide partition to the lipid membrane (with various architectures and degrees of insertion).

2.3.1. Adsorption and binding to the membrane

The association of peptides with membranes should be treated as a partition between two immiscible fluid phases, the aqueous media and the lipid membrane [150].

Wimley and White[150, 151] described a four-step process and the corresponding thermodynamic parameters, comprising interfacial partitioning, folding, insertion and association (Fig. 2.3.1) to describe the folding and bilayer insertion of small hydrophobic peptides. For each step, the standard Gibbs energy change (ΔG°) can be determined or estimated.
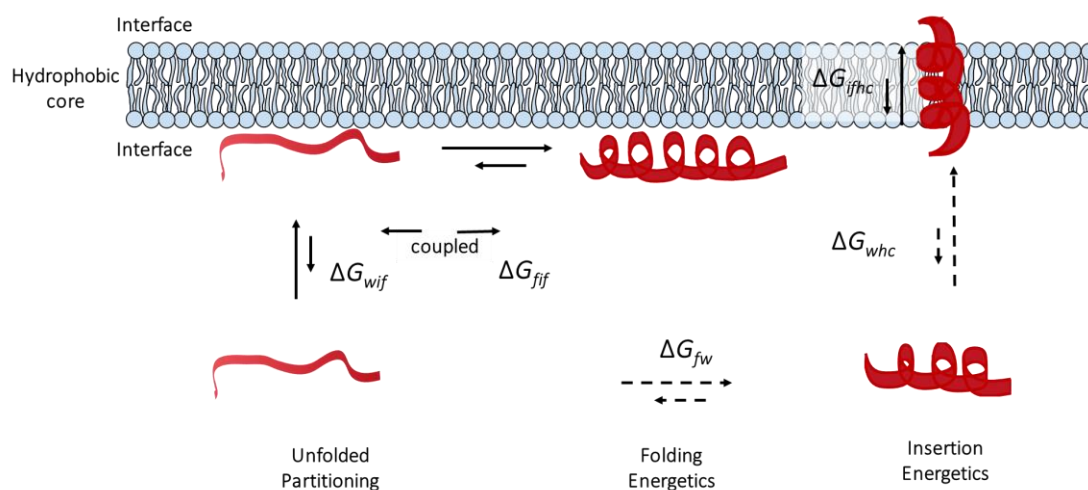
Fig. 2.3.1. Representation of the four-step thermodynamic cycle for describing the energetics of the partitioning, folding, insertion, and association of peptides with lipid bilayers. The process can follow an interfacial path two (solid arrows), a water path (dotted arrows), or a combination of the two. ΔG indicates Gibbs energy change and the subscript indicates a specific step in the cycle: ΔG_{wif} Gibbs energy change of the unfolded chain from water to interface; ΔG_{fif} Gibbs energy change of the folding in the interface; ΔG_{ifhc} Gibbs energy change of the insertion of the folded peptide from the interface to the hydrocarbon core; ΔG_{fw} Gibbs energy change of the folding in water; ΔG_{whc} Gibbs energy change of the insertion of the into the hydrocarbon core. Adapted from[147].

Partitioning of peptides from aqueous solution to membranes is often dominated by electrostatic and hydrophobic interactions between the cationic AMPs and the lipid membranes. For model membranes mimicking bacteria (negatively charged) as AMPs are almost always positively charged, a significant enhancement of AMPs concentration near the membrane surface will occur, compared to its concentration in the bulk. Partition of a charged peptide to a neutral membrane can occur as well, leading to a peptide concentration near the membrane surface that is initially similar to the bulk concentration, and decreases as the partition takes place, due to the positive charge that is increasing at the membrane surface due to peptide partition[86, 115, 152].

Upon the initial interaction of AMPs with the membrane, there is usually a conformational transition of the peptide from unstructured (random) in solution to an acquired secondary structure upon membranes interaction. This increases the peptides partition, as the secondary structure has a better interaction with the membrane, due to its amphipathicity[150, 153]. Peptide's partition may affect the bilayer structure due to the insertion of the hydrophobic moieties. The exact location of the peptide depends on the hydrophobic/hydrophilic balance and forces involved[152].

The partition constant, K_p, can be determined from the equilibrium between peptides and membrane through spectroscopic methods[154], such as fluorescence spectroscopy[155], but also through high sensitivity calorimetric methods, like isothermal titration calorimetry (ITC)[156]. The partition constant can be converted into the standard Gibbs energy change (ΔG^0)[152] as

$$\Delta G^0 = -RT \ln K_p \qquad (2.3.1)$$

The dimensionless partition constant, considering a simple partition equilibrium between the aqueous phase (W) and the lipid bilayer phase (L), can be defined as[157]:

$$K_{p,x} = \frac{\dfrac{n_L^P}{n_L + n_L^P}}{\dfrac{n_W^P}{n_W + n_W^P}} \qquad (2.3.2)$$

where, n_L and n_W are the number of moles of lipid and water, respectively, and n_i^P is the number of moles of peptide present in each phase (L, lipid phase and W, aqueous phase). $K_{p,x}$ can be related to the Nernst partition constant (K_p), by replacing the

amounts of water and lipid by their respective molar volumes, γ_W and γ_L, respectively The two partition constants are related as:

$$K_p = K_{p,x} \times \frac{\gamma_W}{\gamma_L}$$

(2.3.3)

In this thesis, the partition constant of cyclic peptides into model membranes, were determined by fluorescence techniques, as explained in **part III**, **publication V**.

2.3.2. Lipid:peptide molar ratio

The effect of AMPs on pathogen membranes depends usually on the lipid:peptide molar ratio. At low peptide concentration, *i.e.*, high L:P ratios, the AMPs tend to adsorb at the membrane surface, at the level of the lipid headgroup, lying parallel to the lipid bilayer surface. This usually is accompanied by lateral lipid segregation (accumulation of negatively charged lipids close to the AMP), with an increase in local membrane rigidity at *loci* where the peptide is tightly 'bound' to the negatively charged lipid headgroups, changing eventually the permeability and mechanical properties of the membrane, making it less stable. As the peptide content increases (L:P ratio decreases), it eventually reaches a threshold concentration, *i.e.*, the minimum peptide concentration at the surface that is necessary to promote a different structural arrangement and eventually a severe biological effect[158, 159]. After this concentration, AMPs begin to tilt towards a more perpendicular position, inserting into the membrane and forming transmembrane pores or other transmembrane structures. This phenomenon varies with the AMP and membrane lipid composition. It should be noted that these phenomena can also occur in some cases at uncharged membranes (like non-pathogen membranes), but the threshold will be orders of magnitude higher than the ones observed for charged membranes[22, 115].

2.3.3. Peptide insertion and membrane permeability

The most accepted starting mechanism of action for AMPs is the **carpet model** (Fig. 2.3.2). In the **carpet model**, AMPs approach the membrane due to electrostatic interaction and accumulate at the membrane surface, in a parallel orientation, eventually covering all membrane. When partitioned to the membrane (step iii) above), the peptide has its hydrophilic part towards the solution, and the hydrophobic part at

the phospholipid bilayer[160]. Once a threshold concentration is reached, different mechanisms can follow towards destruction of the integrity of the membrane and pathogen death - toroidal or wormhole pores, barrel stave pore or a 'detergent'-like membrane solubilization (Fig. 2.3.2).

In the **'detergent-like' solubilization** the peptide acts as a detergent, forming 'lipid nanodiscs', surrounded by peptide[161, 162], and leads to total membrane destruction[163]. This model is seen for cecropins[164], LL-37[161], trichogin GA IV[165] and some magainins[22, 163, 166]. Another type of membrane micellization has been described, where peptide and lipid form mixed micelles, with cubic structures[22, 89, 167].

In the **toroidal pore model,** after the threshold concentration AMPs turn to a vertical orientation in the membrane, with their polar faces facing the polar head groups of the lipids and their non polar chains the hydrocarbon part of the lipids. Both lipid monolayers will show a continuous bend, forming a water-filled toroidal pore, with the peptides and the lipid head groups at the rime (Fig. 2.3.2). Protegrins, magainins and melittin have been suggested to create this type of transmembrane pore[115, 127, 168, 169]. In some cases, upon pore disintegration some peptides can be translocated to the inner leaflet of the membranes, resulting in cell death[170, 171].

In the **barrel-stave model** (Fig. 2.3.2), AMPs aggregate at the membrane, forming a bundle of peptide helices. In this model, the hydrophobic core of the peptide is aligned with the acyl chains of the phospholipids and the hydrophilic peptide regions form the interior region of pore channels, that result in the cytoplasmic outflow[22, 172]. This arrangement at the membrane may cause disintegration of the pore due to the repulsion of the AMPs charges, being only possible with highly hydrophobic and not too highly charged peptides. It has been reported that increasing peptide content in the membrane leads to an increase in the pore size [146]. Examples of peptides following this mechanism are alamethicin and perforin[173].

The distinguishing feature between **toroidal model** and the **barrel-stave model** is the arrangement of the peptides in the bilayer. In the **barrel-stave pore**, upon insertion in the lipid bilayer, the hydrophobic part of the peptide interacts with the lipid hydrocarbon chains while the hydrophilic portions faces inwards, forming a hydrophilic channel. In **toroidal pores** the polar side of the AMPs interacts with the polar head groups of the lipids, resulting in a continuous bend of the membrane, eventually connecting the two leaflets[22].

The **sinking raft model** (Fig. 2.3.2) is a consequence of a mass imbalance for a particular lipid domain and therefore, a strong membrane curvature is introduced. In this mechanism, the peptide sinks into the membrane and transient pores are formed, with the peptide residing in both leaflets of the membrane[174].
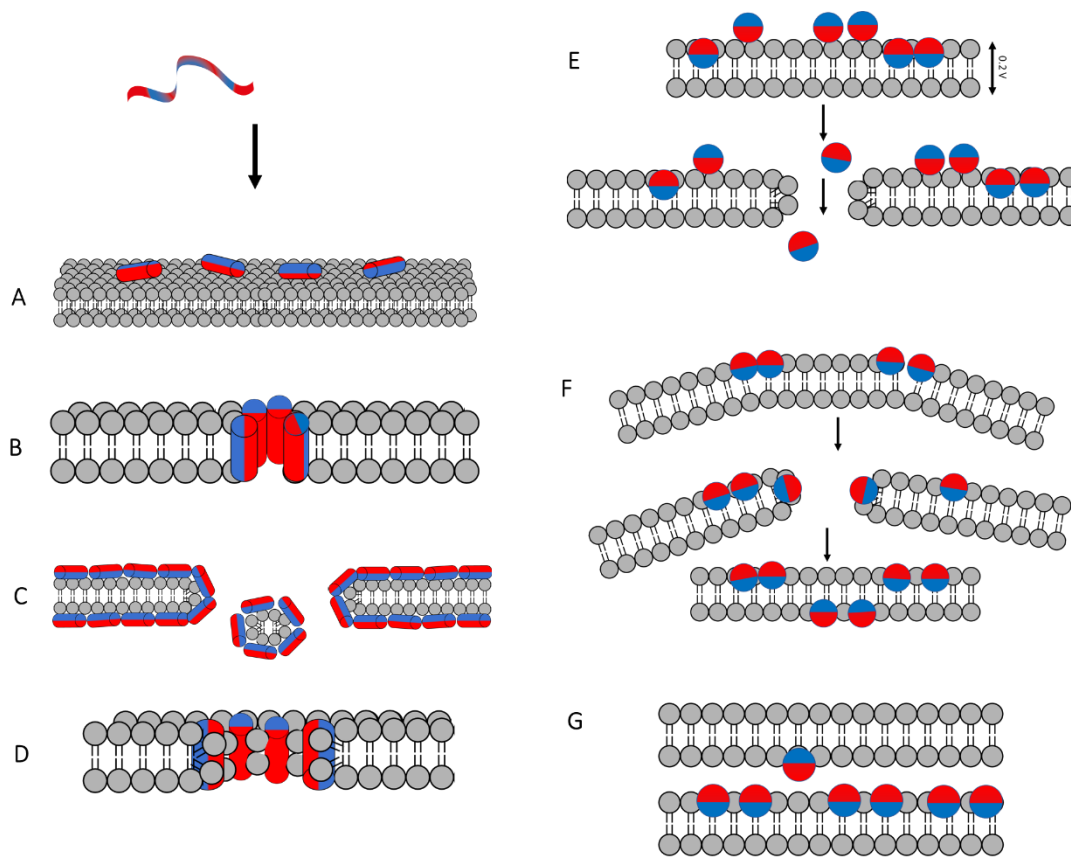
Fig. 2.3.2. Representation of the mode of action of AMPs, where the red region is the hydrophilic and the blue the hydrophobic. **(A)** AMPs with random structure in solution are attracted to the membrane, adopt secondary structure, and cover the membrane surface ("carpet") **(B)** Barrel-stave model, the peptides span the membrane and form a pore with hydrophilic interior; **(C)** Micellization model, the peptide has a detergent-like action and disrupts the membrane structure, forming peptide/lipid mixed micelles; **(D)** Toroidal pore model, the peptide has the hydrophilic part associated with the lipid headgroups, and the hydrophobic part facing the lipid tails; **(E)** Molecular electroporation model, the peptide's interaction with the membrane promotes an electrical potential across the membrane; **(F)** Sinking raft model, the peptide induces a mass imbalance between the two leaflets of the membrane. **(G)** Membrane stacking, induced by the peptide, that becomes intercalated between the lipid layers. Adapted from [22].

The **molecular electroporation model** (Fig. 2.3.2) was proposed to describe the action of some AMPs that show activity without apparent formation of transmembrane pores. In this model, high local electrical fields due to the peptide partition to membrane are enough for transient pore formation. It provides a possible explanation on how the peptides increase membrane permeability without necessarily causing its disruption[22, 175].

The **micellar aggregate channel** is an alternative model that suggests the reorientation and association of the peptide in an unstructured way in the membrane to form micelle-like aggregates that provide channels for the movement of ions across the membrane[176].

In the **membrane stacking model,** upon peptide's interaction with the membrane, an initial disruption of the bilayer occurs, leading to the formation of a multibilayers stacking with peptides intercalated between them, in an *onion-like* structure [177].

In general, in the presence of lipid mixtures, the peptide induces **lipid segregation**, due to its preference for the negatively charged lipids. This phenomenon significantly perturbs the membrane, forming lipid–peptide domains, causing lateral phase segregation in zwitterionic and anionic lipid mixtures, and in some cases, this can lead to the formation of non-lamellar phases at physiologically-relevant conditions. If lipid segregation is the only result of peptide/lipid interactions, small intracellular leakage can occur, as well as membrane depolarization and destabilization, due to changes in curvature strain, affecting the membrane function[13, 20, 89, 146, 178].

AMPs do not need to act through an exclusive mechanism of action [179]. By damaging the bacteria membrane, the ions and pH gradient may change, accompanied by the loss of metabolites, osmotic changes, and all together this eventually ends up in cell death[71, 115, 164] Finally, it should be pointed out that some AMPs translocate to the cytoplasm, and bind to DNA, or inhibit enzymatic activities and protein synthesis, *i.e.*, have internal targets[180], like lactoferrin derived peptides (LFcin)[181], and this can occur with or without permeabilizing the cytoplasmic membrane[115, 182, 183].

2.3.4. Resistance

Although AMP have mostly membrane based mechanisms of action, making resistance more difficult, bacteria can still find mechanisms to circumvent the AMPs' action. Examples are i) surface net charges change, like for *Staphylococcus aureus*, that transports *D*-alanine from the cytoplasm to the surface teichoic acid, causing esterification between teichoic acid and *D*-alanine, which leads to a reduction of the net negative charge; ii) *Salmonella* species that have reduced the fluidity in their outer layer, by adding other components to the lipid A layer, increasing hydrophobicity of the surface and delaying or avoiding peptide insertion and pore formation. Changes in membrane proteins and the degradation of the peptides by proteolytic enzymes are also mechanisms used by bacteria to resist AMP action[115].

2.4. Selectivity

The amphipathic structure and the cationic character of AMPs are fundamental properties that contribute to their selectivity[184, 185].

Although AMPs are membrane-active in prokaryotes, it is known that they possess some, albeit significantly smaller ability to disrupt eukaryotic membranes - it has been observed that 'good' AMPs are usually nonhemolytic at concentrations well above their minimal inhibitory concentrations (MICs, minimum concentration that prevents visible growth of bacteria) [122]. This difference can be associated with the presence of sphingomyelin and cholesterol, that help to attenuate possible perturbations induced by AMPs in eukaryotic membranes[186, 187].

Some AMPs can interact and permeabilize some cancer cells, again as a result of charge effects. Cancer cells carry an additional negative surface net charge as they have a significant presence of PS in the outer leaflet of their plasma membranes, while in normal cells PS are located in the inner leaflet[188] [189]. Cholesterol levels also decrease in cancer cells, enhancing the membrane fluidity and facilitating apoptosis by AMPs. Although the mode of action of AMPs against cancer cells is not well known, it is supposed to be like the ones acting in bacteria, *i.e.*, basically driven by electrostatic attraction[190, 191].

2.4.1. Effect of membrane charge

The most straightforward explanation for AMPs' selectivity is electrostatic attraction. Bacteria membranes have a predominance of anionic phospholipids (see **chapter 1**, **section 1.3** Table 1.1) having thus an overall negative charge (membrane potential of about -140 mV). In contrast, eukaryote cell membranes are mainly composed by zwitterionic phospholipids, having thus a close to neutral net charge (membrane potential of -15 mV)[71, 122]. This leads to a preference of AMPs for bacterial cell wall as compared to mammalian cells[192].

The membrane surface charge depends mainly on the lipid's head groups and leads to the attraction of a cloud of oppositely charged ions. The charges' distribution is ruled by the competition between the electrostatic interactions and the entropy of the ions in solution, leading to a distribution that changes with distance, forming the "diffuse double layer". The ions' accumulation (positive adsorption) or depletion (negative adsorption) at the surface influences the electrostatic interactions between the peptides and the biological membranes [61, 193].

These effects at the membrane surface were found to be well described by the Gouy-Chapman theory[194] (Fig 2.4.1).
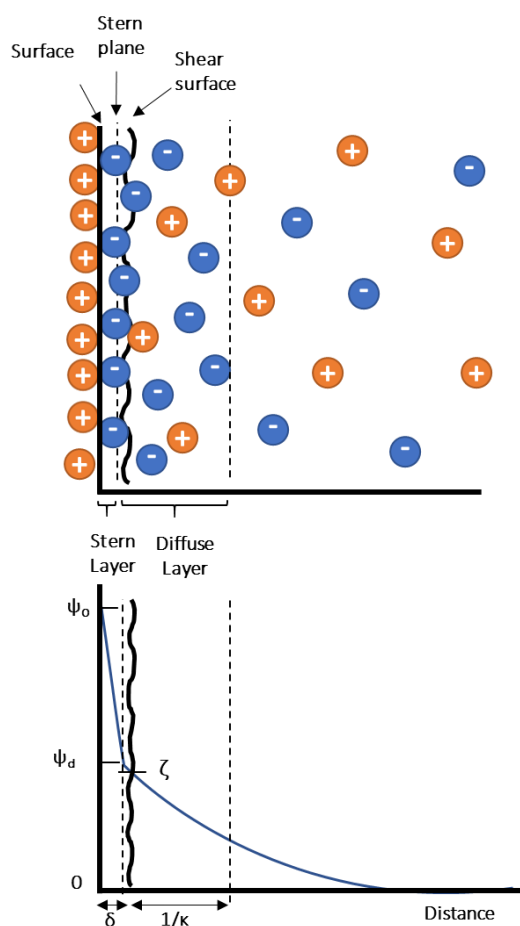
Fig. 2.4.1. Top panel: schematic illustration of the electric double layer according to Stern's model. Here the surface has positive charge, attracts counterions and alters ion's distribution, forming a "diffuse layer" in the adjacent aqueous phase. Bottom panel: electric potential as a function of the distance (x) from the surface predicted by the Gouy-Chapman-Stern theory. (ψ_0), surface potential, (ψ_d), Stern potential, (ζ), Zeta potential, (δ), thickness of Stern layer, ($1/\kappa$) Debye length (distance where charge separation occurs). Adapted from [195].

In brief, one can determine the value of the electric potential as a function of the distance from the membrane surface. Once this value is known, the local concentration of any ionic species can be determined by applying the Gouy-Chapman model using the Boltzmann equation (Eq. 2.4.1)[61, 193, 196]:

$$C(x) = C_0 e^{-zF\psi(x)/RT} \tag{2.4.1}$$

where $C(x)$ is the ion concentration and $\psi(x)$ the electrical potential as function of the distance x from the membrane surface, C_0 is the ion concentration in the bulk, z is the ions' valence, F is the Faraday's constant and RT are the ideal gases constant and the absolute temperature. The potential at the membrane surface (ψ_0) can be predicted using the Gouy-Chapman theory, and can be related to the membrane surface charge

density (σ, the total electric charge per unit of membrane surface area), by use of equation (Eq. 2.4.2)[196]:

$$\sigma = \sqrt{2000\,\varepsilon_0\varepsilon_R RT \sum_i C_{i,0}\,[(e^{-z_i F\psi_0/RT}) - 1]} \tag{2.4.2}$$

where ε_0 is the permittivity of vacuum, ε_R the relative dielectric constant, $C_{i,0}$ is the concentration of ith electrolyte in the bulk aqueous phase, z_i is the charge of the ith species and the other parameters were described above[52, 193]. It should be noted that the pH at the membrane surface it will be different from the one in the bulk, due to the higher concentration of ions of charge opposite to the membrane, changing the apparent pK_a of any groups located here[52, 193].

These theory and equations have been successfully applied to studies of AMP partition to charged lipid membranes, particularly in the determination of partition parameters from ITC experiments[152, 197].

Chapter 3. Antimicrobial Cyclic Peptides

Linear antimicrobial peptides are the most commonly studied[115, 123, 164, 198, 199], and that is also the case in our research group[89, 157, 200-203]. Despite their proven activity, the low stability under physiological conditions has been a major barrier to their therapeutic use, since they can be rapidly cleaved by enzymes *in vivo*, losing rapidly their biological activity[204, 205].

The interest in antimicrobial peptides of cyclic structure started in 1944 with the discovery of the antimicrobial properties of Gramicidin S (Fig. 3.1.1.A), a cyclic decapeptide natural product[206]. Since then, **cyclic peptides (CPs)** (Fig. 3.1.1.B) have been explored in different applications, such as therapeutics, diagnostics, vaccines and as drug leads[207].
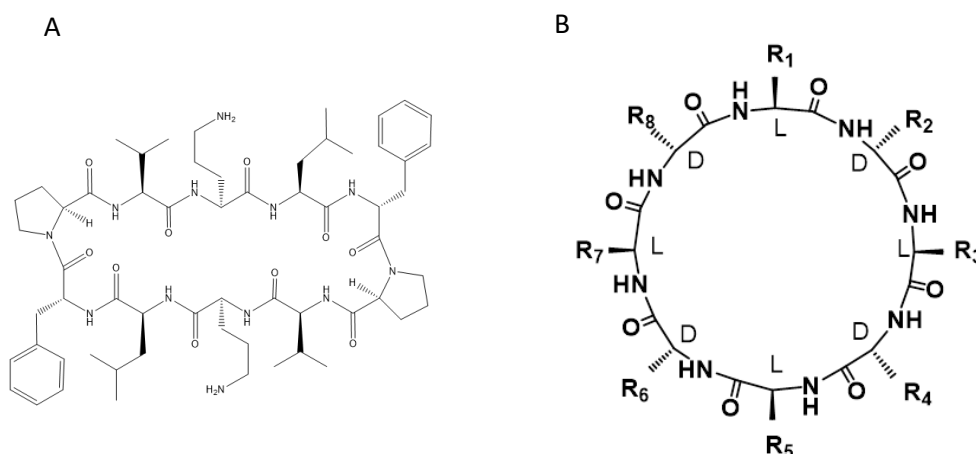
Fig. 3.1.1. A. 2D representation of molecular structure of the cyclic peptide Gramicidin S, discovered in 1944. **B.** Schematic 2D representation of a *D,L*-α-cyclic peptide, of flat ring conformation.

Since then, cyclization of the peptides has been tried with different peptides. The cyclization of peptides increases their rigidity, forcing them to adopt more ordered secondary structures. This structural change has some advantages, when compared to the linear analogues: **i)** decrease of conformational freedom for each constituent within the ring, and consequently the decrease of the entropic term of the Gibbs energy; **ii)** higher binding affinities to receptors; **iii)** higher resistance to endopeptidases when compared to the more flexible linear analogues[208-211].

In 1974, De Santis *et al.*[212] suggested that cyclic peptides with an even number of alternating *D*- and *L*- amino acids could adopt a flat ring conformation, where the NH and the CO groups would be oriented perpendicular to the plane of the ring. They also

stated that tubular structures could be formed by these CPs. In 1993 Ghadiri and co-workers have demonstrated the formation of self-assembled hollow structures, the **self-assembled cyclic peptides nanotubes (SCPNs)** (Fig. 3.1.2) by ring stacking of a *D,L*-α-cyclic peptides (c-[(*L*-Gln-*D*-Ala-*L*-Glu-*D*-Ala)₂])[213].

3.1. Self-Assembled *D,L*-α-Cyclic Peptides

The process of self-assembling of *D,L*-α-cyclic peptides was described as a proton-triggered process, as the protonation favors self-assembling due to the formation of hydrogen bonds between the side chains, together with a decrease in solubility of the CPs [213]. At alkaline pH, the formation of the nanotubes is disfavored, due to the intermolecular repulsive electrostatic interactions of the negatively charged carboxylate side chains of the glutamic acid, that also increases their solubility in the aqueous media. The nanotubes formed were characterized by Fourier-transform infrared spectroscopy, electron microscopy, electron diffraction, and crystal structure modeling. *D-L*-α-[(*L*-Gln-*D*-Ala-*L*-Glu-*D*-Ala)₂] adopted a low energy ring flat conformation with the amide groups perpendicular to the plane of the structure, with an approximate 7 Å internal van der Waals diameter. The flat rings self-assembled in an extensive antiparallel β-sheet structure, creating intermolecular hydrogen bonds between the units, with the residues' side chains pointing outwards, forming a hollow cylindrical structure. This tubular hollow structures were only possible as consequence of steric restrictions due to the alternation of *D,L*- arrangement, creating a hydrophilic core structure lined with the backbone amide functionalities.

Cyclic Peptide

Self-Assembled
Cyclic Peptide
Nanotubes
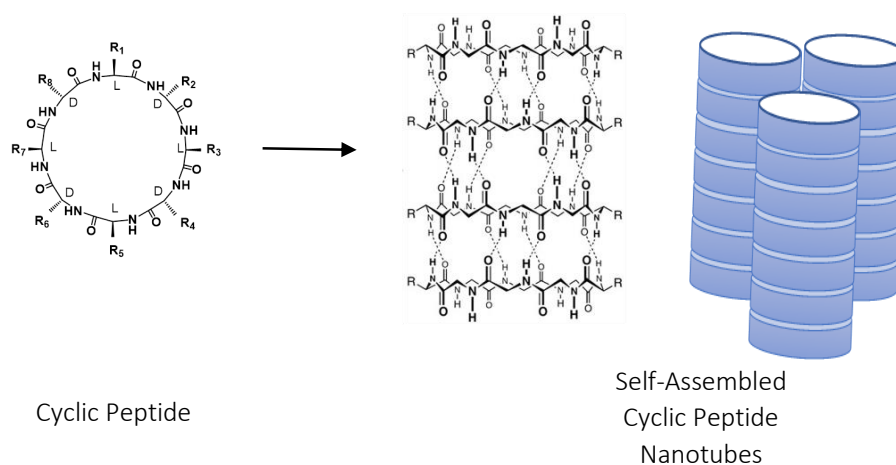
Fig. 3.1.2. Schematic 2D representation of *D,L* -α-cyclic peptide and 3D representation of self-assembled cyclic peptide nanotubes forming with antiparallel β-sheet, one of the proposed macromolecular structures that these peptides can adopt. Adapted from[214].

The use of these cyclic *D,L* peptides presents some advantages: **i)** the internal diameter of the tube can be controlled, as well as same of the outside surface properties, simply by choosing the number and the appropriate amino acid side chains, respectively; **ii)** the physical properties can be modified according to its application, by changing their surface as a consequence of amino acids' choice; and **iii)** they have a robust secondary structure that together with the abundance of *D*-amino acids makes them less degradable by proteases. Such properties prompted the design a variety of amino-acid derived nanotubes with different properties and functions[215-218]. This class of peptides possess unique structural properties that are not found in natural antimicrobial peptides or their modified versions[124, 213]. With the correct design, they can behave as artificial transmembrane channels for ion and glucose transport, solid surface-supported ion sensors, as well as being designed to present antibacterial activity [124, 219, 220]

3.1.1. Antimicrobial properties of *D-L*-α-cyclic peptides

Ghadiri's group proposed the design of *D,L*-α-cyclic peptides targeting Gram-positive and/or Gram-negative bacteria, that could act by increasing membrane permeability and/or forming transmembrane pores that would lead to cell death[124]. The synthesized *D,L*-α–CPs of different number of amino acid residues were shown to self-assemble into macromolecular structures, namely peptide nanotubes, under appropriate conditions. The presence of a surface is a triggering factor for self-assembling, and it was shown that membrane surfaces were not an exception. Thus the concept of possible use of these *D,L*-α-cyclic peptides as antimicrobial peptides emerged, and Ghadiri's groups published the first results in this area[213].

The basic mechanism of these new antimicrobial peptides is like what was described above for the linear AMPs, *i.e.*, an interaction driven by electrostatics[221].

The macromolecular structure and orientation at the membrane depends on the size and external surface of the cyclic peptide. Hydrophobic cyclic peptides will form nanotubes typically oriented perpendicular to the lipid bilayer, to maximize van der Waals contacts with the lipids (Fig. 3.1.3. A). These peptides are used to form transmembrane channels that transport ions and small polar molecules. Amphipathic cyclic peptides, on the other hand, can lie parallel to the membrane surface (Fig. 3.1.3. B), with the hydrophobic part inserted into the membrane, and the hydrophilic part pointing outwards, inserted at the heads' level. These later peptides are believed to permeate membranes through a carpet-like mechanism, changing transmembrane

potential and/or gradient, disrupting the membrane and eventually causing cell death[222].

Altogether, the increased resistance to protease degradation due to the presence of *D*-amino acids allied with the robust secondary structure makes *D-L-*α-cyclic peptides with the ability to self-assemble very promising antimicrobial peptide's candidates[115, 223, 224].
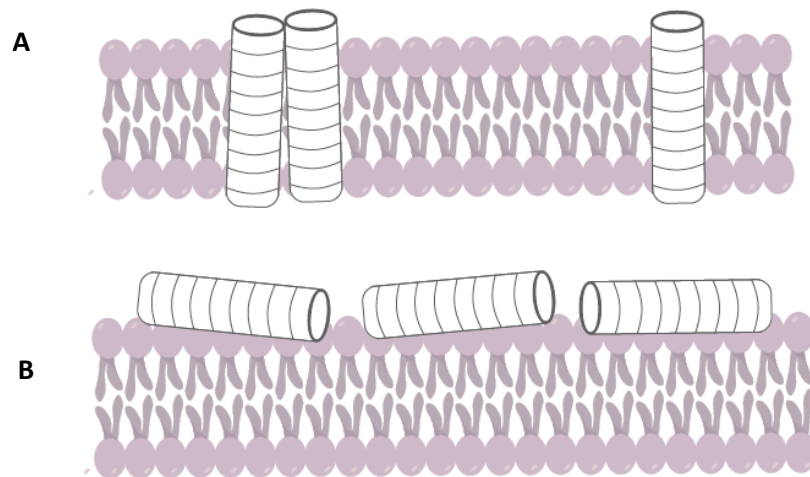
Fig. 3.1. 3. Schematic representation of cyclic peptides' nanotubes **A.** perpendicular to the membrane, **B.** parallel to the membrane. Their relative position depends on the CPs and membrane composition.

Chapter 4. The Problem and the Motivation

Antimicrobial peptides are promising potential alternatives to treat infectious diseases, a subject of high urgency due to the alarming existence of extremely high pathogen acquired resistance to conventional antibiotics. Thus, the search for new and more effective antimicrobial drugs has been growing in the last decade. Cyclic peptides are part of this effort, and those involving *D*-amino acids can become a promising antibiotic group of compounds. Keeping in mind that their properties are dependent on the CP sequence, a question that can be raised is what are the critical factors for new and improved cyclic peptides? This was the main motivation of this thesis work.

Ghadiri *et. al* [124] published a list of CPs with a diversity of structures that could be selective to target bacterial membranes. Thus, a starting cyclic peptide of known structure and recognized antimicrobial activity was chosen as a lead compound (**CP1,** a Ghadiri's peptide), to later designing, synthesize and test new and improved antimicrobial CPs.

CP1, *c*-[RRKWLWLW] has a rather "perfect" amphipathic structure - a part with three consecutive charged residues (two arginines and one lysine) to promote affinity to the negative charged bacterial membranes, and another with repeating tryptophan and leucine amino acids. Even though this CP has a quite good antimicrobial characteristics, it has very low solubility in aqueous solution due to the presence of the three tryptophan residues, requiring the use of the organic solvent DMSO for its solution characterization. Therefore, from this peptide a new peptide was synthetized in University of Santiago de Compostela in Professor Granja's group, with improved aqueous solubility - **CP2,** *c*-[KSKSWPgKQ]. This peptide combines the presence of three charged lysine residues with polar non-charged residues (serine and glutamine) to increase solubility. The presence of propargylglicyne (Pg) allows further modification through the alkyne moiety. The underlined residues are *D*- amino acids.

Thereafter, a second generation of three new and improved CPs was developed in Juan Granja's group, using **CP2** as a template. The lysine was replaced by arginine (**CPR**, *c*-[RSKSWPgKQ]) and a carbon tail of 10 and 14 carbons was added to **CPR**, attached to the Pg group, creating **CPRT10**, *c*-[RSKSWX^{C10}KQ] and **CPRT14,** *c*-[RSKSWX^{C14}KQ], respectively. X that denotes (*S*)-2-amino-3-(1λ^2,2,3-triazol-4-yl)propanoic acid to which a hydrocarbon tail is attached in the case of **CPRT10** and **CPRT14**. The underlined residues are *D*-amino acids. The three peptides

are soluble in water, contain one hydrophobic residue (tryptophan, W, known to increase membrane anchoring), three charged residues (one arginine (R) and two lysines (K)), and three polar non-charged residues (one glutamine (Q) and two serines (S)).

The phospholipid compositions used in this thesis to prepare model membranes that mimic bacterial membranes were DMPG (1,2-dimyristoyl-s*n*-glycero-3-phospho-(1'-rac-glycerol)), DMPE (1,2-dimyristoyl-s*n*-glycero-3-phosphoethanolamine) and binary mixtures of DMPE:DMPG with different molar ratios (3:1,1:1; 1:9) (**Part III**, **publications II – V** and **manuscript VI**). DMPC (1,2-dimyristoyl-s*n*-glycero-3-phosphocholine) was also used to assess the toxicity towards eukaryotic membranes. POPE (1-palmitoyl-2-oleoyl-sn-glycero-3-phosphoethanolamine) and POPG (1-palmitoyl-2-oleoyl-sn-glycero-3-phospho-(1'-rac-glycerol)), lipids with unsaturated chains, where used in the leakage experiments (**Part III**, **publication V**).

The liposomes used were multilamellar large vesicles (MLVs), large unilamellar vesicles (LUVs) and oligolamellar vesicles (OLVs), with significantly different sizes and polydispersity (see preparation methods in **Part II**, **chapter 5** and **Part III**, **publications II – V** and **manuscript VI**).

These peptides' studies are divided into different publications, in **Part III**:

Publication II – Studies of the first generation of cyclic peptides, **CP1** and **CP2**, and their interactions with model membranes of DMPG and DMPE with different charge contents. In this chapter biophysical experimental techniques (DSC and ATR-FTIR with polarized light), were used together with CG-MD simulations to characterize their interactions and macromolecular assemblies when in contact with membranes with varying negative charge content.

Publication III – ATR-FTIR was used to get structural information on **CPR** and **CPRT10** in solution and/or in contact with DMPG membranes, namely characterizing the formation of self-assembled nanotubes. Polarized lens was combined with ATR-FTIR to assess the orientation of the peptides as regarding the lipid membranes.

Publication IV - The combination of biophysical experimental techniques (DSC and ATR-FTIR) and CG-MD simulations was again used to study the second generation cyclic peptides **CPR**, **CPRT10** and **CPRT14**, aiming at understanding their interactions,

macromolecular assemblies and eventually unveil their mechanism of action in membranes composed by DMPG and DMPE with different charge contents.

Publication V – Fluorescence spectroscopy was used to assess the partition of the second generation of cyclic peptides **CPR**, **CPRT10** and **CPRT14**, to membranes of DMPG and DMPE:DMPG (1:1), using the peptides' intrinsic fluorescence. The peptide-induced membrane leakage pattern was followed using an encapsulated fluorescent dye, fluorescein.

Manuscript VI - X-ray scattering techniques (SAXS and WAXS) were used to characterize the CPs influence on the structure of selected lipid model membranes. MLVs of DMPE were characterized, and the effect of **CP1**, **CP2**, **CPR**, **CPRT10** and **CPRT14** on the membrane's repeat distance assessed. Further, the most promising peptides, with proven antimicrobial activity, **CPR**, **CPRT10** and **CPRT14,** were assessed also against OLVs of DMPE:DMPG (3:1), used as bacterial model membranes.

References

1. Roberts, K.; Alberts, B.; Johnson, A.; Lewis, J.; Raff, M.; Walter, P. *Molecular Biology Of The Cell*. 4th Edition ed.; 2002.

2. Cuevas, J. Structure and Function of Membranes. In *Reference Module in Biomedical Sciences*, Elsevier: 2015.

3. Blume, A. Temperature-Induced and Isothermal Phase Transitions of Pure and Mixed Lipid Bilayer Membranes Studied by DSC and ITC. In *Biocalorimetry. Foundations and Contemporary Approaches*, 1st Edition ed.; Bastos, M., Ed. Boca Raton: 2016.

4. Kauzmann, W. Some Factors in the Interpretation of Protein Denaturation. In *Adv. Protein Chem.*, Anfinsen, C. B.; Anson, M. L.; Bailey, K.; Edsall, J. T., Eds. Academic Press: 1959; Vol. 14, pp 1-63.

5. Xu, Y.; Tillman, T. S.; Tang, P. Chapter 3 - Membranes and Drug Action. In *Pharmacology*, Hacker, M.; Messer, W.; Bachmann, K., Eds. Academic Press: San Diego, 2009; pp 31-61.

6. Schaeffer, L. Chapter 14 - The Role of Functional Groups in Drug–Receptor Interactions. In *The Practice of Medicinal Chemistry (Fourth Edition)*, Wermuth, C. G.; Aldous, D.; Raboisson, P.; Rognan, D., Eds. Academic Press: San Diego, 2008; pp 359-378.

7. de Jesus, A. J.; Yin, H. Supramolecular Membrane Chemistry. In *Comprehensive Supramolecular Chemistry II*, Atwood, J. L., Ed. Elsevier: Oxford, 2017; pp 311-328.

8. Stillwell, W. Chapter 10 - Lipid Membrane Properties. In *An Introduction to Biological Membranes (Second Edition)*, Stillwell, W., Ed. Elsevier: 2016; pp 181-220.

9. Chapman, D.; Wallach, D. F. H. *Biological membranes*. 1968.

10. Chapman, D.; Williams, R. M.; Ladbrooke, B. D. Physical studies of phospholipids. VI. Thermotropic and lyotropic mesomorphism of some 1,2-diacyl-phosphatidylcholines (lecithins). **Chemistry and Physics of Lipids 1967,** 1, 445-475.

11. Gennis, R. B. *Biomembranes*. Springer, New York, NY: 1989.

12. Yeagle, P. L. *The Structure of Biological Membranes*. CRC Press: 2011.

13. Luzzati, V. Biological significance of lipid polymorphism: the cubic phases. *Curr. Opin. Struct. Biol.* **1997,** 7, 661-668.

14. Qiu, H.; Caffrey, M. The phase diagram of the monoolein/water system: metastability and equilibrium aspects. *Biomaterials* **2000,** 21, 223-34.

15. Tyler, A. I. I.; Law, R. V.; Seddon, J. M. X-Ray Diffraction of Lipid Model Membranes. In *Methods in Membrane Lipids*, Owen, D. M., Ed. Springer New York: New York, NY, 2015; pp 199-225.

16. Frolov, V. A.; Shnyrova, A. V.; Zimmerberg, J. Lipid polymorphisms and membrane shape. *Cold Spring Harb Perspect. Biol.* **2011,** 3, a004747.

17. Israelachvili, J. N. 20 - Soft and Biological Structures. In *Intermolecular and Surface Forces (Third Edition)*, Israelachvili, J. N., Ed. Academic Press: San Diego, 2011; pp 535-576.

18. Jing, W.; Prenner, E. J.; Vogel, H. J.; Waring, A. J.; Lehrer, R. I.; Lohner, K. Headgroup structure and fatty acid chain length of the acidic phospholipids modulate the interaction of membrane mimetic vesicles with the antimicrobial peptide protegrin-1. *J. Pept. Sci.* **2005,** 11, 735-43.

19. Lombardo, D.; Kiselev, M. A.; Magazù, S.; Calandra, P. Amphiphiles Self-Assembly: Basic Concepts and Future Perspectives of Supramolecular Approaches. *Adv. Condens. Matter Phys.* **2015,** 2015, 151683.

20. Haney, E. F.; Nathoo, S.; Vogel, H. J.; Prenner, E. J. Induction of non-lamellar lipid phases by antimicrobial peptides: a potential link to mode of action. *Chem. Phys. Lipids* **2010,** 163, 82-93.

21. Ruthven N. A. H. Lewis, D. A. M., and Ronald N. McElhaney. Membrane Lipid Molecular Structure

and Polymorphism. In *Lipid Polymorphism and Membrane Properties*, Epand, R. M., Ed. Academic Press: 1997; Vol. 44.

22. Teixeira, V.; Feio, M. J.; Bastos, M. Role of lipids in the interaction of antimicrobial peptides with membranes. *Prog. Lipid Res.* **2012,** 51, 149-77.

23. Tresset, G. The multiple faces of self-assembled lipidic systems. *PMC Biophys* **2009,** 2, 3-3.

24. Calzada, E.; Onguka, O.; Claypool, S. M. Phosphatidylethanolamine Metabolism in Health and Disease. *Int. Rev. Cell. Mol. Biol.* **2016,** 321, 29-88.

25. Zweytick, D.; Tumer, S.; Blondelle, S. E.; Lohner, K. Membrane curvature stress and antibacterial activity of lactoferricin derivatives. *Biochem. Biophys. Res. Commun.* **2008,** 369, 395-400.

26. Koynova, R.; Tenchov, B. Lipids: Phase Transitions. In *Wiley Encyclopedia of Chemical Biology*, pp 1-15.

27. Tenchov, B. On the reversibility of the phase transitions in lipid-water systems. *Chem. Phys. Lipids* **1991,** 57, 165-77.

28.   Seddon, J. M.; Templer, R. H. Chapter 3 - Polymorphism of Lipid-Water Systems. In *Handbook of Biological Physics*, Lipowsky, R.; Sackmann, E., Eds. North-Holland: 1995; Vol. 1, pp 97-160.

29.   Gennis, R. B. The Structures and Properties of Membrane Lipids. In *Biomembranes*, Gennis, R. B., Ed. Springer New York: New York, NY, 1989; pp 36-84.

30.   Demetzos, C. Differential Scanning Calorimetry (DSC): a tool to study the thermal behavior of lipid bilayers and liposomal stability. *J. Liposome Res.* **2008,** 18, 159-73.

31.   Leekumjorn, S.; Sum, A. K. Molecular studies of the gel to liquid-crystalline phase transition for fully hydrated DPPC and DPPE bilayers. *Biochim. Biophys. Acta, Biomembr.* **2007,** 1768, 354-365.

32.   González-Henríquez, C. M.; Villegas-Opazo, V. A.; Sagredo-Oyarce, D. H.; Sarabia-Vallejos, M. A.; Terraza, C. A. Thermal Response Analysis of Phospholipid Bilayers Using Ellipsometric Techniques. *Biosensors* **2017,** 7, 34.

33.   Yeagle, P. L. Chapter 7 - Structures of Lipid Assemblies. In *The Membranes of Cells (Third Edition)*, Yeagle, P. L., Ed. Academic Press: Boston, 2016; pp 115-154.

34.   Seddon, J. M.; Templer, R. H.; Raynes, E. P.; Boden, N. Cubic phases of self-assembled amphiphilic aggregates. *Philos. Trans. Royal Soc. A* **1997,** 344, 377-401.

35.   Koynova, R.; Caffrey, M. Phases and phase transitions of the hydrated phosphatidylethanolamines. *Chem. Phys. Lipids* **1994,** 69, 1-34.

36.   Koynova, R.; Caffrey, M. Phases and phase transitions of the glycoglycerolipids. *Chem. Phys. Lipids* **1994,** 69, 181-207.

37.   Shyamsunder, E.; Gruner, S. M.; Tate, M. W.; Turner, D. C.; So, P. T. C.; Tilcock, C. P. S. Observation of inverted cubic phase in hydrated dioleoylphosphatidylethanolamine membranes. *Biochemistry* **1988,** 27, 2332-2336.

38.   Tenchov, B.; Koynova, R.; Rapp, G. Accelerated formation of cubic phases in phosphatidylethanolamine dispersions. *Biophys. J.* **1998,** 75, 853-866.

39.   Seddon, J. M.; Robins, J.; Gulik-Krzywicki, T.; Delacroix, H. Inverse micellar phases of phospholipids and glycolipids. Invited Lecture. *Phys. Chem. Chem. Phys.* **2000,** 2, 4485-4493.

40.   Garidel, P.; Blume, A. Miscibility of phosphatidylethanolamine-phosphatidylglycerol mixtures as a function of pH and acyl chain length. ***Eur Biophys J* 2000,** 28, 629-38.

41.   Collawn, J. F.; Bebök, Z. Chapter 1 Structure and Functions of Biomembranes. In *Free Radical Effects on Membranes*, Matalon, S., Ed. Academic Press: 2008; Vol. 61, pp 1-21.

42.   Watson, H. Biological membranes. *Essays Biochemistry* **2015,** 59, 43-70.

43.   Yeagle, P. L. Chapter 2 - The Lipids of Biological Membranes. In *The Membranes of Cells (Third Edition)*, Yeagle, P. L., Ed. Academic Press: Boston, 2016; pp 27-56.

44.   Singer, S. J.; Nicolson, G. L. The Fluid Mosaic Model of the Structure of Cell Membranes. *Science* **1972,** 175, 720.

45.   Engelman, D. M. Membranes are more mosaic than fluid. *Nature* **2005,** 438, 578-80.

46.   Luckey, M. *Membrane structural biology: with biochemical and biophysical foundations*. Cambridge University Press: 2014.

47.   Simons, K.; Ikonen, E. Functional rafts in cell membranes. *Nature* **1997,** 387, 569-572.

48.   Simons, K.; Toomre, D. Lipid rafts and signal transduction. *Nat. Rev. Mol. Cell Biol.* **2000,** 1, 31-39.

49.   Rao, M.; Mayor, S. Use of Forster's resonance energy transfer microscopy to study lipid rafts. *Biochim. Biophys. Acta* **2005,** 1746, 221-33.

50.   Silvius, J. R.; Nabi, I. R. Fluorescence-quenching and resonance energy transfer studies of lipid microdomains in model and biological membranes (Review). *Mol. Membr. Biol.* **2006,** 23, 5-16.

51.   Jin, S.; Zhou, F.; Katirai, F.; Li, P.-L. Lipid raft redox signaling: molecular mechanisms in health and disease. *Antioxid Redox Signal* **2011,** 15, 1043-1083.

52.   Gennis, R. B. *Biomembranes: Molecular Structure and Function*. Springer New York: 1989.

53.   Fahy, E.; Subramaniam, S.; Brown, H. A.; Glass, C. K.; Merrill, A. H., Jr.; Murphy, R. C.; Raetz, C. R.; Russell, D. W.; Seyama, Y.; Shaw, W.; Shimizu, T.; Spener, F.; van Meer, G.; VanNieuwenhze, M. S.; White, S. H.; Witztum, J. L.; Dennis, E. A. A comprehensive classification system for lipids. *J. Lipid. Res.* **2005,** 46, 839-61.

54.   Stillwell, W. Chapter 5 - Membrane Polar Lipids. In *An Introduction to Biological Membranes*, Stillwell, W., Ed. Elsevier: San Diego, 2013; pp 57-83.

55.   Vance, J. E. Phospholipid Synthesis and Transport in Mammalian Cells. *Traffic* **2015,** 16, 1-18.

56.   Alcorn, J. L. Pulmonary Surfactant Trafficking and Homeostasis. In *Lung Epithelial Biology in the Pathogenesis of Pulmonary Disease*, Sidhaye, V. K.; Koval, M., Eds. Academic Press: Boston, 2017; pp 59-75.

57.   Uphoff, A.; Hermansson, M.; Haimi, P.; Somerharju, P. Chapter 11 - Analysis of complex lipidomes. In *Medical Applications of Mass Spectrometry*, Vékey, K.; Telekes, A.; Vertes, A., Eds. Elsevier: Amsterdam, 2008; pp 223-249.

58.   Stillwell, W. Chapter 5 - Membrane Polar Lipids. In *An Introduction to Biological Membranes (Second Edition)*, Stillwell, W., Ed. Elsevier: 2016; pp 63-87.

59.   Merrill, A. H. CHAPTER 13 - Sphingolipids. In *Biochemistry of Lipids, Lipoproteins and Membranes (Fifth Edition)*, Vance, D. E.; Vance, J. E., Eds. Elsevier: San Diego, 2008; pp 363-397.

60.   Nelson, D. L. *Lehninger principles of biochemistry*. Fourth edition. New York : W.H. Freeman, 2005.: 2005.

61.   Chapman, D. *Biomembrane Structure and Function*. Palgrave Macmillan UK: 1983.

62.   Volkman, J. Sterols in microorganisms. *Appl. Microbiol. Biotechnol.* **2003,** 60, 495-506.

63.   Gordon, M. H. FATS | Classification. In *Encyclopedia of Food Sciences and Nutrition (Second Edition)*, Caballero, B., Ed. Academic Press: Oxford, 2003; pp 2287-2292.

64.   Myant, N. B. Chapter 3 - The Distribution of Sterols and Related Steroids in Nature. In *The Biology of Cholesterol and Related Steroids*, Myant, N. B., Ed. Butterworth-Heinemann: 1981; pp 123-159.

65.   Simons, K.; Sampaio, J. L. Membrane organization and lipid rafts. *Cold Spring Harb. Perspect. Biol.* **2011,** 3, a004697-a004697.

66.   Pozo Navas, B.; Lohner, K.; Deutsch, G.; Sevcsik, E.; Riske, K. A.; Dimova, R.; Garidel, P.; Pabst, G. Composition dependence of vesicle morphology and mixing properties in a bacterial model membrane system. *Biochim. Biophys. Acta* **2005,** 1716, 40-8.

67.   Virtanen, J. A.; Cheng, K. H.; Somerharju, P. Phospholipid composition of the mammalian red cell membrane can be rationalized by a superlattice model. *Proc. Natl. Acad. Sci. U. S. A.* **1998,** 95, 4964-4969.

68.   Rothman, J. E.; Lenard, J. Membrane asymmetry. *Science* **1977,** 195, 743-753.

69.   Cole, L. A. Evolution of Chemical, Prokaryotic, and Eukaryotic Life. In *Biology of Life*, Cole, L. A., Ed. Academic Press: 2016; pp 93-99.

70.   Parker, J. Bacteria. In *Encyclopedia of Genetics*, Brenner, S.; Miller, J. H., Eds. Academic Press: New York, 2001; pp 146-151.

71.   Lohner, K.; Sevcsik, E.; Pabst, G. Chapter Five Liposome-Based Biomembrane Mimetic Systems: Implications for Lipid–Peptide Interactions. In *Advances in Planar Lipid Bilayers and Liposomes*, Leitmannova Liu, A., Ed. Academic Press: 2008; Vol. 6, pp 103-137.

72.   Pajerski, W.; Ochonska, D.; Brzychczy-Wloch, M.; Indyka, P.; Jarosz, M.; Golda-Cepa, M.; Sojka, Z.; Kotarba, A. Attachment efficiency of gold nanoparticles by Gram-positive and Gram-negative bacterial strains governed by surface charges. *J. Nanoparticle Res.* **2019,** 21, 186.

73.   Sohlenkamp, C.; Geiger, O. Bacterial membrane lipids: diversity in structures and pathways. *FEMS Microbiol. Rev.* **2016,** 40, 133-159.

74.   Barak, I.; Muchova, K. The role of lipid domains in bacterial cell processes. *Int. J. Mol. Sci.* **2013,** 14, 4050-65.

75.   Bogdanov, M.; Pyrshev, K.; Yesylevskyy, S.; Ryabichko, S.; Boiko, V.; Ivanchenko, P.; Kiyamova, R.; Guan, Z.; Ramseyer, C.; Dowhan, W. Phospholipid distribution in the cytoplasmic membrane of Gram-negative bacteria is highly asymmetric, dynamic, and cell shape-dependent. *Sci. Adv.* **2020,** 6, eaaz6333.

76.   Christensen, H.; Garton, N. J.; Horobin, R. W.; Minnikin, D. E.; Barer, M. R. Lipid domains of mycobacteria studied with fluorescent molecular probes. *Mol. Microbiol.* **1999,** 31, 1561-72.

77.   Fishov, I.; Woldringh, C. L. Visualization of membrane domains in Escherichia coli. *Mol. Microbiol.* **1999,** 32, 1166-72.

78.   Mileykovskaya, E.; Dowhan, W. Visualization of phospholipid domains in Escherichia coli by using the cardiolipin-specific fluorescent dye 10-N-nonyl acridine orange. *J. Bacteriol.* **2000,** 182, 1172.

79.   Kawai, F.; Shoda, M.; Harashima, R.; Sadaie, Y.; Hara, H.; Matsumoto, K. Cardiolipin Domains in Bacillus subtilis Marburg Membranes. *J. Bacteriol.* **2004,** 186, 1475.

80.   Hiraoka, S.; Matsuzaki, H.; Shibuya, I. Active increase in cardiolipin synthesis in the stationary growth phase and its physiological significance in Escherichia coli. *FEBS Lett* **1993,** 336, 221-4.

81.   Gidden, J.; Denson, J.; Liyanage, R.; Ivey, D. M.; Lay, J. O. Lipid Compositions in Escherichia coli and Bacillus subtilis During Growth as Determined by MALDI-TOF and TOF/TOF Mass Spectrometry. *Int. J. Mass. Spectrom.* **2009,** 283, 178-184.

82.   Epand, R. F.; Pollard, J. E.; Wright, J. O.; Savage, P. B.; Epand, R. M. Depolarization, bacterial membrane composition, and the antimicrobial action of ceragenins. *Antimicrob. Agents Chemother.* **2010,** 54, 3708-13.

83.   Mileykovskaya, E.; Dowhan, W. Role of membrane lipids in bacterial division-site selection. *Curr. Opin. Microb.* **2005,** 8, 135-142.

84.   Andrade, S.; Ramalho, M. J.; Loureiro, J. A.; Pereira, M. C. Liposomes as biomembrane models: Biophysical techniques for drug-membrane interaction studies. *J. Mol. Liq.* **2021,** 334, 116141.

85.   Adão, R.; Cruz, P. F.; Vaz, D. C.; Fonseca, F.; Pedersen, J. N.; Ferreira-da-Silva, F.; Brito, R. M. M.; Ramos, C. H. I.; Otzen, D.; Keller, S.; Bastos, M. DIBMA nanodiscs keep α-synuclein folded. *Biochim. Biophys. Acta* **2020,** 1862, 183314.

86.   Hollmann, A.; Martinez, M.; Maturana, P.; Semorile, L. C.; Maffia, P. C. Antimicrobial Peptides: Interaction With Model and Biological Membranes and Synergism With Chemical Antibiotics. *Front. Chem.* **2018,** 6, 204.

87.   Wodlej, C.; Riedl, S.; Rinner, B.; Leber, R.; Drechsler, C.; Voelker, D. R.; Choi, J. Y.; Lohner, K.; Zweytick, D. Interaction of two antitumor peptides with membrane lipids - Influence of phosphatidylserine and cholesterol on specificity for melanoma cells. *PLoS One* **2019,** 14, e0211187.

88.   Hädicke, A.; Blume, A. Interaction of Short Pentavalent Cationic Peptides with Negatively Charged DPPG Monolayers and Bilayers: Influence of Peptide Modifications on Binding. *J. Phys. Chem. B* **2018,** 122, 10522-10534.

89.   Bastos, M.; Silva, T.; Teixeira, V.; Nazmi, K.; Bolscher, J. G.; Funari, S. S.; Uhrikova, D. Lactoferrin-derived antimicrobial peptide induces a micellar cubic phase in a model membrane system. *Biophys. J.* **2011,** 101, L20-2.

90.   Bai, G.; Nichifor, M.; Bastos, M. Association and Phase Behavior of Cholic Acid-Modified Dextran and Phosphatidylcholine Liposomes. *J. Phys. Chem. Lett.* **2010,** 1, 932-936.

91.   Reuter, M.; Schwieger, C.; Meister, A.; Karlsson, G.; Blume, A. Poly-l-lysines and poly-l-arginines induce leakage of negatively charged phospholipid vesicles and translocate through the lipid bilayer upon electrostatic binding to the membrane. *Biophys. Chem.* **2009,** 144, 27-37.

92.   Knobloch, J.; Suhendro, D. K.; Zieleniecki, J. L.; Shapter, J. G.; Köper, I. Membrane–drug interactions studied using model membrane systems. *Saudi J. Biol. Sci.* **2015,** 22, 714-718.

93.   Loura;, L. M. S.; Almeida, R. F. M. d. *Tópicos de Biofísica de Membranas.* 2004.

94.   Angelova, M. I.; Soléau, S.; Méléard, P.; Faucon, F.; Bothorel, P. In *Preparation of giant vesicles by external AC electric fields. Kinetics and applications*, Trends in Colloid and Interface Science VI, Darmstadt, 1992//, 1992; Helm, C.; Lösche, M.; Möhwald, H., Eds. Steinkopff: Darmstadt, 1992; pp 127-131.

95.   Milcovich, G.; Lettieri, S.; Antunes, F. E.; Medronho, B.; Fonseca, A. C.; Coelho, J. F. J.; Marizza, P.; Perrone, F.; Farra, R.; Dapas, B.; Grassi, G.; Grassi, M.; Giordani, S. Recent advances in smart biotechnology: Hydrogels and nanocarriers for

tailored bioactive molecules depot. *Advances in Colloid and Interface Science* **2017,** 249, 163-180.

96.   Ventola, C. L. The antibiotic resistance crisis: part 1: causes and threats. *Pharm. Ther.* **2015,** 40, 277-283.

97.   Munita, J. M.; Arias, C. A. Mechanisms of Antibiotic Resistance. *Microbiol. Spectrum* **2016,** 4, 10.1128/microbiolspec.VMBF-0016-2015.

98.   Organization, W. H. *Antimicrobial resistance: global report on surveillance.* 2014.

99.   Direção-Geral da Saúde (DGS), P. Prevenção e Controlo de Infeções e de Resistência aos Antimicrobianos em números - 2014. http://www.dgs.pt/estatisticas-de-saude/estatisticas-de-saude/publicacoes/portugal-controlo-da-infecao-e-resistencia-aos-antimicrobianos-em-numeros-2014.aspx

100.   Gould, I. M.; Bal, A. M. New antibiotic agents in the pipeline and how they can help overcome microbial resistance. *Virulence* **2013,** 4, 185-191.

101.   Dhingra, S.; Rahman, N. A. A.; Peile, E.; Rahman, M.; Sartelli, M.; Hassali, M. A.; Islam, T.; Islam, S.; Haque, M. Microbial Resistance Movements: An Overview of Global Public Health Threats Posed by Antimicrobial Resistance, and How Best to Counter. *Front. Public Health* **2020,** 8, 535668.

102.   Europe, W. H. O. W. Antimicrobial resistance. https://www.who.int/news-room/fact-sheets/detail/antimicrobial-resistance

103.   Europe, W. H. O. W. Preventing the COVID-19 pandemic from causing an antibiotic resistance catastrophe.

104.   Rawson, T. M.; Moore, L. S. P.; Zhu, N.; Ranganathan, N.; Skolimowska, K.; Gilchrist, M.; Satta, G.; Cooke, G.; Holmes, A. Bacterial and Fungal Coinfection in Individuals With Coronavirus: A Rapid Review To Support COVID-19 Antimicrobial Prescribing. *Clin. Infect. Dis.* **2020,** 71, 2459-2468.

105.   Brown, K. L.; Hancock, R. E. W. Cationic host defense (antimicrobial) peptides. *Curr. Opin. Immunol.* **2006,** 18, 24-30.

106.   Tossi, A.; Sandri, L.; Giangaspero, A. Amphipathic, α-helical antimicrobial peptides. *Biopolymers* **2000,** 55, 4-30.

107.   Wang, G.; Li, X.; Wang, Z. APD2: the updated antimicrobial peptide database and its application in peptide design. *Nucleic Acids Res.* **2009,** 37, D933-7.

108.   Zhao, X.; Wu, H.; Lu, H.; Li, G.; Huang, Q. LAMP: A Database Linking Antimicrobial Peptides. *PLOS ONE* **2013,** 8, e66557.

109.   Wang, G. The antimicrobial peptide database provides a platform for decoding the design principles of naturally occurring antimicrobial peptides. *Protein Sci.* **2020,** 29, 8-18.

110. Hoskin, D. W.; Ramamoorthy, A. Studies on anticancer activities of antimicrobial peptides. *Biochim. Biophys. Acta* **2008,** 1778, 357-75.

111. Hsieh, I. N.; Hartshorn, K. L. The Role of Antimicrobial Peptides in Influenza Virus Infection and Their Potential as Antiviral and Immunomodulatory Therapy. *Pharmaceuticals* **2016,** 9, 53.

112. Delattin, N.; Brucker, K.; Cremer, K.; Cammue, B. P.; Thevissen, K. Antimicrobial Peptides as a Strategy to Combat Fungal Biofilms. *Curr. Top Med. Chem.* **2017,** 17, 604-612.

113. Zhao, H.; Kinnunen, P. K. J. Modulation of the activity of secretory phospholipase A2 by antimicrobial peptides. *Antimicrob. Agents Chemother.* **2003,** 47, 965-971.

114. Bjorn, C.; Hakansson, J.; Myhrman, E.; Sjostrand, V.; Haug, T.; Lindgren, K.; Blencke, H. M.; Stensvag, K.; Mahlapuu, M. Anti-infectious and anti-inflammatory effects of peptide fragments sequentially derived from the antimicrobial peptide centrocin 1 isolated from the green sea urchin, Strongylocentrotus droebachiensis. *AMB Express* **2012,** 2, 67.

115. Brogden, K. A. Antimicrobial peptides: pore formers or metabolic inhibitors in bacteria? *Nat. Rev. Microbiol.* **2005,** 3, 238-50.

116. Gordon, Y. J.; Romanowski, E. G.; McDermott, A. M. A review of antimicrobial peptides and their therapeutic potential as anti-infective drugs. *Curr. Eye Res.* **2005,** 30, 505-515.

117. Mahlapuu, M.; Håkansson, J.; Ringstad, L.; Björn, C. Antimicrobial Peptides: An Emerging Category of Therapeutic Agents. *Front. Cell. Infect. Microbiol.* **2016,** 6.

118. Mahlapuu, M.; Björn, C.; Ekblom, J. Antimicrobial peptides as therapeutic agents: opportunities and challenges. *Crit. Rev. Biotechnol.* **2020,** 40, 978-992.

119. Haug, B. E.; Strom, M. B.; Svendsen, J. S. M. The Medicinal Chemistry of Short Lactoferricin-Based Antibacterial Peptides. *Curr. Med. Chem.* **2007,** 14, 1-18.

120. Silva, T.; Moreira Ana, C.; Nazmi, K.; Moniz, T.; Vale, N.; Rangel, M.; Gomes, P.; Bolscher Jan, G. M.; Rodrigues Pedro, N.; Bastos, M.; Gomes Maria, S.; Dunman, P. Lactoferricin Peptides Increase Macrophages' Capacity To Kill Mycobacterium avium. *mSphere* 2, e00301-17.

121. Carmona, G.; Rodriguez, A.; Juarez, D.; Corzo, G.; Villegas, E. Improved protease stability of the antimicrobial peptide Pin2 substituted with D-amino acids. *Protein J.* **2013,** 32, 456-66.

122. Matsuzaki, K. Control of cell selectivity of antimicrobial peptides. *Biochim. Biophys. Acta* **2009,** 1788, 1687-92.

123.   Güell, I.; Cabrefiga, J.; Badosa, E.; Ferre, R.; Talleda, M.; Bardají, E.; Planas, M.; Feliu, L.; Montesinos, E. Improvement of the Efficacy of Linear Undecapeptides against Plant-Pathogenic Bacteria by Incorporation of D-Amino Acids. *Appl. Environ. Microbiol.* **2011,** 77, 2667.

124.   Fernandez-Lopez, S.; Kim, H. S.; Choi, E. C.; Delgado, M.; Granja, J. R.; Khasanov, A.; Kraehenbuehl, K.; Long, G.; Weinberger, D. A.; Wilcoxen, K. M.; Ghadiri, M. R. Antibacterial agents based on the cyclic D,L-α-peptide architecture. *Nature* **2001,** 412, 452-5.

125.   Gough, M.; Hancock, R. E.; Kelly, N. M. Antiendotoxin activity of cationic peptide antimicrobial agents. *Infect. Immun.* **1996,** 64, 4922-7.

126.   Giuliani, A.; Pirri, G.; Nicoletto, S. Antimicrobial peptides: an overview of a promising class of therapeutics. *Open Life Sci.* **2007,** 2, 1-33.

127.   Yeaman, M. R.; Yount, N. Y. Mechanisms of Antimicrobial Peptide Action and Resistance. *Pharmacol. Rev.* **2003,** 55, 27-55.

128.   Gagnon, M. C.; Strandberg, E.; Grau-Campistany, A.; Wadhwani, P.; Reichert, J.; Burck, J.; Rabanal, F.; Auger, M.; Paquin, J. F.; Ulrich, A. S. Influence of the Length and Charge on the Activity of α-Helical Amphipathic Antimicrobial Peptides. *Biochemistry* **2017,** 56, 1680-1695.

129.   Dathe, M.; Nikolenko, H.; Meyer, J.; Beyermann, M.; Bienert, M. Optimization of the antimicrobial activity of magainin peptides by modification of charge. *FEBS Lett.* **2001,** 501, 146-50.

130.   Lyu, Y.; Yang, Y.; Lyu, X.; Dong, N.; Shan, A. Antimicrobial activity, improved cell selectivity and mode of action of short PMAP-36-derived peptides against bacteria and Candida. *Sci. Rep.* **2016,** 6, 27258.

131.   Hong, S. Y.; Park, T. G.; Lee, K.-H. The effect of charge increase on the specificity and activity of a short antimicrobial peptide. *Peptides* **2001,** 22, 1669-1674.

132.   Jiang, Z.; Vasil, A. I.; Hale, J. D.; Hancock, R. E.; Vasil, M. L.; Hodges, R. S. Effects of net charge and the number of positively charged residues on the biological activity of amphipathic α-helical cationic antimicrobial peptides. *Biopolymers* **2008,** 90, 369-83.

133.   Edwards, I. A.; Elliott, A. G.; Kavanagh, A. M.; Zuegg, J.; Blaskovich, M. A.; Cooper, M. A. Contribution of Amphipathicity and Hydrophobicity to the Antimicrobial Activity and Cytotoxicity of beta-Hairpin Peptides. *ACS Infect. Dis.* **2016,** 2, 442-450.

134.   Yeaman, M. R.; Yount, N. Y. Mechanisms of antimicrobial peptide action and resistance. *Pharmacol Rev* **2003,** 55, 27-55.

135.   Yin, L. M.; Edwards, M. A.; Li, J.; Yip, C. M.; Deber, C. M. Roles of Hydrophobicity and Charge Distribution of Cationic Antimicrobial Peptides in Peptide-Membrane Interactions. *J. Biol. Chem.* **2012,** 287, 7738-7745.

136.   Chen, Y.; Guarnieri, M. T.; Vasil, A. I.; Vasil, M. L.; Mant, C. T.; Hodges, R. S. Role of peptide hydrophobicity in the mechanism of action of α-helical antimicrobial peptides. *Antimicrob. Agents Chemother.* **2007,** 51, 1398-406.

137.   Falla, T. J.; Hancock, R. E. Improved activity of a synthetic indolicidin analog. *Antimicrob. Agents Chemother.* **1997,** 41, 771-5.

138.   Smirnova, M. P.; Afonin, V. G.; Shpen, V. M.; Tiagotin Iu, V.; Kolodkin, N. I. Structure-function relationship between analogues of the antibacterial peptide indolicidin. I. Synthesis and biological activity of analogues with increased amphipathicity and elevated net positive charge of the molecule. *Bioorg Khim* **2004,** 30, 458-65.

139.   Jenssen, H.; Hamill, P.; Hancock, R. E. W. Peptide Antimicrobial Agents. *Clin. Microbiol. Rev.* **2006,** 19, 491-511.

140.   Haney, E. F.; Hunter, H. N.; Matsuzaki, K.; Vogel, H. J. Solution NMR studies of amphibian antimicrobial peptides: Linking structure to function? *Biochim. Biophys. Acta, Biomembr.* **2009,** 1788, 1639-1655.

141.   Bechinger, B.; Gorr, S. U. Antimicrobial Peptides: Mechanisms of Action and Resistance. *J. Dent. Res.* **2017,** 96, 254-260.

142.   Broekman, D. C.; Zenz, A.; Gudmundsdottir, B. K.; Lohner, K.; Maier, V. H.; Gudmundsson, G. H. Functional characterization of codCath, the mature cathelicidin antimicrobial peptide from Atlantic cod (Gadus morhua). *Peptides* **2011,** 32, 2044-2051.

143.   Wang, J.; Ma, K.; Ruan, M.; Wang, Y.; Li, Y.; Fu, Y. V.; Song, Y.; Sun, H.; Wang, J. A novel cecropin B-derived peptide with antibacterial and potential anti-inflammatory properties. *PeerJ* **2018,** 6, e5369-e5369.

144.   Andreu, D.; Ubach, J.; Boman, A.; Wåhlin, B.; Wade, D.; Merrifield, R. B.; Boman, H. G. Shortened cecropin A-melittin hybrids Significant size reduction retains potent antibiotic activity. *FEBS Lett.* **1992,** 296, 190-194.

145.   Crichton, R. R. Structural and Molecular Biology for Chemists. In *Biological Inorganic Chemistry*, Crichton, R. R., Ed. Elsevier: Amsterdam, 2008; pp 43-76.

146.   Nguyen, L. T.; Haney, E. F.; Vogel, H. J. The expanding scope of antimicrobial peptide structures and their modes of action. *Trends Biotechnol.* **2011,** 29, 464-72.

147.   White, S. H.; Wimley, W. C. Hydrophobic interactions of peptides with membrane interfaces. *Biochim. Biophys. Acta, Rev. Biomembr.* **1998,** 1376, 339-52.

148. Krainer, G.; Hartmann, A.; Anandamurugan, A.; Gracia, P.; Keller, S.; Schlierf, M. Ultrafast Protein Folding in Membrane-Mimetic Environments. *J. Mol. Biol.* **2018,** 430, 554-564.

149. Schrodinger, L. *The AxPyMOL Molecular Graphics Plugin for Microsoft PowerPoint, Version 1.8*, 2015.

150. White, S. H.; Wimley, W. C.; Ladokhin, A. S.; Hristova, K. Protein folding in membranes: determining energetics of peptide-bilayer interactions. *Methods Enzymol* **1998,** 295, 62-87.

151. White, S. H.; Wimley, W. C. MEMBRANE PROTEIN FOLDING AND STABILITY: Physical Principles. *Annu. Rev. Biophys. Biomol. Struct.* **1999,** 28, 319-365.

152. Seelig, J. Thermodynamics of lipid–peptide interactions. *Biochim. Biophys. Acta, Biomembr.* **2004,** 1666, 40-50.

153. White, S. H.; Wimley, W. C. Hydrophobic interactions of peptides with membrane interfaces. *Biochimica et Biophysica Acta (BBA) - Reviews on Biomembranes* **1998,** 1376, 339-352.

154. Loura, L. M.; de Almeida, R. F.; Coutinho, A.; Prieto, M. Interaction of peptides with binary phospholipid membranes: application of fluorescence methodologies. *Chem. Phys. Lipids* **2003,** 122, 77-96.

155. Teixeira, V.; Feio, M. J.; Rivas, L.; De la Torre, B. G.; Andreu, D.; Coutinho, A.; Bastos, M. Influence of lysine N(ε)-trimethylation and lipid composition on the membrane activity of the cecropin A-melittin hybrid peptide CA(1-7)M(2-9). *J. Phys. Chem. B* **2010,** 114, 16198-208.

156. Klinger, J.; Keller, S. Peptide–Membrane Interactions Studied by Isothermal Titration Calorimetry. In *Biocalorimetry. Foundations and Contemporary Approaches*, 1st Edition ed.; Bastos, M., Ed. Boca Raton: 2016.

157. Bastos, M.; Bai, G.; Gomes, P.; Andreu, D.; Goormaghtigh, E.; Prieto, M. Energetics and partition of two cecropin-melittin hybrid peptides to model membranes of different composition. *Biophys. J.* **2008,** 94, 2128-41.

158. Huang, H. W. Action of Antimicrobial Peptides: Two-State Model. *Biochemistry* **2000,** 39, 8347-8352.

159. Melo, M. N.; Ferre, R.; Castanho, M. A. Antimicrobial peptides: linking partition, activity and high membrane-bound concentrations. *Nat. Rev. Microbiol.* **2009,** 7, 245-50.

160. Huan, Y.; Kong, Q.; Mou, H.; Yi, H. Antimicrobial Peptides: Classification, Design, Application and Research Progress in Multiple Fields. *Front. Microbiol.* **2020,** 11, 582779.

161.   Sevcsik, E.; Pabst, G.; Richter, W.; Danner, S.; Amenitsch, H.; Lohner, K. Interaction of LL-37 with Model Membrane Systems of Different Complexity: Influence of the Lipid Matrix. *Biophys. J.* **2008,** 94, 4688-4699.

162.   Bondar, A. N.; Keller, S. Lipid Membranes and Reactions at Lipid Interfaces: Theory, Experiments, and Applications. *J. Membr. Biol.* **2018,** 251, 295-298.

163.   Shai, Y. Mechanism of the binding, insertion and destabilization of phospholipid bilayer membranes by α-helical antimicrobial and cell non-selective membrane-lytic peptides. *Biochim. Biophys. Acta, Biomembr.* **1999,** 1462, 55-70.

164.   Bechinger, B.; Lohner, K. Detergent-like actions of linear amphipathic cationic antimicrobial peptides. *Biochim. Biophys. Acta* **2006,** 1758, 1529-39.

165.   Stella, L.; Mazzuca, C.; Venanzi, M.; Palleschi, A.; Didonè, M.; Formaggio, F.; Toniolo, C.; Pispisa, B. Aggregation and Water-Membrane Partition as Major Determinants of the Activity of the Antibiotic Peptide Trichogin GA IV. *Biophys. J.* **2004,** 86, 936-945.

166.   Yamaguchi, S.; Huster, D.; Waring, A.; Lehrer, R. I.; Kearney, W.; Tack, B. F.; Hong, M. Orientation and dynamics of an antimicrobial peptide in the lipid bilayer by solid-state NMR spectroscopy. *Biophys. J.* **2001,** 81, 2203-14.

167.   Silva, T.; Adão, R.; Nazmi, K.; Bolscher, J. G. M.; Funari, S. S.; Uhríková, D.; Bastos, M. Structural diversity and mode of action on lipid membranes of three lactoferrin candidacidal peptides. *Biochim. Biophys. Acta, Biomembr.* **2013,** 1828, 1329-1339.

168.   Hallock, K. J.; Lee, D.-K.; Ramamoorthy, A. MSI-78, an analogue of the magainin antimicrobial peptides, disrupts lipid bilayer structure via positive curvature strain. *Biophys. J.* **2003,** 84, 3052-3060.

169.   Matsuzaki, K.; Murase, O.; Fujii, N.; Miyajima, K. An Antimicrobial Peptide, Magainin 2, Induced Rapid Flip-Flop of Phospholipids Coupled with Pore Formation and Peptide Translocation. *Biochemistry* **1996,** 35, 11361-11368.

170.   Nicolas, P. Multifunctional host defense peptides: intracellular-targeting antimicrobial peptides. *FEBS J.* **2009,** 276, 6483-96.

171.   Rivas, L.; Luque-Ortega, J. R.; Andreu, D. Amphibian antimicrobial peptides and Protozoa: lessons from parasites. *Biochim. Biophys. Acta* **2009,** 1788, 1570-81.

172.   Kumar, P.; Kizhakkedathu, J. N.; Straus, S. K. Antimicrobial Peptides: Diversity, Mechanism of Action and Strategies to Improve the Activity and Biocompatibility In Vivo. *Biomolecules* **2018,** 8.

173.   Wiesner, J.; Vilcinskas, A. Antimicrobial peptides: the ancient arm of the human immune system. *Virulence* **2010,** 1, 440-64.

174. Pokorny, A.; Almeida, P. F. F. Kinetics of Dye Efflux and Lipid Flip-Flop Induced by δ-Lysin in Phosphatidylcholine Vesicles and the Mechanism of Graded Release by Amphipathic, α-Helical Peptides. *Biochemistry* **2004,** 43, 8846-8857.

175. Miteva, M.; Andersson, M.; Karshikoff, A.; Otting, G. Molecular electroporation: a unifying concept for the description of membrane pore formation by antibacterial peptides, exemplified with NK-lysin. *FEBS Lett* **1999,** 462, 155-8.

176. Powers, J. P.; Hancock, R. E. The relationship between peptide structure and antibacterial activity. *Peptides* **2003,** 24, 1681-91.

177. Silva, T.; Claro, B.; Silva, B. F. B.; Vale, N.; Gomes, P.; Gomes, M. S.; Funari, S. S.; Teixeira, J.; Uhríková, D.; Bastos, M. Unravelling a Mechanism of Action for a Cecropin A-Melittin Hybrid Antimicrobial Peptide: The Induced Formation of Multilamellar Lipid Stacks. *Langmuir* **2018,** 34, 2158-2170.

178. Epand, R. M.; Epand, R. F. Lipid domains in bacterial membranes and the action of antimicrobial agents. *Biochim. Biophys. Acta* **2009,** 1788, 289-94.

179. Arouri, A.; Dathe, M.; Blume, A. Peptide induced demixing in PG/PE lipid mixtures: a mechanism for the specificity of antimicrobial peptides towards bacterial membranes? *Biochim. Biophys. Acta* **2009,** 1788, 650-9.

180. Nguyen, L. T.; Schibli, D. J.; Vogel, H. J. Structural studies and model membrane interactions of two peptides derived from bovine lactoferricin. *J. Pept. Sci.* **2005,** 11, 379-89.

181. Haukland, H. H.; Ulvatne, H.; Sandvik, K.; Vorland, L. H. The antimicrobial peptides lactoferricin B and magainin 2 cross over the bacterial cytoplasmic membrane and reside in the cytoplasm. *FEBS Lett* **2001,** 508, 389-93.

182. Li, Y.; Xiang, Q.; Zhang, Q.; Huang, Y.; Su, Z. Overview on the recent study of antimicrobial peptides: origins, functions, relative mechanisms and application. *Peptides* **2012,** 37, 207-215.

183. Hale, J. D.; Hancock, R. E. Alternative mechanisms of action of cationic antimicrobial peptides on bacteria. *Expert Rev. Anti. Infect. Ther.* **2007,** 5, 951-9.

184. Zasloff, M. Antimicrobial peptides of multicellular organisms. *Nature* **2002,** 415, 389-395.

185. Hancock, R. E. W.; Sahl, H.-G. Antimicrobial and host-defense peptides as new anti-infective therapeutic strategies. *Nat. Biotechnol.* **2006,** 24, 1551-1557.

186. Matsuzaki, K.; Sugishita, K.; Fujii, N.; Miyajima, K. Molecular Basis for Membrane Selectivity of an Antimicrobial Peptide, Magainin 2. *Biochemistry* **1995,** 34, 3423-3429.

187.   McIntosh, T. J.; Simon, S. A. ROLES OF BILAYER MATERIAL PROPERTIES IN FUNCTION AND DISTRIBUTION OF MEMBRANE PROTEINS. *Annu. Rev. Biophys. Biomol. Struct.* **2006,** 35, 177-198.

188.   Wodlej, C.; Riedl, S.; Rinner, B.; Leber, R.; Drechsler, C.; Voelker, D. R.; Choi, J.-Y.; Lohner, K.; Zweytick, D. Interaction of two antitumor peptides with membrane lipids–Influence of phosphatidylserine and cholesterol on specificity for melanoma cells. *PLOS ONE* **2019,** 14, e0211187.

189.   Bevers, E. M.; Comfurius, P.; Zwaal, R. F. Regulatory mechanisms in maintenance and modulation of transmembrane lipid asymmetry: pathophysiological implications. *Lupus* **1996,** 5, 480-7.

190.   Beloribi-Djefaflia, S.; Vasseur, S.; Guillaumond, F. Lipid metabolic reprogramming in cancer cells. *Oncogenesis* **2016,** 5, e189.

191.   Tornesello, A. L.; Borrelli, A.; Buonaguro, L.; Buonaguro, F. M.; Tornesello, M. L. Antimicrobial Peptides as Anticancer Agents: Functional Properties and Biological Activities. *Molecules* **2020,** 25, 2850.

192.   Steinstraesser, L.; Kraneburg, U.; Jacobsen, F.; Al-Benna, S. Host defense peptides and their antimicrobial-immunomodulatory duality. *Immunobiology* **2011,** 216, 322-333.

193.   Andelman, D. Electrostatic Properties of Membranes: The Poisson-Boltzmann Theory. In *Structure and Dynamics of Membranes - From Cells to Vesicles*, Lipowsky, R.; Sackmann, E., Eds. North-Holland: 1995; Vol. 1, pp 603-642.

194.   Walz, D.; Teissié, J.; Milazzo, G. *Bioelectrochemistry of Membranes.* Birkhäuser Basel: 2012.

195.   Shaw, D. J. 7 - Charged interfaces. In *Introduction to Colloid and Surface Chemistry (Fourth Edition)*, Shaw, D. J., Ed. Butterworth-Heinemann: Oxford, 1992; pp 174-209.

196.   Simon, S. A.; McIntosh, T. J. *Peptide-Lipid Interactions.* Elsevier Science: 2002.

197.   Vargas, C.; Klingler, J.; Keller, S. Membrane partitioning and translocation studied by isothermal titration calorimetry. *Methods Mol Biol* **2013,** 1033, 253-71.

198.   Hilpert, K.; Fjell, C. D.; Cherkasov, A. Short linear cationic antimicrobial peptides: screening, optimizing, and prediction. *Methods Mol. Biol.* **2008,** 494, 127-59.

199.   Oren, Z.; Shai, Y. Mode of action of linear amphipathic α-helical antimicrobial peptides. *J. Pept. Sci.* **1998,** 47, 451-463.

200.   Abrunhosa, F.; Faria, S.; Gomes, P.; Tomaz, I.; Pessoa, J. C.; Andreu, D.; Bastos, M. Interaction and lipid-induced conformation of two cecropin-melittin hybrid

peptides depend on peptide and membrane composition. *J. Phys. Chem. B.* **2005,** 109, 17311-9.

201.   Adão, R.; Nazmi, K.; Bolscher, J.; Bastos, M. C- and N-truncated antimicrobial peptides from LFampin 265 - 284: Biophysical versus microbiology results. *Journal of Pharmacy And Bioallied Sciences* **2011,** 3, 60-69.

202.   Adao, R.; Seixas, R.; Gomes, P.; Pessoa, J. C.; Bastos, M. Membrane structure and interactions of a short Lycotoxin I analogue. *J. Pept. Sci.* **2008,** 14, 528-34.

203.   Adao, R.; Nazmi, K.; Bolscher, J. G.; Bastos, M. C- and N-truncated antimicrobial peptides from LFampin 265 - 284: Biophysical versus microbiology results. *J. Pharm. Bioallied. Sci.* **2011,** 3, 60-9.

204.   Zompra, A. A.; Galanis, A. S.; Werbitzky, O.; Albericio, F. Manufacturing peptides as active pharmaceutical ingredients. *Future Med. Chem.* **2009,** 1, 361-77.

205.   Otvos, L. Peptide-Based Drug Design: Here and Now. In *Peptide-Based Drug Design*, Otvos, L., Ed. Humana Press: Totowa, NJ, 2008; pp 1-8.

206.   Gause, G.; Brazhnikova, M. Gramicidin S and its use in the Treatment of Infected Wounds. *Nature* **1944,** 154, 703-703.

207.   Choi, J. S.; Joo, S. H. Recent Trends in Cyclic Peptides as Therapeutic Agents and Biochemical Tools. *Biomol. Ther.* **2020,** 28, 18-24.

208.   Tapeinou, A.; Matsoukas, M. T.; Simal, C.; Tselios, T. Review cyclic peptides on a merry-go-round; towards drug design. *Biopolymers* **2015,** 104, 453-61.

209.   Du, X.; Li, Y.; Xia, Y. L.; Ai, S. M.; Liang, J.; Sang, P.; Ji, X. L.; Liu, S. Q. Insights into Protein-Ligand Interactions: Mechanisms, Models, and Methods. *Int. J. Mol. Sci.* **2016,** 17.

210.   Horton, D. A.; Bourne, G. T.; Smythe, M. L. Exploring privileged structures: The combinatorial synthesis of cyclic peptides. *Mol. Diversity* **2000,** 5, 289-304.

211.   Joo, S. H. Cyclic peptides as therapeutic agents and biochemical tools. *Biomol. Ther.* **2012,** 20, 19-26.

212.   De Santis, P.; Morosetti, S.; Rizzo, R. Conformational Analysis of Regular Enantiomeric Sequences. *Macromolecules* **1974,** 7, 52-58.

213.   Ghadiri, M. R.; Granja, J. R.; Milligan, R. A.; McRee, D. E.; Khazanovich, N. Self-assembling organic nanotubes based on a cyclic peptide architecture. *Nature* **1993,** 366, 324-327.

214.   Hartgerink, J. D.; Granja, J. R.; Milligan, R. A.; Ghadiri, M. R. Self-Assembling Peptide Nanotubes. *J. Am. Chem. Soc.* **1996,** 118, 43-50.

215.   Rodríguez-Vázquez, N.; García-Fandiño, R.; Amorín, M.; Granja, J. R. Self-assembling α,γ-cyclic peptides that generate cavities with tunable properties. *Chem. Sci.* **2016,** 7, 183-187.

216.	Sanchez-Quesada, J.; Ghadiri, M. R.; Bayley, H.; Braha, O. Cyclic Peptides as Molecular Adapters for a Pore-Forming Protein. *J. Am. Chem. Soc.* **2000,** 122, 11757-11766.

217.	Motesharei, K.; Ghadiri, M. R. Diffusion-Limited Size-Selective Ion Sensing Based on SAM-Supported Peptide Nanotubes. *J. Am. Chem. Soc.* **1997,** 119, 11306-11312.

218.	Ashkenasy, N.; Horne, W. S.; Ghadiri, M. R. Design of self-assembling peptide nanotubes with delocalized electronic states. *Small* **2006,** 2, 99-102.

219.	Ghadiri, M. R.; Granja, J. R.; Buehler, L. K. Artificial transmembrane ion channels from self-assembling peptide nanotubes. *Nature* **1994,** 369, 301-304.

220.	Granja, J. R.; Ghadiri, M. R. Channel-Mediated Transport of Glucose across Lipid Bilayers. *J. Am. Chem. Soc.* **1994,** 116, 10785-10786.

221.	González-Freire, E.; Novelli, F.; Pérez-Estévez, A.; Seoane, R.; Amorín, M.; Granja, J. R. Double orthogonal click reactions for the development of antimicrobial peptide nanotubes. *Chemistry* **2020**.

222.	Calvelo, M.; Granja, J. R.; Garcia-Fandino, R. Competitive double-switched self-assembled cyclic peptide nanotubes: a dual internal and external control. *Phys. Chem. Chem. Phys.* **2019,** 21, 20750-20756.

223.	Mika, J. T.; Moiset, G.; Cirac, A. D.; Feliu, L.; Bardaji, E.; Planas, M.; Sengupta, D.; Marrink, S. J.; Poolman, B. Structural basis for the enhanced activity of cyclic antimicrobial peptides: the case of BPC194. *Biochim. Biophys. Acta* **2011,** 1808, 2197-205.

224.	García-Fandiño, R.; Amorín, M.; Castedo, L.; Granja, J. R. Transmembrane ion transport by self-assembling α,γ-peptide nanotubes. *Chem. Sci.* **2012,** 3, 3280-3285.

PART II
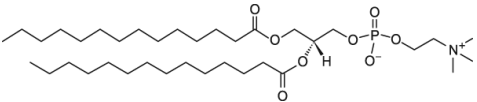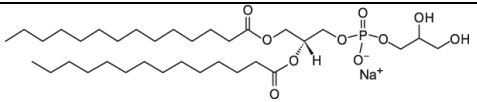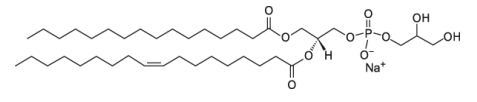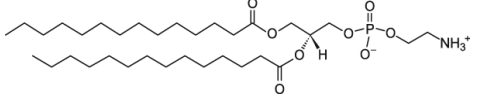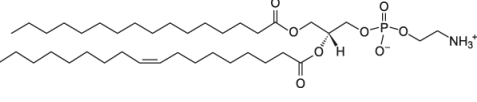
Experimental Section

Chapter 5. Preparation of Lipid Model Membranes

5.1. Materials

All lipids used in this thesis were purchased from Avanti Polar Lipids, Alabama, USA and used as received (Table 5.1).

Table 5. 1. Name, Temperature of gel to liquid crystalline phase transition (T_m), structure and M_w of each lipid used in this thesis.

Phospholipids	T_m/°C	Structure	M_w/gmol^{-1}
PHOSPHATIDYLCHOLINE			
DMPC 14:0 PC 1,2-dimyristoyl-*sn*-glycero-3-phosphocholine	24		677.50
PHOSPHATIDYLGLYCEROL			
DMPG 14:0 PG 1,2-dimyristoyl-*sn*-glycero-3-phospho-(1'-rac-glycerol)	23		688.43
POPG 16:0-18:1 PG 1-palmitoyl-2-oleoyl-*sn*-glycero-3-phospho-(1'-rac-glycerol)	-2		770.51
PHOSPHATIDYLETHANOLAMINE			
DMPE 14:0 PE 1,2-dimyristoyl-*sn*-glycero-3-phosphoethanolamine	50		635.45
POPE 16:0-18:1 PE 1-palmitoyl-2-oleoyl-*sn*-glycero-3-phosphoethanolamine	25*		717.53

* POPE presents also a fluid to hexagonal transition, at 71°C

All other reagents were from Merck, Germany. All solutions were prepared using ultra-pure water from a Millipore system, with resistivity 18.2 MΩ cm at 25 °C.

5.2. Lipid Film Preparation

The pure lipid or the mixtures at different molar ratios were weighted in a Mettler Toledo balance (± 0.0005 g) in appropriate amounts and dissolved in a round bottom flask in an azeotropic mixture of chloroform/methanol (87.4:12.6 %(v/v)), since at this proportion chloroform and methanol form an azeotropic mixture, which guarantees that the solvent composition is maintained through the solvent evaporation process. A lipid film was obtained by evaporating the azeotropic mixture, either under vacuum at a rotary evaporator at 70 °C or under a slow flux of N_2. The films were then kept over-night under high vacuum (< 10 mbar) to remove any trace of the organic solvents.

Thereafter, the lipid films were then hydrated for 30 minutes with i) a previously warmed buffer HEPES (10 mM HEPES, 150 mM NaCl, 0.02% NaN_3, 1 mM EDTA, pH 7.45, with 0.7% DMSO when **CP1** is studied), for **DSC**, **fluorescence** and **SAXS** experiments; ii) water for **ATR-FTIR** experiments; iii) with a 40 mM carboxyfluorescein solution for **leakage** experiments - at *ca*. 10 °C above the gel-to-liquid crystalline phase transition temperature (T_m).

The lipids suspension obtained after hydration underwent several cycles of vortex/incubation at a temperature above T_m, creating a multilamellar vesicles suspension (MLVs). The MLVs were frozen in liquid nitrogen and thawed above T_m, a sequence repeated 3 times.

In the case of the samples used in **SAXS** (**manuscript VI**), peptide solutions prepared in the same buffer as the liposomes, were added at different lipid-to-peptide (L:P) ratios to the MLVs (DMPE) and OLVs (PE:PG) suspensions, and the samples were incubated for 30 min above T_m. The samples were then transferred with a long needle syringe to into glass capillaries (Spezialglas Markröhrchen 1.5 mm capillaries; Glass Technik 37 & Konstruktion – Müller & Müller OHG, Germany), and centrifuged for 2 min at 2000 g. This step was carefully repeated until a deposit and a significant amount of supernatant in the capillaries were seen, to guarantee that all samples were studied at high water contents. Lastly, the capillaries were sealed by a melted commercial wax.

When large unilamellar vesicles (LUVs) were used (see **Publications II – V**), they were then obtained through extrusion of the MLVs using two staked polycarbonate filters with a pore diameter of 100 nm (Whatman, Nucleopore (NJ, USA)), in either a 10 mL stainless steel extruder from Lipex Biomembranes Inc. (Vancouver, Canada), under

inert (N_2) atmosphere (**DSC** in **publications II** and **IV, Fluorescence** samples for **publication V**), or with a manually powered extruder of 500 μL capacity (Liposofast-Basic (BPS, UK)) (**ATR-FTIR**, **publications II, III** and **IV**, and **leakage** samples, **publication V**). Three sequences of extrusion/vortex/freeze-thaw were made, followed by 15-20 passages through the extruder. The final phospholipid concentration was determined using a modified version of the Bartlett phosphate assay[1].

The average particle size of the obtained LUVs was measured by dynamic light scattering (DLS) on a Malvern Zetasizer Nano ZS from Malvern Instruments (Malvern, UK). The measurements were performed above the transition temperature (T_m) at a total lipid concentration of 0.1 mM, using a He-Ne laser (wavelength 633 nm) as a source of incident light, and operating at a scattering angle of 173°.

The Buffer properties (refractive index, density and viscosity) to be used in the DLS measurements were determined at 37°C and 60°C (see Supplementary Material of **publication II**).
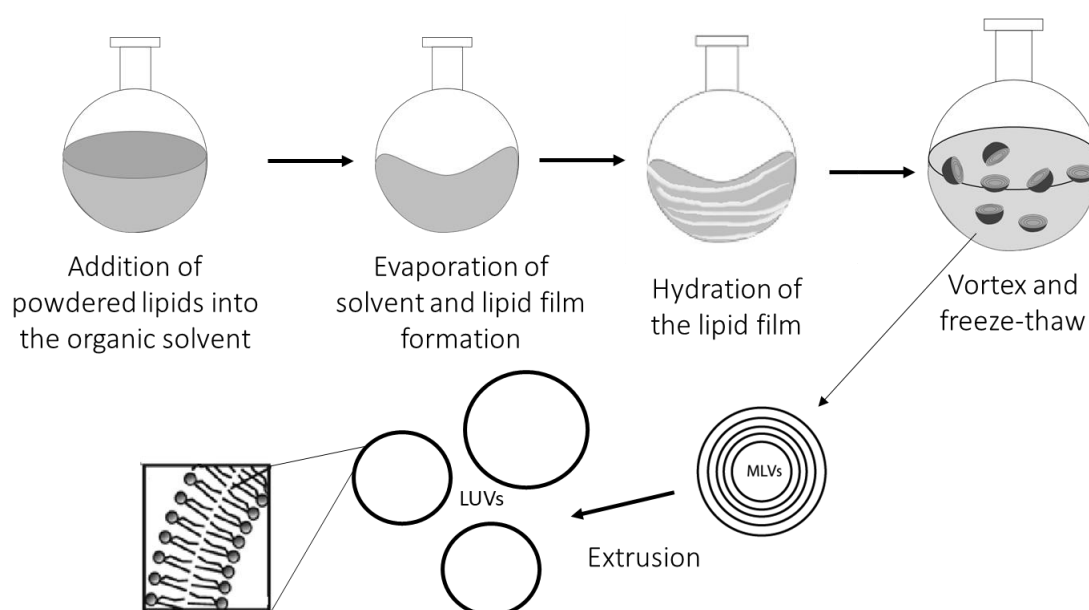
Fig. 5.2.1. Schematic representation of liposome's preparation, involving all steps of solubilization in the organic solvent, evaporation, hydration, vortex and freeze-thaw, and final form (MLVs and LUVs).

Chapter 6. Biophysical Techniques Used in the Study of the Interactions of Antimicrobial Cyclic Peptides and Lipid Model Membranes

6.1. Differential Scanning Calorimetry

Phospholipids have thermotropic changes transitions, *i.e.*, phase transitions induced by temperature change (see **chapter 1**, **section 1.1**)., that are thus very easy to determine by differential scanning calorimetry (DSC). Differential scanning calorimetry is an experimental technique that follows the heat capacity of a system as a function of temperature change, under controlled rate conditions. This technique is fundamental for determination of lipid temperature-induced phase transitions[2-5] and has emerged as a most valuable tool to study peptide-membrane interactions.

To study the interaction of cyclic peptides with different bacterial membrane models, a power-compensated DSC (VP-DSC by MicroCal/Malvern) was used. In this apparatus the sample cell and the reference cell are heated (or cooled) at constant temperature rate, at constant pressure, in a block is surrounded by an adiabatic jacket (Fig. 6.1. A). During the scan, the same power is delivered to both cells by the heaters positioned under each cell. When a thermal event occurs in the sample cell, the power delivered to this cell is either decreased on increased (depending on the exothermic or endothermic nature of the process), to still keep the temperature difference between the two sides close to zero. The differential power between the two cells, reference and sample, (DP), will rise in the positive or negative direction, if endo- or exothermic processes occur, respectively. The power signal is recorded as a function of time (heat flux) and can thus be easily converted to heat capacity (Cp) as a function of temperature by use of then scanning rate[6, 7], *i.e.,* using the ratio between the heat flux ($\frac{dQ}{dt}$) and the scanning rate ($\frac{dT}{dt}$):

$$Cp = \frac{dQ}{dt} \Big/ \frac{dT}{dt} = \frac{dQ}{dT} \tag{6.1.1}$$

From this, the enthalpy of transition ($\Delta_{trans}H$) can be obtained by integration of the C_p vs T curve, in the appropriate transition interval[8], as:

$$\Delta_{\text{trans}}H = \int_{T_1}^{T_2} Cp \ dT \qquad (6.1.2)$$

Integrating the curve C_p/T as a function of T provides the entropy change of the phase transition as:

$$\Delta S = \int_{T1}^{T2} \frac{C_p(T)}{T} \ dT \qquad (6.1.3)$$

The DSC experiment provides also information on the transition temperature (T_{m}), which is the temperature of maximum C_{p}, and insight into the cooperativity of the thermotropic phase transition, as it is proportional to the peak width[9]. The van't Hoff enthalpy (ΔH_{VH}) is derived from the shape analysis of the calorimetric C_{p}=f(T) data, but can be easily estimated as:

$$\Delta H_{VH} = \frac{4 \times R \times T_m^2 \times C_{p,max}(T_m)}{\Delta_{trans}H} \qquad (6.1.4)$$

Importantly, the ratio $\Delta H_{\text{VH}}/\Delta_{\text{trans}}H$ provides the size of cooperative domain, *i.e.*, the number of lipids per cooperative unit at the phase transition.

The half width at half height of the transition (HWHH) is widely used to compare the cooperative of the transitions. As an example, we can see the gel to fluid phase transition of MLVs and LUVs, prepared from the same lipid. (Fig 6.1.C). The transition peak for MLVs will appear as a much sharper peak as compared to then one for LUVs, and consequently smaller values of HWHH are obtained for the former.

The DSC can be used as screening tool to establish the influence of a component added to the liposome preparation, being an easy and fundamental tool in this regard, as it produces a 'fingerprint' of the interactions. In present study, DSC was used to characterize the effect of the peptides on the lipid model membrane's phase transitions. In all cases, the effect of the peptide on the transition shape, width, T_{m} and $\Delta_{\text{trans}}H$ was observed and analyzed to understand the peptide/lipid interactions present.

A

B

C
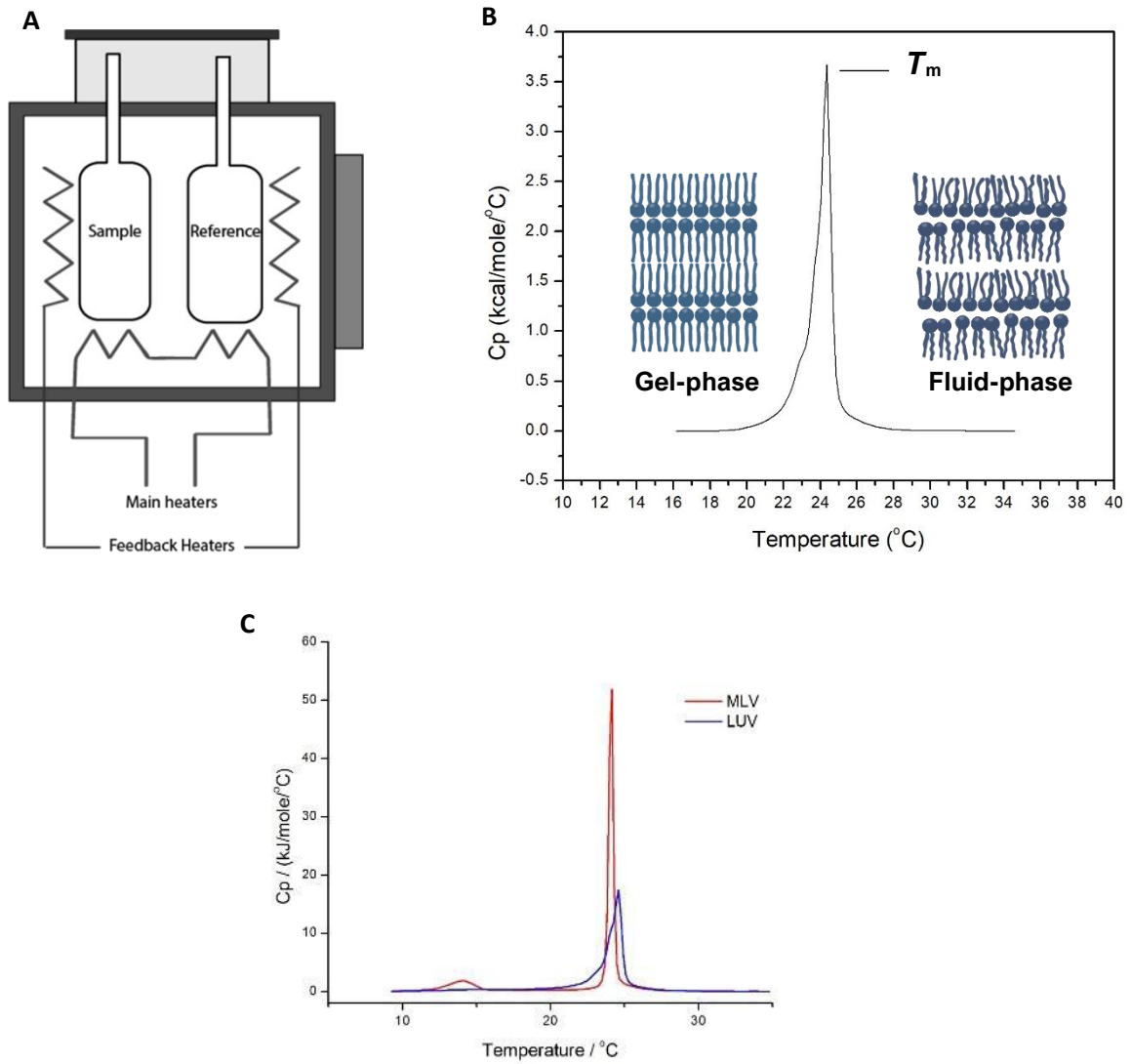
Fig. 6. 1. A. Schematic representation of the DSC apparatus here used. Temperature differences between the reference cell and the sample cell are measured and the difference is maintained close to zero by a feedback heating system. **B.** Thermogram of main lipid transition, gel to fluid phase, where T_m is the temperature of maximum C_p **C.** Thermograms for MLVs and LUVs of the same lipid, DMPC. Differences can be observes as regarding maximum in the intensity of the peaks, cooperativity (HWHH), and the presence of clearly seen pre-transition for MLVs[10].

6.2. Polarized Attenuated Total Reflection Fourier Transform Infrared Spectroscopy

Attenuated total reflection Fourier transform infrared spectroscopy (ATR-FTIR) is a useful method for the identification of the chemical nature, orientation, and conformation of molecules at an interface. As shown in publications **II**, **III** and **IV**, this spectroscopic technique allows structural characterization of peptides and proteins, as well as their interactions with membranes, without the need of external labelling probes, and with only a few micrograms of sample[11-14].

FTIR spectroscopy uses modulated, mid-infrared energy, and the infrared light is absorbed at specific frequencies that are directly related to the atom-to-atom vibrational bond energies in the molecule. When the bond energy of the vibration and the energy of mid-infrared light are equivalent, the bond can absorb that energy. As different bonds in a molecule vibrate at different energies, they will absorb at different wavelengths of the IR radiation. The position (frequency) and the intensity of these individual absorption bands contribute to the overall spectrum, creating a characteristic fingerprint of the molecule.

ATR-FTIR directs an infrared light beam through a trapezoidal high refractive index medium, transparent to the infrared radiation of interest, resulting in an evanescent wave at the reflecting interface (Fig. 6.2). Therefore, the ATR accessory measures the changes that occur in an internally reflected Infra Red (IR) beam when it comes in contact with the sample. As a result, in regions of the IR spectrum where the sample absorbs energy, the evanescent wave will be attenuated. The attenuated beam returns to the crystal, and exits its opposite end, being finally directed to the detector in the IR spectrometer, which records the attenuated IR beam as an interferogram signal, which can then be used to generate an IR spectrum.

A total reflection of the beam when it impinges on the surface of the internal reflection element (IRE) occurs below a critical angle, and is dependent on the refractive index of the material and on the external medium[15]. An evanescent wave, whose amplitude falls off exponentially with the distance, z^*, from the interface, with a characteristic decay length (depth of penetration, d_p), is created by the superimposition of incoming and reflected waves, aligned with the normal of the totally reflecting surface[11, 16]. The relation between these parameters can be found in Eq. 6.2.1.

$$E = E_0 \exp^{-z^*/d_p}$$
(6.2.1)

where E_0 is the time averaged electric field intensity at the interface, in the rarer medium (medium whose particles are loosely packed), E, is the time averaged field intensity in the rarer medium at a distance z^* from the interface and d_p is the depth of penetration of the evanescent field.

$$d_p = \frac{\lambda/n_1}{2\pi\sqrt{(\sin^2\theta - \left(\frac{n_2}{n_1}\right)^2)}} \qquad (6.2.2)$$

where λ is the wavelength of the IR light, n_1 and n_2 are index of the internal reflection element and external medium, respectively, and θ is the angle of incidence. This evanescent field makes the interaction between infrared light and the sample on the surface of the IRE possible, within the penetration depth of the field. Thus, the samples should be as must possible in contact with the IRE, and for this, films of membranes, with or without proteins or peptides are produced, simply by evaporating the solvent prior to the measurement[11, 17].
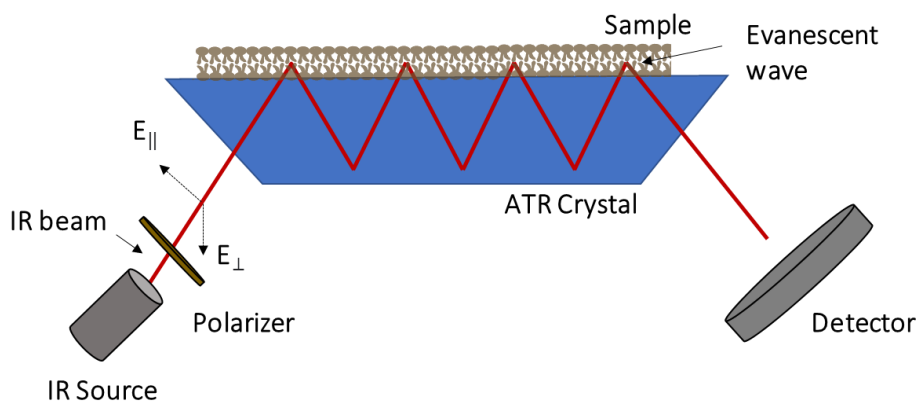
Fig. 6. 2. Representation of the light pathway of an ATR-FTIR system (from IR Source to the detector). The IR beam passes through the ATR crystal that has the sample on the top. The evanescent wave penetrates and is absorbed by the sample. The polarizer generates parallel (***E****ll*) and perpendicular polarized incident beam (***E****⊥).* Adapted from[18].

All molecules present in the path of the evanescent field contribute to the spectrum, where different bands need to be analyzed to obtain structural information. In this study, as the goal is to study antimicrobial *D,L*-α-cyclic interactions with lipid membranes, as well as to determine their relative position, the lipid membrane spectrum needs to be obtained with the phospholipids parallel to surface and in close contact with the IRE surface. To this, a lipid film is produced at the crystal surface by slowly evaporating the LUV suspension under a stream of nitrogen, obtaining oriented

multilayer stacks, as described previously[11, 17]. The same procedure is adopted for the peptide in solution and when the suspension contains mixtures of lipid and peptide.

The study is performed in two steps: **i)** analysis of the ATR-FTIR spectra to get **structural information** on the peptides in solution and/or in contact with the membranes, and **ii)** analysis of **ATR-FTIR dichroic spectra** acquired by using a polarizer, with subsequent calculation of the dichroic ratios.

Structural information on the peptides can be obtained by the analysis of amide I (1600-1700 cm^{-1}) and amide II (1510-1580 cm^{-1}) absorption bands. These bands help in revealing secondary structures that peptides and proteins may adopt in/without the presence of lipids. The main absorption bands associated with the lipid groups are i) the ester carbonyl stretching band (~1730 cm^{-1}) that is sensitive to hydrogen bonding and is used to monitor hydration at the membrane-water interface and ii) the methylene vibrations of the fatty acyl chains (~2850 cm^{-1} for symmetric stretch and ~2920 cm^{-1} for antisymmetric stretch), that can be related with the physical properties of lipids under various conditions, being very sensitive indicators of hydrocarbon chain-melting phase transitions[19, 20].

When polarized lens is used together with ATR-FTIR (polarized ATR-FTIR), information about the orientation of phospholipids in the lipid membrane and of the peptides relative to the membrane normal can be obtained. For this, the dichroic ratio (R^{ATR}) is calculated from the ratio of the integrated absorption for parallel ($A_\parallel$) *vs* perpendicular ($A_\perp$) polarized incident light[11, 21]:

$$\mathbf{R^{ATR}} = \frac{\mathbf{A_\parallel}}{\mathbf{A_\perp}} = \frac{\int \mathbf{A_\parallel}(\upsilon)\,\mathbf{d\upsilon}}{\int \mathbf{A_\parallel}(\upsilon)\,\mathbf{d\upsilon}} \tag{6.2.3}$$

In Eq. 6.2.3 $\int A_i(\upsilon)\,d\upsilon$ denotes the absorbances integrated through an entire absorbance band for parallel or perpendicular polarized incident light. The lipid in the bilayer as well as the present peptides/proteins can have fluctuations, and dichroic ratio can thus be related to an orientational order parameter (S). For axially symmetric distributions (R=1), it is possible to calculate order parameters as:

$$S = (3\,cos^2\theta^* - 1)/2 \tag{6.2.4}$$

where θ^* is the angle between the main axis of symmetry of the element of interest also denominated as molecular director, and the membrane normal. When the

molecules suffer a perturbation, they will present an angle tilt (γ_0), relative to the IR beam (R≠1)[11, 16, 20]:

$$R = 1 + 3 \, sin^2 \gamma \, S \, / \, (1 - S)$$
(6.2.5)

where S is the order parameter between the angle of the transition dipole moment and the normal of IRE and γ is the angle of incidence of the IR beam. γ can be related to γ_0 by the Snell's law, and the refractive index (n)[20]:

$$\gamma = sin^{-1}(\sin \gamma_0 \, /n)$$
(6.2.6)

Qualitative analysis of dipole moment deviations is important to determine peptides' orientation for certain groups and can be obtained from the subtraction of $A_\perp$ to $A_\parallel$ polarized spectra. As an example, if the difference spectra show a negative peak for the Amide I band together with a positive one for the Amide II band (related to the amide C=O bonds) we can conclude that the peptide lies parallel to the membrane plane.

6.3. Fluorescence

Fluorescence spectroscopy is versatile technique that can be applied characterize the partition of molecules to model membrane systems if they possess a fluorophore. It is an extremely sensitivity technique, of minimal induced perturbation, where intrinsic timescale is appropriate to follow dynamic processes that take place in membranes [22-26]
   Fluorescence is a type of luminescence, where the emission of light from a molecule (fluorophore) occurs, caused by absorption of photons, exciting a molecule to excited states[27]. The mechanism of the excitation/relaxation in the molecule can be illustrated through the Jablonski diagram (Fig. 6.3. A).

A

B
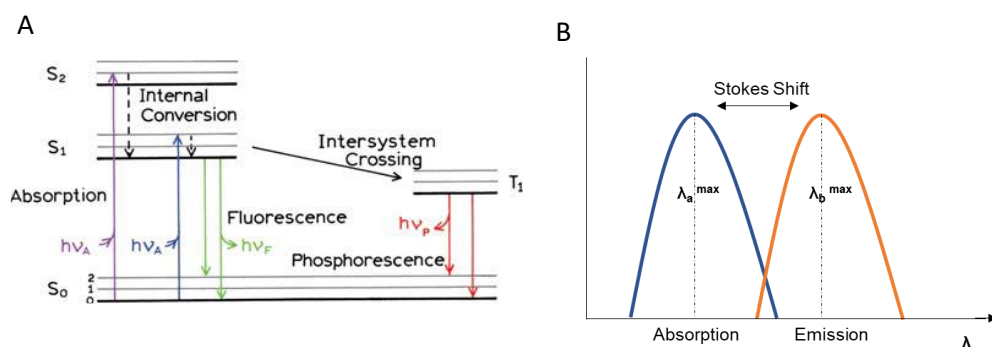
Fig. 6. 3. A. Jablonski diagram showing the occurrence of fluorescence emission after excitation (absorption) of an electron from the singlet ground state (S_0) to the excited state (S_2). Other effects are also represented[27]. **B.** Representation of the Stokes shift, *i.e.*, the difference in wavelength/energy between the excitation and emission spectra, reflecting the difference in absorption and emission energies.

Following light absorption by the fluorophore, the excitation process from the ground state (S_0) to the excited state level (S_1 or S_2) is very fast. After excitation, the molecule is quickly relaxed to the lowest vibrational level of the excited electronic state (S_1). This process, called internal conversion, occurs on a timescale of picoseconds or less. Fluorescence emission occurs as the fluorophore returns from the singlet electronic excited state to any vibrational state of the electronic ground state (S_0). Fluorescence emission typically occurs at longer wavelengths, *i.e.*, lower energy of emission as compared to absorbance -this shift is known as Stokes Shift (Fig. 6.3. B). and the emission spectra are usually independent of the excitation wavelength[27].

In this thesis, we used fluorescence mainly to follow peptide's partition to the membranes. In this case, the fluorophore was the amino acid tryptophan, present in all the studied cyclic peptides. Tryptophan has a dominant indole group that absorbs near 280 nm and emits near 340 nm. Its emission spectrum is highly sensitive to solvent polarity and its emission may be blue shifted if buried and shift to longer wavelengths if exposed to the solvent. For the partition studies we used steady state fluorescence (SS) and time-resolved fluorescence spectroscopy (TRFS). Fluorescence techniques were further use in the study of the peptides induced leakage experiments, and in this case using an extrinsic fluorophore, carboxyfluorescein, that was encapsulated in the model membranes (**publication V**).

Detailed information on the mathematic framework and models used with these techniques can be found in the referred **publication V**.

6.4. X-ray Diffraction

X-ray diffraction (or scattering) is a fundamental method for the determination of structure of condensed and soft matter [28]. In diffraction measurements, an X-ray photon beam with a specific wavelength interacts with an electron cloud of atoms of a sample and scatters elastically, *i.e.*, without losing or taking up energy from the atoms.

When a X-ray beam hits a lyotropic liquid crystal, due to their long range periodicity and short range disorder, a reduced number of sharp diffraction peaks from the sample appears. These diffracted beams should be as sharp as the incident beam, although due to a variety of factors, like crystallite size, disorder, or homogeneity, they can be broadened[29, 30]. The incident X-ray beam on a set of periodic points in a lattice may lead to the maximum diffraction in certain directions, in which scattered X-rays are in the same phase [31]. Therefore, diffraction peaks, referred to as Bragg peaks and represented by diffraction patterns, are obtained by the reflection of different planes, spatially averaged[32-34]. Each of these Bragg peak fits with a specific lattice plane due to reciprocal lattice points, as explained next.

The electron density profile (recorded intensity) needs to be transformed by the Fourier transform, where a form factor $F(q)$ is obtained, that varies as a function of the modulus of the scattering vector q, resulting from the photon wavelength λ and the scattering angle 2Θ[32]:

$$q = \frac{4\pi sin\theta}{\lambda}$$
(6.4.1)

The intensity distribution of a system can be affected by particle size, volume, contrast (electron density), sample to detector distance, resolution, or beam collimation.
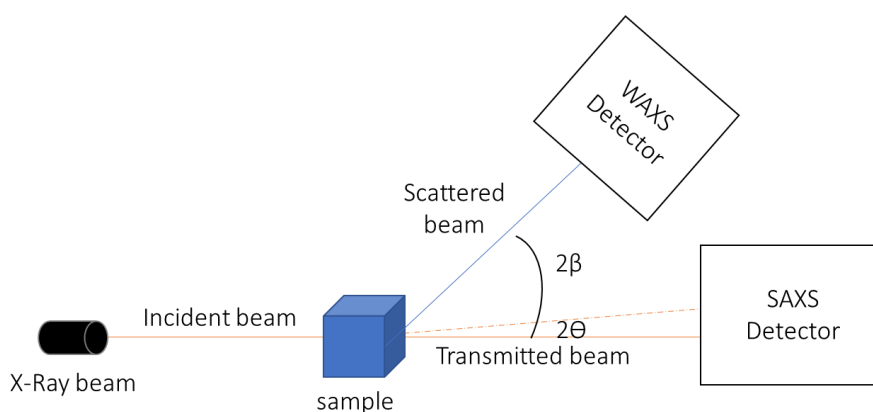
Fig. 6. 4. Schematic representation of X-Ray scattering setup, with WAXS and SAXS detector, where 2Θ is the scattering angle for SAXS detector and 2β for the WAXS detector.

X-ray techniques can be used to study lipid systems, since they allow to study positional correlations of lipid aggregates on various length scales. The lipids' electron density in lamellar phases varies across the lipid bilayer (Fig. 6.5). X-rays are sensitive to the electron rich phosphate of the headgroup, and quite insensitive to the choline group, thus the corresponding electron density profile can be represented by the summation of three Gaussians distributions, two centered at the electrodense lipid head groups and one of negative amplitude in the middle of the bilayer, where the hydrocarbon chains meet.[32][35, 36].
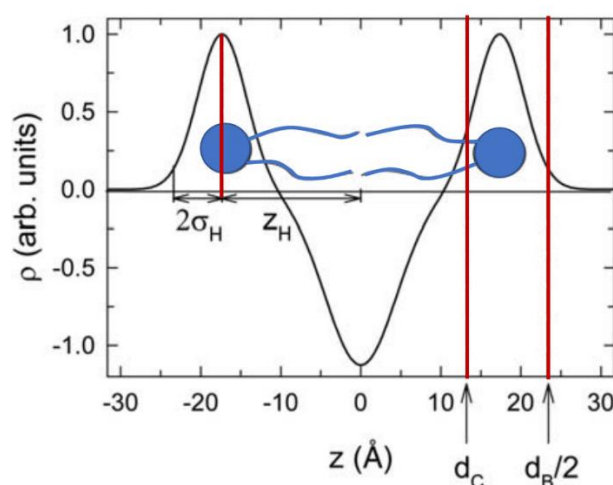
Fig. 6. 5. The electron density profile of lipid bilayers across the membrane, represented by the summation of three Gaussians. Z_H is the position of the headgroup, i.e., corresponds to the distance between half of the lipid's headgroup and the end of the tail (the double layer center), and $2\sigma_H$ is twice the head's width. The membrane thickness, d_B, and the boundary of the hydrocarbon region, $2d_C$, can be determined using parameters from the gel phase, by following $d_B=2(Z_H+2\sigma_H)$[36]. Adapted from[32].

X-ray diffraction measurements are a powerful tool to give structural information on lipid mesophases as well as on polymorphic changes in the lipid bilayer. They are widely applied to lipid model membranes, as lipid dispersions in water form structures with long-range periodic order that will diffract the X-rays in a particular pattern, depending on the existent phase and the respective space group[37, 38].

Lipid studies use mostly Small Angle X-ray Scattering (SAXS) and Wide Angle X-ray Scattering (WAXS). In the case of SAXS, X-rays of wavelength 0.1-0.2 nm are scattered by the lipid/water sample at very low angles (0.1 – 10º). Using this angular range provides information on the characteristic distances of partially ordered materials such as multilamellar liposome preparations. As regarding WAXS, information is gathered on structures of sub-nanometer size, using angles > 5º. Therefore, the small angle region of the diffraction pattern in SAXS measurements is used to identify the symmetry that defines the phase, providing structural information on macromolecules

with sizes between 5-25 nm, with repeat distances in partially ordered samples up to 150 nm, while WAXS can give information on the molecular packing, or the short-range organization, *i.e.,* the packing of the lipid acyl chains, being used to differentiate between the various lamellar phases[37].

If an ordered mesophase is present (*e.g.* lamellar, hexagonal or cubic phases), sharp Bragg peaks will appear in the low-angle region of the diffraction pattern. These Bragg reflections have reciprocal spacing in characteristic ratios for each phase allowing their identification (Table 6.1) [39].

Table 6. 1. Lipid mesophases and the respective order ratios of the Bragg reflections that allow their identification by X-ray. *d* is the repeat distance in lamellar phases, and h, k, and l are the Miller indices that characterize hexagonal and cubic phases.

Mesophase	index
Lamellar $S_l = l/d$	1,2,3,4,…
Hexagonal $S_{hk} = 2(h^2+k^2-hk)^{1/2}/\sqrt{3}a$	$1, \sqrt{3}, 2, \sqrt{7}, 3, \sqrt{12}, \sqrt{13}, …$
Cubic $S_{hkl} = (h^2+k^2+l^2)^{1/2}/a$	$1, \sqrt{2}, \sqrt{3}, 2, \sqrt{5}, \sqrt{6}, \sqrt{8}, 3, …$

$(S_{hkl} = 1/d_{hkl})$

The crystallographic space group to which the phase belongs is determined once the lattice type is identified, although a corrected Bragg peaks' detection is not always simple in these soft matter systems, due to the thermal disorder inherent in liquid-crystalline phases, which decreases the intensities at larger diffraction angles [39].

Besides of structures' determination, it is also possible to derive bilayer thickness from SAXS, through the application of Bragg's law, measuring the distance between the theoretical planes:

$$2d_{hkl} \, sin\Theta = n\lambda \qquad\qquad (6.4.2)$$

Where n is the order of the reflection, λ is the wavelength of radiation, d_{hkl} is the distance between repeated planes in the lattice, and 2θ is the scattering angle[39]. X-ray scattering experiments are thus ideal for studying the structure and dynamics of lipid membranes, as well as their structural changes induced by changes in temperature, pressure, pH, ionic strength, etc. As regarding the aim of this thesis, the

focus is on possible membrane structural changes induced by the antimicrobial peptides - in lattice parameters and/or in the disappearance or appearance of different phases[30]. The analysis of structural changes induced by the studied antimicrobial cyclic peptides are reported in **manuscript VI**.

6.5. Dynamic Light Scattering

Dynamic light scattering (DLS) is a useful tool for the determination of the hydrodynamic radii of macromolecules, from the determined translational diffusion coefficient $(D_{\tau'})$[40]. Light scattering measures the amount of light scattered by a particle in solution at some angle relative to the incident light beam, where the emitted light has the same wavelength as the incident light. In solution, particles usually present Brownian motion caused by thermal density fluctuations in the solvent[41], that are dependent on their size, temperature, and solvent viscosity[42]. In DLS, when a monodisperse spherical particle is isolated, the fluctuations in intensity of the scattered light at a single angle are detected and analyzed with an autocorrelation function, against short delay times (τ')[43]:

$$g\left(\tau'\right) = 1 + b \exp\left(-2D_{\tau'}\, q^2 \tau'\right) \tag{6.5.1}$$

where b is a constant depending on the optics and the geometry of the instrument, τ' is the characteristic time decay, $D_{\tau'}$ is the translational diffusion coefficient and q is the scattering vector. This last parameter is provided experimentally by the scattering angle (θ') and the wavelength of the incident light (λ), depends on the solvent refractive (n_0), and their overall relationship can be expressed as[43, 44]:

$$|q| = \frac{4\pi n_0}{\lambda \sin\left(\frac{\theta}{2}\right)} \tag{6.5.2}$$

In the used Malvern Zetasizer DLS instrument a correlogram is generated where a raw correlation function is plotted against the delay time (τ'), and $D_{\tau'}$ is obtained by data fitting. If the particle can be considered a sphere (in our case the lipid vesicles LUVs), $D_{\tau'}$ can used to calculate the hydrodynamic radius from the Stokes-Einstein equation:

$$R_h = \frac{k_B T}{6\pi\eta D_{\tau'}} \tag{6.5.3}$$

where R_h is the hydrodynamic radius, defined as the radius of a hypothetical sphere that diffuses at the same rate as the particle under investigation, k_{B} is Boltzmann's constant (1.380×10^{-23} kg.m^2.s^{-2}.K^{-1})[45], T is the absolute temperature, η is the viscosity of the medium and $D_{\tau'}$ the translational diffusion coefficient[46-48]

The polydispersity index (PDI) is another important parameter that can be obtained from DLS measurements, as it characterized the dispersion of the LUVs prepared. PDI is calculated by the square of the standard deviation divided by the mean particle diameter. The PDI value may vary from 0 to 1, and in our preparations we always obtained values < 0.1, showing that we got monodisperse LUVs[49, 50].

DLS was used only used as a complementary method in the present thesis, to characterize the liposomes' size and size distribution.

6.6. Molecular Dynamic Simulations

Biophysical experimental techniques are used to understand the functional structure, dynamics, and interactions involved in biological systems or their appropriate models. Although biophysical techniques have evolved immensely in the past decades, some limitations are still present, hardening the task of characterization and understand of the macromolecules, especially in complex environments. As such, gathering computational simulations with experimental techniques is a comprehensive approach that provides complementary information and thus helps the understanding of the studied phenomena. Molecular dynamics (MD) simulations have been used to reveal molecular motion at the atomic scale, in simple or even complex systems, and therefore have been widely used as a tool for studying the structural properties and dynamical behavior of biological systems, from peptides to proteins and also lipid membranes[51-54]. In MD simulations at the atomic scale the forces between atoms are calculated at every time step, to provide information on the structures and dynamics of the studied system. This type of simulations is defined as **all-atom MD simulations (AA-MD)**[55]. In AA-MD the complexity of the simulations increases with the number of atoms, and consequently the consumption of calculation time is very large. To bring MD simulations from the atomic scale to the mesoscale, the reduction of the systems complexity must be considered, by grouping atoms together into single particles called 'beads' – this is done in the approach called **Coarse-grained molecular dynamics (CG-MD)**. CG-MD is the most popular MD technique, due to calculation time constraints (with consequent costs), as each bead can represent three to five heavy

atoms together with their hydrogen atoms, and the bonds are not explicitly modeled. The coarse-grained models reduce the degrees of freedom in the system by up to an order of magnitude, and the effective forces between these CG beads can be derived from all-atom simulation trajectories. This *mapping* has the goal to replace functional groups by corresponding beads with representative levels of polarity and affinities to other chemical groups[56, 57].
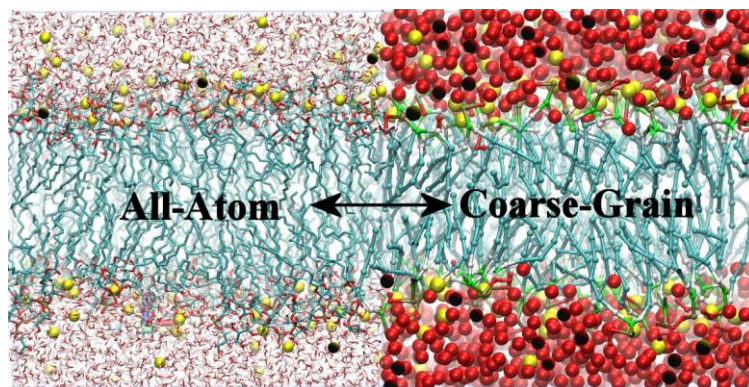
Fig. 6. 6. Example of conversion of complexity between All-Atom and Coarse Grain

In **publications II** and **IV** we present CG-simulations for the studied CPs and lipid systems. These studies were performed by co-workers and the conditions used are there well described. This technique was used to get detailed information of CPs in solution and their model membrane interactions, showing the macromolecular structures/assembling adopted. The overall discussion of experimental information and CG-MD results lead to a deeper understanding of the studied systems.

6.7. Isothermal Titration Calorimetry

Isothermal Titration calorimetry (ITC) is the golden calorimetric technique to directly determine the thermodynamic parameters associated to any interaction event. In biocalorimetry, that refers to process like the association of drugs, biological ligands or peptides to proteins or enzymes, as well as to lipid model membranes[58-62].

ITC presents very significant advantages for this goal, such as allowing the interaction to be monitored in solution, not requiring labelling of the reactants and has a high-content information in a single experiment (as will be shown below). This richness usually counteracts its often-referred disadvantages, such as being a time consuming and low throughput technique, requiring significant sample consuming and being often difficult to model, leading to intricate data analysis.

The most sensitive ITC instruments, called micro- and sometimes even nano-calorimeters are designed as twin instruments, with two identical cells. They can work based on heat conduction or power compensation principles. The one used in this thesis was of the power compensation type, where the twin cells (measuring and reference cells) are enclosed in an adiabatic jacket, working basically at constant pressure and temperature. Each cell has a heater, and under resting condition they deliver the same power to each side, keeping the temperature difference between the side close to zero ($\Delta T \approx 0$). The measuring cell contains the **titrand**, and the reference cell the solvent in use. The typical ITC experiment consists on the sequential addition of aliquots of chosen, defined volume of the **titrant** solution (contained in a motor driven precision syringe) into the **titrand** contained in the measuring cell, resulting in either an exothermic or endothermic reaction depending on the partition/binding process under study[63] (Fig. 6.7). When a reaction occurs between the titrand and the titrant, a momentaneous temperature change takes place in the measuring cell, which is promptly compensated by a feedback system that operates to keep the temperature difference between the sides close to zero ($\Delta T \approx 0$). Therefore, the power delivered to the measuring cell is either increased or decreased, depending of the process being endothermic or exothermic[64].
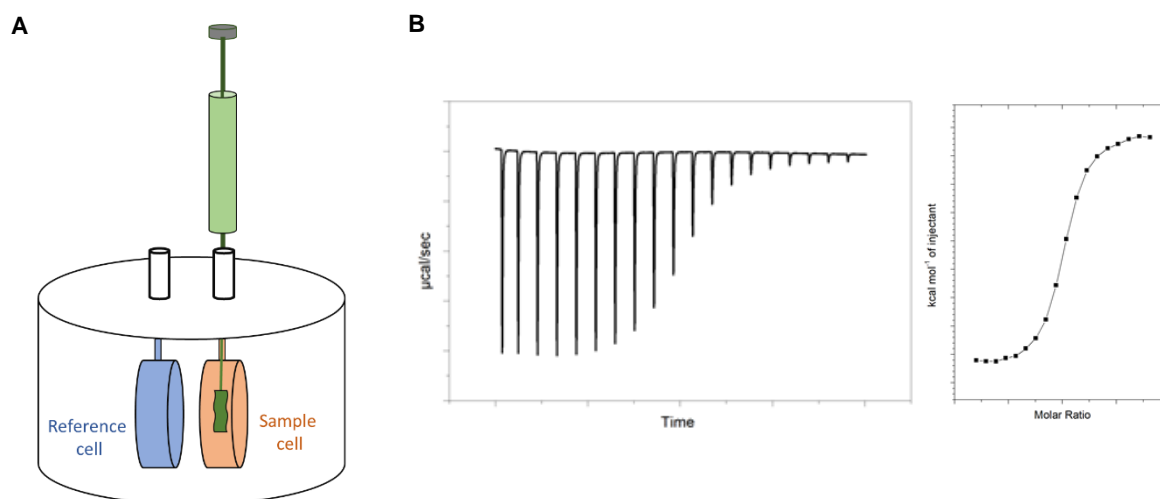
Fig. 6. 7. A. Typical schematic representation of the used ITC instrument. **B. left panel.** Example of an exothermic binding reaction titration curve. **Right panel.** Corresponding heat exchange *per* injection (obtained from the integration of each peak), plotted as a function of the molar ratio between the titrant and the titrand in the in the cell after each injection

The heat exchange involved in the binding/partition can be quantitatively determined by integration of the power *vs* time curves, *i.e.*, in the initial data processing

the integral of each peak is automatically multiplied by the calibration constant and divided by the number of moles of the chosen reactant. Fitting an appropriate model to the obtained data (Fig 6.7 B, right panel) with the will give us the enthalpy change (ΔH) and the binding affinity, K_a (in ligand binding experiments) or the partition constant K_p (in partition experiments). From these, the standard Gibbs energy change ($\Delta G°$) can be calculated using the equation[65]:

$$\Delta G° = -RT \ln K \tag{6.7.1}$$

where R is the gas constant and T is the absolute temperature. Note that different notations are sometimes used in ligand binding experiments, namely the binding affinity or association constant (K_a) and the dissociation constant (K_d), but they are easily related as $K_a = 1/K_d$ [66]. From the thermodynamic parameters $\Delta H°$ and $\Delta G°$, the standard change in entropy ($\Delta S°$) can also be calculated as:

$$\Delta G° = \Delta H° - T\Delta S° \tag{6.7.2}$$

Another parameter is obtained from most software dealing with ligand binding ITC data, often referred to as n value or the "stoichiometry" value for the binding reaction. It should be stressed that n only represents the stoichiometry if the concentrations of titrant and titrand are known with high accuracy. In other cases, as the "binding stoichiometry" is usually implicit in the binding model chosen for data analysis, the parameter n reflects the possible uncertainties in the concentrations of titrant and titrand. In different softwares used for ITC data treatment it is possible to choose whether the correction factor/competent fraction n (or its complementary value, the reactant incompetent fraction) is to be applied to the titrant (in the syringe) or to the titrand (in the cell). These and other important issues in ITC experiments are discussed in **publication VII**.

One important aspect to be considered for obtaining isothermal titration calorimetric experiment with high quality, is the calculation of the "*c-value*" when planning the experiment. It equals the product of the binding affinity and the actual concentration of the titrand solution ($[P]_0$) in the measuring cell (the total binding site concentration) or by the ratio to the dissociation constant as [63, 66]:

$$c = n K_a [P]_0 = n [P]_0 / K_d \tag{6.7.3}$$

As can be seen in Fig. 6.8 the shape of the curve changes significantly with the
c-value.
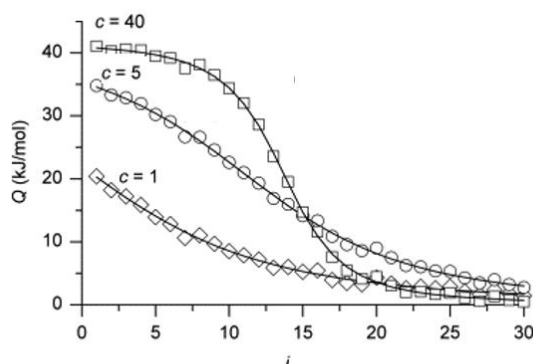
Fig. 6. 8. Plot of ITC titrations representing the heat of injection *vs.* injection number simulated for different c values. Adapted from[67].

When $c > 1$, an inflection point will appear in the binding, a condition needed for proper determination of K values in ligand-binding experiments. Previously the recommended c values were $50 < c < 500$, but more recently S. Keller *et al*[67], suggested that $c= 40$ still produce good ITC curves, based on analysis of the noise levels typical of present instruments.

To accurately measure the thermodynamic parameters characterizing the interactions between the species contained in the syringe (titrand) and in the cell (titrant), one should perform careful measurements in a precise, well-maintained, and calibrated ITC instrument. Thus, appropriated standardization tests should be used regularly to evaluate the instrument performance, together with the use of appropriate metrics for comparing precision and accuracy, and also to evaluate inter-experiment variability. In **publication VII**, a very thorough multi-laboratory benchmark standardization study is presented, using two test reactions, the binding of Ca^{2+} or Mg^{2+} to ethylenediaminetetraacetic acid (EDTA), in different buffer conditions, at 25°C. (Fig. 6.9).
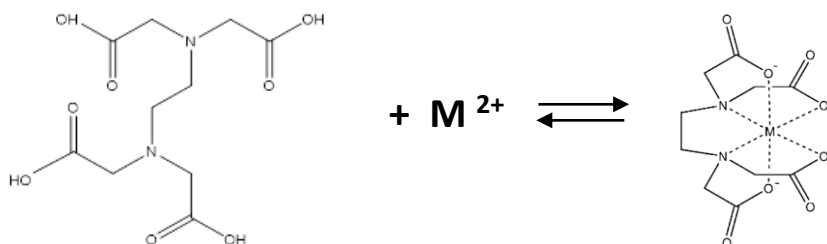
Fig. 6. 9. Drawings representing the species involved in the chemical reactions studied in **publication VII** where M^{2+} represents either Ca^{2+} or Mg^{2+}.

The experimental details used are well described in **publication VII**, together with data analysis using different softwares and discussion of the possible influence of instrument and/or user. This work was performed in the beginning of this thesis work, as the initial plan included the use of ITC to characterize the partition of the peptides to lipid model membranes. Finally, only preliminary experiments of some peptides and lipids systems were performed, and they are thus not included in this thesis.

References

1.   Bartlett, G. R. Phosphorus assay in column chromatography. *J biol chem* **1959,** 234, 466-468.

2.   Lohner, K.; Prenner, E. J. Differential scanning calorimetry and X-ray diffraction studies of the specificity of the interaction of antimicrobial peptides with membrane-mimetic systems. *Biochim. Biophys. Acta, Biomembr.* **1999,** 1462, 141-156.

3.   Abrunhosa, F.; Faria, S.; Gomes, P.; Tomaz, I.; Pessoa, J. C.; Andreu, D.; Bastos, M. Interaction and lipid-induced conformation of two cecropin-melittin hybrid peptides depend on peptide and membrane composition. *J. Phys. Chem. B.* **2005,** 109, 17311-9.

4.   Silva, T.; Adão, R.; Nazmi, K.; Bolscher, J. G. M.; Funari, S. S.; Uhríková, D.; Bastos, M. Structural diversity and mode of action on lipid membranes of three lactoferrin candidacidal peptides. *Biochim. Biophys. Acta, Biomembr.* **2013,** 1828, 1329-1339.

5.   Adão, R.; Nazmi, K.; Bolscher, J.; Bastos, M. C- and N-truncated antimicrobial peptides from LFampin 265 - 284: Biophysical versus microbiology results. *Journal of Pharmacy And Bioallied Sciences* **2011,** 3, 60-69.

6.   Höhne, G. W. H.; Hemminger, W.; Flammersheim, H. J. *Differential Scanning Calorimetry: An Introduction for Practitioners*. Springer Berlin Heidelberg: 2013.

7.   Gill, P.; Moghadam, T. T.; Ranjbar, B. Differential scanning calorimetry techniques: applications in biology and nanoscience. *J. Biomol. Tech.* **2010,** 21, 167-193.

8.   Ladbury, J. E.; Doyle, M. L. *Biocalorimetry 2: Applications of Calorimetry in the Biological Sciences*. Wiley: 2005.

9.   Demetzos, C. Differential Scanning Calorimetry (DSC): a tool to study the thermal behavior of lipid bilayers and liposomal stability. *J. Liposome Res.* **2008,** 18, 159-73.

10.   Bastos, M.; Águas, A. C. P. *Using DSC to characterize thermotropic phase transitions in lipid bilayer membranes. The basics of liposome sample preparation and DSC studies*; 2016.

11.   Goormaghtigh, E.; Raussens, V.; Ruysschaert, J.-M. Attenuated total reflection infrared spectroscopy of proteins and lipids in biological membranes. *Biochim. Biophys. Acta, Rev. Biomembr.* **1999,** 1422, 105-185.

12.   Tatulian, S. A. Structural Characterization of Membrane Proteins and Peptides by FTIR and ATR-FTIR Spectroscopy. In *Lipid-Protein Interactions: Methods and Protocols*, Kleinschmidt, J. H., Ed. Humana Press: Totowa, NJ, 2013; pp 177-218.

13.   Goormaghtigh, E.; Cabiaux, V.; Ruysschaert, J.-M. Determination of Soluble and Membrane Protein Structure by Fourier Transform Infrared Spectroscopy. In *Physicochemical Methods in the Study of Biomembranes*, Hilderson, H. J.; Ralston, G. B., Eds. Springer US: Boston, MA, 1994; pp 405-450.

14.   Woods, D. A.; Bain, C. D. Total internal reflection spectroscopy for studying soft matter. *Soft Matter* **2014,** 10, 1071-1096.

15.   Ausili, A.; Sánchez, M.; Gómez-Fernández, J. C. Attenuated total reflectance infrared spectroscopy: A powerful method for the simultaneous study of structure and spatial orientation of lipids and membrane proteins. *Biomed. Spectrosc. Imaging* **2015,** 4, 159-170.

16.   Goormaghtigh, E.; Ruysschaert, J. M.; Brasseur, R. Polarized attenuated total reflection spectroscopy as a tool to investigate the conformation and orientation of membrane components. In *Molecular description of biological membranes components by computer aided conformational analysis*, 1990; pp 285-332.

17.   Derenne, A.; Claessens, T.; Conus, C.; Goormaghtigh, E. Infrared Spectroscopy of Membrane Lipids. In *Encyclopedia of Biophysics*, 2013; pp 1074-1081.

18.   Ausili, A.; Sánchez, M.; Gómez-Fernández, J. C. Attenuated total reflectance infrared spectroscopy: A powerful method for the simultaneous study of structure and spatial orientation of lipids and membrane proteins. *Biomedical Spectroscopy and Imaging* **2015,** 4, 159-170.

19.   Lewis, R. N. A. H.; McElhaney, R. N. Membrane lipid phase transitions and phase organization studied by Fourier transform infrared spectroscopy. *Biochim. Biophys. Acta, Biomembr.* **2013,** 1828, 2347-2358.

20.   Tamm, L. K.; Tatulian, S. A. Infrared spectroscopy of proteins and peptides in lipid bilayers. *Q. Rev. Biophys.* **1997,** 30, 365-429.

21.   Bechinger, B.; Ruysschaert, J. M.; Goormaghtigh, E. Membrane helix orientation from linear dichroism of infrared attenuated total reflection spectra. *Biophys. J.* **1999,** 76, 552-63.

22.   Bocchinfuso, G.; Bobone, S.; Mazzuca, C.; Palleschi, A.; Stella, L. Fluorescence spectroscopy and molecular dynamics simulations in studies on the mechanism of membrane destabilization by antimicrobial peptides. *Cell. Mol. Life. Sci.* **2011,** 68, 2281-301.

23.   Rusu, L.; Gambhir, A.; McLaughlin, S.; Rädler, J. Fluorescence correlation spectroscopy studies of Peptide and protein binding to phospholipid vesicles. *Biophys. J.* **2004,** 87, 1044-1053.

24.   Teixeira, V.; Feio, M. J.; Rivas, L.; De la Torre, B. G.; Andreu, D.; Coutinho, A.; Bastos, M. Influence of lysine N(ε)-trimethylation and lipid composition on the membrane activity of the cecropin A-melittin hybrid peptide CA(1-7)M(2-9). *J. Phys. Chem. B* **2010,** 114, 16198-208.

25.   Melo, A. M.; Fedorov, A.; Prieto, M.; Coutinho, A. Exploring homo-FRET to quantify the oligomer stoichiometry of membrane-bound proteins involved in a cooperative partition equilibrium. *Phys. Chem. Chem. Phys.* **2014,** 16, 18105-18117.

26.   Loura, L. M.; de Almeida, R. F.; Coutinho, A.; Prieto, M. Interaction of peptides with binary phospholipid membranes: application of fluorescence methodologies. *Chem. Phys. Lipids* **2003,** 122, 77-96.

27.   Lakowicz, J. R. *Principles of Fluorescence Spectroscopy*. Springer US: 2007.

28.   Boldon, L.; Laliberte, F.; Liu, L. Review of the fundamental theories behind small angle X-ray scattering, molecular dynamics simulations, and relevant integrated application. *Nano Rev.* **2015,** 6, 25661.

29.   Karlovská, J.; Williams, A. A.; Macri, R. V.; Gandour, R. D.; Funari, S. S.; Uhríková, D.; Balgavý, P. Synchrotron SAX and WAX diffraction study of a hydrated very long-chain, dendritic amphiphile+DPPC mixture. *Colloids Surf., B* **2007,** 54, 160-164.

30.   Silva, T.; Claro, B.; Silva, B. F. B.; Vale, N.; Gomes, P.; Gomes, M. S.; Funari, S. S.; Teixeira, J.; Uhríková, D.; Bastos, M. Unravelling a Mechanism of Action for a Cecropin A-Melittin Hybrid Antimicrobial Peptide: The Induced Formation of Multilamellar Lipid Stacks. *Langmuir* **2018,** 34, 2158-2170.

31.   Tyler, A. I.; Law, R. V.; Seddon, J. M. X-ray diffraction of lipid model membranes. In *Methods in membrane lipids*, Springer: 2015; pp 199-225.

32.   Lohner, K.; Sevcsik, E.; Pabst, G. Chapter Five Liposome-Based Biomembrane Mimetic Systems: Implications for Lipid–Peptide Interactions. In *Advances in Planar Lipid Bilayers and Liposomes*, Leitmannova Liu, A., Ed. Academic Press: 2008; Vol. 6, pp 103-137.

33.   Lipfert, J.; Doniach, S. Small-angle X-ray scattering from RNA, proteins, and protein complexes. *Annu. Rev. Biophys. Biomol. Struct.* **2007,** 36, 307-27.

34.   Da Vela, S.; Svergun, D. I. Methods, development and applications of small-angle X-ray scattering to characterize biological macromolecules in solution. *CRSB* **2020,** 2, 164-170.

35.   Pabst, G.; Rappolt, M.; Amenitsch, H.; Laggner, P. Structural information from multilamellar liposomes at full hydration: Full q-range fitting with high quality x-ray data. *Phys. Rev. E* **2000,** 62, 4000-4009.

36.   Pabst, G.; Katsaras, J.; Raghunathan, V. A.; Rappolt, M. Structure and Interactions in the Anomalous Swelling Regime of Phospholipid Bilayers. *Langmuir* **2003,** 19, 1716-1722.

37.   Tyler, A. I.; Law, R. V.; Seddon, J. M. X-ray diffraction of lipid model membranes. *Methods Mol. Biol.* **2015,** 1232, 199-225.

38.   Staudegger, E.; Prenner, E. J.; Kriechbaum, M.; Degovics, G.; Lewis, R. N. A. H.; McElhaney, R. N.; Lohner, K. X-ray studies on the interaction of the antimicrobial peptide gramicidin S with microbial lipid extracts: evidence for cubic phase formation. *Biochim. Biophys. Acta, Biomembr.* **2000,** 1468, 213-230.

39.   Seddon, J. M.; Templer, R. H. Chapter 3 - Polymorphism of Lipid-Water Systems. In *Handbook of Biological Physics*, Lipowsky, R.; Sackmann, E., Eds. North-Holland: 1995; Vol. 1, pp 97-160.

40.   Stetefeld, J.; McKenna, S. A.; Patel, T. R. Dynamic light scattering: a practical guide and applications in biomedical sciences. *Biophys. Rev.* **2016,** 8, 409-427.

41.   Chapter 6 - Physics of electrorheological fluids. In *Studies in Interface Science*, Hao, T., Ed. Elsevier: 2005; Vol. 22, pp 235-340.

42.   Harding, S. E.; Jumel, K. Light Scattering. *Curr. Protoc. Protein Sci.* **1998,** 11, 7.8.1-7.8.14.

43.   Bhattacharjee, S. DLS and zeta potential - What they are and what they are not? *J. Control Release* **2016,** 235, 337-351.

44.   Lorber, B.; Fischer, F.; Bailly, M.; Roy, H.; Kern, D. Protein analysis by dynamic light scattering: methods and techniques for students. *Biochem. Mol. Biol. Educ.* **2012,** 40, 372-82.

45.   Eite Tiesinga, P. J. M., David B. Newell, and Barry N. Taylor. The 2018 CODATA Recommended Values of the Fundamental Physical Constants. In Web Version 8.1 ed.; Database developed by J. Baker, M. D., and S. Kotochigova, Ed. 2018 CODATA recommended values (Version 8.1), 2020.

46.   Harding, S. Protein hydrodynamics. In 1999; Vol. 2, pp 271-305.

47.   Cummins, H. *Photon Correlation and Light Beating Spectroscopy*. Springer US: 2013.

48.   Gilroy, E. L.; Hicks, M. R.; Smith, D. J.; Rodger, A. Viscosity of aqueous DNA solutions determined using dynamic light scattering. *Analyst* **2011,** 136, 4159-4163.

49.   Raval, N.; Maheshwari, R.; Kalyane, D.; Youngren-Ortiz, S. R.; Chougule, M. B.; Tekade, R. K. Chapter 10 - Importance of Physicochemical Characterization of

Nanoparticles in Pharmaceutical Product Development. In *Basic Fundamentals of Drug Delivery*, Tekade, R. K., Ed. Academic Press: 2019; pp 369-400.

50.   Clayton, K. N.; Salameh, J. W.; Wereley, S. T.; Kinzer-Ursem, T. L. Physical characterization of nanoparticle size and surface modification using particle scattering diffusometry. *Biomicrofluidics* **2016,** 10, 054107-054107.

51.   Calvelo, M.; Granja, J. R.; Garcia-Fandino, R. Competitive double-switched self-assembled cyclic peptide nanotubes: a dual internal and external control. *Phys. Chem. Chem. Phys.* **2019,** 21, 20750-20756.

52.   Claro, B.; Gonzalez-Freire, E.; Calvelo, M.; Bessa, L. J.; Goormaghtigh, E.; Amorin, M.; Granja, J. R.; Garcia-Fandino, R.; Bastos, M. Membrane targeting antimicrobial cyclic peptide nanotubes - an experimental and computational study. *Colloids Surf., B* **2020,** 196, 111349.

53.   Gonzalez, M. A.; Bresme, F. Membrane–Ion Interactions Modify the Lipid Flip-Flop Dynamics of Biological Membranes: A Molecular Dynamics Study. *J. Phys. Chem. B* **2020,** 124, 5156-5162.

54.   Antunes, E.; Azoia, N. G.; Matama, T.; Gomes, A. C.; Cavaco-Paulo, A. The activity of LE10 peptide on biological membranes using molecular dynamics, in vitro and in vivo studies. *Colloids Surf., B* **2013,** 106, 240-7.

55.   Bond, P. J.; Holyoake, J.; Ivetac, A.; Khalid, S.; Sansom, M. S. Coarse-grained molecular dynamics simulations of membrane proteins and peptides. *J. Struct. Biol.* **2007,** 157, 593-605.

56.   Marrink, S. J.; Risselada, H. J.; Yefimov, S.; Tieleman, D. P.; de Vries, A. H. The MARTINI Force Field: Coarse Grained Model for Biomolecular Simulations. *J. Phys. Chem. B* **2007,** 111, 7812-7824.

57.   Shinoda, W.; DeVane, R.; Klein, M. L. Multi-property fitting and parameterization of a coarse grained model for aqueous surfactants. *Mol. Simul.* **2007,** 33, 27-36.

58.   Samelo, J.; Mora, M. J.; Granero, G. E.; Moreno, M. J. Partition of Amphiphilic Molecules to Lipid Bilayers by ITC: Low-Affinity Solutes. *ACS Omega* **2017,** 2, 6863-6869.

59.   Heerklotz, H.; Tsamaloukas, A. D.; Keller, S. Monitoring detergent-mediated solubilization and reconstitution of lipid membranes by isothermal titration calorimetry. *Nat. Protoc.* **2009,** 4, 686-97.

60.   Bai, G.; Nichifor, M.; Bastos, M. Association and Phase Behavior of Cholic Acid-Modified Dextran and Phosphatidylcholine Liposomes. *J. Phys. Chem. Lett.* **2010,** 1, 932-936.

61.   Adão, R.; Bai, G.; Loh, W.; Bastos, M. Chemical calibration of Isothermal Titration Calorimeters: An evaluation of the dilution of propan-1-ol into water as a test reaction using different calorimeters, concentrations, and temperatures. *J. Chem. Thermodyn.* **2012,** 52, 57-63.

62.   Abraham, T.; Prenner, E. J.; Lewis, R. N. A. H.; Mant, C. T.; Keller, S.; Hodges, R. S.; McElhaney, R. N. Structure–activity relationships of the antimicrobial peptide gramicidin S and its analogs: Aqueous solubility, self-association, conformation, antimicrobial activity and interaction with model lipid membranes. *Biochim. Biophys. Acta, Biomembr.* **2014,** 1838, 1420-1429.

63.   Srivastava, V. K.; Yadav, R. Chapter 9 - Isothermal titration calorimetry. In *Data Processing Handbook for Complex Biological Data Sources*, Misra, G., Ed. Academic Press: 2019; pp 125-137.

64.   Microcal Inc., N., MA. VP-ITC Instruction Manual.

65.   Velazquez-Campoy, A.; Claro, B.; Abian, O.; Höring, J.; Bourlon, L.; Claveria-Gimeno, R.; Ennifar, E.; England, P.; Chaires, J. B.; Wu, D.; Piszczek, G.; Brautigam, C.; Tso, S.-C.; Zhao, H.; Schuck, P.; Keller, S.; Bastos, M. A multi-laboratory benchmark study of isothermal titration calorimetry (ITC) using Ca2+ and Mg2+ binding to EDTA. *Eur. Biophys. J.* **2021**.

66.   Bastos, M.; Velazquez-Campoy, A. Isothermal titration calorimetry (ITC): a standard operating procedure (SOP). *Eur. Biophys. J.* **2021**.

67.   Broecker, J.; Vargas, C.; Keller, S. Revisiting the optimal cvalue for isothermal titration calorimetry. *Analytical Biochemistry* **2011,** 418, 307-309.

PART III

**Results
and Discussion**

I.   **"Design and applications of cyclic peptides"**

Barbara Claro, Margarida Bastos and Rebeca Garcia-Fandiño **(2018)**, In *Peptide Applications in Biomedicine, Biotechnology and Bioengineering*, S. Koutsopoulos, Woodhead Publishing: 87-129

Design and applications of cyclic peptides

4

Barbara Claro, Margarida Bastos and Rebeca Garcia-Fandino
University of Porto, Porto, Portugal

4.1 Introduction

Peptides are known for their ability to influence physiological and biochemical functions of life, as neurotransmitters, neuromodulators, during the cell−cell communication upon interaction with receptors, or during metabolism and reproduction [1]. They have the capability to bind to particular targets in vivo while not interfering so significantly with the immune system as their endogenous protein counterparts. Moreover, the high diversity of their constituent building blocks and their reduced toxicity make them promising platforms for therapeutics in different areas of science and technology. As such, they have been the subject of an increased amount of studies in the past few decades [2−7]. Despite encouraging results, one of the major barriers to the therapeutic use of linear peptides is their low stability under physiological conditions. Linear peptides are usually rather rapidly cleaved by enzymes in vivo, losing their biological activity [8,9]. To overcome these obstacles, diverse peptide modifications have been proposed [10−13]. The development of new peptide-based systems obtained through cyclization of linear peptides was recently considered one of the most promising approaches, due to a series of advantages that will be discussed below [14,15].

Constraining a peptide into a cyclic structure decreases the conformational freedom for each constituent within the ring and forces the molecule into an ordered secondary structure [16]. Although considered a simplistic approach [17,18], it was suggested that the advantage of cyclization resulted from the increase in rigidity being translated into a decrease of the entropic term of the Gibbs energy, thus providing superior binding affinities than natural binders to a receptor [19,20]. Other studies show that they present a higher resistance to endopeptidases when compared to the more flexible linear analogues [21−26]. For CPs the increase in rigidity is frequently followed by the formation of preferred side-chain conformations. Thus, the structural arrangement of the side chains is frequently the most important factor in the molecular recognition process, using the peptide backbone as a template for their orientation [27]. Cyclization was also shown to increase the propensity for β-turn formation, which is believed to improve binding affinity [28−30]. Another suggested advantage of cyclization is that the elimination of charged termini in CPs can enhance membrane permeability [31], although it has been demonstrated that a peptide does not cross the membrane better simply because it is cyclized, but because of its structural features [32]. Additionally, the lack of both amino and

carboxyl termini makes CPs less prone to hydrolysis by exopeptidases [33], decreasing off-target side effects [34], and thus leading to substantially enhanced metabolic stability and specificity [35−38]. Furthermore, CPs are significantly smaller compared to proteins and therefore more affordable due to lower manufacturing costs through various chemical methods [39].

4.2   Cyclic peptides in nature

Gene-encoded CPs were originally believed to be aberrations in the peptide world. The discovery of Gramicidin S in 1944 by Gause and Brazhnikova during the Second World War marked a "before and after" in the history of CPs [40]. The number of CPs disclosed has continually grown, with thousands of CPs known at present. Most arise from natural CPs and have been extensively used in pharmaceutical and agricultural applications as active ingredients obtained from natural extracts (bacteria, fungi, plants, animal venoms) [41−45]. The major advantage of Nature-derived CPs is that despite Nature never having faced the need to create a CP that encompasses all important drug-like properties (such as protection against serum enzymes), evolution has already done the work of selecting a set of bioactive peptide scaffolds that may be advantageous for drug-discovery purposes, since natural sources contain a rich diversity of CPs and CP-like structures. The structures of these naturally occurring CPs range from large peptides (∼70 residues) containing mainly α-helical arrangements, to small β-hairpins (12−14 residues), as shown in Fig. 4.1 [45,46]. Most of them share a common function: the defense-related or toxic properties against microbes and/or insects, exhibiting a wide variety of unusual and potent biological activities

Gramicidin S is an example of CPs obtained from bacteria (Fig. 4.1). It is a cyclic decapeptide, extracted nonribosomally from the soil bacterium *Aneurinibacillus*, with an antiparallel β-sheet constructed by two identical pentapeptides joined head to tail, formally written as cyclo(-Val-Orn-Leu-D-Phe-Pro-)$_2$ [47,48]. Tyrocidines are antibiotics with different structures, differing only in the analogue-type substitutions of the aromatic residues—Tyrocidine A, B, and C (Fig. 4.1) [49]. They are the major constituent of tyrothricin, which also contains gramicidin, produced by the bacteria *Bacillus brevis*, found in soil [50]. Cyclosporin is an immunosuppressive agent used to prevent organ rejection in transplantation surgery. This cyclic undecapeptide with high lipophilicity is produced as a secondary metabolite by strains of fungi *Cylindrocarpum lucidum* Booth and *Tolypocladium inflatum* Gams isolated from soil samples. Seven of its eleven amide bonds are N-methylated, adopting different conformations depending on the environment in which they are located [23,51]. Some ribosomally synthesized CPs produced in bacteria include for example AS-48 [52], which is intensively used in food preservation because of its activity against *Salmonella* and *Listeria*, or lactocyclicin Q and garvicin ML, isolated from cheese and Mallard ducks, respectively, extremely stable and with antimicrobial activity [53,54]. Vancomycin [55] is a
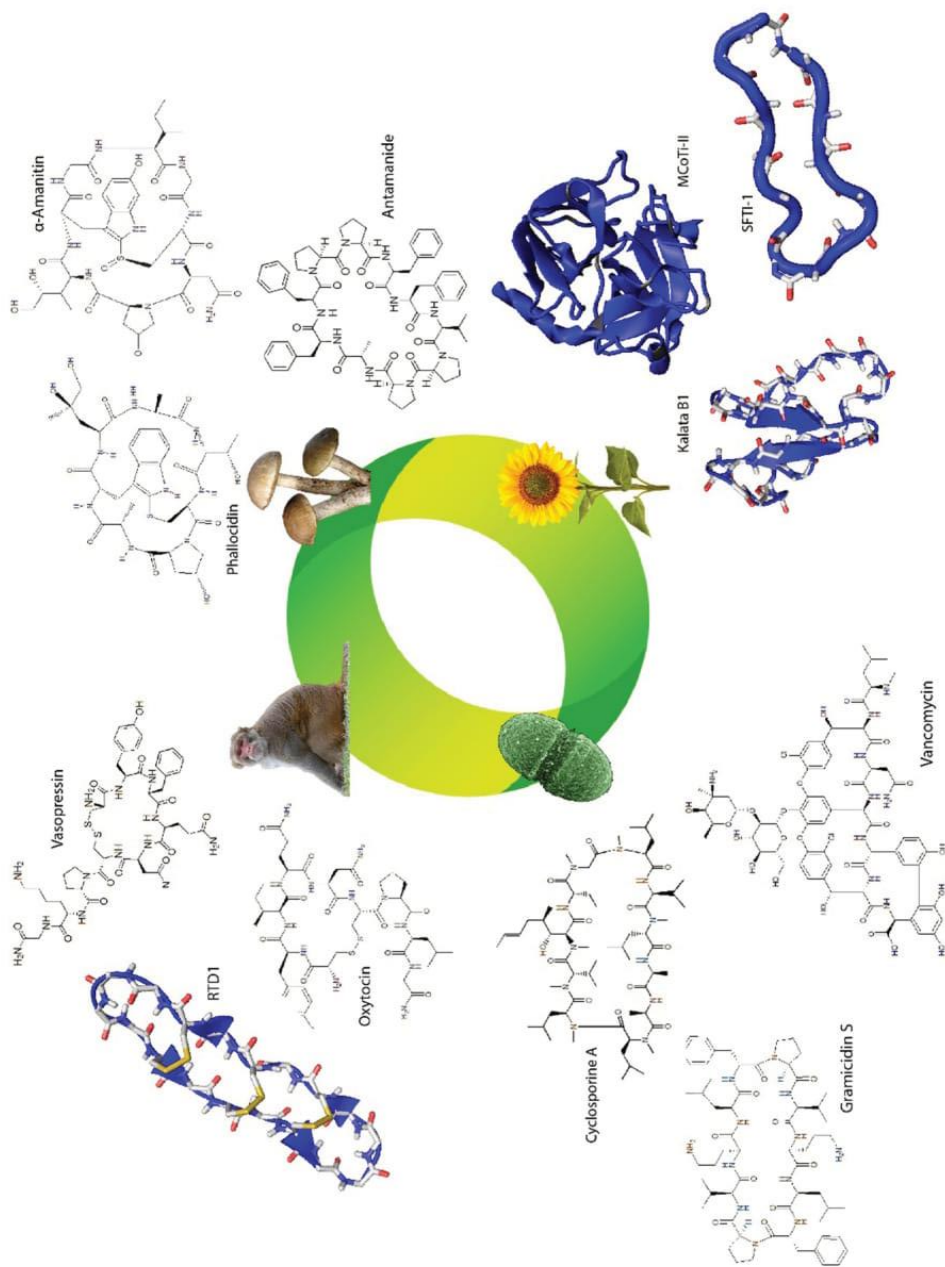
Figure 4.1 Examples of natural CPs obtained from bacteria, fungi, plants, and animals.

branched tricyclic glycosylated nonribosomal peptide produced by the Actinobacteria *Nocardia orientalis* and used as the last resort in hospitals to treat drug-resistant Gram-positive bacterial infections. Its biosynthesis occurs via different nonribosomal protein synthases (NRPSs). The molecule consists of a seven-membered peptide chain that is formed by parts of three phenylglycine systems, two chlorinated tyrosine units, aspartic acid, and N-methylleucine. Two ether bonds and a carbon−carbon bond join the various substituents on the peptide chain into three large rings. A disaccharide, composed of glucose and vancosamine, is also present but is not part of the cyclic structure.

Some CPs found in fungi are, for example, the highly toxic alpha-amanitin (Fig. 4.1) and phallocidin, targeting RNA polymerase II and F-actin, respectively [56]. They are ribosomally expressed and differ from other CPs by having an internal crosslink, which is not a disulfide bond. The mushroom metabolite antamanide [44,57], isolated from the lethal *Amanita phalloides*, is another immunosuppressant consisting on a cyclic decapeptide containing one valine residue, four proline residues, one alanine residue, and four phenylalanine residues. It has been shown that altering any of the proline residues (or the phenylalanine residues to tyrosine or L-cyclohexylalanine) reduces the immunosuppressive activity to zero [58].

The largest family of CPs found in plants is the cyclotides [59,60]. They have been found in more than 20 species from the *Violaceae*, *Rubiaceae*, *Cucurbitaceae*, *Fabaceae*, and *Solanaceae* plant families. More than 280 sequences have been reported so far (http://www.cybase.org.au/), but it has been predicted that the cyclotide class might comprise more than 50,000 members [41]. Cyclotides are 28−37 amino acids (AA) in size and have a cystine knotted arrangement of three disulfide bonds. One of the best known examples is Kalata-B1 [61], an amphipathic peptide containing 29 AA residues. Two of the largest cyclotides, MCoTI-I and MCoTI-II, are also trypsin inhibitors, and are found in the seeds of a bitter melon from Vietnam. Another type of CP in plants is sunflower trypsin inhibitors. Sunflower trypsin inhibitor-1 (SFTI-1) [62] is a 14-residue peptide with one disulfide bond that is extracted from the seeds of the common sunflower, and is a potent trypsin inhibitor.

Some primates express CPs called θ-defensins as a part of their immune system, and to date, they are the only known ribosomally synthesized CPs in mammals [63,64]. The characteristic structural motif of the θ-defensins is the cyclic cystine ladder, including a CP backbone and three parallel disulfide bonds. In contrast to the cyclic cystine knot, which characterizes the plant cyclotides, the cyclic cystine ladder has not been described as a structural motif. Some examples are RTD-1 [65], isolated from macaque leukocytes and some recent naturally occurring isoforms, isolated from baboon leukocytes [66]. Oxytocin [67] and vasopressin [68,69] are peptide hormones released by the primate posterior pituitary gland. They are nonapeptides with a single disulfide bridge, differing only by two substitutions in the amino acid sequence. Both are examples of CPs already in the market, being originally discovered as hormones found in mammals and later used as the "starting point" in drug design in the pharmaceutical industry.

4.3 Types of cyclic peptides: classification

4.3.1 Size

A number of CPs has been discovered in Nature and they vary greatly in structure and size, from the smallest CPs in fungi containing only seven residues to the largest in bacteria comprising 78 residues (Fig. 4.2) [71]. Small peptide cycles (five to six amino acids) have shown in recent studies acceptable bioavailability and good stability against enzymatic degradation, providing good skeletons for drug design [72,73]. Overall, the smaller the size of the CPs, the higher the conformational restraints and the smaller the observable flexibility [74]. Synthetic macrocycles composed by large rings (in the 600−1500 molecular weight range) are also very promising, and are very useful, for example, in protein−protein interactions [75].

Ring size is a significant factor in the success of the synthesis of a CP. Whereas six-membered rings are quite easy to synthesize, 7−15-membered rings are less accessible. In the case of small-to-medium-sized rings, the ground-state E geometry
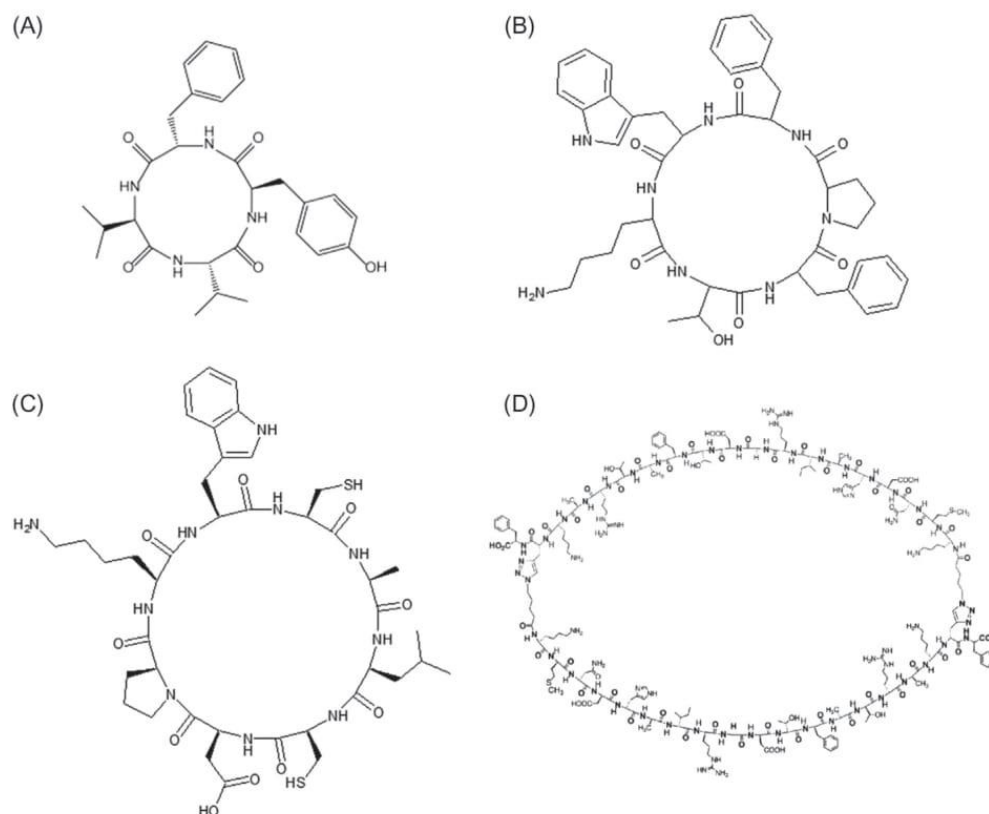
Figure 4.2 Examples of CPs with different sizes: (A) Cyclo(D-Tyr-L-Phe-D-Val-L-Val) with four residues; (B) Cyclo(Pro-Phe-Trp-Lys-Thr-Phe) with six residues; (C) Cyclo(L-Cys-L-Ala-L-Leu-L-Cys-L-Asp-L-Pro-L-Lys-L-Trp) with eight residues; and (D) "Duoboros" with 18 residues [70].

of the peptide bond is not a favorable conformation for the linear peptide to be cyclized, since the two ends that must react are too far apart from each other. This problem is not present in larger ring sizes since they can accommodate *E* peptide bonds. On the other hand, the synthesis of these large macrocycles demands special conditions to avoid intermolecular reactivity [76].

4.3.2   Number of rings

Although most of the CPs known or designed are monocyclic, Nature has also created many peptides with multicyclic motifs. Some naturally occurring bicyclic peptides are, for example, α-amanitin (Fig. 4.1) [77,78], phalloidin [58] (Fig. 4.1), bouvardin [79,80] (Fig. 4.3), moroidin [81,82] (Fig. 4.3), SFTI-1 [62], or the θ-defensins [63,64] (Fig. 4.1). Typical linkages formed in ribosomal peptides are disulfide, amide, thioether, or ester bonds. In nonribosomal peptides, additional cyclization chemistries are found, such as biaryl or biaryl ether linkages. These peptidic structures contain two macrocyclic rings with limited conformational flexibility, which can enhance their overall binding properties. Furthermore, their small size affords a number of advantages over large proteins, including access to
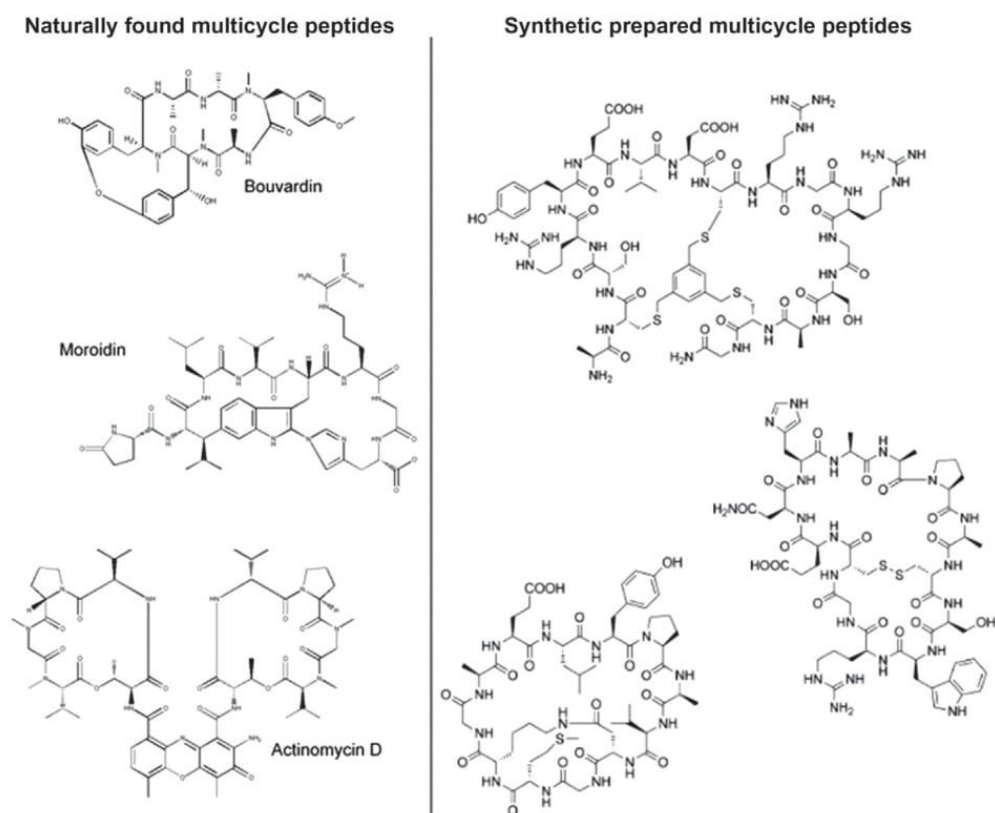
Figure 4.3 Examples of multicyclic peptides found in Nature (left) or chemically synthesized (right).

chemical synthesis, better tissue penetration, and alternative routes of administration, such as topical application. Owing to their attractive features, bicyclic peptides are attracting increased interest for biological use (Fig. 4.3) [83−88].

Examples of natural CPs containing more than two cyclic units in their structure are also known, i.e., nisin [89], mersacidin [90], actinomycin D [91], or vancomycin [55]. Many of these polycyclic peptides consist of cycles sequentially organized along the peptide backbone. In these molecules, the conformational constraints imposed by the polycyclic backbone enable them to adopt a defined structure in solution, which is crucial for their biological activity and advantageous toward enhancing their cell penetration properties and stability against proteolysis. A recent review has summarized the properties of existing polycyclic peptide drugs relating them to their interesting molecular architectures [92].

4.3.3 Physical properties

Based on their structures and biological function, CPs have been classified into different families (Table 4.1) [93]:

1. Highly charged (cationic or anionic) CPs with membrane-disrupting (antimicrobial peptides (AMPs)) and membrane-penetrating properties (CPPs). Cyclic AMPs have emerged as good antimicrobial candidates due to their robust secondary structure and high activity [94−98]. One of the most representative examples is CPs composed of amino acids of opposite alternating chirality (L and D), in which all side chains are exposed to the outer surface of the structure leaving an empty internal hole, which favors the formation of a nanotube by self-assembly of the different units at the membrane site (see Section 4.7) [99,100].

2. Nonpolar CPs enclosing lipophilic modifications to the amide backbone. These CPs exhibit a wide range of biological activities, many of them associated with penetrating properties into eukaryotic cells by passive diffusion. Nonpolar CPs are characterized by a predominance of aliphatic residues, the presence of D-amino acids, and N-methylation of backbone amides. The CPs in this category, whose crystal structures have been solved, often contain one or more β-turns that are templates for various patterns of intramolecular hydrogen bonds. Since they do not interact with membranes electrostatically, it has been speculated that the penetration mechanism is similar to most small drug molecules. Some of the most representative examples of the nonpolar CPs are the already-mentioned cyclosporin A [101] or the K^+ ionophore valinomycin. Other examples include argyrin B, cyclomarin or CSA (homodetic "all-amide" peptides) destruxin B, aureobasidin A, HUN-7293/CT08 or guangomide A (depsipeptides), lissoclinamide 7, patellamide D, ascidiacyclamide or trunkamide (pattelamide-like CPs, derived from ribosomally synthesized sequences of alternating lipophilic and Ser, Thr, or Cys residues), phakellistatins (proline-rich peptides), coibamide A, didemnin B, YM254890, selenamide, luzopeptin, callynormine A (heterodetic CPs) [93]. A detailed review has summarized a large number of examples of CPs of this family [93].

3. Mixed-polarity CPs, with amphiphilic features but with action not limited to microbial targets. Their mechanism of action does not depend on membrane-disrupting or membrane-penetrating ability. They exhibit activity in mammalian cells that suggests intracellular targets, as they are supposed to enter the cell through a passive membrane diffusion or other mechanisms not well known yet. Some representative examples of this group are

Table 4.1 Classification of CPs according to their physical properties

Classification of CPs		Structural features	Representative cyclic peptides	Biological activitiy
Charge	Cationic	Cationic residues present (e.g., Arg or Lys)	Gramicidin S, polymyxin B	AMP/CPP
	Anionic	Anionic residues present (e.g., Asp or Glu)	Gramicidin A	AMP/CPP
Mixed polarity		May contain a lipid tail	Largamide, pseudodesmin A, microcin, papuamides, thiostrepton	Activity in mammalian cells but not limited to microbial targets
Nonpolar		Predominance of aliphatic residues (e.g., Gly, Ala, Val, Leu or Ile), presence of D-amino acids, or N-methylation of backbone amides	Aureobasidin A, argyrin B, aureobasidin, guangomide A, cyclomarin, CSA, Destruxin B	Penetrating properties into eukaryotic cells by passive diffusion or other mechanisms not well known
Cyclotides and cysteine-knot proteins		Multiple disulfide bonds and multiloop conserved structures	Kalata B1, Bowman—Birk trypsin inhibitor	Membrane permeation of the cysteine knot

    kahalilide F [102] and also other CPs with a lipid tail appended, such as largamide, pseudodesmin A, the papuamides, thiostrepton or microcin [103].

4. Cyclotides and cysteine-knot proteins, are small (2−8 kDa) proteins with unusual topologies and notable oral activity. They are backbone-cyclized microproteins that contain multiple disulfide bonds and a conserved multiloop structure [61,104,105]. Some representative examples of CPs from this family are the already mentioned Kalata B1 [61] or the Bowman−Birk inhibitor. The mechanism of membrane permeation of this type of CPs is not yet well established. A recent review has summarized the available chemical or biological methods for production of these interesting CPs [106].

4.3.4 Type of cyclization

The ring structure of a CP can be formed by linking one end of the peptide to the other by an amide bond, or other chemically stable bonds such as, e.g., lactone,

ether, or thioether disulfide [107]. Based on the type of bond that comprises the ring, CPs can be divided into three main categories: (1) homodetic (containing only peptide bonds); (2) heterodetic (diverse functional groups are also employed to connect the amino acids); and (3) complex, consisting of a mixture of homodetic and heterodetic linkages (Fig. 4.4). Linear peptides can be cyclized not only by joining the N-termini connects with the C-termini of the terminal peptides (head-to-tail bond), but also by linking amine and carboxylic functions in amino acid side chains, giving side-chain-to-head or side-chain-to-tail connections. It has been demonstrated that the position of cyclization within the sequence will constrain particular motifs and alternative geometries and will affect the binding affinity of CPs [108,109]. Tapeinou et al. have recently summarized the cyclization strategies according to the following classification [19,27,110]:

- N-to-C or head-to-tail cyclization (homodetic)—this is the simplest and most common cyclization, where the peptide bond is formed between the N-terminus amino group and the C-terminus carboxyl group [111,112]. It has been inferred that the ring size is the most important factor for the head-to-tail macrocyclization. For peptides containing more than seven amino acids the ring closure is not problematic, although for smaller peptides the ring connection should be chosen carefully to avoid problems. Furthermore, the incorporation of turn-inducing structural elements embedded along the linear precursor can also result in a more efficient macrocyclization [13,113].
- Cyclotides—the peptide bond is formed head-to-tail and the ring is usually strengthened by three disulfide bonds [59,114].
- Side chain-to-one of the termini cyclization (head-to-side chain or side chain-to-tail (heterodetic))—the bond is formed between the N- or C-terminus and the side chain functional group of amino acids [26].
- Side-chain-to-side-chain or backbone cyclization—the bond is formed between two side chains of amino acids (homodetic and heterodetic) [115−118]. Through this methodology, a bridge is created from a backbone amide nitrogen or a Cα carbon atom to any other position, introducing restrains into the linear peptide and leaving the peptide chain termini free [119]. In order to be effective, the side-chain-to-side-chain macrocyclization can involve a condensation reaction between side chains under high dilution to minimize unwanted intermolecular processes such as oligo- and polymerizations [120]. This cyclization is advantageous for peptide hormones that are often found as N-terminal primary amide, for example [121].
- Disulfide—the disulfide bond is formed between two thiol groups (cysteine) [122]. Disulfide cyclizations are easy to generate but require that two cysteines be included in the sequence, and the disulfide bond may be subject to reduction and reoxidation into unintended configurations.
- Thioether—the thioether bond is formed between the side chain thiol group of a cysteine and the α-carbon atom of an amino acid [123].

4.3.5 Type of building blocks

To improve the potency of a CP, additional diversity has been obtained through the incorporation of noncanonical amino acids (e.g., D-amino acids, ornithine, hydroxyproline, N-methylated residues, or other non-natural amino acids) [13,124−129] or
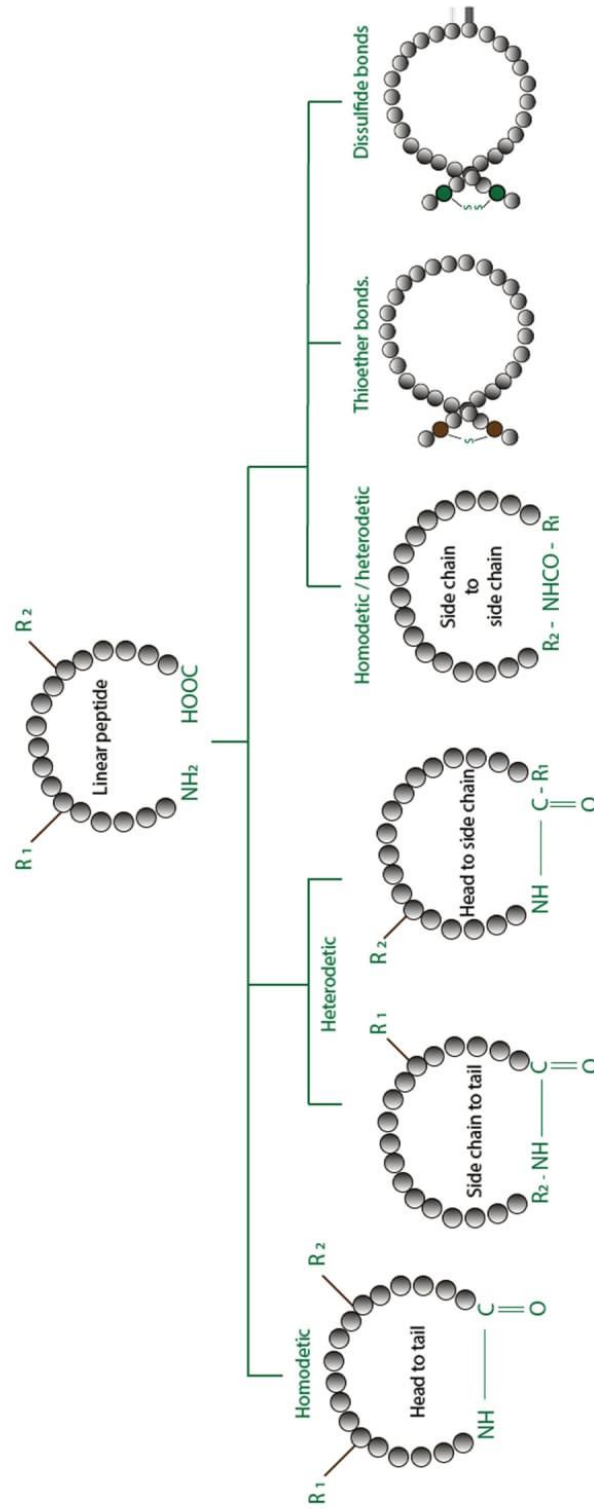
Figure 4.4 Principal categories of cyclization according to the type of bonds that comprise the ring of CP.

by means of peptide structural modifications. The introduction of small groups or the replacement of the canonical amino acids by noncanonical ones influences the entire CP backbone, unlike for the linear peptides where it only affects the insertion area [130]. Amino acid side-chain alterations also change the behavior of the CPs. The most commonly reported side-chain alteration in CPs is cysteine bridging, which is easily formed by oxidation of two thiol functions of the amino acid side chains. Disulfide bonds play an important role in constraining peptide conformations, although the resulting cycles usually retain considerable flexibility and are easily cleaved under physiological conditions [76,131].

Several reviews have been published about CPs containing noncanonical amino acids, mainly related to the application of peptide nanotubes by self-assembly (self-assembled cyclic peptide nanotubes (SCPNs), see Section 4.7) [132,133]. SCPNs have been assembled from CPs with α-amino acids (α-CPs) comprising 4 [134], 6 [135−137], 8 [138−141], 10 [142,143], or 12 [144] residues, resulting in internal diameters ranging from 2 up to 13 Å. The chemistry of SCPNs can also be altered by using chiral β^3-amino acid residues (Fig. 4.5) [145,146]. The inner surfaces of D, L-α- and β-PNTs are hydrophilic, and it is not possible to modify their pore properties by introducing functional groups because all the amino acid side chains have to point outwards and pseudoequatorially. However, this shortcoming is overcome if cyclic γ-amino acids are used, as has been proven by Granja's group through the design, synthesis, and characterization of a new class of CP composed of alternating α-amino acids and *cis*-3-aminocyclohexanecarboxylic acid (γ-Ach) [147]. The use

Figure 4.5 Examples of CPs containing noncanonical amino acids.

of a γ-amino acid with a hydroxyl group at C2 has also allowed the incorporation of different groups that modify the internal properties of the CPs [148,149]. Another synthetic route to modify the lumen chemistry of CPs was obtained by means of the insertion into the peptide sequence of an unnatural amino acid containing a methyl functional group pointing toward the inside of the pore (Fig. 4.5) [150]. Other examples of modifications of the original Ghadiri CPs include the use of δ-amino acids [151], ε-amino acids [152,153], CPs derived from dialkylmalonic acid and containing disulfide bridges between the two terminal cysteines to close the ring [154], or pseudopeptidic macrocyclics [155] (Fig. 4.5). The introduction of moieties that are not amino acids, e.g., to generate peptidomimetics, can enhance diversity [156], specificity, and functionality, but it may be accompanied by an increase in toxicity compared to that associated with CPs of natural amino acids. On the other hand, N-methylation patterns that facilitate the formation of transannular (intramolecular) hydrogen bonds are related with good passive permeability and oral bioavailability [157]. Recent reviews address N-methylation in peptides from synthetic and conformational perspectives [73,158,159].

4.3.6 Type of secondary structure

CPs are now known to reproduce peptide backbones constrained to strand, sheet, helix, turn, or loop conformations (Fig. 4.6). A recent review summarizes the most significative examples over the last 20 years of CPs that mimic this type of structure, and identifies some additional restraints incorporated into natural cyclic

Figure 4.6 Examples of short synthetic peptide sequences that can be induced to fold into protein-like bioactive conformations (strands, helices, turns) by cyclization [160].

peptides and synthetic macrocyclic peptidomimetics that refine peptide structure and confer desired biological properties [160].

4.4   Methods for the design of cyclic peptides

One of the main sources of inspiration for designing CPs is Nature itself. Cybase [161] is an online database of known natural and non-natural head-to-tail cyclic proteins, i.e., proteins that possess a cyclic backbone in which the N- and C-termini have been joined with a conventional amide bond. This database includes several cyclotide entries (plant-made defense proteins (such as the kalata proteins), primate rhesus θ-defensins (RTDs) with increased biological activities, such as anti-HIV activity), which are used as lead molecules for drug design [114].

   There are several approaches to the design of CPs depending on the application for which they are aimed. Presently there are two main approaches in drug design. The first consists of intentional modifications of known cyclic analogues that may or may not have affinity against a target. Rational design requires the knowledge of the role of each residue so that cyclization occurs at the amino acid positions least important for the retention of the activity of the linear peptide. Some examples have included mutated or grafted natural cyclotides [162,163] or modified cyclic hormones to obtain enhanced compounds towards different targets [164,165] (i.e., melanocortin [166,167], gonadotropin releasing hormone [168−172], or somatostatin [173]). In many cases cyclization of linear peptides was used to obtain enhanced pharmacological agents, many of them targeting protein−protein interactions (PPIs) [168−170,172,174−181]. The second approach is used when little is known about the target (e.g., receptor) or the ligand (the CP to be designed). This second approach uses combinatorial syntheses to identify lead compounds and usually involves: (1) screening methods to identify biological function; (2) synthesis of libraries based on linear peptides; and (3) mutagenesis studies driven by trial and error [182,183]. Several groups have reviewed the topic of library generation [184−187], with *phage display* (see below) or *combinatorial methods* being some of the most common methods to create screening libraries. The two approaches are not mutually exclusive. Lead compounds identified by combinatorial synthesis can be optimized through rational approaches to determine the best analogue. Likewise, peptides designed through rational approaches can be optimized by iterative replacement of each amino acid (Fig. 4.7) [188]. The combination of both approaches has led to successful examples of CPs with pharmacological activity [189].

   During the design of CP many variables need to be optimized, experimentally generated, tested, and analyzed, making the overall process tedious and time consuming. Furthermore, the ambitious challenge of understanding the mechanisms of action of CPs would require atomic resolution, which is still unattainable by most experimental techniques known today. Hence, computational approaches to the design of new CPs can provide a better understanding of their sequence−structure relationships and would greatly benefit CP development attempts [190,191].
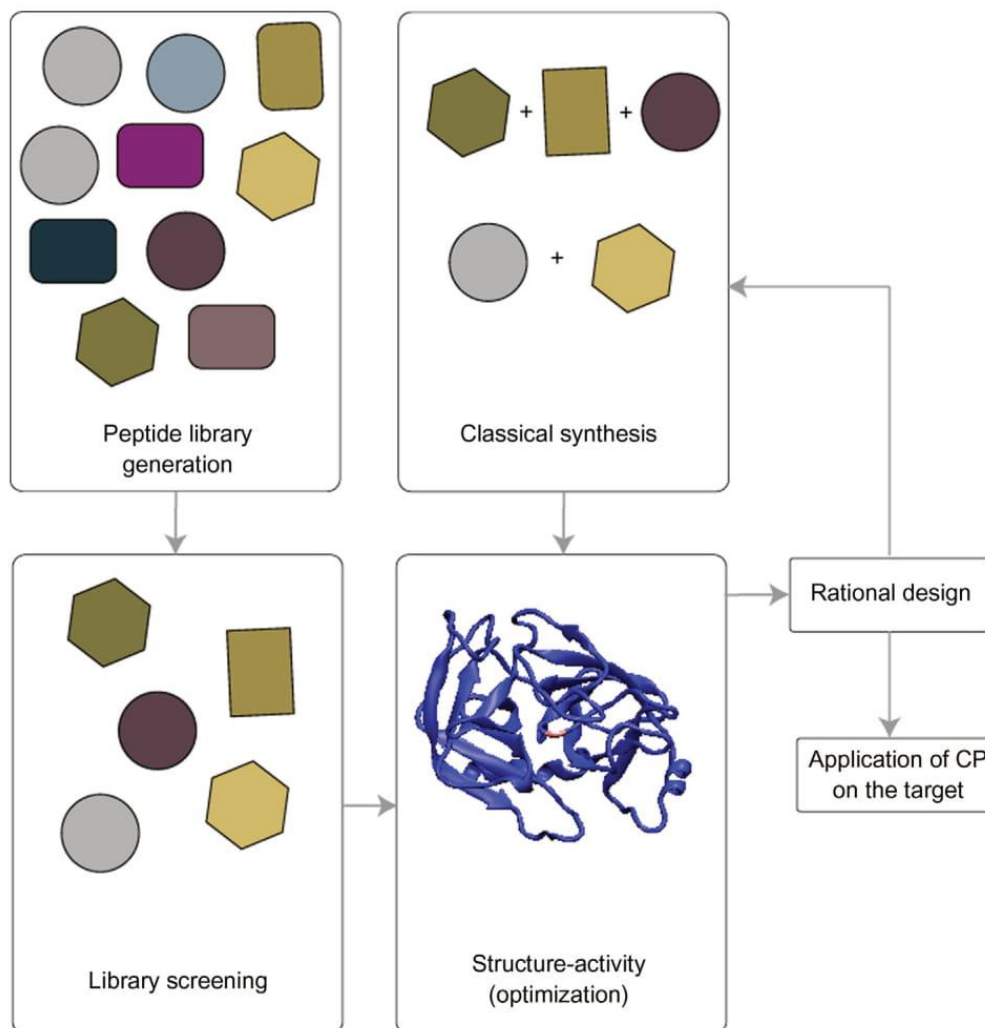
Figure 4.7 Main approaches to identify lead compounds using combinatorial synthesis and/or rational design.

Several recent reviews have summarized computational methods to generate CP libraries for virtual screening, as well as current efforts to accurately predict the conformations adopted by CPs [192−195]. Although several software tools have been developed (i.e., CycloP [196], PLOP [197,198], Peplook [199,200], PEPstrMOD [201], PEP-FOLD [202,203], I-TASSER [204]) and constitute valuable complementary tools, the reliability of these prediction algorithms is highly related to sampling CP conformational space (using algorithms based on distance geometry [205−207], stochastic search [208], or systematic search [209,210], among others) and to accurately describing CP energetics. Furthermore, it is important to remember that most biological systems are not static. To understand how structure and function are related one ought to visualize molecules in action. Complete

understanding of the processes at the molecular level requires the ability to watch molecules as they react, interact, or transform in real time by structurally characterizing the often short-lived transient species and intermediates. Indeed, obtaining high-resolution (temporal and spatial) information about dynamic processes is extremely challenging. In this regard, molecular modeling techniques, mainly molecular dynamics (MD) simulations, may provide useful working hypotheses of the mechanism of action in different environments.

Over the last few years, computational chemistry has played an important role in drug design with validation in wet laboratories. Docking methods employed in computational drug design have been coupled with MD simulations to predict the occurrence of complexes [192,211]. MD simulations have also been employed to investigate the mechanism of cyclic AMPs at the membrane level (see some examples in Fig. 4.8) [212−215,217,218]. Nevertheless, the invaluable insights provided by computer modeling in this area are still in their early days. For example, the absence of reliable systematic studies focused on the comparison of different computational methodologies, or on AMP interactions with different types of lipid bilayers, just to name a few cases, is striking. There are also very few attempts that included more than one membrane-active molecule [219], and there is a lack of quantitative information at comparable time-scales as those employed in wet-labs due to the difficulty in simulating events that span this relevant range. To address the difficulties introduced by the ring strain in the free energy barriers between
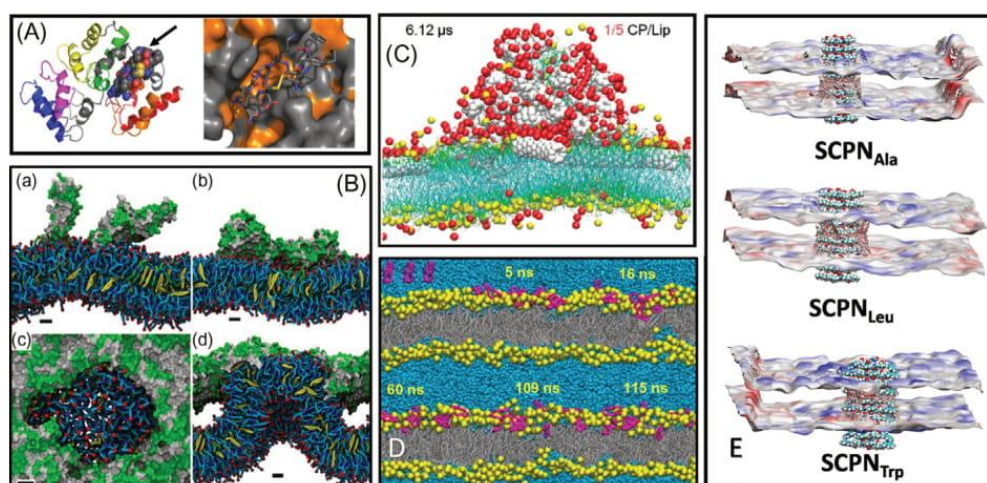
Figure 4.8 Some examples of Docking and MD simulations applied to the study of CPs on membranes. (A) Complex between the calcium-binding protein calbindin-D28K and the cyclic peptide (CKFSIKNRQC) shown as spheres, and detail of the binding site, representing in orange the hydrophobic patches [212]. (B) CG-MD simulation of the progressive membrane association and disruption activity of kB1 [213]. (C) CG-MD simulations of a CP [RRKWLWLW] aggregate interacting with a POPE-POPG membrane [214]. (D) MD simulation of the BPC194 CP interacting with a lipid bilayer [215]. (E) Local membrane thickness for three SCPNs composed of α,γ-CPs [216].

conformations, a variety of enhanced sampling methods, such as REMD [220−224] or META and BE-META simulations [15,225,226] have been applied to help accelerate the sampling process [227−231]. It is clear that for a full understanding of functional dynamics a combination of these methods with structural and spectroscopic techniques is required, to allow the generation of dynamic structural models consistent with all available experimental data. Algorithm improvements, parallelization and specialized hardware have been tried extensively to systematically explore events in the microsecond scale, and MD simulation times and size are now beginning to extend into ranges where direct comparison and experimental testing (EPR, NMR, OCD, AFM, and SAXS) [232,233] are starting to become feasible. Advances in coarse-grain (CG) methodology, which considers appropriately chosen groups of atoms as single interacting centers, have allowed access to unprecedented time-scales in MD simulations, extending them towards biologically relevant time-scales (see, e.g., Fig. 4.8B,C) [213,214,234]. Furthermore, while CG models offer researchers means of accelerating the discovery process, further acceleration is possible through the use of advanced computer hardware, such as graphical processing units (GPUs) [235]. By intelligently combining these techniques it might be possible to address the main limitations of computational techniques applied to CPs, such as structure generation, sampling, and also the accuracy of applying to CPs the force-fields commonly employed for linear peptides and proteins, which remains to be determined [236,2,37].

4.5   Approaches to the preparation of CPs

Most of the CPs produced by Nature involve ribosomal synthesis, comprising mRNA translation to peptide chains of L-amino acids, often posttranslationally modified and cyclized by enzymes [238,239]. However, Nature also widely uses nonribosomal synthesis, making use of enzymes to catalyze the assembly of non-proteinogenic amino acids and derivatives followed by cyclization [240,241]. Encouraged by the existence of natural CPs with biological activity, synthetic chemists and biologists have invested great effort in the development of tools to obtain biologically active CP compounds. These efforts have included both genetic and synthetic methods [23].

The genetic methods (Fig. 4.9) include phage display, intein-based CPs, and mRNA display.

In *phage display technology* [242] (Fig. 4.9A) a gene encoding a protein of interest is inserted into a phage coat protein gene, inducing the phage to display the protein (or peptide) on its surface while containing the gene for the protein (or the peptide) on its inside. Usually, peptides are displayed on the N-terminus, middle, or C-terminus of coat proteins, and are not meant to be cyclic. However, cyclization can be obtained by disulfide bridge formation. One of the main disadvantages of this method is that phage display is limited to natural, ribosomal amino acids. An important point in this methodology is that phage display has been used to generate
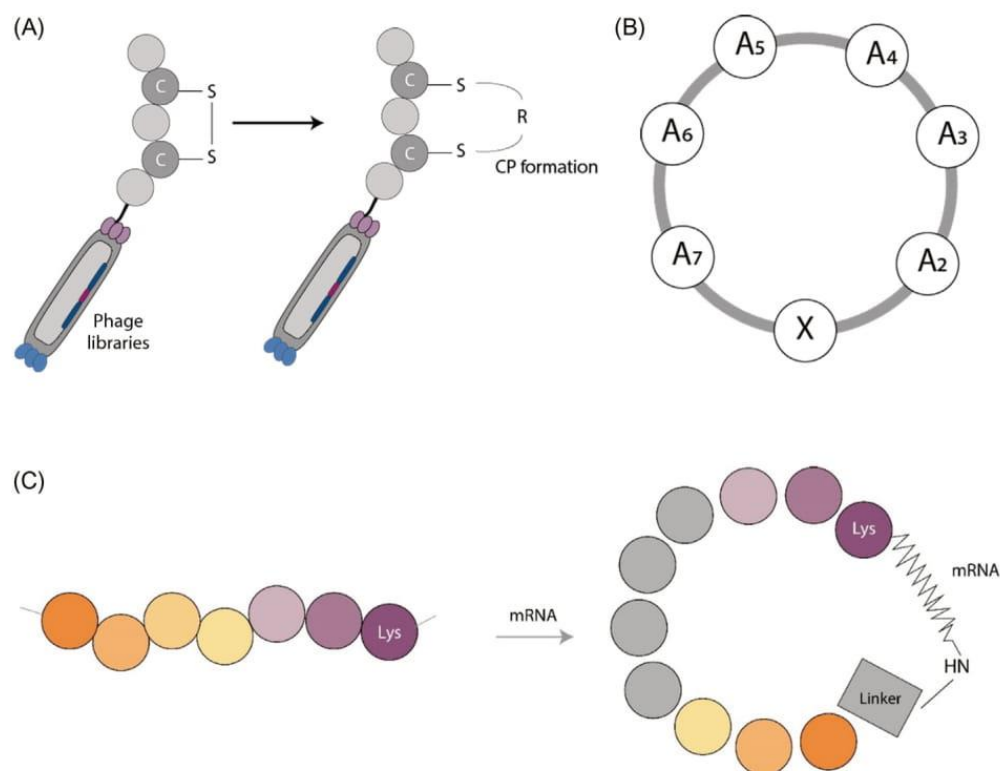
Figure 4.9 Genetic methods to produce CPs: (A) phage display, (B) intein-based CPs, and (C) mRNA display.

screening libraries [243,244]. Furthermore, databases and computational tools have played an important role in phage display study [245,246].

Inteins refer to protein sequences that are spliced out during maturation [247,248]. SICLOPPS (split-intein circuit ligation of peptides and proteins) is a valuable tool to develop CP libraries using a *trans*-intein DnaE protein [249]. The CP formed from SICLOPPS takes a general structure cyclo (XA$_1$A$_2$A$_3$...An), where X is either Cys or Ser (Fig. 4.9B). The main disadvantages of these methods are the requirement of Cys (or Ser) residue in the sequences, the limitation of the choice of the amino acids to ribosomal amino acids and that CPs can only be prepared in vivo.

The method of *mRNA display* (Fig. 4.9C) is an in vitro method of displaying peptides/proteins coupled to the encoding mRNA that has been recently modified to prepare CPs [250,251]. Some of its limitation are poor efficiency, failure of the cyclization reaction when there are multiple Lys residues in the sequence, and undesired dimerization between two mRNA−peptide hybrid molecules mediated by crosslinker.

The synthetic method includes chemical synthesis strategies in *solution* and *solid-phase* [19]. Several groups have summarized the various synthetic methods used to generate CPs [76,107,131,252]. The *solution-phase peptide synthesis*

method has been widely used to synthesize individual peptides. Popular synthetic strategies are based on orthogonally protected precursors at specific functional groups, which are selectively deprotected during peptide synthesis [120,253]. However, the long synthesis time and the laboriousness of the purification, usually reducing overall yields, has led to almost complete substitution of solution-phase by solid-phase peptide synthesis in most research laboratories [254]. The main advantage of solid-supported peptide synthesis and macrocyclizations is that simple washing and filtration are often enough for reasonable purification [255]. To cyclize peptides on a solid support, the linear precursor is most commonly anchored to the support through the side chain of a trifunctional amino acid. A protecting-group strategy of at least three dimensions of orthogonality is required to construct the linear peptide, deprotect the N- and C-termini, cyclize in a head-to-tail, and finally cleave the product from the solid support [76,253,256]. Innovative straightforward protocols involving solid-phase peptide synthesis, followed by in-solution fragment coupling, have been introduced to improve the yield and facilitate the synthesis of large polypeptides [76,257−260].

Solid-phase peptide synthesis in combination with intramolecular native chemical ligation [261] is one of the most common methods of producing synthetic CPs (Fig. 4.10). It allows partial automation and the incorporation of non-native or posttranslationally modified amino acid equivalents that would be difficult to incorporate in peptides produced recombinantly.

The synthetic methods involve individual synthesis (individual compounds are synthesized separately), parallel synthesis (the synthetic intermediates are split during the synthesis and used in later steps), as well as split-and-pool synthesis (where the starting material is split in *n* portions, reacted with *n* building blocks, and recombined in one flask for the second step, repeating this procedure many times. It allows the preparation of peptide libraries in large scales). Recent development of a CP library based on split-and-pool synthesis allows on-bead screening, in-solution screening, and microarray screening of CPs for biological activity [23].

4.6 Limitations of cyclic peptides

Although CPs often show improvements in binding affinity, specificity, or stability when compared to their linear analogues, due to the imposition of constrained geometries, it is important to note that cyclization does not necessarily lead to improvements in all, or sometimes even in any, of these properties [262]. Certain linear peptides can contain sequences that can support rigid structures recognized by targeted receptors without the need for cyclization [263]. There are also cases where peptide cyclization worsens the biological activity of the linear analogues [264] and even linear analogues of native CPs displaying a similar or superior binding affinity to targeted receptors as compared with their cyclic counterparts [265]. Furthermore, peptide cyclization was shown to sometimes decrease the degree of cell membrane penetration. It has been suggested that the lower cell penetration of
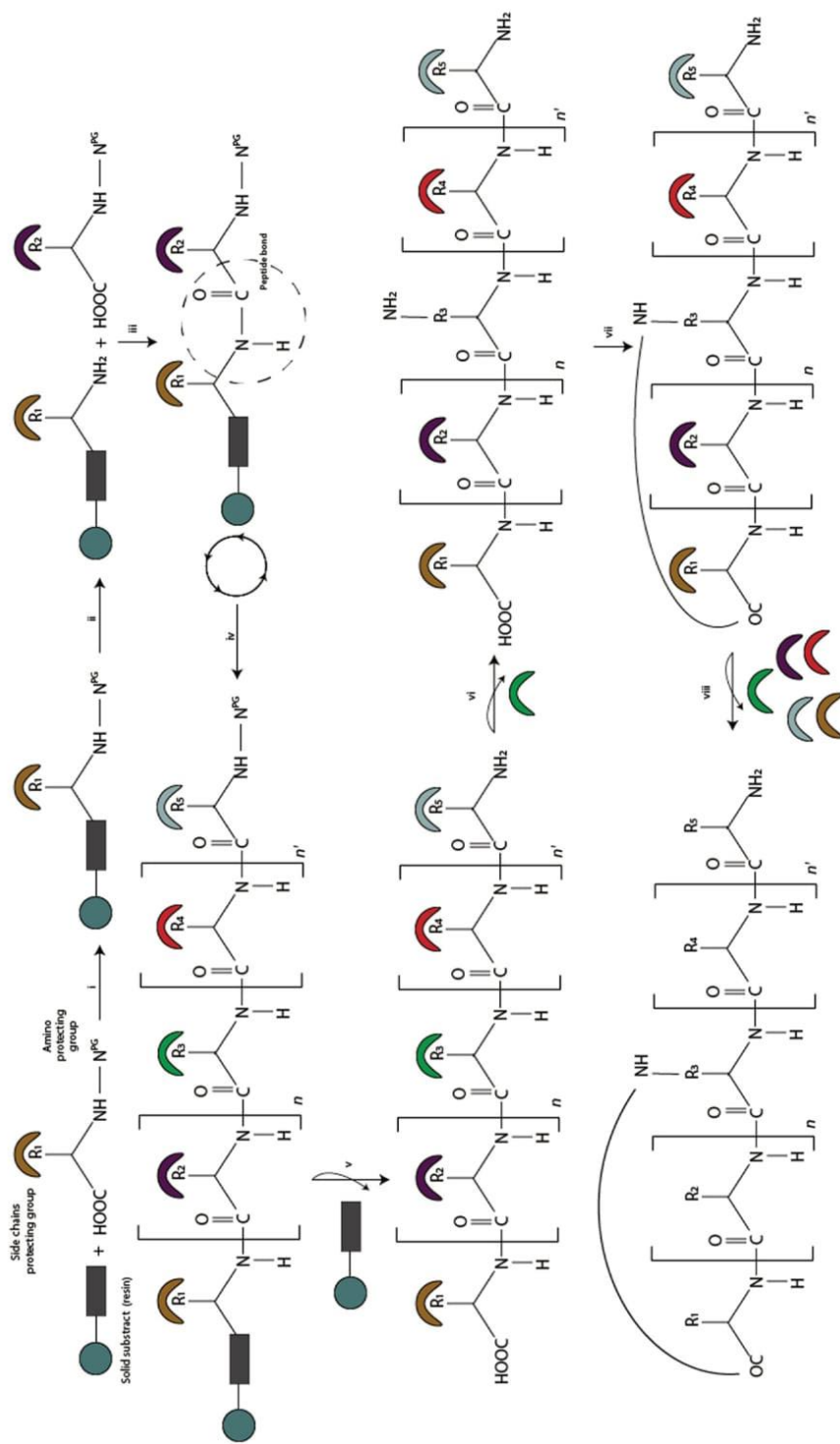
Figure 4.10 Visual representation of the solid-state synthesis of a side chain-to-tail CP. (i) The first amino acid is loaded to the solid support via the carboxyl group, followed by (ii) the removal of the NPG−amino protected group. Afterwards, (iii) the amino group with the activated carboxyl group, of the second amino acid, is coupled and (iv) so as the following amino acids. (v) A cleavage of the resins occurs and also (vi) a selective removal of the side chain amino protected groups. A (vii) cyclization between the side chain amino group and the C-terminal carboxyl group takes place and (viii) a final deprotection of the side chain of the protected groups finishes the cyclization.

particular CPs could be due to a reduction in the enthalpy of interaction with the membrane, contributing to a less favorable internalization [266].

Another important limitation is the fact that scaling-up the production of CPs from a research laboratory to an industrial level is not as accessible as in noncyclized peptides. CPs generally demand a ligation strategy that must be integrated within the synthesis procedure, complicating the chemistry and thus the scaling-up process. Furthermore, the absence of charges on the N- and C-termini reduces the effectiveness of proteomic sequencing techniques, such as mass spectrometry and Edman degradation, making quality control and characterization efforts more complicated than in linear peptides.

4.7 Applications of cyclic peptides

CPs have been widely exploited over recent years, enabling their use in different applications, such as therapeutics, diagnostics, vaccines, and agriculture, among others.

CPs have played a rather important role in *pharmaceutical research* as biomedically useful agents or as lead compounds in drug development [6,23,267]. In the past peptides have been considered poor drug molecules due to various reasons, with probably the most important drawbacks being their quick metabolization/degradation and the fact that many peptides do not usually cross the cell membrane as some small molecules do. However, there has been a rebirth of interest in peptides and CPs in recent years. This is partly because both pharmaceutical companies and academic researchers have realized that these molecules afford quick access to the underexploited level intermediate between traditional small organic molecules and the higher molecular weight space of proteins and antibodies [93,268]. CPs are considered good drug leads and useful therapeutics and biochemical tools, due to the structural features mentioned in the previous sections. Structural rigidity combined with different peptide sequences can provide binding toward target molecules. They can also be more selective when compared to small molecules, while being smaller than protein molecules, such as antibodies and growth factors, and they can more closely reproduce specific interactions involved in PPIs [23]. The constant progress on synthesis and purification strategies, together with a significant decrease in amino acid prices have promoted sustained growth in the use of CPs as therapeutically relevant targets in the drug market [92]. Some representative examples used in the current pharmaceutical market to treat different diseases include *cyclosporine A* and cyclic citrullinated peptides for rheumatoid arthritis [269,270], *azathioprine* for ulcerative colitis [271], *somatostatin* analogues for advanced metastatic colorectal cancer, diabetic retinopathy or pancreatic and gastrointestinal cancers [272,273], *alcitonin* used in osteoporosis and hypercalcemia treatments [274], *ziconotide* indicated for severe chronic pain [275], *eptifibatide* for myocardial infarction [276], and analogues of myelin basic protein (MBP) and myelin oligodendrocyte glycoprotein (MOG) which have shown promising results for multiple

sclerosis [277,278]. *Cyclotides* also exhibit different therapeutic activities such as antimicrobial, [279] anti-HIV [280], and anticancer [281], but they are not in use as drugs because of their cytotoxicity [104].

Nearly all known natural CPs display high *antibacterial activity*. Tyrothricin [49], the first commercialized antibiotic and still used in the clinic today (Tyrosur) or vancomycin [55] are examples of CPs with antimicrobial activity already used in therapeutics. AMPs share amphiphilicity and cationic structural properties with CPPs. Thus, CPPs can present potential application as AMPs with dual actions as both antibiotics and possible molecular transporter properties [282]. However, many of the known CPs are also hemolytic and thus lack the selectivity required for use as a human antibiotic. Efforts to develop CPs as antibiotics in vivo are directed towards the development of analogues that possess greater selectivity for bacterial cells over erythrocytes, and represent an emerging field with very promising initial results.

In recent years it was proposed to use CPs as *agricultural fungicides*, in the control of plant diseases [283]. Antimicrobial CPs that are active against plant pathogens have a wide spectrum of activity (e.g., *Alternaria, Botrytis, Cochliobolus, Geotrichum, Penicillium, Sclerotinia, Fusarium* species, and *Magnaporthe grisea*), probably due to similarity with the fungal cell wall, where antimicrobial CPs are active. However, there are several concerns that need to be solved prior to extended application of CPs in agriculture, such as the selective toxicity for pathogenic fungi over their hosts and the synergistic effects with other fungicides.

The cyclization of peptides has a very promising potential in *drug delivery*. CPP-mediated intracellular nano-drug delivery systems (nano-DDS) can improve delivery of water-insoluble drugs, negatively charged molecules (i.e., DNA, siRNA, phosphopeptides) and proteins [284]. Furthermore, cyclic CPPs containing specific amino acids have been shown to have different geometries, different affinities, and different mechanisms for similar targets as compared to linear CPPs. Thus, CPs can be designed to be used as nuclear delivery vehicles of anticancer compounds targeting DNA. The functionalization of CPs with tumor-targeting moieties can be used as a strategy for selective cancer cell targeting and to enhance nuclear targeting of anticancer drugs. Cyclic CPPs can be also covalently conjugated to active drug cargos to generate prodrugs (chemically modified analogues of an active metabolite) that can improve the pharmacokinetic and pharmacodynamic (PK/PD) properties of the drug. Therefore, an increase in the application of a new generation of CPs for the delivery of a wide range of drugs and biomolecules is to be expected. A representative example is, e.g., a novel drug-delivery system comprised of alternating tryptophan and arginine in a cyclic octapeptide [WR]4 recently presented by Parang and coworkers [285]. They showed that the optimal balance between electrostatic and hydrophobic interactions of the CPs (drug carrier) and phosphopeptides (transporters which give on/off signals to many enzymes through interactions with protein kinases), led to the formation of circular vesicle-like nanostructures (25−60 nm in diameter) with improved intracellular phosphopeptide delivery. Compared to its linear counterpart this delivery system had higher enzymatic stability, improved cell permeability, bypassed endosomal uptake and allowed the nuclear targeting

and cellular delivery of impermeable phosphopeptides [286]. Cyclic [W(RW)4] was conjugated with Dox through an appropriate linker to afford cyclic [W(RW)4]−Dox, a cyclic prodrug ([W(RW)4] − Dox) that can be used to enhance the cellular retention of the drug in the treatment of ovarian cancer [287]. Very recently, it has been found that a novel class of pH-sensitive CPs containing tryptophan and glutamic acid residues have potential applications for targeting tumors and translocation of polar cargo molecules across the cellular membrane. These peptides might have application not only in targeting of acidic diseased tissue, but might also find very interesting applications in cosmetics and skin care products [288].

CPs have also been used as surfactants, showing promising ability for stabilization of silver nanoparticles [283]. These studies established a new class of surfactant-like cyclic peptide that self-assembled into nanostructures and could have potential application for the stabilization of silver nanoparticles and protein biomolecules. Since then, CPs have been used in nano-DDS-containing metal nanoparticles (metal nano-DDSs), which have emerged as effective tools for the treatment of various diseases. The formation of [WR]5-capped gold nanoparticles was shown to enhance the intracellular delivery of model anti-HIV drugs, phosphopeptides, and siRNA [289,290], exhibiting higher molecular transporting potency when compared with the linear counterparts. It has been recently demonstrated that a noncell-penetrating cyclic peptide can be converted to an efficient intracellular drug transporter through capping of the gold nanoparticles [289]. In an aqueous solution of chloroaurate this cyclic peptide formed a gold-capped CP delivery system. It was loaded with hydrophobic drugs (including doxorubicin, lamivudine, emtricitabine, and stavudine) in an equal molar ratio and showed improved cellular uptake and retention when used as a molecular transporter [291]. The generated cyclic peptide-capped selenium nanoparticles (CP−SeNPs) using a CP composed of five tryptophan, four arginine, and one cysteine [W5R4C], can potentially be used as nanosized delivery tools for negatively charged biomolecules and anticancer drugs [292].

Other applications behind CPs have been multifunctional nanoparticles for targeted cancer imaging, cancer therapy, and to identify peptide-targeting ligands. The application of CPs in the *imaging of angiogenesis* (formation of new blood vessels) is another promising approach. Cyclic arginine−glycine−asparatic acid, known as RGD-peptide, is responsible for binding integrin $\alpha_v\beta_3$. Integrins are heterodimeric molecular marker membrane receptors comprised of an α- and a β-subunit that mediate interactions between cells and the extracellular matrix [293]. This CP plays a key role in tumor angiogenesis and metastasis, whereas its expression is significantly upregulated in invasive tumor cells of certain cancers. Cyclic RGD-peptide has also been used for tumor cell targeting due to its high selectivity and affinity for different integrin subtypes [294−296]. The ability to visualize noninvasively and yet to quantify $\alpha_v\beta_3$ integrin expression level in vivo is a property that allows the understanding of the relationship between integrin level and tumor growth and spread. A series of cyclic RGD-peptides were labeled with different radionuclides for positron emission tomography and single-photon emission computed tomography imaging showing tumor targeting efficacy and in vivo pharmacokinetic profiles [297−300].

In addition, cyclo-RGD compound can be used to deliver nanoparticles filled with anticancer drug to the area where the tumor is growing [301].

Many studies have investigated the self-assembly process of CPs. Modification and functionalization of the surface of CP nanostructures can be achieved through reactions with the various side chains of the amino acids present on the CP [302]. By carefully designing the repeating CP unit and optimizing the self-assembly conditions, CP nanostructures can be tailored to meet the needs of specific applications (Fig. 4.11). However, few applications have been developed so far using these self-assembled nanostructures. This is due to the present lack of understanding of the mechanisms of self-assembly and the influence of various parameters on the self-assembling process [303]. It has been recently demonstrated that it is possible to control the supramolecular peptide architecture and the formation of nanotubes or nanoparticles using three different methods—phase equilibrium, pH-driven, and pH-sensitive methods [304]. The dimensions of the self-assembled nanostructures were found to be strongly influenced by the CP concentration, side chain modification, pH value, reaction time, stirring intensity, and sonication time.

SCPNs (Fig. 4.11) are structures built up by stacking CPs, reported for the first time by Ghadiri and coworkers, based on cyclic polypeptides with an even number of alternating D- and L-amino acids [99,305]. They are stabilized by hydrogen bonds—the amino acid side chains are directed outwards while the carbonyl and the amino groups of the peptide backbone are directed perpendicularly to the ring. In this conformation, antiparallel β-sheet-type interactions can be established between CPs in such a way that they stack on top of each other. These structures have attracted special attention due to the ease of modification of their structural and functional properties and because they can adopt a particular orientation by
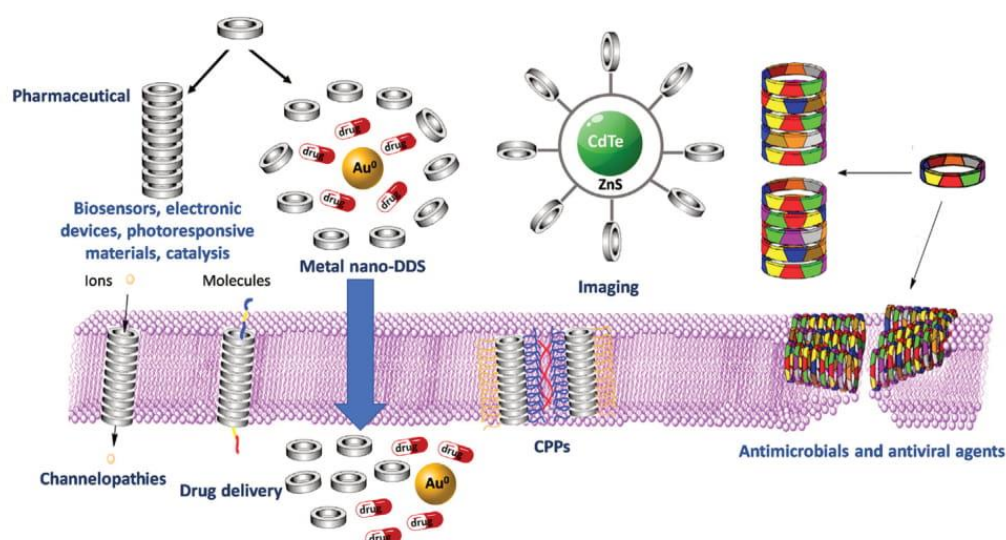
Figure 4.11 Schematic representation of some of the most important applications of self-assembled CPs into SCPNs or nanoparticles.

appropriate choice of the amino acid side chain functionalities and the ring size of the peptide subunit employed. In addition, due to the *Cn* symmetry of the backbone skeleton, nonsymmetrical CPs can form an infinite number of different structures, due to the interstrand rotation between two consecutive CPs, to form nonequivalent interactions for each β-sheet. Appropriate unit design and optimization of conditions for self-assembly allows the nanotube properties to be tailored for specific applications [306]. These nanostructures can be used in artificial photosystems, biosensors, antimicrobials and antiviral agents, electronic devices, photoresponsive materials, selective transmembrane transport channels, catalysis, and drug delivery [135,302,307,308]. Regarding their use in drug delivery, they can be used as artificial ion channels and pores [138]. For example, SCPNs composed of (W-D-L)4-Q-D-L and applied to the delivery of the antitumor drug 5-fluorouracil (5-FU) rapidly reached a high level of penetration into tumor cells where the drug effect was strengthened as the dosage of the cyclic peptide increased. This increase was associated with the CP improving the transport of the drug into the target cell [309]. Results from MD simulations showed that the 5-FU molecule was transported by hopping through different potential energy minima distributed along the subunits of the nanotube [309].

While almost all the SCPNs that have been developed so far have hydrophilic inner surfaces and can only permeate polar molecules, it is possible to modulate the inner properties of particular peptide nanotubes. As was discussed in Section 4.3, α,γ-SCPN [147,310,311] are composed of CPs alternating D-α-amino acids and (1*S*,3*S*)-3-aminocycloalkanecarboxylic acids. γ-Amino acids impose each ring in antiparallel orientation between each two subunits and the side chains of the amino acids are on the outside of the nanotube. This structure generates a partly hydrophobic cavity, which can be modulated by simple chemical modification of the β-carbon of the cyclic γ-amino acids, allowing the tuning of the transport properties of the nanotube. The group of Prof. JR Granja has recently developed a synthetic strategy that allows preparation of γ-amino acids modified at C2 position [148,149], α,γ-SCPN, with promising applications ranging from ion separation to antimicrobial therapy [133,312,313]. Other approximations to create peptide nanotubes with tunable interiors are, for example, the addition of 3-amino-2-methyl benzoic acid in the D,L-alternating primary sequence of the cyclic peptide [150]. The modulation of the external properties of SCPNs allows the design of CPs that self-assemble into lipid membranes, changing their permeability and resistance properties [314]. In these studies it was shown that depending on their sequences the formed SCPNs can be oriented either perpendicularly to the lipid membrane (hydrophobic CPs) [135,141] or in parallel (amphipathic CPs) (Fig. 4.11) [315]. The consequences of this orientation determine the effect caused in the lipid membrane. Hydrophobic CPs form hydrophobic transmembrane channels that can efficiently transport ions and small polar molecules. On the other hand, amphipathic CPs have disruptive properties on the membrane, conferring them a high antimicrobial activity. It was shown that cationic amphiphilic CPs selectively interact with bacterial membranes of Gram-positive bacteria and provided good protection against mice infected with MRSA (meticillin-resistant *Staphylococcus aureus*) [316]. The

structural studies suggest a *carpet-type mechanism* that decreases the membrane stability, dissipating the membrane potential and leading eventually to cell death. One key feature that makes these CPs particularly promising antimicrobial peptides is that in principle the CPs by themselves should not be toxic. It is the membrane interaction that triggers the nanotube formation, having a supramolecular structure in the active form.

The use of SCPNs as *biosensors* has also been described. Studies based on ion channels modified with cyclic D,L-α-octapeptides have shown the ability to detect various polyanionic organic molecules, including the second messenger inositol tris-phosphate. These nanotubes inserted into self-assembled organosulfur monolayers supported on gold films have also shown the capability of diffusion-limited size-selective ion sensing [315]. Overall, these new results are very important to the development of a new class of biosensors and optical devices.

4.8 Concluding remarks

CPs have several structural features that improve the hydrophobicity of native linear counterparts providing conformational stability and enhanced affinity to a certain target. Cyclization of linear peptides also increases the resistance to cleavage by proteolytic enzymes and membrane permeability, leading to superior bioavailability.

Several natural CPs have recently emerged as templates for drug design due to their resistance to chemical or enzymatic hydrolysis and high selectivity to receptors. Apart from several naturally occurring cyclic peptides already in use, biologically active cyclic peptides were developed in recent years with genetic and synthetic approaches. Although not all cyclization strategies and constrained geometries enhance these properties to the same extent, CPs may be obtained with particular characteristics that allow them to be used in various important applications, such as therapeutics, agriculture, or diagnostics.

The development of practical protocols that mimic the power of Nature's strategies remains paramount for the advancement of novel CPs. From increased knowledge of the action of CPs in Nature, it might be possible to optimize ways they could be used in different applications. However, in most cases, the three-dimensional structures of naturally occurring CPs are still unknown, and efforts to determine their structures can provide many important new lessons for synthetic chemists. Furthermore, without the ability to understand dynamic structural changes, the design and creation of new CPs will rely on empirical rule-based approaches as well as on a fair degree of serendipity. More importantly, developing a greater understanding of the relationship between the structure of CPs and their activity and combining this knowledge with the current advances in rational drug design, peptide synthesis, and structure determination will result in the development of novel and more potent CPs. This will contribute to improved treatment of human diseases, such as cancer, infection, neurodegeneration and autoimmunity, as well as to other important applications related to nanotechnology.

References

[1] N. Sewald, H.-D. Jakubke, Introduction and background, Peptides: Chemistry and Biology, Wiley-VCH Verlag GmbH & Co. KGaA, 2009, pp. 1−4.

[2] B. Zhong, C. Zhang, S. Guo, C. Zhang, Rational design of cyclic peptides to disrupt TGF-B/SMAD7 signaling in heterotopic ossification, J. Mol. Graph. Model. 72 (2017) 25−31.

[3] R.P. Hicks, Antibacterial and anticancer activity of a series of novel peptides incorporating cyclic tetra-substituted Cα amino acids, Bioorg. Med. Chem. 24 (18) (2016) 4056−4065.

[4] M. Bastos, G. Bai, P. Gomes, D. Andreu, E. Goormaghtigh, M. Prieto, Energetics and partition of two cecropin-melittin hybrid peptides to model membranes of different composition, Biophys. J. 94 (6) (2008) 2128−2141.

[5] M. Bastos, T. Silva, V. Teixeira, K. Nazmi, J.G. Bolscher, S.S. Funari, et al., Lactoferrin-derived antimicrobial peptide induces a micellar cubic phase in a model membrane system, Biophys. J. 101 (3) (2011) L20−L22.

[6] K. Fosgerau, T. Hoffmann, Peptide therapeutics: current status and future directions, Drug Discov. Today 20 (1) (2015) 122−128.

[7] R.E.W. Hancock, H.G. Sahl, Antimicrobial and host-defense peptides as new anti-infective therapeutic strategies, Nat. Biotechnol. 24 (12) (2006) 1551−1557.

[8] A.A. Zompra, A.S. Galanis, O. Werbitzky, F. Albericio, Manufacturing peptides as active pharmaceutical ingredients, Future Med. Chem. 1 (2) (2009) 361−377.

[9] L. Otvos, Peptide-based drug design: here and now, in: L. Otvos (Ed.), Peptide-Based Drug Design, Humana Press, Totowa, NJ, 2008, pp. 1−8.

[10] D. Goodwin, P. Simerska, I. Toth, Peptides as therapeutics with enhanced bioactivity, Curr. Med. Chem. 19 (26) (2012) 4451−4461.

[11] V.M. Ahrens, R. Frank, S. Boehnke, C.L. Schütz, G. Hampel, D.S. Iffland, et al., Receptor-mediated uptake of boron-rich neuropeptide Y analogues for boron neutron capture therapy, ChemMedChem 10 (1) (2015) 164−172.

[12] J.M. Mason, Design and development of peptides and peptide mimetics as antagonists for therapeutic intervention, Future Med. Chem. 2 (12) (2010) 1813−1822.

[13] G. Luca, M. Rossella De, C. Lucia, Chemical modifications designed to improve peptide stability: incorporation of non-natural amino acids, pseudo-peptide bonds, and cyclization, Curr. Pharm. Des. 16 (28) (2010) 3185−3203.

[14] M. Brindisi, S. Maramai, S. Brogi, E. Fanigliulo, S. Butini, E. Guarino, et al., Development of novel cyclic peptides as pro-apoptotic agents, Eur. J. Med. Chem. 117 (2016) 301−320.

[15] H. Yu, Y.-S. Lin, Toward structure prediction of cyclic peptides, Phys. Chem. Chem. Phys. 17 (6) (2015) 4210−4219.

[16] M. Guharoy, P. Chakrabarti, Secondary structure based analysis and classification of biological interfaces: identification of binding motifs in protein−protein interactions, Bioinformatics 23 (15) (2007) 1909−1918.

[17] J.E. DeLorbe, J.H. Clements, B.B. Whiddon, S.F. Martin, Thermodynamic and structural effects of macrocyclic constraints in protein−ligand interactions, ACS Med. Chem. Lett. 1 (8) (2010) 448−452.

[18] J. DeLorbe, J. Clements, M. Teresk, A. Benfield, H. Plake, L. Millspaugh, et al., Thermodynamic and structural effects of conformational constraints in protein−ligand interactions. Entropic paradox associated with ligand preorganization, J. Am. Chem. Soc. 131 (46) (2009) 16758−16770.

Design and applications of cyclic peptides   113

[19]   A. Tapeinou, M.-T. Matsoukas, C. Simal, T. Tselios, Review cyclic peptides on a merry-go-round; towards drug design, Pept. Sci. 104 (5) (2015) 453−461.

[20]   X. Du, Y. Li, Y.-L. Xia, S.-M. Ai, J. Liang, P. Sang, et al., Insights into protein−ligand interactions: mechanisms, models, and methods, Int. J. Mol. Sci. 17 (2) (2016) 144.

[21]   P. Edman, Chemistry of amino acids and peptides, Annu. Rev. Biochem. 28 (1959) 69−96.

[22]   D.A. Horton, G.T. Bourne, M.L. Smythe, Exploring privileged structures: the combinatorial synthesis of cyclic peptides, Mol. Divers. 5 (4) (2000) 289−304.

[23]   S.H. Joo, Cyclic peptides as therapeutic agents and biochemical tools, Biomol. Ther. 20 (1) (2012) 19−26.

[24]   F.J. Duffy, M. Devocelle, D.C. Shields, Computational approaches to developing short cyclic peptide modulators of protein−protein interactions, in: P. Zhou, J. Huang (Eds.), Computational Peptidology, Springer New York, New York, 2015, pp. 241−271.

[25]   T.S. Young, D.D. Young, I. Ahmad, J.M. Louis, S.J. Benkovic, P.G. Schultz, Evolution of cyclic peptide protease inhibitors, Proc. Nat. Acad. Sci. U.S.A. 108 (27) (2011) 11052−11056.

[26]   K. Shibata, T. Suzawa, S. Soga, T. Mizukami, K. Yamada, N. Hanai, et al., Improvement of biological activity and proteolytic stability of peptides by coupling with a cyclic peptide, Bioorg. Med. Chem. Lett. 13 (15) (2003) 2583−2586.

[27]   K. Jensen, Peptide and Protein Design for Biopharmaceutical Applications, Wiley, 2009.

[28]   M.S. Lee, B. Gardner, M. Kahn, H. Nakanishi, The three-dimensional solution structure of a constrained peptidomimetic in water and in chloroform observation of solvent induced hydrophobic cluster, FEBS Lett. 359 (2−3) (1995) 113−118.

[29]   K. Uma, R. Kishore, P. Balaram, Stereochemical constraints in peptide design: analysis of the influence of a disulfide bridge and an α-aminoisobutyryl residue on the conformation of a hexapeptide, Biopolymers 33 (6) (1993) 865−871.

[30]   D. Lau, L. Guo, R. Liu, J. Marik, K. Lam, Peptide ligands targeting integrin α3β1 in non-small cell lung cancer, Lung Cancer 52 (3) (2006) 291−297.

[31]   T. Rezai, B. Yu, G.L. Millhauser, M.P. Jacobson, R.S. Lokey, Testing the conformational hypothesis of passive membrane permeability using synthetic cyclic peptide diastereomers, J. Am. Chem. Soc. 128 (8) (2006) 2510−2511.

[32]   Y.-U. Kwon, T. Kodadek, Quantitative comparison of the relative cell permeability of cyclic and linear peptides, Chem. Biol. 14 (6) (2007) 671−677.

[33]   G. Hussack, T. Hirama, W. Ding, R. MacKenzie, J. Tanha, Engineered single-domain antibodies with high protease resistance and thermal stability, PLoS One 6 (11) (2011) e28218.

[34]   M. Lindgren, M. Hällbrink, A. Prochiantz, Ü. Langel, Cell-penetrating peptides, Trends Pharmacol. Sci. 21 (3) (2000) 99−103.

[35]   E. Cini, G. Bifulco, G. Menchi, M. Rodriquez, M. Taddei, Synthesis of enantiopure 7-substituted azepane-2-carboxylic acids as templates for conformationally constrained peptidomimetics, Eur. J. Org. Chem. 2012 (11) (2012) 2133−2141.

[36]   G. Grigoryan, A.W. Reinke, A.E. Keating, Design of protein-interaction specificity gives selective bZIP-binding peptides, Nature 458 (7240) (2009) 859−864.

[37]   A. Grauer, B. König, A. Peptidomimetics, Versatile route to biologically active compounds, Eur. J. Org. Chem. 2009 (30) (2009) 5099−5111.

[38]   D.J. Mandell, T. Kortemme, Computer-aided design of functional protein interactions, Nat. Chem. Biol. 5 (11) (2009) 797−807.

[39]   N. Terrett, Drugs in middle space, MedChemComm 4 (3) (2013) 474−475.

Peptide Applications in Biomedicine, Biotechnology and Bioengineering

[40] G.F. Gause, M.G. Brazhnikova, Gramicidin S and its use in the treatment of infected wounds, Nature 154 (3918) (1944) 703−803.

[41] K. Thell, R. Hellinger, E. Sahin, P. Michenthaler, M. Gold-Binder, T. Haider, et al., Oral activity of a nature-derived cyclic peptide for the treatment of multiple sclerosis, Proc. Nat. Acad. Sci. U.S.A. 113 (15) (2016) 3960−3965.

[42] H.-S. Lee, H.J. Shin, K.H. Jang, T.S. Kim, K.-B. Oh, J. Shin, Cyclic peptides of the nocardamine class from a marine-derived bacterium of the genus *Streptomyces*, J. Nat. Prod. 68 (4) (2005) 623−625.

[43] V.A. Burns, B.G. Bobay, A. Basso, J. Cavanagh, C. Melander, Targeting RNA with cysteine-constrained peptides, Bioorg. Med. Chem. Lett. 18 (2) (2008) 565−567.

[44] D.J. Craik, Seamless proteins tie up their loose ends, Science 311 (5767) (2006) 1563.

[45] N. Daly, D. Wilson, D. Craik, Cyclic peptides from plants and their promise in drug design, Aust. Biochem. 43 (2) (2012) 7−9.

[46] D. Craik, A. Poth, M. Colgrave, M. Akcan, B. Oku, A. Chan, et al., Discovery and applications of naturally occurring cyclic peptides, Planta Med. 77 (12) (2011) 1231−2231.

[47] T. Mogi, K. Kita, Gramicidin S and polymyxins: the revival of cationic cyclic peptide antibiotics, Cell. Mol. Life Sci. 66 (23) (2009) 3821.

[48] E. Conti, T. Stachelhaus, M.A. Marahiel, P. Brick, Structural basis for the activation of phenylalanine in the non-ribosomal biosynthesis of gramicidin S, EMBO J. 16 (14) (1997) 4174.

[49] H.D. Mootz, M.A. Marahiel, The tyrocidine biosynthesis operon of *Bacillus brevis*: complete nucleotide sequence and biochemical characterization of functional internal adenylation domains, J. Bacteriol. 179 (21) (1997) 6843−6850.

[50] F. Lipmann, R. Roskoski, W. Gevers, H. Kleinkauf, Tyrocidine biosynthesis by three complementary fractions from *Bacillus brevis* (ATCC 8185), Biochemistry 9 (25) (1970) 4839−4845.

[51] S.A. Survase, L.D. Kagliwal, U.S. Annapure, R.S. Singhal, Cyclosporin A: a review on fermentative production, downstream processing and pharmacological applications, Biotechnol. Adv. 29 (4) (2011) 418−435.

[52] P. Martinez Viedma, H. Abriouel, N. Ben Omar, R. Lucas Lopez, A. Galvez, Inhibition of spoilage and toxigenic *Bacillus* species in dough from wheat flour by the cyclic peptide enterocin AS-48, Food Control. 22 (5) (2011) 756−761.

[53] J. Borrero, D.A. Brede, M. Skaugen, D.B. Diep, C. Herranz, I.F. Nes, et al., Characterization of Garvicin ML, a novel circular bacteriocin produced by *Lactococcus garvieae* DCC43, isolated from Mallard ducks (*Anas platyrhynchos*), Appl. Environ. Microbiol. 77 (1) (2011) 369−373.

[54] N. Sawa, T. Zendo, J. Kiyofuji, K. Fujita, K. Himeno, J. Nakayama, et al., Identification and characterization of lactocyclicin Q, a novel cyclic bacteriocin produced by *Lactococcus* sp strain QU 12, Appl. Environ. Microbiol. 75 (6) (2009) 1552−1558.

[55] A.V.R. Rao, M.K. Gurjar, K.L. Reddy, A.S. Rao, Studies directed toward the synthesis of vancomycin and related cyclic-peptides, Chem. Rev. 95 (6) (1995) 2135−2167.

[56] H.E. Hallen, H. Luo, J.S. Scott-Craig, J.D. Walton, Gene family encoding the major toxins of lethal Amanita mushrooms, Proc. Nat. Acad. Sci. U.S.A. 104 (48) (2007) 19097−19101.

[57] A.T. Bockus, C.M. McEwen, R.S. Lokey, Form and function in cyclic peptide natural products: a pharmacokinetic perspective, Curr. Top. Med. Chem. 13 (7) (2013) 821−836.

Design and applications of cyclic peptides   115

[58] T. Wieland, H. Faulstich, Amatoxins, phallotoxins, phallolysin, and antamanide —
      biologically-active components of poisonous amanita mushrooms, CRC Crit. Rev.
      Biochem. 5 (3) (1978) 185−260.

[59] D.J. Craik, N.L. Daly, T. Bond, C. Waine, Plant cyclotides: a unique family of cyclic
      and knotted proteins that defines the cyclic cystine knot structural motif, J. Mol. Biol.
      294 (5) (1999) 1327−1336.

[60] T. Mahatmanto, Review seed biopharmaceutical cyclic peptides: from discovery to
      applications, Biopolymers 104 (6) (2015) 804−814.

[61] O. Saether, D.J. Craik, I.D. Campbell, K. Sletten, J. Juul, D.G. Norman, Elucidation of
      the primary and three-dimensional structure of the uterotonic polypeptide Kalata B1,
      Biochemistry 34 (13) (1995) 4147−4158.

[62] M.L.J. Korsinczky, H.J. Schirra, D.J. Craik, Sunflower trypsin inhibitor-1, Curr. Protein
      Pept. Sci. 5 (5) (2004) 351−364.

[63] N. Venkataraman, A.L. Cole, P. Ruchala, A.J. Waring, R.I. Lehrer, O. Stuchlik, et al.,
      Reawakening retrocyclins: ancestral human defensins active against HIV-1, PLoS Biol.
      7 (4) (2009) 720−729.

[64] A.C. Conibear, K.J. Rosengren, P.J. Harvey, D.J. Craik, Structural characterization of
      the cyclic cystine ladder motif of theta-defensins, Biochemistry 51 (48) (2012)
      9718−9726.

[65] Y.Q. Tang, J. Yuan, G. Osapay, K. Osapay, D. Tran, C.J. Miller, et al., A cyclic
      antimicrobial peptide produced in primate leukocytes by the ligation of two truncated
      alpha-defensins, Science 286 (5439) (1999) 498−502.

[66] A.E. Garcia, G. Osapay, P.A. Tran, J. Yuan, M.E. Selsted, Isolation, synthesis, and
      antimicrobial activities of naturally occurring theta-defensin isoforms from baboon
      leukocytes, Infect. Immun. 76 (12) (2008) 5883−5891.

[67] D.W. Urry, M. Ohnishi, R. Walter, Secondary structure of the cyclic moiety of the pep-
      tide hormone oxytocin and its deamino analog, Proc. Nat. Acad. Sci. 66 (1) (1970)
      111−116.

[68] S. Granier, S. Terrillon, R. Pascal, H. Déméné, M. Bouvier, G. Guillon, et al., A cyclic
      peptide mimicking the third intracellular loop of the V2 vasopressin receptor inhibits
      signaling through its interaction with receptor dimer and G protein, J. Biol. Chem. 279
      (49) (2004) 50904−50914.

[69] M. Manning, J.P. Przybylski, A. Olma, W.A. Klis, M. Kruszynski, N.C. Wo, et al., No
      requirement of cyclic conformation of antagonists in binding to vasopressin receptors,
      Nature 329 (6142) (1987) 839−840.

[70] S. Punna, J. Kuzelka, Q. Wang, M.G. Finn, Head-to-tail peptide cyclodimerization by
      copper-catalyzed azide-alkyne cycloaddition, Angew. Chem. Int. Ed. 44 (15) (2005)
      2215−2220.

[71] D.J. Craik, N.L. Daly, I. Saska, M. Trabi, K.J. Rosengren, Structures of naturally occur-
      ring circular proteins from bacteria, J. Bacteriol. 185 (14) (2003) 4011−4021.

[72] A. Bryan, L. Joseph, J.A. Bennett, H.I. Jacobson, T.T. Andersen, Design and synthesis
      of biologically active peptides: a "tail" of amino acids can modulate activity of syn-
      thetic cyclic peptides, Peptides 32 (12) (2011) 2504−2510.

[73] J.E. Bock, J. Gavenonis, J.A. Kritzer, Getting in shape: controlling peptide bioactivity
      and bioavailability using conformational constraints, ACS Chem. Biol. 8 (3) (2013)
      488−499.

[74] C. Ramakrishnan, P.K.C. Paul, K. Ramnarayan, Cyclic peptides — small and big and
      their conformational aspects, J. Biosci. 8 (1) (1985) 239−251.

[75] E.M. Driggers, S.P. Hale, J. Lee, N.K. Terrett, The exploration of macrocycles for drug discovery—an underexploited structural class, Nat. Rev. Drug Discov. 7 (7) (2008) 608−624.

[76] C.J. White, A.K. Yudin, Contemporary strategies for peptide macrocyclization, Nat. Chem. 3 (7) (2011) 509−524.

[77] D.A. Bushnell, P. Cramer, R.D. Kornberg, Structural basis of transcription: alpha-amanitin-RNA polymerase II cocrystal at 2.8 A resolution, Proc. Nat. Acad. Sci. U.S.A. 99 (3) (2002) 1218−1222.

[78] F. Enjalbert, S. Rapior, J. Nouguier-Soule, S. Guillon, N. Amouroux, Treatment of amatoxin poisoning: 20-year retrospective analysis, J. Toxicol. Clin. Toxicol. 40 (6) (2002) 715−757.

[79] S.D. Jolad, J.J. Hoffmann, S.J. Torrance, R.M. Wiedhopf, J.R. Cole, S.K. Arora, et al., Bouvardin and deoxybouvardin, anti-tumor cyclic hexapeptides from bouvardia-ternifolia (*Rubiaceae*), J. Am. Chem. Soc. 99 (24) (1977) 8040−8045.

[80] M. Zalacain, E. Zaera, D. Vazquez, A. Jimenez, The mode of action of the anti-tumor drug bouvardin, an inhibitor of protein-synthesis in eukaryotic cells, FEBS Lett. 148 (1) (1982) 95−97.

[81] T.W.C. Leung, D.H. Williams, J.C.J. Barna, S. Foti, P.B. Oelrichs, Structural studies on the peptide moroidin from laportea moroides, Tetrahedron 42 (12) (1986) 3333−3348.

[82] S.D. Kahn, P.M. Booth, J.P. Waltho, D.H. Williams, Computer-assisted structure determination − structure of the peptide moroidin from laportea-moroides, J. Org. Chem. 54 (8) (1989) 1901−1904.

[83] C. Heinis, T. Rutherford, S. Freund, G. Winter, Phage-encoded combinatorial chemical libraries based on bicyclic peptides, Nat. Chem. Biol. 5 (7) (2009) 502−507.

[84] A. Angelini, L. Cendron, S. Chen, J. Touati, G. Winter, G. Zanotti, et al., Bicyclic peptide inhibitor reveals large contact interface with a protease target, ACS Chem. Biol. 7 (5) (2012) 817−821.

[85] S. Chen, J. Morales-Sanfrutos, A. Angelini, B. Cutting, C. Heinis, Structurally diverse cyclisation linkers impose different backbone conformations in bicyclic peptides, ChemBioChem 13 (7) (2012) 1032−1038.

[86] W. Lian, P. Upadhyaya, C.A. Rhodes, Y. Liu, D. Pei, Screening bicyclic peptide librar-ies for protein−protein interaction inhibitors: discovery of a tumor necrosis factor-alpha antagonist, J. Am. Chem. Soc. 135 (32) (2013) 11990−11995.

[87] J.S. Quartararo, P. Wu, J.A. Kritzer, Peptide bicycles that inhibit the Grb2 SH2 domain, ChemBioChem 13 (10) (2012) 1490−1496.

[88] R. Roodbeen, B. Paaske, L. Jiang, J.K. Jensen, A. Christensen, J.T. Nielsen, et al., Bicyclic peptide inhibitor of urokinase-type plasminogen activator: mode of action, ChemBioChem 14 (16) (2013) 2179−2188.

[89] J. Lubelski, R. Rink, R. Khusainov, G.N. Moll, O.P. Kuipers, Biosynthesis, immunity, regulation, mode of action and engineering of the model lantibiotic nisin, Cell. Mol. Life Sci. 65 (3) (2008) 455−476.

[90] C. Chatterjee, M. Paul, L.L. Xie, W.A. van der Donk, Biosynthesis and mode of action of lantibiotics, Chem. Rev. 105 (2) (2005) 633−683.

[91] H. Lackner, 3-Dimensional structure of actinomycins, Angew. Chem. Int. Ed. Engl. 14 (6) (1975) 375−386.

[92] V. Baeriswyl, C. Heinis, Polycyclic peptide therapeutics, ChemMedChem 8 (3) (2013) 377−384.

Design and applications of cyclic peptides   117

[93] T.B. Andrew, M.M. Cayla, R.S. Lokey, Form and function in cyclic peptide natural products: a pharmacokinetic perspective, Curr. Top. Med. Chem. 13 (7) (2013) 821−836.

[94] A. Stavrakoudis, I.G. Tsoulos, Z.O. Shenkarev, T.V. Ovchinnikova, Molecular dynamics simulation of antimicrobial peptide arenicin-2: β-hairpin stabilization by noncovalent interactions, Pept. Sci. 92 (3) (2009) 143−155.

[95] R.E.W. Hancock, M.G. Scott, The role of antimicrobial peptides in animal defenses, Proc. Nat. Acad. Sci. U.S.A. 97 (16) (2000) 8856−8861.

[96] K. Matsuzaki, Control of cell selectivity of antimicrobial peptides, Biochim. Biophys. Acta 1788 (8) (2009) 1687−1692.

[97] M.R. Yeaman, N.Y. Yount, Mechanisms of antimicrobial peptide action and resistance, Pharmacol. Rev. 55 (1) (2003) 27.

[98] M. Zasloff, Antimicrobial peptides of multicellular organisms, Nature 415 (6870) (2002) 389−395.

[99] M.R. Ghadiri, J.R. Granja, R.A. Milligan, D.E. McRee, N. Khazanovich, Self-assembling organic nanotubes based on a cyclic peptide architecture, Nature 366 (6453) (1993) 324−327.

[100] K. Rosenthal-Aizman, G. Svensson, A. Undén, Self-assembling peptide nanotubes from enantiomeric pairs of cyclic peptides with alternating D and L amino acid residues, J. Am. Chem. Soc. 126 (11) (2004) 3372−3373.

[101] P.F. Augustijns, T.P. Bradshaw, L.S.L. Gan, R.W. Hendren, D.R. Thakker, Evidence for a polarized efflux system in Caco-2 cells capable of modulating cyclosporine A transport, Biochem. Biophys. Res. Commun. 197 (2) (1993) 360−365.

[102] J. Gao, M.T. Hamann, Chemistry and biology of kahalalides, Chem. Rev. 111 (5) (2011) 3208−3235.

[103] D.W. Lee, B.S. Kim, Antimicrobial cyclic peptides for plant disease control, Plant Pathol. J. 31 (1) (2015) 1−11.

[104] N.L. Daly, K.J. Rosengren, D.J. Craik, Discovery, structure and biological activities of cyclotides, Adv. Drug Deliv. Rev. 61 (11) (2009) 918−930.

[105] L. Skjeldal, L. Gran, K. Sletten, B.F. Volkman, Refined structure and metal binding site of the Kalata B1 peptide, Arch. Biochem. Biophys. 399 (2) (2002) 142−148.

[106] Y.L. Li, T. Bi, J.A. Camarero, Chemical and biological production of cyclotides, Adv. Bot. Res. 76 (2015) 271−303.

[107] J.S. Davies, The cyclization of peptides and depsipeptides, J. Pept. Sci. 9 (8) (2003) 471−501.

[108] A. Kumar, G. Ye, Y. Wang, X. Lin, G. Sun, K. Parang, Synthesis and structure−activity relationships of linear and conformationally constrained peptide analogues of CIYKYY as Src tyrosine kinase inhibitors, J. Med. Chem. 49 (11) (2006) 3395−3401.

[109] N. Assa-Munt, X. Jia, P. Laakkonen, E. Ruoslahti, Solution structures and integrin binding activities of an RGD peptide with two isomers, Biochemistry 40 (8) (2001) 2373−2378.

[110] C. Gilon, C. Mang, E. Lohof, A. Friedler, H. Kessler, Synthesis of cyclic peptides, in: M. Goodman, C. Toniolo, L. Moroder, A. Felix (Eds.), Synthesis of Peptides and Peptidomimetics, G. Thieme, 2002.

[111] Y.-U. Kwon, T. Kodadek, Encoded combinatorial libraries for the construction of cyclic peptoid microarrays, Chem. Commun. (Camb). (44) (2008) 5704−5706.

[112] C.M. Deber, V. Madison, E.R. Blout, Why cyclic peptides? Complementary approaches to conformations, Acc. Chem. Res. 9 (3) (1976) 106−113.

[113] S. Jiang, Z. Li, K. Ding, P.P. Roller, Recent progress of synthetic studies to peptide and peptidomimetic cyclization, Curr. Org. Chem. 12 (17) (2008) 1502−1542.

[114] D.J. Craik, J.E. Swedberg, J.S. Mylne, M. Cemazar, Cyclotides as a basis for drug design, Expert Opin. Drug Discov. 7 (3) (2012) 179−194.

[115] K.S. Harris, T. Durek, Q. Kaas, A.G. Poth, E.K. Gilding, B.F. Conlan, et al., Efficient backbone cyclization of linear peptides by a recombinant asparaginyl endopeptidase, Nat. Commun. 6 (2015) 10199.

[116] A. Piserchio, G.D. Salinas, T. Li, J. Marshall, M.R. Spaller, D.F. Mierke, Targeting specific PDZ domains of PSD-95: structural basis for enhanced affinity and enzymatic stability of a cyclic peptide, Chem. Biol. 11 (4) (2004) 469−473.

[117] P. Grieco, P.M. Gitu, V.J. Hruby, Preparation of "side-chain-to-side-chain" cyclic peptides by Allyl and Alloc strategy: potential for library synthesis, J. Pept. Res. 57 (3) (2001) 250−256.

[118] S.R. Tala, S.M. Schnell, C. Haskell-Luevano, Microwave-assisted solid-phase synthesis of side-chain to side-chain lactam-bridge cyclic peptides, Bioorg. Med. Chem. Lett. 25 (24) (2015) 5708−5711.

[119] C. Gilon, D. Halle, M. Chorev, Z. Selincer, G. Byk, Backbone cyclization: a new method for conferring conformational constraint on peptides, Biopolymers 31 (6) (1991) 745−750.

[120] Lundquist, J.C. Pelletier, A new tri-orthogonal strategy for peptide cyclization, Org. Lett. 4 (19) (2002) 3219−3221.

[121] C.G. Ullman, L. Frigotto, R.N. Cooley, In vitro methods for peptide display and their applications, Brief. Funct. Genomics 10 (3) (2011) 125−134.

[122] M. Hahn, D. Winkler, K. Welfle, R. Misselwitz, H. Welfle, H. Wessner, et al., Cross-reactive binding of cyclic peptides to an anti-TGFα antibody Fab fragment: an X-ray structural and thermodynamic analysis, J. Mol. Biol. 314 (2) (2001) 293−309.

[123] M. Akamatsu, P.P. Roller, L. Chen, Z.-Y. Zhang, B. Ye, T.R. Burke Jr, Potent inhibition of protein-tyrosine phosphatase by phosphotyrosine-mimic containing cyclic peptides, Bioorg. Med. Chem. 5 (1) (1997) 157−163.

[124] G. Luca, C. Giuliana, T. Alessandra, S. Federico, M. Rossella De, C. Gianpaolo, Cyclopeptide analogs for generating new molecular and 3D diversity, Comb. Chem. High Throughput Screen 12 (10) (2009) 929−939.

[125] A. Fernández-Tejada, F. Corzana, J.H. Busto, A. Avenoza, J.M. Peregrina, Conformational effects of the non-natural α-methylserine on small peptides and glycopeptides, J. Org. Chem. 74 (24) (2009) 9305−9313.

[126] A. Fernández-Tejada, F. Corzana, J.H. Busto, G. Jiménez-Osés, J.M. Peregrina, A. Avenoza, Non-natural amino acids as modulating agents of the conformational space of model glycopeptides, Chemistry 14 (23) (2008) 7042−7058.

[127] J. Schwochert, R. Turner, M. Thang, R.F. Berkeley, A.R. Ponkey, K.M. Rodriguez, et al., Peptide to peptoid substitutions increase cell permeability in cyclic hexapeptides, Org. Lett. 17 (12) (2015) 2928−2931.

[128] S. Chen, D. Gfeller, S.A. Buth, O. Michielin, P.G. Leiman, C. Heinis, Improving binding affinity and stability of peptide ligands by substituting glycines with D-amino acids, ChemBioChem 14 (11) (2013) 1316−1322.

[129] A.C. Rand, S.S.F. Leung, H. Eng, C.J. Rotter, R. Sharma, A.S. Kalgutkar, et al., Optimizing PK properties of cyclic peptides: the effect of side chain substitutions on permeability and clearance, MedChemComm 3 (10) (2012) 1282−1289.

Design and applications of cyclic peptides   119

[130] O. Demmer, A.O. Frank, H. Kessler, Design of cyclic peptides, in: K. Jensen (Ed.), Peptide and Protein Design for Biopharmaceutical Applications, John Wiley & Sons, Ltd., 2009.
[131] J.N. Lambert, J.P. Mitchell, K.D. Roberts, The synthesis of cyclic peptides, J. Chem. Soc. Perkin Trans. 1 (5) (2001) 471−484.
[132] R. Garcia-Fandino, M. Amorin, J.R. Granja, Synthesis of supramolecular nanotubes, Supramolecular Chemistry: From Molecules to Nanomaterials, John Wiley & Sons, Ltd, 2012.
[133] J. Montenegro, M.R. Ghadiri, J.R. Granja, Ion channel models based on self-assembling cyclic peptide nanotubes, Acc. Chem. Res. 46 (12) (2013) 2955−2965.
[134] T. Suga, S. Osada, H. Kodama, Formation of ion-selective channel using cyclic tetra-peptides, Bioorg. Med. Chem. 20 (1) (2012) 42−46.
[135] S. Fernandez-Lopez, H.-S. Kim, E.C. Choi, M. Delgado, J.R. Granja, A. Khasanov, et al., Antibacterial agents based on the cyclic D,L-[alpha]-peptide architecture, Nature 412 (6845) (2001) 452−455.
[136] J. Taira, S. Osada, R. Hayashi, T. Ueda, M. Jelokhani-Niaraki, H. Aoyagi, et al., Trans-bilayer ion conduction by proline containing cyclic hexapeptides and effects of amino acid substitutions on ion conducting properties, Bull. Chem. Soc. Jpn. 83 (6) (2010) 683−688.
[137] J.T. Fletcher, J.A. Finlay, M.E. Callow, J.A. Callow, M.R. Ghadiri, A combinatorial approach to the discovery of biocidal six-residue cyclic D,L-α-peptides against bacteria, MRSA and E. coli and the aiofouling algae Ulva linza and Navicula perminuta, Chemistry 13 (14) (2007) 4008−4013.
[138] M.R. Ghadiri, J.R. Granja, L.K. Buehler, Artificial transmembrane ion channels from self-assembling peptide nanotubes, Nature 369 (6478) (1994) 301−304.
[139] J. Sanchez-Quesada, M.R. Ghadiri, H. Bayley, O. Braha, Cyclic peptides as molecular adapters for a pore-forming protein, J. Am. Chem. Soc. 122 (48) (2000) 11757−11766.
[140] H.S. Kim, J.D. Hartgerink, M.R. Ghadiri, Oriented self-assembly of cyclic peptide nanotubes in lipid membranes, J. Am. Chem. Soc. 120 (18) (1998) 4417−4424.
[141] L. Motiei, S. Rahimipour, D.A. Thayer, C.-H. Wong, M.R. Ghadiri, Antibacterial cyclic D,L-[small alpha]-glycopeptides, Chem. Commun. (25) (2009) 3693−3695.
[142] J.R. Granja, M.R. Ghadiri, Channel-mediated transport of glucose across lipid bilayers, J. Am. Chem. Soc. 116 (23) (1994) 10785−10786.
[143] J. Sánchez-Quesada, H. Sun Kim, M.R. Ghadiri, A synthetic pore-mediated transmembrane transport of glutamic acid, Angew. Chem. Int. Ed. 40 (13) (2001) 2503−2506.
[144] N. Khazanovich, J.R. Granja, D.E. McRee, R.A. Milligan, M.R. Ghadiri, Nanoscale tubular ensembles with specified internal diameters. Design of a self-assembled nano-tube with a 13-[angstrom] pore, J. Am. Chem. Soc. 116 (1994) 6011−6012.
[145] D. Seebach, E. Dubost, R.I. Mathad, B. Jaun, M. Limbach, M. Löweneck, et al., New open-chain and cyclic tetrapeptides, consisting of α-, β2-, and β3-amino-acid residues, as somatostatin mimics − a survey, Helv. Chim. Acta 91 (9) (2008) 1736−1786.
[146] K. Gademann, M. Ernst, D. Hoyer, D. Seebach, Synthesis and biological evaluation of a cyclo-β-tetrapeptide as a somatostatin analogue, Angew. Chem. Int. Ed. 38 (9) (1999) 1223−1226.
[147] M. Amorín, L. Castedo, J.R. Granja, New cyclic peptide assemblies with hydrophobic cavities: the structural and thermodynamic basis of a new class of peptide tanotubes, J. Am. Chem. Soc. 125 (10) (2003) 2844−2845.

[148] C. Reiriz, M. Amorin, R. Garcia-Fandino, L. Castedo, J.R. Granja, Alpha-gamma-cyclic peptide ensembles with a hydroxylated cavity, Org. Biomol. Chem. 7 (21) (2009) 4358−4361.

[149] N. Rodriguez-Vazquez, R. Garcia-Fandino, M. Amorin, J.R. Granja, Self-assembling alpha, gamma-cyclic peptides that generate cavities with tunable properties, Chem. Sci. 7 (1) (2016) 183−187.

[150] R. Hourani, C. Zhang, R. van der Weegen, L. Ruiz, C. Li, S. Keten, et al., Processable cyclic peptide nanotubes with tunable interiors, J. Am. Chem. Soc. 133 (39) (2011) 15296−15299.

[151] S. Leclair, P. Baillargeon, R. Skouta, D. Gauthier, Y. Zhao, Y.L. Dory, Micrometer-sized hexagonal tubes self-assembled by a cyclic peptide in a liquid crystal, Angew. Chem. Int. Ed. 43 (3) (2004) 349−353.

[152] W.S. Horne, C.D. Stout, M.R. Ghadiri, A heterocyclic peptide nanotube, J. Am. Chem. Soc. 125 (31) (2003) 9372−9376.

[153] J.H. van Maarseveen, W.S. Horne, M.R. Ghadiri, Efficient route to C2 symmetric heterocyclic backbone modified cyclic peptides, Org. Lett. 7 (20) (2005) 4503−4506.

[154] S. Guha, A. Banerjee, Self-assembled robust dipeptide nanotubes and fabrication of dipeptide-capped gold nanoparticles on the surface of these nanotubes, Adv. Funct. Mater. 19 (12) (2009) 1949−1961.

[155] I. Alfonso, M. Bru, M.I. Burguete, E. García-Verdugo, S.V. Luis, Structural diversity in the self-assembly of pseudopeptidic macrocycles, Chemistry 16 (4) (2010) 1246−1255.

[156] C. Qin, X. Bu, X. Wu, Z. Guo, A chemical approach to generate molecular diversity based on the scaffold of cyclic decapeptide antibiotic tyrocidine A, J. Comb. Chem. 5 (4) (2003) 353−355.

[157] T.R. White, C.M. Renzelman, A.C. Rand, T. Rezai, C.M. McEwen, V.M. Gelev, et al., On-resin N-methylation of cyclic peptides for discovery of orally bioavailable scaffolds, Nat. Chem. Biol. 7 (11) (2011) 810−817.

[158] J. Chatterjee, F. Rechenmacher, H. Kessler, N-methylation of peptides and proteins: an important element for modulating biological functions, Angew. Chem. Int. Ed. 52 (1) (2013) 254−269.

[159] E. Biron, J. Chatterjee, O. Ovadia, D. Langenegger, J. Brueggen, D. Hoyer, et al., Improving oral bioavailability of peptides by multiple N-methylation: somatostatin analogues, Angew. Chem. Int. Ed. 47 (14) (2008) 2595−2599.

[160] T.A. Hill, N.E. Shepherd, F. Diness, D.P. Fairlie, Constraining cyclic peptides to mimic protein structure motifs, Angew. Chem. Int. Ed. 53 (48) (2014) 13020−13041.

[161] C.K.L. Wang, Q. Kaas, L. Chiche, D.J. Craik, CyBase: a database of cyclic protein sequences and structures, with applications in protein discovery and engineering, Nucleic Acids Res. 36 (Database issue) (2008) D206−D210.

[162] A.G. Poth, L.Y. Chan, D.J. Craik, Cyclotides as grafting frameworks for protein engineering and drug design applications, Pept. Sci. 100 (5) (2013) 480−491.

[163] L.Y. Chan, S. Gunasekera, S.T. Henriques, N.F. Worth, S.-J. Le, R.J. Clark, et al., Engineering pro-angiogenic peptides using stable, disulfide-rich cyclic scaffolds, Blood 118 (25) (2011) 6709.

[164] E. Emanuele, M. Arra, S. Pesenti, Vasopressin and oxytocin as neurohormonal mediators of MDMA (ecstasy) sociosexual behavioural effects, Med. Hypotheses 67 (5) (2006) 1250−1251.

[165] M. Manning, A. Misicka, A. Olma, K. Bankowski, S. Stoev, B. Chini, et al., Oxytocin and vasopressin agonists and antagonists as research tools and potential therapeutics, J. Neuroendocrinol. 24 (4) (2012) 609−628.

[166] R. Eliasen, N.L. Daly, B.S. Wulff, T.L. Andresen, K.W. Conde-Frieboes, D.J. Craik, Design, synthesis, structural and functional characterization of novel melanocortin agonists based on the cyclotide Kalata B1, J. Biol. Chem. 287 (48) (2012) 40493−40501.

[167] A.V. Mayorov, M. Cai, E.S. Palmer, Z. Liu, J.P. Cain, J. Vagner, et al., Solid-phase peptide head-to-side chain cyclodimerization: discovery of C(2)-symmetric cyclic lactam hybrid α-melanocyte-stimulating hormone (MSH)/agouti-signaling protein (ASIP) analogues with potent activities at the human melanocortin receptors, Peptides 31 (10) (2010) 1894−1905.

[168] D. Laimou, T. Katsila, J. Matsoukas, A. Schally, K. Gkountelias, G. Liapakis, et al., Rationally designed cyclic analogues of luteinizing hormone-releasing hormone: enhanced enzymatic stability and biological properties, Eur. J. Med. Chem. 58 (2012) 237−247.

[169] S.C. Koerber, J. Rizo, R.S. Struthers, J.E. Rivier, Consensus bioactive conformation of cyclic GnRH antagonists defined by NMR and molecular modeling, J. Med. Chem. 43 (5) (2000) 819−828.

[170] J.E. Rivier, R.S. Struthers, J. Porter, S.L. Lahrichi, G. Jiang, L.A. Cervini, et al., Design of potent dicyclic (4−10/5−8) gonadotropin releasing hormone (GnRH) antagonists, J. Med. Chem. 43 (5) (2000) 784−796.

[171] J.E. Rivier, J. Porter, L.A. Cervini, S.L. Lahrichi, D.A. Kirby, R.S. Struthers, et al., Design of monocyclic (1−3) and dicyclic (1−3/4−10) gonadotropin releasing hormone (GnRH) antagonists, J. Med. Chem. 43 (5) (2000) 797−806.

[172] R.J. Bienstock, J. Rizo, S.C. Koerber, J.E. Rivier, A.T. Hagler, L.M. Gierasch, Conformational analysis of a highly potent dicyclic gonadotropin-releasing hormone antagonist by nuclear magnetic resonance and molecular dynamics, J. Med. Chem. 36 (22) (1993) 3265−3273.

[173] D. D'Addona, A. Carotenuto, E. Novellino, V. Piccand, J.C. Reubi, A. Di Cianni, et al., Novel sst5-selective somatostatin dicarba-analogues: synthesis and conformation−affinity relationships, J. Med. Chem. 51 (3) (2008) 512−520.

[174] A. Kling, P. Lukat, D.V. Almeida, A. Bauer, E. Fontaine, S. Sordello, et al., Targeting DnaN for tuberculosis therapy using novel griselimycins, Science 348 (6239) (2015) 1106.

[175] O. Demmer, A.O. Frank, F. Hagn, M. Schottelius, L. Marinelli, S. Cosconati, et al., A conformationally frozen peptoid boosts CXCR4 affinity and anti-HIV activity, Angew. Chem. Int. Ed. 51 (32) (2012) 8110−8113.

[176] E. Miranda, I.K. Nordgren, A.L. Male, C.E. Lawrence, F. Hoakwie, F. Cuda, et al., A cyclic peptide inhibitor of HIF-1 heterodimerization that inhibits hypoxia signaling in cancer cells, J. Am. Chem. Soc. 135 (28) (2013) 10418−10425.

[177] R.P. Morse, J.L.E. Willett, P.M. Johnson, M. Zheng, A. Credali, A. Iniguez, et al., Diversification of β-augmentation interactions between CDI toxin/immunity proteins, J. Mol. Biol. 427 (23) (2015) 3766−3784.

[178] J.E. Rivier, G. Jiang, R.S. Struthers, S.C. Koerber, J. Porter, L.A. Cervini, et al., Design of potent dicyclic (1−5/4−10) gonadotropin releasing hormone (GnRH) antagonists, J. Med. Chem. 43 (5) (2000) 807−818.

[179] B. Zhao, X. Wei, W. Li, R.S. Udan, Q. Yang, J. Kim, et al., Inactivation of YAP oncoprotein by the Hippo pathway is involved in cell contact inhibition and tissue growth control, Genes Dev. 21 (21) (2007) 2747−2761.

Peptide Applications in Biomedicine, Biotechnology and Bioengineering

[180] Z. Zhang, Z. Lin, Z. Zhou, H.C. Shen, S.F. Yan, A.V. Mayweg, et al., Structure-based design and synthesis of potent cyclic peptides inhibiting the YAP−TEAD protein−protein interaction, ACS Med. Chem. Lett. 5 (9) (2014) 993−998.

[181] S. Bonetto, L. Spadola, A.G. Buchanan, L. Jermutus, J. Lund, Identification of cyclic peptides able to mimic the functional epitope of IgG1-Fc for human Fc gamma RI, FASEB J. 23 (2) (2009) 575−585.

[182] S.E. Blondelle, K. Lohner, Combinatorial libraries: a tool to design antimicrobial and antifungal peptide analogues having lyric specificities for structure-activity relationship studies, Biopolymers 55 (1) (2000) 74−87.

[183] S.E. Blondelle, C. Pinilla, C.S. Boggiano, Synthetic combinatorial libraries as an alternative strategy for the development of novel treatments for infectious diseases, Comb. Chem. 369 (2003) 322−344.

[184] M.A. Gallop, R.W. Barrett, W.J. Dower, S.P.A. Fodor, E.M. Gordon, Applications of combinatorial technologies to drug discovery. 1. Background and peptide combinatorial libraries, J. Med. Chem. 37 (9) (1994) 1233−1251.

[185] C.P. Scott, E. Abel-Santos, A.D. Jones, S.J. Benkovic, Structural requirements for the biosynthesis of backbone cyclic peptide libraries, Chem. Biol. 8 (8) (2001) 801−815.

[186] O.H. Aina, J. Marik, R. Liu, D.H. Lau, K.S. Lam, Identification of novel targeting peptides for human ovarian cancer cells using "one-bead one-compound" combinatorial libraries, Mol. Cancer Ther. 4 (5) (2005) 806.

[187] O.H. Aina, R. Liu, J.L. Sutcliffe, J. Marik, C.-X. Pan, K.S. Lam, From combinatorial chemistry to cancer-targeting peptides, Mol. Pharm. 4 (5) (2007) 631−651.

[188] C. Qin, X. Bu, X. Zhong, N.L. Joyce Ng, Z. Guo, Optimization of antibacterial cyclic decapeptides, J. Comb. Chem. 6 (3) (2004) 398−406.

[189] M.D. Galsky, N.J. Vogelzang, P. Conkling, E. Raddad, J. Polzer, S. Roberson, et al., A phase I trial of LY2510924, a CXCR4 peptide antagonist, in patients with advanced cancer, Clin. Cancer Res. 20 (13) (2014) 3581.

[190] K. Barreto, C.R. Geyer, Screening combinatorial libraries of cyclic peptides using the yeast two-hybrid assay, in: W. Xiao (Ed.), Yeast Protocols, Springer New York, New York, 2014, pp. 273−309.

[191] K. Grabowska, A.K. Puszko, P.F.J. Lipiński, A.K. Laskowska, B. Wileńska, E. Witkowska, et al., Design, synthesis and in vitro biological evaluation of a small cyclic peptide as inhibitor of vascular endothelial growth factor binding to neuropilin-1, Bioorg. Med. Chem. Lett. 26 (12) (2016) 2843−2846.

[192] S.M. McHugh, J.R. Rogers, S.A. Solomon, H. Yu, Y.-S. Lin, Computational methods to design cyclic peptides, Curr. Opin. Chem. Biol. 34 (2016) 95−102.

[193] S.E. Allen, N.V. Dokholyan, A.A. Bowers, Dynamic docking of conformationally constrained macrocycles: methods and applications, ACS Chem. Biol. 11 (1) (2016) 10−24.

[194] G. Sliwoski, S. Kothiwale, J. Meiler, E.W. Lowe, Computational methods in drug discovery, Pharmacol. Rev. 66 (1) (2014) 334−395.

[195] S. Kalyaanamoorthy, Y.-P.P. Chen, Structure-based drug design to augment hit discovery, Drug Discov. Today 16 (17−18) (2011) 831−839.

[196] F.J. Duffy, M. Verniere, M. Devocelle, E. Bernard, D.C. Shields, A.J. Chubb, CycloPs: generating virtual libraries of cyclized and constrained peptides including nonnatural amino acids, J. Chem. Inf. Model. 51 (4) (2011) 829−836.

[197] D.J. Mandell, E.A. Coutsias, T. Kortemme, Sub-angstrom accuracy in protein loop reconstruction by robotics-inspired conformational sampling, Nat. Methods 6 (8) (2009) 551−552.

[198] M.P. Jacobson, D.L. Pincus, C.S. Rapp, T.J.F. Day, B. Honig, D.E. Shaw, et al., A hierarchical approach to all-atom protein loop prediction, Proteins 55 (2) (2004) 351−367.

[199] J. Beaufays, L. Lins, A. Thomas, R. Brasseur, In silico predictions of 3D structures of linear and cyclic peptides with natural and non-proteinogenic residues, J. Pept. Sci. 18 (1) (2012) 17−24.

[200] A. Thomas, S. Deshayes, M. Decaffmeyer, M.H. Van Eyck, B. Charloteaux, R. Brasseur, Prediction of peptide structure: how far are we? Proteins 65 (4) (2006) 889−897.

[201] S. Singh, H. Singh, A. Tuknait, K. Chaudhary, B. Singh, S. Kumaran, et al., PEPstrMOD: structure prediction of peptides containing natural, non-natural and modified residues, Biol. Direct 10 (1) (2015) 73.

[202] P. Thevenet, Y. Shen, J. Maupetit, F. Guyon, P. Derreumaux, P. Tuffery, PEP-FOLD: an updated de novo structure prediction server for both linear and disulfide bonded cyclic peptides, Nucleic Acids Res. 40 (2012) W288−W293.

[203] Y. Shen, J. Maupetit, P. Derreumaux, P. Tufféry, Improved PEP-FOLD approach for peptide and miniprotein structure prediction, J. Chem. Theory Comput. 10 (10) (2014) 4745−4758.

[204] Y. Zhang, I-TASSER server for protein 3D structure prediction, BMC Bioinformatics 9 (2008) 40.

[205] S. Izrailev, F. Zhu, D.K. Agrafiotis, A distance geometry heuristic for expanding the range of geometries sampled during conformational search, J. Comput. Chem. 27 (16) (2006) 1962−1969.

[206] F. Zhu, D.K. Agrafiotis, Self-organizing superimposition algorithm for conformational sampling, J. Comput. Chem. 28 (7) (2007) 1234−1239.

[207] P. Bonnet, D.K. Agrafiotis, F. Zhu, E. Martin, Conformational analysis of macrocycles: finding what common search methods miss, J. Chem. Inf. Model. 49 (10) (2009) 2242−2259.

[208] A. Rayan, H. Senderowitz, A. Goldblum, Exploring the conformational space of cyclic peptides by a stochastic search method, J. Mol. Graph. Model. 22 (5) (2004) 319−333.

[209] J. Li, T. Ehlers, J. Sutter, S. Varma-O'Brien, J. Kirchmair, CAESAR: a new conformer generation algorithm based on recursive buildup and local rotational symmetry consideration, J. Chem. Inf. Model. 47 (5) (2007) 1923−1932.

[210] P.C.D. Hawkins, A.G. Skillman, G.L. Warren, B.A. Ellingson, M.T. Stahl, Conformer generation with OMEGA: algorithm and validation using high quality structures from the Protein Databank and Cambridge Structural Database, J. Chem. Inf. Model. 50 (4) (2010) 572−584.

[211] U.S.F. Tambunan, A.A. Parikesit, Y. Dephinto, F.R.P. Sipahutar, Computational design of drug candidates for influenza A virus subtype H1N1 by inhibiting the viral neuraminidase-1 enzyme, Acta Pharm. 64 (2) (2014) 157−172.

[212] B.G. Bobay, L.R. Butler, J. Cavana, Computational design of cyclic peptide inhibitors of the anti-apoptotic protein Calbindin-D28K, Biochem. Pharmacol. 3 (4) (2014) 142.

[213] W. Nawae, S. Hannongbua, M. Ruengjitchatchawalya, Defining the membrane disruption mechanism of kalata B1 via coarse-grained molecular dynamics simulations, Sci. Rep. 4 (2014) 3933.

[214] A. Khalfa, M. Tarek, On the antibacterial action of cyclic peptides: insights from coarse-grained MD simulations, J. Phys. Chem. B. 114 (8) (2010) 2676−2684.

[215] A.D. Cirac, G. Moiset, J.T. Mika, A. Kocer, P. Salvador, B. Poolman, et al., The molecular basis for antimicrobial activity of pore-forming cyclic peptides, Biophys. J. 100 (10) (2011) 2422−2431.

[216] R. Garcia-Fandino, A. Pineiro, J.L. Trick, M.S.P. Sansom, Lipid bilayer membrane perturbation by embedded nanopores: a simulation study, ACS Nano 10 (3) (2016) 3693−3701.

[217] C.D. Fjell, J.A. Hiss, R.E.W. Hancock, G. Schneider, Designing antimicrobial peptides: form follows function, Nat. Rev. Drug Discov. 11 (1) (2012) 37−51.

[218] G. Maccari, M. Di Luca, R. Nifosi, F. Cardarelli, G. Signore, C. Boccardi, et al., Antimicrobial peptides design by evolutionary multiobjective optimization, PLoS Comput. Biol. 9 (9) (2013) e1003212.

[219] C.F. Lopez, S.O. Nielsen, G. Srinivas, W.F. Degrado, M.L. Klein, Probing membrane insertion activity of antimicrobial polymers via coarse-grain molecular dynamics, J. Chem. Theory Comput. 2 (3) (2006) 649−655.

[220] V.A. Voelz, K.A. Dill, I. Chorny, Peptoid conformational free energy landscapes from implicit-solvent molecular simulations in AMBER, Biopolymers 96 (5) (2011) 639−650.

[221] J.M. Damas, L.C.S. Filipe, S.R.R. Campos, D. Lousa, B.L. Victor, A.M. Baptista, et al., Predicting the thermodynamics and kinetics of helix formation in a cyclic peptide model, J. Chem. Theory Comput. 9 (11) (2013) 5148−5157.

[222] A.M. Razavi, W.M. Wuest, V.A. Voelz, Computational screening and selection of cyclic peptide hairpin mimetics by molecular simulation and kinetic network models, J. Chem. Inf. Model. 54 (5) (2014) 1425−1432.

[223] E. Yedvabny, P.S. Nerenberg, C. So, T. Head-Gordon, Disordered structural ensembles of vasopressin and oxytocin and their mutants, J. Phys. Chem. B. 119 (3) (2015) 896−905.

[224] A.E. Wakefield, W.M. Wuest, V.A. Voelz, Molecular simulation of conformational pre-organization in cyclic RGD peptides, J. Chem. Inf. Model. 55 (4) (2015) 806−813.

[225] A. Spitaleri, M. Ghitti, S. Mari, L. Alberici, C. Traversari, G.-P. Rizzardi, et al., Use of metadynamics in the design of isoDGR-based $\alpha_v\beta_3$ antagonists to fine-tune the conformational ensemble, Angew. Chem. Int. Ed. 50 (8) (2011) 1832−1836.

[226] C. Paissoni, M. Ghitti, L. Belvisi, A. Spitaleri, G. Musco, Metadynamics simulations rationalise the conformational effects induced by N-methylation of RGD cyclic hexapeptides, Chemistry 21 (40) (2015) 14165−14170.

[227] Y. Sugita, Y. Okamoto, Replica-exchange molecular dynamics method for protein folding, Chem. Phys. Lett. 314 (1−2) (1999) 141−151.

[228] D.J. Earl, M.W. Deem, Parallel tempering: theory, applications, and new perspectives, Phys. Chem. Chem. Phys. 7 (23) (2005) 3910−3916.

[229] A. Laio, M. Parrinello, Escaping free-energy minima, Proc. Natl. Acad. Sci. U.S.A. 99 (20) (2002) 12562−12566.

[230] S. Piana, A. Laio, A bias-exchange approach to protein folding, J. Phys. Chem. B. 111 (17) (2007) 4553−4559.

[231] P. Labute, LowModeMD—Implicit low-mode velocity filtering applied to conformational search of macrocycles and protein loops, J. Chem. Inf. Model. 50 (5) (2010) 792−800.

[232] J. Burck, S. Roth, P. Wadhwani, S. Afonin, N. Kanithasen, E. Strandberg, et al., Conformation and membrane orientation of amphiphilic helical peptides by oriented circular dichroism, Biophys. J. 95 (8) (2008) 3872−3881.

[233] A.S. Ulrich, Solid state 19F NMR methods for studying biomembranes, Prog. Nucl. Magn. Reson. Spectrosc. 46 (1) (2005) 1−21.

[234] V. Tozzini, Coarse-grained models for proteins, Curr. Opin. Struct. Biol. 15 (2) (2005) 144−150.

[235] J.D. Owens, M. Houston, D. Luebke, S. Green, J.E. Stone, J.C. Phillips, GPU computing, Proc. IEEE 96 (5) (2008) 879−899.

[236] Y. Goldtzvik, M. Goldstein, R. Benny Gerber, On the crystallographic accuracy of structure prediction by implicit water models: tests for cyclic peptides, Chem. Phys. 415 (2013) 168−172.

[237] H. Geng, F. Jiang, Y.-D. Wu, Accurate structure prediction and conformational snalysis of cyclic peptides with residue-specific force fields, J. Phys. Chem. Lett. 7 (10) (2016) 1805−1810.

[238] W.Y. Xu, L.L. Li, L.C. Du, N.H. Tan, Various mechanisms in cyclopeptide production from precursors synthesized independently of non-ribosomal peptide synthetases, Acta Biochim. Biophys. Sin. (Shanghai) 43 (10) (2011) 757−762.

[239] P.G. Arnison, M.J. Bibb, G. Bierbaum, A.A. Bowers, T.S. Bugni, G. Bulaj, et al., Ribosomally synthesized and post-translationally modified peptide natural products: overview and recommendations for a universal nomenclature, Nat. Prod. Rep. 30 (1) (2013) 108−160.

[240] S.A. Sieber, M.A. Marahiel, Molecular mechanisms underlying nonribosomal peptide synthesis: approaches to new antibiotics, Chem. Rev. 105 (2) (2005) 715−738.

[241] M.A. Fischbach, C.T. Walsh, Assembly-line enzymology for polyketide and nonribosomal peptide antibiotics: logic, machinery, and mechanisms, Chem. Rev. 106 (8) (2006) 3468−3496.

[242] G.P. Smith, Filamentous fusion phage: novel expression vectors that display cloned antigens on the virion surface, Science 228 (4705) (1985) 1315−1317.

[243] J.R. Hsiao, Y. Chang, Y.L. Chen, S.H. Hsieh, K.F. Hsu, C.F. Wang, et al., Cyclic alphavbeta6-targeting peptide selected from biopanning with clinical potential for head and neck squamous cell carcinoma, Head Neck 32 (2) (2010) 160−172.

[244] K.E. Duncan, B.R. Dempsey, L.E. Killip, J. Adams, M.L. Bailey, G.A. Lajoie, et al., Discovery and characterization of a nonphosphorylated cyclic peptide inhibitor of the peptidylprolyl isomerase, Pin1, J. Med. Chem. 54 (11) (2011) 3854−3865.

[245] J. Huang, B.B. Ru, P. Dai, Bioinformatics resources and tools for phage display, Molecules 16 (1) (2011) 694−709.

[246] J. Huang, B.B. Ru, P. Zhu, F.L. Nie, J. Yang, X.Y. Wang, et al., MimoDB 2.0: a mimotope database and beyond, Nucleic Acids Res. 40 (D1) (2012) D271−D277.

[247] F.B. Perler, E.O. Davis, G.E. Dean, F.S. Gimble, W.E. Jack, N. Neff, et al., Protein splicing elements: inteins and exteins—a definition of terms and recommended nomenclature, Nucleic Acids Res. 22 (7) (1994) 1125−1127.

[248] F.B. Perler, Protein splicing mechanisms and applications, IUBMB Life 57 (7) (2005) 469−476.

[249] C.P. Scott, E. Abel-Santos, M. Wall, D.C. Wahnon, S.J. Benkovic, Production of cyclic peptides and proteins in vivo, Proc. Nat. Acad. Sci. U. S. A. 96 (24) (1999) 13638−13643.

[250] S.W. Millward, T.T. Takahashi, R.W. Roberts, A general route for post-translational cyclization of mRNA display libraries, J. Am. Chem. Soc. 127 (41) (2005) 14142−14143.

[251] S.W. Millward, S. Fiacco, R.J. Austin, R.W. Roberts, Design of cyclic peptides that bind protein surfaces with antibody-like affinity, ACS Chem. Biol. 2 (9) (2007) 625−634.
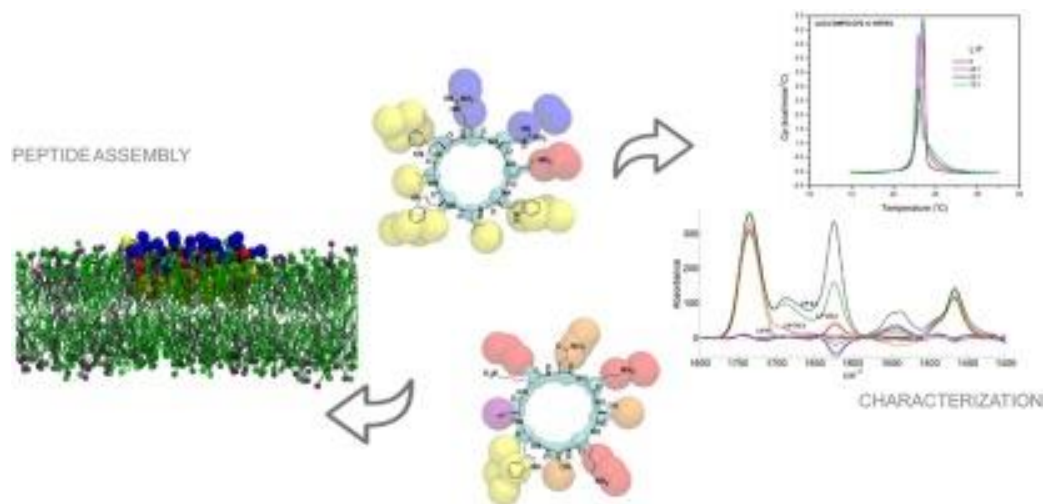
[252] K.D. Kopple, Synthesis of cyclic peptides, J. Pharm. Sci. 61 (9) (1972) 1345−1356.

[253] S.A. Kates, N.A. Solé, C.R. Johnson, D. Hudson, G. Barany, F. Albericio, A novel, convenient, three-dimensional orthogonal strategy for solid-phase synthesis of cyclic peptides, Tetrahedron Lett. 34 (10) (1993) 1549−1552.

[254] R.B. Merrifield, Solid phase peptide synthesis. I. The synthesis of a tetrapeptide, J. Am. Chem. Soc. 85 (14) (1963) 2149−2154.

[255] G.T. Bourne, S.W. Golding, R.P. McGeary, W.D.F. Meutermans, A. Jones, G.R. Marshall, et al., The development and application of a novel safety-catch linker for BOC-based assembly of libraries of cyclic peptides,1, J. Org. Chem. 66 (23) (2001) 7706−7713.

[256] O. Demmer, I. Dijkgraaf, M. Schottelius, H.J. Wester, H. Kessler, Introduction of functional groups into peptides via N-alkylation, Org. Lett. 10 (10) (2008) 2015−2018.

[257] G. Koopmanschap, E. Ruijter, R.V.A. Orru, Isocyanide-based multicomponent reactions towards cyclic constrained peptidomimetics, Beilstein J. Org. Chem. 10 (2014) 544−598.

[258] J.M. Smith, J.R. Frost, R. Fasan, Emerging strategies to access peptide macrocycles from genetically encoded polypeptides, J. Org. Chem. 78 (8) (2013) 3525−3531.

[259] V.R. Pattabiraman, J.W. Bode, Rethinking amide bond synthesis, Nature 480 (7378) (2011) 471−479.

[260] J.M. Smith, F. Vitali, S.A. Archer, R. Fasan, Modular assembly of macrocyclic organo−peptide hybrids using synthetic and genetically encoded precursors, Angew. Chem. Int. Ed. 50 (22) (2011) 5075−5080.

[261] R.J. Clark, J. Jensen, S.T. Nevin, B.P. Callaghan, D.J. Adams, D.J. Craik, The engineering of an orally active conotoxin for the treatment of neuropathic pain, Angew. Chem. Int. Ed. 49 (37) (2010) 6545−6548.

[262] Á. Roxin, G. Zheng, Flexible or fixed: a comparative review of linear and cyclic cancer-targeting peptides, Future Med. Chem. 4 (12) (2012) 1601−1618.

[263] G. Colombo, F. Curnis, G.M. De Mori, A. Gasparri, C. Longoni, A. Sacchi, et al., Structure-activity relationships of linear and cyclic peptides containing the NGR tumor-homing motif, J. Biol. Chem. 277 (49) (2002) 47891−47897.

[264] G.J. Mizejewski, M. Muehlemann, M. Dauphinee, Update of alpha fetoprotein growth-inhibitory peptides as biotherapeutic agents for tumor growth and metastasis, Chemotherapy 52 (2) (2006) 83−90.

[265] W.R. Baumbach, T.A. Carrick, M.H. Pausch, B. Bingham, D. Carmignac, I.C. Robinson, et al., A linear hexapeptide somatostatin antagonist blocks somatostatin activity in vitro and influences growth hormone release in rats, Mol. Pharmacol. 54 (5) (1998) 864−873.

[266] J. Zhong, Y. Chau, Antitumor activity of a membrane lytic peptide cyclized with a linker sensitive to membrane type 1-matrix metalloproteinase, Mol. Cancer Ther. 7 (9) (2008) 2933−2940.

[267] M. Katsara, T. Tselios, S. Deraos, G. Deraos, M.T. Matsoukas, E. Lazoura, et al., Round and round we go: cyclic peptides in disease, Curr. Med. Chem. 13 (19) (2006) 2221−2232.

[268] C.A. Lipinski, F. Lombardo, B.W. Dominy, P.J. Feeney, Experimental and computational approaches to estimate solubility and permeability in drug discovery and development settings, Adv. Drug Deliv. Rev. 64 (2012) 4−17.

[269] A.R. Hamel, F. Hubler, A. Carrupt, R.M. Wenger, M. Mutter, Cyclosporin A prodrugs: design, synthesis and biophysical properties, J. Pept. Res. 63 (2) (2004) 147−154.

[270] T.W.J. Huizinga, C.I. Amos, A.H.M. van der Helm-van Mil, W. Chen, F.A. van Gaalen, D. Jawaheer, et al., Refining the complex rheumatoid arthritis phenotype based on specificity of the HLA-DRB1 shared epitope for antibodies to citrullinated proteins, Arthritis. Rheum. 52 (11) (2005) 3433−3438.

[271] E.F. Stange, S.P.L. Travis, S. Vermeire, W. Reinisch, K. Geboes, A. Barakauskiene, et al., European evidence-based consensus on the diagnosis and management of ulcerative colitis: definitions and diagnosis, J. Crohns Colitis 2 (1) (2008) 1−23.

[272] R. Colucci, C. Blandizzi, N. Ghisu, T. Florio, M. Del Tacca, Somatostatin inhibits colon cancer cell growth through cyclooxygenase-2 downregulation, Br. J. Pharmacol. 155 (2) (2008) 198−209.

[273] M.D. Culler, K. Oberg, R. Arnold, E.P. Krenning, I. Sevilla, J.A. Diaz, Somatostatin analogs for the treatment of neuroendocrine tumors, Cancer Metastasis Rev. 30 (1) (2011) 9−17.

[274] C.H. Chesnut, M. Azria, S. Silverman, M. Engelhardt, M. Olson, L. Mindeholm, Salmon calcitonin: a review of current and future therapeutic indications, Osteoporos. Int. 19 (4) (2008) 479−491.

[275] A. Schmidtko, J. Lotsch, R. Freynhagen, G. Geisslinger, Ziconotide for treatment of severe chronic pain, Lancet 375 (9725) (2010) 1569−1577.

[276] K. Ley, J. Rivera-Nieves, W.J. Sandborn, S. Shattil, Integrin-based therapeutics: biological basis, clinical use and new drugs, Nat. Rev. Drug Discov. 15 (3) (2016) 173−183.

[277] T. Tselios, V. Apostolopoulos, I. Daliani, S. Deraos, S. Grdadolnik, T. Mavromoustakos, et al., Antagonistic effects of human cyclic MBP87-99 altered peptide ligands in experimental allergic encephalomyelitis and human T-cell proliferation, J. Med. Chem. 45 (2) (2002) 275−283.

[278] T. Tselios, M. Aggelidakis, A. Tapeinou, V. Tseveleki, I. Kanistras, D. Gatos, et al., Rational design and synthesis of altered peptide ligands based on uman myelin oligodendrocyte glycoprotein 35-55 epitope: inhibition of chronic experimental autoimmune encephalomyelitis in mice, Molecules 19 (11) (2014) 17968−17984.

[279] J.P. Tam, Y.A. Lu, J.L. Yang, K.W. Chiu, An unusual structural motif of antimicrobial peptides containing end-to-end macrocycle and cystine-knot disulfides, Proc. Nat. Acad. Sci. U.S.A. 96 (16) (1999) 8913−8918.

[280] C.K.L. Wang, M.L. Colgrave, K.R. Gustafson, D.C. Ireland, U. Goransson, D.J. Craik, Anti-HIV cyclotides from the Chinese medicinal herb *Viola yedoensis*, J. Nat. Prod. 71 (1) (2008) 47−52.

[281] S.L. Gerlach, R. Rathinakumar, G. Chakravarty, U. Goransson, W.C. Wimley, S.P. Darwin, et al., Anticancer and chemosensitizing abilities of cycloviolacin O2 from *Viola odorata* and psyle cyclotides from *Psychotria leptothyrsa*, Biopolymers 94 (5) (2010) 617−625.

[282] D. Oh, J.D. Sun, A.N. Shirazi, K.L. LaPlante, D.C. Rowley, K. Parang, Antibacterial activities of amphiphilic cyclic cell-penetrating peptides against multidrug-resistant pathogens, Mol. Pharm. 11 (10) (2014) 3528−3536.

[283] D. Mandal, R.K. Tiwari, A.N. Shirazi, D. Oh, G.F. Ye, A. Banerjee, et al., Self-assembled surfactant cyclic peptide nanostructures as stabilizing agents, Soft Matter 9 (39) (2013) 9465−9475.

[284] D. Mandal, A.N. Shirazi, K. Parang, Cell-penetrating homochiral cyclic peptides as nuclear-targeting molecular transporters, Angew. Chem. Int. Ed. 50 (41) (2011) 9633−9637.

[285] A.N. Shirazi, R.K. Tiwari, D. Oh, A. Banerjee, A. Yadav, K. Parang, Efficient delivery of cell impermeable phosphopeptides by a cyclic peptide amphiphile containing tryptophan and arginine, Mol. Pharm. 10 (5) (2013) 2008−2020.

Peptide Applications in Biomedicine, Biotechnology and Bioengineering

[286] A.N. Shirazi, D. Oh, R.K. Tiwari, B. Sullivan, A. Gupta, G.D. Bothun, et al., Peptide amphiphile containing arginine and fatty acyl chains as molecular transporters, Mol. Pharm. 10 (12) (2013) 4717−4727.

[287] A.N. Shirazi, R. Tiwari, B.S. Chhikara, D. Mandal, K. Parang, Design and biological evaluation of cell-penetrating peptide-doxorubicin conjugates as prodrugs, Mol. Pharm. 10 (2) (2013) 488−499.

[288] D. Weerakkody, A. Moshnikova, N.S. El-Sayed, R.C. Adochite, G. Slaybaugh, J. Golijanin, et al., Novel pH-sensitive cyclic peptides, Sci. Rep. 6 (2016) 31322.

[289] A.N. Shirazi, D. Mandal, R.K. Tiwari, L.R. Guo, W. Lu, K. Parang, Cyclic peptide-capped gold nanoparticles as drug delivery systems, Mol. Pharm. 10 (2) (2013) 500−511.

[290] A.N. Shirazi, K.L. Paquin, N.G. Howlett, D. Mandal, K. Parang, Cyclic peptide-capped gold nanoparticles for enhanced siRNA delivery, Molecules 19 (9) (2014) 13319−13331.

[291] A.N. Shirazi, R.K. Tiwari, D. Oh, B. Sullivan, K. McCaffrey, D. Mandal, et al., Surface decorated gold nanoparticles by linear and cyclic peptides as molecular transporters, Mol. Pharm. 10 (8) (2013) 3137−3151.

[292] A.N. Shirazi, R.K. Tiwari, D. Oh, B. Sullivan, A. Kumar, Y.A. Beni, et al., Cyclic peptide-selenium nanoparticles as drug transporters, Mol. Pharm. 11 (10) (2014) 3631−3641.

[293] Y. Takada, X. Ye, S. Simon, The integrins, Genome Biol. 8 (5) (2007) 215.

[294] J.D. Hood, D.A. Cheresh, Role of integrins in cell invasion and migration, Nat. Rev. Cancer 2 (2) (2002) 91−100.

[295] H. Jin, J. Varner, Integrins: roles in cancer development and as treatment targets, Br. J. Cancer 90 (3) (2004) 561−565.

[296] X. Chen, P.S. Conti, R.A. Moats, In vivo near-infrared fluorescence imaging of integrin $\alpha_v\beta_3$ in brain tumor xenografts, Cancer Res. 64 (21) (2004) 8009.

[297] X. Chen, R. Park, M. Tohme, A.H. Shahinian, J.R. Bading, P.S. Conti, MicroPET and autoradiographic imaging of breast cancer αv-integrin expression using 18F- and 64Cu-labeled RGD peptide, Bioconjug. Chem. 15 (1) (2004) 41−49.

[298] X. Chen, R. Park, A.H. Shahinian, M. Tohme, V. Khankaldyyan, M.H. Bozorgzadeh, et al., 18F-labeled RGD peptide: initial evaluation for imaging brain tumor angiogenesis, Nucl. Med. Biol. 31 (2) (2004) 179−189.

[299] R. Haubner, B. Kuhnast, C. Mang, W.A. Weber, H. Kessler, H.-J. Wester, et al., [18F]Galacto-RGD: synthesis, radiolabeling, metabolic stability, and radiation dose estimates, Bioconjug. Chem. 15 (1) (2004) 61−69.

[300] M.L. Janssen, W.J. Oyen, I. Dijkgraaf, L.F. Massuger, C. Frielink, D.S. Edwards, et al., Tumor targeting with radiolabeled αvβ3 integrin binding peptides in a nude mouse model, Cancer Res. 62 (21) (2002) 6146.

[301] E.A. Murphy, B.K. Majeti, L.A. Barnes, M. Makale, S.M. Weis, K. Lutu-Fuga, et al., Nanoparticle-mediated drug delivery to tumor vasculature suppresses metastasis, Proc. Nat. Acad. Sci. U.S.A. 105 (27) (2008) 9343−9348.

[302] R.J. Brea, C. Reiriz, J.R. Granja, Towards functional bionanomaterials based on self-assembling cyclic peptide nanotubes, Chem. Soc. Rev. 39 (5) (2010) 1448−1456.

[303] P. Kumaraswamy, R. Lakshmanan, S. Sethuraman, U.M. Krishnan, Self-assembly of peptides: influence of substrate, pH and medium on the formation of supramolecular assemblies, Soft Matter 7 (6) (2011) 2744−2754.

II.   **"Membrane targeting antimicrobial cyclic peptide nanotubes – an experimental and computational study"**
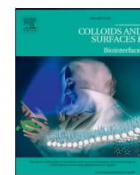
Bárbara Claro, Eva González-Freire, Martin Calvelo, Lucinda J. Bessa, Erik Goormaghtigh, Manuel Amorín, Juan R. Granja, Rebeca Garcia-Fandiño, Margarida Bastos **(2020)**, *Colloids and Surfaces B: Biointerfaces,*196, 111349

Membrane targeting antimicrobial cyclic peptide nanotubes – an experimental and computational study

Bárbara Claro [a], Eva González-Freire [b], Martin Calvelo [b], Lucinda J. Bessa [c], Erik Goormaghtigh [d], Manuel Amorín [b], Juan R. Granja [b], Rebeca Garcia-Fandiño [a,b,*], Margarida Bastos [a,*]

[a] CIQUP, Centro de Investigação em Química, Departamento de Química e Bioquímica, Faculdade de Ciências, Universidade do Porto, Porto, Portugal
[b] Centro Singular de Investigación en Química Biolóxica e Materiais Moleculares (CiQUS), Departamento de Química Orgánica, Universidade de Santiago de Compostela, 15782 Santiago de Compostela, Spain
[c] LAQV/Requimte, Departamento de Química e Bioquímica, Faculdade de Ciências da Universidade do Porto, Porto, Portugal
[d] Structure and Function of Biological Membranes, Center for Structural Biology and Bioinformatics, ULB, Brussels, Belgium

ARTICLE INFO

ABSTRACT

The search of new antibiotics, particularly with new mechanisms of action, is nowadays a very important public health issue, due to the worldwide increase of resistant pathogens. Within this effort, much research has been done on antimicrobial peptides, because having the membrane as a target, they represent a new antibiotic paradigm. Among these, cyclic peptides (CPs) made of sequences of D- and L-amino acids have emerged as a new class of potential antimicrobial peptides, due to their expected higher resistance to protease degradation. These CPs are planar structures that can form Self-assembled Cyclic Peptide Nanotubes (SCPNs), in particular in the presence of lipid membranes. Aiming at understanding their mechanism of action, we used biophysical experimental techniques (DSC and ATR-FTIR) together with Coarse-grained molecular dynamics (CG-MD) simulations, to characterize the interaction of these CPs with model membranes of different electrostatic charges' contents. DSC results revealed that the CPs show a strong interaction with negatively charged membranes, with differences in the strength of interactions depending on peptide and on membrane charge content, at odds with no or mild interactions with zwitterionic membranes. ATR-FTIR suggested that the peptides self-assemble at the membrane surface, adopting mainly a β-structure. The experiments with polarized light showed that in most cases they lie parallel to the membrane surface, but other forms and orientations are also apparent, depending on peptide structure and lipid:peptide ratio. The nanotube formation and orientation, as well as the dependence on membrane charge were also confirmed by the CG-MD simulations. These provide detail on the position and interactions, in agreement with the experimental results. Based on the findings reported here, we could proceed to the design and synthesis of a second-generation CPs, based on CP2 (soluble peptide), with increased activity and reduced toxicity.

1. Introduction

The indiscriminate use of antibiotics over the past decades and bacteria ability to adapt to hostile conditions led to an increase in antibiotic-resistance to the point of becoming a major world's public health concern [1]. Despite intensive research in this area for decades, there is an urgent need for new antibiotic paradigm(s). Antimicrobial peptides (AMPs) appeared as a promising alternative to conventional therapeutics, as they are based on a different mechanism of action, *i.e.*, they mainly target the bacterial membrane [2–4], reducing thus the

tendency to induce antimicrobial resistance. AMPs are present as part of the innate immune system of most organisms, they present structural and functional diversity and are active against Gram-positive and Gram-negative bacteria, viruses and fungi [5–8].

Most AMPs studied so far are linear, although some cyclic versions have also been studied, presenting very good activity [9,10]. A more unusual approach was proposed in 1993 by Ghadiri and co-workers, namely the use of cyclic *D-L-α*-cyclic peptides (*D-L-α*-CPs) [11]. These peptides, with an even number of alternating *D*- and *L*-α amino acids, can adopt the structure of a flat ring in which the amide groups are oriented perpendicular to the plane of the ring. The radial disposition of the side chains outwards the channel modifies the external properties of the nanotube, allowing the modulation of their formation and properties [12]. Under appropriate conditions, the CPs can self-assemble into a hollow structure through the formation of β-sheet type arrangement to form tubular structures called self-assembled cyclic peptide nanotubes, SCPNs [13,14]. Due to their robust secondary structure and proven antimicrobial activity [9,15], combined with a high resistance to protease degradation, SCPNs with appropriate amino acid composition are currently seen as very promising antimicrobial candidates [9,13,16,17]. Other key features that make these CPs very promising antimicrobial peptides are the fact that individual CPs should have a reduced toxicity but the interaction with the membrane should trigger the nanotube formation, being this supramolecular structure the active form [18].

Although different mechanisms of action have been proposed in the literature [4,5,19], the mechanisms by which AMPs in general and SCPNs in particular kill bacteria are not fully understood. They share two major features – they target the bacterial membrane and have electrostatic interactions as the main initial driving force, as the cationic AMPs interact with the anionic headgroups of the phospholipids (more abundant at the outer surface of the bacteria's membrane), and this feature characterizes their specificity. Accumulation and eventual rearrangements of AMPs at the lipid membrane leads to membrane segregation/permeabilization, to the formation of pores, membrane micellization or membrane disruption and aggregation [8,20–23]. Overall, these interactions will cause perturbation/disruption of the membrane, with possible perturbation of cell wall biosynthesis or cell division, and/or translocation across the membrane, and eventually to cell death [5].

Biophysical studies with model membranes have been widely used to characterize the interactions of AMPs with membranes [24–26], and various models have been proposed thereafter [22]. The plethora of proposed models stresses the complexity of the problem. In some cases, different mechanisms have been proposed for the same peptide, depending on the specific techniques and experimental conditions used to investigate them [27]. The main reason for the lack of clarity on the mechanism of membrane destabilization by therapeutic peptides is related to the difficulties involved in the application of atomic-resolution structural techniques (X-ray and neutron diffraction and NMR spectroscopy) to these systems. Although significant advances are being achieved in these approaches [8,24,26,28], determination of the structure of peptides, proteins and other molecules in membranes is still a challenge, and the experimental conditions needed by these techniques often deflect from the physiological ones. In this regard, Molecular Dynamics (MD) simulations may provide the necessary bridges to achieve a complete understanding of membrane/antimicrobial agent interaction processes [29]. Advances in computer power and methodology, including coarse-grained (CG) resolution [30], which considers appropriately chosen groups of atoms as single interacting centres, or the use of GPUs (graphics processing unit), have made possible to systematically explore events in the microsecond scale. Computing times and molecular sizes of MD simulation are now beginning to extend into ranges where direct comparison and experimental testing are starting to be feasible [31,32], stressing the synergistic potential of a combined *in-silico/in-vitro* approach in the characterization of the membrane destabilization process by

antimicrobial molecules. As such, the MD approach has been widely used in this area, providing very useful insight into AMPs action [9] and of the effects and location at the membrane [33–37].

In present work, we have used both approaches to address the SCPNs/model membrane interactions: a) biophysical characterization by differential scanning calorimeter (DSC), dynamic light scattering (DLS) and attenuated total reflection Fourier transform infrared spectroscopy (ATR-FTIR), and b) coarse-grained Molecular Dynamics simulations (CG-MD).

Two *D,L*-α-CPs were studied, here designated as **CP1** and **CP2** (Fig. 1 and Table 1). Our approach was to start with a CP of known antimicrobial action (**CP1**) [14], and design a new one thereafter (**CP2**), with improved aqueous solubility (**CP1** has very low solubility in aqueous media, requiring the use of DMSO, a solvent commonly used in biophysical/medical studies). **CP1** is characterized by an amphipathic structure that contains three basic residues to promote its affinity for the negatively charged bacterial membranes [14]. This peptide has a high antibacterial activity, both *in vitro* and *in vivo*. Its mechanism of action remains speculative, although some studies have been carried out to help to elucidate it [38]. **CP2**, on the other hand, combines the presence of three charged residues (Lys) with polar non-charged residues to increase solubility. The design of this CP was based on its simple and hydrophilic character. **CP2** presents quite good activity [16−32 μg/mL for gram positive bacteria (S. aureus or *S. epidermidis*) E. González-Freire, F. Novelli, A. Pérez-Estévez, R. Seoane, M. Amorín and J. R. Granja, manuscript in preparation) and allows simple further modification through the alkyne moiety.

As models for bacterial membranes we used 1,2-dimyristoyl-*sn*-glycero-3-phosphoethanolamine (DMPE) and 1,2-dimyristoyl-*sn*-glycero-3-phospho-(1'-*rac*-glycerol) (DMPG), since phosphoethanolamine (PE) and phospho-(1'-*rac*-glycerol) (PG) lipids are known to be the main constituents of Gram negative (*e.g.*, in *E. coli* there are 25 % PG and 75 % PE) and PG is the main component of Gram positive (57 % in *S. aureus* and 70 % in *B. subtilis*) plasma membranes [39]. In order to vary significantly the negative content of the membranes, to span a wide range of pathogens mimics and understand the role of membrane charge in the antimicrobial mechanism, we used mixtures of DMPE:DMPG at different molar ratios (3:1, 1:1, 1:9), as well as pure DMPE and DMPG.

2. Experimental

2.1. Materials and methods

2.1.1. Synthetic procedures

Peptides **CP1** and **CP2** were prepared using conventional Fmoc/ᵗBu solid-phase peptide synthesis following the synthetic scheme illustrated in Scheme S1 (see Supplementary Material) [14]. Briefly, the linear peptide sequence was prepared in 2-chlorotrytil chloride resin through the conventional Fmoc/ᵗBu method [40]. First residue (Lys) was attached to the solid support through its side chain and the linear peptide was growth. The resulting linear peptide was cyclized prior to cleavage with trifluoroacetic acid cocktail [41]. For more details about the synthetic procedure and CPs characterization, see Supplementary Material Fig. S1-S4.

2.1.2. Preparation of liposomes

1,2-dimyristoyl-sn-glycero-3-phosphocholine (DMPC), 1,2-dimyristoyl-*sn*-glycero-3-phosphoethanolamine (DMPE) and 1,2-dimyristoyl-*sn*-glycero-3-phospho-(1'-*rac*-glycerol) (DMPG) (Avanti Polar Lipids, Alabama, USA) at different molar ratios were weighted and dissolved in an azeotropic mixture of chloroform/methanol (87.4:12.6 (v/v)) in a round bottom flask. A lipid film was obtained by evaporating the azeotropic mixture under vacuum in a rotary evaporator at 70 °C. The resulting film was then kept under high vacuum (< 10 mbar) overnight to remove any trace of the organic solvents. The dry lipid film was hydrated for 30 min at *ca.* 10 °C above the gel-to-liquid crystalline phase
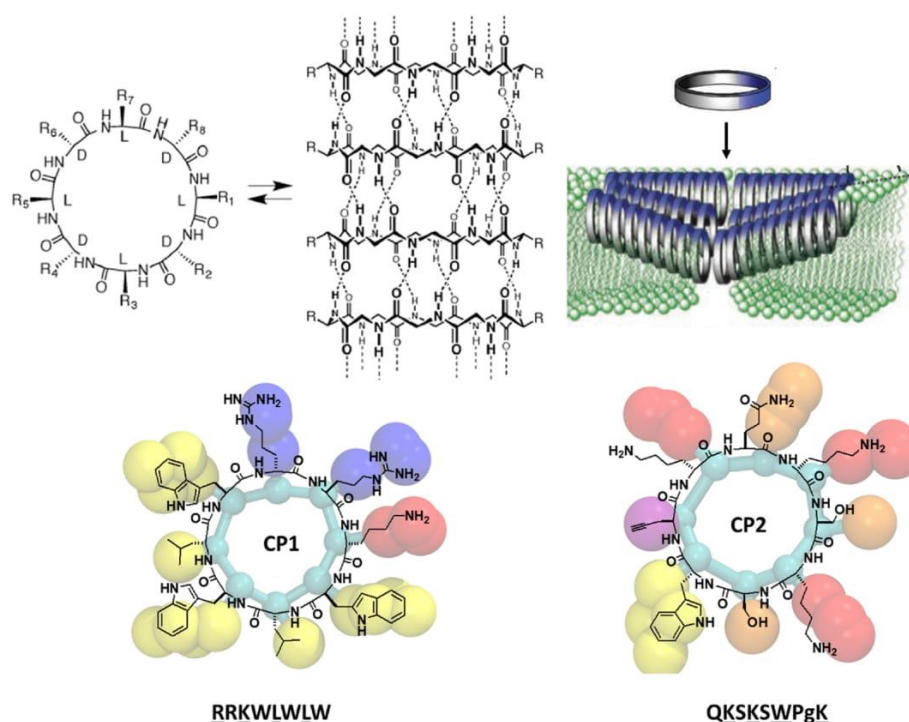
Fig. 1. Top: Schematic representation of the self-assembly of *D,L*-α-CPs into nanotubes (antiparallel β-sheet structure) and one of the proposed models for their interaction with lipid bilayers. Down: In plane and 3D structures of the peptides **CP1** and **CP2** used in this study, together with their sequence, where the underlined amino acids are *D*-residues. Lys are represented in red, Arg in blue, and purple represents the alkyne moiety. The rest of the residues of the SCNP are shown in yellow. Pg stands for propargylglycine (For interpretation of the references to colour in this figure legend, the reader is referred to the web version of this article.).

Table 1
Cyclic Peptides' information.

Peptide	Sequence	Molecular weight/(g/mol)	Buffer used
CP1	RRKWLWLW	1224.70	HEPES/DMSO*
CP2	QKSKSWPgK**	1041.18	HEPES

* DMSO (0.7 %) is needed due to **CP1** low solubility in aqueous media.
** Pg stands for propargylglycine.

transition temperature (T_m) with i) a previously heated buffer (HEPES (10 mM HEPES, 150 mM NaCl, 0.02 % NaN$_3$, 1 mM EDTA, pH 7.45) for **CP2** and HEPES/DMSO (10 mM HEPES, 150 mM NaCl, 0.02 % NaN$_3$, 1 mM EDTA, 0.7 % DMSO, pH 7.45) for **CP1**) for the DSC experiments; and ii) water for the ATR-FTIR experiments. Thereafter, cycles of vortex/incubation above T_m were performed, leading to multilamellar vesicles suspension (MLVs). The resulting MLVs were frozen in liquid nitrogen and thawed above T_m (three freeze/thaw cycles). Large unilamellar vesicles (LUVs) were obtained by extrusion of the MLVs in either a 10 mL stainless steel extruder (Lipex Biomembranes Inc., Vancouver, Canada), under inert (N$_2$) atmosphere, using two staked polycarbonate filters with a pore diameter of 100 nm (Whatman, Nucleopore, NJ, USA) or a mini extruder from Liposofast Basic (BPS, UK) using polycarbonate filters with a pore diameter of 100 nm (Whatman, Nucleopore, NJ, USA). Three sequences of extrusion/vortex/freeze-thaw were made, followed by 10–20 passages through the extruder. The final phospholipid concentration was determined using a modified version of the Bartlett phosphate assay [42].

2.2. Dynamic light scattering (DLS)

Dynamic light scattering (DLS) on a Malvern Zetasizer Nano ZS (Malvern Instruments, Malvern, UK) was used for measuring the average particle size of the LUVs. The measurements were performed above the transition temperature (T_m) at a total lipid concentration of 0.1 mM,

using a He-Ne laser (wavelength 633 nm) as a source of incident light, and operating at a scattering angle of 173°. Refractive index (Anton Paar, Abbemat 300) and density (Anton Paar, DMATM 4500 M) and viscosity (Lovis 2000ME) were determined for both types of buffers at 37 °C and 60 °C, for the parameters to be used in the DLS measurements (see Table S1 in Supplementary Material). The samples obtained were monodisperse, with a particle size of ~117 nm, and a polydispersity index always <0.1.

2.3. Differential scanning calorimetry (DSC)

DSC measurements were performed in a MicroCal VP-DSC microcalorimeter from Malvern (Worcestershire, UK). Blank experiments with buffer in both cells were performed prior to sample loading, for subsequent blank correction. Three successive heating scans were performed for each sample, against buffer in the reference cell, at a scanning rate of 60 °C/hour, in a temperature range that depends on the lipid system. In the case of lipid/peptides mixtures, the sample mixtures were prepared immediately before the experiment by adding the desired amount of the CP to the LUVs suspension and transferred to the measuring cell. As the mixtures were not incubated above T_m prior to measurements, a difference always exists between the first and following scans, as the interaction is always better with the fluid phase. Unless otherwise stated, the results shown here are for the second scan. To guarantee that all samples had the same thermal history, the sample preparation and handling (lag time at low temperature, time between mixtures, and start of the experiment) were kept constant in all experiments. The transition temperature (T_m) and the transition enthalpy change ($\Delta_{trans}H$) were calculated by integration of the blank corrected heat capacity *vs* temperature curve (*Cp vs*. temperature), using a linear baseline. The respective half width at half height (HWHH) was also determined in all cases.

2.4. Attenuated total reflection Fourier transform infrared spectroscopy (ATR-FTIR)

The measurements were carried out in two different instruments and places (see Supplementary Material). In both cases, all peptide solutions and lipid suspensions were prepared in water for these experiments, as the drying process preclude the use of NaCl, and buffer could not be used due to superimposition of absorption bands.

Peptide and liposomes were mixed at desired lipid:peptide ratios (L:P) and the mixtures were incubated for 30 min at *ca* 10 °C above the transition temperature of the respective lipid system. A 2 μL sample was deposited on the diamond crystal and the solvent was slowly evaporated under a gentle N$_2$ flux through a pipette tip, to spread the liquid over the useful crystal surface, making a film as uniform as possible. While evaporating, capillary forces flatten the membranes, which spontaneously formed oriented multilayer arrangements [43].

The determination of molecular orientations by ATR-FTIR spectroscopy was reviewed by Goormaghtigh and Ruysschaert [44]. With that aim, the dichroic spectra were also recorded with parallel and perpendicular polarized incident light (with respect to the incidence plane), and the spectra scaled to the same lipid carbonyl vibration intensity. The dichroic spectrum is the difference between the spectra recorded with parallel and perpendicular polarization, using an appropriate multiplying factor for the perpendicular spectrum upon subtraction, to take into account the differences in the relative power of the evanescent fields [45]. The difference spectra, as well as the various dichroic ratios $\left(R = \frac{A_\parallel}{A_\perp}\right)$ were calculated with the program "Kinetics Spectra", developed in MatLab by Erik Goormaghtigh [46,47].

The background spectra used in the ATR-FTIR measurement was recorded in air.

2.5. Coarse-grained Molecular Dynamics (CG-MD) simulations

Coarse-grained molecular dynamics (CG-MD) simulations of **CP1** and **CP2** interacting with bacterial cytoplasmic membrane models composed of different mixtures of DMPC, DMPE and DMPG lipid bilayers were carried out to provide a better understanding of their mode of action.

As a first approximation, it was assumed that the CPs self-assemble into peptide nanotubes at the membrane, introducing restraints to maintain the tubular structure. Although some authors have proposed some modifications of the CG parameters for CPs [38], we decided to use the standard simulation parameters corresponding to the polarizable MARTINI force field (martini v2.2 P) [48,49], together with the use of distance restraints between all the backbone particles to maintain the cylindrical morphology. This approach allows the spontaneous insertion and reorientation of the SCPN into the lipid bilayer. The CG topologies for the CPs were built using the martinize.py tool [50]. The bonds and charges of the CPs were manually modified to create the cycles. P5 type particles were used for describing the backbone of each amino acid. In order to keep the cylindrical shape, characteristic of nanotubes, during all the simulation time, additional distance restraints (k = 1000 kJ·mol^{-1} nm^{-2}) were added for all the P5-P5 pairs. Subsequent CG-MD simulations of the preformed nanotubes in the membrane, releasing the restraints and limiting them to those necessary to maintain the CP opened and flat were also carried out, following Tarek's strategy [38]. Thus, for describing P5-P5 bond interactions, a harmonic potential was used, defining the equilibrium distance at 3.8 Å and a force constant of 6275 kJ·mol^{-1} nm^{-2}. The P5-P5-P5 angle was described using a harmonic angle potential with θ_0 of 135° and a force constant of 627 kJ·mol^{-1} rad^{-2}. In order to keep the planarity of the lateral chains, the P5$_1$-P5$_2$-P5$_3$-(lateral chain particle)$_2$ improper dihedral was described using a harmonic potential with ξ_0 = 180° and a force constant of 418 kJ·mol^{-1} rad^{-2}.

The CPs were obtained from previous nanotube models [11], taking

the conformation that seems to lead to a better interaction between the CPs. The membrane structures were prepared using the CHARMM membrane builder [51–56]. The parameters for DMPC, DMPE and DMPG were the standard ones provided from the Martini developers [48,57,58].

The MD-CG calculations were carried out at 300 K using the V-rescale thermostat [59] and the Parrinello–Rahman barostat [60] with semi-isotropic pressure coupling. A time step of 25 fs was used for all simulations. At least 1 μs was carried out in each case. All the simulations were done using GROMACS 5.1.2 [61].

3. Results and discussion

3.1. DSC

The results obtained in the DSC experiments for the two peptides, **CP1** and **CP2** and the five model membrane systems of DMPE and DMPG are shown in Fig. 2 and Table 2. For all systems, various ratios of lipid to peptide (L:P) were tested, and their DSC profile and derived thermodynamic parameters (T_m and $\Delta_{trans}H$) are compared to the ones observed for the respective pure lipid system. Due to low solubility of **CP1** in HEPES buffer we had to also use DMSO in the solvent mixture, which limited the possible L:P ratio for this peptide, as we did not want to increase the DMSO content in the aqueous media above 0.7 %, as the lipid membrane starts to be disturbed (unpublished results).

When membranes of pure DMPG are used (Fig. 2 A,B) a modest decrease in T_m, accompanied by a small curve broadening is observed as the peptides content increases, together with the appearance of a small, broad shoulder at temperatures above T_m. As regarding $\Delta_{trans}H$, in the case of **CP1** we observe a gradual decrease as L:P decreases, whereas the values obtained for **CP2** do not change significantly. This indicates that **CP1** interacts more strongly than **CP2** with DMPG. The obtained results are consistent with peptide/lipid aggregation/precipitation of part of the lipid system, leading to the presence of two populations: one of liposomes slightly disturbed by a small amount of surface bound peptide, yielding a DSC profile and T_m similar to the pure lipid system, and another formed by aggregated bilayers, intercalated with peptides strongly bound to the surface of the negatively charged lipids, mainly by electrostatic attraction (corresponding to the broad shoulder at higher temperature). We have previously observed a similar behavior with other peptides and DMPG [62].

Analyzing now the profiles and parameters obtained for the DMPE: DMPG mixtures, we will discuss the effects of introducing a zwitterionic lipid (PE) in the membrane and the consequent decrease in membrane's negative charge. Overall, the transition in the mixed membranes without peptide are broader, as expected, due to the structural difference between the two lipids. They are not expected to mix ideally, particularly in the gel phase, but at pH 7.45 PE:PG mixing is favored with the formation of ion pairs, that facilitates the hydration of PE head groups [63]. The behavior for DMPE:DMPG mixtures ranging from 0:1 to 1:0 has been extensively studied by Blume's group [63–65]. Starting with the system DMPE:DMPG (1:9) (Fig. 2C and D), we observe a large difference in behavior between the two peptides. **CP1** induces a clear demixing of the lipid system, with a peak at a temperature close to pure DMPG (23.0 °C), whose intensity decreases upon increasing the peptide content until it disappears at L:P ratio of 18:1, and another peak centered around 31.0 °C, that conversely increases with peptide content. The first peak corresponds to peptide associated with DMPG, and its intensity decrease is in line with what is observed in pure PG, reflecting aggregated lipid (PG)/peptide precipitation, whereas the peak at higher temperature reflects a mixture rich in PE that still contain some traces of PG and peptide. The increase in PE of this fraction justifies the increase in transition temperature for the lipid mixture, as the T_m obtained for pure DMPE was 50.0 °C, consistent with the reported value of 48.8 °C aqueous solution with 100 mM NaCl at pH 7 [63]. In the case of **CP2**, the effect is much less intense - the transition curve for all L:P ratios was
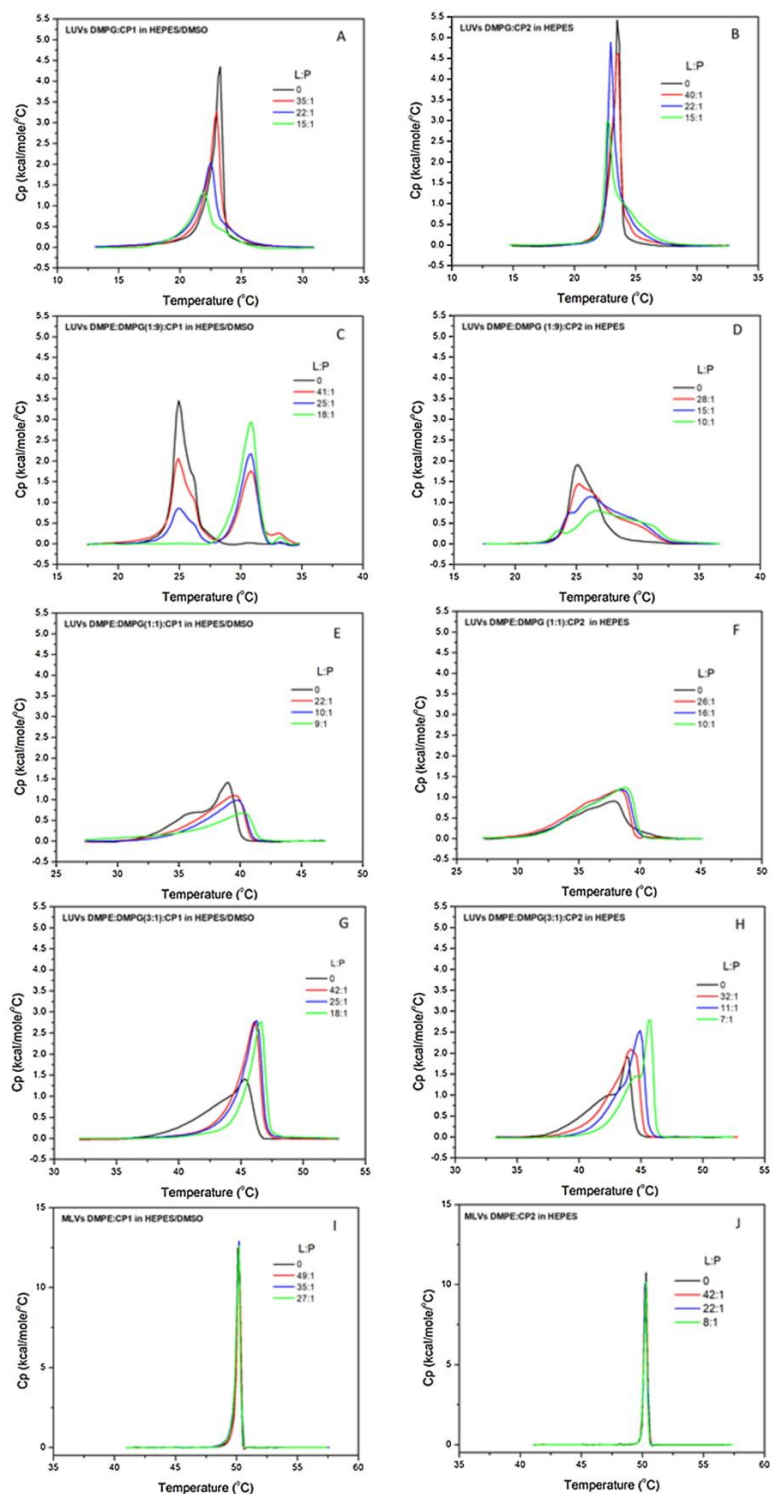
Fig. 2. DSC curves for mixtures of the two peptides **CP1** (left) and **CP2** (right) with model membranes of DMPE:DMPG. A,B: pure DMPG; C,D: DMPE:DMPG (1:9); E, F: DMPE:DMPG (1:1); G,H: DMPE:DMPG (3:1) and I,J: pure DMPE. The molar ratios of lipid to peptide (L:P) for each curve are shown in each plot. The results are all for the second scan (For interpretation of the references to colour in this figure legend, the reader is referred to the web version of this article.).

5

Table 2

Thermodynamic parameters T_m, $\Delta_{trans}H$ and HWHH (half width at half height) for the gel to liquid crystalline phase transition for the different lipid systems here studied, in the absence and presence of the cyclic peptides at various L:P molar ratios. The estimated uncertainty in T_m is ±0.2 °C, and in $\Delta_{trans}H$ is ±1 kJ/mol (within series uncertainties).

	CP1				CP2			
	L:P	T_m/ °C	HWHH/°C	ΔH/(kJ/mol)	L:P	T_m/ °C	HWHH/°C	ΔH/(kJ/mol)
DMPG	0	23.3	0.8	35	0	23.5	0.7	20
	35:1	23.0	1.0	33	40:1	23.6	1.0	23
	22:1	22.5	1.4	30	22:1	22.9	0.7	22
	15:1	21.9	1.9	20	15:1	22.7	0.8	21
DMPE:DMPG (1:9)	0	24.9	1.4	26	0	25.1	2.4	32
	41:1	24.9	1.9	16	28:1	25.1	3.5	39
		30.8	1.5	12				
	25:1	24.9	1.9	7	15:1	26.1	5.9	38
		30.9	1.5	17				
	18:1	30.9	1.7	22	10:1	26.8	6.6	32
DMPE:DMPG (1:1)	0	38.9	2.7	25	0	37.8	4.9	31
	22:1	39.5	3.9	40	26:1	38.4	4.9	40
	10:1	39.7	3.5	32	16:1	38.5	4.9	38
	9:1	40.3	3.9	30	10:1	38.8	4.9	40
DMPE:DMPG (3:1)	0	45.3	3.2	23	0	43.9	2.2	25
	42:1	46.1	1.7	26	321	44.1	2.5	31
	25:1	46.3	1.7	27	11:1	44.9	1.7	26
	18:1	46.6	1.5	23	7:1	45.8	1.7	25
DMPE (MLVs)	0	50.2	0.3	25	0	50.3	0.3	14
	49:1	50.1	0.5	21	42:1	50.2	0.5	16
	35:1	50.2	0.3	25	22:1	50.2	0.3	14
	27:1	50.2	0.3	24	8:1	50.2	0.3	14

significantly broadened, and a small peak at lower temperatures and a broad one at higher temperatures are apparent, indicating that some segregation takes place, but no clear demixing is present, as seen for **CP1**. The differences show clearly the stronger interaction of **CP1** with negatively charged membranes. These results are in accordance with the literature, as the ability of linear and CPs to demix PE:PG membranes has been reported [65]. As regarding the behavior of the two other DMPE:DMPG lipid systems at increasing PE content (1:1 and 3:1) no complete demixing is observed, but T_m shifts to higher temperatures, in a magnitude that increases with peptide content (up to around 38−40 °C for the 1:1 lipid system and close or higher than 45 °C for the 3:1 lipid system). Furthermore, for **CP1**, the width of the transition peaks decreases upon addition of the peptide, whereas that is not clear for **CP2**. Both observations are consistent with membrane segregation and PG/peptide aggregation, stronger for **CP1**, with consequent relative increase in DMPE content in the membrane mixture. We believe that the contribution of the lower transition temperature peak is not detected because of the lower PG content of the membrane lipid system [26,62]. It should be stressed that for the system with higher PE content, 3:1, more significant differences are observed between the two peptides, as expected – for **CP1** the curves are relatively insensitive to the L:P ratio, probably as all PG is taken by the peptide at all L:P proportions, whereas for **CP2** a more progressive increase in T_m is observed, due to the weaker interaction of this peptide with PG. Finally, the interaction of both peptides with pure DMPE was also followed by DSC, and no detectable interaction was observed for either peptide, at any L:P ratios tested (Fig. 2I and J). This observation does not preclude any interaction, it just shows that if it exists, it is not reflected in strong changes in DSC profile, indicating that the peptides are not disturbing the hydrocarbon chains arrangement or interacting with the heads in a way that DSC can detect. As will be seen later (see MD section), by MD we see that the peptides can interact with both lipids, although in a different manner.

3.2. ATR-FTIR

The ATR-FTIR experiments were performed to obtain information on the possible self-assembly of the peptides at the membrane, as well as on their position relative to the membrane plane, derived from the dichroic spectra.

Experiments were first performed with DMPC, as that was the membrane model used by Ghadiri's group in their initial work with this type of peptides [13]. Thereafter we did ATR-FTIR with five lipid model systems, pure DMPG and DMPE:DMPG at molar ratios 1:9, 1:1 and 3:1. The results for DMPC and **CP1** and **CP2** can be seen in Fig. 3A and B.

In the case of **CP1**, the appearance of the amide I frequency at 1630 cm^{-1} (perpendicular component, strong) together with a weak band at ~1688 cm^{-1} (parallel component, weak) and the amide II band at ~1530 cm^{-1} are altogether consistent with the characteristic features of a pure antiparallel β-sheet structure, in agreement with Ghadiri et al. [13]. Furthermore, the negative dichroism of the β-sheet (negative peaks at 1630 cm^{-1}) indicates that the amide C=O are largely parallel to the membrane, *i.e.*, the peptide nanotube lays parallel to the membrane surface [47], at odds with the perpendicular position obtained by Ghadiri with the ion channel forming hydrophobic peptide (*c*-[L̲QL̲WL̲WL̲W]) [13]. We can further observe that the difference peak increases with the decreasing L:P ratio (*i.e.*, higher peptide content). As regarding **CP2**, we also observe the amide I frequency at 1630 cm^{-1} and the amide II band at ~1530 cm^{-1}, but the band at ~1688 cm^{-1} is very strong and broad. A separate calculation of the side chain contributions revealed that only a minor fraction of this broad band may be explained by their contribution. Therefore, one can suggest that the spectra indicate that a significant fraction of the structure does not adopt a typical extended antiparallel β-sheet structure, and "turns" (these can contribute in the 1680 cm^{-1} region) [66], parallel sheet or other non-periodic structures are probably also present. Further, the amount of these other structures increases with the increase in peptide content. Altogether, this suggests that **CP2** also forms some β-sheet structure at the lipid surface, but also other forms, and has a much less defined orientation as regarding the membrane, as the difference spectra are not so conclusive as for **CP1**. The dichroic ratio for the strong amide I band (perpendicular component) was chosen to quantitatively assess the peptide nanotube orientation. To evaluate the lipid chain orientation, the symmetric and antisymmetric CH$_2$ stretches [$R(\nu_{as}(CH_2))$, $R(\nu_s(CH_2))$] were used. Finally two lipid head components were used to asses lipid orientation and order, namely the fatty acid carbonyl ester stretch [$R(\nu(CO))$] and the symmetric stretching of the PO$_2$- group, for the phosphate head group [$R(\nu_s(PO_2))$]. The values obtained for the dichroic ratios (parallel to perpendicular, $R = \frac{A_{\parallel}}{A_{\perp}}$) for the lipid part, $R(\nu_{as}(CH_2))$,
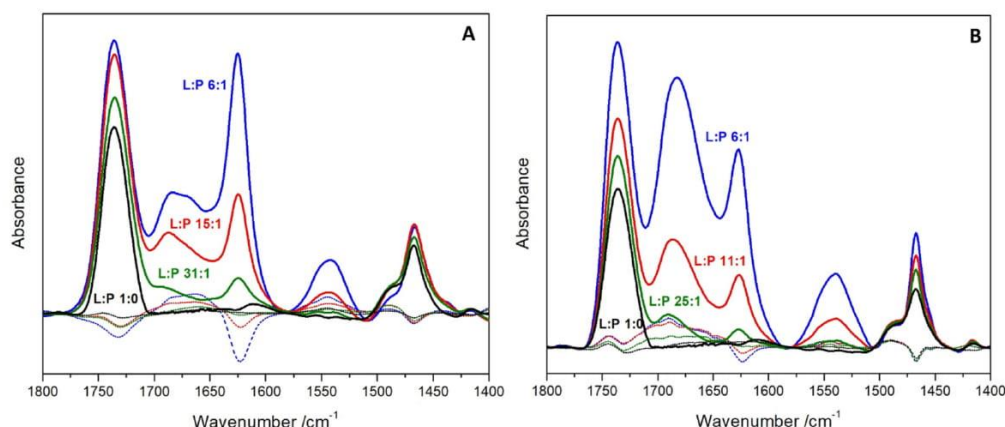
Fig. 3. ATR-FTIR results for DMPC and its mixtures with **CP1** (A) and **CP2** (B). The molar ratios are shown in each curve. The dichroic spectra (dashed lines, same color code) when polarizers were used at right angles are also shown for the various ratios (difference between the parallel and perpendicular spectra), clearly showing the negative peaks at 1630 cm^{-1} (For interpretation of the references to colour in this figure legend, the reader is referred to the web version of this article.).

$R(v_s(CH_2))$, $R(v(C=O))$ and $R(v_s(PO_2))$ indicate that **CP1** disturbs more the hydrocarbon part of the lipids than **CP2**. This is in line with our DSC studies for these peptides with DMPC (Fig. S5) that show that **CP1** interacts mildly with DMPC, lowering the phase transition temperature. This temperature reduction is consistent with penetration of the peptide into the lipid hydrocarbon part, which is facilitated by Trp residues, whereas **CP2**, as expected due to its low hydrophobic content, does not interact with these lipid membranes, as revealed by the invariance of the DSC curves.

We proceed now to the analysis of the results obtained for the negatively charged (DMPG) and mixed DMPE:DMPG membranes that were also studied by ATR-FTIR, both as considering the characteristic frequencies observed in the ATR-FTIR spectra and the values obtained for the dichroic ratios. The results are overall similar for all these lipid systems tested, and thus the lipid system DMPE:DMPG (1:9) is here presented as an example, with the results obtained for **CP1** and **CP2** with this lipid system shown in Fig. 4.

For both peptides we also observe here the appearance of the amide I frequency at ~1630 cm^{-1}, together with the amide II band at ~1530 cm^{-1}, consistent with the characteristic features of an antiparallel β-sheet structure. Nevertheless, here again some differences are observed between the spectra of both peptides. For **CP2**, the band at ~1688 cm^{-1} is always stronger than the band at 1630 cm^{-1} (Fig. 4), at

odds with **CP1**. We suggest as above (see discussion for DMPC and **CP2**), that part of this broad band is due to the presence of non-typical β-sheet structures and/or other non-periodic structures, and its presence increases with the increase in peptide content in the mixtures. Further, at odds with what was observed with DMPC, the intensities for **CP2** are usually larger than for **CP1**. This could reflect either a stronger binding of **CP2** or a larger destruction of the membranes in the case of **CP1**. Considering our DSC results, the fact that the organization into nanotubes seems stronger for **CP1** (reflected here in a more clear antiparallel β-sheet form for this peptide) and the known higher antimicrobial activity of **CP1**, we believe that these relative intensities reflect more the larger membrane destruction in the case of **CP1**.

For the analysis of the dichroic ratios for all these lipid systems, a curve fitting to three bands in the range 1800-1600 cm^{-1} was performed, to improve the quality of the calculated R values. The fittings obtained for DMPE:DMPG (1:9) with **CP1** and **CP2** considering peaks at 1740, 1670 and in the deconvolution are shown in Fig. S6A and S6B. For easier visualization, the R values obtained are plotted for both peptides and all membrane systems, as a function of the increase in peptide content (Fig. 5). For **CP1** and **CP2** the overall picture of the effect of the peptides on the R values is similar – for all membrane systems, the R values for the lipid chain orientation $[R(v_{as}(CH_2))$ and $R(v_s(CH_2))]$ as well as for lipid head components $[R(v(C=O))$ and $R(v_s(PO_2))]$ decrease in the presence
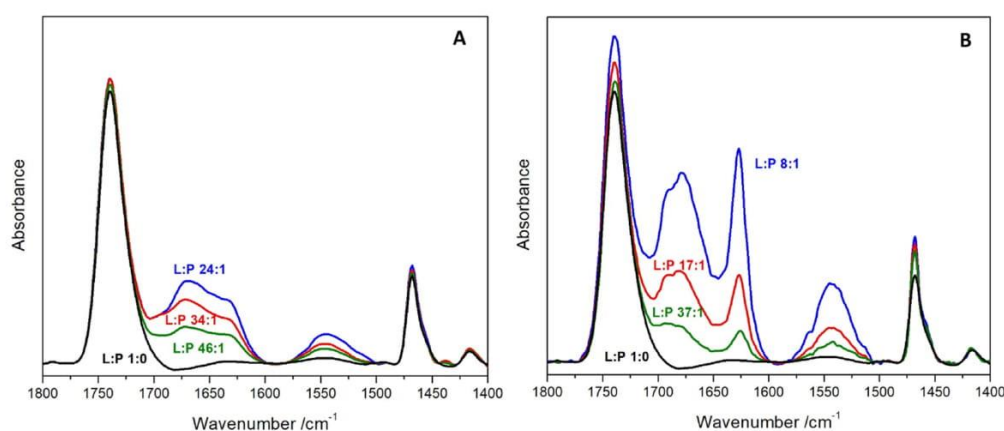

Fig. 4. ATR-FTIR results for DMPE:DMPG (1:9) with **CP1** (A) and **CP2** (B). The molar ratios are shown in each curve (For interpretation of the references to colour in this figure legend, the reader is referred to the web version of this article).
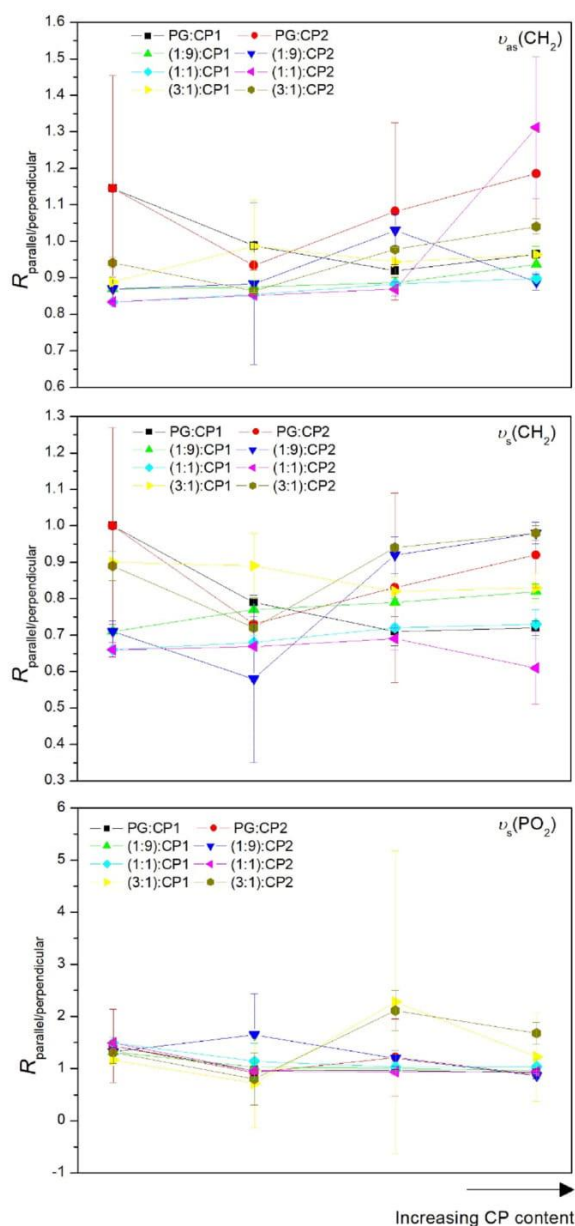
Fig. 5. Dichroic Ratio for Amide I, $v_{as}(CH_2)$, $v_s(CH_2)$ and $v_{as}(PO_2)$ for **CP1** and **CP2** and the lipid systems studied, plotted as a function of increasing peptide content along *xx* axis (left to right) (For interpretation of the references to colour in this figure legend, the reader is referred to the web version of this article.).

of the peptide, when compared to the pure lipid system, but they do not change significantly as a function of L:P ratio. Further, the change in the values for the lipid head components are larger than the ones found for the lipid chain order. This indicates that both CPs interact mainly with the polar heads of the lipids, a conclusion in line with the ones derived from the DSC results, as explained above. As regarding the amide I, the *R* values does not change significantly with peptide content. It can be further observed that the amide I dichroic ratio is always similar to the lipid $v(C=O)$ dichroic ratio, an additional indication of parallel arrangement to the membrane surface.

3.3. CG-MD simulations

Previous CG-MD simulations carried out by Tarek et al. [38], performed at various concentrations of **CP1** interacting with POPE:POPG (3:1), had suggested a type of mechanism in which the peptides first self-assemble at the membrane interface forming amphipathic nanotubes with the hydrophilic surface pointing towards the membrane/aqueous interface. Starting from different approaches, *i.e.* individual CPs, preassembled CP clusters or a random distribution of CPs, lipids and water, Tarek et al. CG-MD simulations' suggested that the interaction with the membrane is triggered by strong electrostatic interactions between the charged peptides and the lipid head groups, resulting in a coating of the lipid interface [38]. Thus, in order to try to further decipher the mechanism of action of **CP1** and **CP2**, CG-MD simulations of preassembled nanotubes composed of eight units of these CPs (herein called **SCPN1** and **SCPN2**, depending of the type of CP that they are composed, **CP1** or **CP2**, respectively) were carried out in presence of different membrane compositions (see *Methods*): DMPC, DMPC:DMPG (3:1), DMPE:DMPG (3:1) and DMPE:DMPG (1:9). Among the possible relative conformations that the CPs can adopt along the nanotube, we decided to assume an antiparallel structure in which all the Trp are aligned along the nanotube (Fig. 6A-B). As far as CP concentration is concerned, we decided to carry out a comparative study between the two peptides using in each case just a single unit of **SCPN1** and **SCPN2**, as each SCPN has 8 CPs, to understand the basis of initial interaction of each nanotube with the different membrane compositions.

The nanotubes are placed initially in the vicinity of the membrane in a random orientation, and they rapidly bind spontaneously to the membrane interface (Fig. 6C-E). In the case of **SCPN2**, and independently of the membrane composition, the nanotube interacts with the membrane having its hydrophobic region oriented towards the hydrophobic core of the membrane while the hydrophilic groups remain close to the head group region, pointing towards the solvent. A similar interaction with the membrane was found for the preassembled **SCPN1** (Fig. 6D) when the lipid composition was DMPC, DMPC:DMPG (3:1) and DMPE:DMPG (3:1). In those cases, the Arg residues are oriented towards the water, while close to the head group region, and the hydrophobic part towards the hydrocarbon part of the bilayer. However, for the model membrane with highest PG content, DMPE:DMPG (1:9), we observed a twirl of **SCPN1**, yielding a structure with the Arg residues pointing towards the lipids' headgroups of the bilayer (Fig. 6D) with the rest of the nanotube exposed to the aqueous media. Although this disposition must have a high energy cost due to the orientation of the SCPN's hydrophobic part towards water, this must be compensated by the strong electrostatic interactions between the PG negative-charged head groups and the Arg residues. It should be pointed out that the artificial restraints applied to maintain the nanotube force the CPs positive charges to be kept together, leading to a possible overestimation of the electrostatic contribution compared to the real unrestrained system (*vide infra*). In this case, **SCPN1** is not so deeply inserted into the bilayer as compared to the other membrane compositions here studied, as a consequence of the strong interaction between Arg residues and the lipids, together with the absence of hydrophobic interactions between the Trp and Leu residues with the aliphatic part of the membrane.

It should be noted that a replica of the simulation starting with the **SCPN1** interacting with the membrane trough the hydrophobic region (Fig. S9) confirmed that this other orientation was also stable and maintained along the simulated times.

The tilt angles of the preassembled nanotubes calculated with respect to the perpendicular axis of the membrane are represented in Fig. 7. Lower tilt angles are observed for **SCPN2** as compared to **SCPN1**, in consonance with less deep membrane penetration, except for **SCPN1** when is interacting with DMPE:DMPG (1:9) membrane. In this case the tilt angle is of a magnitude similar to the ones observed for **SCPN2**. It is worth mentioning that the interaction of **SCPN1** with all other lipid membranes here tested (DMPC, DMPC:DMPG 3:1, DMPE:DMPG 3:1) is
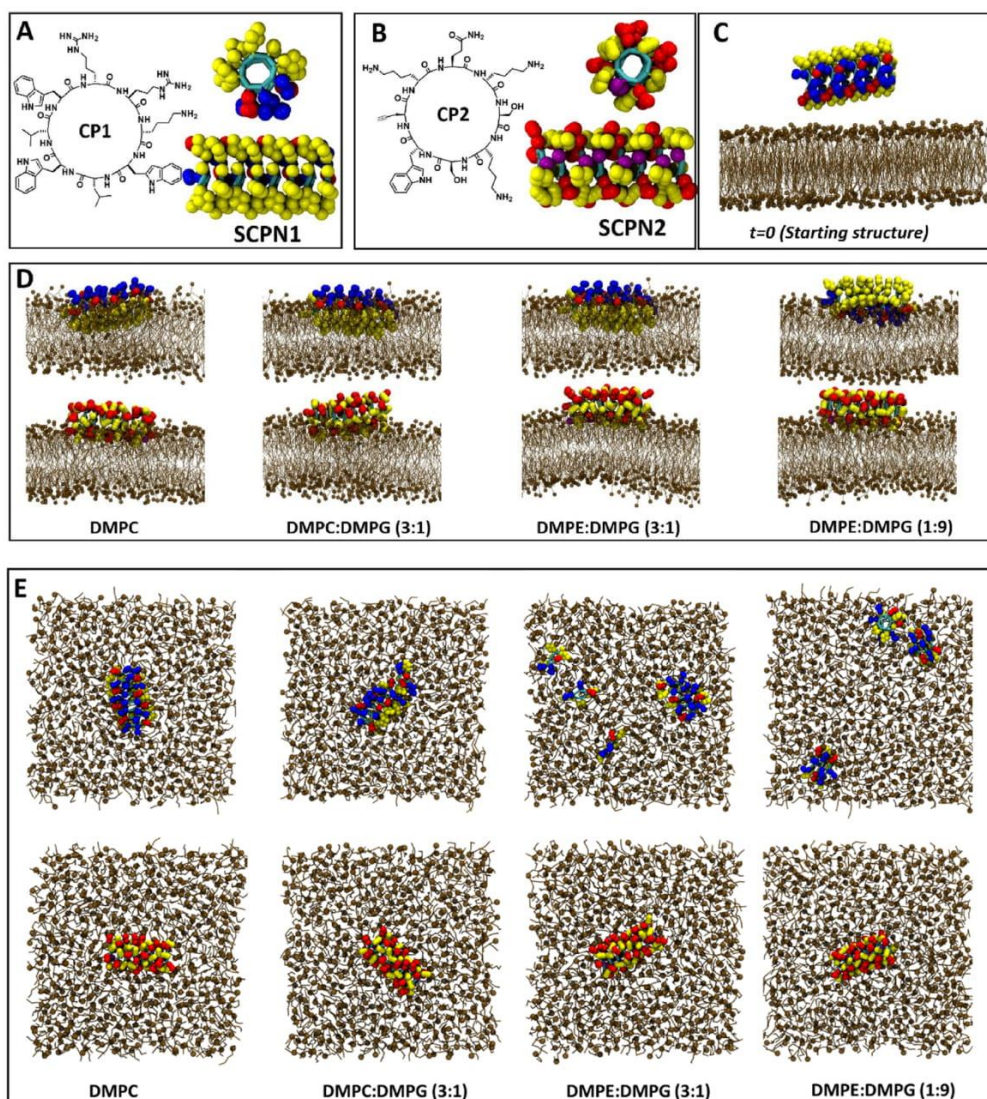
Fig. 6. 2D and CG-structure for **CP1** (A) and **CP2** (B) forming the corresponding SCPNs constructed by the stacking of eight cyclic units (**SCPN1** and **SCPN2**). Lys are represented in red, Arg in blue, and purple represents the alkyne moiety. The remaining residues of the SCNP are shown in yellow. In the initial structure at t = 0 the SCPN is outside the membrane, leading to a spontaneous insertion (C) after 1 μs. Section D shows the corresponding snapshots at t = 1 μs for the CG-MD simulation of **SCPN1** (top) and **SCPN2** (down) in presence of different model membrane systems, using restraints to force the nanotube topology. It can be seen that in the case of the DMPE:DMPG (1:9) membrane and **SCPN1,** the Arg are directed towards the membrane surface, in contrast to what happens in the other membrane compositions. Section E shows the corresponding snapshots at t = 1.5 μs [**SCPN1** (top) and **SCPN2** (down)], where the last 500 ns were carried out releasing the restraints to maintain the nanotube structure and just keeping those necessary to maintain the CP flat conformation (for lateral side views see Fig. S7). Water molecules have been removed for clarity (For interpretation of the references to colour in this figure legend, the reader is referred to the web version of this article.).

really strong. The **SCPN1** penetrates the hydrophobic region of the membranes interacting even with the opposite layer, which makes sense due to its high Trp content, a peptide know to act as 'anchor' to the membrane (see videos pc.mp4, pcpg31.mp4 and pepg31.mp4, Supplementary Material). The twirled orientation found in the case of **SCPN1** and the DMPE:DMPG 1:9 composition (see video pepg19.mp4, Supplementary Material) leads to a weaker interaction with the membrane, at least at the initial step of the mechanism, under the assumption of the applied restraints to the nanotube (*vide infra*).

To further characterize **SCPN1** and evaluate the stability of the preformed nanotubes upon membrane insertion, we did another set of CG-MD simulations, starting from the structures generated after 1 μs of

simulation. These structures were released of the nanotube restraints while keeping those that maintain the CPs flat conformation. In these calculations the originally assumed nanotubes were only maintained for the membranes lacking PE (Fig. 6E and Fig S7). The disassembling of the nanotubes in presence of DMPE:DMPG (3:1) and DMPE:DMPG (1:9) membranes is accompanied by an increase in the number of contacts between the CPs and the lipids of these membranes. This occurs contrary to what was observed in the membranes containing PC, where the number of contacts between the CPs and the lipids is very similar after the releasing of the nanotube restraints (Fig. 8). Thus, the releasing of the restraints that force the formation of the nanotube led to a better accommodation of the CPs and consequently an increase of the contacts
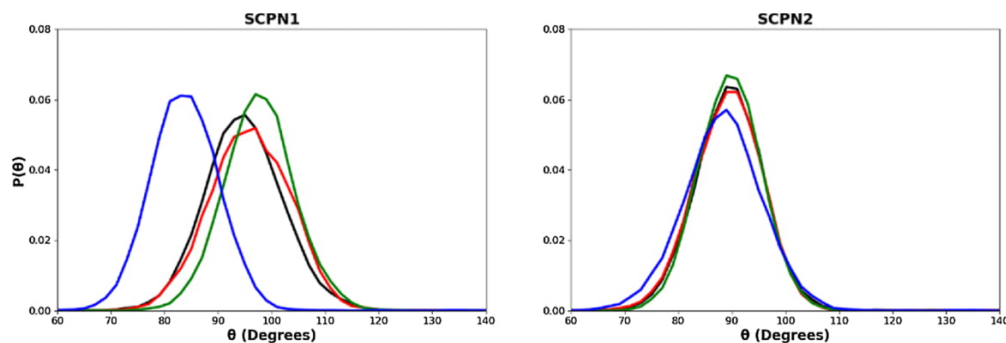
Fig. 7. Probability distribution of the tilt angles for the corresponding SCPNs (**SCPN1** and **SCPN2**) with respect to the *z*-axis of the membrane. (DMPC in black, DMPC:DMPG (3:1) in red, DMPE:DMPG (3:1) in green and DMPE:DMPG (1:9) in blue) (For interpretation of the references to colour in this figure legend, the reader is referred to the web version of this article.).
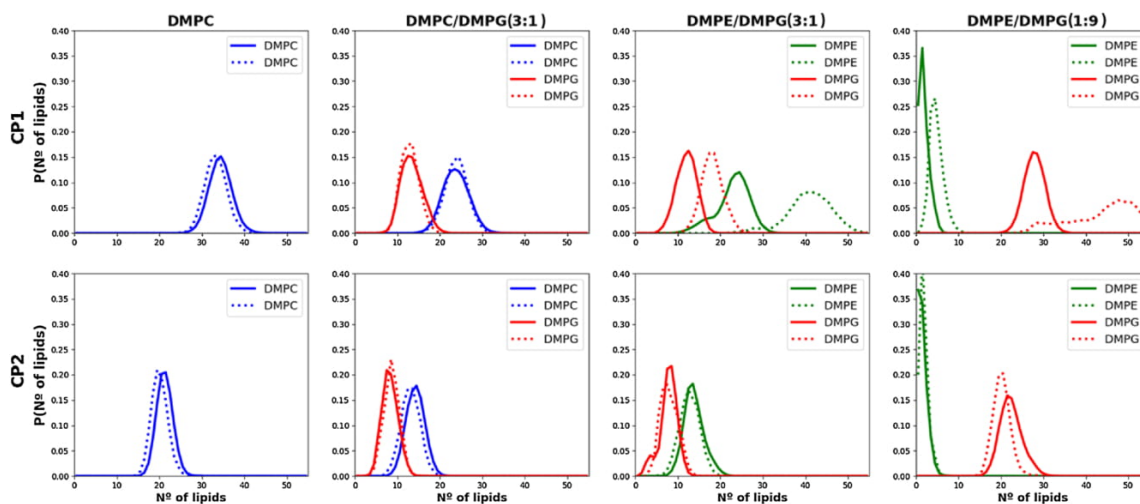

Fig. 8. Probability distribution of the number of contacts between **SCPN1** (top) and **SCPN2** (down), respectively, and the different lipids composing the membrane. Blue for DMPC, red for DMPG and green for DMPE. Dashed lines correspond to the MD simulations after the releasing of the initial restraints (For interpretation of the references to colour in this figure legend, the reader is referred to the web version of this article.).

of the CPs with PE and PG lipids. Therefore, these structural changes result in the destabilization of the nanotube. It is worth noting that different replicas were carried out and, in all cases, the **SCPN1** is dissembled (Fig S8). This disassembling gives rise to several small clusters formed by **CP1** units. Analogously, in the case of **SCPN1** with DMPE:DMPG (1:9) we also carried out a replica of the simulation in which we started with the **SCPN1** immersed in the membrane through the hydrophobic region (Figure S9). As it was mentioned, whereas this orientation was also stable and maintained when the nanotube was restrained, the release of the restraints also led to the partial disassembly of **SCPN1**. However, assuming a different CP stacking for **SCPN1**, in which the Trp are just partially aligned with each other (Fig. S10), the resulting nanotube structure was preserved even in absence of restraints. The rotation of the different CP units that form the nanotube [67,68] seems to be a key factor for their interaction with different membranes (Fig. S10A). It is very likely that different relative orientations of the CPs that constitute the nanotube can be adopted in the presence of membrane of different compositions, opening the door to a mechanism of adaptability of these systems to the environment through alternative rotations, to maximize the favorable interactions with the membrane. In this regard, it is interesting to note that this alternative conformation for **SCPN1** did not maintain the nanotube structure when the constraints

were released, for the model membrane system DMPE:DMPG (3:1) (Fig. S10).

Similar studies were carried out for **SCPN2**, using a preassembled nanotube composed by 8 units of **CP2** (see Methods), and no considerable differences were found with respect to the orientation of this nanotube, depending on the membrane composition. In all cases (Fig. 6D), the Lys residues were oriented towards the aqueous media, leaving the Trp and the alkyne moiety close to the aliphatic part of the lipids of the membrane.

Subsequent CG-MD simulations, starting from these structures and releasing the restraints of the nanotube **SCPN2** just to maintain the CPs in the flat conformation led in all cases to the conservation of the originally assumed nanotubes (Fig. 6E and Fig. S11). Just as with **SCPN1**, the releasing of the restraints applied to **SCPN2** is also translated into an increase in the degree of the number of contacts between the **CP2** units and the lipids (Fig. 8). The main contacts occurring with negatively charged lipids, even though they are present in reduced proportion in DMPC:DMPG (3:1) or DMPE:DMPG (3:1) systems, suggests that the interaction with the anionic phospholipids is the main driving force to the association of the CP with the membranes. This is even more clearly shown for **SCPN2.** It should be noted that the global number of contacts between the lipids and **CP2** is lower than for **CP1**, for all the four model

membrane systems studied (Fig. 8).

The tilt angles of the nanotubes calculated with respect to the perpendicular axis of the membrane are more homogenous for **SCPN2** than for **SCPN1**, presenting similar values for all the membrane compositions (Fig. 7). As mentioned before, the lower tilt angle formed by **SCPN2** in the DMPC membrane compared to the one formed by **SCPN1** in an analogous composition reveals its lower tendency to interact with the DMPC membrane. This is in agreement with the invariance of the DSC and also with the lower toxicity for this system.

4. Conclusions

Overall, the results obtained from the different approaches here described allow us to better characterize the interactions of **CP1** and **CP2** with model membranes, and try to rationalize their antimicrobial activity.

DSC shows that both peptides interact with negatively charged membranes, but differences can be found in the strength of interactions (**CP1** stronger than **CP2**), eventually reaching a significant difference for the system DMPE:DMPG (1:9), where **CP1** is actually able to effectively segregate the two lipid components (two separated peaks), whereas **CP2** presents similar features, but to a very small extent (only the appearance of shoulders). This result for **CP1** and DMPE:DMPG (1:9) is in line with what was observed in the CG-MD simulations, where a different arrangement of the peptide at the membrane surface is observed. The results from CG-MD (Fig. 7) led to the idea that a second layer of peptide could be formed, protecting the hydrophobic part of the nanotube from the aqueous environment. This could lead to the capacity of the peptides from the second layer to interact with another membrane, or even to disrupt the membrane leading to lipid bilayer stacking, as we have observed with another antimicrobial peptide [26]. Although no CG-MD studies were performed for the pure DMPG lipid system, we suggest that the same type of mechanism could be at stake with these membranes.

For all membrane systems with various PG contents, the results show an interaction mainly at the headgroups level, as shown by DSC and in the ATR-FTIR analysis of the changes of vibrations for the phosphate and hydrocarbon parts of the lipids. Further, by CG-MD we saw that the main contacts occur with negatively charged lipids, suggesting that the interaction with the anionic phospholipids is the main driving force to the association of the CP with the membranes. Altogether the results and the differences observed are in line with the microbiology screening study performed (E. González-Freire, F. Novelli, A. Pérez-Estévez, R. Seoane, M. Amorín and J. R. Granja, manuscript in preparation) for the two peptides and Gram-positive and Gram-negative bacteria, where **CP1** was found to be active, particularly against Gram-positive bacteria, and **CP2** was found to have moderate/low activity against the same bacteria. This might be due to the lower content of hydrophobic residues, or to weaker amphipathic character. It also complies with the observation in ATR-FTIR that when **CP1** or **CP2** and negative phospholipids are involved, other structures are also present at the membrane surface, together with pure β-sheet-based nanotubes, but this effect is much stronger for **CP2**, as although this peptide can form some nanotubes at the lipid membrane, it clearly has a mixture of structures when partly negatively charged membranes are used. It should be also noted that the global number of contacts between the lipids and **CP2** is lower than for **CP1**, for all the four model membrane systems studied. Further, the pointed larger intensities observed for **CP2** in the presence of negatively charged phospholipids and the quoted DSC results lead us to suggest that this could explain at least partly the weaker antimicrobial activity of **CP2** – as shown by ATR-FTIR, and assumed in part of the CG-MD studies, **CP2** only interacts at the interface with phospholipid heads (DSC and ATR-FTIR), has a limited segregation capacity (DSC), and the various forms taken by the peptide on interaction with the bacterial membranes would be less effective, *i.e.*, less destructive than the ones taken by **CP1**.

The fact that **CP1** activity was particularly high against Gram-positive bacteria with very high PG contents in the cytosol membrane

also correlates well with our results, where the membrane perturbation was in all cases more severe with membranes with higher PG content. Further, our DSC results found no detectable interaction of the peptides with DMPE, which could at least partly explain the lower activity against Gram-negative bacteria such as *E. coli*, where the PE content is high.

Finally, the results obtained for DMPC are very interesting, as we have used in the past this membrane composition as a crude model for eukaryotic membranes, and we found excellent agreement between the DSC results and toxicity tests [8].In the present study, the DSC experiments showed that **CP1** interacts with DMPC, whereas **CP2** does not. Curiously, as discussed above, ATR-FTIR revealed that both peptides form antiparallel β-sheets at the membrane plane, with **CP1** showing clearly a β-sheet at the membrane surface while **CP2** showed a less well-defined structure. Nevertheless, the values obtained for the dichroic ratios indicate that **CP1** disturbs more the hydrocarbon part of the lipids than **CP2**. This could indicate that **CP2** only 'sees' the membrane as a platform for nanotube formation, as observed for these type of *D,L-α*-CPs in other experimental conditions, but does not penetrate and disturb DMPC membrane significantly, in perfect agreement with our DSC results [11].

Developing a greater comprehension of the relationship between structure of antimicrobial molecules and antimicrobial activity against bacterial membranes as well as toxicity towards mammalian cell will ultimately enable the design of more efficient and selective "intelligent" materials of this type that can be used instead of conventional antibiotics. The present results contribute to this effort, as they did corroborate the activity of **CP1**, shed light into possible mechanism of action and bacterial selectivity, and further point to its possible toxicity. **CP2**, on the other hand, did prove to be a weak antimicrobial peptide, with possible reasons for the diminished activity discussed above. This lead us already to the design and synthesis of next generation peptides, taking **CP2** as a template (for its expected lack of toxicity and high solubility), but introducing changes that based on these results we anticipate will increase potency.

References

[1] L. Fernández, R.E.W. Hancock, Adaptive and mutational resistance: role of porins and efflux pumps in drug resistance, Clin. Microbiol. Rev. 25 (4) (2012) 661–681, https://doi.org/10.1128/cmr.00043-12.

[2] N.B. da Cunha, N.B. Cobacho, J.F.C. Viana, L.A. Lima, K.B.O. Sampaio, S.S. M. Dohms, A.C.R. Ferreira, C. de la Fuente-Núñez, F.F. Costa, O.L. Franco, S. C. Dias, The next generation of antimicrobial peptides (AMPs) as molecular therapeutic tools for the treatment of diseases with social and economic impacts, Drug Discov. Today 22 (2) (2017) 234–248, https://doi.org/10.1016/j.drudis.2016.10.017.

[3] K. Midura-Nowaczek, A. Markowska, Antimicrobial peptides and their analogs: searching for new potential therapeutics, Perspect. Med. Chem. 6 (2014) 73–80, https://doi.org/10.4137/PMC.S13215.

[4] W.C. Wimley, K. Hristova, Antimicrobial peptides: successes, challenges and unanswered questions, J. Membr. Biol. 239 (1-2) (2011) 27–34, https://doi.org/10.1007/s00232-011-9343-0.

[5] C.D. Fjell, J.A. Hiss, R.E.W. Hancock, G. Schneider, Designing antimicrobial peptides: form follows function, Nat. Rev. Drug Discov. 11 (2011) 37–51, https://doi.org/10.1038/nrd3591.

[6] M. Mahlapuu, J. Håkansson, L. Ringstad, C. Björn, Antimicrobial peptides: an emerging category of therapeutic agents, Front. Cell. Infect. Microbiol. 6 (194) (2016), https://doi.org/10.3389/fcimb.2016.00194.

[7] A.T.Y. Yeung, S.L. Gellatly, R.E.W. Hancock, Multifunctional cationic host defence peptides and their clinical applications, Cell. Mol. Life Sci. 68 (13) (2011) 2161, https://doi.org/10.1007/s00018-011-0710-x.

[8] T. Silva, R. Adão, K. Nazmi, J.G.M. Bolscher, S.S. Funari, D. Uhríková, M. Bastos, Structural diversity and mode of action on lipid membranes of three lactoferrin candidacidal peptides, Biochim. Acta Biomembr. 1828 (5) (2013) 1329–1339, https://doi.org/10.1016/j.bbamem.2013.01.022.

[9] J.T. Mika, G. Moiset, A.D. Cirac, L. Feliu, E. Bardaji, M. Planas, D. Sengupta, S. J. Marrink, B. Poolman, Structural basis for the enhanced activity of cyclic antimicrobial peptides: the case of BPC194, Biochim. Biophys. Acta Biomembr. 1808 (9) (2011) 2197–2205, https://doi.org/10.1016/j.bbamem.2011.05.001.

[10] M. Wu, R.E.W. Hancock, Improved derivatives of Bactenecin, a cyclic dodecameric antimicrobial cationic peptide, Antimicrob. Agents Chemother. 43 (5) (1999) 1274–1276, https://doi.org/10.1128/AAC.43.5.1274.

[11] M.R. Ghadiri, J.R. Granja, R.A. Milligan, D.E. McRee, N. Khazanovich, Self-assembling organic nanotubes based on a cyclic peptide architecture, Nature 366 (6453) (1993) 324–327, https://doi.org/10.1038/366324a0.

[12] N. Rodríguez-Vázquez, M. Amorín, J.R. Granja, Recent advances in controlling the internal and external properties of self-assembling cyclic peptide nanotubes and dimers, Org. Biomol. Chem. 15 (21) (2017) 4490–4505, https://doi.org/10.1039/C7OB00351J.

[13] H.S. Kim, J.D. Hartgerink, M.R. Ghadiri, Oriented self-assembly of cyclic peptide nanotubes in lipid membranes, J. Am. Chem. Soc. 120 (18) (1998) 4417–4424, https://doi.org/10.1021/ja9735315.

[14] S. Fernandez-Lopez, H.-S. Kim, E.C. Choi, M. Delgado, J.R. Granja, A. Khasanov, K. Kraehenbuehl, G. Long, D.A. Weinberger, K.M. Wilcoxen, M.R. Ghadiri, Antibacterial agents based on the cyclic d,l-α-peptide architecture, Nature 412 (2001) 452–455, https://doi.org/10.1038/35086601.

[15] Anna D. Cirac, G. Moiset, Jacek T. Mika, A. Koçer, P. Salvador, B. Poolman, Siewert J. Marrink, D. Sengupta, The molecular basis for antimicrobial activity of pore-forming cyclic peptides, Biophys. J. 100 (10) (2011) 2422–2431, https://doi.org/10.1016/j.bpj.2011.03.057.

[16] R. García-Fandiño, M. Amorín, L. Castedo, J.R. Granja, Transmembrane ion transport by self-assembling α,γ-peptide nanotubes, Chem. Sci. 3 (11) (2012) 3280–3285, https://doi.org/10.1039/c2sc21068a.

[17] R.-V. Nuria, H.L. Ozores, G. Arcadio, G.-F. Eva, F. Alberto, P. Michele, M.P. Juan, O. Juan, M. Javier, G.-F. Rebeca, A. Manuel, R.G. Juan, Membrane-targeted self-assembling cyclic peptide nanotubes, Curr. Top. Med. Chem. 14 (23) (2014) 2647–2661, https://doi.org/10.2174/1568026614666141215143431.

[18] H. Cui, B. Xu, Supramolecular medicine, Chem. Soc. Rev. 46 (21) (2017) 6430–6432, https://doi.org/10.1039/C7CS90102J.

[19] L.A. Calderon, A.M. Soares, R.G. Stábeli, Anuran Antimicrobial Peptides: an alternative for the development of nanotechnological based therapies for multi-drug-resistant infections, Signpost Open J. Biochem. Biotech. 1 (2012) 1–11.

[20] K.A. Brogden, Antimicrobial peptides: pore formers or metabolic inhibitors in bacteria? Nat. Rev. Microbiol. 3 (3) (2005) 238–250, https://doi.org/10.1038/nrmicro1098.

[21] L.T. Nguyen, E.F. Haney, H.J. Vogel, The expanding scope of antimicrobial peptide structures and their modes of action, Trends Biotechnol. 29 (9) (2011) 464–472, https://doi.org/10.1016/j.tibtech.2011.05.001.

[22] V. Teixeira, M.J. Feio, M. Bastos, Role of lipids in the interaction of antimicrobial peptides with membranes, Prog. Lipid Res. 51 (2) (2012) 149–177, https://doi.org/10.1016/j.plipres.2011.12.005.

[23] L. Yang, T.A. Harroun, T.M. Weiss, L. Ding, H.W. Huang, Barrel-stave model or toroidal model? A case study on melittin pores, Biophys. J. 81 (3) (2001) 1475–1485, https://doi.org/10.1016/S0006-3495(01)75802-X.

[24] M. Bastos, T. Silva, V. Teixeira, K. Nazmi, J.G. Bolscher, S.S. Funari, D. Uhrikova, Lactoferrin-derived antimicrobial peptide induces a micellar cubic phase in a model membrane system, Biophys. J. 101 (3) (2011) 20–22, https://doi.org/10.1016/j.bpj.2011.06.038.

[25] M. Reuter, C. Schwieger, A. Meister, G. Karlsson, A. Blume, Poly-l-lysines and poly-l-arginines induce leakage of negatively charged phospholipid vesicles and translocate through the lipid bilayer upon electrostatic binding to the membrane, Biophys. Chem. 144 (1-2) (2009) 27–37, https://doi.org/10.1016/j.bpc.2009.06.002.

[26] T. Silva, B. Claro, B.F.B. Silva, N. Vale, P. Gomes, M.S. Gomes, S.S. Funari, J. Teixeira, D. Uhríková, M. Bastos, Unravelling a mechanism of action for a cecropin A-melittin hybrid antimicrobial peptide: the induced formation of multilamellar lipid stacks, Langmuir 34 (5) (2018) 2158–2170, https://doi.org/10.1021/acs.langmuir.7b03639.

[27] E. Sevcsik, G. Pabst, A. Jilek, K. Lohner, How lipids influence the mode of action of membrane-active peptides, Biochim. Biophys. Acta 1768 (10) (2007) 2586–2595, https://doi.org/10.1016/j.bbamem.2007.06.015.

[28] M. Hong, Structure, topology, and dynamics of membrane peptides and proteins from solid-state NMR spectroscopy, J. Phys. Chem. B 111 (35) (2007) 10340–10351, https://doi.org/10.1021/jp073652j.

[29] J. Mondal, A brief appraisal of computational modeling of antimicrobial peptides' activity, Drug Dev. Res. 80 (1) (2019) 28–32, https://doi.org/10.1002/ddr.21472.

[30] G.E. Balatti, E.E. Ambroggio, G.D. Fidelio, M.F. Martini, M. Pickholz, Differential interaction of antimicrobial peptides with lipid structures studied by coarse-grained molecular dynamics simulations, Molecules 22 (10) (2017) 1775, https://doi.org/10.3390/molecules22101775.

[31] N.A. Berglund, T.J. Piggot, D. Jefferies, R.B. Sessions, P.J. Bond, S. Khalid, Interaction of the antimicrobial peptide polymyxin B1 with both membranes of E. coli: a molecular dynamics study, PLoS Comput. Biol. 11 (4) (2015), e1004180, https://doi.org/10.1371/journal.pcbi.1004180.

[32] S. Khalid, N.A. Berglund, P.J. Bond, T.J. Piggot, Molecular dynamics simulations reveal mechanistic details of polymyxin penetration into both membranes of E. coli, Biophys. J. 108 (2) (2015) 549a, https://doi.org/10.1371/journal.pcbi.1004180.

[33] A. Boags, P.-C. Hsu, F. Samsudin, P.J. Bond, S. Khalid, Progress in molecular dynamics simulations of Gram-negative bacterial cell envelopes, J. Phys. Chem. Lett. 8 (11) (2017) 2513–2518, https://doi.org/10.1021/acs.jpclett.7b00473.

[34] A. Hollmann, M. Martinez, P. Maturana, L.C. Semorile, P.C. Maffia, Antimicrobial peptides: interaction with model and biological membranes and synergism with chemical antibiotics, Front. Chem. 6 (204) (2018), https://doi.org/10.3389/fchem.2018.00204.

[35] J. Parkin, M. Chavent, S. Khalid, Molecular simulations of Gram-negative bacterial membranes: a vignette of some recent successes, Biophys. J. 109 (3) (2015) 461–468, https://doi.org/10.1016/j.bpj.2015.06.050.

[36] G. Shahane, W. Ding, M. Palaiokostas, H.S. Azevedo, M. Orsi, Interaction of antimicrobial lipopeptides with bacterial lipid bilayers, J. Membr. Biol. 252 (4) (2019) 317–329, https://doi.org/10.1007/s00232-019-00068-3.

[37] L. Zhao, Z. Cao, Y. Bian, G. Hu, J. Wang, Y. Zhou, Molecular dynamics simulations of human antimicrobial peptide LL-37 in model POPC and POPG lipid bilayers, Int. J. Mol. Sci. 19 (4) (2018) 1186, https://doi.org/10.3390/ijms19041186.

[38] A. Khalfa, M. Tarek, On the antibacterial action of cyclic peptides: insights from coarse-grained MD simulations, J. Phys. Chem. B 114 (8) (2010) 2676–2684, https://doi.org/10.1021/jp9064196.

[39] N. Malanovic, K. Lohner, Gram-positive bacterial cell envelopes: the impact on the activity of antimicrobial peptides, Biochim. Biophys. Acta Biomembr. 1858 (5) (2016) 936–5946, https://doi.org/10.1016/j.bbamem.2015.11.004.

[40] L.A. Carpino, G.Y. Han, 9-Fluorenylmethoxycarbonyl function, a new base-sensitive amino-protecting group, J. Am. Chem. Soc. 92 (19) (1970) 5748–5749, https://doi.org/10.1021/ja00722a043.

[41] V. Dartois, J. Sanchez-Quesada, E. Cabezas, E. Chi, C. Dubbelde, C. Dunn, J. Granja, C. Gritzen, D. Weinberger, M.R. Ghadiri, T.R. Parr, Systemic antibacterial activity of novel synthetic cyclic peptides, Antimicrob. Agents Chemother. 49 (8) (2005) 3302–3310, https://doi.org/10.1128/AAC.49.8.3302-3310.2005.

[42] G.R. Bartlett, Phosphorus assay in column chromatography, J. Biol. Chem. 234 (3) (1959) 466–468.

[43] U.P. Fringeli, H.H. Günthard, Infrared membrane spectroscopy. Membrane Spectroscopy, Springer, 1981, pp. 270–332, https://doi.org/10.1007/978-3-642-81537-9_6.

[44] E. Goormaghtigh, J.M. Ruysschaert, R. Brasseur, Polarized Attenuated Total Reflection Spectroscopy as a Tool to Investigate the Conformation and Orientation of Membrane Components, Molecular Description of Biological Membranes Components by Computer Aided Conformational Analysis, CRC Press Inc, 1990, pp. 285–332, https://doi.org/10.1201/9780429291777-11.

[45] B. Bechinger, J.-M. Ruysschaert, E. Goormaghtigh, Membrane helix orientation from linear dichroism of infrared attenuated total reflection spectra, Biophys. J. 76 (1) (1999) 552–563, https://doi.org/10.1016/S0006-3495(99)77223-1.

[46] E. Goormaghtigh, Infrared spectroscopy: data analysis, in: G.C.K. Roberts (Ed.), Encyclopedia of Biophysics, Springer Berlin Heidelberg, Berlin, Heidelberg, 2013, pp. 1049–1057, https://doi.org/10.1007/978-3-642-16712-6_111.

[47] E. Goormaghtigh, V. Raussens, J.-M. Ruysschaert, Attenuated total reflection infrared spectroscopy of proteins and lipids in biological membranes, Biochim. Biophys. Acta, Rev. Biomembr. 2 (1422) (1999) 105–185, https://doi.org/10.1016/s0304-4157(99)00004-0.

[48] S.J. Marrink, H.J. Risselada, S. Yefimov, D.P. Tieleman, A.H. de Vries, The MARTINI force field: coarse grained model for biomolecular simulations, J. Phys. Chem. B 111 (27) (2007) 7812–7824, https://doi.org/10.1021/jp071097f.

[49] L. Monticelli, S.K. Kandasamy, X. Periole, R.G. Larson, D.P. Tieleman, S.-J. Marrink, The MARTINI coarse-grained force field: extension to proteins, J. Chem. Theory Comput. 4 (5) (2008) 819–834, https://doi.org/10.1021/ct700324x.

[50] D.H. de Jong, G. Singh, W.D. Bennett, C. Arnarez, T.A. Wassenaar, L.V. Schäfer, X. Periole, D.P. Tieleman, S.J. Marrink, Improved parameters for the martini coarse-grained protein force field, J. Chem. Theory Comput. 9 (1) (2012) 687–697, https://doi.org/10.1021/ct300646g.

[51] S. Jo, T. Kim, W. Im, Automated builder and database of protein/membrane complexes for molecular dynamics simulations, PLoS One 2 (9) (2007) e880, https://doi.org/10.1371/journal.pone.0000880.

[52] S. Jo, T. Kim, V.G. Iyer, W. Im, CHARMM-GUI: a web-based graphical user interface for CHARMM, J. Comput. Chem. 29 (11) (2008) 1859–1865, https://doi.org/10.1002/jcc.20945.

[53] S. Jo, J.B. Lim, J.B. Klauda, W. Im, CHARMM-GUI Membrane Builder for mixed bilayers and its application to yeast membranes, Biophys. J. 97 (1) (2009) 50–58, https://doi.org/10.1016/j.bpj.2009.04.013.

[54] J. Lee, X. Cheng, J.M. Swails, M.S. Yeom, P.K. Eastman, J.A. Lemkul, S. Wei, J. Buckner, J.C. Jeong, Y. Qi, CHARMM-GUI input generator for NAMD, GROMACS, AMBER, OpenMM, and CHARMM/OpenMM simulations using the CHARMM36 additive force field, J. Chem. Theory Comput. 12 (1) (2015) 405–413, https://doi.org/10.1021/acs.jctc.5b00935.

[55] J. Lee, D.S. Patel, J. Ståhle, S.-J. Park, N.R. Kern, S. Kim, J. Lee, X. Cheng, M. A. Valvano, O. Holst, CHARMM-GUI membrane builder for complex biological membrane simulations with glycolipids and lipoglycans, J. Chem. Theory Comput. 15 (1) (2018) 775–786, https://doi.org/10.1021/acs.jctc.8b01066.

[56] E.L. Wu, X. Cheng, S. Jo, H. Rui, K.C. Song, E.M. Dávila-Contreras, Y. Qi, J. Lee, V. Monje-Galvan, R.M. Venable, CHARMM-GUI membrane builder toward realistic biological membrane simulations, J. Comput. Chem. 35 (27) (2014) 1997–2004, https://doi.org/10.1002/jcc.23702.

[57] S.J. Marrink, A.H. De Vries, A.E. Mark, Coarse grained model for semiquantitative lipid simulations, J. Phys. Chem. B 108 (2) (2004) 750–760, https://doi.org/10.1021/jp036508g.

[58] T.A. Wassenaar, H.I. Ingólfsson, R.A. Böckmann, D.P. Tieleman, S.J. Marrink, Computational lipidomics with insane: a versatile tool for generating custom membranes for molecular simulations, J. Chem. Theory Comput. 11 (5) (2015) 2144–2155, https://doi.org/10.1021/acs.jctc.5b00209.

[59] G. Bussi, D. Donadio, M. Parrinello, Canonical sampling through velocity rescaling, J. Chem. Phys. 126 (1) (2007), 014101, https://doi.org/10.1063/1.2408420.

[60] M. Parrinello, A. Rahman, Polymorphic transitions in single crystals: a new molecular dynamics method, J. Appl. Phys. 52 (12) (1981) 7182–7190, https://doi.org/10.1063/1.328693.

[61] M.J. Abraham, T. Murtola, R. Schulz, S. Páll, J.C. Smith, B. Hess, E. Lindahl, GROMACS: High performance molecular simulations through multi-level parallelism from laptops to supercomputers, SoftwareX 1 (2015) 19–25, https://doi.org/10.1016/j.softx.2015.06.001.

[62] F. Abrunhosa, S. Faria, P. Gomes, I. Tomaz, J.C. Pessoa, D. Andreu, M. Bastos, Interaction and lipid-induced conformation of two cecropin−melittin hybrid peptides depend on peptide and membrane composition, J. Phys. Chem. B 109 (36) (2005) 17311–17319, https://doi.org/10.1021/jp051572e.

[63] P. Garidel, A. Blume, Miscibility of phosphatidylethanolamine-phosphatidylglycerol mixtures as a function of pH and acyl chain length, Eur. Biophys. J. 28 (8) (2000) 629–638, https://doi.org/10.1007/s002490050003.

[64] A. Arouri, M. Dathe, A. Blume, Peptide induced demixing in PG/PE lipid mixtures: a mechanism for the specificity of antimicrobial peptides towards bacterial membranes? Biochim. Biophys. Acta Biomembr. 1788 (3) (2009) 650–659, https://doi.org/10.1016/j.bbamem.2008.11.022.

[65] S. Finger, A. Kerth, M. Dathe, A. Blume, The efficacy of trivalent cyclic hexapeptides to induce lipid clustering in PG/PE membranes correlates with their antimicrobial activity, Biochim. Biophys. Acta Biomembr. 1848 (11, Part A) (2015) 2998–3006, https://doi.org/10.1016/j.bbamem.2015.09.012.

[66] L.K. Tamm, S.A. Tatulian, Infrared spectroscopy of proteins and peptides in lipid bilayers, Q. Rev. Biophys. 30 (4) (1997) 365–429, https://doi.org/10.1017/s0033583597003375.

[67] M.J. Pérez-Alvite, M. Mosquera, L. Castedo, J. Granja, Toward the rational design of molecular rotors ion sensors based on α,γ-cyclic peptide dimers, Amino Acids 41 (2011) 621–628, https://doi.org/10.1007/s00726-011-0886-2.

[68] M. Panciera, E. González-Freire, M. Calvelo, M. Amorín, J.R. Granja, Induced α, γ-cyclic peptide rotodimer recognition by nucleobase scaffolds, Pept. Sci. 112 (1) (2020), https://doi.org/10.1002/pep2.24132 e24132.

SUPPLEMENTARY MATERIAL

Membrane targeting antimicrobial cyclic peptide nanotubes– an experimental and computational study

Bárbara Claro[a], Eva González-Freire[b], Martin Calvelo[b], Lucinda J. Bessa[c], Erik Goormaghtigh[d], Manuel Amorín[b], Juan R. Granja[b], Rebeca Garcia-Fandiño[a, b,*], Margarida Bastos[a,*]

[a] CIQUP, Centro de Investigação em Química, Departamento de Química e Bioquímica, Faculdade de Ciências, Universidade do Porto, Porto, Portugal;
[b] Centro Singular de Investigación en Química Biolóxica e Materiais Moleculares (CiQUS), Departamento de Química Orgánica, Universidade de Santiago de Compostela, 15782 Santiago de Compostela, Spain
[c] LAQV/Requinte, Departamento de Química e Bioquímica, Faculdade de Ciências da Universidade do Porto, Porto, Portugal
[d] Structure and Function of Biological Membranes, Center for Structural Biology and Bioinformatics, ULB, Brussels, Belgium

A. Materials and Methods of CPs Synthesis

Commercially available *N*-Boc-α-amino acids, *N*-[(dimethylamino)-1H-1,2,3-triazolo[4,5-b]pyridin-1-ylmethylene]-*N*-methylmethanaminium hexafluorophosphate *N*-oxide (*N*-HATU), *N*-[(1H-benzotriazol-1-yl)-(dimethylamino)methylene]-*N*-methylmethanaminium hexafluorophosphate *N*-oxide (*N*-HBTU) and *N*-[(1Hbenzotriazol-1-yl)-(dimethylamino)methylene]-*N*-methylmethanaminium tetrafluoroborate *N*-oxide (*N*-TBTU)[2] were all used as obtained from Sigma-Aldrich, Novabiochem, Applied Biosystems, Bachem or Iris Biotech. Deuterated solvents (CDCl$_3$ and D$_2$O) were obtained from Aldrich. All other reagents obtained from commercial suppliers were used without further purification unless otherwise noted. Dichloromethane and piperidine were dried and distilled over calcium hydride. *N*,*N*-Diisopropylethylamine (DIEA) was dried and distilled over calcium hydride, and then redistilled over ninhydrin.[3,4]

Analytical thin-layer chromatography was performed on E. Merck silica gel 60 F$_{254}$ plates. Compounds which were not UV active were visualized by dipping the plates in a ninhydrin solution and heating. Silica gel flash chromatography was performed using E. Merck silica gel (type 60SDS, 230-400 mesh). Solvent mixtures for chromatography are reported as v/v ratios. HPLC purification was carried out on Phenomenex Luna 5 µm silica column with CH$_2$Cl$_2$/MeOH gradients between 100 and 85:15 (normal phase) and Zorbax C18, Phenomenex Luna 5µm C18 and Agilent Eclipse XDB-C18 columns with H$_2$O MiliQ® (0.1% TFA)/MeCN (0.1% TFA) gradients between 100 and 5:95 (reverse phase). Purifications using HPLC systems were carried out using Hitachi D-7000, Agilent 1100, Jasco 4000 and Waters 2489 instruments.

Proton nuclear magnetic resonance (^{1}H NMR) spectra were recorded on Varian Inova 750 MHz, Varian-Inova 500 Mhz, Varian-Mercury 300 MHz or Bruker WM 250 MHz spectrometers. Chemical shifts (δ) were reported in parts per million (ppm) relative to tetramethylsilane, and the coupling constants (*J*) were reported in Hz. ^{1}H NMR splitting patterns are designated as singlet (s), doublet (d), triplet (t), quartet (q) or pentuplet (p). Splitting patterns that could not be easily interpreted are designated as multiplet (m) or broad (br). Carbon nuclear magnetic resonance (^{13}C NMR) spectra were recorded on Varian-Inova 500 MHz, Varian-Mercury 300 MHz or Bruker WM 250 MHz spectrometers. Carbon resonances were assigned using distortionless enhancement by polarization transfer (DEPT) spectra obtained with phase angles of 135°.

[2] L. A. Carpino, H. Imazumi, A. El-Faham, F. J. Ferrer, C. Zhang, Y. Lee, B. M. Foxman, P. Henklein, C. Hanay, C. Mügge, H. Wenschuh, J. Klose, M. Beyermann, M. Bienert, The uronium/guanidinium peptide coupling reagents: finally the true uronium salts. Angew. Chem. Int. Ed. 41(2002) 441-445.

[3] H. C Brown, Organic Synthesis via Boranes, Ed. John Wiley & Sons, (1975).

[4] D. D. Perrin, W. I. F. Armarego, Purification of Laboratory Chemicals, Ed. Pergamon Press, (1988).

Electrospray (ESI) mass spectra were recorded on a Bruker BIOTOF II mass spectrometer. Fast Atom Bombardment (FAB+) mass spectra were recorded on a Micromass Autospec spectrometer employing disulfide, glycerol or thioglycerol as matrix. FT-IR measurements were made on a JASCO FT/IR-400 and PerkinElmer FT-IR Spectrum Two spectrophotometers using 5-10 mM in CHCl₃ and placed in a CaF₂ solution IR cell.

^{1}H NMR Assignments of Cyclic Peptides (CPs). The signals of the ^{1}H NMR spectra of the peptides in CDCl₃ were identified from the corresponding double-quantum-filled 2D COSY, TOCSY and/or NOESY and ROESY spectra acquired at concentration and temperature indicated. Mixing times (~250 ms or 400 ms) were not optimized. Spectra were typically acquired using Bruker standard pulse sequences on 300 and 500 MHz apparatuses, and were referenced relative to residual proton resonances in CDCl₃ (at 7.26 ppm).

A.1. Synthesis of CP1

The cyclic peptide was prepared manually in solid phase using 2-Chlorotrytil chloride resin (2CTC, 400 mg, 1.6 mmol Cl⁻/g resin). Firstly, the resin was soaked in freshly distilled DCM (3 mL) for 1 hour. The solvent was filtered off, and a solution of *N*-α-(9-Fluorenylmethyloxycarbonyl)-l-Lysine allyl ester hydrochloride (340 mg, 0.83 mmol) and DIEA (200 μL, 1.25 mmol) in freshly distilled DCM (3 mL) was added to the resin. After 2 h, the solvent was filtered off and the resin was washed with DCM (4 mL). A mixture of DCM-MeOH-DIEA (8.5:1:0.5, 3 mL) was added and the resin was shaken twice for 10 min, then washed with DCM (3 x 2 mL) and DMF (3 x 2 mL). The resin was dried in under high vacuum and the loading was determined by quantification of the Fmoc group. For this, a small portion of the resin (ca 10 mg) was treated with a solution of piperidine in DMF (20% v/v, 2 mL) for 30 min. An aliquot of this solution (20 μL) is diluted to 1 mL DMF and the absorbance was read between 290-301 nm. The concentration of the dibenzofulvene-piperidine adduct is obtained by using the extinction coefficients tabulated in the literature.[5] All the resin (400 mg, 0.56 mmol Fmoc/g resin, 0.224 mmol) was used for the synthesis of the peptide. The next amino acids were introduced in the resin following the deprotecting-coupling sequence: the Fmoc group was removed by treatment

---

[5] S. Eissler, M. Kley, D. Bächle, G. Loidl, T. Meier and D. Samson, *J. Pept. Sci.*; 23 (2017) 757–762

with piperidine/DMF (1:4, 2-3 mL) for 20 min. The resin was washed with DMF (6 mL) and then the resin was treated with a solution of Fmoc-protected amino acid (0.672 mmol, 3 equiv mmol), HBTU (250 mg, 0.672 mmol, 3 equiv) and DIEA (0.214 mL, 1.3 mmol, 6 equiv) in DMF (3 mL). The resin was shaken for 40 min and then washed with DMF (3 mL). After the coupling of the last amino acid, we proceed to remove the protecting groups of the N- and C-terminal groups in order to carry out the cyclization. To avoid overpressure in this step, the resin was divided in two. A solution of $Pd(PPh_3)$ was prepared in situ, mixing $Pd(OAc)_2$ (6.3 mg, 0.028 mmol, 0.25 equiv) and PPh_3 (36.68 mg, 0.14 mmol, 1.25 equiv) in dry DCM (3 mL). A solution of *N*-methylmorpholine (86.3 µL, 0.784 mmol, 7 equiv) and phenylsilane (96.6 µL 0.784 mmol, 7 equiv) was added to the mixture and, finally, to the resin. The suspension was stirred overnight. The resin was put together and washed with DCM (3 x 3 mL), sodium diethyldithiocarbamate (0.5% w/v in DMF, 2 x 4 mL, 20 min) DIEA in DMF (10% v/v, 3 x 2 mL), and DMF (3 x 3 mL). The resin was stirred with piperidine/DMF for 30 min. Then, it was washed with DMF (6 x 2 mL), DIEA in DMF (10% v/v, 3 x 2 mL), LiCl en DMF (0.8 M, 3 x 2 mL) and DMF (3 x 3 mL).

Cyclization was carried out by adding a solution of TBTU (215 mg, 0.672 mmol, 3 equiv) and DIEA (0.214 mL, 1.3 mmol, 6 equiv) in DMF (3 mL) and the suspension was stirred for 12 h. After washing with DMF (3 mL), the reaction was repeated twice in the same conditions.

The peptide was released from the resin by treatment with freshly prepared TFA cocktail (TFA-H_2O-TIS 0.95:0.025:0.025, 3 mL) for 2 h and then filtered. The resin was washed with TFA (0.5 mL) and the combined fractions were evaporated to 1-2 mL by bubbling argon. The concentrated solution was added dropwise to cold diethyl ether (10 mL diethyl ether/ml TFA). The resulting precipitate was centrifuged for 10 min at 3500 rpm. The supernatant was discarded and the solid was dried under vacuum. The sample was dissolved in MilliQ water and purified by semipreparative HPLC using a C18 column [isocratic of 70:30 H_2O (0.1% TFA)-ACN (0.1% TFA) (5 min) and gradient of 70:30 to 50:50 H_2O (0.1% TFA)-ACN (0.1% TFA) (30 min)] to give **CP1**. (52 mg, 19%). (ref) [Agilent SB-C18 column, H_2O (0.1% TFA)/ACN (0.1% TFA). 100:0 →100:0 (2 min) and 100:0 → 25:75 (19 min)] (R_t = 9.0 min). **MS (ESI, H_2O):** 1226.7 (10, [M+1H]⁺), 613.5 (100, [M+2H]²⁺). **HRMS** (ESI): Calcd for: $C_{63}H_{88}N_{18}O_8$ [M+H]⁺: 1225.7114; found 1225.7105. **FTIR (neat)**: v = 3279 (amide A), 1650 (amide I), 1529 cm⁻¹ (amide II).

A.2. Synthesis of CP2:

The cyclic peptide was prepared in solid phase using Fmoc Rink Amide resin (400 mg, 0.71 mmol/g resin). Firstly, the resin was swollen in DCM for 1 hour. Then, the Fmoc group was removed by treatment with piperidine/DMF (1:4, 2-3 mL) for 20 min and the first amino acid was coupled by its side chain, using HBTU and DIEA, in the same way than any coupling described above. The procedure was the same for the eight amino acids. The removal of the allyl group was carried out for 5 hours instead of stirring overnight to avoid the reduction of the propargyl group. The cyclization and cleaveage was carried out as it was described above. The sample was dissolved in MilliQ water and purified by semipreparative HPLC using a C18 column [isocratic of 100:0 H_2O (0.1% TFA)-ACN (0.1% TFA) (5 min) and gradient of 100:0 to 60:40 H_2O (0.1% TFA)-ACN (0.1% TFA) (30 min)] to give **CP1**. (48 mg, 18%). [Agilent SB-C18 column, H_2O (0.1% TFA)/ACN (0.1% TFA). 100:0 →100:0 (2 min) and 100:0 → 25:75 (19 min)] (R_t = 9.1 min). **MS** (ESI, H_2O): 968.5 (25, [M+1H]$^+$), 484.9 (100, [M+2H]$^{2+}$), 323.6 (8, [M+3H]$^{3+}$). **HRMS** (ESI): Calcd for: $C_{45}H_{70}N_{13}O_{11}$ [M+1H]$^+$: 968.5316; found 968.5312. **FTIR (neat)**: v = 3273 (amide A), 1669, 1623 (amide I), 1535 cm^{-1} (amide II).
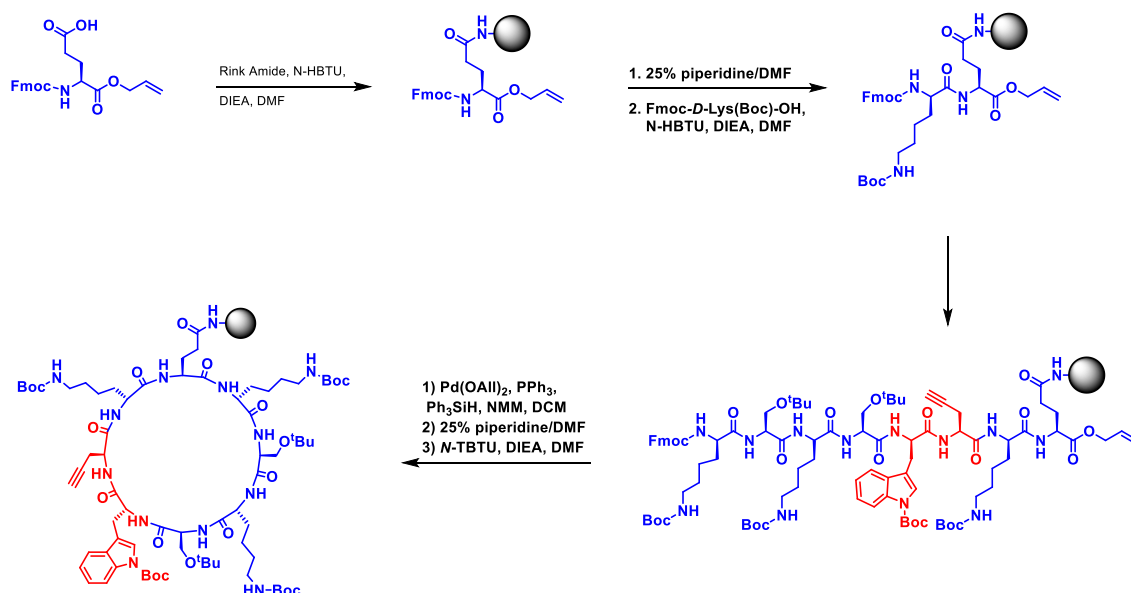
Scheme S1 General scheme for the solid phase synthesis of CPs, illustrating the synthesis of **CP2**.
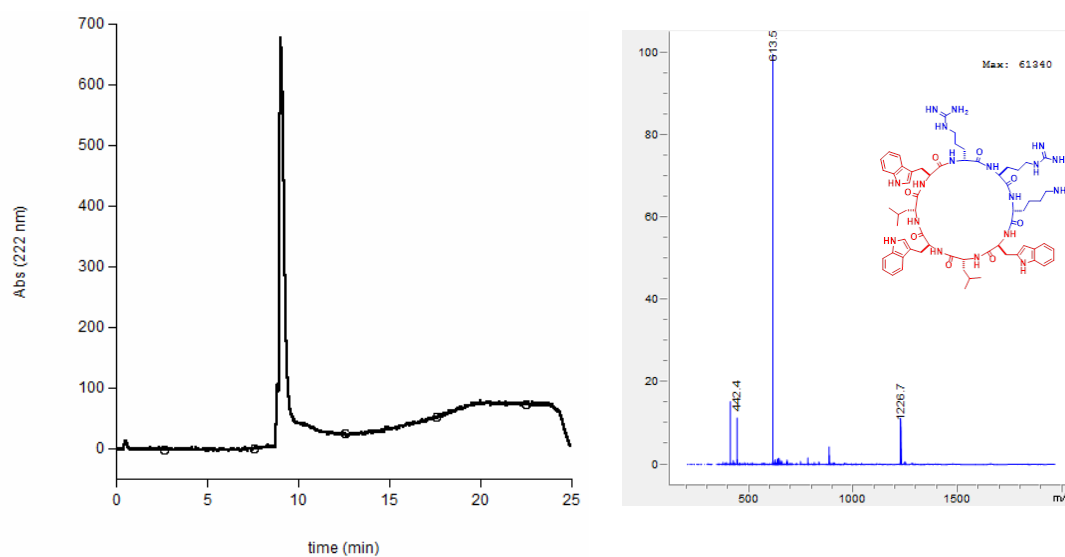
Fig. S1 RP-HPLC for **CP1** [Agilent SB-C18 column, H_2O (0.1% TFA)/ACN (0.1% TFA). 100:0 →100:0 (2 min) and 100:0 → 25:75 (19 min)] (R_t = 9.0 min). Absorbance at 222 nm.
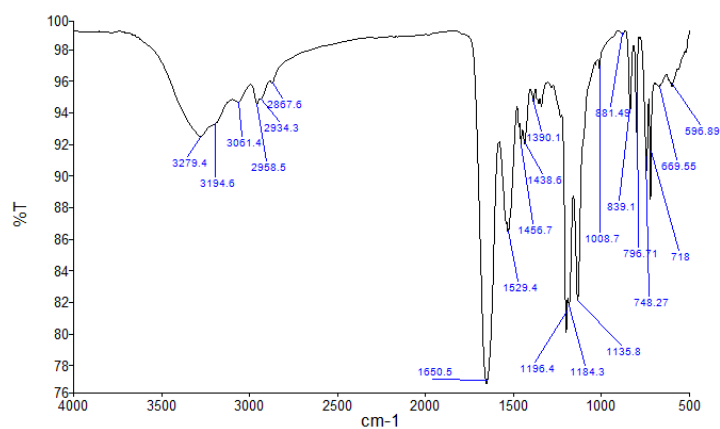
Fig. S2 FT-IR (neat, 298 K) spectra for **CP1.**
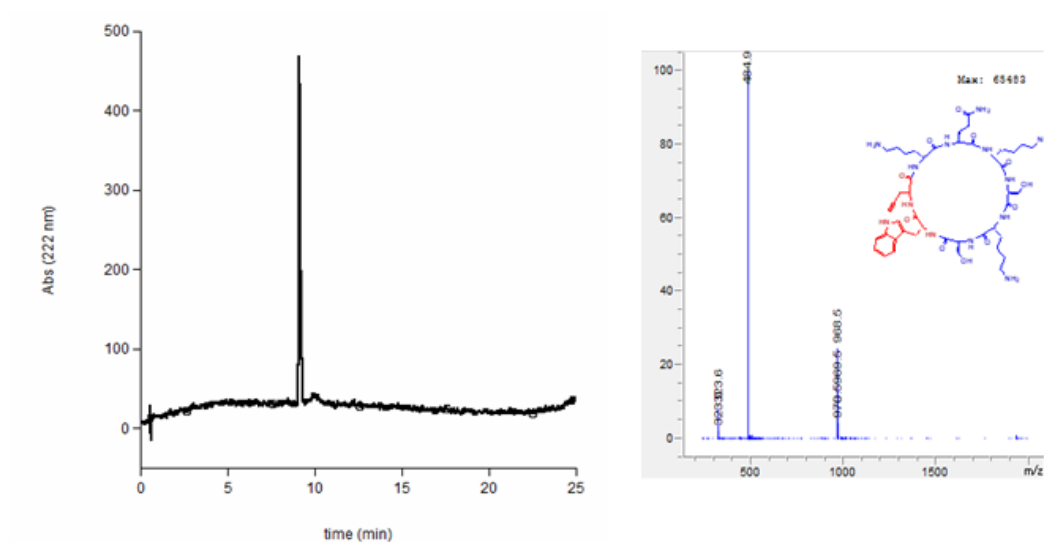
Fig. S3 RP-HPLC for **CP2** [Agilent SB-C18 column, H_2O (0.1% TFA)/ACN (0.1% TFA). 100:0 →100:0 (2 min) and 100:0 → 25:75 (19 min)] (R_t = 9.1 min). Absorbance at 222 nm.
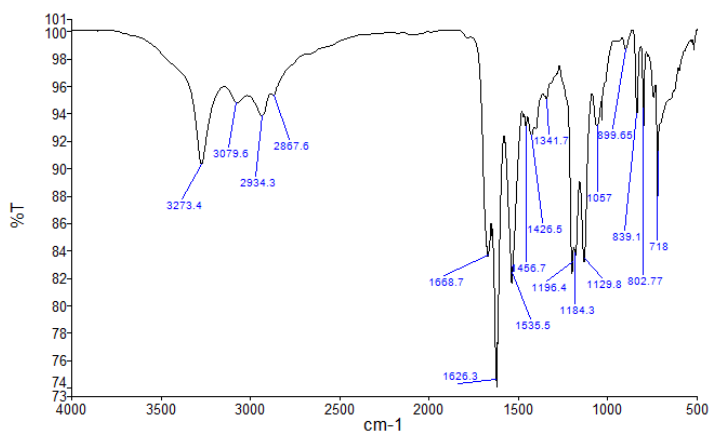
Fig. S4 FT-IR (neat, 298 K) spectra for **CP2.**

B. Materials and Methods FTIR

The measurements were carried out in two different instruments and places. In Brussels, Attenuated Total Reflection Infrared (ATR-FTIR) spectra were recorded on a Bruker IFS 55 infrared spectrophotometer equipped with a liquid-nitrogen-cooled MCT detector. The internal reflection element was a diamond with an aperture angle of 45°. A total of 128 scans were accumulated for each spectrum. Spectra were recorded at a nominal resolution of 2 cm^{-1}. The spectrophotometer was continuously purged with a nitrogen flow.

In Porto, a Spectrum Two FTIR Spectrometer (PerkinElmer, EUA) equipped with diamond internal reflection element from GladiATR Accessory S2PE (PIKE Technologies Inc, EUA) was used. The angle of incidence was also 45 °. FTIR spectra were taken using the PerkinElmer Spectrum software, between 4000 and 550 cm^{-1}, and 32 scans were recorded for each spectrum, at a resolution of 4 cm^{-1}. A grid polarizer KRS-5 from Specac was adapted to the instrument, to enable dichroic spectra to be recorded.

C. Buffer characterization

Table S1 Determined buffer properties for the parameter values needed in the DLS setup.

Buffer	Temperature/°C	Refractive Index/nD	Density/g.cm^{-3}	Viscosity/mPa.s
HEPES	37	1.33298	1.00086	0.715
	60	1.32897	0.99090	0.485
HEPES /DMSO	37	1.33399	1.00184	0.727
	60	1.33194	0.99126	0.507

D. Complementary DSC results
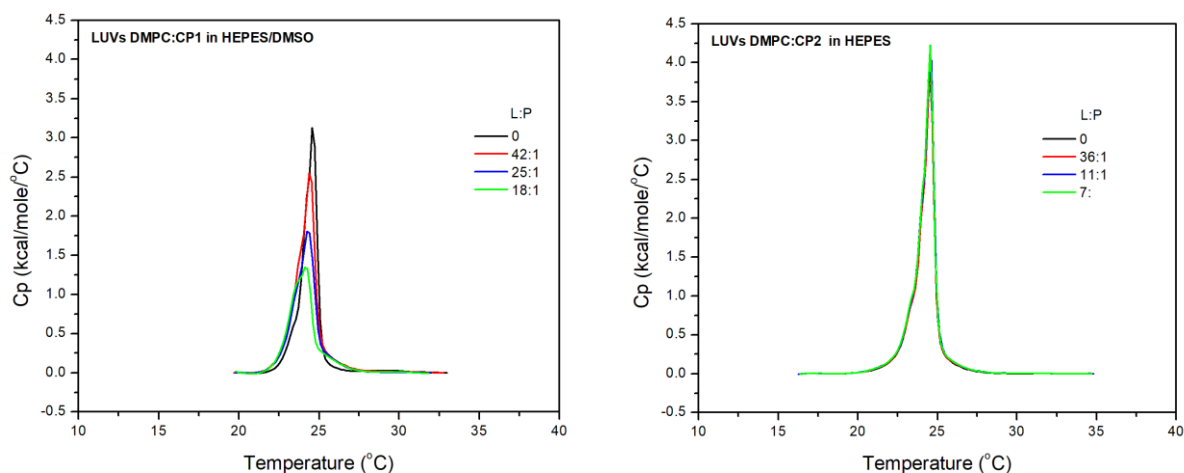
Fig. S5 DSC results for **CP1** and DMPC in HEPES/DMSO and for **CP2 and DMPC** in HEPES

E. Complementary ATR-FTIR results
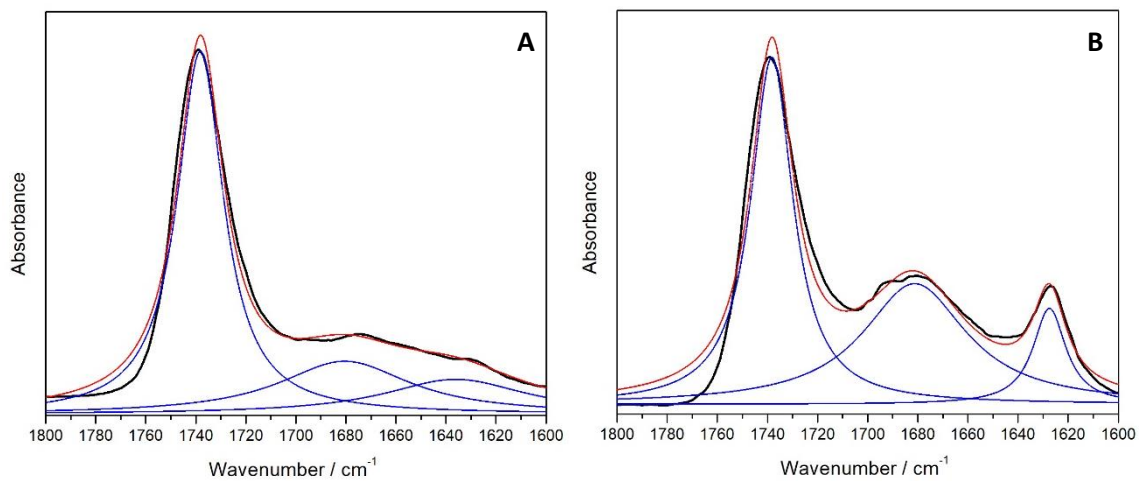
Fig. S6 (A) DMPE:DMPG(1:9):**CP1** L:P34:1 – fitting between 1800-1600 cm^{-1}
   (B) DMPE:DMPG(1:9):**CP2** L:P17:1 – fitting between 1800-1600 cm^{-1}

F. **Complementary MD results**
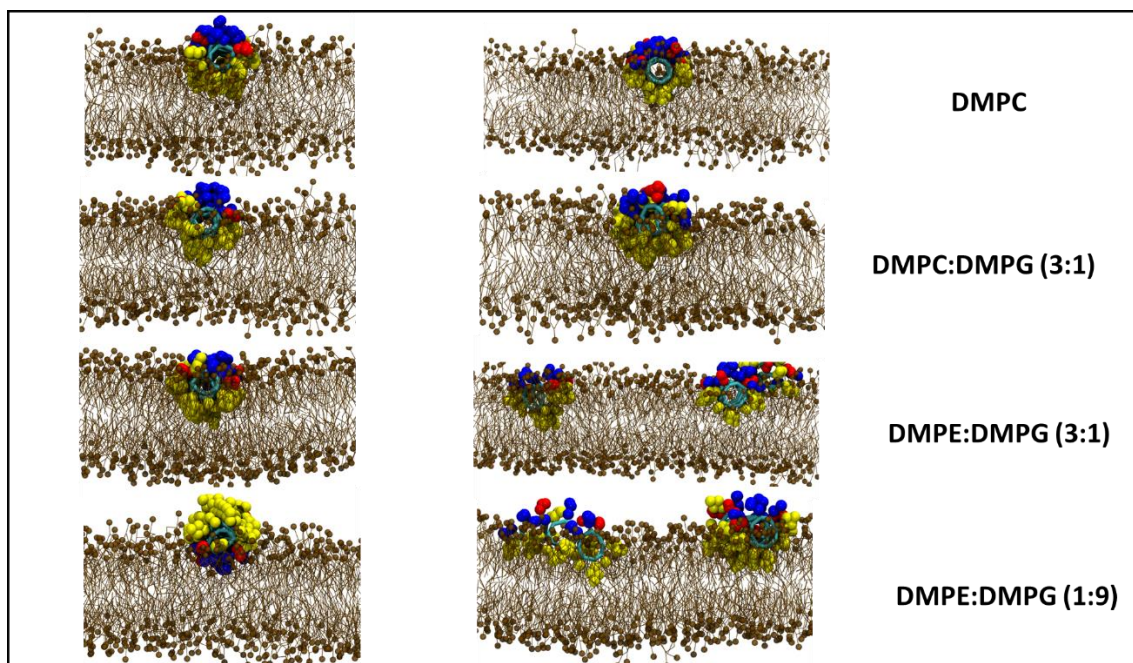
Fig. S7 Lateral side views for the structures represented in Figure 6D-E for **SCPN1,** corresponding to snapshots at t=1 µs for the CG-MD simulation of **SCPN1** in presence of different model membrane systems, using restraints to force the nanotube topology (**left column**) and snapshots at t=1.5 µs, where the last 500 ns were carried out releasing the restraints and limiting them to those necessary to maintain the CP opened and plane but not forcing the formation of the SCPN (**right column**). Lys are represented in red, Arg in blue. The rest of the residues of the SCNP are shown in yellow.
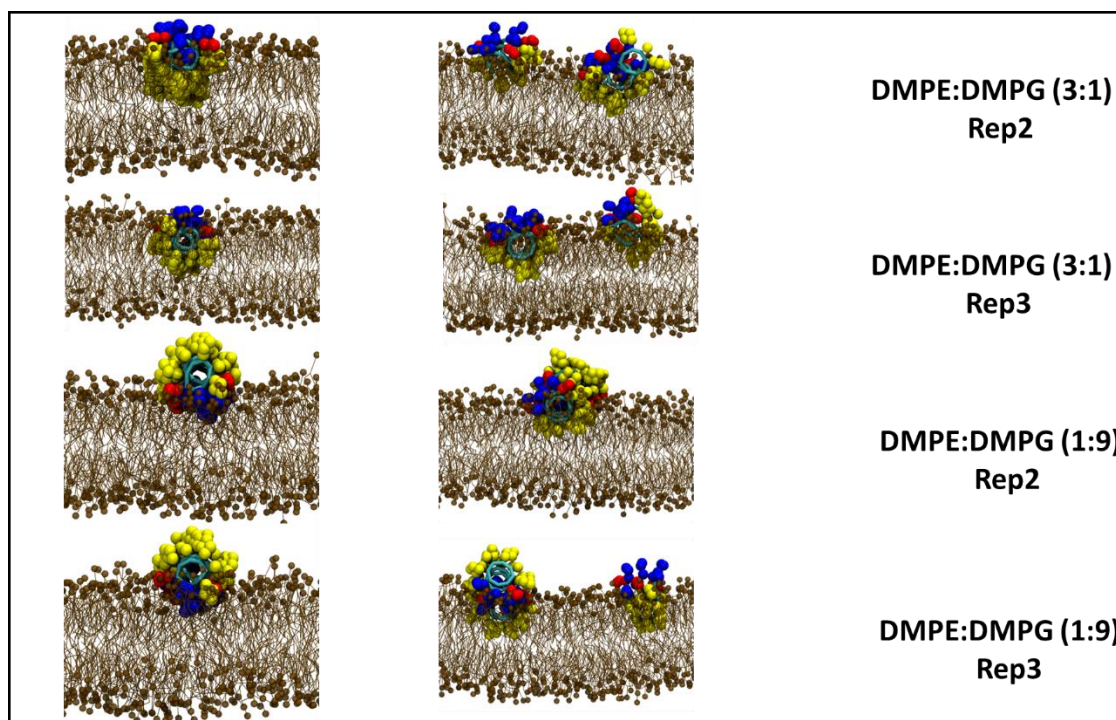
Fig. S8 Two additional replicas **SCPN1** in presence of DMPE:DMPG (3:1) and DMPE:DMPG (1:9), same conditions as previous, *i.e.*, corresponding to snapshots at t=1 μs for the CG-MD simulation of **SCPN1** in presence of different model membrane systems, using restraints to force the nanotube topology (**left column**) or to snapshots at t=1.5 μs, where the last 500 ns were carried out releasing the restraints and limiting them to those necessary to maintain the CP opened and plane but not forcing the formation of the SCPN (**right column**). Lys are represented in red, Arg in blue. The rest of the residues of the SCNP are shown in yellow.
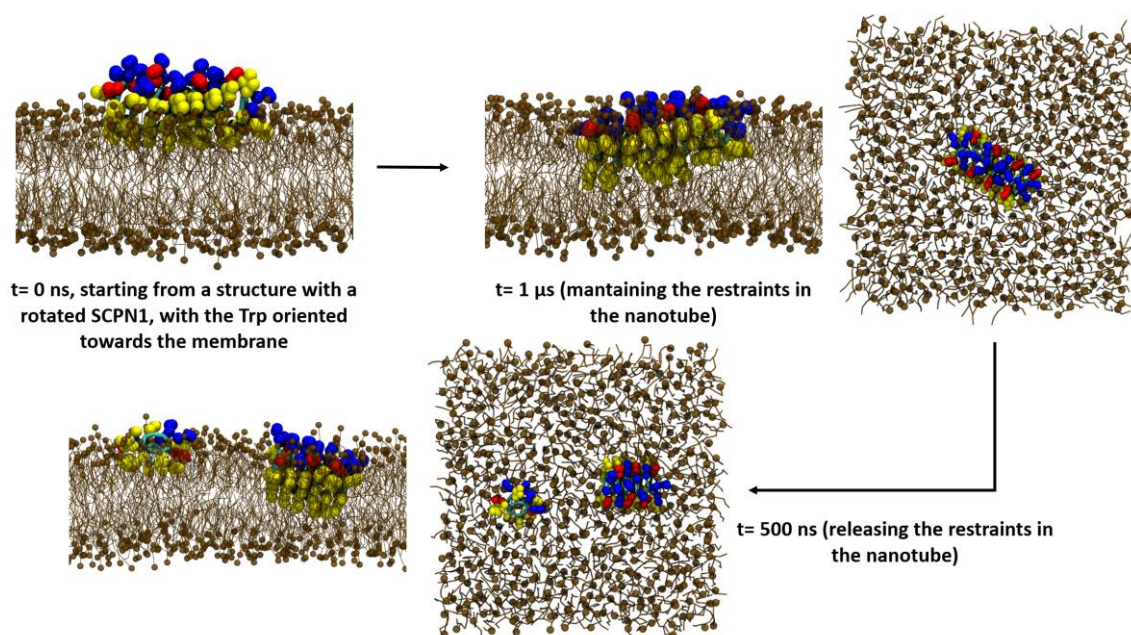
Fig. S9 Results of the MD simulation for DMPE:DMPG (1:9) and CP1, starting from a structure with a rotated **SCPN1**, with the Trp inserted in the membrane. After 1 µs, the nanotube is more inserted into the membrane, but after the releasing of the restraints, it is partially destroyed.
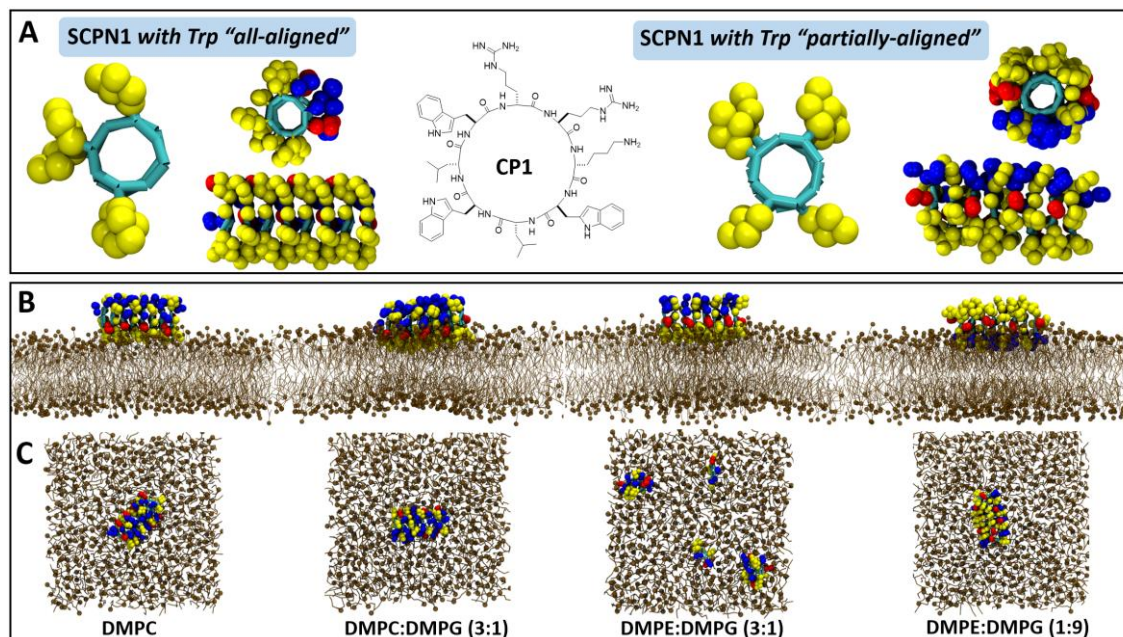
Fig. S10 Results of the MD simulation starting from a structure with a different conformation of SCPN1 where the Trp are not all aligned (A). In the initial structure at t=0 the SCPN is outside the membrane, thus leading to a spontaneous insertion after 1 μs. Structures in the middle (B) show the corresponding snapshots at t=1 μs for the CG-MD simulation of SCPN1 in presence of different model membrane systems, using restraints to force the nanotube topology. It can be noted that for CP1 the Arg are again directed towards the DMPE:DMPG (1:9) membrane, in contrast to what happens in the other membrane compositions. Down figures (C) show the corresponding snapshots at t=1.5 μs, where the last 500 ns were carried out releasing the restraints and limiting them to those necessary to maintain the CP opened and plane but not forcing the formation of the SCPN. In this case the nanotube is maintained in presence of DMPE:DMPG (1:9).
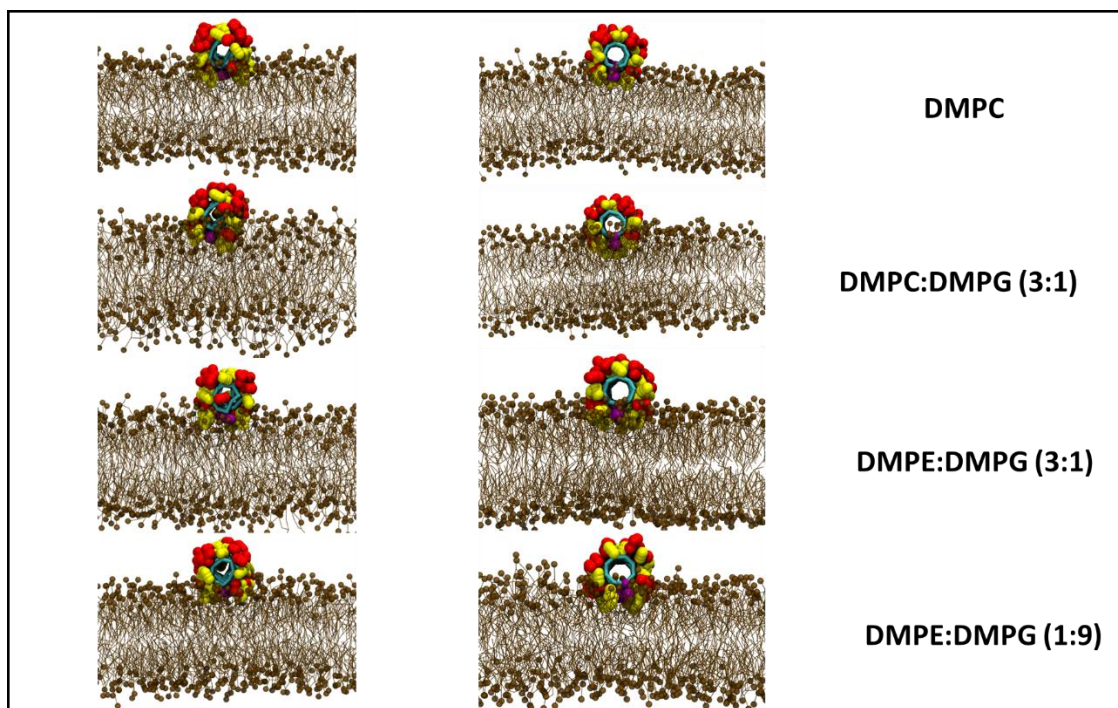
Fig. S11 Lateral side views for the structures represented in Figure 6D-E, for **SCPN2** corresponding to snapshots at t=1 μs for the CG-MD simulation of **SCPN2** in presence of different model membrane systems, using restraints to force the nanotube topology (**left column**) or snapshots at t=1.5 μs, where the last 500 ns were carried out releasing the restraints and limiting them to those necessary to maintain the CP opened and plane but not forcing the formation of the SCPN (**right column**). Lys are represented in red, Arg in blue, and purple represents the alkyne moiety. The rest of the residues of the SCNP are shown in yellow.

Video S1 for DMPC, DMPC:DMPG (3:1), DMPE:DMPG (3:1) and **SCPN1**, showing that it penetrates the hydrophobic region of the membranes to even interact with the opposite layer.

https://nubeusc-my.sharepoint.com/:f:/g/personal/martin_calvelo_souto_usc_es/EuXlUOT2vgBArcgM5GEgkFYBwuT4JpPOsrZxxQYlsjIkPQ?e=ePT7uT

III.   **"Attenuated total reflection-Fourier transform infrared spectroscopy: a tool to characterize antimicrobial cyclic peptide–membrane interactions"**

Bárbara Claro, Erik Goormaghtigh, Margarida Bastos **(2021),** *European Biophysics Journal*, 50, 629–639

ORIGINAL ARTICLE

Attenuated total reflection-Fourier transform infrared spectroscopy: a tool to characterize antimicrobial cyclic peptide–membrane interactions

Bárbara Claro[1] · **Erik Goormaghtigh[2]** · **Margarida Bastos[1]**

Abstract

Attenuated total reflection-Fourier transform infrared spectroscopy (ATR-FTIR) has been used for the structural characterization of peptides and their interactions with membranes. Antimicrobial peptides (AMPs) are part of our immune system and widely studied in recent years. Many linear AMPs have been studied, but their cyclization was shown to enhance the peptide's activity. We have used cyclic peptides (CPs) of an even number of alternating D- and L-α-amino acids, an emerging class of potential AMPs. These CPs can adopt a flat-ring shape that can stack into an antiparallel structure, forming intermolecular hydrogen bonds between different units, creating a tubular β-sheet structure - self-assembled cyclic peptide nanotubes (SCPNs). To get the structural information on peptides in solution and/or in contact with membranes, Amide I and II absorptions are used as they can adopt frequency and shape band characteristics that are influenced by the strength of existing hydrogen bonds between the amide CO and NH involved in secondary structures such as helix, β-sheet or aperiodic structures. The combination of polarized lens with ATR-FTIR provides an important tool to study the orientation of peptides when interacting with lipid membranes as the information can be derived on the position relative to the membrane normal. This work shows how ATR-FTIR used together with polarized light was successfully used to characterize structurally two CPs (RSKSWPgKQ and RSKSWX^{C10}KQ) in solution and upon interaction with negatively charged membranes of DMPG, assessing the formation and orientation of tubular structures (SCPNs) that were shown to be enhanced by the presence of the lipid membrane.

Keywords Antimicrobial peptides · D,L-α-Cyclic peptides · Self-assembled cyclic peptide nanotubes · ATR-FTIR · Polarization · Lipid membranes

Introduction

Spectroscopy techniques are an extremely useful method to identify the chemical nature, orientation and conformation of molecules at an interface (Goormaghtigh et al. 1994;

Special Issue: COST Action CA15126, MOBIEU: Between atom and cell.

✉ Margarida Bastos
  mbastos@fc.up.pt

1   Departamento de Química e Bioquímica, Centro de
    Investigação em Química, Faculdade de Ciências, CIQUP,
    Universidade do Porto, Porto, Portugal

2   Structure and Function of Biological Membranes, Center
    for Structural Biology and Bioinformatics, ULB, Brussels,
    Belgium

Woods and Bain 2014). Attenuated total reflection-Fourier transform infrared spectroscopy (ATR-FTIR) is a fast detection technique with a strong signal that has been successfully used in structural characterization of biological systems such as membranes, proteins or peptides and their association. This method records a wide spectral range in a single spectrum, covering the vibrational frequencies of different chemical groups, allowing the structural characterization of the interactions of peptides, proteins, drugs or others with membranes, without the need of external labeling probes (Goormaghtigh et al. 1999; Tatulian 2013). In ATR-FTIR, a beam of infrared light passes through a high refractive index medium, transparent to the infrared radiation, resulting in an evanescent wave at the reflecting interface. When the beam impinges on the surface of the internal reflection element (IRE), below a critical angle, it is entirely reflected. The beam can then create several internal total reflections until

reaching the end of the IRE, transmitting the information to the detector. In this phenomenon, the superimposition of incoming and reflected waves gives rise to a standing wave within the IRE. This standing wave (evanescent wave) is aligned with the normal of the totally reflecting surface. Beyond the reflecting interface, an electromagnetic disturbance exists. The evanescent wave is characterized by its amplitude which falls off exponentially with the distance from the interface. All molecules present in the evanescent wave contribute to the spectrum (Derenne et al. 2013; Goormaghtigh et al. 1999).

Lipid membranes can be deposited on the internal reflection element as oriented multilayer stacks by drying the solvent of the membrane suspension. The lipid film formed should have the phospholipids in the membrane parallel to the surface and be in close contact with the internal reflection element surface to allow interaction with the evanescent field (Derenne et al. 2013; Goormaghtigh et al. 1999).

To get structural information on peptides or proteins in solution and/or in contact with membranes Amide I absorption band has been mostly used. This band shows the contributions from the C=O stretching vibration (76%) of the amide groups and a lower contribution from the CN stretching vibration (14%). Amide II appears to be significantly less "pure", arising from NH bending (43%) and CN stretching (29%) vibrations. Both Amide I and II absorptions can adopt frequency and shape band characteristics that are influenced by the strength of existing hydrogen bonds, involving the amide C=O and NH that are involved in secondary structure, be it helix, β-sheet or aperiodic secondary structures (Hayashi and Mukamel 2008; Torii and Tasumi 1992; Yılmaz et al. 2020). The combination of polarized lens with ATR-FTIR (polarized ATR-FTIR) is presently an important tool to study the orientation of peptides and proteins when interacting with lipid membranes, providing information on the position of their secondary structural elements relative to the membrane normal. When the dipole transition moment is parallel to the electric field, the infrared light absorption is going to be maximal. For a membrane deposited on the IRE, its molecules and their respective dipole moments will have the same orientation with respect to a normal to the IRE. The orientation information for the peptides is determined by measuring the spectral intensity while changing the orientation of the incident light with the polarizer, and through calculation of the dichroic ratio (R^{ATR}). The dipole is essentially oriented along the C=O bonds, and thus a negative dichroism indicates the amide C=O bonds that are oriented in the plane of the membrane. To compute the peptide orientation with respect to the lipid membrane from experimental dichroic ratios, we need to know several parameters, among which the refractive index of the peptide in the absorbance band, the orientational distribution function of the transition dipole with respect to the secondary structure main symmetry axis, and the spread of the lipid membrane as regarding the IRE. Further to this, indeed the computation depends on the model used to describe the system. It should be mentioned that in thin films (much thinner than the wavelength) the field is usually considered to be constant over the film thickness, whereas in thick films the evanescent field does not penetrate the whole depth of the sample (Bechinger et al. 1999). In our experimental conditions, the intensity of the evanescent wave falls at 1/e after ca. 0.5 μm, i.e., with a penetration depth that is much larger than the molecular dimensions.

The dichroic ratio (R^{ATR}) of the Amide I or Amide II bands provides orientational order parameters. It is obtained from the ratio of the integrated absorption for parallel versus perpendicular polarized incident light, $R^{ATR} = A^{parallel}/A^{perpendicular}$ (Bechinger et al. 1999). As such, polarized ATR-FTIR can be a very helpful technique in the study, the orientation and the secondary structure of antimicrobial cyclic peptides upon membrane interaction, and thus help to unravel their mechanism of action.

Antimicrobial peptides (AMPs) are known for many years, as they are part of our immune system (Brogden 2005; Kumar et al. 2018; Torres et al. 2019), and their smart design is a very promising road to overcome bacterial resistance due to their alternative mechanism of action (they target the membrane) and their high selectivity for prokaryotic cells (Brogden and Brogden 2011; Junkes et al. 2011; Mika et al. 2011). Studies of AMPs that exhibit linear structure have been performed in the past years (Adão et al. 2011; Bastos et al. 2008; Blume and Kerth 2013; Marquette and Bechinger 2018; Silva et al. 2018), although cyclization of linear peptides enhanced the peptide activity (Appelt et al. 2008; Dathe et al. 2004; Fernandez-Lopez et al. 2001; Gunasekera et al. 2020).

Cyclic peptides (CPs) of an even number of alternating D- and L-α-amino acids have emerged as a new class of potential AMPs. They can adopt a flat-ring-shaped conformation, where the amide groups of the backbone arrange perpendicular to the plane of the structure. The flat rings, under certain conditions, can stack into an antiparallel structure, forming intermolecular hydrogen bonds between the CPs, creating a tubular β-sheet structure that has been referred to as self-assembled cyclic peptide nanotubes (SCPNs). The alternation of D- and L-amino acids in the CP's sequence places the peptide's side chains pointing to the outside of the nanotube, creating a hollow tubular core, and the presence of hydrophobic side chains favors its partition into the lipid membrane (Ghadiri et al. 1993; Hartgerink et al. 1996; Kim et al. 1998). A wise design of the CPs, by choosing the number of amino acids to control the diameter of the nanotube and their composition to vary the properties of the nanotube's outer surface to improve specificity, allows to modulate their characteristics to improve antimicrobial

performance. The nanotube formation is facilitated by membrane interaction, this supramolecular structure being the active form (Brea et al. 2010). The presence of D-amino acids leads to resistance to protease degradation that allied with the robust secondary structure and proven antimicrobial activity, which make SCPNs currently very promising antimicrobial candidates (García-Fandiño et al. 2012; Kim et al. 1998; Mika et al. 2011; Nuria et al. 2014).

This work aims at showing how ATR-FTIR used together with polarized light can assist us in successfully characterizing the structure, the antimicrobial D, L-α-cyclic peptides and their interactions with lipid membranes. With this method, we were able to assess the formation of tubular structures and to show that they were enhanced by the presence of the lipid membrane, and finally derive the orientation of the formed nanotube. As such it constitutes a 'proof of concept' for the use of this technique in the antimicrobial peptide's biophysical research area.

We used two D,L-α-cyclic peptides (CP), here designated as **ARG** (RSKSWPgKQ) and **ARG-C10** [RSKSWX^{C10}KQ, where X denotes (S)-2-amino-3-(1λ2, 2, 3-triazol-4-yl)propanoic acid], where the C10 hydrocarbon tail is appended (Fig. 1). These are two second-generation peptides of another cyclic peptide previously studied in our group (Claro et al. 2020), where one of the lysines (K) was substituted by one arginine. The peptides show good antimicrobial activity, particularly for Gram-positive bacteria (González-Freire et al. 2020). Based on these microbiological studies, we used here as model membranes large unilamellar vesicles (LUVs) of 1,2-dimyristoyl-sn-glycero-3-phospho-(1′-rac-glycerol) (DMPG).

Materials and methods

Preparation and size characterization of prepared liposomes

1,2-Dimyristoyl-sn-glycero-3-phospho-(1′-rac-glycerol) (DMPG) was purchased from Avanti Polar Lipids (AL, USA). The lipid was weighed in the appropriate amount and dissolved in an azeotropic mixture of chloroform/methanol [87.4:12.6 % (v/v)] in a round-bottom flask. The lipid film was obtained by evaporating the azeotropic mixture under a flux of N_2 and then kept overnight under high vacuum (< 10 mbar) to remove any trace of the organic solvents. The lipid film was then hydrated for 30 min with a previously heated milli-Q water at ca. 10 °C above the gel-to-liquid crystalline phase transition temperature (T_m). The suspension was subjected to a number of vortex/incubation above T_m cycles until a multilamellar vesicle suspension (MLVs) was formed. The MLVs was later frozen in liquid nitrogen and thawed above T_m three times. After the
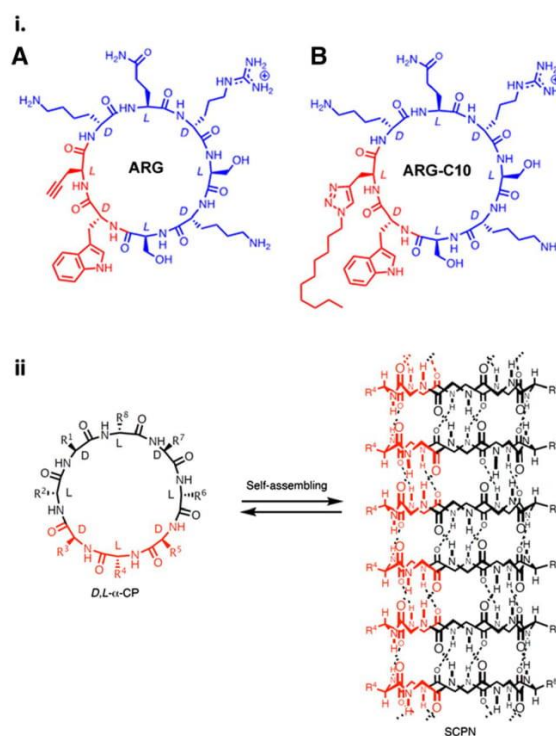
Fig. 1 Upper panel (i) D,L-α-cyclic peptides amino acid sequence. **a ARG** (RSKSWPgKQ) and **b ARG-C10** (RSKSWX^{C10} KQ). *X* denotes (*S*)-2-amino-3-(1λ2,2,3-triazol-4-yl)propanoic acid. Lower panel (ii): self-assembly of CP into nanotubes (β-sheet structure)

freeze and thaw cycles, large unilamellar vesicles (LUVs) were obtained by extrusion of the MLVs suspension, using a manually powered extruder designed for use with small samples, 0.5 mL capacity Liposofast-Basic (BPS, UK), with polycarbonate filters [pore diameter of 100 nm from Whatman, Nucleopore (NJ, USA)]. Three sequences of extrusion/vortex/freeze–thaw were made, followed by 30–40 passages through the 100 nm polycarbonate filters. The size of the LUVs was confirmed by dynamic light scattering (DLS) from Malvern Zetasizer Nano ZS (Malvern Instruments, Malvern, UK), being smaller than 120 nm, and with a polydispersity index always < 0.1. The final phospholipid concentration was determined using the modified version of the Bartlett phosphate assay (Bartlett 1959).

Attenuated total reflection-Fourier transform infrared spectroscopy

Attenuated total reflection infrared spectra were recorded on a spectrum two FTIR spectrometer (PerkinElmer, EUA) equipped with diamond internal reflection element from GladiATR Accessory S2PE (PIKE Technologies Inc, EUA).

FTIR spectra were taken using the PerkinElmer Spectrum software, with a 45° angle of incidence, between 4000 and 550 cm^{-1} and 32 scans were recorded for each spectrum, at a resolution of 4 cm^{-1}. A grid polarizer KRS-5 from Specac was adapted to the instrument, to enable dichroic spectra to be recorded.

The peptides and lipid suspension were prepared in water, and the pH of all samples was adjusted to 7.45 with a pH meter from Mettler Toledo Five Easy and a pH electrode Mettler Toledo LE438. No interference was found by the small salt amounts of salt introduced by the pH adjustment, as verified by comparison of the spectra before and after pH adjustment. The mixtures of peptide and liposomes were prepared with different lipid:peptide molar ratios (L:P) and incubated for 30 min at ca. 10 °C above the lipid transition temperature (previously determined by us by DSC) (Claro et al. 2020). A film with an oriented multilayer arrangement was obtained by depositing a 2 μL sample on the diamond crystal and evaporating the solvent under a gentle N$_2$ flux. The slow evaporation helps the capillary forces to flatten the membranes, getting a well-spread membrane film, and the absence of solvent reduces the water vapor contributions (Fringeli and Günthard 1981). The background spectra used in the ATR-FTIR measurement were recorded in air.

Each mixture was repeated three times, with independent sample films, from the same L:P mixture. Further to this, three independent L:P mixtures were prepared, and each measured three times.

The structural model assumed here, already used in previous studies of this type of peptides (Ghadiri et al. 1993; Kim et al. 1998), assumes that the 'stackable', flat-ring CPs have a conformationally restricted backbone amide, where the H-bonding C=O and NH moieties are aligned with the axis of the nanotube. In this case, the IR-active amide modes mirror the orientation of the nanotube assembly. Polarized ATR-FTIR allows an evaluation of the molecular orientations of the peptide at the membrane by following the amide's peptide and the lipid components by their dichroic spectra, recorded with parallel and perpendicular polarized incident light (with respect to the incidence plane) (Goormaghtigh et al. 1990; Kim et al. 1998). The spectra are scaled to the same lipid carbonyl vibration intensity, and thereafter, the dichroic spectrum is obtained through the difference between the recorded parallel spectra with perpendicular polarization. A multiplying factor for the perpendicular spectrum upon subtraction is used, due to the differences in the relative power of the evanescent fields (Bechinger et al. 1999). The difference spectra, as well as the various dichroic ratios ($R = \frac{A_{\parallel}}{A_{\perp}}$), were calculated with the program "Kinetics Spectra", developed in MatLab by Erik Goormaghtigh (Bechinger et al. 1999; Goormaghtigh 2013).

Results and discussion

ATR-FTIR studies of **ARG** and **ARG-C10** with/without oriented lipid membranes were performed to obtain information on their possible self-assembly alone and at the membrane, together with their orientation relative to the membrane plane, through the dichroic spectra.

The spectra of the pure CP are shown in Fig. 2a for **ARG** and in Fig. 2b for **ARG-C10**. The contributions of

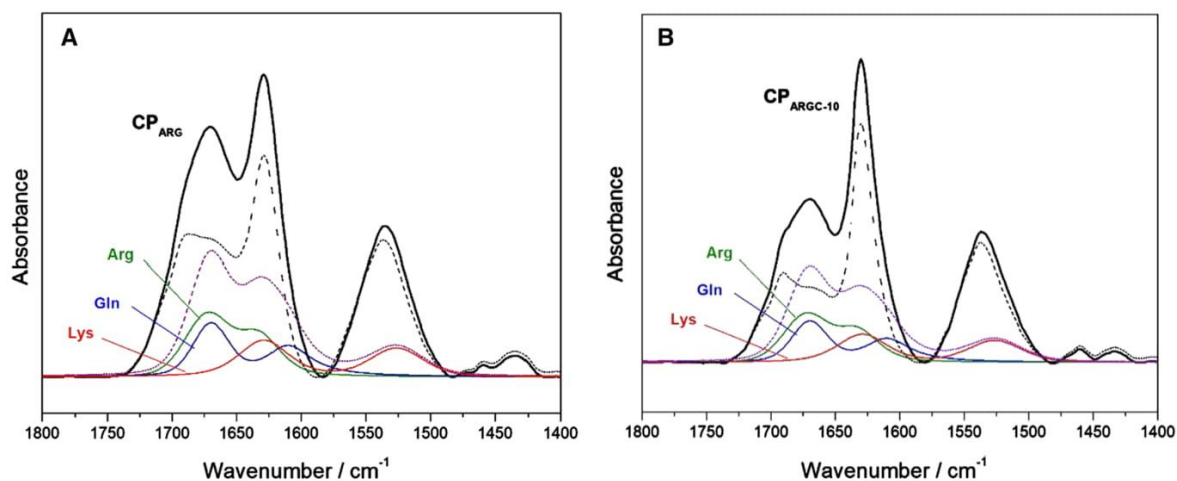**Fig. 2** ATR-FTIR spectra for **ARG a** and **ARG-C10 b** deposited in the crystal, from an aqueous solution that was evaporated with a gentle N$_2$ flux. Together with the peptide spectra the figure also shows the ones for each amino acid side chain contributions (Arg, Gln and Lys), as well as the resultant spectra (sum) of their contributions (dashed purple) and the CPs' corrected spectra thereof (dashed black)

the side chains of the amino acids Gln, Arg, and Lys (the ones that give a significant contribution) were calculated for each peptide with the data treatment program Kinetics, and the respective spectra are also plotted in Fig. 2a, b. In an undeuterated spectrum, the sum of the side chain contributions usually represents about 10% of the Amide I intensity. Although usually this contribution is not taken into account when the band shape is analyzed for the determination of the secondary structure (Goormaghtigh 2009), their consideration could help to improve the comparison of the peptide band pattern in the absence and presence of lipid. The amino acid residue's contribution is the same for both peptides, as they have the same aa sequence (Fig. 2a, b).

In the spectra for **ARG** and **ARG-C10**, for the Amide I band, we observe peaks at 1675 cm^{-1} [that has been attributed to a β-turn structure (Tatulian 2013)], a stronger one at 1625 cm^{-1} [associated with a β-sheet structure (Kim et al. 1998)], and for the Amide II, we see a peak at 1540 cm^{-1}. The relative intensities of the two Amide I peaks are similar for the two peptides—the peak at 1625 cm^{-1} is in both cases more intense than the one at 1675 cm^{-1}, but the difference in intensities is larger for **ARG-C10**. These results indicate that β-sheet nanotube structures form at the crystal surface, but clearly other structures are also present, possibly some β-turn structures. The Amide II band at 1540 cm^{-1} can represent intermolecularly hydrogen-bonded amide groups. Although we have in this region an overlap with the bending vibrations of NH$_3^+$ of the Lys (~ 1526 cm^{-1}) (Tamm and Tatulian 1997), the difference is significant (Fig. 2) and, therefore, we take this as an indication of the presence of hydrogen-bonded amide groups between different peptide rings. These structures for the peptide alone are in line with

the reported hydrogen-bonded antiparallel β-sheet tubular structure observed by Ghadiri et al. for another pure peptide of this general type in the solid state (cyclo[(L-Trp-D-Leu)$_3$-L-Gln-D-Leu]) (Ghadiri et al. 1993; Hartgerink et al. 1996). The hypothesis that the CPs can form clusters in the absence of a membrane was proposed by Tarek for another cyclic peptide of this type in aqueous solution (Khalfa and Tarek 2010), and more recently this was also observed by Granja et al. (González-Freire et al. 2020).

After obtaining the spectra for the CPs alone, we did the ATR-FTIR experiments with different peptide/lipid mixtures, prepared as explained above, to characterize structurally the peptide/membrane assembly.

Taking the L:P 10:1 ratio as an example (mixture with highest peptide content), we can see that when **ARG** or **ARG-C10** is mixed with DMPG (Fig. 3a, b), we also see for the Amide I band a broad peak centered around 1675 cm^{-1} and another one at 1625 cm^{-1} (β-sheet structure), and for the Amide II, a peak at 1540 cm^{-1}. Interestingly, the relative intensities of the two Amide I peaks are reversed for **ARG-C10**, where the intensity is now higher at 1675 cm^{-1}, whereas for **ARG** the peak at 1625 cm^{-1} is still more intense than the one at 1675 cm^{-1}. It should be noted that the Amide II peak at 1540 cm^{-1} has been reported as evidencing the occurrence of strong, intermolecularly hydrogen-bonded amide groups (Naumann et al. 1987). These spectral features were already observed in previous studies from our group with similar peptides (Claro et al.2020), as well as in Ghadiri's original reports of studies with D,L-α-cyclic peptides (Kim et al. 1998). The peak around 1730 cm^{-1} is characteristic of the C=O stretch of the lipids, and it does partly overlap with the amide bands, but that does not affect

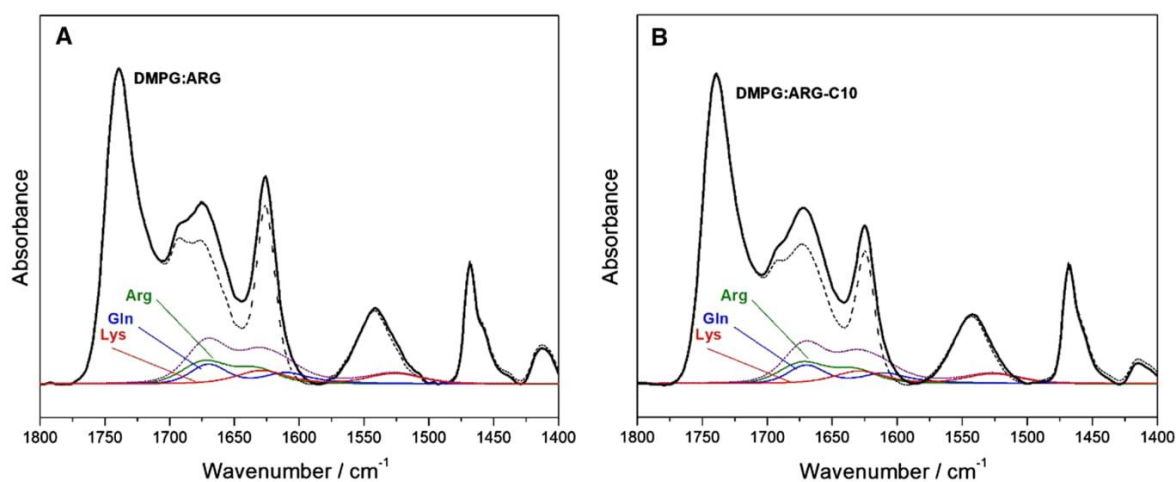**Fig. 3** ATR-FTIR spectra for DMPG: **ARG** (**a**) and DMPG: **ARG-C10** (**b**) both at L:P 10:1 (highest peptide content). Together with the peptide spectra, the contributions of the side chains of the amino acids Gln, Arg, and Lys are also plotted. The resultant spectra (sum) of the amino acid side chain contributions are represented in purple and the corrected spectra thereof in dashed black

our conclusions, as the data were treated after spectra deconvolution (Fig. 4).

The calculation of the side chain contributions (dashed lines in Fig. 3) reveals that they represent a minor contribution to the overall shape of the band, much less significant than in the peptide-alone case (Fig. 2). Therefore, its presence does not change the conclusions from the data treatment, as the peaks would be slightly less intense, but would not change relative position, and thus we did proceed with the raw spectrum, to avoid the errors due to excessive data reduction.

We did further analysis of the obtained spectra in the range 1800–1600 cm^{-1}, by curve fitting to deconvolute the observed peaks in this range. An example of such fitting for L:P ratio 10:1 is presented in Fig. 4 for both peptides. This deconvolution reveals clearly for both peptides the presence of the parallel component (weak) of the Amide I peak at ~ 1690 cm^{-1}, taken together with the perpendicular component (strong) of the Amide I peak frequency at 1625 cm^{-1} points to antiparallel β -sheets (Kim et al. 1998; Tamm and Tatulian 1997). This analysis allows us to estimate the percentage of the various β-structures present, as indicative values: 22% of β-turns/aggregated structures and 80% β-sheet for **ARG** (Fig. 4a), and 54% of β-turns/aggregated structures and 46% of β-sheet structures for **ARG-C10** (Fig. 4b). For the other L:P ratios (31:1 and 23:1), we did obtain, respectively, 17 and 15% of β-turns/aggregated structures and 87 and 84% β-sheet for ARG, whereas for **ARG-C10** we obtained, respectively, 15 and 17% of β-turns/aggregated structures and 85 and 83% β-sheet. González-Freire et al. (2020) concluded for a similar structure from **ARG-C10** by fluorescence measurements with thioflavin T (ThT), as they observed the typical fluorescence enhancement with peptide

concentration increase that is characteristic of formation of β-sheet type structures. They further suggest that in this case nanotube formation must be a cooperative process with a critical point around 12 µM. The significantly higher value for the β-turns/aggregated structures, observed for **ARG-C10**, particularly at the highest peptide content, is in line with the observation of fibers for this peptide in the studies of González-Freire et al. (2020).

When ATR-FTIR experiments are performed with polarized light, we can also evaluate the orientation of the peptide as regarding the membrane plane, by observing the peptide's amide band for the subtracted dichroic spectra (‖—⊥). Figure 5 shows a detailed example for **ARG** and DMPG at L:P 10:1, and shows that when subtracting the parallel spectra (blue line) to the perpendicular spectra (black spectra) with appropriate scaling factor (Bechinger et al. 1999), a negative dichroism at 1625 cm^{-1} is observed, indicating that the peptide nanotube arranges parallel to the membrane surface.

The same feature was found for the other L:P ratios, as well as for **ARG-C10**. Therefore, for clarity of the plots, we show now in Fig. 6 only the transmission spectra together with the difference dichroic spectra (‖—⊥) (dashed lines), for all lipid:peptide ratios (L:P) here studied. When **ARG** is mixed with DMPG (Fig. 6a), we observe an increase in the absorption peaks (solid lines) when the peptide content increases, i.e., the L:P decreases. We also observe an increase in the negative dichroism intensity of the β-sheet peak at 1625 cm^{-1} (dashed lines), indicating that the peptide nanotube arranges parallel to the membrane surface, i.e., the C=O of the amide is oriented parallel to the membrane (Goormaghtigh et al. 1999). The positive dichroism of the Amide II peak (1540 cm^{-1}) is also in agreement with the parallel β-sheet position. For **ARG-C10** (Fig. 6b)
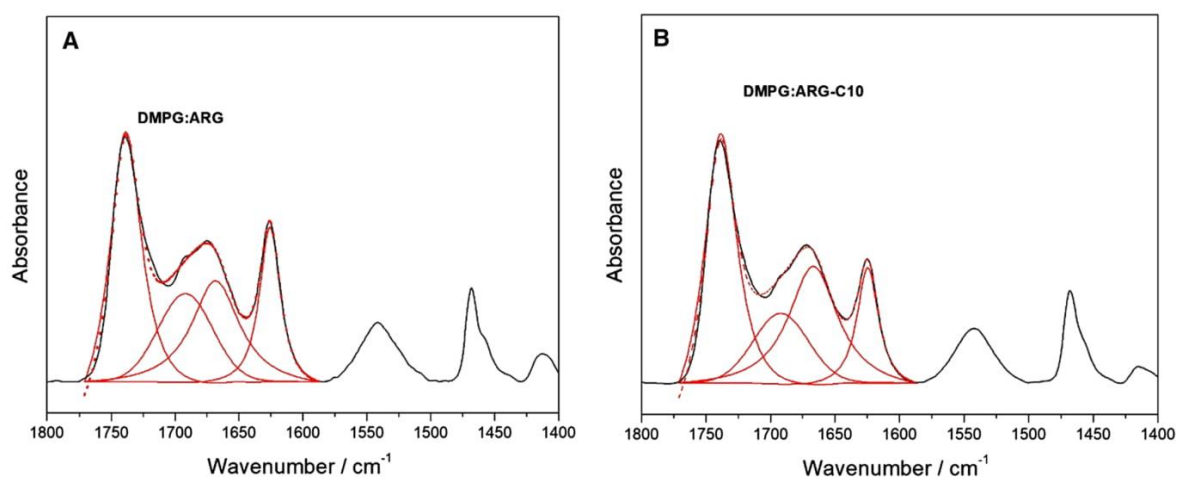
Fig. 4 ATR-FTIR spectra for DMPG: **ARG** (**a**) and DMPG: **ARG-C10** (**b**) at L:P 10:1. These spectra show the fittings obtained by the Fourier self-deconvolution method (red lines) as well as their sum (dashed line) between 1800 and 1600 cm^{-1}
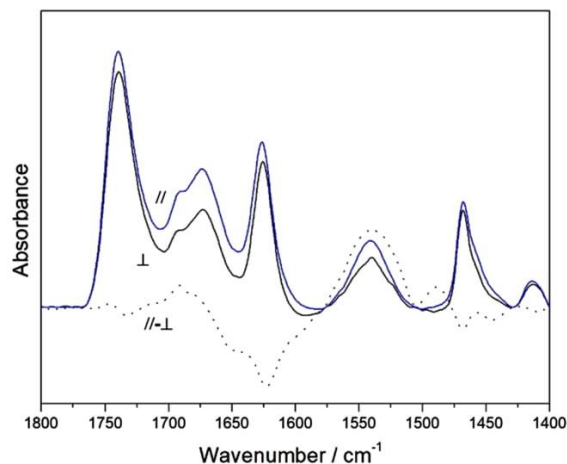
Fig. 5 Dichroic spectra for DMPG with **ARG** at L:P 10:1. The parallel (blue) and the perpendicular (black) spectra presented were obtained when a polarizer was used at right angles, and the subtracted dichroic (dashed line) was calculated as the difference between the parallel and perpendicular spectra

similar features are observed as the difference spectra are also negative at 1625 cm^{-1}, but the difference spectra are less intense. Taking these results together with the finding above that for **ARG-C10**, the % of other structures is much more significant at L:P ratio 10 than for **ARG**, we conclude that the presence of the carbon tail in **ARG-C10** is changing the peptide arrangement when in contact with negatively charged DMPG membranes, particularly at higher contents.

To quantitatively assess the lipid and peptide orientation and the changes induced by the CPs in the lipid chain orientation, dichroic ratios and the respective tilt angles for different components were calculated.

For DMPG, the symmetric [$\nu_s(CH_2)$] and antisymmetric [$\nu_{as}(CH_2)$] CH$_2$ stretches were used to evaluate the lipid chain orientation and to calculate the respective dichroic ratios (R^{ATR}), whereas the same information (orientation and dichroic rations) for the lipid heads was obtained through the symmetric stretch of the lipid headgroup components, ν_s (CO) and ν_s (PO$_2$). The calculated dichroic ratio for each component [$R\nu_s(CH_2)$, $R\nu_{as}(CH_2)$, $R\nu_s(CO)$ and $R\nu_s(PO_2)$] was obtained from the ratio of the integrated absorption for parallel vs perpendicular polarized incident light (Table 1).

As mentioned above, the film is prepared by slowly evaporating the solvent to allow the formation of a film as uniform as possible, in close contact with IRE, as it is known that oriented multilayer systems are easily obtained using this methodology (Bechinger et al. 1999). As stated in "Introduction", the conclusions drawn are indeed affected by the model—our results are derived in all cases from the "Kinetics" software (referred to above) in the absence and presence of the peptides, and assuming that the lipid bilayers were oriented perfectly parallel to the crystal surface, the tilts of the heads and CH$_2$ chains were obtained.

Without peptides, the hydrocarbon chains of DMPG presented an average tilt angle of 10° (average of the ν_{as} (CH$_2$) and ν_s (CH$_2$) angles) and the phosphate group, PO$_2$, a tilt of 65.2° with respect to the surface normal. When **ARG** is added to DMPG, the hydrocarbon chain and the headgroup's angle increase, whereas for **ARG-C10**, the hydrocarbon
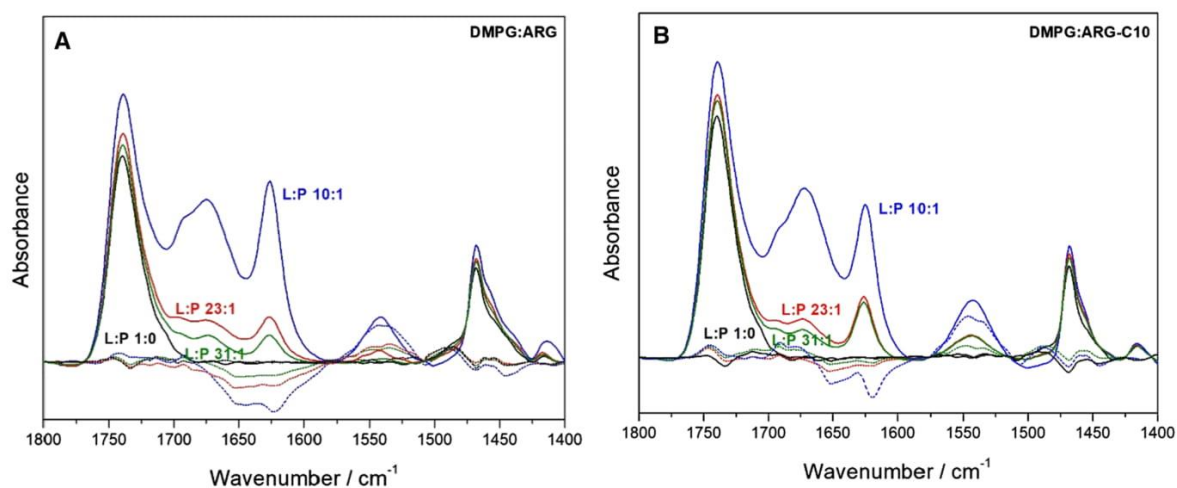
Fig. 6 ATR-FTIR results for DMPG (black line) and its mixtures with **ARG** (**a**) and **ARG-C10** (**b**). The lipid: peptide molar ratios (L:P) are shown in each curve (increasing in peptide concentration appears as decreasing L:P ratios). The dichroic spectra for the various ratios (dashed lines, same color code) are also shown, obtained when a polarizer was used at right angles, and calculated as the difference between the parallel and perpendicular spectra, with appropriate scaling

Table 1 Dichroic ratios and respective angles for ν_{as} (CH$_2$), ν_s (CH$_2$), ν_s(PO$_2$) and Amide I for **ARG** and **ARG-C10** when mixed with DMPG, for the different L:P ratios

	L:P	ν_{as} (CH$_2$) 2920 cm^{-1}	ν_s (CH$_2$) 2850 cm^{-1}	(CO) 1730 cm^{-1}	ν_s(PO$_2$) 1085 cm^{-1}	Amide I 1600–1700 cm^{-1}
DMPG						
R^{ATR}	1:0	**0.82 ± 0.01**	**0.70 ± 0.02**	**1.08 ± 0.01**	**1.10 ± 0.02**	**–**
Angle/deg		**11.3 ± 0.2**	**7.9 ± 0.4**	**–**	**65.2 ± 0.3**	**–**
ARG						
R^{ATR}	31	0.88 ± 0.01	0.72 ± 0.01	1.04 ± 0.01	1.06 ± 0.01	1.24 ± 0.01
Angle/deg		12.9 ± 0.2	8.5 ± 0.3	–	66.0 ± 0.3	15.4 ± 0.4
R^{ATR}	23	0.89 ± 0.01	0.74 ± 0.01	1.03 ± 0.01	1.04 ± 0.01	1.15 ± 0.02
Angle/deg		13.2 ± 0.2	9.1 ± 0.3	–	66.3 ± 0.2	11.7 ± 0.6
R^{ATR}	10	0.977 ± 0.003	0.85 ± 0.01	1.06 ± 0.03	0.98 ± 0.04	1.07 ± 0.02
Angle/deg		15.8 ± 0.1	12.1 ± 0.2	–	67.5 ± 0.7	8.6 ± 0.7
ARG-C10						
R^{ATR}	31	0.89 ± 0.01	0.74 ± 0.02	1.04 ± 0.01	1.11 ± 0.03	1.20 ± 0.05
Angle/deg		13.3 ± 0.2	9.0 ± 0.5	–	65.1 ± 0.5	14 ± 2
R^{ATR}	23	0.89 ± 0.02	0.73 ± 0.02	1.05 ± 0.01	1.11 ± 0.01	1.18 ± 0.01
Angle/deg		13.2 ± 0.5	8.6 ± 0.5	–	65.0 ± 0.1	12.8 ± 0.2
R^{ATR}	10	0.94 ± 0.01	0.79 ± 0.01	1.07 ± 0.01	1.03 ± 0.07	1.10 ± 0.04
Angle/deg		14.6 ± 0.3	10.3 ± 0.3	–	66.6 ± 1.3	10 ± 2

Note 1: The uncertainty assigned to each parameter is the average deviation between different ATR-FTIR experiments for the same lipid, peptide or L:P ratio

Note 2: The values for the dichroic ratios and respective angles for the lipid, DMPG, are represented in bold to facilitate comparison with the corresponding data for the peptides

chain also increases with peptide content increase, but the headgroups' angle remains the same (within uncertainty) (see Table 1 and Fig. 7).

To analyze the peptide angle, we did deconvolution of each polarized spectra (‖ and ⊥) in the range 1800–1600 cm^{-1}, as described above for the transmission spectra.

The peptide tilt angle can be analyzed by the Amide I (perpendicular component), which is the backbone C=O stretch (Table 1). When we compare the difference of the tilt angles for the peptides with the average tilt angles for DMPG (10°), we see that the peptide angle is only somewhat higher (except for the higher L:P ratio), indicating that the position of the nanotube is parallel, confirming our qualitative evaluation (Fig. 6).

In Fig. 7 and Table 1, we compare the R^{ATR} values obtained in the presence of peptides with the ones for the pure lipid system. The R^{ATR} values for the lipid hydrocarbon chain orientation [Rν_{as} (CH$_2$) and Rν_s (CH$_2$)] show an increase with the peptide concentration, being higher for ARG at L:P 10:1. As regarding the lipid headgroup component [Rν_s (PO$_2$)], for **ARG**, it decreases as the peptide content increases, whereas for **ARG-C10** it is about constant until the highest peptide content, where it drops significantly. In all cases, the values are higher for **ARG-C10**. We also observe that the R^{ATR} values for the lipid head component are less affected than the ones for the chains.

Conclusions

ATR-FTIR showed that both **ARG** and **ARG-C10** form b-sheet type nanotubes at the crystal surface, as revealed by the intense peak at 1625 cm^{-1}, characteristic of β-sheet structure. When CPs are mixed with DMPG at increasing peptide contents, an overall increase in the intensity of the absorption peaks indicates a strong electrostatic interaction with DMPG, and that the amount of β-sheet type structures is increased in the presence of DMPG membranes. The spectra showed that other structures are also present, particularly for **ARG-C10**. The significantly higher value of the percentual content of these other structures for this peptide, particularly at the highest peptide content that can be seen as revealing the presence of aggregated strands, is in line with the observation of fibers in the studies of Granja et al. (González-Freire et al. 2020). This could also justify its higher peptide antimicrobial activity, as observed by the same authors.

Due to the use of polarized light, our data could reveal both qualitatively and quantitatively that the peptides lie
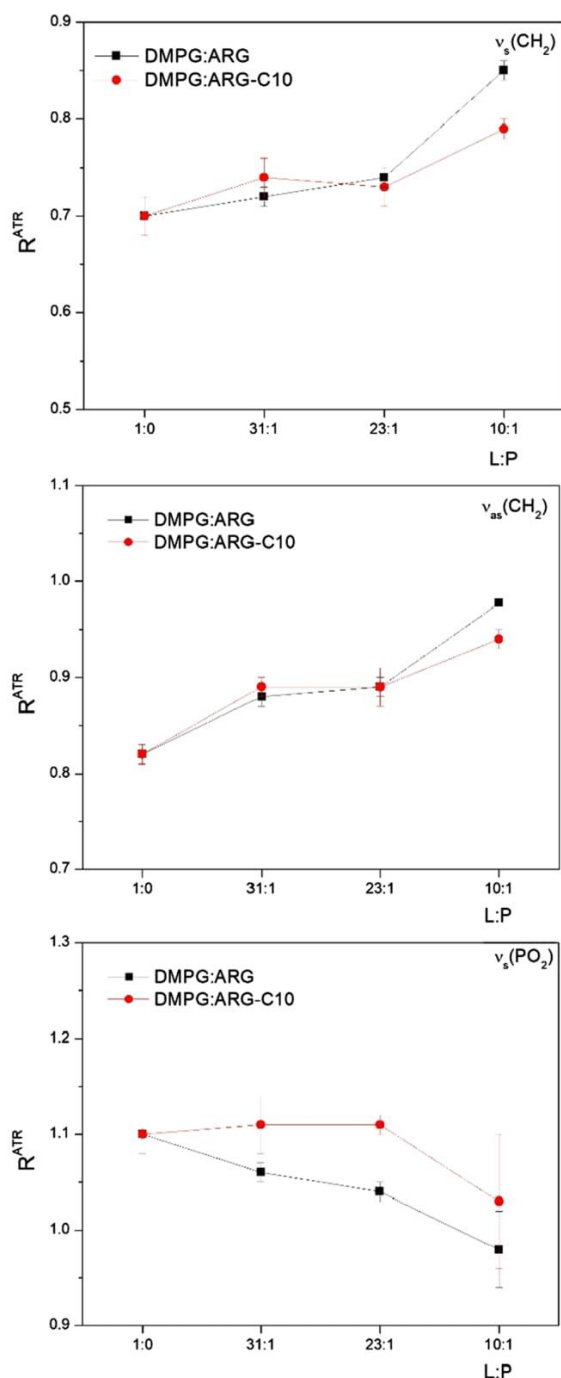
Fig. 7 Dichroic ratio for Amide I, Rν_s (CH$_2$), Rν_{as} (CH$_2$) and Rν_s (PO$_2$) as a function of L:P ratio (peptide content increases in along xx axis), for **ARG** and **ARG-C10** and DMPG. The uncertainty assigned to each parameter is the average deviation between different ATR-FTIR experiments for the same lipid, peptide or L:P ratio

mostly parallel to the membrane surface, as it is typical for antimicrobial peptides, at least at initial concentration levels. Finally, also derived from the use of polarized light the level of perturbation of both the lipids' head and chains could be assessed through the calculation of the dichroic ratios (R^{ATR}) for chosen components.

Overall, this study helped us to characterize structurally the CPs/membrane interactions, providing results that are in line with the antimicrobial action of these peptides, and offered potential structural reasons for the observed difference in antimicrobial potency. However, this technique does not provide information on the length of the nanotubes, which could be an important factor. In our previous paper (Claro et al. 2020) we started MD simulations assuming 8 CP per nanotube, as proposed in the literature (Ghadiri et al. 1993), but realized from the calculations that the CP per nanotube is not constant and depends on peptide and surface composition. We will thus continue to use this technique in parallel with others in our studies of these next-generation cyclic antimicrobial peptides to design more efficient and selective antimicrobial peptides.

References

Adão R, Nazmi K, Bolscher JGM, Bastos M (2011) C- and N-truncated antimicrobial peptides from LFampin 265–284: Biophysical versus microbiology results. J Pharm BioAllied Sci 3:60–69. https://doi.org/10.4103/0975-7406.76467

Appelt C, Wessolowski A, Dathe M, Schmieder P (2008) Structures of cyclic, antimicrobial peptides in a membrane-mimicking environment define requirements for activity. J Pept Sci 14:524–527. https://doi.org/10.1002/psc.924

Bartlett GR (1959) Phosphorus assay in column chromatography. J Biol Chem 234:466–468 (**PMID: 13641241**)

Bastos M, Bai G, Gomes P, Andreu D, Goormaghtigh E, Prieto M (2008) Energetics and partition of two cecropin-melittin hybrid peptides to model membranes of different composition. Biophys J 94:2128–2141. https://doi.org/10.1529/biophysj.107.119032

Bechinger B, Ruysschaert J-M, Goormaghtigh E (1999) Membrane helix orientation from linear dichroism of infrared attenuated total reflection spectra. Biophys J 76:552–563. https://doi.org/10.1016/S0006-3495(99)77223-1

Blume A, Kerth A (2013) Peptide and protein binding to lipid monolayers studied by FT-IRRA spectroscopy. Biochim. Biophys. Acta, Biomembr 1828:2294–2305. https://doi.org/10.1016/j.bbamem.2013.04.014

Brea RJ, Reiriz C, Granja JR (2010) Towards functional bionanomaterials based on self-assembling cyclic peptide nanotubes. Chem Soc Rev 39:1448–1456. https://doi.org/10.1039/B805753M

Brogden KA (2005) Antimicrobial peptides: pore formers or metabolic inhibitors in bacteria? Nat Rev Microbiol 3:238–250. https://doi.org/10.1038/nrmicro1098

Brogden NK, Brogden KA (2011) Will new generations of modified antimicrobial peptides improve their potential as pharmaceuticals? Int J Antimicrob Agents 38:217–225. https://doi.org/10.1016/j.ijantimicag.2011.05.004

Claro B, González-Freire E, Calvelo M, Bessa LJ, Goormaghtigh E, Amorín M, Granja JR, Garcia-Fandiño R, Bastos M (2020) Membrane targeting antimicrobial cyclic peptide nanotubes—an experimental and computational study. Colloids Surf B 196:111349. https://doi.org/10.1016/j.colsurfb.2020.111349

Dathe M, Nikolenko H, Klose J, Bienert M (2004) Cyclization increases the antimicrobial activity and selectivity of arginine- and tryptophan-containing hexapeptides. Biochemistry 43:9140–9150. https://doi.org/10.1021/bi035948v

Derenne A, Claessens T, Conus C, Goormaghtigh E (2013) Infrared spectroscopy of membrane lipids. In: Roberts GCK (ed) Encyclopedia of biophysics. Springer, Berlin, pp 1074–1081. https://doi.org/10.1007/978-3-642-16712-6_558

Fernandez-Lopez S, Kim H-S, Choi EC, Delgado M, Granja JR, Khasanov A, Kraehenbuehl K, Long G, Weinberger DA, Wilcoxen KM, Ghadiri MR (2001) Antibacterial agents based on the cyclic D,L-α-peptide architecture. Nature 412:452. https://doi.org/10.1038/35086601

Fringeli UP, Günthard HH (1981) Infrared membrane spectroscopy. In: Grell E (ed) Membrane spectroscopy. Springer, Berlin, pp 270–332. https://doi.org/10.1007/978-3-642-81537-9_6

García-Fandiño R, Amorín M, Castedo L, Granja JR (2012) Transmembrane ion transport by self-assembling α, γ-peptide nanotubes. Chem Sci 3:3280–3285. https://doi.org/10.1039/C2SC21068A

Ghadiri MR, Granja JR, Milligan RA, McRee DE, Khazanovich N (1993) Self-assembling organic nanotubes based on a cyclic peptide architecture. Nature 366:324–327. https://doi.org/10.1038/366324a0

González-Freire E, Novelli F, Pérez-Estévez A, Seoane R, Amorín M, Granja JR (2020) Double orthogonal click reactions for the development of antimicrobial peptide nanotubes. Eur J Chem. https://doi.org/10.1002/chem.202004127

Goormaghtigh E (2009) FTIR data processing and analysis tools. Adv Biomed Spectrosc 2:104–128. https://doi.org/10.3233/978-1-60750-045-2-104

Goormaghtigh E (2013) Infrared spectroscopy: data analysis. In: Roberts GCK (ed) Encyclopedia of biophysics. Springer, Berlin, pp 1049–1057. https://doi.org/10.1007/978-3-642-16712-6_111

Goormaghtigh E, Ruysschaert JM, Brasseur R (1990) Polarized attenuated total reflection spectroscopy as a tool to investigate the conformation and orientation of membrane components. A molecular description of biological membranes components by computer aided conformational analysis. CRC Press, Boca Raton, pp 285–332

Goormaghtigh E, Cabiaux V, Ruysschaert J-M (1994) Determination of soluble and membrane protein structure by Fourier transform infrared spectroscopy. In: Hilderson HJ, Ralston GB (eds) Physicochemical methods in the study of biomembranes. Springer, Boston, pp 405–450. https://doi.org/10.1007/978-1-4615-1863-1_10

Goormaghtigh E, Raussens V, Ruysschaert J-M (1999) Attenuated total reflection infrared spectroscopy of proteins and lipids in biological

membranes. Biochim Biophys Acta Rev Biomembr 1422:105–185. https://doi.org/10.1016/S0304-4157(99)00004-0

Gunasekera S, Muhammad T, Strömstedt AA, Rosengren KJ, Göransson U (2020) Backbone cyclization and dimerization of LL-37-derived peptides enhance antimicrobial activity and proteolytic stability. Front Microb 11:168. https://doi.org/10.3389/fmicb.2020.00168

Hartgerink JD, Granja JR, Milligan RA, Ghadiri MR (1996) Self-assembling peptide nanotubes. J Am Chem Soc 118:43–50. https://doi.org/10.1021/ja953070s

Hayashi T, Mukamel S (2008) Two-dimensional vibrational lineshapes of Amide III, II, I and A bands in a helical peptide. J Mol Liq 141:149–154. https://doi.org/10.1016/j.molliq.2008.02.013

Junkes C, Harvey RD, Bruce KD, Dölling R, Bagheri M, Dathe M (2011) Cyclic antimicrobial R-, W-rich peptides: the role of peptide structure and E. coli outer and inner membranes in activity and the mode of action. Eur Biophys J 40:515–528. https://doi.org/10.1007/s00249-011-0671-x

Khalfa A, Tarek M (2010) On the antibacterial action of cyclic peptides: insights from Coarse-Grained MD simulations. J Phys Chem B 114:2676–2684. https://doi.org/10.1021/jp9064196

Kim HS, Hartgerink JD, Ghadiri MR (1998) Oriented self-assembly of cyclic peptide nanotubes in lipid membranes. J Am Chem Soc 120:4417–4424. https://doi.org/10.1021/ja9735315

Kumar P, Kizhakkedathu JN, Straus SK (2018) Antimicrobial peptides: diversity, mechanism of action and strategies to improve the activity and biocompatibility in vivo. Biomolecules 8:24. https://doi.org/10.3390/biom8010004

Marquette A, Bechinger B (2018) Biophysical investigations elucidating the mechanisms of action of antimicrobial peptides and their synergism. Biomolecules 8:22. https://doi.org/10.3390/biom8020018

Mika JT, Moiset G, Cirac AD, Feliu L, Bardaji E, Planas M, Sengupta D, Marrink SJ, Poolman B (2011) Structural basis for the enhanced activity of cyclic antimicrobial peptides: the case of BPC194. Biochim Biophys Acta 1808:2197–2205. https://doi.org/10.1016/j.bbamem.2011.05.001

Naumann D, Labischinski H, Rönspeck W, Barnickel G, Bradaczek H (1987) Vibrational spectroscopic analysis of LD-sequential, bacterial cell wall peptides: an IR and Raman study. Biopolymers 26:795–817. https://doi.org/10.1002/bip.360260603

Nuria R-V, Ozores HL, Arcadio G, Eva G-F, Alberto F, Michele P, Juan MP, Juan O, Javier M, Rebeca G-F, Manuel A, Juan RG (2014) Membrane-targeted self-assembling cyclic peptide nanotubes. Curr Trends Med Chem 14:2647–2661. https://doi.org/10.2174/1568026614666141215143431

Silva T, Claro B, Silva BFB, Vale N, Gomes P, Gomes MS, Funari SS, Teixeira J, Uhríková D, Bastos M (2018) Unravelling a mechanism of action for a Cecropin A-Melittin hybrid antimicrobial peptide: the induced formation of multilamellar lipid stacks. Langmuir 34:2158–2170. https://doi.org/10.1021/acs.langmuir.7b03639

Tamm LK, Tatulian SA (1997) Infrared spectroscopy of proteins and peptides in lipid bilayers. Q Rev Biophys 30:365–429. https://doi.org/10.1017/s0033583597003375

Tatulian SA (2013) Structural characterization of membrane proteins and peptides by FTIR and ATR-FTIR spectroscopy. In: Kleinschmidt JH (ed) Lipid-protein interactions: methods and protocols. Humana Press, Totowa, pp 177–218. https://doi.org/10.1007/978-1-62703-275-9_9

Torii H, Tasumi M (1992) Model calculations on the Amide-I infrared bands of globular proteins. J Chem Phys 96:3379–3387. https://doi.org/10.1063/1.461939

Torres MDT, Sothiselvam S, Lu TK, de la Fuente-Nunez C (2019) Peptide design principles for antimicrobial applications. J Mol Biol 431:3547–3567. https://doi.org/10.1016/j.jmb.2018.12.015

Woods DA, Bain CD (2014) Total internal reflection spectroscopy for studying soft matter. Soft Matter 10:1071–1096. https://doi.org/10.1039/C3SM52817K

Yılmaz İ, Yıldız Ö, Korkmaz F (2020) Structural properties of an engineered outer membrane protein G mutant, OmpG-16SL, investigated with infrared spectroscopy. J Biomol Struct Dyn 38:2104–2115. https://doi.org/10.1080/07391102.2019.1624617

Publisher's Note Springer Nature remains neutral with regard to jurisdictional claims in published maps and institutional affiliations.

IV. **"Macromolecular assembly and membrane activity of antimicrobial *D,L*-α-Cyclic peptides"**

Bárbara Claro, Antonio Peón, Eva González-Freire, Erik Goormaghtigh, Manuel Amorín, Juan R. Granja, Rebeca Garcia-Fandiño, Margarida Bastos

Manuscript submitted for publication

Macromolecular assembly and membrane activity of antimicrobial *D,L*-α-Cyclic peptides

Bárbara Claro[1], Antonio Peón[1], Eva González-Freire[2], Erik Goormaghtigh[3], Manuel Amorín[2], Juan R. Granja[2], Rebeca Garcia-Fandiño*[1,2], Margarida Bastos*[1]

[1]CIQUP, Centro de Investigação em Química, Departamento de Química e Bioquímica, Faculdade de Ciências, Universidade do Porto, Porto, Portugal;

[2]Centro Singular de Investigación en Química Biolóxica e Materiais Moleculares (CiQUS), Departamento de Química Orgánica, Universidade de Santiago de Compostela, 15782 Santiago de Compostela, Spain

[3]Structure and Function of Biological Membranes, Center for Structural Biology and Bioinformatics, ULB, Brussels, Belgium

KEYWORDS. Antimicrobial Peptides, *D,L*-α-cyclic peptides, Self-Assembled Cyclic Peptide Nanotubes, Differential Scanning Calorimetry, polarized ATR-FTIR, Coarse-Grained Molecular Dynamics Simulations.

Statistical summary of the article:

Total number of words in main text – 5847

Figures - 7

Abstract

Antimicrobial peptides are viewed as a promising alternative to conventional antibiotics, as their activity through membrane targeting makes them less prone to resistance development. Among them, antimicrobial *D,L*-α-cyclic peptides (CPs) have been proposed as an alternative, specially due to their cyclic nature and to the presence of *D*- amino acids that increases their resistance to proteases. In present work, second generation *D,L*-α-cyclic peptides with proven antimicrobial activity are shown to form complex macromolecular assemblies in the presence of membranes. We addressed the CPs:membrane interactions through a combination of experimental techniques (DSC and ATR-FTIR) with Coarse grained molecular dynamics (CG-MD) simulations, aiming at understanding their interactions, macromolecular assemblies and eventually unveil their mechanism of action. DSC shows that the interaction depends heavily on the

negatively charge content of the membrane and on lipid/peptide ratio, suggesting different mechanisms for the different peptides and lipid systems. CG-MD proved that CPs can self-assemble at the lipid surface as nanotubes or micellar aggregates, depending on the peptide, in agreement with ATR-FTIR results. Finally, our results shed light into possible mechanisms of action of the peptides with pending hydrocarbon tail, namely membrane extensive segregation and/or membrane disintegration through the formation of disk-like lipid/peptide aggregates.

1. Introduction

The development of new, intelligent nanomaterials, capable of self- organization replying to external stimuli, has been studied in the recent years, and a number of different applications can be found in the literature [1-6]. Although a variety of different materials have been studied, the structural similarity with natural peptides and proteins that are the main molecular building blocks in nature makes the use of peptide-derived materials the most common approach towards biocompatibility [7-9]. Some of these peptide-derived new molecules were shown to self-assemble into structures such as nanotubes, due their broad conformational, chemical and functional features [10-12]. One such group of compounds are supramolecular structures called self-assembling cyclic peptide nanotubes (SCPNs), build from cyclic peptides (CPs) with an even number of alternating *D*- and -*L*-α-amino acids, as illustrated by Ghadiri and co-workers [3]. These new materials have been shown to be able to form artificial transmembrane channels for ions, or to act as good alternative to antimicrobial candidates, depending on peptide side chains composition and hydrophobicity [3, 13-15]. These *D,L*-α-cyclic peptides (*D,L*-α-CPs) can adopt a planar ring structure with side chains pointing outwards of the nanotube. Within the appropriate environment, individual CPs can stack in a *β*-sheet structure, creating intermolecular hydrogen bond networks along the growing axis, forming the SCPNs [11, 16].

Antimicrobial resistance is considered as one of the major global health issues of the 21st century [17], as the current therapeutic strategies are no longer appropriate to fight infection and drug-resistant pathogens. In this combat, antimicrobial peptides (AMPs), also known as host defense peptides [18], are currently in the spotlight as a good alternative to the conventional therapeutics to overcome bacterial resistance, as their main target is the bacterial membrane and they induce significantly lower resistance

[19]. AMPs are produced by a variety of organisms and present a diversity of functional and structural properties [20, 21], but exhibit common basic features - they are usually cationic, with amphipathic structure, they have a small number of amino acids and they are active against Gram-positive and Gram-negative bacteria, fungi and viruses [20, 21]. Different mechanisms of action have been proposed for AMPs [22-24], all causing membrane perturbation and/or destruction. Their action is triggered by electrostatic interactions, the first driving force for interaction with the membranes, as the cationic AMPs interact with the anionic membrane surface (negative headgroups) of pathogens. Thereafter there is usually accumulation and rearrangement at the membrane, leading to membrane micellization, segregation/permeabilization, pore formation or aggregation [25-27]. Amphipathic cationic D,L-α-CPs, have been shown to be potent antimicrobials whose mechanism of action is related with the nanotube formation that is facilitated by membrane interaction, being this supramolecular structure the main active form [28]. The robust secondary structure allied with the presence of D-amino acid residues reduces the resistance against proteases, making SCPNs promising antimicrobial candidates [13, 14, 16, 29-31]. Therefore, the design of new SCPNs with good antimicrobial activity is a very attractive application of these peptides, for their possible significant contribution to worldwide wealth.

We combined experimental techniques (differential scanning calorimeter (DSC) and attenuated total reflection Fourier transform infrared spectroscopy (ATR-FTIR)) with coarse-grained Molecular Dynamics simulations (CG-MD) to characterize and rationalize the interactions of three second generation CPs of proven antimicrobial activity [32] with lipid model membranes.

The antimicrobial D,L-α-CPs used in this study are designated as **CPR,** c-[RSKSWPgKQ] , **CPRT10,** c-[RSKSWX^{C10}KQ] and **CPRT14,** c-[RSKSWX^{C14}KQ] (Fig. 1), and were designed as second generation peptides, based on a CP previously reported by our group, there called CP2 [13]. In the amino acid sequence the use of brackets indicates that the peptides have a cyclic structure, the underlined amino acids are D-amino acids and X denotes (S)-2-amino-3-(1λ^2,2,3-triazol-4-yl)propanoic acid. **CPR**, **CPRT10** and **CPRT14** are soluble in water and they contain one hydrophobic residue (tryptophan (W)), known to increase membrane anchoring, three charged residues (one arginine (R) and two lysines (K)), and three polar non-charged residues (one glutamine (Q) and two serines (S)). **CPRT10** and **CPRT14** differ from **CPR** as they have a ten and fourteen carbons' tails, respectively, linked to the propargylglycine

group (Pg) through a copper catalyzed azide–alkyne cycloaddition (CuAAC reaction). All three CPs present good antimicrobial activity, mainly against Gram positive bacteria [32].

DMPE (1,2-dimyristoyl-*sn*-glycero-3-phosphoethanolamine) and DMPG (1,2-dimyristoyl-*sn*-glycero-3-phospho-(1'-rac-glycerol)) are used as simple models for the bacterial membrane, since they are known to have a significant presence in Gram-negative and Gram-positive bacteria cytosolic membrane. Although the lipid composition varies quite significantly among pathogens, typically Gram-negative bacteria have a higher PE content and Gram-positive bacteria a higher PG content [33]. As our peptides showed the highest activity towards Gram-positive bacteria [32], we chose mixture with high PG content, *i.e.*, pure DMPG membranes and mixtures of DMPE:DMPG at different molar ratios (1:1) and (1:9). Further to these, we also used DMPE alone, to assess its role on the interactions of the peptides with the lipid mixtures. Finally eukaryotic membranes are mimicked by using 1,2-dimyristoyl-*sn*-glycero-3-phosphocholine (DMPC), as a control for toxicity, as has been seen in different studies a remarkable correlation between toxicity and DSC AMP:PC profile [26, 34-39].
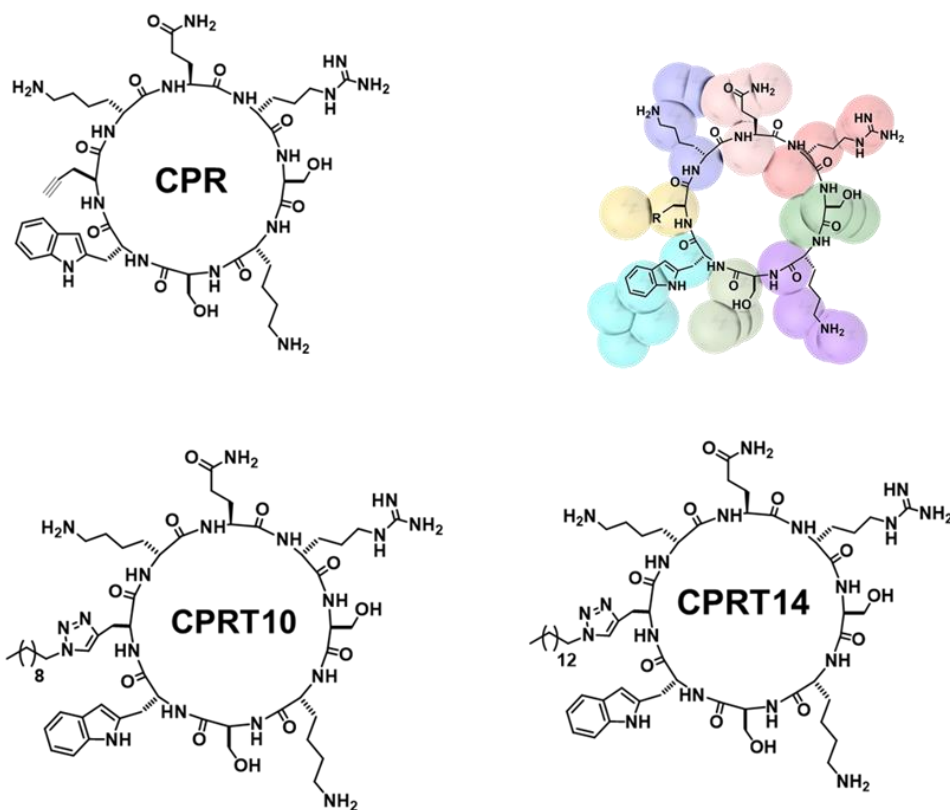
Fig. 1. Structures of the peptides studied here: **CPR,** c-[RSKSWPgKQ], **CPRT10,** c-[RSKSWX^{C10}KQ] and **CPRT14,** c-[RSKSWX^{C14}KQ]. In the amino acid composition here shown the use of brackets indicates that the peptides have a cyclic structure, the underlined amino acids are D-amino acids and X denotes (S)-2-amino-3-(1λ^2,2,3-triazol-4-yl)propanoic acid. The beads of a Coarse-Grained model for the Molecular Dynamics simulation are represented for **CPR**. Amino acid residues are colored as follow: Gln-1 (rose), Arg-2 (brick-red), Ser-3 (dark green), Lys-4 (violet), Ser-5 (soft green), Trp-6 (cyan), R tail (gold), Lys-8 (dark blue).

2. Experimental

2.1 Materials and Methods

Hexafluorophosphate benzotriazole tetramethyl uronium (N-HBTU), tetrafluoroborate benzotriazole tetramethyl uronium (N-TBTU), and the α-amino acids were purchased from Iris Biotech, Novabiochem, Advanced Chemtech, Aldrich, and/or GL Biochem (Shangai) Ltd. Rink Amide resin was purchased from Novabiochem. Triisopropylsilane (TIS) and diisopropylethylamine (DIEA) were purchased from Sigma-Aldrich, Germany. All solvents were HPLC grade purchased from Aldrich or Fisher Scientific, and they were used without additional purification, except the dry DCM, which were distilled with CaH$_2$. Synthesis grade DMF was used to synthesize the peptides on solid phase.

1,2-dimyristoyl-sn-glycero-3-phosphocholine (DMPC), 1,2-dimyristoyl-sn-glycero-3-phosphoethanolamine (DMPE) and 1,2-dimyristoyl-sn-glycero-3-phospho-(1'-rac-glycerol) (DMPG) were from Avanti Polar Lipids, Alabama, USA, and used as received. The water used was in all cases high purity Millipore water. The buffer was prepared with HEPES, NaCl, NaN$_3$ and EDTA all purchased from Sigma-Aldrich, Germany.

2.1.1. Synthetic procedures

Peptides **CPR**, **CPRT10** and **CPRT14** were synthesized manually by standard Fmoc solid phase peptide synthesis protocols [40-43]. See Supplementary Material for details about synthetic procedure and CPs characterization.

2.1.2. Preparation of Liposomes

Liposomes of DMPE, DMPG and DMPC and their mixtures at different molar ratios were prepared by the lipid film method, as described in detail in Supplementary Material.

2.1.3. Differential Scanning Calorimetry

Differential Scanning Calorimetry measurements were performed in a MicroCal VP-DSC microcalorimeter from Malvern (Worcestershire, UK), by following the same protocol as published by our group before [13, 38]. Details on the procedure can be found in Supplementary Material.

2.1.4. Coarse-grained Molecular Dynamics simulations

Coarse-grained molecular dynamics (CG-MD) simulations of **CPR**, **CPRT10** and **CPRT14** interacting with membrane models of DMPE, DMPG and their mixtures were carried out. The CG parameters used for CPs were those corresponding to the polarizable MARTINI force field (Martini v2.2 polar amino acids and polarizable water) [44, 45], together with the use of distance restraints between all the backbone particles to maintain the cyclic conformation (Fig. 1). The CG topologies for the CPs were built using the martinize.py tool [46] and subsequently modified using local code. Computational details can be found in Supplementary Material.

2.1.5. Attenuated Total Reflection Fourier Transform Infrared Spectroscopy

ATR-FTIR measurements followed the same protocol as published before [13, 47]. The measurements were carried in a Spectrum Two FTIR Spectrometer (PerkinElmer, EUA) equipped with diamond internal reflection element from GladiATR Accessory S2PE (PIKE Technologies Inc, EUA). The details of the procedure can be found in Supplementary Material.

3. Results and discussion

3.1. DSC

The DSC thermograms for each model membrane system, as well as for their mixtures with **CPR**, **CPRT10** and **CPRT14** at different L:P ratios can be found in Fig. 2. After the first DSC scan full equilibration was attained, and from the second all scans were identical, as common in similar studies [13, 38, 48]. The data obtained were treated and

integrated after baseline correction, either as one peak or using multi-peak deconvolution. The obtained thermograms are shown in Fig. 2 for the 3 peptides and the 4 lipid systems. The thermodynamic parameters retrieved (T_m and $\Delta_{trans}H$) are presented in Table S1.

Overall, it can be seen in Fig 2 that the behavior of **CPR** is different from the obtained for the other two peptides with tail, **CPRT10** and **CPRT14**. Observing the results obtained at high PG contents, (Fig. 2A for pure DMPG and 2D for DMPE:DMPG (1:9)), we can see that when **CPR** is mixed with either lipid system (Fig. 2Aand 2D) a small shoulder appears above the T_m (25ºC), which relative importance increases with increase in peptide content (L:P decrease), representing almost half of the total enthalpy change for the largest peptide content It should be also noted that the temperature for the main transition is maintained (Table S1). Altogether, this indicates that the interaction between this peptide and the negatively charged membrane is mainly electrostatic and at the surface, with no significant penetration of the lipid's hydrocarbon core. This suggests a phase separation into peptide poor and peptide rich domains in the membrane, as also found previously by Sevcsik *et al* [49]. These authors suggest that the shoulder reflects the presence of a quasi-interdigitated phase, that they confirmed by X-ray. According to Sevcsik *et al* [49] this creates a void in the membrane that is compensated by moving the inner lipid layer towards the hydrophobic part of the peptide nanotube. We believe that we could have the same situation here, as this is compatible with the DSC tracing observed. Further, our MD results (see below) support that the peptide forms nanotubes at the membrane, maintains a surface position, and that after an initial approach electrostatically driven (with the Arg facing the membrane, interacting with the lipid's headgroups) it rotates turning the Trp towards the hydrocarbons chains.

In the case of the other two peptides, **CPRT10** and **CPRT14**, the results observed for the two PG rich lipid systems must be evaluated separately. For **CPRT10** and DMPG (Fig. 2 B) we observe a small decrease in T_m for the lowest peptide content (27:1), and thereafter we have two peaks superimposed, one centered at T_m of the pure DMPG and another at about 1ºC lower (Table S1), showing that the peptide is destabilizing the lipid membrane. As regarding **CPR14** and DMPG (Fig. 2 C), after an initial decrease in T_m of ~1ºC for the lowest peptide content, we have again a peak splitting, but of different characteristics – at the L:P ratio 22:1 we have two transition both of just slightly enlarged width as compared to pure lipid, but at the highest peptide content, 12:1, the

pattern shows a sharp peak centered around 20 ^{o} that coexists with a broad peak centered about 22ºC (see peak deconvolution for these ratios in Fig S2). We interpret these results as showing that at high peptide content part of the membrane forms most likely disk-like peptide aggregates, that undergo a broad transition and coexist with DMPG with small amount of peptide. A similar situation was already described for another antimicrobial peptide, LL-37 by Sevcsik *et al* [33, 49]. The distinctly different behavior of these 2 peptides as compared to **CPR** can be ascribed to the presence of the 10 and 14 hydrocarbon tails.

The effect of decreasing the membrane's negative charge by adding a zwitterionic lipid, DMPE, can be seen in Fig. 2D to 2I. When DMPE and DMPG are mixed, a broader profile in the transition curve appears as expected, due to structural mismatch between the two lipids. However, at pH 7.45, the formation of ion pairs facilitates PE headgroup's hydration, stabilizing the lipid mixture [50]. The behavior of **CPR** with the model membrane DMPE:DMPG (1:9) was already described above (Fig. 2D), as it is similar to what is observed with pure DMPG. For the two peptides with tail, **CPRT10** and **CPRT14** (Fig. 2E,F), we observe a clear segregation within the membrane, with the appearance of peaks at lower temperatures. Again, some differences exist between **CPRT10** and **CPRT14** – for **CPRT10** the peak around 25ºC is maintained (peptide poor domain), with a small increase in width as the peptide content increases, and a peak at lower temperature appears (peptide-rich), which temperature decreases for the highest peptide content, but its relative importance is maintained (in terms of enthalpy); for **CPRT14** a similar patter appears, with the main peak maintained, but already changed at the highest peptide content, whereas the peptide-rich part of the membrane appears to be formed by 'patches' of different composition, as more than one peak appears at lower temperatures. This is indeed the results of both a longer hydrocarbon tail, that drives a more significant partition of **CPRT14** to the lipid membranes, as well as the capacity of this peptide to also interact with DMPE, as will be seen below. Overall this segregation reflects in the preferential association of the positively charged cyclic peptides with DMPG, as the associated peptide-rich peak(s) appear at temperatures lower than the T_m for the DMPE:DMPG mixture (DMPG has a T_m of 23.2ºC and DMPE 50.3ºC), and the remaining regions, richer in PE:PG and some associated CP, show peaks at temperature similar to the original lipid mixture. The ability of linear and cyclic peptides to induce segregation and domain formation within

PE:PG membranes has been reported by our group for different CPs, as well as by other groups using different antimicrobial peptides [13, 48, 51].

As regarding the interactions with the model membranes with even lower negative charge content, DMPE:DMPG (1:1) (Fig. 2 G-I) we observe for the three CPs an a peak with increased T_m, reflecting most likely the depletion of DMPG from part of the membrane, leaving a lipid mixture with composition that approaches DMPE as the CP content increases. As before, **CPR** does not induce lipid segregation with membrane domain formation, whereas in the case of **CPRT10** and **CPRT14** a second, low temperature peak is clearly seen, close to the T_m of pure DMPG (Fig 2H,I and Table S1). This shows that these two peptides induce a phase separation in DMPE:DMPG (1:1) mixtures, giving rise to a DMPG-rich peak that was depleted from the mixed membrane by the peptides, that is in equilibrium with the remaining membrane mainly composed of DMPE, possibly still with some DMPG and CP associated, as its transition temperature is lower than the one we determined to pure DMPE membranes, 50.3ºC. This behavior was also found for different antimicrobial peptides, by our group as well as others [13, 52, 53].

The interaction of the CPs with pure DMPE (Fig. 2 J-L) was also followed by DSC, and it is clear in Fig. 2J that **CPR** hardly interact with DMPE, **CPRT10** show a clear but small change in the thermal profile, that is not strong enough to be reflected in a significant change in thermodynamic parameters (see Table S1), whereas for **CPRT14** the $\Delta_{trans}H$ decrease significantly with L:P decrease, indicating that this peptide somehow interacts with this rather zwitterionic lipid. Our MD results (see CG-MD section) indicate that a small number of peptides **CPRT10** and **CPRT14** bury the aliphatic tail and the adjacent Trp in the membrane, either through isolated CP units or through small associated peptides over the surface. Nevertheless, it is difficult to interpret the observed DSC effect, as there is no change in T_m, as one would expect if the tails or hydrophobic moieties of the peptide would penetrate the hydrophobic core the DMPE, we only see a decrease in $\Delta_{trans}H$, thus the number of penetrating peptides must be small and thus its effect not revealed by DSC.

Finally, the interaction of these peptides with DMPC was also tested, often used as a simplified model membrane for eukaryotic cells, and we have been obtaining a remarkable parallel between toxicity and interaction with DMPC membranes [26, 34, 37, 39, 54]. The results are shown in Fig. S1 and Table S2, showing that **CPR** does not

interact at all with this membrane system, whereas **CPRT10** and **CPRT14** show a mild interaction.

Overall, our results suggest that the presence of the hydrocarbon tail changes significantly the peptide:membrane interactions. **CPRT10** and **CPT14** are shown to form different types of micellar aggregates in solution [32] and in the presence of then membrane (see results and discussion in CG-MD section) thus depending on the energetic balance between peptide's micellar aggregates and membrane partition they can also act in a 'surfactant-like' manner at high peptide contents.
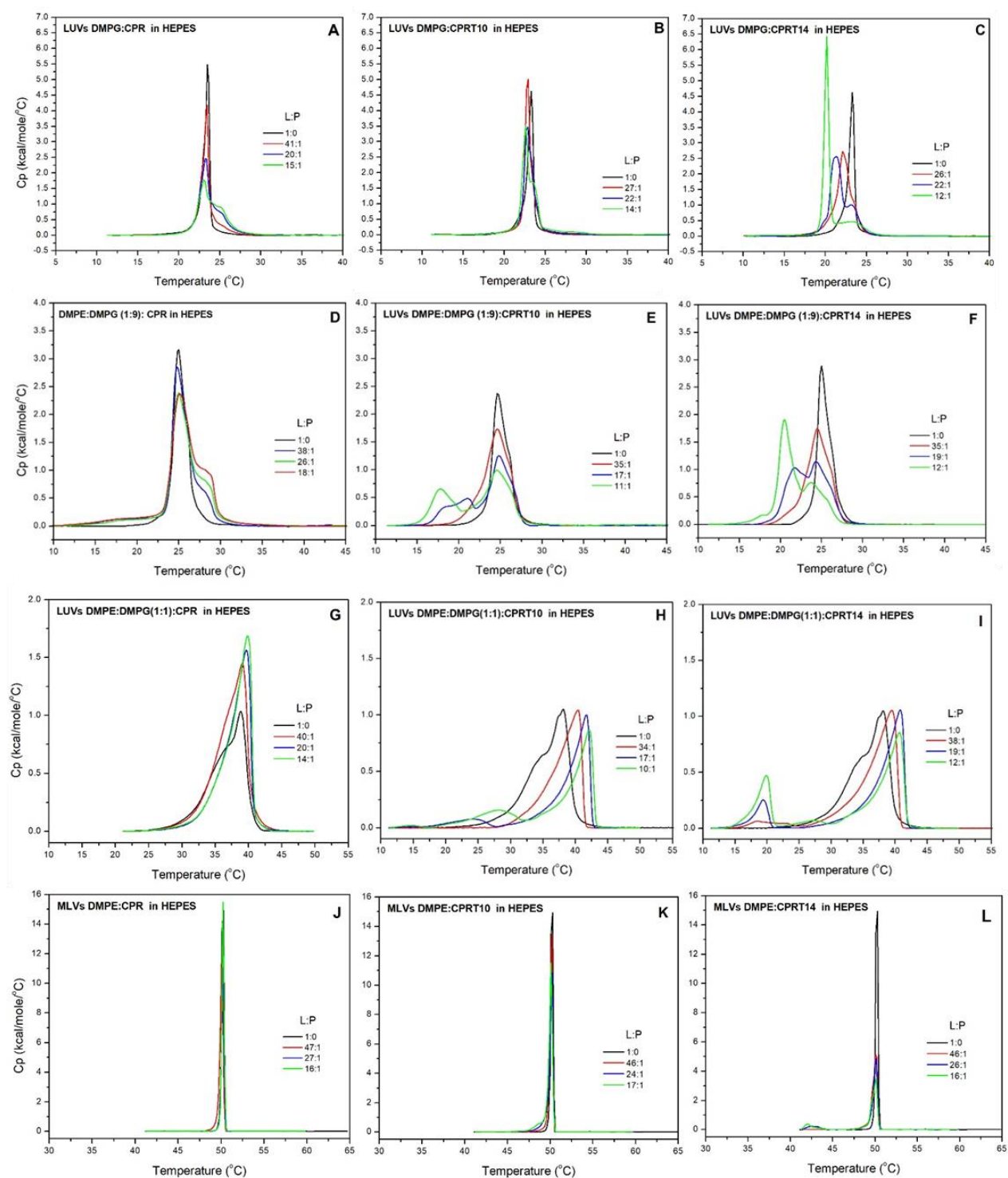
Fig. 2. DSC curves for mixtures of the three cyclic peptides **CPR** (left panel), **CPRT10** (middle panel) and **CPRT14** (right panel) with model membranes of DMPG, DMPE and their mixtures. A,B,C: LUVs of DMPG; D,E,F: LUVs of DMPE:DMPG (1:9); G,H,I: LUVs of DMPE:DMPG (1:1); J,K,L: MLVs of DMPE. The molar ratios of lipid to peptide (L:P) for each curve are shown in each plot. The DSC profiles shown are all for the second scan. Note that the y scales for the different lipid systems are different.

3.2. CG-MD

In order to try to further decipher the mechanism of action of **CPR**, **CPRT10** and **CPRT14**, CG-MD simulations of 160 CP units placed randomly (representing a molar ratio of lipid to peptide 3:1), were carried out in the presence of the same membrane compositions that were studied experimentally: DMPE, DMPE:DMPG (1:1), DMPE:DMPG (1:9) and DMPG.

The CG-MD simulations show a significant difference in the behavior of the peptide **CPR** when compared to those bearing a hydrophobic tail, **CPRT10** and **CPRT14**, in agreement with DSC results. The most remarkable contrast is that whereas **CPR** units self-assemble into small or medium-size nanotubes (up to 5 CP units), the presence of T10 and T14 tails induce the formation of mostly micellar aggregates in **CPRT10** and **CPRT14**. In these micellar assemblies, the CPs are acting as the hydrophilic "head" regions in contact with surrounding solvent, sequestering the hydrophobic tail regions in the micelle center (Fig. 3 and Fig. S3-S6).
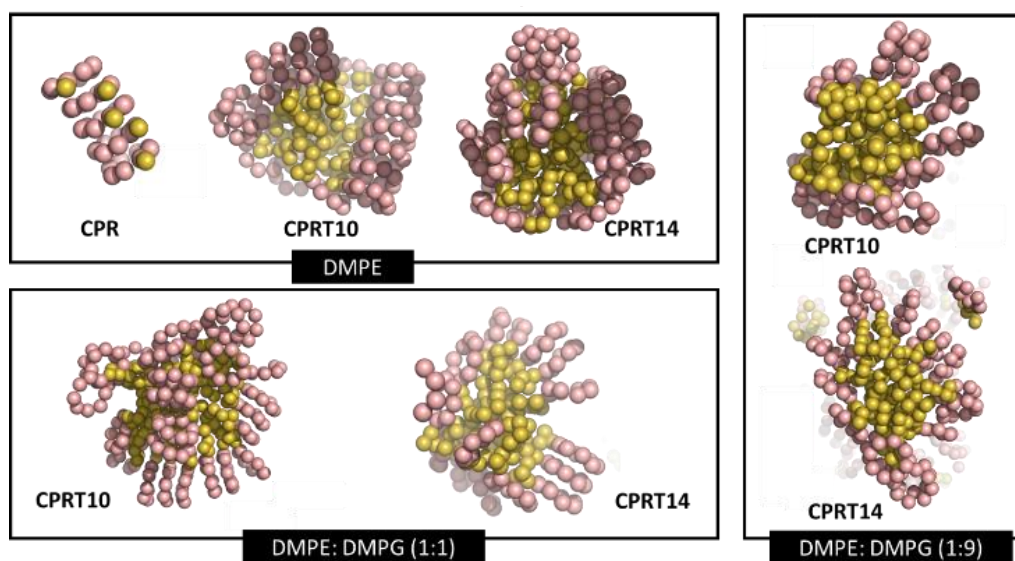
Fig. 3. Detail of some structures found in the last snapshot (t=2 μs) of the CG-MD simulations of **CPR**, **CPRT10** and **CPRT14** in different membrane compositions.

The study outcomes suggest that the interaction of the different peptides is significantly sensitive to the membrane composition. The interaction with the DMPE membrane exhibits for the three peptides a markedly different behavior from the rest of lipid compositions here studied. A feature common to all simulations carried out in presence of DMPE is that there is very little (**CPRT10** and **CPRT14**) on no (**CPR**) insertion of the peptides into the membrane (Fig. 4 and Fig. S3-S6). Overall, these computational findings are in agreement with DSC experimental evidence reported above, which

suggests that the studied peptides do not interact strongly with liposomes composed only of DMPE. Regarding the differences between the three peptides in the presence of this membrane model, the peptides with the tail continue to associate mostly into micellar aggregates (**CPRT14** and **CPRT10**) as in solution, whereas **CPR** forms short nanotubes. Some (few) peptides **CPRT10** and **CPRT14** bury the aliphatic tail and the adjacent Trp in the membrane, either through isolated CP units or through small nanotubes over the surface (Fig. 4 and Fig. S4-S6).

The interaction of **CPR** with the DMPE membrane takes place mostly through the residues Trp and Lys adjacent to Pg (bearing the alkyne moiety) (Fig. 5). The presence of T10 tail significantly increases the number of contacts between **CPRT10** and DMPE membrane, through this hydrocarbon moiety, together with the neighboring Trp, and also through the adjacent Lys to a minor extent (Fig. 5 and Fig. S5). The longest tail, however, drastically reduces the number of contacts between **CPRT14** and the DMPE membrane (Fig. 5 and Fig. S6). Although the residues interacting mostly with the membrane are the same as for **CPRT10** (the hydrocarbon tail, Trp and the adjacent Lys), the number of interactions shows a significant decrease (about 4 times less than the previous peptide). Curiously, by DSC a larger effect of **CPRT14** is observed, although difficult to interpret, as stated above.

The influence of DMPE is still significant for DMPE:DMPG (1:1). The presence of 50% DMPE in the bilayer leads to a smaller interaction of the peptides with the membrane when compared to membrane models with higher DMPG contents (Fig. 4, Fig. S4-S6). In any case, the number of contacts between all CPs and DMPE:DMPG (1:1) substantially increases when compared to the pure DMPE membrane (Fig. 5, second column)
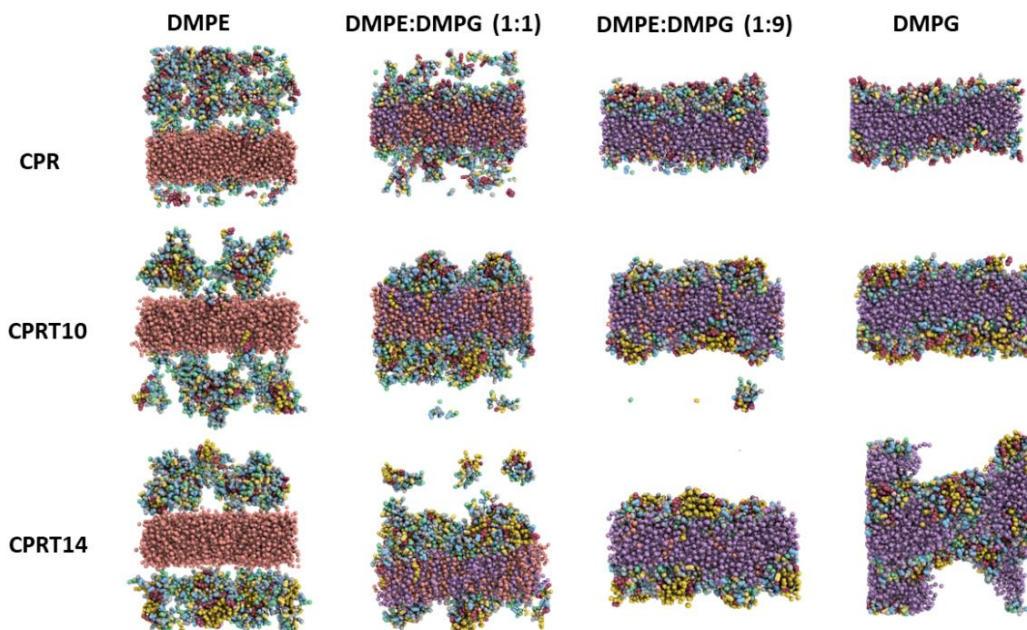
Fig. 4. Lateral view of the last snapshots at t=2 μs from the CG-MD simulation of 160 units of **CPR**, **CPRT10** and **CPRT14**, respectively, in the presence of different membrane compositions: DMPE, DMPE:DMPG (1:1), DMPE:DMPG (1:9) and DMPG. DMPE lipids are represented in orange whereas DMPG lipids are represented in purple. Each residue in the CP is represented in a different color. Water molecules have been removed for clarity. Top view is represented in Fig. S3. The figure was rendered using PyMOL (The PyMOL Molecular Graphics System, Version 2.5 Schrödinger, LLC).

A clear difference is found again in the behavior of **CPR** when compared to the peptides bearing the hydrocarbon tails, **CPRT10** and **CPRT14**, in presence of this lipid composition: whereas in the case of **CPR** the interaction with the membrane is dominated by the Trp and the Lys adjacent to the Pg residue, the highest number of contacts between **CPRT10** and **CPRT14** and the DMPE:DMPG (1:1) corresponds to the Arg residue (Fig. 5, second column). Interestingly, as can be observed from the graphics, the interaction with Arg was also prevalent for **CPR** at this membrane composition at the beginning of the CG-MD simulation, but as the simulation progresses, these Arg-membrane contacts are replaced by the interaction with Trp and Lys mentioned previously. Overall, the common aspects for the peptide/membrane interaction, namely electrostatic interactions and the role of Trp in the membrane anchoring, is the behavior expected for AMPS, and were also observed with other CPs in previous works [13, 34]: the electrostatic interaction between the charged residues of the CP and the charged heads of the lipids would be the driving force attracting the

peptides towards the membrane; once there, the peptides turn around, inserting their hydrophobic residues into the membrane. What is remarkable is how clear this shows up in the **CPR** simulation results (Fig. 5). It is also noteworthy that once this happens, the number of contacts between Trp and Lys and the membrane significantly increase (up to 1200-1400, and they seem to be still evolving) with respect to the initial electrostatic contacts between Arg and the membrane, suggesting that this interaction is much more favorable, *i.e.*, energetically more stable. In the case of **CPRT10** and **CPRT14** the electrostatic interaction with the membrane takes place mainly through the Arg charged residues in the first steps of the simulation. However, it should be noted that within the simulated time (2 μs), most of **CPRT10** and **CPRT14** units are not able to turn around and introduce their hydrophobic tails inside the membrane, at odds with **CPR**, as clearly seen in Fig. 5. In fact, as it can be appreciated in Fig. 5, although the main membrane interaction between **CPRT10** and **CPRT14** takes place through the Arg residue, there are some contacts with the DMPE:DMPG (1:1) membrane through the T10 and T14 tails already at this simulation time. The insertion of the hydrophobic tails in the membrane involves breaking the micellar aggregates and this behavior could not be observed within the simulation times studied here. However, the extension of some of the CG-MD simulations for longer periods (20 μs), led, indeed, to much more tails inserted in the membrane (see an example for **CPRT10** and **CPRT14** in Fig. S7-S8). These finding are in agreement with the DSC results, as the strong interaction of **CPRT10** and **CPRT14** with DMPG leads to segregation, and the appearance of DMPE rich and DMPE poor domains within the membrane. When the DMPG content increases further, in DMPE:DMPG (1:9) and finally in pure DMPG, the predominant interaction between all CPs and both membranes is electrostatic, as can be clearly visualized from the number of contacts of the individual residues (Fig. 5, columns 3-4). However, in the case of **CPR**, the system seems to be still evolving towards the typical behavior observed in previous membrane systems, mainly DMPE:DMPG (1:1): a decreasing of Arg-membrane interaction in favor of a correlated increase in the number of contacts through Trp and the adjacent residues in the sequence, Ser and Pg. Again this is in agreement with our DSC results, where we did suggest above the possible appearance of a quasi-interdigitated phase for **CPR** and DMPE:DMPG (1:9 and pure DMPG), that can only take place if the apolar part of the peptide's nanotubes face the hydrocarbon chains of the lipid membrane (see above DSC discussion). No significant differences were observed for the interactions of **CPRT10** and **CPRT14** with DMPE:DMPG (1:9),

except for a slightly higher number of Arg-membrane contacts in the case of **CPRT14**. However, in the case of pure DMPG, that is no longer the case, as a strong distortion of the membrane can be observed. Whereas up to 1 μs the behavior of **CPRT14** is very similar to **CPRT10**, after that the number of contacts between Arg and the membrane significantly decreases, together with an increase in the number of contacts between the T14 tail and the membrane, all this accompanied by a great distortion and final collapse of the membrane system (Fig. 5, column 4 and Fig. 4). These observations match perfectly with the DSC results found for **CPRT14** and DMPG at the highest peptide content, where we concluded that lipid-peptide disks are formed, that lead to membrane disintegration.
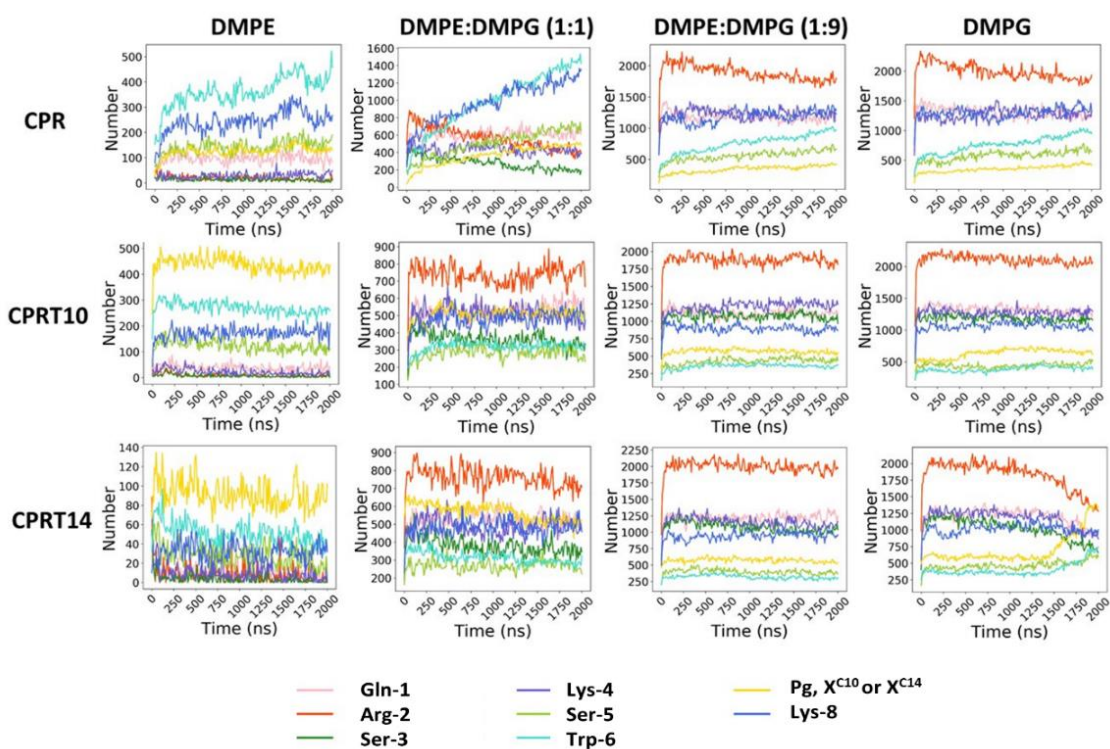
Fig. 5. Number of contacts within 0.6 nm between any pair of atoms of each amino acid of **CPR**, **CPRT10** or **CPRT14** and the corresponding membrane compositions, DMPE, DMPE:DMPG (1:1), DMPE:DMPG (1:9) and DMPG, respectively over 2 microseconds. Note that the scales in all cases are not the same on purpose, to facilitate the visualization of the lines. Matplotlib [55] library was used to produce the figures.

3.3. ATR-FTIR

ATR-FTIR was used to characterize structurally the CPs self-assembly when interacting with different model membranes. The use of polarized ATR-FTIR allowed us to assess their orientation relative to the membrane plane.

The structural changes in peptide organization and their possible effect on the lipid bilayer's structure was extensively studied by ATR-FTIR by our group for these three peptides, and the initial results obtained for **CPR** and **CPRT10** when mixed with DMPG liposomes were already reported [47]. In that study, we reported for both peptides the presence in the amide I band of a peak centered around 1675 cm^{-1} and another at 1625 cm^{-1}, associated with the presence of β-turn [56] and β-sheet [16] structures, respectively. The spectrum also showed a peak for the amide II at 1540 cm^{-1}, representing intermolecularly hydrogen-bonded amide groups together with unbound N-H, providing evidence for nanotube formation in the presence of DMPG membranes [16, 47]. Deconvolution of the peaks revealed in the case of these two peptides the presence of the parallel component of the amide I peak at ~1690 cm^{-1} (weak) together with the perpendicular component (strong) at 1625 cm^{-1}, indicating the possible presence of antiparallel β-sheets. The position of the aggregates as regarding the membrane was derived from the results obtained when using polarized light, where the obtained negative dichroism at 1625 cm^{-1} indicated that the formed structures laid parallel to the membrane plane [47, 57]. Considering the results obtained by MD above (CG-MD section), it is possible that the observed dichroism is not too strong as many of the peptides are involved in aggregates, of micellar type, and do not associated into well-formed nanotubes.

When similar measurements were made with **CPRT14** and DMPG, at different L:P ratios, we observe the same type and position of peaks, as reported for **CPR** and **CPRT10** - the amide I band also has two peaks, one around 1675 cm^{-1} and other at 1625 cm^{-1}, associated with the possible presence of β-turn [56] and β-sheet [16] structures, respectively (Fig. 6). Additionally, for higher CP contents, the spectra show a well-defined peak at ~1692 cm^{-1}, indicating the presence of either antiparallel β-sheet structure or aggregated strands [58], and the peak for the amide II at 1540 cm^{-1} is also present. Two interesting observations for this system should be referred: i) the peak at 1625 cm^{-1} has higher intensity for the middle L:P ratio, 23:1 when compared to L:P 10:1 and further ii) the peak at 1625 cm^{-1} is higher than the peak at 1675 cm^{-1} for L:P 23:1 while the opposite is observed for 10:1. These can be associated with the formation of

new structures, possibly aggregated structures, as by DSC we observe a decrease in the T_m and clear domain formation with increase in peptide content, and our MD results suggest the formation of self-assembled/aggregated structures, and that they interact with the membrane while partly maintaining the micellar aggregates (see CG-MD section). We should stress that in our previous publication [47], we did a curve fitting to deconvolute the observed peaks in the range 1800–1600 cm^{-1}, and we did the same here for **CPRT14**. This deconvolution allowed us to estimate the percentage of the various β-structures present, as indicative values, and the values retrieved were 80% β-sheet and 22% of β-turns/aggregated structures for **CPR**, as opposed to 46% of β-sheet and 54% of β-turns/aggregated structures and 40% of β-sheet and 60% of β-turns/aggregated structures for **CPRT10** and **CPRT14**, respectively. These results fit very well with what was found here in our MD results, where **CPR** formed predominantly nanotubes with β-sheet structure as opposed to the peptides with tail, that induced domain formation within the lipid membrane, composed of lipid and micellar-like aggregates at high peptide contents. Finally, it is worth mentioning that the self/association of **CPRT10** and **CPRT14** was experimentally verified by González-Freire *et al* [32] by fluorescence measurements with thioflavin T (ThT), obtaining critical aggregation values of ~13 μM and ~4.5 μM for **CPRT10** and **CPRT14,** respectively.
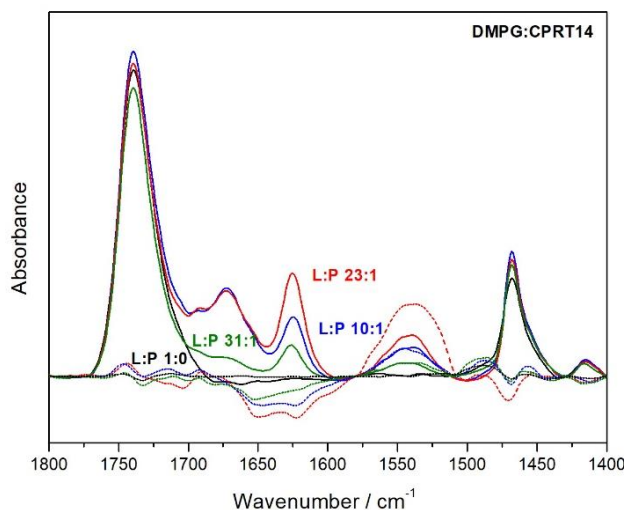
Fig. 6. ATR-FTIR results for DMPG (black line, L:P 1:0) and its mixtures with **CPRT14**. The different molar ratios for the mixtures, L:P, are shown in each curve. The dichroic spectra for the various ratios (dashed lines, same color code) are also shown and calculated as the difference between the parallel and perpendicular spectra, with

appropriate scaling. Note that the negative dichroism at 1465 cm^{-1} (v_δ (CH$_2$) with dipole perpendicular to the chain) also confirms that the membranes are oriented parallel to the support, as stated in the text.

A qualitative analysis of the orientation of the nanotubes or aggregated structures was obtained through the use of ATR-FTIR with polarized light. The orientation as regarding the membrane plane was evaluated by subtracting spectra recorded with the perpendicular incident light from spectra obtained with the parallel incident light ($\parallel$ - $\perp$), multiplied by an appropriate factor [59]. Negative deviations of the difference spectra at 1625 cm^{-1} (dashed lines, Fig. 6), whose intensity increases with increasing peptide content, indicates that the peptide C=O bond arranges perpendicular to the membrane normal axis - the nanotubes are thus oriented parallel to the membrane normal axis. The positive dichroism of the amide II peak (1540 cm^{-1}) (Fig. 6) is also in line that orientation [57, 59].

The structural effect of the peptides in the presence of the membranes was also studied for other model membrane systems, namely DMPE:DMPG (1:9) and (1:1) (see Supplementary material Fig. S9 and S10). In Fig. 7 we did plot the spectra for the different CPs in DMPG, DMPE:DMPG (1:9) and (1:1), at a chosen L:P molar ratio, L:P 10:1, to compare the influence of the membrane charge in the structure and nanotube/aggregates' formation. For DMPG with the different peptides (Fig. 7 A), the amide I band peaks (1675 cm^{-1} and 1625 cm^{-1}), and the peak for the amide II (1540 cm^{-1}) associated with the presence of β-sheet/aggregated structures and intermolecular interactions respectively, are present for the three CPs. When we compare the relative intensities, we see that overall, there is a trend in peak intensity depending on peptide, being the peaks for **CPR** the highest, followed by **CPRT10** and then **CPRT14**. Indeed, this reflects the fact found by MD that **CPR** forms mainly nanotubes at the lipid surface, whereas **CPRT10** and **CPRT14** form mainly micellar aggregates, with few nanotubes (see CG-MD section).

When we add 10% of DMPE to the negatively charged DMPG (Fig.7 B) we observe the presence of the same peaks in the amide I and amide II band, but two striking differences are apparent - the increase in intensity of the 1625 cm^{-1} peak for all peptides, this peak becoming more intense than the one at 1675 cm^{-1} in the same amide band, and the decrease in the intensities for the C=O 1740 cm^{-1} for the mixture with **CPRT14**. Indeed, this points to the presence of other aggregated structures, as the peaks at 1675

cm^{-1} and 1692 cm^{-1} (*β*-turns or antiparallel *β*-sheet or aggregated strands [58]) are evident, in line with our DSC observation of a peak splitting (see above DSC section) and the MD results below for **CPRT10** and **CPRT14**. The decrease in the intensity of the C=O band (1740 cm^{-1}) and the peak at 1675 cm^{-1} for DMPE:DMPG (1:9):**CPRT14**, may indicate the presence of aggregates/other type of structures, associated with peptide micellar state, as already stated above, as well as the partial destruction of the lipid membrane. Again, these observations are in line with the DSC and MD findings, as we observe some membrane segregation, with parts of the membrane richer in DMPG and peptide, and other parts richer in DMPE.

For DMPE:DMPG (1:1) (Fig. 7 C) we observe for all CPs the same peaks and similar decrease in the intensity of C=O band (1740 cm^{-1}), as we described for the system DMPE:DMPG (1:9). In the case of **CPR**, the spectra suggest that most self-assembled structures are *β*-sheet type, as we have a low intensity peak at 1625 cm^{-1}, in agreement with the MD results. Again, for this model membrane system, the spectra for **CPRT14** suggest the presence of aggregates/other type of structures, in line with the DSC and MD results. Further, these findings are also in line with the observation for **CPRT14** of an arrangement of self-assembled peptides with a filamentous structure, in the studies of González-Freire *et al*, when the peptides were studied in a solution (without membranes) by STEM microscopy [32].

Overall, as regarding the position of the macromolecular structures relative to the membranes, obtained from the polarized spectra for lipid systems here studied (results not shown), the negative dichroism indicates that the nanotubes structures formed by **CPR** as well as the aggregates formed by **CPRT10** and **CPRT14** lay parallel to the membrane, thus adopting the same orientation already reported in the presence of DMPG membranes in previous studies [47] and here for **CPRT14**.
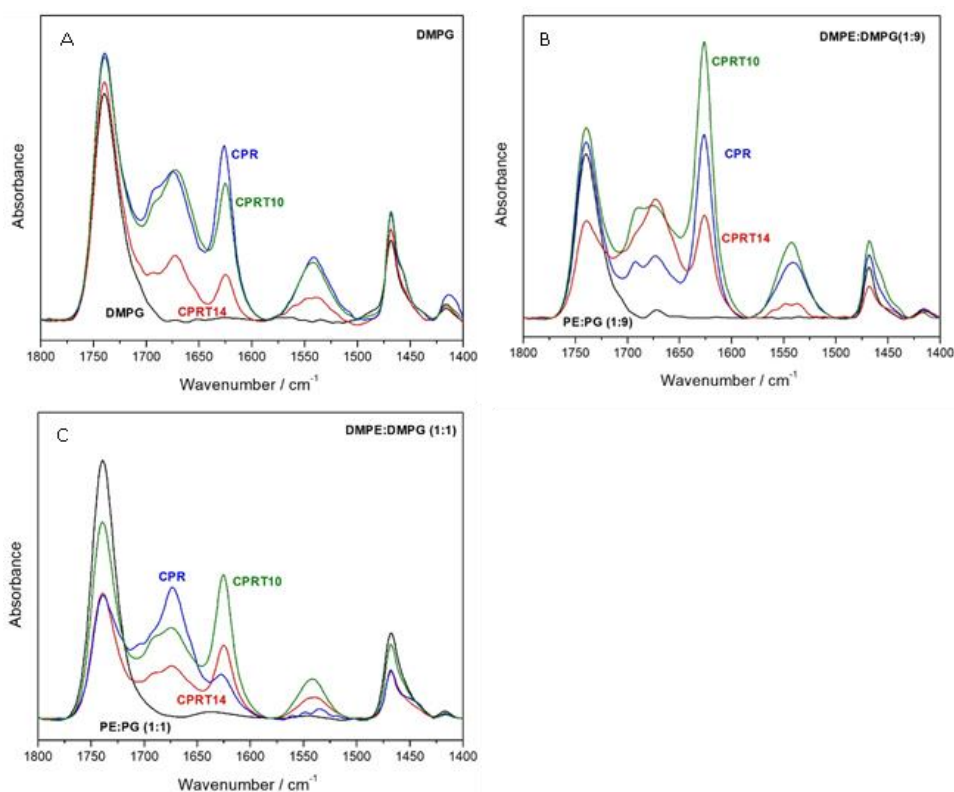
Fig. 7. ATR-FTIR results for **CPR**, **CPRT10** and **CPRT14** mixed with DMPG (A), DMPE:DMPG(1:9) (B) and DMPE:DMPG(1:1) (C), at L:P 10:1 molar ratio. The color code for the different spectra is: pure lipid (black), and mixtures with **CPR** (blue), with **CPRT10** (green) and **CPRT14** (red).

CONCLUSIONS

This work presents an orthogonal study using biophysical experiments (DSC and ATR-FTIR) and CG-MD simulations of peptide/lipid model membranes mimicking bacteria membranes, aiming at understanding the mechanism of action of second generation *D,L*-α-cyclic peptides, with proven antimicrobial activity. The CPs here studied share the same sequence but differ in the presence of a hydrophobic tail of ten (**CPRT10**) or fourteen (**CPRT14**) carbons that replaces a Pg in the original sequence (**CPR**).

DSC results showed that the presence of negative charge in the membrane is a requirement for a strong interaction of the three peptides, as **CPR** and C**PRT10** do not interact and **CPRT14** just weakly with the zwitterionic DMPE. Further, it is shown that the interaction depends on charge content and on peptide, being stronger for the cyclic peptides with a tail and for the more negatively charged membranes. Importantly, the

CG-MD results show that the macromolecular structures adopted by the three peptides are different – mostly short nanotubes in the case of **CPR**, and mainly micellar-type aggregates in the case of **CPRT10** and **CPRT14**, in line with results presented by González-Freire *et al* [32]. These finding corroborate the interpretations we suggest for the observed DSC profiles, showing a distinct behavior of **CPR** as compared to the other two peptides with tail. This is also supported by our FTIR-ATR results, where the amide I band peaks and the peak for the amide II, associated with the presence of *β*-sheet/aggregated structures and intermolecularly interactions respectively, are present for all three CPs. Further, they show that there is a trend in peak intensity depending on peptide, being the peaks for **CPR** the highest, followed by **CPRT10** and then **CPRT14**, related to the formation of a lower number of nanotubes in the case of **CPRT10** and **CPRT14** when compared to **CPR**. Finally, these results can help the understanding of the antimicrobial activity found for these peptides - very weak for **CPR**, very active and fast for **CPRT10**, and very active but slower for **CPRT14**. Although **CPR** is also interacting strongly to the negatively charged membranes, it is not destructive, as it shows a mild degree of membrane penetration and no significant segregation in mixed membranes. On the contrary, the two peptides with tail have a strong electrostatic interaction with negatively charged membranes, leading to membrane disintegration at high peptide contents in the case of **CPRT14** (with peptide lipid discs formation, detergent like behavior), and to extensive domain formation in the case of **CPRT10.** For less negatively charged mixed membranes, both peptides induce membrane segregation, that must impair cell function in real pathogen systems. The observed faster effect of **CPRT10** as compared to **CPRT14** may be due to the weaker tendency of this peptide to form micellar aggregates, making its partition to the membrane more favorable and faster.

ACKNOWLEDGMENTS

ABBREVIATIONS

CPs, cyclic peptides; SCPNs, cyclic peptide nanotubes; AMPs, antimicrobial peptides; MD, molecular dynamics; CG, coarse-grained resolution; DSC, differential scanning calorimetry; ATR-FTIR, attenuated total reflection Fourier – infrared spectroscopy; Pg, propargylglycine group; DMPE, 1,2-dimyristoyl-sn-glycero-3-phosphoethanolamine; DMPG, 1,2-dimyristoyl-sn-glycero-3-phospho-(1'-rac-glycerol); DMPC, 1,2-dimyristoyl-sn-glycero-3-phosphocholine; PE, phosphoethanolamine; PG, phospho-(1'-rac-glycerol); T_m, transition temperature; Cp, heat capacity; Gln, Glutamine; Arg, Arginine ; Ser, Serine; Lys, Lysine; Trp, Tryprophan; DCM, dichloromethane; HPLC, High-Performance Liquid Chromatography; HEPES, 4-(2-hydroxyethyl)-1-piperazineethanesulfonic acid; EDTA, Ethylenediamine tetra-acetic acid; FMOC, fluorenylmethoxycarbonyl protecting group; LUVs, Large unilamellar vesicles;

REFERENCES

[1] I. A. Banerjee, L. Yu, H. Matsui, Location-Specific Biological Functionalization on Nanotubes: Attachment of Proteins at the Ends of Nanotubes Using Au Nanocrystal Masks, Nano Lett. 3 (2003) 283-287.
[2] C. Cheng, C. Zhang, X. Gao, Z. Zhuang, C. Du, W. Chen, 3D Network and 2D Paper of Reduced Graphene Oxide/Cu2O Composite for Electrochemical Sensing of Hydrogen Peroxide, Anal. Chem. 90 (2018) 1983-1991.
[3] M.R. Ghadiri, J.R. Granja, R.A. Milligan, D.E. McRee, N. Khazanovich, Self-assembling organic nanotubes based on a cyclic peptide architecture, Nature 366 (1993) 324-327.
[4] Q. Hu, H. Li, L. Wang, H. Gu, C. Fan, DNA Nanotechnology-Enabled Drug Delivery Systems, Chem. Rev. 119(10) (2019) 6459-6506.
[5] A.O. Oluwole, B. Danielczak, A. Meister, J.O. Babalola, C. Vargas, S. Keller, Solubilization of Membrane Proteins into Functional Lipid-Bilayer Nanodiscs Using a Diisobutylene/Maleic Acid Copolymer, Angew. Chem. Int. Ed. 56 (2017) 1919-1924.

[6] M.C. Roco, Nanotechnology: convergence with modern biology and medicine, Curr. Opin. Biotechnol. 14 (2003) 337-346.

[7] A. Ivankin, L. Livne, A. Mor, G.A. Caputo, W.F. DeGrado, M. Meron, B. Lin, D. Gidalevitz, Role of the Conformational Rigidity in the Design of Biomimetic Antimicrobial Compounds, Angew. Chem. Int. Ed. 49 (2010) 8462-8465.

[8] S. Keller, I. Sauer, H. Strauss, K. Gast, M. Dathe, M. Bienert, Membrane-Mimetic Nanocarriers Formed by a Dipalmitoylated Cell-Penetrating Peptide, Angew. Chem. Int. Ed. 44 (2005) 5252-5255.

[9] M. Xiong, Z. Han, Z. Song, J. Yu, H. Ying, L. Yin, J. Cheng, Bacteria-Assisted Activation of Antimicrobial Polypeptides by a Random-Coil to Helix Transition, Angew. Chem. Int. Ed. 56 (2017) 10826-10829.

[10] V.S. Bystrov, I.K. Bdikin, A. Heredia, R.C. Pullar, E.D. Mishina, A.S. Sigov, A.L. Kholkin, Piezoelectricity and ferroelectricity in biomaterials: from proteins to self-assembled peptide nanotubes, Piezoelectric nanomaterials for biomedical applications, Springer, 2012.

[11] I.W. Hamley, Soft Matter Nanotechnology. From Structure to Function Edited by Xiadong Chen and Harald Fuchs, . Angew. Chem. Int. Ed. 55 (2016) 3262-3262.

[12] R.V. Ulijn, A.M. Smith, Designing peptide based nanomaterials, Chem. Soc. Rev. 37 (2008) 664-675.

[13] B. Claro, E. González-Freire, M. Calvelo, L.J. Bessa, E. Goormaghtigh, M. Amorín, J.R. Granja, R. Garcia-Fandiño, M. Bastos, Membrane targeting antimicrobial cyclic peptide nanotubes – an experimental and computational study, Colloids Surf. B - Biointerfaces (2020) 111349.

[14] S. Fernandez-Lopez, H.-S. Kim, E.C. Choi, M. Delgado, J.R. Granja, A. Khasanov, K. Kraehenbuehl, G. Long, D.A. Weinberger, K.M. Wilcoxen, M.R. Ghadiri, Antibacterial agents based on the cyclic d,l-[alpha]-peptide architecture, Nature 412 (2001) 452-455.

[15] J.D. Hartgerink, J.R. Granja, R.A. Milligan, M.R. Ghadiri, Self-Assembling Peptide Nanotubes, J. Am. Chem. Soc. 118 (1996) 43-50.

[16] H.S. Kim, J.D. Hartgerink, M.R. Ghadiri, Oriented Self-Assembly of Cyclic Peptide Nanotubes in Lipid Membranes, J. Am. Chem. Soc. 120 (1998) 4417-4424.

[17] S. Hernando-Amado, T.M. Coque, F. Baquero, J.L. Martínez, Defining and combating antibiotic resistance from One Health and Global Health perspectives, Nature Microbiol.4 (2019) 1432-1442.

[18] P. Kumar, J.N. Kizhakkedathu, S.K. Straus, Antimicrobial Peptides: Diversity, Mechanism of Action and Strategies to Improve the Activity and Biocompatibility In Vivo, Biomolecules 8 (2018) 24.

[19] O. Fleitas, O.L. Franco, Induced Bacterial Cross-Resistance toward Host Antimicrobial Peptides: A Worrying Phenomenon, Front. Microbiol. 7 (2016) 381-381.

[20] R.I. Lehrer, T. Ganz, Antimicrobial peptides in mammalian and insect host defence, Curr. Opin. Immunol. 11 (1999) 23-27.

[21] J.T. Mika, G. Moiset, A.D. Cirac, L. Feliu, E. Bardaji, M. Planas, D. Sengupta, S.J. Marrink, B. Poolman, Structural basis for the enhanced activity of cyclic antimicrobial peptides: the case of BPC194, Biochim. Biophys. Acta 1808(9) (2011) 2197-205.

[22] L.A. Calderon, A.M. Soares, R.G. Stábeli, Anuran Antimicrobial Peptides: an alternative for the development of nanotechnological based therapies for multi-drug-resistant infections, Signpost. Open J. Biochem. Biotech. 1 (2012) 1-11.

[23] C.D. Fjell, J.A. Hiss, R.E. Hancock, G. Schneider, Designing antimicrobial peptides: form follows function, Nat. Rev. Drug Discovery 11 (2011) 37-51.

[24] W.C. Wimley, K. Hristova, Antimicrobial peptides: successes, challenges and unanswered questions, J. Membr. Biol. 239 (2011) 27-34.

[25] Brogden, K. A. Antimicrobial peptides: pore formers or metabolic inhibitors in bacteria? Nature rev. microbiol. 3 (2005), 238.

[26] T. Silva, R. Adão, K. Nazmi, J.G.M. Bolscher, S.S. Funari, D. Uhríková, M. Bastos, Structural diversity and mode of action on lipid membranes of three lactoferrin candidacidal peptides, Biochim. Biophys. Acta, Biomembr. 1828 (2013) 1329-1339.

[27] V. Teixeira, M.J. Feio, M. Bastos, Role of lipids in the interaction of antimicrobial peptides with membranes, Prog. Lipid Res. 51 (2012) 149-177.

[28] R.J. Brea, C. Reiriz, J.R. Granja, Towards functional bionanomaterials based on self-assembling cyclic peptide nanotubes, Chem. Soc. Rev. 39 (2010) 1448-1456.

[29] R. García-Fandiño, M. Amorín, L. Castedo, J.R. Granja, Transmembrane ion transport by self-assembling α,γ-peptide nanotubes, Chem. Sci. 3 (2012) 3280-3285.

[30] W.S. Horne, C.M. Wiethoff, C. Cui, K.M. Wilcoxen, M. Amorin, M.R. Ghadiri, G.R. Nemerow, Antiviral cyclic d,l-α-peptides: Targeting a general biochemical pathway in virus infections, Bioorg. Med. Chem. 13 (2005) 5145-5153.

[31] R.-V. Nuria, H.L. Ozores, G. Arcadio, G.-F. Eva, F. Alberto, P. Michele, M.P. Juan, O. Juan, M. Javier, G.-F. Rebeca, A. Manuel, R.G. Juan, Membrane-Targeted Self-Assembling Cyclic Peptide Nanotubes, Curr. Trends Med. Chem. 14 (2014) 2647-2661.

[32] E. González-Freire, F. Novelli, A. Pérez-Estévez, R. Seoane, M. Amorín, J.R. Granja, Double orthogonal click reactions for the development of antimicrobial peptide nanotubes, Chem. Eur. J. 27 (2020) 3029 – 3038.

[33] K. Lohner, DSC studies on the modulation of membrane lipid polymorphism and domain organization by antimicrobial peptides, in: M. Bastos (Ed.) Biocalorimetry: foundations and contemporary approaches. CRC Press, Boca Raton 2016, chapter 9.

[34] F. Abrunhosa, S. Faria, P. Gomes, I. Tomaz, J.C. Pessoa, D. Andreu, M. Bastos, Interaction and Lipid-Induced Conformation of Two Cecropin−Melittin Hybrid Peptides Depend on Peptide and Membrane Composition, J. Phys. Chem., B 109(36) (2005) 17311-17319.

[35] R. Adão, K. Nazmi, J.G.M. Bolscher, M. Bastos, C- and N-truncated antimicrobial peptides from LFampin 265 – 284: Biophysical versus microbiology results, J. Pharm. BioAllied Sci.3(1) (2011) 60-69.

[36] M. Bastos, G. Bai, P. Gomes, D. Andreu, E. Goormaghtigh, M. Prieto, Energetics and Partition of Two Cecropin-Melittin Hybrid Peptides to Model Membranes of Different Composition, Biophys. J. 94 (2008) 2128-2141.

[37] J.G. Bolscher, R. Adão, K. Nazmi, P.A. van den Keybus, W. van 't Hof, A.V. Nieuw Amerongen, M. Bastos, E.C. Veerman, Bactericidal activity of LFchimera is stronger and less sensitive to ionic strength than its constituent lactoferricin and lactoferrampin peptides, Biochimie 91 (2009) 123-32.

[38] T. Silva, B. Claro, B.F.B. Silva, N. Vale, P. Gomes, M.S. Gomes, S.S. Funari, J. Teixeira, D. Uhríková, M. Bastos, Unravelling a Mechanism of Action for a Cecropin A-Melittin Hybrid Antimicrobial Peptide: The Induced Formation of Multilamellar Lipid Stacks, Langmuir 34 (2018) 2158-2170.

[39] V. Teixeira, M.J. Feio, L. Rivas, B.G. De la Torre, D. Andreu, A. Coutinho, M. Bastos, Influence of Lysine Nε-Trimethylation and Lipid Composition on the Membrane Activity of the Cecropin A-Melittin Hybrid Peptide CA(1−7)M(2−9), J. Phys. Chem., B 114 (2010) 16198-16208.

[40] L.Carpino, A.; G. Y. Han, 9-Fluorenylmethoxycarbonyl function, a new base-sensitive amino-protecting group. J. Am. Chem. Soc. 92 (1970) 5748-5749.

[41] J. M. Palomo, Solid-phase peptide synthesis: an overview focused on the preparation of biologically relevant peptides. RSC Advances 4 (2014) 32658-32672.

[42] P. Rovero, L. Quartara, G. Fabbri, Synthesis of cyclic peptides on solid support, Tetrahedron Letters, 32 (1991) 2639-2642.

[43] V. Dartois.; J. Sanchez-Quesada; E.Cabezas; Chi, E.; C. Dubbelde; C. Dunn; J. Granja; C. Gritzen; D. Weinberger; M. R. Ghadiri; Jr T. R. Parr, Systemic antibacterial activity of novel synthetic cyclic peptides. Antimicrob. Agents Chemother 49 (2005) 3302-10.

[44] S.J. Marrink, H.J. Risselada, S. Yefimov, D.P. Tieleman, A.H. de Vries, The MARTINI Force Field: Coarse Grained Model for Biomolecular Simulations, J. Phys. Chem. B 111 (2007) 7812-7824.

[45] L. Monticelli, S.K. Kandasamy, X. Periole, R.G. Larson, D.P. Tieleman, S.-J. Marrink, The MARTINI Coarse-Grained Force Field: Extension to Proteins, J. Chem. Theory Comput. 4 (2008) 819-834.

[46] D.H. de Jong, G. Singh, W.F.D. Bennett, C. Arnarez, T.A. Wassenaar, L.V. Schäfer, X. Periole, D.P. Tieleman, S.J. Marrink, Improved Parameters for the Martini Coarse-Grained Protein Force Field, J. Chem. Theory Comput. 9 (2013) 687-697.

[47] B. Claro, E. Goormaghtigh, M. Bastos, Attenuated total reflection Fourier transform infrared spectroscopy: a tool to characterize antimicrobial cyclic peptide/membrane interactions, Eur. Biophys. J., S. Ed. dedicated to COST Action CA15126, MOBIEU: Between atom and cell, 2020.

[48] S. Finger, A. Kerth, M. Dathe, A. Blume, The efficacy of trivalent cyclic hexapeptides to induce lipid clustering in PG/PE membranes correlates with their antimicrobial activity, Biochim. Biophys. Acta, Biomembr., 1848 (2015) 2998-3006.

[49] E. Sevcsik, G. Pabst, A. Jilek, K. Lohner, How lipids influence the mode of action of membrane-active peptides, Biochim. Biophys. Acta, Biomembr., 1768 (2007) 2586-2595.

[50] P. Garidel, A. Blume, Miscibility of phosphatidylethanolamine-phosphatidylglycerol mixtures as a function of pH and acyl chain length, Eur.Biophys. J., 28 (2000) 629-638.

[51] A. Arouri, M. Dathe, A. Blume, Peptide induced demixing in PG/PE lipid mixtures: A mechanism for the specificity of antimicrobial peptides towards bacterial membranes?, Biochim. Biophys. Acta, Biomembr., 1788 (2009) 650-659.

[52] R. Adão, P.F. Cruz, D.C. Vaz, F. Fonseca, J.N. Pedersen, F. Ferreira-da-Silva, R.M.M. Brito, C.H.I. Ramos, D. Otzen, S. Keller, M. Bastos, DIBMA nanodiscs keep α-synuclein folded, Biochim. Biophys. Acta, Biomembr., 1862 (2020) 183314.

[53] A. Blume, Temperature induced and isothermal phase transitions of pure and mixed lipid bilayer membranes studied by DSC and ITC, in: M. Bastos (Ed.) Biocalorimetry: foundations and contemporary approaches. CRC Press, Boca Raton 2016, chapter 6

[54] R. Adão, R. Seixas, P. Gomes, J.C. Pessoa, M. Bastos, Membrane structure and interactions of a short Lycotoxin I analogue, J. Pept. Sci., 14 (2008) 528-534.

[55] J.D. Hunter, Matplotlib: A 2D Graphics Environment, Comput. Sci. Eng., 9 (2007) 90-95.

[56] S.A. Tatulian, Structural Characterization of Membrane Proteins and Peptides by FTIR and ATR-FTIR Spectroscopy, in: J.H. Kleinschmidt (Ed.) Lipid-Protein Interactions: Methods and Protocols, Humana Press, Totowa, NJ, 2013.

[57] E. Goormaghtigh, V. Raussens, J.-M. Ruysschaert, Attenuated total reflection infrared spectroscopy of proteins and lipids in biological membranes, Biochim. Biophys. Acta, Rev. Biomembr, 1422 (1999) 105-185.

[58] L.K. Tamm, S.A. Tatulian, Infrared spectroscopy of proteins and peptides in lipid bilayers, Q. Rev. Biophys., 30 (1997) 365-429.

[59] B. Bechinger, J.-M. Ruysschaert, E. Goormaghtigh, Membrane helix orientation from linear dichroism of infrared attenuated total reflection spectra, Biophys. J., 76 (1999) 552-563.

Supplementary Material

Macromolecular assembly and membrane activity of antimicrobial *D,L*-α-Cyclic peptides

Bárbara Claro[1], Antonio Peón[1], Eva González-Freire[2], Erik Goormaghtigh[3], Manuel Amorín[2], Juan R. Granja[2], Rebeca Garcia-Fandiño[*1,2], Margarida Bastos[*1]

[1]CIQUP, Centro de Investigação em Química, Departamento de Química e Bioquímica, Faculdade de Ciências, Universidade do Porto, Porto, Portugal;

[2]Centro Singular de Investigación en Química Biolóxica e Materiais Moleculares (CiQUS), Departamento de Química Orgánica, Universidade de Santiago de Compostela, 15782 Santiago de Compostela, Spain

[3]Structure and Function of Biological Membranes, Center for Structural Biology and Bioinformatics, ULB, Brussels, Belgium

A.1. Methods

A.1.1. Cyclic peptide synthesis

HPLC (High-Performance Liquid Chromatography) semi-preparative purification was carried out on Hitachi D-7000 and Jasco LC-4000 with an Agilent Eclipse XDB-C18 column. HPLCcoupled with mass spectrometry (HPLC-MS) analysis were carried out on Agilent Technologies 1260 Infinity II associated with a 6120 Quadrupole LC-MS using an Agilent SB-C18 column.

Nuclear Magnetic Resonance (NMR) spectra were recorded on a Varian Inova 500 MHz. D2O, and H2O/D2O were the solvents employed to obtain the NMR. Chemical shifts are reported in ppm referenced to TMS (δ = 0.00 ppm) or to the solvent signals, HOD (δ = 4.79 ppm). Spin multiplicities are reported as a singlet (s), doublet (d), triplet (t), multiplet (m) or broad (b). The coupling constants (J) are given in Hz.

High Resolution mass determination (HR-MS) using ESI-MS were acquired in a Bruker MicroTof II mass spectrometer. Mass peaks are expressed in units of mass per unit of load (m/z).

FT-IR measurements were performed on a Perkin Elmer Spectrum Two ATR-FTIR, placing the sample directly on its diamond plate (neat) as a thin film.

Peptide *c*-[QRSKSWPgK] (CPR) was synthesized by manual Fmoc solid phase peptide synthesis, using Fmoc-Rink Amide resin (400 mg, loading 0.7 mmol/g), which was swelled in DCM (HPLC, 3 mL) for 1 hour in a peptide synthesis vessel prior synthesis. The removal of the Fmoc protecting group was carried out using a solution of piperidine in DMF (25%, 2 mL) for 15 min and then the solvent was filtered off, and the resin was washed with DMF (6 x 2 mL). The first amino acid was attached to the resin by its side chain. Therefore, protected glutamic acid (Fmoc-Glu-OAll, 3 equiv) in DMF (3 mL) was preactivated by treating with *N*-HBTU (3 equiv) followed by addition of DIEA (3 equiv) and the resulting mixture was manually shacked for 1 minute before addition to the resin. The coupling was carried out for 40 minutes by shaking the resulting mixture at room temperature, after which the resin solution was filtered off and then washed with DMF (3 x 2 mL). The procedures of deprotection and coupling were repeat for the other seven amino acids.

Once the linear peptide was completed, it was cyclized while it was still attached to the solid support. For that purpose, the allyl group was removed using a solution of [Pd(PPh$_3$)$_4$] prepared *in situ* as a result of mixing Pd(OAc)$_2$ (0.25 equiv) and PPh$_3$ (1.25 equiv) in dry DCM (2 mL) and stirring under Ar for 30 min. Then, phenylsilane (7 equiv) and 4-methylmorpholine (7 equiv) were added, and the resulting mixture was added over the resin under Ar and the mixture was shaked for 4-5 hours. After that, the

solution was filtered off and the resin washed with DCM (3 x 2 mL), DMF (3 x 2 mL), sodium diethyldithiocarbamate in DMF (0.5%, 2 x 2 mL, 15 min), DMF (2 x 2 mL), DIEA in DMF (10%, 2 x 2 mL) and finally DMF (3 x 2 mL). Then, the Fmoc was removed, as usual, by treating it with piperidine in DMF (25%, 1 x 2 mL, 30 min). The solution was removed, and the resin washed with DMF (6 x 2 mL), DIEA in DMF (5%, 3 x 2 mL), LiCl in DMF (0.8 M, 3 x 2 mL), DMF (3 x 2 mL). The cyclization reaction was carried out in the presence of N-TBTU (3 equiv) and DIEA (6 equiv) in DMF (3 mL) for 12 hours at room temperature. After this time, the resulting solution was filtered off and the resin washed DMF (3 x 2 mL) and DCM (3 x 2 mL).

Finally, the peptide was deprotected and cleaved from the resin by treating the resin at room temperature with a cleavage cocktail of TFA, TIS and H_2O (95:2.5:2.5, 1 mL per 50 mg of resin) for 2 hours.[6] Then, the mixture was filtered, the resin washed with TFA (1 mL) and the peptide was precipitated from the solution by addition of Et_2O (20 mL per 1 mL of TFA). After repeated washing with diethyl ether, the precipitate was dried under vacuum, dissolved in H_2O (5-10 mL depending on the peptide solubility), and purified by reverse phase semi-preparative high-performance liquid chromatography (RP-HPLC) using a C18 column [H_2O (0.1% TFA)/ ACN (0.1% TFA) 100:0 (5 min) and 100:0 to 25:75 H_2O (0.1% TFA)-ACN (0.1% TFA) (30 min)] to give 80 mg of **CPR** (30% yield). [R_t = 9.6 min, H_2O (0.1% TFA)/ACN (0.1% TFA) 100:0 (2 min) and 100:0 → 25:75 (19 min)]. **ESI-MS** m/z (%): 996.5 (20, $[M+1H]^+$), 499.0 (100, $[M+2H]^{2+}$), 333.1 (10, $[M+3H]^{3+}$). **HRMS** (ESI): Calcd for: $C_{45}H_{69}N_{15}O_{11}$, 996.5373; found, 996.5374. **FTIR (neat)**: v = 3279 (amide A), 1668, 1620 (amide I), 1535 cm^{-1} (amide II).

Synthesis of CPRT10:

For the preparation of this peptide, 1-azidodecane was immediately prepared before the click reaction on the solid support. Therefore, NaN_3 (6 equiv) and the corresponding 1-bromodecane (6 equiv) were mixed in DMF (1 mL) for 24 hours at 40 °C and the resulting 1-azidodecane was used without further purification. Then, DMF (0.2 mL), piperidine (0.3 mL), 1-azidodecane (6 equiv), CuI (5 equiv), sodium ascorbate (5 equiv), and DIEA (10 equiv) were added to 150 mg of peptide modified resin and the mixture was purged with argon for 5 minutes. The resulting reaction mixture was shaken at room temperature for 36 hours. After the reaction was completed, the supernatant solution was removed and the resin was washed with DCM (3 x 2 mL), DMF (3 x 2 mL), piperidine in DMF (20%, 2 x 3 mL, 15 min), DMF (3 x 2 mL), MilliQ H_2O (2 x 2 mL, 10 min), DMF (3 x 2 mL), and DCM (3 x 2 mL), prior to cleavage. The resulting powder was

---

[6] D. A. Pearson, M. Blanchette, M. L. Baker, C. A. Guindon, Tetrahedron Lett. 30 (1989) 2739–2742.

solubilized in H_2O and purified in reverse phase HPLC [Phenomenex Luna C18 (2) 100A column, H_2O (0.1% TFA)/ ACN (0.1% TFA) 100:0 (5 min), 100:0 → 25:75 (30 min) to provide 21 mg of **CPRT10** (17% yield). [Agilent SB-C18 column, H_2O (0.1% TFA)/ACN (0.1% TFA) 100:0 (2 min) and 100:0 → 25:75 (19 min)]. [R_t = 14.5 min, H_2O (0.1% TFA)/ACN (0.1% TFA) 100:0 (2 min) and 100:0 → 25:75 (19 min)]. **MS** (ESI, H_2O): 1180.7 (20, $[M+1H]^+$), 590.6 (100, $[M+2H]^{2+}$), 394.1 (25, $[M+3H]^{3+}$). **HRMS** (ESI): Calcd for: $C_{55}H_{90}N_{18}O_{11}Na$, 1201.6926; found 1201.6929. **FTIR (neat)**: v = 3279 (amide A), 1664, 1627 (amide I), 1539 cm^{-1} (amide II).

Synthesis of CPRT14:

Following the general protocol of the SPPS, **CPR** was grown and cycled in the solid support. Then, the click chemistry was carried out with tetradecyl azide and, finally, the cleavage of the resin. The resulting powder was solubilized in H_2O and purified in reverse phase HPLC [Phenomenex Luna C18 (2) 100A column, H_2O (0.1% TFA)/ ACN (0.1% TFA) 100:0 → 100:0 (0 → 5 min), 100:0 → 25:75 (5 → 35 min) to provide 16 mg of **CPRT14** (13% yield). [Agilent SB-C18 column, H_2O (0.1% TFA)/ACN (0.1% TFA). 100:0 → 100:0 (2 min) and 100:0 → 25:75 (19 min)]. [R_t = 16.8 min, H_2O (0.1% TFA)/ACN (0.1% TFA) 100:0 (2 min) and 100:0 → 25:75 (19 min)]. **MS** (ESI, H_2O): 1235.7 (15, $[M+1H]^+$), 618.5 (100, $[M+2H]^{2+}$), 412.8 (22, $[M+3H]^{3+}$). **HRMS** (ESI): Calcd for: $C_{59}H_{98}N_{18}O_{11}Na$ $[M+Na]^+$: 1257.7554; found 1257.7555. **FTIR (neat)**: v = 3273 (amide A), 1664, 1620 (amide I), 1539 cm^{-1} (amide II).

Peptide CPR: *c*-[R̲SK̲SW̲XK̲Q]
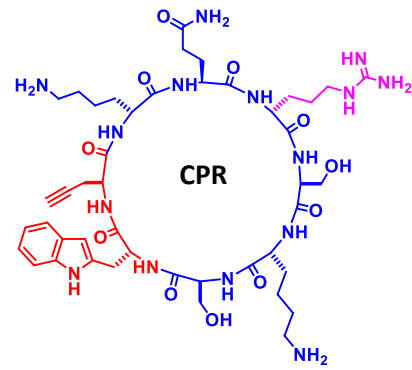
RP-HPLC: [Agilent SB-C18 column, H_2O (0.1% TFA)/ACN (0.1% TFA) 100:0 (2 min) and 100:0 → 25:75 (19 min)] (R_t = 9.6 min). Absorbance at 222 nm.
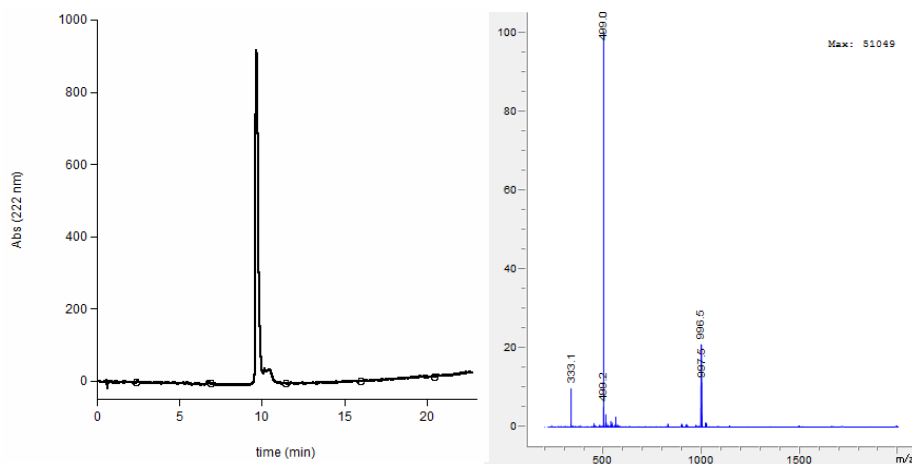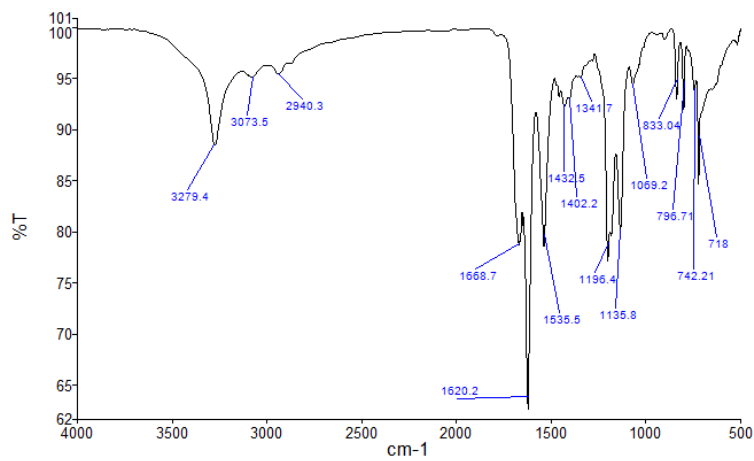
FT-IR (neat, 298 K)

Peptide CPRT10: *c*-[RSKSWX^{C10}KQ]
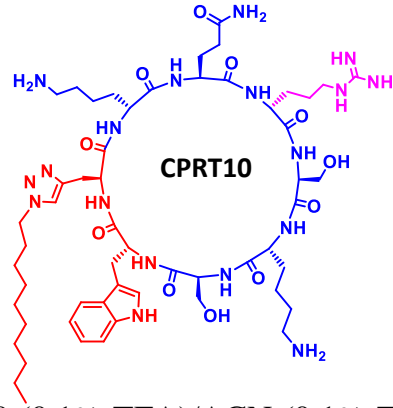
RP-HPLC: [Agilent SB-C18 column, H$_2$0 (0.1% TFA)/ACN (0.1% TFA) 100:0 (2 min) and 100:0 → 25:75 (19 min)] (R_t = 14.5 min). Absorbance at 222 nm.
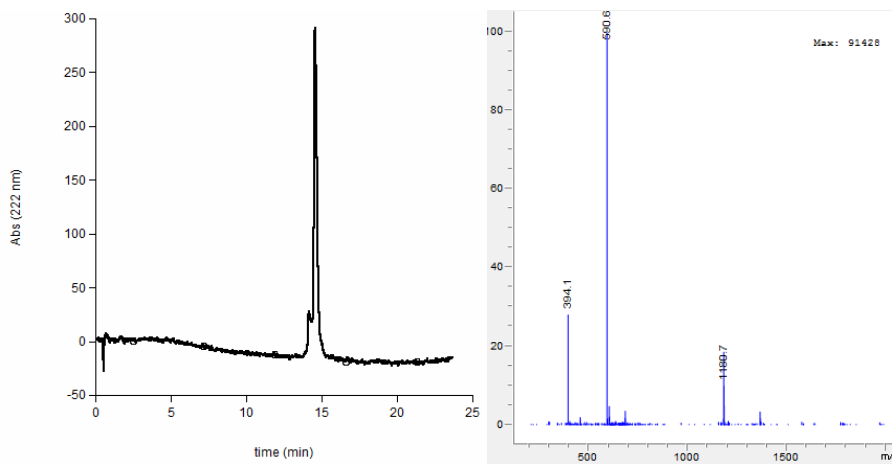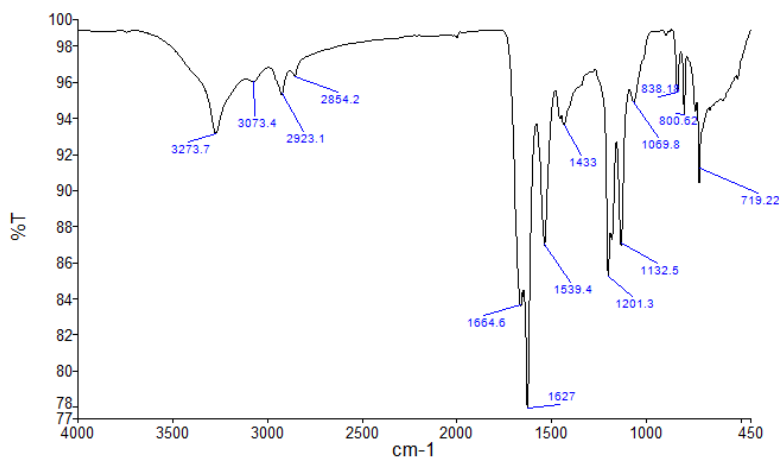
FT-IR (neat, 298 K):

¹H-NMR: (2 mM, H₂O/D₂O, 300 K, 500 MHz)
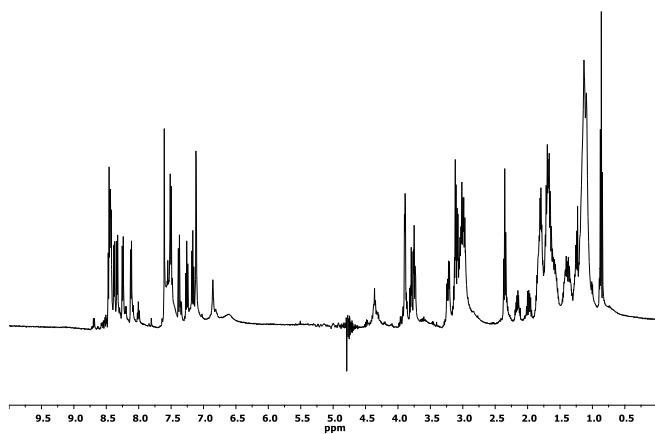
TOCSY: (2 mM, H₂O/D₂O, 300 K, 500 MHz)
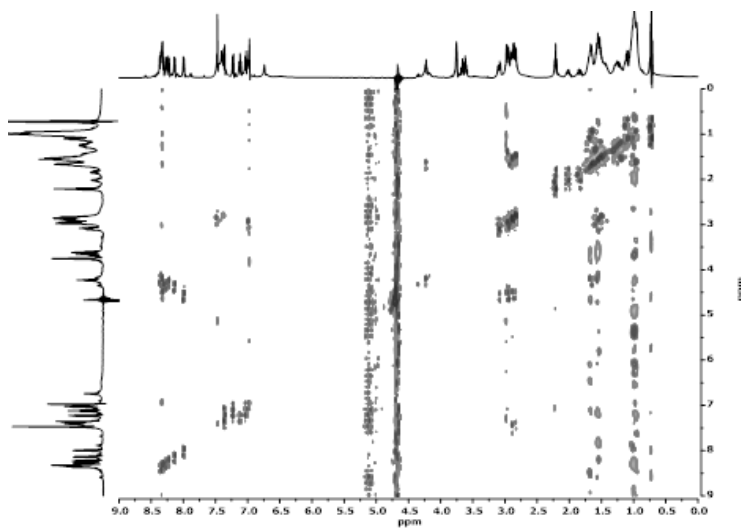
COSY: (2 mM, H₂O/D₂O, 300 K, 500 MHz)
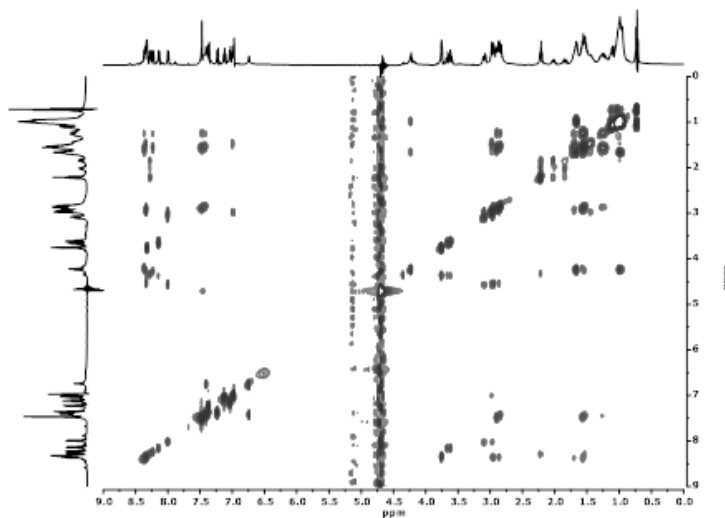
Peptide CPRT14: *c*-[RSKSWX^{C14}KQ]
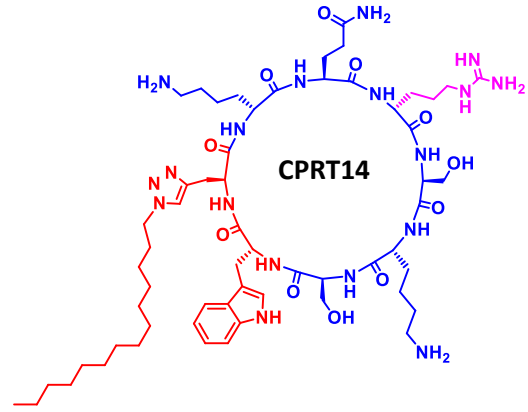
RP-HPLC: [Agilent SB-C18 column, H_2O (0.1% TFA)/ACN (0.1% TFA) 100:0 (2 min) and 100:0 → 25:75 (19 min)] (R_t = 16.8 min). Absorbance at 222 nm.
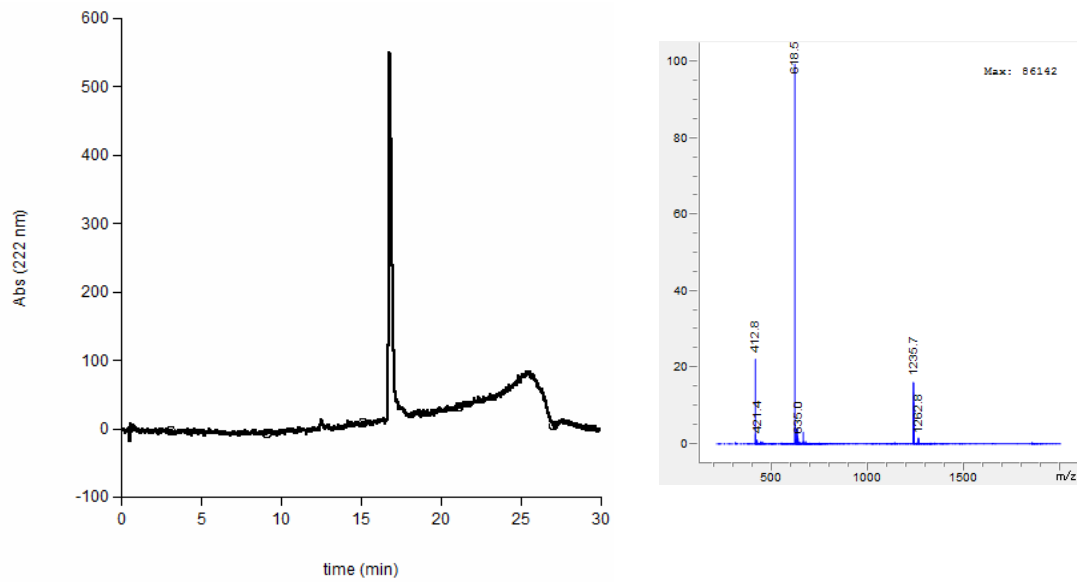
FT-IR (neat, 298 K):
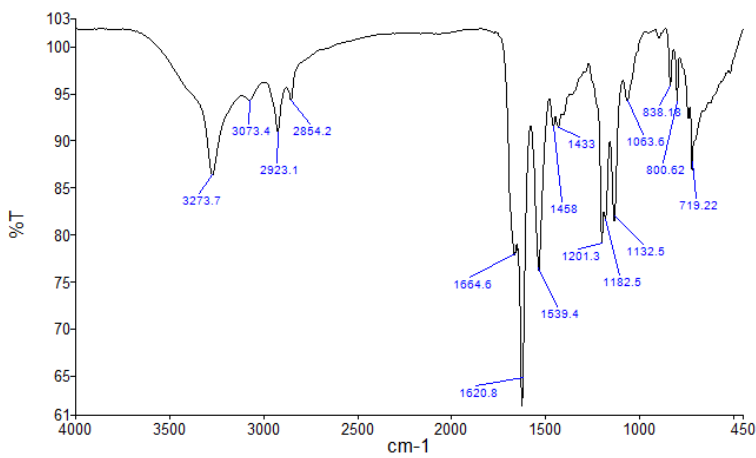
¹H-NMR: (2 mM, H₂O/D₂O, 300 K, 500 MHz)
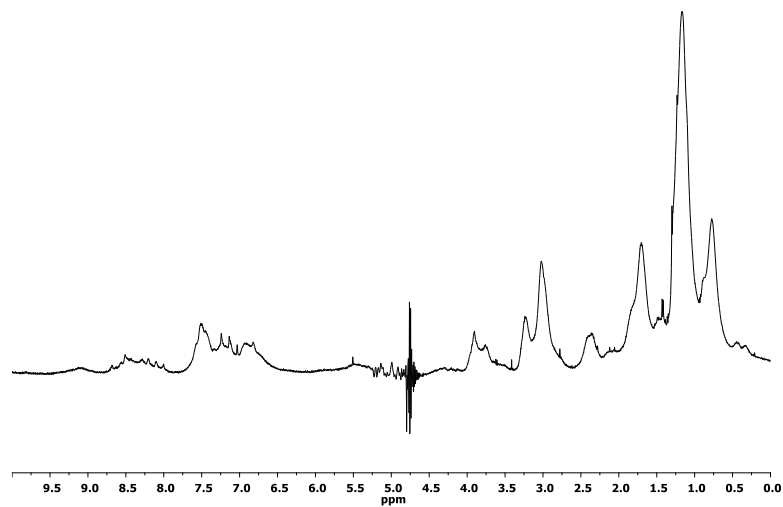
A.1.2. Preparation of Liposomes

DMPE, DMPG and DMPC and their mixtures at different molar ratios were weighted in appropriate amounts and dissolved in a round bottom flask in an azeotropic mixture of chloroform/methanol (87.4:12.6 %(v/v)). A lipid film was obtained by evaporating the azeotropic mixture (either under vac-uum at a rotary evaporator at 70 °C for DSC or under a flux of N_2 for ATR-FTIR) and then kept over-night under high vacuum (< 10 mbar) to remove any trace of the organic solvents.

The lipid film was then hydrated for 30 minutes with a previously heated buffer HEPES (10 mM HEPES, 150 mM NaCl, 0.02% NaN3, 1 mM EDTA, pH 7.45) - for DSC experiments - or with water - for ATR-FTIR experiments - at *ca*. 10 °C above the gel-to-liquid crystalline phase transition temperature (T_m). Thereafter the suspension underwent several cycles of vortex/incubation, at a temperature above Tm, creating a multilamellar vesicles suspension (MLVs). The MLVs were frozen in liquid nitrogen and thawed above T_m, a cycle repeated 3 times. Large unilamellar vesicles (LUVs) were then obtained through extrusion of the MLVs, using two staked polycarbonate filters with a pore diameter of 100 nm (Whatman, Nucleopore (NJ, USA)), in either a 10 mL stainless steel extruder from Lipex Biomembranes Inc. (Vancouver, Canada), under inert (N2) atmosphere (DSC samples), or with a manually powered extruder of 500 μL capacity (Liposofast-Basic (BPS, UK)) (ATR-FTIR samples. Three sequences of extrusion/vortex/freeze-thaw were made, followed by 15-20 passages through the extruder. The final phospholipid concentration was determined using a modified version of the Bartlett phosphate assay[7].

The average particle size of the LUVs was measured by dynamic light scattering (DLS) on a Malvern Zetasizer Nano ZS from Malvern Instruments (Malvern, UK). The measurements were performed above the transition temperature (T_m) at a total lipid concentration of 0.1 mM, using a He-Ne laser (wavelength 633 nm) as a source of incident light, and operating at a scattering angle of 173°. The pre-pared samples were monodisperse, with a particle size of ~110 nm, and a polydispersity index (PDI) always <0.1. The Buffer properties (refractive index, density and viscosity) to be used in the DLS measurements were determined at 37°C and 60°C (Refractive index in an Anton Paar, Abbemat 300, density in an Anton Paar, DMATM 4500M and viscosity in a Lovis 2000ME).

---

[7] G.R. Bartlett, Phosphorus assay in column chromatography, J. Biol. Chem. 234 (1959) 466-468.

A.2. DSC

A.2.1. Methodology

In brief, prior to sample loading, blank experiments with buffer in both cells were performed, for subsequent blank correction. The temperature scans were performed at a scanning rate of 60 °C/hour, and three successive heating scans for each sample were always performed, against buffer in the reference cell. The DSC profiles shown are all for the second scan, as the first scan usually differs from following ones because the peptides are added to the liposome suspension at room temperature just prior to the DSC experiment, and the mixtures were not incubated above transition temperature (T_m) prior to measurements. As all samples studied here provided repetitive scans after the second, the results shown here are for the second scan. All the samples were prepared immediately before each measurement by adding the desired amount of the CPs to the LUVs suspension and transferred to the measuring cell, to guarantee that all samples had the same thermal history. The T_m and the transition enthalpy change ($\Delta_{trans}H$) were obtained by integration of the blank corrected heat capacity vs temperature curve (Cp vs. temperature), using a linear baseline. In cases where a peak splitting was apparent, the curve was deconvoluted and the parameters for each peak are presented.

Table S1. Thermodynamic parameters for the gel to liquid crystalline phase transitions (T_m, $\Delta_{trans}H$) that were obtained from the thermograms represented in Figure 2, for the different lipid systems and peptides here studied, at different L:P molar ratios.

	L:P	Peak number	T_m/°C	$\Delta_{trans}H$/(kJ/mol)	L:P	Peak number	T_m/°C	$\Delta_{trans}H$/(kJ/mol)	L:P	Peak number	T_m/°C	$\Delta_{trans}H$/(kJ/mol)
			CPR				**CPRT10**				**CPRT14**	
DMPG	1:0	1	23.4	23	1:0	1	23.2	27	1:0	1	23.2	27
	41:1	1	23.3	22	27:1	1	22.9	30	26:1	1	22.2	34
		2	25.6	1								
	20:1	1	23.2	19	22:1	1	23.3	15	22:1	1	23.3	10
		2	25.1	7		2	22.7	15		2	21.2	22
	15:1	1	23.0	13	14:1	1	23.6	11	12:1	1	20.1	21
		2	24.9	12		2	22.6	20		2	22.2	14
DMPE:DMPG(1:9)	1:0	1	25.0	30	1:0	1	24.8	31	1:0	1	25.0	30
	38:1	1	24.9	14	35:1	1	24.6	31	35:1	1	24.6	23
		2	26.3	18						2	22.0	5
	26:1	1	25.0	12	17:1	1	25.1	17	19:1	1	24.4	18
		2	26.6	21		2	20.2	11		2	21.7	17
	18:1	1	25.0	12	11:1	1	24.6	19	12:1	1	23.6	17
		2	26.6	21		2	18.2	11		2	20.5	15
										3	17.7	2
DMPE:DMPG (1:1)	1:0	1	38.8	25	1:0	1	38.0	30	1:0	1	38.0	31
	40:1	1	39.1	32	34:1	1	40.5	24	38:1	1	39.4	26
										2	20.2	2
	20:1	1	39.6	29	17:1	1	41.7	19	19:1	1	40.7	22
						2	23.5	2		2	19.5	22.0
	14:1	1	39.8	30	10:1	1	42.2	16	12:1	1	40.6	18
						2	28.2	5		2	19.9	6
DMPE (MLVs)	1:0	1	50.3	25	1:0	1	50.3	25	1:0	1	50.3	25
	47:1	1	50.0	24	46:1	1	50.2	24	46:1	1	50.0	16
	27:1	1	50.2	17	24:1	1	50.2	24	26:1	1	50.0	16
										2	42.7	3
	16:1	1	50.2	21	17:1	1	50.1	28	16:1	1	50.1	17
						2	48.7	3		2	42.0	2

Notes: 1. The estimated uncertainties in the thermodynamic parameters are for the same series: ±0.3 °C for T_m and ± 1 kJ/mol for $\Delta_{trans}H$, whereas between series they are ±1 °C for T_m and ± 3 kJ/mol for $\Delta_{trans}H$.

In some cases two or three peaks are apparent, and in those cases they are evaluated separately.
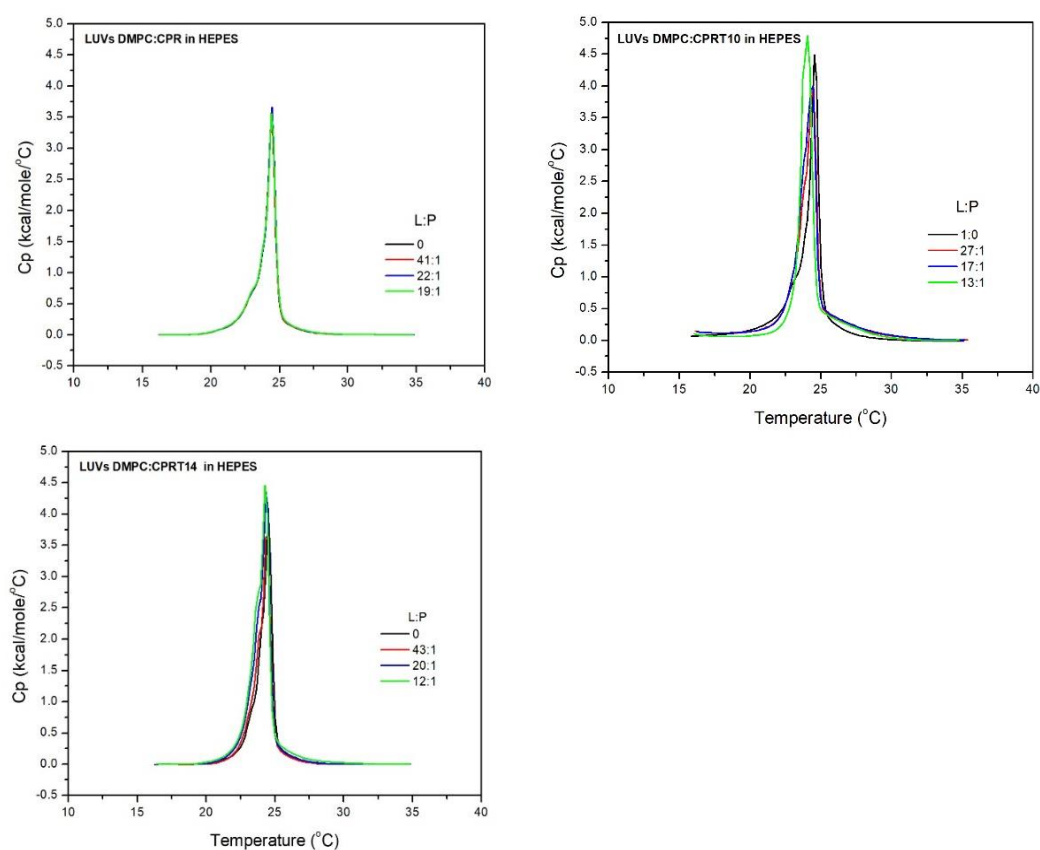
Fig. S1. DSC curves for mixtures of the three peptides **CPR** (A), **CPRT10** (B) and **CPRT14** (C) with model membranes of DMPC to test the toxicity of the three peptides. The molar ratios of lipid to peptide (L:P) for each curve are shown in each plot. The results are all for the second scan.

Table S2. Thermodynamic parameters T_m and $\Delta_{trans}H$ and for the gel to liquid crystalline phase transition for DMPC in the absence and presence of the CPs at various L:P molar ratios.

		CPR			CPRT10			CPRT14	
	L:P	T_m/°C	ΔH/(kJ/mol)	L:P	T_m/°C	ΔH/(kJ/mol)	L:P	T_m/°C	ΔH/(kJ/mol)
DMPC	**1:0**	24.5	19	**1:0**	24.5	28	**1:0**	24.5	20
	36:1	24.4	19	**27:1**	24.5	32	**43:1**	24.5	19
	27:1	24.5	19	**22:1**	24.5	34	**20:1**	24.4	24
	17:1	24.4	19	**13:1**	24.1	31	**12:1**	24.4	26
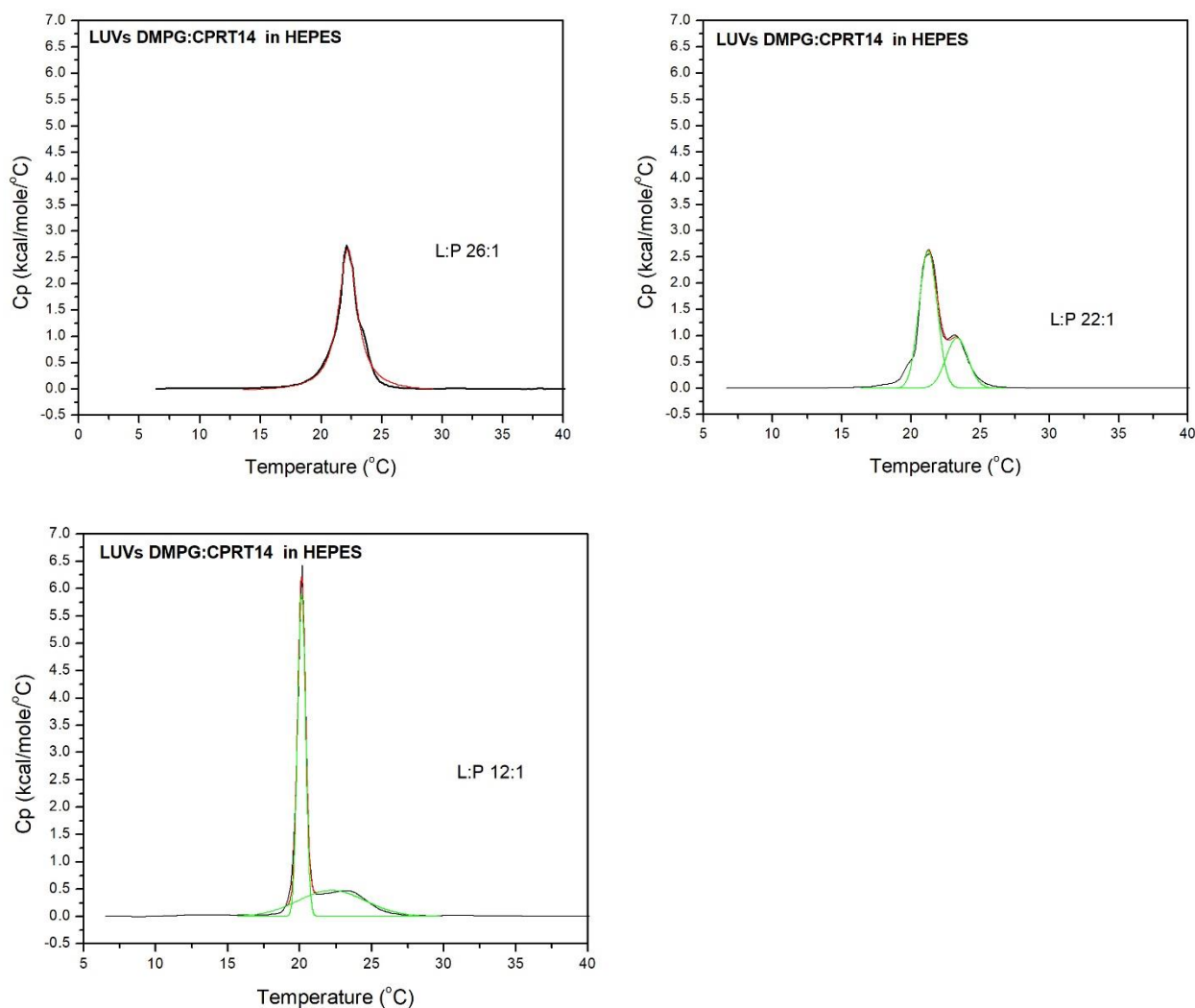
Fig. S2. DSC curves for mixtures of **CPRT14** with model membranes of DMPG. The molar ratios of lipid to peptide (L:P) for each curve are shown in each plot, and the green curves represent the peak deconvolution. The results shown are all for the second scan.

A3. CG-MD

A.3.1. Methodology

Coarse-grained molecular dynamics (CG-MD) simulations of **CPR**, **CPRT10** and **CPRT14** interacting with membrane models of DMPE, DMPG and their mixtures were carried out. The CG parameters used for CPs were those corresponding to the polarizable MARTINI force field (Martini v2.2 polar amino acids and polarizable water)[8], together with the use of distance restraints between all the backbone particles to maintain the cyclic morphology.

In a preliminary work with related peptides[9] we assumed that the CPs self-assembled into peptide nanotubes at the membrane, introducing restraints to maintain the tubular structure and leaving the CPs free once the nanotube was inserted. This approximation allows the quick insertion and reorientation of the SCPNs into the lipid bilayer at the cost of losing spontaneity in the self-assembling process, which could lead to important consequences: length of the nanotube, prevalence of some rotamer conformers, etc. Therefore, in present work, CG-MD simulations were carried out starting from a 'soup' of randomly distributed CP units and studying their spontaneous self-assembly in the presence of a membrane of different compositions, and approach also considered by Tarek *et al*[10].

The CG parameters used for CPs were those corresponding to the polarizable MARTINI force field (Martini v2.2 polar amino acids and polarizable water)[3], together with the use of distance restraints between all the backbone particles to maintain the cyclic morphology (Fig. 1). The CG topologies for the CPs were built using the martinize.py tool[11] . The bonds and charges of the CPs were manually modified to create the cycles. P5 type particles were used for describing the backbone of each amino acid. With the objective of maintaining the cycle open, the P5-P5-

---

[8] a) S.J. Marrink, H.J. Risselada, S. Yefimov, D.P. Tieleman, A.H. de Vries, The MARTINI Force Field: Coarse Grained Model for Biomolecular Simulations, J. Phys. Chem. B 111 (2007) 7812-7824; b) L. Monticelli, S.K. Kandasamy, X. Periole, R.G. Larson, D.P. Tieleman, S.-J. Marrink, The MARTINI Coarse-Grained Force Field: Extension to Proteins, J. Chem. Theory Comput. 4 (2008) 819-834.

[9] B. Claro, E. González-Freire, M. Calvelo, L.J. Bessa, E. Goormaghtigh, M. Amorín, J.R. Granja, R. Garcia-Fandiño, M. Bastos, Membrane targeting antimicrobial cyclic peptide nanotubes – an experimental and computational study, Colloids Surf., B (2020) 111349

[10] A. Khalfa, M. Tarek, On the Antibacterial Action of Cyclic Peptides: Insights from Coarse-Grained MD Simulations, J. Phys. Chem. B, 114 (2010) 2676-2684.

[11] D.H. de Jong, G. Singh, W.F.D. Bennett, C. Arnarez, T.A. Wassenaar, L.V. Schäfer, X. Periole, D.P. Tieleman, S.J. Marrink, Improved Parameters for the Martini Coarse-Grained Protein Force Field, J. Chem. Theory Comput. 9 (2013) 687-697.

P5 angle was described using a harmonic angle potential with θ_0 of 135° and a force constant of 627 kJ·mol^{-1}·rad^{-2}. In order to keep the planarity of the lateral chains, the P51-P52-P53-(lateral chain particle)^2 improper dihedral was described using a harmonic potential with $\xi_0 = 180°$ and a force constant of 418 kJ·mol^{-1}·rad^{-2}.

The CPs structures were obtained from previous models[4]. The membrane structures were prepared using the CHARMM-GUI Membrane Builder[12]. The parameters for DMPC, DMPE and DMPG were the standard ones provided from the Martini developers (Martini v2.0 lipids)[3a] [13]. Four membrane models composed of different mixtures of DMPE, DMPE:DMPG (1:1), DMPE:DMPG (1:9) and DMPG were mixed with 160 units of the corresponding peptides (CPR, CPRT10 and CPRT14), leading to a molar ratio of lipid to peptide (3:1). All membranes used were also simulated in absence of peptides, for comparison. The CG-MD calculations were carried out at 37 °C (310.15 K) using the V-rescale thermostat[14] and the Parrinello−Rahman

[12] a) S. Jo, T. Kim, W. Im, Automated Builder and Database of Protein/Membrane Complexes for Molecular Dynamics Simulations, PLOS ONE 2 (2007) e880; b) S. Jo, T. Kim, V.G. Iyer, W. Im, CHARMM-GUI: A web-based graphical user interface for CHARMM, J. Comput. Chem. 29 (2008) 1859-1865; c) S. Jo, J.B. Lim, J.B. Klauda, W. Im, CHARMM-GUI Membrane Builder for Mixed Bilayers and Its Application to Yeast Membranes, Biophys. J. 97 (2009) 50-58; d) J. Lee, X. Cheng, J.M. Swails, M.S. Yeom, P.K. Eastman, J.A. Lemkul, S. Wei, J. Buckner, J.C. Jeong, Y. Qi, S. Jo, V.S. Pande, D.A. Case, C.L. Brooks, A.D. MacKerell, J.B. Klauda, W. Im, CHARMM-GUI Input Generator for NAMD, GROMACS, AMBER, OpenMM, and CHARMM/OpenMM Simulations Using the CHARMM36 Additive Force Field, J. Chem. Theory Comput 12 (2016) 405-413; e) J. Lee, D.S. Patel, J. Ståhle, S.-J. Park, N.R. Kern, S. Kim, J. Lee, X. Cheng, M.A. Valvano, O. Holst, Y.A. Knirel, Y. Qi, S. Jo, J.B. Klauda, G. Widmalm, W. Im, CHARMM-GUI Membrane Builder for Complex Biological Membrane Simulations with Glycolipids and Lipoglycans, J. Chem. Theory Comput. 15(2019) 775-786; f) E.L. Wu, X. Cheng, S. Jo, H. Rui, K.C. Song, E.M. Dávila-Contreras, Y. Qi, J. Lee, V. Monje-Galvan, R.M. Venable, J.B. Klauda, W. Im, CHARMM-GUI Membrane Builder toward realistic biological membrane simulations, J. Comput. Chem., 35 (2014) 1997-2004.

[13] a) S.J. Marrink, A.H. de Vries, A.E. Mark, Coarse Grained Model for Semiquantitative Lipid Simulations, J. Phys. Chem. B, 108 (2004) 750-760; b) T.A. Wassenaar, H.I. Ingólfsson, R.A. Böckmann, D.P. Tieleman, S.J. Marrink, Computational Lipidomics with insane: A Versatile Tool for Generating Custom Membranes for Molecular Simulations, J. Chem. Theory Comput., 11 (2015) 2144-2155.

[14] G. Bussi, D. Donadio, M. Parrinello, Canonical sampling through velocity rescaling, J. Chem. Phys., 126 (2007) 014101.

barostat[15] with semi-isotropic pressure coupling. A time step of 20 fs was used for all simulations. In each case, all simulations were run at least within 2 μs and using GROMACS version 2019.3[16]. The analysis was carried out with GROMACS' tools and home-made scripts.
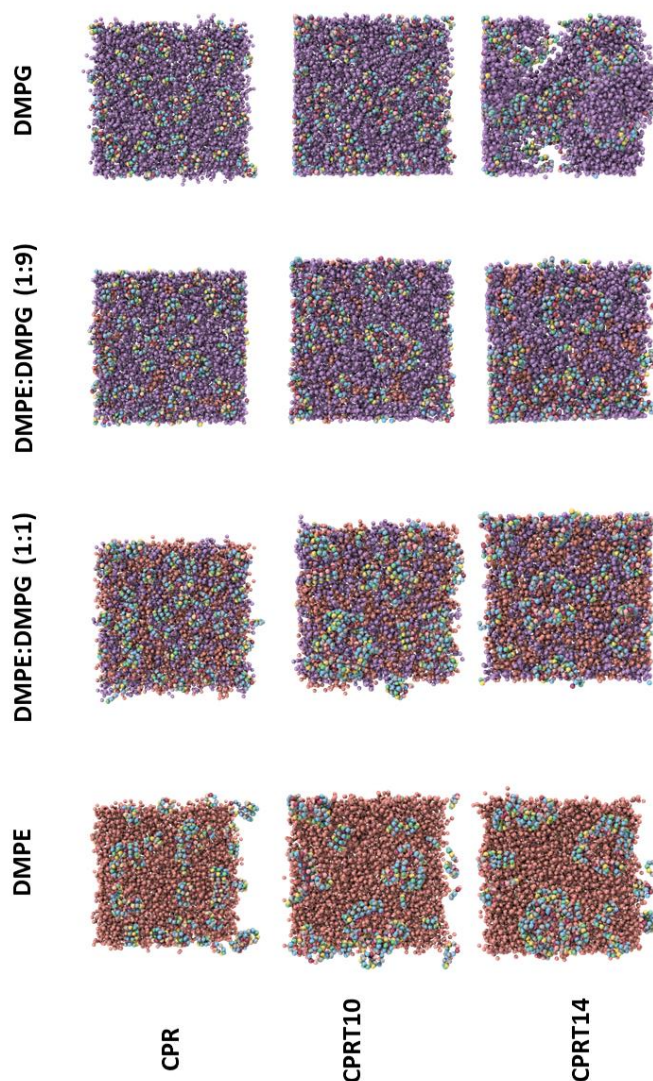
Fig. S3. Top view of the last snapshots at t=2 μs from the CG-MD simulation of 160 units of **CPR**, **CPRT10** and **CPRT14**, respectively in the presence of different membrane compositions: DMPE, DMPE:DMPG (1:1), DMPE:DMPG (1:9) and DMPG. DMPE lipids are represented in orange whereas DMPG lipids are represented in purple. Each residue in the CP is represented in a different color. Water molecules have been removed for clarity.

---

[15] M. Parrinello, A. Rahman, Polymorphic transitions in single crystals: A new molecular dynamics method, J. Appl. Phys., 52 (1981) 7182-7190.

[16] D.v.d.S. M.J. Abraham, E. Lindahl, B. Hess, and the GROMACS development team, GROMACS User Manual version 2019.3, 2019.

DMPE

DMPE:DMPG(1:1)

DMPE:DMPG(1:9)

DMPG
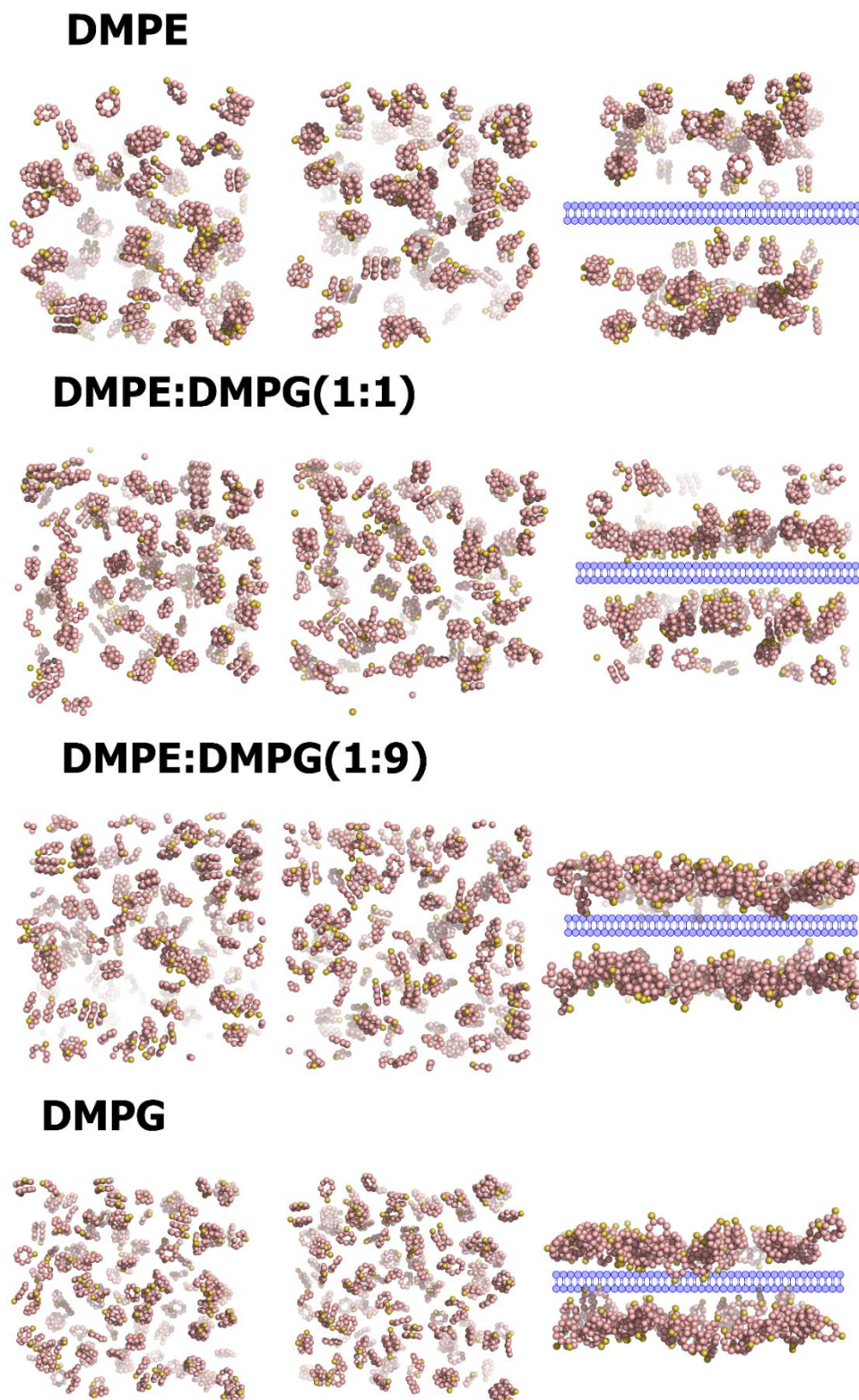
Fig. S4. Last frame (t=2 μs) of the MD simulations of 160 units of **CPR** in different membrane compositions. The Pg group is represented in yellow, all other amino acid residues in pink. Water and lipids are removed for clarification. The membrane drawing is just to help the visualization.

DMPE

DMPE:DMPG(1:1)

DMPE:DMPG(1:9)

DMPG
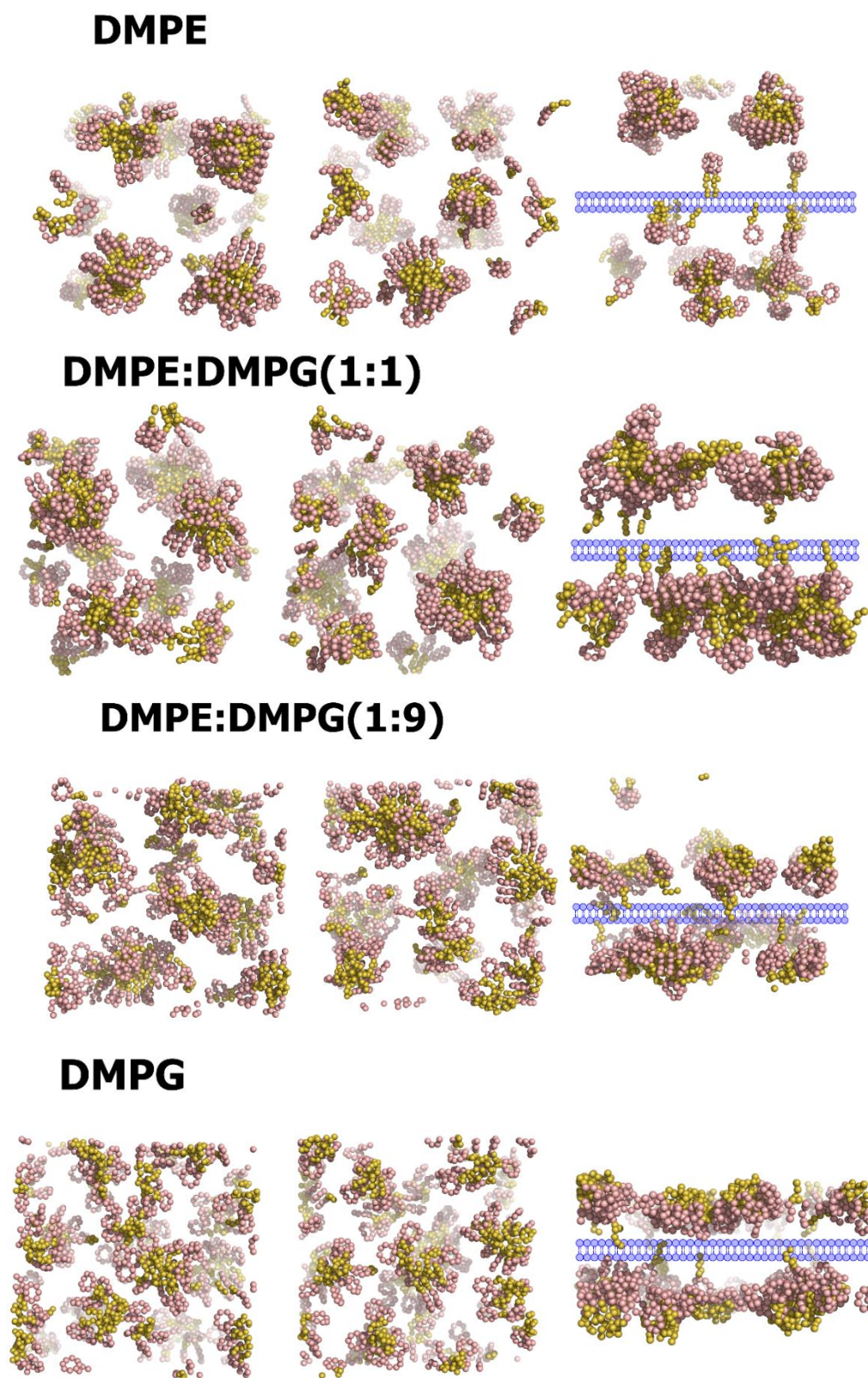
Fig. S5. Last frame (t=2 μs) of the MD simulations of 160 units of **CPRT10** in different membrane compositions. The C10-alkyl tail is represented in yellow, all other amino acid residues in pink. Water and lipids are removed for clarification. The membrane drawing is just to help the visualization.
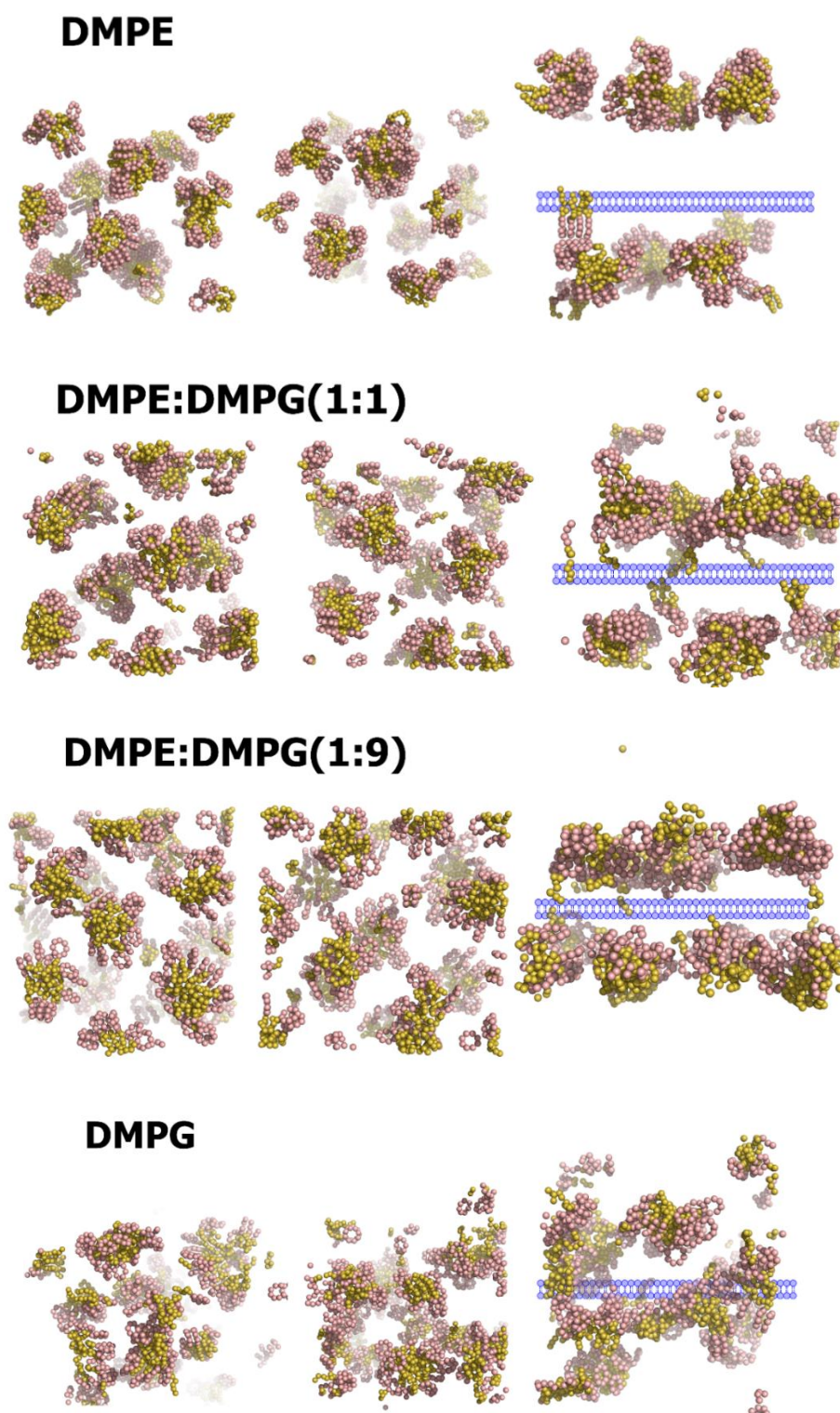
Fig. S6. Last frame (t=2 μs) of the MD simulations of 160 units of **CPRT14** in different membrane compositions. The C14-alkyl tail is represented in yellow, all other amino acid residues in pink. Water and lipids are removed for clarification. The membrane drawing is just to help the visualization.

DMPE:DMPG 1:1

t=2 microseconds   t=20 microseconds
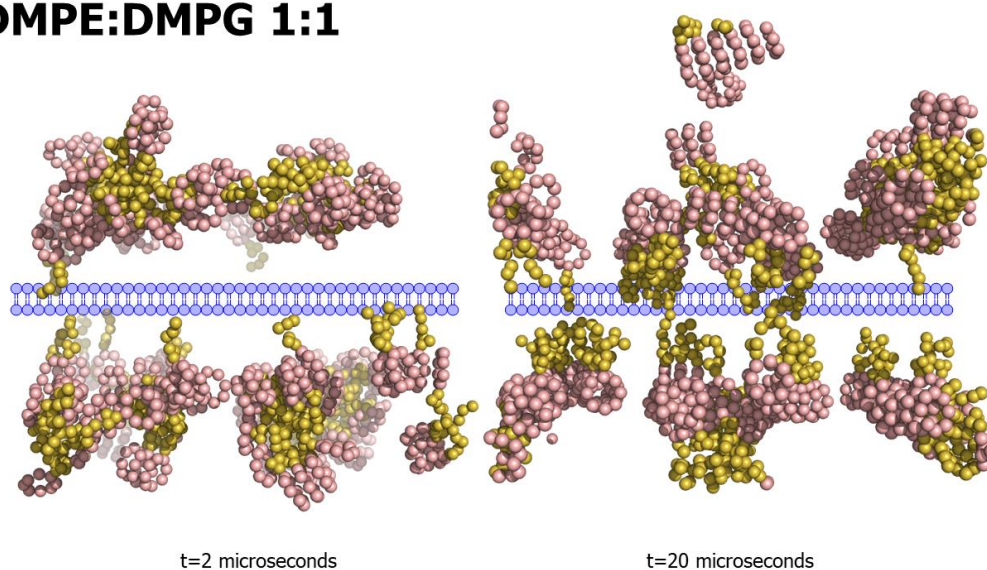
Fig. S7. MD simulations of 160 units of system **CPRT10** in DMPE:DMPG(1:1) at different times (2 microseconds and 20 microseconds). The C10-alkyl tail is represented in yellow, all other amino acid residues in pink. Water and lipids are removed for clarification. The membrane drawing is just to help the visualization.

DMPE:DMPG 1:1

t=2 microseconds   t=20 microseconds
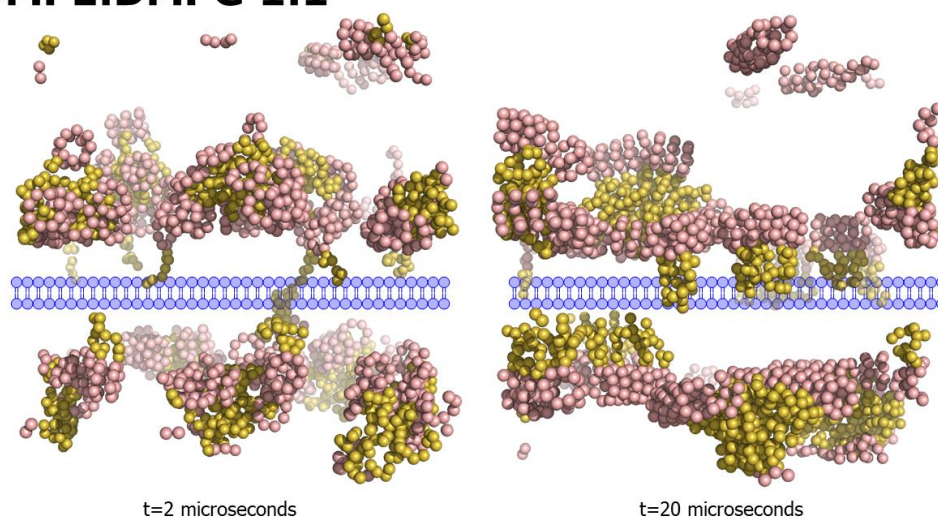
Fig. S8. MD simulations of 160 units of system **CPRT14** in DMPE:DMPG(1:1) at different times (2 microseconds and 20 microseconds). The C14-alkyl tail is represented in yellow, all other amino acid residues in pink. Water and lipids are removed for clarification. The membrane drawing is just to help the visualization.

A4. ATR-FTIR

A.4.1. Methodology

The incidence angle was 45° and 32 scans were recorded for each spectrum between 4000 and 550 cm^{-1}, at a resolution of 4 cm^{-1}. The dichroic spectra were measured with an adapted grid polarizer KRS-5 from Specac.

All samples were prepared in salt-free water with the pH adjusted to 7.45 with a pH meter Five Easy and an electrode LE438 from Mettler Toledo. The mixtures of CPs and lipids were mixed at appropriate Lipid:Peptide (L:P) molar ratios and incubated at ca 10 °C above the transition temperature of the respective lipid system for 30 min. A 2 µL sample was deposited on the diamond crystal and the solvent was slowly evaporated under a gentle N_2 flux to spread the liquid over the useful crystal surface, making an oriented multilayer film. While evaporating, capillary forces flatten the membranes, which spontaneously form these oriented multilayer arrangements[17].

The background spectra were recorded in air and all the measurements were carried out at room tem-perature. All spectra were analyzed with the program "Kinetics Spectra"[18].

---

[17] U.P. Fringeli, H.H. Günthard, Infrared membrane spectroscopy, Membrane spectroscopy, Springer 1981, 270-332.

[18] E. Goormaghtigh, J.M. Ruysschaert, R. Brasseur, Polarized attenuated total reflection spectroscopy as a tool to investigate the conformation and orientation of membrane components, Molecular description of biological membranes components by computer aided conformational analysis, (1990) 285-332.
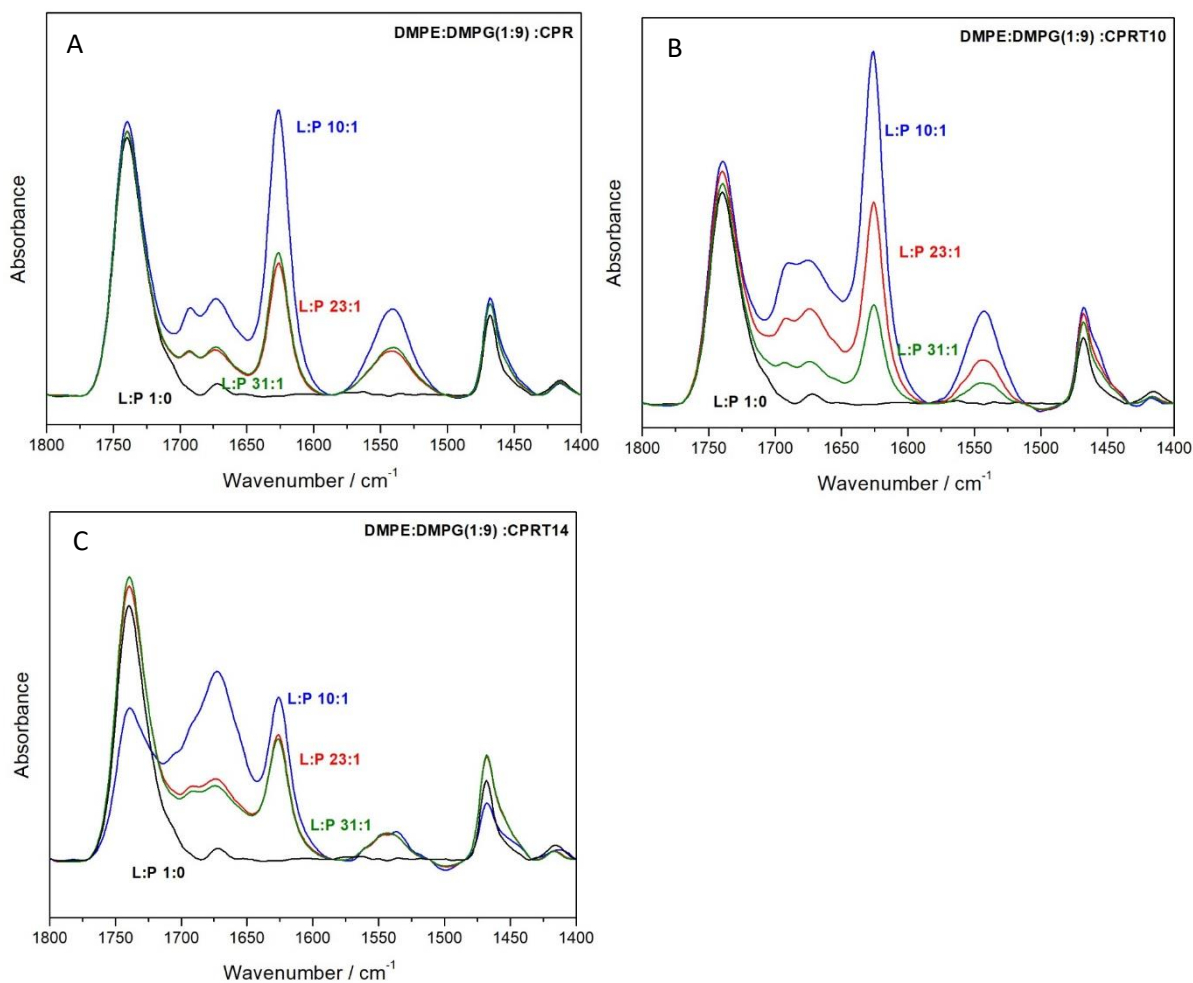
Fig. S9. ATR-FTIR results for DMPE:DMPG (1:9) with **CPR** (A), **CPRT10** (B) and **CPRT14** (C). The molar ratios are shown in each curve.
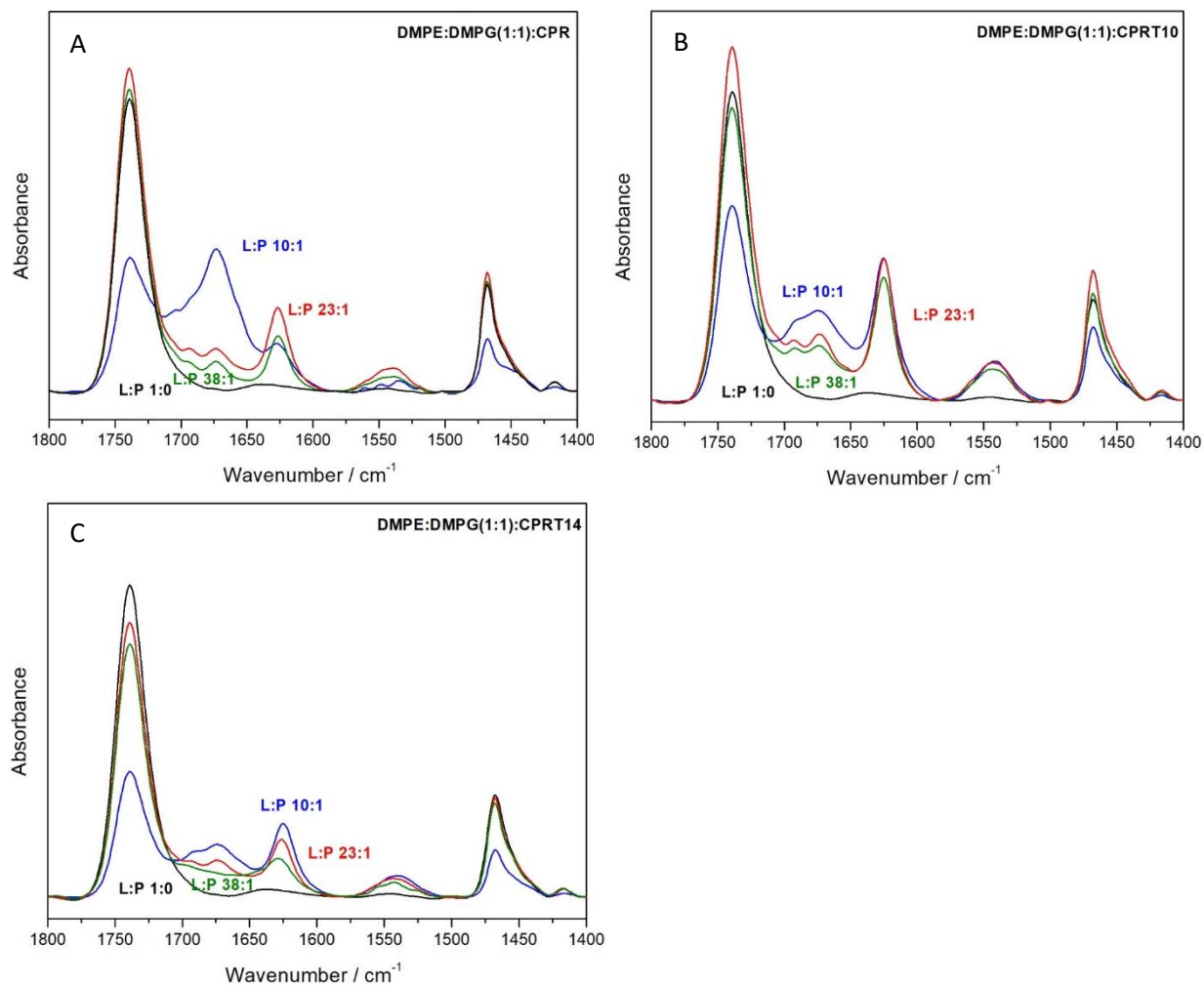
Fig. S10. ATR-FTIR results for DMPE:DMPG (1:1) with **CPR** (A), **CPRT10** (B) and **CPRT14** (C). The molar ratios are shown in each curve.

V. **"Partition of antimicrobial *D-L*-α-Cyclic Peptides into bacterial model membranes"**

Bárbara Claro, Eva González-Freire, Juan R. Granja, Rebeca Garcia-Fandiño, Jana Gallová, Daniela Uhríková, Aleksander Fedorov, Ana Coutinho, Margarida Bastos

Partition of antimicrobial *D-L-α*-Cyclic Peptides into bacterial model membranes

Bárbara Claro[a], Eva González-Freire[b], Juan R. Granja[b], Rebeca Garcia-Fandiño[a,b], Jana Gallová[c], Daniela Uhríková[c], Aleksander Fedorov[d], Ana Coutinho[d,e*], Margarida Bastos [a,*]

[a] CIQUP, Centro de Investigação em Química, Departamento de Química e Bioquímica, Faculdade de Ciências, Universidade do Porto, Porto, Portugal;

[b] Centro Singular de Investigación en Química Biolóxica e Materiais Moleculares (CiQUS), Departamento de Química Orgánica, Universidade de Santiago de Compostela, 15782 Santiago de Compostela, Spain

[c] Faculty of Pharmacy, Comenius University in Bratislava, 832 32 Bratislava, Slovak Republic

[d] iBB – Institute for Bioengineering and Biosciences, Department of Bioengineering, Instituto Superior Técnico, Universidade de Lisboa, 1049-001 Lisboa, Portugal

[e] Department of Chemistry and Biochemistry, Faculdade de Ciências, Universidade de Lisboa, 1749-016 Lisboa, Portugal

Corresponding authors: Margarida Bastos (mbastos@fc.up.pt)

Ana Coutinho (ana.coutinho@tecnico.ulisboa.pt)

Keywords: Antimicrobial Peptides, *D,L*- α -cyclic peptides, Self-Assembled Nanotubes, Time Resolved Fluorescence Spectroscopy, Steady-state Fluorescence Spectroscopy

19

Abstract

Fluorescence spectroscopy is used to characterize the partition of three second generation *D,L*-α-cyclic peptides to two lipid model membranes. The peptides have proven antimicrobial activity, particularly against Gram positive bacteria, and the model membranes are formed of either with 1,2-dimyristoyl-sn-glycero-3-phospho-(1'-rac-glycerol) (DMPG) or its mixture with 1,2-dimyristoyl-sn-glycero-3-phosphoethanolamine (DMPE), at a molar ratio of (1:1). The peptide's intrinsic fluorescence was used in the Steady State and/or Time Resolved Fluorescence Spectroscopy experiments, showing that the peptides bind to the membranes, and the extent of their partition is thereof quantified. The peptide-induced membrane leakage was followed using an encapsulated fluorescent dye.

Overall, the partition is mainly driven by electrostatics, but also involves hydrophobic interactions. The introduction of a hydrocarbon tail in one of the residues of the parent peptide, **CPR**, adjacent to the tryptophan (Trp) residue, significantly improves the partition of the modified peptides, **CPRT10** and **CPRT14,** to both membrane systems. Further, we show that the length of the tail is the main distinguishing factor for the extension of the partition process.

The parent peptide induces very limited leakage, at odds with the peptides with tail, that promote fast leakage, increasing in most cases with peptide concentration, and being almost complete for the highest peptide concentration and negatively charged membranes.

Overall, the results help the unravelling of the antimicrobial action of these peptides and are well in line with their proven high antimicrobial activity.

1. Introduction

The excessive use and misuse of antibiotic therapy led through the years to the presently alarming situation due to the huge increase of multi-resistant pathogens [1-3]. In the last decades, several attempts were followed to tackle this problem, searching for solutions that might counteract, or at least minimize, antibiotic resistance. The study of natural antimicrobial peptides (AMPs), known to be present in the defense systems of all forms of life [4,5], together with their production and synthetic modification towards more effective ones, has been an innovative scientific research area within this important global health care issue.

Most AMPs are cationic at physiological pH, promoting their strong interaction with the negatively charged headgroups of the phospholipid, that are more abundant at the outer surface of bacteria, leading to a desired specificity towards bacterial cells. Further, they usualy adopt an amphipathic conformation that facilitates their anchoring/translocation and destruction of the pathogen's lipid bilayers [4,6].

Several AMPs' mechanisms of action have been proposed in the litterature [7-9], but in many cases their actual action remains elusive, and clearly depends on peptide and pathogen. Pore formation, membrane segregation/permeabilization, eventualy leading to membrane micellization, disruption and aggregation are all phenomena that have been observed, resulting from rearrangements of AMPs at the lipid membrane. These processes are accompanied by the leakage of vital components, such as ions and other metabolites, leading to cell death [4,10-14].

Most studied AMPs are linear, but recently it has been shown that cyclization enhances the antimicrobial activity [15-18]. Within this group, D,L-α-cyclic peptides (D,L-α-CPs) with an even number of D- and L- α-amino acids are viewed as a new class of potential AMPs [11,17,19]. The amide groups present in

the backbone of the cyclic peptides (CPs) arrange perpendicularly to the plane of the cyclic structure, in a flat-ring-shape conformation. Under appropriate conditions, intermolecular hydrogen bonds are formed between the rings, creating tubular β-sheet structures, referred to as self-assembled cyclic peptide nanotubes (SCPNs). The antimicrobial CPs also form cationic amphiphilic nanotubes, as the natural AMPs. In the presence of lipid membranes, these supramolecular structures are easily formed, being in many cases the active form of CPs. The properties of the nanotubes can be altered, most commonly by varying the number and/or the type of amino acids present, thereby changing the diameter and outer surface of the nanotube [20,21]. This allows the tunning of the antimicrobial activity. The presence of *D*-amino acids in the CPs structure increases their resistance to protease degradation, making these cyclic peptides very promising antimicrobial candidates [11,20,22,23]. Although the mechanisms by which they kill bacteria are not yet fully understood, they seem to follow the usual antimicrobial peptide's pattern - the positive side chains of the amino acids in the peptides that are pointing outwards target the bacterial membrane through electrostatic interactions and the hydrophobic side chains help the partition into the lipid membrane [19,22,24].

We have previously performed biophysical experiments (Differential Scanning Calorimetry, DSC, and Attenuated Total Reflection-Fourier Transformed InfraRed spectroscopy, ATR-FTIR) combined with Molecular Dynamics (MD) simulations to characterize the interaction of a plethora of these antimicrobial *D,L*-α-CPs with different lipid model membranes. In this work, we focused on three second generation *D,L*-α-cyclic peptides, designated as **CPR** (*c*-[RSKSWPgKQ])**, CPRT10** (*c*-[RSKSWX^{C10}KQ]) and **CPRT14** (*c*-

[RSKSWX^{C14}KQ]) [25] (the underlined residues are *D*-amino acids), which were developed based on previously studied antimicrobial cyclic peptides [11, 17], and showed very good antimicrobial activity, particularly against gram positive bacteria [26]. **CPR**, **CPRT10** and **CPRT14** contain one arginine (R) and two lysines (K) (three charged residues, net charge +3), a glutamine (Q) and two serines (S) (three polar non-charged residues) and a tryptophan (W) (a hydrophobic residue). The three peptides have a propargylglycine residue (Pg), or the corresponding "Clickabled" derivatives, noted by X, that represents (*S*)-2-amino-3-(1-alkyl-1λ^2,2,3-triazol-4-yl)propanoic acid to which a hydrocarbon tail is attached in the case of **CPRT10** and **CPRT14**, with ten and fourteen CH_2 groups, respectively. To further clarify their mechanism of action, we have now used fluorescence spectroscopy to characterize both their partition to lipid membranes and the peptide-induced membrane leakage pattern of a self-quenched encapsulated fluorescent dye. In the case of the partition experiments, we took advantage of the intrinsic fluorescence properties of the CPs, as they all share a Trp residue. As regarding the membrane permeabilization studies we used an extrinsic fluorescent probe, carboxyfluorescein (CF), to follow its peptide-induced leakage kinetics from liposomes.

Large unilamellar vesicles (LUVs) of pure 1,2-dimyristoyl-*sn*-glycero-3-phospho-(1'-*rac*-glycerol) (DMPG) and its mixture with 1,2-dimyristoyl-*sn*-glycero-3-phosphoethanolamine (DMPE), at a molar ratio of (1:1) were used as models for bacterial membranes. For the leakage studies with CF, 1-palmitoyl-2-oleoyl-*sn*-glycero-3-phospho-(1'-*rac*-glycerol) (POPG), as well as its mixture with 1-palmitoyl-2-oleoyl-*sn*-glycero-3-phosphoethanolamine (POPE) at the same molar ratio as in the partition studies, (1:1) were used instead because the

acyl chains of DMPE and DMPG were found to be too short to efficiently

encapsulate the fluorescent dye (results not shown).
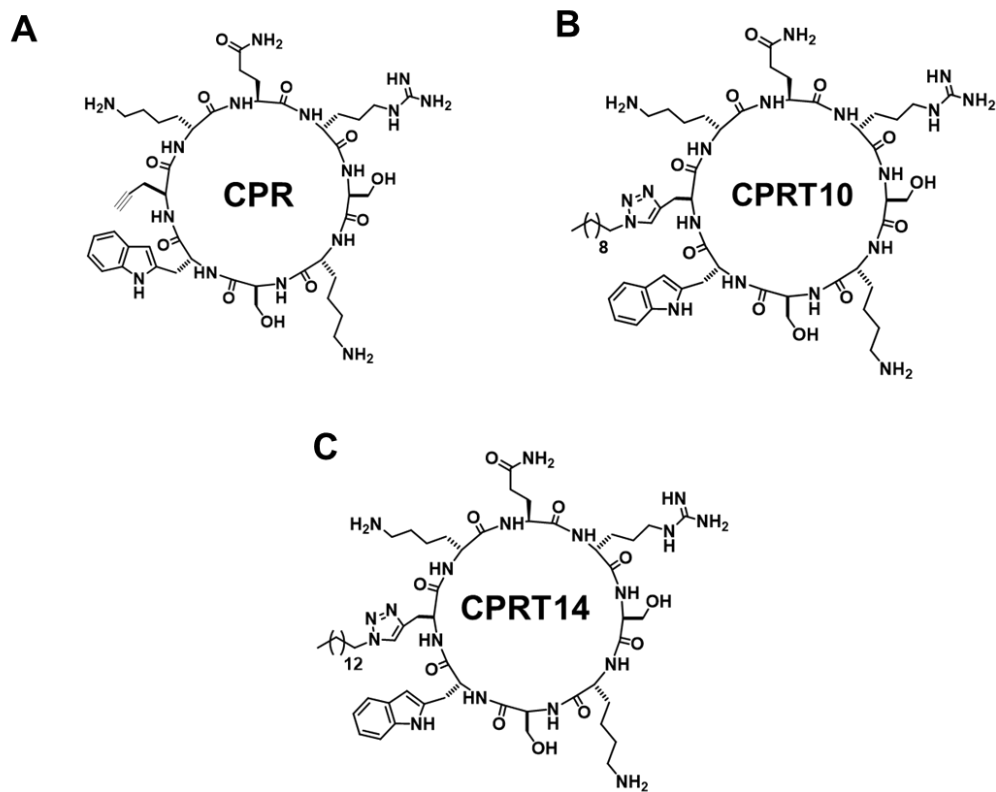
Fig. 1 *D,L*-α-cyclic peptides **A) CPR** (*c*-[RSKSWPgKQ]), **B) CPRT10** (*c*-[RSKSWX^{C10}KQ]) and **C) CPRT14** (*c*-[RSKSWX^{C14}KQ]). In the amino acid composition Pg denotes propargylglycine, while X denotes (*S*)-2-amino-3-(1-alkyl-1λ^2,2,3-triazol-4-yl) propanoic acid and the underline residues are *D*-amino acids.

2. Materials and Methods

2.1. Preparation and Size Characterization of Liposomes for the Partition Studies

Large Unilamellar Vesicles (LUVs) were obtained as described in our previous studies [11,25]. The lipids DMPE and DMPG (Avanti Polar Lipids, Alabama, USA) were dissolved in chloroform/methanol [87.4:12.6 %(v/v)], either as pure DMPG or as a 1:1 mixture, and subsequently dried overnight under vacuum to obtain a film. Thereafter the lipid film was hydrated with buffer [HEPES (10 mM HEPES, 150 mM NaCl, 0.02% NaN_3, 1 mM EDTA), all purchased from Sigma-Aldrich, Germany), pH 7.45]. The MLVs suspension, obtained after several cycles of vortex/incubation, at a temperature above T_m, was then frozen in liquid nitrogen and thawed above T_m, repeating 3 times. LUVs were obtained by extrusion of the MLVs in a 10 mL stainless steel extruder from Lipex Biomembranes Inc. (Vancouver, Canada), under inert (N_2) atmosphere using two staked polycarbonate filters with a pore diameter of 100 nm [Whatman, Nucleopore (NJ, USA)]. The final phospholipid concentration was determined using a modified version of the Bartlett phosphate assay [11, 27] and the average particle size of the LUVs were measured by dynamic light scattering (DLS) after preparation and in the following day before use. Average particle diameters between 110-115 nm were always obtained, with polydispersity indexes always <0.1.

2.2. Preparation of Liposomes for the Leakage experiments

10 mM solutions of POPG and its (1:1) mixture with POPE were prepared for the leakage experiments following the same lipid film procedure described above. The Multilamellar Vesicle's Suspension (MLVs) was obtained using a different hydration solution. A 40mM CF (Sigma-Aldrich, Germany) solution was prepared beforehand, by dissolving initially the required amount of the dye in 50 μL of a 1 mol/dm^3 NaOH

solution, to which the buffer described above [HEPES (10 mM HEPES, 150 mM NaCl, 0.02% NaN_3, 1 mM EDTA, pH 7.45] was added dropwise under stirring, until the desired final volume was obtained. Finally, the pH was adjusted to 7.45 as before. The suspensions of MLVs with CF were then extruded to obtained LUVs loaded with CF, by using a manually powered extruder Liposofast-Basic (BPS, UK), with 0.5 mL capacity, and two superimposed 100 nm pore diameter polycarbonate filters [Whatman, Nucleopore (NJ, USA)], covered with aluminum foil to protect the solution from light. Three sequences of extrusion/vortex/freeze-thaw cycles were made, followed by 30-40 passages through the polycarbonate filters. The size of the liposomes was also confirmed by DLS, with values between 110-115 nm.

Upon extrusion, the excess of CF that remained free in solution (*i.e.,* CF not encapsulated inside the LUVs), was removed from the LUVs suspension, following a procedure adapted from Huláková S. *et al*. [28]. To this end, three independent preparations of 0.5 g of Sephadex™ G-50 were weighted, soaked with 7mL of buffer and kept for 24h in the refrigerator. Thereafter, each soaked Sephadex™ G-50 sample were transferred into three different columns made of 5 ml disposable syringe, with a glass microfiber filter (Whatman GF/B) placed at the bottom of the syringe, and the columns were centrifuged at 1000 g for 5 min to remove the excess buffer. Afterwards, the prepared 10 mM LUVs were added dropwise to the top of one of the Sephadex™ G-50 columns, and allowed to rest for 5 min. This column was then centrifuged for 7 min at 500 g, followed by 3 min at 1000 g. The LUVs suspension recovered from the first column was subsequently passed through the second column, with the same centrifugation cycle, *i.e.,* 7 min at 500 g, followed by 3 min at 1000 g. This process was repeated with the third column. Altogether this process improved the efficiency of removal of nonencapsulated CF. The total lipid concentration was rigorously

determined thereafter using a modified version of the Bartlett phosphate assay [11, 27] and the average particle size of the LUVs were measured by DLS. The lipid suspensions were then diluted to the desired lipid concentration to be used in the leakage studies, namely, a total lipid concentration of 52 μM and 42 μM for POPG and POPE:POPG (1:1), respectively.

3. Experimental methods

3.1. Steady-State fluorescence intensity and anisotropy measurements

To assess the partition of the CPs to the model membranes by steady-state fluorescence measurements, stock peptide solutions were prepared, and their concentration determined by UV-VIS by measuring their absorbance at 280 nm, and using a molar extinction coefficient, ε, of 5690 $M^{-1}cm^{-1}$. From these, peptide solutions at 10 μM for **CPR** and **CPRT10**, and 13 μM for **CPRT14** were prepared in HEPES buffer. Then, an appropriate volume of the 3 mM stock solution of DMPG or DMPE:DMPG (1:1) LUVs were added to each CP solution, covering the range 0 – 1000 μM in phospholipid concentration, to obtain independent samples at different lipid:peptide ratios (L:P). The measurements were carried either on a HORIBA Jobin Yvon Fluorolog-3-21 spectrofluorometer (Kyoto, Japan), equipped with a FI-3751 thermoelectric temperature controller (Wavelength Electronics) or on a SLM-AMINCO 8100 spectrofluorometer (SLM Instruments Inc., Urbana, IL) with temperature controlled by a thermostatic bath (Julabo F25, Houston, TX, USA). The mixtures were prepared and allowed to equilibrate for 30 min at 45°C prior to the fluorescence measurements performed at 38ºC, in 0.5 cm x 0.5 cm quartz cuvettes (Hellma, Belgium) with constant stirring, after an equilibration period of 1 min. The samples were excited at 280 nm and their emission spectra were collected between 290-450 nm. The integration time was 0.5 s

and the slits were 5 nm or 4 nm for both the emission and the excitation settings for the

HORIBA Jobin Yvon Fluorolog and SLM AMINCO 8100 spectrofluorometers,

respectively. For the steady-state fluorescence anisotropy measurements, the samples

were excited at 280 nm and the emission was at 340 nm. The slits were 10 nm for both

the emission and the excitation, respectively, for HORIBA Jobin Yvon Fluorolog, and 8

nm and 16 nm for excitation and the emission settings, respectively, for the SLM

AMINCO 8100. The background intensities were always considered and subtracted

from the measured sample fluorescence intensities. In the fluorescence anisotropy

measurements, the range of lipid concentrations was low enough to prevent any

artificial depolarization of the fluorescence emitted by the CPs.

The spectral center-of-mass (intensity-weighted average emission wavelength, $< \lambda >$) of

the CPs emission spectra was calculated according to:

$$\langle \lambda \rangle = \sum_{i=1}^{N} (I_i \lambda_i) / \sum_{i=1}^{N} (I_i) \tag{1}$$

where I_i is the fluorescence intensity value for each wavelength, λ_i [29].

The steady-state fluorescence anisotropies, $\langle r \rangle$, were obtained by measuring the

polarized components of the fluorescence emission according to:

$$\langle r \rangle = \frac{I_{VV} - G I_{VH}}{I_{VV} + 2 G I_{VH}} \tag{2}$$

Where I_{VV} and I_{VH} are the fluorescence intensities for the parallel and horizontal

emission component, both recorded when the sample is excited with vertically polarized

light. The *G*-factor, defined as I_{HV}/I_{HH}, is an instrumental correction factor for the

different sensitivity of the detection system of the instrument for the vertical and

horizontal polarized light. This factor considers the transmission efficiency of the

monochromator to the polarization of the light and helps to correct the measurements for experimental artifacts [30, 31]. The background intensities for the lipid suspension without CPs were always considered and subtracted from the measured sample intensities.

3.2. Time-resolved fluorescence intensity and anisotropy measurements

Time-resolved fluorescence measurements (TRFS) were performed by the time-correlated single-photon timing technique (TCSPT) [30]. Fluorescence intensity decays, I(t), with picosecond resolution were obtained at 38 ºC by exciting the samples at 282 nm using a frequency doubled dye laser Rhodamine 6G laser (Coherent 701-2), cavity dumped (3.7 MHz repetition rate), synchronously pumped by a mode-locked Ar laser (514.5 nm, Coherent Innova 400-10). The emission was detected at 340 nm by a Hamamatsu R-2809 MCP photomultiplier (Jobin-Yvon HR320 monochromator) with an emission polarizer set at the magic angle (54.7º) relative to the vertically polarized excitation beam. The instrument response function (IRF) was recorded while the excitation light was scattered by a Ludox solution [silica and colloidal water solution (Aldrich, Milwaukee, USA)].

The fluorescence intensity decays were collected using a multichannel analyzer with a time window of 1024 channels, typically using a time scale of 12.2 or 16.3 ps/channel. The complex decay of tryptophan residues was described by a sum of exponentials as:

$$I(t) = \sum_{t=1}^{n} \alpha_i e^{-t/\tau_1} \tag{3}$$

where α_i is the normalized amplitude and τ_i *is* the lifetime for the ith decay component. The fractional fluorescence intensity, f_i, associated to each decay component i is:

$$f_i = \alpha_i \tau_i / \sum_{t=1}^{n} \alpha_i \tau_i \qquad (4)$$

and the amplitude-weighted mean fluorescence lifetime, $\bar{\tau}$, was calculated according to:

$$\bar{\tau} = \sum_{t=1}^{n} \alpha_i \tau_i \qquad (5)$$

This parameter is proportional to the area under the fluorescence intensity decay curve and consequently to the fluorescence quantum yield of the fluorophore in the absence of static quenching [32].

The two orthogonal components of the fluorescence emitted by the sample, parallel, $I_{//}(t)$, and perpendicular, $I_{\perp}(t)$, to the plane of polarization of the excitation beam, were also recorded sequentially by automatically alternating the orientation of the emission polarizer every 30 or 60 s. The time-resolved fluorescence polarization measurements were then globally analyzed as previously described [32, 33] by fitting the anisotropy decay curves, r(t), with a sum of discrete exponential terms:

$$r(t) = \sum_{i=1}^{n} \beta_i \exp(-t/\phi_i) + r_{\infty} \qquad (6)$$

Here, β_i and ϕ_i are the normalized amplitude and the rotational correlation time of the ith decay component of the anisotropy, respectively, and r_{∞} is the residual anisotropy [32]. The fluorescence intensity and anisotropy decays were analyzed using the TRFA Data Processer Advanced version 1.4 from the Scientific Software Technologies Center (Belarusian State University) as previously described [33]. The usual criteria (reduced

$\chi^2 < 1.3$ and a random distribution of weighted residuals and autocorrelation plots) were used to evaluate the goodness of the fits [30].

3.3. Steady-State fluorescence measurements in Carboxyfluorescein leakage experiments

Possible leakage of the lipid membranes induced by the cyclic peptides was followed using the loaded CF LUVs. The experiments were performed in a PTI QuantaMaster™ 8075-21 HORIBA spectrofluorometer (HORIBA Scientific), equipped with a 75-W short arc Xenon lamp (UXL-75XE, Ushio Inc. Japan), and a single emission/excitation monochromator.

The peptide concentrations used were 1, 5 and 10 μM, and the lipid concentrations were 52 μM and 42 μM, for POPG and POPE:POPG (1:1).

The CPs were added to the LUVs at 27 °C and the data were recorded at an excitation and emission wavelength of 492 nm and 517 nm, respectively. The excitation/emission slits were 2/2 nm, with 5 points acquired per second, and the measurements were recorded for ~20 min. The fluorescence intensity of CF-loaded vesicles was initially recorded for 120 s, the time point of CPs addition to each system. The change in fluorescence intensity continued to be recorded until it reached a stable value. At this point, 10 μL of a 0.1% (v/v) Triton™-X-100 (Sigma-Aldrich, Germany) solution was added, to obtain 100% release of the entrapped CF.

4. Determination of Partition Constants

Considering a simple partition equilibrium between the aqueous phase (W) and the lipid bilayer phase (L), the partition constant of the CPs to the model membranes can be described according to Eq. (7) [34]:

$$K_{p,x} = \frac{\dfrac{n_L^P}{n_L + n_L^P}}{\dfrac{n_W^P}{n_W + n_W^P}} \tag{7}$$

where $K_{p,x}$ is a dimensionless mole-fraction partition constant of the peptide, n_L and n_W are the number of moles of lipid and water, respectively, and n_i^P is the number of moles of peptide present in each phase (i can be L, lipid phase or W, aqueous phase). Considering that $n_W \gg n_W^P$, and $n_L \gg n_L^P$, as high membrane-bound concentrations of the peptides are avoided to prevent deviations from the ideal partitioning model due to peptide/peptide interactions at the water/membrane surface or in the lipid bilayer, Eq. (7) can be simplified as:

$$K_{p,x} = \frac{\dfrac{n_L^P}{n_L}}{\dfrac{n_W^P}{n_W}} \tag{8}$$

This expression for $K_{p,x}$ can also be related to the Nernst partition constant, $(K_p = [(n_L^P/V_L)/(n_W^P/V_W)])$, by simply replacing the volumes of water and lipid by their respective molar volumes, γ_W and γ_L, respectively, leading to:

$$K_p = K_{p,x} \times \frac{\gamma_W}{\gamma_L} \tag{9}$$

In this study, we have used this formalism as applied to fluorescence data to study the influence of membrane lipid composition on the partition behavior of each CP.

For the time-resolved fluorescence measurements, Eq. (10) was fitted to the experimental values of the amplitude-weighted mean fluorescence lifetime, $\bar{\tau}$, as a function of the lipid concentration in the outer leaflet, $|L|$, to retrieve the molar fraction

partition constant, K_p, and the mean fluorescence lifetime of each CP in the lipid phase, $\bar{\tau}_L$

$$\bar{\tau} = \frac{\bar{\tau}_W + K_p \ \gamma_L \ |L| \ \bar{\tau}_L}{1 + K_p \ \gamma_L \ |L|} \tag{10}$$

The values used throughout for the lipid molar volumes, γ_L, were 0.66 $dm^3.mol^{-1}$ for DMPG and 0.64 $dm^3.mol^{-1}$ for DMPE:DMPG (1:1).

In the case of steady-state fluorescence anisotropy measurements, Eq. (11) shows its relation to the lipid concentration in a simple two-state partition system [35]:

$$< r >_{SS} = \frac{< r >_w \left((\gamma_L[L])^{-1} - 1\right) + < r >_L K_p \varepsilon_L \varphi_L / (\varepsilon_w \varphi_w)}{(\gamma_L[L])^{-1} - 1 + K_p \varepsilon_L \varphi_L / (\varepsilon_w \varphi_w)} \tag{11}$$

where $< r >_W$ and $< r >_L$ are the anisotropies of the cyclic peptide in the aqueous and in the lipid phases, and ε_i and φ_i are the molar absorption coefficient and fluorescence quantum yield of CP in each phase ($i=$ W, aqueous phase and $i=$ L, lipid phase, respectively). If $\varepsilon_w \approx \varepsilon_L$ and $\gamma_L[L] << 1$ conditions present in our experimental conditions, Eq. (11) becomes [35]:

$$< r >_{SS} = \frac{< r >_w \left((\gamma_L[L])^{-1} - 1\right) + < r >_L K_p (\varphi_L / \varphi_w)}{(\gamma_L[L])^{-1} - 1 + K_p (\varphi_L / \varphi_w)} \tag{12}$$

This Eq. was fitted to the obtained values of the steady-state anisotropy as a function of lipid concentration (outer leaflet).

In both cases the data were analyzed using the Origin software 7.0.

5. Results and discussion

5.1. Fluorescence properties of the cyclic peptides in buffer

Trp residues are excellent reporters of their local environment since their fluorescence emission properties are extremely sensitive to the polarity of the surrounding medium [36]. The spectral center-of-mass of the three CPs, $<\lambda>$, was calculated from the corrected fluorescence emission spectra obtained for **CPR**, **CPRT10** or **CPTR14** in buffer, and are summarized in Table 1. The spectral center-of-mass of the three CPs is $<\lambda>\sim$ 363nm (Table 1), very close to $<\lambda>=$ 366nm obtained for the reference compound *N*-acetyl-*L*-tryptophanamide, revealing the full exposure of their Trp residues to the aqueous solution. The fluorescence intensity decays obtained for the three CPs were well described by three exponential terms with lifetime components $\tau_1=$ 0.31 $\pm$ 0.04 ns, $\tau_2=$ 1.23 $\pm$ 0.07 ns and $\tau_3=$ 2.9 $\pm$ 0.2 ns, respectively (Table S1). The fractional intensities associated with the intermediate and long-lived lifetime components ($f_2=$ 0.59 $\pm$ 0.04 and $f_3=$ 0.34 $\pm$ 0.06, respectively) were clearly dominant in all three cases.

Table 1. Fluorescence emission properties of **CPR**, **CPRT10** and **CPRT14** in aqueous buffer or in the presence of 500 μM (outer leaflet) DMPG or DMPE:DMPG (1:1) LUVs at 38 ºC (spectral center-of-mass, $<\lambda>$, mean fluorescence lifetime, $\bar{\tau}$, and steady-state fluorescence anisotropy, $< r >_{SS}$).

Peptide	Medium	$<\lambda>$ (nm)	$\bar{\tau}$ (ns)	$< r >_{SS}$
CPR	Buffer	364	1.3	0.016 ± 0.005
	DMPG	351	1.7	0.072 ± 0.004
	DMPE:DMPG (1:1)	360	1.5	0.050 ± 0.004
CPRT10	Buffer	363	1.2	0.016 ± 0.003
	DMPG	349	2.1	0.086 ± 0.006
	DMPE:DMPG (1:1)	350	2.4	0.087 ± 0.005
CPRT14	Buffer	362	1.2	0.025 ± 0.007
	DMPG	351	2.1	0.090 ± 0.009
	DMPE:DMPG (1:1)	350	2.2	0.121 ± 0.011

The time resolved fluorescence anisotropy of each peptide in buffer decayed monoexponentially to zero at long times (Fig. 2), indicating that there was no significant self-association of the studied CPs in solution at this concentration and temperature. Furthermore, the very short rotational correlation times recovered from these fluorescence anisotropy decays, $\phi_1 \sim 200 - 400$ ps (Table 2), agree with the expected small hydrodynamic volumes for these low molecular weight cyclic peptides. Accordingly, and given the similarities in the mean fluorescence lifetime of the peptides, the steady-state fluorescence anisotropies measured for **CPR**, **CPRT10** or **CPTR14** in aqueous solution were also very low ($< r >_{SS} \sim 0.02 - 0.03$ (Table 1)). In

conclusion, both the steady-state and time-resolved anisotropy measurements indicate that the CPs studied here remained essentially monomeric in solution at the low peptide concentration of 10 μM and the temperature of 38 °C used in these assays. This non-associative behavior at 10 μM is in line with the reported critical association concentration (*cac*) of 13-15 μM for **CPRT10,** and is only slightly higher than the recently reported **CPRT14** *cac* ~ 5 μM [26]. It should be noted that while the intrinsic's peptide's fluorescence (Trp) was exploited here, the authors used two extrinsic fluorescent probes, Nile red and Thioflavine T, to monitor the self-association of the CPs in aqueous solution. Furthermore, a different buffer (PBS 10 mM, 107 mM NaCl, pH 7.4) and a significantly lower temperature, 20 °C (compared to 38 °C here) were used in the former study.
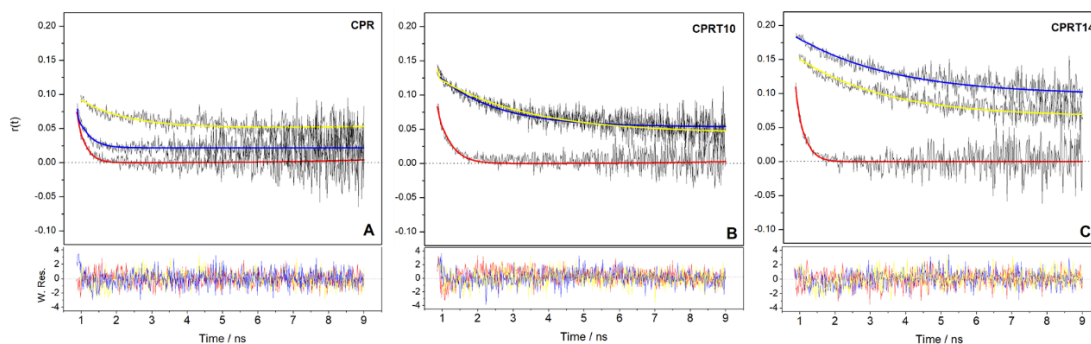
Fig. 2 – Time-resolved fluorescence anisotropy of **CPR** (A), **CPRT10** (B) and **CPRT14** (C) in the absence (buffer) and in the presence of lipid vesicles. The experimental data (black curves) at 38 °C and the corresponding fits are shown for the measurements performed in buffer (red curves) as well as in the presence of 500 μM (outer leaflet) DMPG (yellow curves) or DMPE:DMPG (1:1) (blue curves). The fitted parameters (rotational correlation time, ϕ_1, amplitude, β_1, and residual anisotropy, r_∞) are summarized in Table 2. The weighted residues (W. Res.) are also displayed under each anisotropy decay. The anisotropy decays were measured using a time scale of 12.2 or 16.5 ps/channel.

Table 2. Time-resolved fluorescence anisotropy parameters (rotational correlation time, ϕ_1, amplitude, β_1, and residual anisotropy, r_∞) for **CPR**, **CPRT10** and **CPRT14** in

aqueous buffer or in the presence of 500 μM (outer leaflet) DMPG or DMPE:DMPG (1:1) vesicles at 38 °C.

Peptide	Medium	β_1	ϕ_1 (ns)	r_∞	$r(0)$	χ^2
CPR	Buffer	0.085	0.20		0.085	1.001
	DMPG	0.045	1.4	0.050	0.095	1.276
	DMPE:DMPG (1:1)	0.050	0.31	0.022	0.072	
CPRT10	Buffer	0.083	0.34		0.083	1.179
	DMPG	0.080	2.5	0.042	0.122	1.218
	DMPE:DMPG (1:1)	0.075	1.6	0.054	0.129	1.061
CPRT14	Buffer	0.079	0.46		0.079	1.280
	DMPG	0.088	2.5	0.066	0.154	1.282
	DMPE:DMPG (1:1)	0.085	2.7	0.099	0.184	1.159

5.2. CP partition to DMPG vesicles

The interaction of **CPR**, **CPRT10** and **CPTR14** with lipid membranes was first studied using large unilamellar anionic vesicles prepared with DMPG. The fluorescence emission spectra of all CPs were progressively blue-shifted as the lipid concentrations varied between 5-500 μM (outer leaflet) DMPG, indicating that the Trp residue of each peptide is moving from an aqueous (polar) to the lipid surface (less polar environment). The overall change in the spectral center-of-mass was very similar for the three CPs studied at concentrations up to 500 μM of lipid (outer leaflet) [Δ<λ>~ - 12 nm (Fig. 3A and Table 1)], although much less lipid was required for **CPRT10**, and particularly **CPRT14**, to reach their plateau values of <λ>~ 350nm (Fig. 3A). Since the deeper the penetration of the indole group of the Trp residue in a lipid membrane, the larger the

blue shift in its emission spectra is [37], all CPs must share a similar shallow location

upon fully binding to the membrane surface.
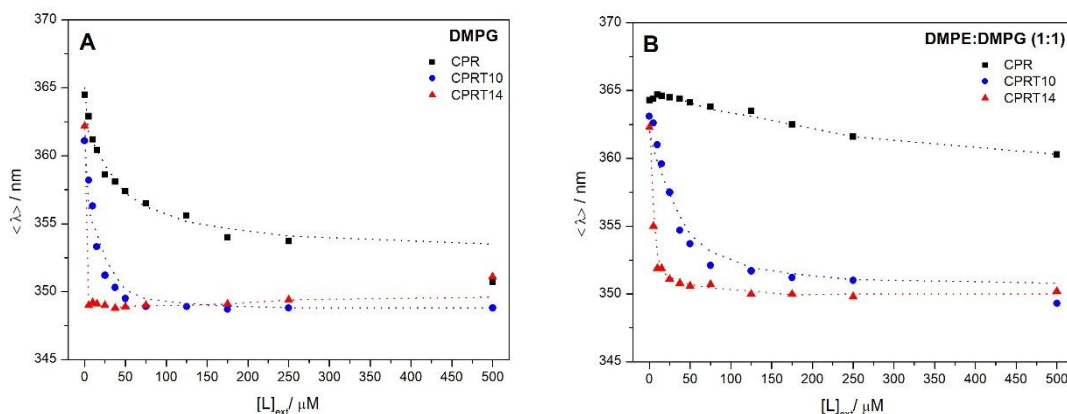
Fig.3 – CP binding to lipid vesicles monitored by steady-state fluorescence spectroscopy. The changes in the spectral center-of-mass, $<\lambda>$, of **CPR** (black squares), **CPRT10** (blue circles) and **CPRT14** (red triangles) were measured as a function of lipid concentration (here represented as outer leaflet lipid concentration, $([L])_{ext}$) using DMPG (A) and DMPE:DMPG (1:1) (B) vesicles at 38 °C. The dashed lines are just a 'guide for the eye'.

Concomitantly to the spectral alterations, there was an increase in the fluorescence

intensity of **CPR**, **CPRT10** and **CPRT14** with the lipid concentration used. However,

since the peptide-membrane interaction was strongly electrostatically driven, it was

accompanied by some peptide-induced vesicle aggregation and precipitation. Therefore,

we sought to use the amplitude-weighted mean fluorescence lifetime, $\bar{\tau}$ as a function of

lipid concentration to determine the partition constant, K_p of each CP studied, in both

lipid systems. The performance of time-resolved fluorescence measurements avoids

possible artifacts caused by significant light scattering from the vesicle suspension

and/or peptide-induced liposome flocculation that is known to occur in these systems

[34, 38]. In addition, the lifetime of a fluorophore is usually an intrinsic molecular

property dependent on its environment but independent of its concentration, *i.e.*, it is an absolute measurement, at variance with its steady-state fluorescence intensity.

The mean fluorescence lifetime of the hydrocarbon-modified peptides, **CPRT10** and **CPRT14**, increased hyperbolically from $\bar{\tau} \sim 1.3$ ns up to $\bar{\tau} \sim 2.1$ ns with the DMPG concentration added to the solution (Table S1 and Fig. 4A). All fluorescence intensity decays for these CPs were again adequately fitted by a triple exponential function, but the fractional intensities associated with the intermediate and long-lived lifetimes of τ_2= 1.6 ns and τ_3= 3.8 ns now reached f_2= 0.29 and f_3= 0.66, respectively, at the highest lipid concentration (outer leaflet) used (Table S1). Eq. (10) was non-linearly fitted to the $\bar{\tau}$ *vs* lipid concentration data (outer leaflet) and the obtained parameters K_p and $\bar{\tau}_L$ are presented in Table 3. By increasing the length of the hydrophobic tail from C10 to C14, the partition constant of **CPRT14** towards DMPG membranes increased by an order of magnitude compared to the one obtained for **CPRT10**: $(2.6 \pm 0.6) \times 10^5$ *vs* $(2.2 \pm 0.5) \times 10^4$, respectively (Table 3). Since the mean fluorescence lifetime, $\bar{\tau}$, is proportional to the quantum yield in the absence of static contributions, it can be also concluded that the quantum yield of the membrane-anchored peptides, **CPRT10** and **CPRT14**, is approximately 2-fold higher than the value presented by either CP in aqueous solution.
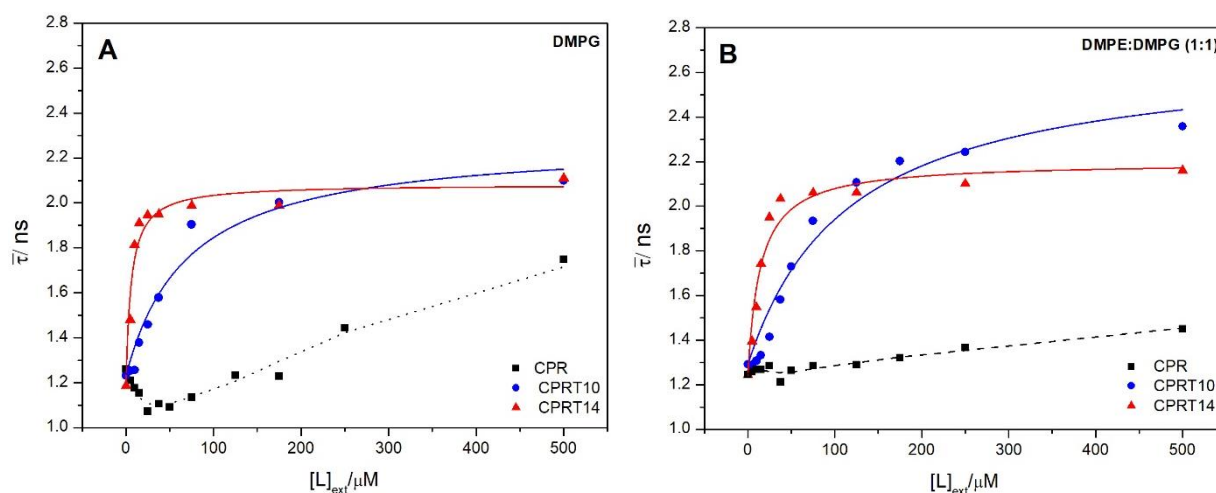
Fig. 4 – CP binding to lipid vesicles monitored by time-resolved fluorescence spectroscopy. The changes in the amplitude-weighted mean fluorescence lifetime, $\bar{\tau}$, of **CPR** (black squares), **CPRT10** (blue circles) and **CPRT14** (red triangles) were measured as a function of lipid concentration (outer leaflet, $[L])_{ext}$) using DMPG (A) and DMPE:DMPG (1:1) (B) lipid vesicles at 38°C. The solid lines correspond to the best fit of Eq. (10) to the TRFS data, and the dashed lines in the case of **CPR** are just a 'guide for the eye'. The parameters retrieved for **CPRT10** and **CPRT14**, K_p and $\bar{\tau}_L$ are summarized in Table 3.

In the case of **CPR**, a more complex, biphasic behavior was detected. The mean fluorescence lifetime of the peptide initially decreased with the lipid concentration, reaching a minimum of ~1.07 ns at 25 μM (outer leaflet) of DMPG, and then progressively increased with the lipid concentration used (Fig. 4A). These results are consistent with the occurrence of self-quenching [39] when a high surface concentration of peptide is reached at very low L:P ratios [33] which, in turn, most probably drives the self-association of **CPR** into nanotubes at the membrane surface [25]. The membrane induced self-association is in line with our previous results, where MD studies showed that at high peptide concentration **CPR** self-assembles into nanotubes at DMPG membrane surface [25]. Upon increasing the lipid concentration, the membrane-bound **CPR** becomes progressively diluted among the lipid vesicles, thereby effectively preventing fluorescence self-quenching from occuring. Since this is no longer a simple two-state equilibrium system between monomeric free and membrane-bound peptide, a K_p value for **CPR** cannot be obtained from fitting Eq. (10) to the lifetime data. Interestingly, it seems that the introduction of the alkyl chain prevents **CPRT10** and **CPRT14** from experiencing this self-quenching effect, likely due to adverse orientational effects between the quencher groups and the Trp residues.

The binding of **CPR** and its lipid derivatives **CPRT10** and **CPRT14** to the anionic lipid vesicles was also studied through fluorescence anisotropy measurements to gain some insight into the motional restrictions that affect the tryptophan residue when the CP is inserted into the membrane surface.

Representative time-resolved anisotropy decay curves obtained for each peptide in the presence of 500 μM (outer leaflet) DMPG LUVs are shown in Fig. 2. The fitted parameters are presented in Table 2. The fluorescence depolarization kinetics of each CP reaches a residual, time-independent value different from zero, *i.e.*, a limiting anisotropy r_∞, which is indicative of a restricted motion of its Trp side chain on the time scale of the experiment, due to its membrane binding. The CPs also displayed a single rotational correlation time which reached $\phi_1 \sim$ 2.5 ns for the fully membrane-bound **CPRT10** and **CPRT14** peptides, and 1.4 ns for **CPR**. The anisotropy values obtained at time zero, $r(0)$, for **CPRT10** and **CPRT14** were very close to the fundamental anisotropy of Trp [r_0(280nm)$\sim$ 0.15] [40], indicating that no significant fast depolarization motions of the Trp residues took place below the time resolution of our equipment.

Fig. 5 shows that the anisotropy of all CPs steadily increased upon addition of DMPG LUVs. As the peptides are adsorbed/interacting with the membrane there is a concomitant decrease in their rotational dynamics, *i.e.,* the Trp residue locates in a more ordered environment, probably confined at the phospholipid-water interface by electrostatic interaction with the anionic phospholipids. It should be noted that the anisotropy of each cyclic peptide is a linear combination of its limiting values in the aqueous solution and lipid phases, $<r>_W$ and $<r>_L$, respectively, weighted by the fluorescence quantum yield and molar fraction of the cyclic peptide in each phase [30]. Since $Q \sim \bar{\tau}_L/\bar{\tau}_W \sim$ 1.8 -2.1 (Table 3), the membrane-bound molar fraction of each CP

dominates the $<r>_{SS}$ values. For **CPRT14**, this effect results in a very sharp increase of $<r>_{SS}$ with lipid concentration, precluding retrieval of a K_p value from anisotropy data. On the other hand, a two-parameter fitting procedure of Eq. (12) to the data yielded a $K_p = (6.6 \pm 2.3) \times 10^4$ and $<r>_L = 0.091 \pm 0.005$ for **CPRT10** (Table 3) in good agreement with the partition constant obtained from the lifetime data. For **CPR**, and assuming, as above, that the relative increase in its quantum yield is identical to the value obtained for the two alkyl-modified peptides (*Q=1.8*), fitting of Eq. (12) to the steady state anisotropy data lead to $K_p = (2.5 \pm 0.5) \times 10^4$ and $<r>_L = 0.075 \pm 0.004$. The obtained K_p is of the same order of magnitude of the one obtained for **CPRT10**, whereas the limiting $<r>_L$ value is somewhat smaller. Nevertheless, as seen above (Table 2) the limiting anisotropy r_∞ are similar for the three CPs in DMPG, namely 0.05, 0.04 and 0.06, pointing to a similar restricted motion of the Trp side chain, due to CP's membrane binding. The lower value retrieved for **CPR** must thus be associated with the fact that for this peptide the partition equilibrium is coupled to peptide oligomerization at the membrane, as reflected in the $\bar{\tau}$ *vs* lipid concentration plots (Fig. 4 and discussion above), and is also in line with our previous results, as this peptide was shown by MD to form peptide nanotubes at the lipid membrane surface at high peptide concentrations [25].
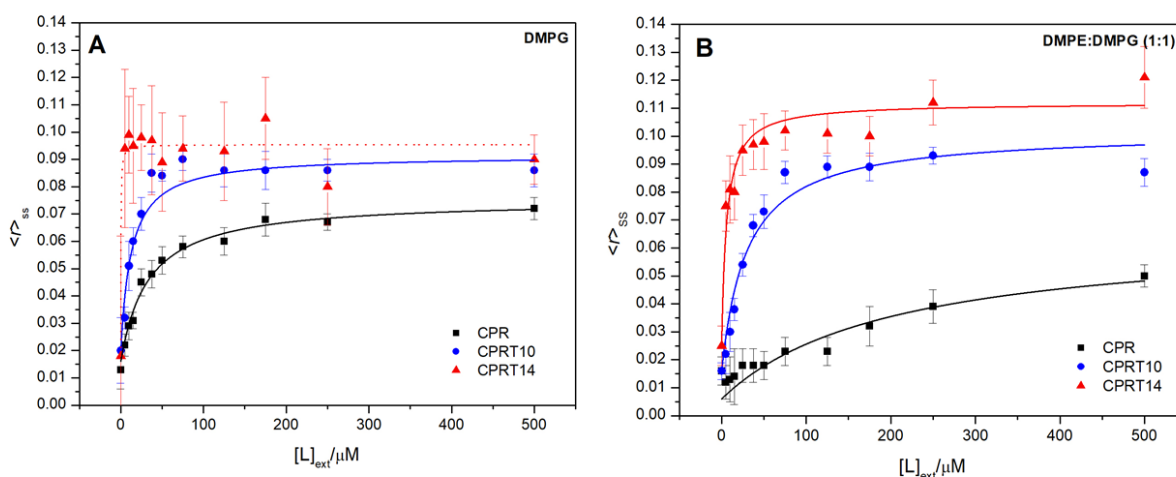
Fig. 5–CP binding to lipid vesicles monitored by steady-state fluorescence anisotropy. The changes in the fluorescence anisotropy, $<r>_{SS}$, of **CPR** (black squares), **CPRT10** (blue circles) and **CPRT14** (red triangles) were measured as a function of lipid concentration (outer leaflet, $[L])_{ext}$) using DMPG (A) and DMPE:DMPG 1:1 (B) lipid vesicles at 38ºC. The solid lines correspond to the best fit of Eq. (12) to the data and the fitted partition constants, K_p and $<r>_L$ are summarized in Table 3. The dashed lines used for **CPRT14** and DMPG are just a 'guide for the eye'. The error bars represent the mean deviation of ten repeated scans.

5.3. CP partition to DMPE:DMPG (1:1) vesicles

In order to evaluate the relative contribution of electrostatic and hydrophobic interactions to the energetics of CP binding to the lipid vesicles, the partition experiments were repeated for **CPR**, **CPRT10** and **CPRT14** but now employing DMPE:DMPG (1:1) vesicles. Altogether, the steady-state and time-resolved fluorescence measurements revealed that **CPR** partition to these membranes was much weaker than to DMPG LUVs. In short, there was only a very small change in the spectral center-of-mass of **CPR** ($\Delta<\lambda>$= -4 nm, Table 1) and increase in its mean fluorescence lifetime (Fig. 4B) upon addition of increasing concentrations of these mixed lipid vesicles. The anisotropy decay of **CPR** in the presence of concentrations up

to 500 μM (outer leaflet) of the DMPE:DMPG (1:1) vesicles was also very similar to its decay in aqueous solution (Fig. 2 A). Assuming, as above, that the relative increase in its quantum yield is identical to the values obtained for the two hydrocarbon-modified peptides with this mixed membrane system, a correction factor $Q=1.9$ was calculated for **CPR** from the average of the $\bar{\tau}_L/\bar{\tau}_W$ values obtained in this case for the two peptides with a tail. The fitting of Eq. (12) to the steady state anisotropy data obtained for **CPR** (Fig. 5 B) lead to a very low $K_p= (1.2 \pm 0.4)\times 10^3$, showing the adverse effect of DMPE on the partition of **CPR** to the mixed DMPE:DMPG (1:1) membrane, compatible with our previous finding that this peptide does not partition to DMPE membranes [25]. In conclusion, **CPR** binding to the studied lipid membranes is strongly electrostatically driven, in agreement with the overall polar character of this cyclic peptide and its net charge of +3.

The modification of **CPR** with a hydrocarbon chain of 10 or 14 carbons significantly changed this behavior, since the partition of **CPRT10** and **CPRT14** is now strongly dependent on the length of the hydrophobic tail, but essentially independent of the anionic content of the membranes. The overall blue-shift displayed by the emission spectra of both lipid-modified peptides and the increase in their mean fluorescence lifetimes (Table 1 and Fig. 4 B), as well as the variation in their fluorescence anisotropy with the lipid concentration (Fig. 5 B) were very similar for DMPG and DMPE:DMPG (1:1) vesicles. A quantitative analysis of both the lifetime and anisotropy data confirmed this behavior since very similar partition constants were obtained for each cyclic peptide towards the anionic and mixed lipid vesicles, being the partition coefficient always one order of magnitude higher for **CPRT14** compared to **CPRT10** (Table 3).

Table 3. Partition constants, K_p, limiting mean fluorescence lifetimes, $\bar{\tau}_L$, and anisotropies, $< r >_L$, obtained for the interaction of **CPR**, **CPRT10** and **CPRT14** with

the lipid systems DMPG and DMPE:DMPG (1:1) at 38 $^{\circ}$C. The parameters are retrieved from fitting Eq. (10) to the time-resolved fluorescence data (K_p and $\bar{\tau}_L$), and fitting of Eq. (12) to the steady state anisotropy data (K_p and $< r >_L$). The uncertainties represent the errors obtained from the non-linear fits.

Peptide	Lipid vesicles	Time-resolved fluorescence data [*]		Steady-state anisotropy data [**]		
		K_p	$\bar{\tau}_L$ (ns)	K_p	$< r >_L$	$\bar{\tau}_L/\bar{\tau}_W$
CPR	DMPG	-	-	$(2.5 \pm 0.5) \times 10^4$	0.075 ± 0.004	1.8
	DMPE:DMPG (1:1)	-	-	$(1.2 \pm 0.4) \times 10^3$	0.10 ± 0.02	1.9
CPRT10	DMPG	$(2.2 \pm 0.5) \times 10^4$	2.3 ± 0.1	$(6.6 \pm 2.3) \times 10^4$	0.091 ± 0.005	1.8
	DMPE:DMPG (1:1)	$(1.3 \pm 0.3) \times 10^4$	2.7 ± 0.1	$(2.1 \pm 0.5) \times 10^4$	0.108 ± 0.008	2.1
CPRT14	DMPG	$(2.6 \pm 0.6) \times 10^5$	2.08 ± 0.04	-	-	1.8
	DMPE:DMPG (1:1)	$(1.1 \pm 0.2) \times 10^5$	2.20 ± 0.04	$(1.7 \pm 0.6) \times 10^5$	0.109 ± 0.005	1.8

[*] Eq. (10) was fitted to the mean fluorescence lifetime data displayed in Fig.4.

[**] Eq. (12) was fitted to the steady-state anisotropy data displayed in Fig. 5 while keeping a fixed $\bar{\tau}_L/\bar{\tau}_W$ ratio.

6. Leakage

Leakage studies are a very effective technique to detect the formation of membrane pores and/or membrane destruction, and thus a very important method to confirm the antimicrobial peptides' action on the phospholipid membrane. CF encapsulated in the inner aqueous phase of unilamellar vesicles was used to follow the dye release by action of the cyclic peptides' on lipid membranes of POPG and POPE:POPG (1:1). CF entrapped at high concentration in the aqueous compartment of liposomes is self-quenched, and upon its release from the vesicle it becomes diluted into the surrounding media and therefore its fluorescence emission will increase over time and thus the release can be monitored.

The complete leakage curves (including Triton X-100 addition) measured for the same concentration of lipid vesicles (~50 μM) and three different peptide concentrations (*i.e.,* at different L:P ratios) are shown in Fig. 6 for POPG (left panel, A,B,C) and POPE:POPG (1:1) lipid vesicles (right panel, D,E,F).

CPR induces very small leakage, except for POPG (Fig. 6A) membranes and a L:P (5:1) ratio. This result can be understood considering the behavior reported above and in our previous work [25]. The results for the mean fluorescence lifetime (Fig 4A) were rationalized as reflecting the occurrence of self-quenching [39] when a high surface concentration of peptide is reached at very low L:P ratios (5:1), driving the self-association of **CPR** into nanotubes at the membrane surface, as we had previously also found [25]. At L:P (5:1) there is a very high peptide concentration at the membrane, and thus nanotubes are formed and this in turn can lead to the observed high leakage, through a slow process as it involves self-association and leakage. In the case of POPE:POPG (1:1) (Fig. 6D), no significant leakage was observed at any L:P ratio, reflecting the reduction in membrane partition for this peptide as a results of the high

POPE content of the lipid vesicles. Altogether these results also comply with the very low antimicrobial activity reported for this peptide [26].
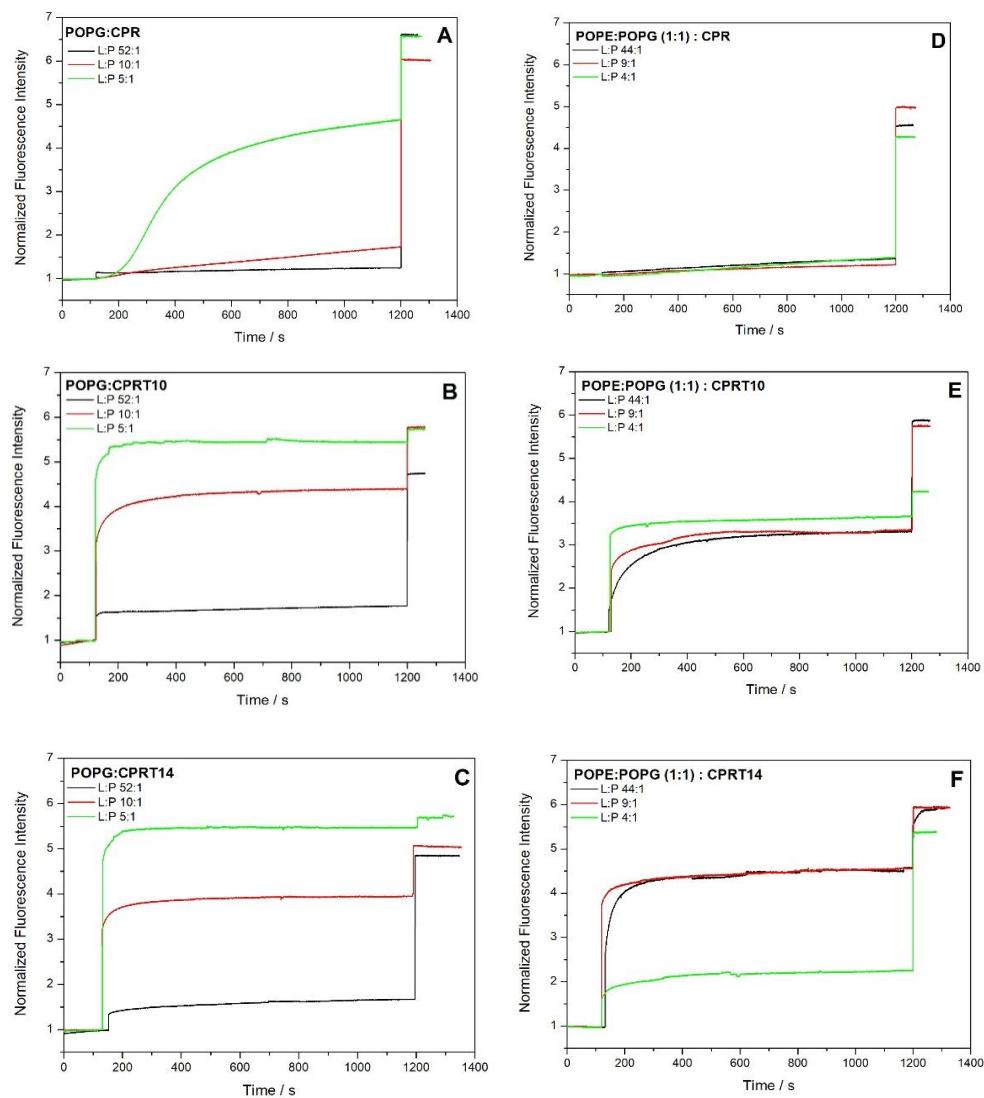
Fig. 6. Influence of lipid composition and peptide concentration on the CP-induced leakage of CF from liposomes. Complete curves of fluorescence intensity *vs* time for the CPs-induced leakage of CF from POPG (left panel) and POPE:POPG (1:1) (right panel) vesicles as function of time. In both cases the three used L:P ratios are plotted for each peptide and membrane system, with the peptide and lipid concentrations referred to in Material and Methods. The plots show the increase in the fluorescence signal at peptides' addition (120 s), and a final total CF release at TritonX-100's addition (1200 s), normalized to the fluorescence intensity before peptides' addition.

CPRT10 promotes a higher leakage in POPG lipid system as compared to POPE:POPG for L:P 10:1 and 5:1(Fig. 6 B,E), but in both cases a plateau is rapidly reached for all L:P ratios. As expected, in each case the leakage increases as the peptide concentration increases. Although we stated above that for **CPRT10** and **CPRT14** the partition was more dependent on the size of the hydrocarbon tail than on the lipid system, the K_p was nevertheless higher (about twice) for the fully negatively charged system, in line with the leakage results.

Finally, **CPRT14** has a similar behavior for the negatively charged system POPG, *i.e.*, inducing a leakage that increases with increase in peptide concentration (Fig.6 C). Curiously, a different behavior is observed for POPE:POPG (1:1) (Fig. 6F) at the highest peptide concentration, 10 μM (L:P 4:1), where the leakage significantly decreases (plateau occurs at about half of the normalized fluorescence intensity). This can be associated with the possible formation of micellar type aggregates for **CPRT14** at this concentration and temperature. If occurring, this might reduce the leakage, as we would have competition between self-association and partition, with two possible occurrences – dissociation of micellar type aggregates followed by partition to the membrane, or partition of the aggregates, that would be less effective. The fact that this is not seen for POPG (Fig 6.C) must result from the very strong membrane interaction with fully negatively charged membranes, that can overcome the self-assembling in solution, being energetically more favorable. This possibility would be in line with the previously determined *cac* (4.5 μM), for this peptide at room temperature (20 °C) [26], similar to what we used here in the leakage experiments (27 °C). As such, it does not contradict our findings here that at 10 μM and 38 °C the peptide was not associated in buffer, as the higher temperature should counteract the self-association. Finally, these observations correlate well with the higher antimicrobial activity of **CPRT10** and

CPRT14 as compared to **CPR**, particularly against Gram (+) pathogens, with previously reported low MIC values of *e.g.,* 16 µg·mL^{-1} against *Staphylococcus aureus*, 2 µg·mL^{-1} against *Staphylococcus epidermidis* [26].

7. Conclusions

The use of fluorescence spectroscopy allowed us to characterize the partition of these three peptides (parent peptide **CPR** and its derivatives with pending alkyl chains of 10 and 14 CH$_2$ groups, **CPRT10** and **CPRT14**, respectively) to two different lipid model membrane systems. Steady-state fluorescence measurements showed that the peptides bind to the membrane (blue shift of the maximum intensity for the Trp), and the extent of their partition could be quantified by either steady-state anisotropies and/or TRFS.

Our results clearly show that **CPR** has a lower partition to the membranes as compared to the hydrocarbon tail-modified peptides, particularly for the mixed membrane system DMPE:DMPG (1:1). The partition is mainly driven by electrostatics, with low membrane penetration, in full agreement with our previous results by other methods (DSC, FTIR and MD) [25] and with its very low antimicrobial activity [26].

The introduction of a hydrocarbon tail adjacent to the Trp residue, in **CPRT10** and **CPRT14**, significantly improved the partition to both membrane systems. Further to this, our results show that the length of the tail became the main distinguishing factor for the extension of the partition process – values of a similar order of magnitude were obtained for each peptide in both membrane systems, whereas in both cases K_p is about one order of magnitude higher for **CPRT14**.

Complementary to the partition we could also characterize the leakage behavior in both membrane systems. These studies indicated that **CPR** induces a limited leakage, at odds with the peptides with tail. **CPRT10 and CPRT14** induce fast leakage, which increases

in most cases with peptide concentration, being almost complete for the highest peptide
concentration and PG membranes. Overall, these results not only quantify the partition
process and allow distinction between the parent peptide (**CPR**) and its derivatives with
a hydrocarbon tail, but also rationalize the proven much higher antimicrobial activity of
CPRT10 and **CPRT14**.

ACKNOWLEDGMENT

REFERENCES

[1] D.I. Andersson, D. Hughes, Antibiotic resistance and its cost: is it possible to reverse resistance?, Nat. Rev. Micro., 8 (2010) 260-271. https://doi.org/10.1038/nrmicro2319.
[2] M. Fillion, G. Valois-Paillard, A. Lorin, M. Noël, N. Voyer, M. Auger, Membrane interactions of synthetic peptides with antimicrobial potential: effect of electrostatic interactions and amphiphilicity, Probiotics & Antimicro. Prot., 7 (2015) 66-74. https://doi.org/10.1007/s12602-014-9177-z.
[3] A. Li, P.Y. Lee, B. Ho, J.L. Ding, C.T. Lim, Atomic force microscopy study of the antimicrobial action of Sushi peptides on Gram negative bacteria, Biochim. Biophys. Acta, Biomembr., 1768 (2007) 411-418. https://doi.org/10.1016/j.bbamem.2006.12.010
[4] V. Teixeira, M.J. Feio, M. Bastos, Role of lipids in the interaction of antimicrobial peptides with membranes, Prog. Lipid Res., 51 (2012) 149-177. https://doi.org/10.1016/j.plipres.2011.12.005.

[5] M.S. Zharkova, D.S. Orlov, O.Y. Golubeva, O.B. Chakchir, I.E. Eliseev, T.M. Grinchuk, O.V. Shamova, Application of Antimicrobial Peptides of the Innate Immune System in Combination With Conventional Antibiotics—A Novel Way to Combat Antibiotic Resistance?, Front. Cell. Infect. Microbiol., 9 (2019) 128. https://doi.org/10.3389/fcimb.2019.00128.

[6] M. Wilmes, B.P.A. Cammue, H.-G. Sahl, K. Thevissen, Antibiotic activities of host defense peptides: more to it than lipid bilayer perturbation, Nat. Prod. Rep, 28 (2011) 1350-1358. https://doi.org/10.1039/C1NP00022E.

[7] L.A. Calderon, A.M. Soares, R.G. Stábeli, Anuran Antimicrobial Peptides: an alternative for the development of nanotechnological based therapies for multi-drug-resistant infections, Signpost Open J Biochem Biotech, 1 (2012) 1-11.

[8] C.D. Fjell, J.A. Hiss, R.E.W. Hancock, G. Schneider, Designing antimicrobial peptides: form follows function, Nat. Rev. Drug Discov., 11 (2011) 37-51. https://doi.org/10.1038/nrd3591.

[9] W.C. Wimley, K. Hristova, Antimicrobial peptides: successes, challenges and unanswered questions, J. Membr. Biol., 239 (2011) 27-34. https://doi.org/10.1007/s00232-011-9343-0.

[10] K.A. Brogden, Antimicrobial peptides: pore formers or metabolic inhibitors in bacteria?, Nat. Rev. Microbiol., 3 (2005) 238-250. https://doi.org/10.1038/nrmicro1098.

[11] B. Claro, E. González-Freire, M. Calvelo, L.J. Bessa, E. Goormaghtigh, M. Amorín, J.R. Granja, R. Garcia-Fandiño, M. Bastos, Membrane targeting antimicrobial cyclic peptide nanotubes – an experimental and computational study, Colloids Surf. B, 196 (2020) 111349. https://doi.org/10.1016/j.colsurfb.2020.111349.

[12] L.T. Nguyen, E.F. Haney, H.J. Vogel, The expanding scope of antimicrobial peptide structures and their modes of action, Trends Biotechnol., 29 (2011) 464-472. https://doi.org/10.1016/j.tibtech.2011.05.001.

[13] T. Silva, R. Adão, K. Nazmi, J.G.M. Bolscher, S.S. Funari, D. Uhríková, M. Bastos, Structural diversity and mode of action on lipid membranes of three lactoferrin candidacidal peptides, Biochim. Biophys. Acta, Biomembr., 1828 (2013) 1329-1339. http://doi.org/10.1016/j.bbamem.2013.01.022.

[14] L. Yang, T.A. Harroun, T.M. Weiss, L. Ding, H.W. Huang, Barrel-stave model or toroidal model? A case study on melittin pores, Biophys.J., 81 (2001) 1475-1485. http://doi.org/10.1016/S0006-3495(01)75802-X.

[15] C. Appelt, A. Wessolowski, M. Dathe, P. Schmieder, Structures of cyclic, antimicrobial peptides in a membrane-mimicking environment define requirements for activity, J. Pept. Sci., 14 (2008) 524-527. http://doi.org/ 10.1002/psc.924.

[16] M. Dathe, H. Nikolenko, J. Klose, M. Bienert, Cyclization increases the antimicrobial activity and selectivity of arginine-and tryptophan-containing hexapeptides, Biochemistry, 43 (2004) 9140-9150. http://doi.org/10.1021/bi035948v.

[17] S. Fernandez-Lopez, H.-S. Kim, E.C. Choi, M. Delgado, J.R. Granja, A. Khasanov, K. Kraehenbuehl, G. Long, D.A. Weinberger, K.M. Wilcoxen, M.R. Ghadiri, Antibacterial agents based on the cyclic *D,L*-α-peptide architecture, Nature, 412 (2001) 452-455. http://doi.org/10.1038/35086601

[18] S. Gunasekera, T. Muhammad, A.A. Strömstedt, K.J. Rosengren, U. Göransson, Backbone Cyclization and Dimerization of LL-37-Derived Peptides Enhance Antimicrobial Activity and Proteolytic Stability, Front. Microbiol, 11 (2020) 168. https://doi.org/10.3389/fmicb.2020.00168.

[19] J.D. Hartgerink, J.R. Granja, R.A. Milligan, M.R. Ghadiri, Self-Assembling Peptide Nanotubes, J. Am. Chem. Soc., 118 (1996) 43-50. https://doi.org/10.1021/ja953070s.

[20] R. García-Fandiño, M. Amorín, L. Castedo, J.R. Granja, Transmembrane ion transport by self-assembling α,γ-peptide nanotubes, Chem. Sci., 3 (2012) 3280-3285. https://doi.org/10.1039/C2SC21068A.

[21] K. Rosenthal-Aizman, G. Svensson, A. Undén, Self-assembling peptide nanotubes from enantiomeric pairs of cyclic peptides with alternating D and L amino acid residues, J. Am. Chem. Soc., 126 (2004) 3372–3373. https://doi.org/10.1021/ja0372659

[22] H.S. Kim, J.D. Hartgerink, M.R. Ghadiri, Oriented Self-Assembly of Cyclic Peptide Nanotubes in Lipid Membranes, J. Am. Chem. Soc., 120 (1998) 4417-4424. https://doi.org/10.1021/ja9735315.

[23] R.-V. Nuria, H.L. Ozores, G. Arcadio, G.-F. Eva, F. Alberto, P. Michele, M.P. Juan, O. Juan, M. Javier, G.-F. Rebeca, A. Manuel, R.G. Juan, Membrane-Targeted Self-Assembling Cyclic Peptide Nanotubes, Curr. Top. Med. Chem., 14 (2014) 2647-2661. http://doi.org/10.2174/1568026614666141215143431.

[24] M.R. Ghadiri, J.R. Granja, L.K. Buehler, Artificial transmembrane ion channels from self-assembling peptide nanotubes, Nature, 369 (1994) 301-304. https://doi.org/10.1038/369301a0.

[25] B. Claro, A. Peón, E. González-Freire, E. Goormaghtigh, M. Amorín, J.R. Granja, R. Garcia-Fandiño, M. Bastos, Macromolecular assembly and membrane activity of antimicrobial *D,L*-α-Cyclic peptides, Colloids Surf. B, Submitted (2021).

[26] E. González-Freire, F. Novelli, A. Pérez-Estévez, R. Seoane, M. Amorín, J.R. Granja, Double orthogonal click reactions for the development of antimicrobial peptide nanotubes, Chem. Eur. J., 27 (2020) 3029-3038. https://doi.org/10.1002/chem.202004127

[27] G.R. Bartlett, Phosphorus assay in column chromatography, J. Biol. Chem., 234 (1959) 466-468.

[28] S. Huláková, B. Fulier, J. Gallová, P. Balgavý, Effect of N-dodecyl-N,N-dimethylamine N-oxide on unilamellar liposomes, Eur. J. Pharm. Sci., 60 (2013) 7-13. https://doi.org/10.2478/afpuc-2013-0021

[29] C.A. Royer, C.J. Mann, C.R. Matthews, Resolution of the fluorescence equilibrium unfolding profile of trp aporepressor using single tryptophan mutants, Protein Sci., 2 (1993) 1844-1852. http://doi.org/ 10.1002/pro.5560021106

[30] J. Lakowicz, Principles of Fluorescence Spectroscopy, third ed., Springer, Boston, MA 2006.

[31] R.F.M. de Almeida, L.M.S. Loura, M. Prieto, A. Watts, A. Fedorov, F.J. Barrantes, Structure and dynamics of the γM4 transmembrane domain of the acetylcholine receptor in lipid bilayers: insights into receptor assembly and function, Mol. Membr. Biol., 23 (2006) 305-315. http://doi.org/ 10.1080/09687860600703613

[32] J.A. Poveda, M. Prieto, J.A. Encinar, J.M. González-Ros, C.R. Mateo, Intrinsic Tyrosine Fluorescence as a Tool To Study the Interaction of the Shaker B "Ball" Peptide with Anionic Membranes, Biochemistry, 42 (2003) 7124-7132. http://doi.org/ 10.1021/bi027183h

[33] A.M. Melo, A. Fedorov, M. Prieto, A. Coutinho, Exploring homo-FRET to quantify the oligomer stoichiometry of membrane-bound proteins involved in a cooperative partition equilibrium, Phys. Chem. Chem. Phys., 16 (2014) 18105-18117. http://doi.org/10.1039/C4CP00060A

[34] M. Bastos, G. Bai, P. Gomes, D. Andreu, E. Goormaghtigh, M. Prieto, Energetics and partition of two cecropin-melittin hybrid peptides to model membranes of different composition, Biophys.J., 94 (2008) 2128-2141. http://doi.org/10.1529/biophysj.107.119032

[35] N.C. Santos, M. Prieto, M.A.R.B. Castanho, Quantifying molecular partition into model systems of biomembranes: an emphasis on optical spectroscopic methods, Biochim. Biophys. Acta, Biomembr., 1612 (2003) 123-135. https://doi.org/10.1016/S0005-2736(03)00112-3

[36] A.H. Clayton, W.H. Sawyer, Site-specific tryptophan fluorescence spectroscopy as a probe of membrane peptide structure and dynamics, Eur. Biophys. J., 31 (2002) 9-13. http://doi.org/10.1007/s002490100182.

[37] C.R. Mateo, R.F.M.d. Almeida, L.M.S. Loura, M. Prieto, From lipid phases to membrane protein organization: fluorescence methodologies in the study of lipid-protein interactions, in: M. C.R., G. J., V. J., G.-R. J.M. (Eds.) Protein-Lipid Interactions: New Approaches and Emerging Concepts, vol. 9, Springer, Berlin, Heidelberg, 2006.

[38] V. Teixeira, M.J. Feio, L. Rivas, B.G. De la Torre, D. Andreu, A. Coutinho, M. Bastos, Influence of Lysine Nε-Trimethylation and Lipid Composition on the Membrane Activity of the Cecropin A-Melittin Hybrid Peptide CA(1−7)M(2−9), J. Phys. Chem. B, 114 (2010) 16198-16208. http://doi.org/ 10.1021/jp106915c

[39] M. Rodrigues, A. Santos, B.G. de la Torre, G. Rádis-Baptista, D. Andreu, N.C. Santos, Molecular characterization of the interaction of crotamine-derived nucleolar targeting peptides with lipid membranes, Biochim. Biophys. Acta, Biomembr., 1818 (2012) 2707-2717. https://doi.org/10.1016/j.bbamem.2012.06.014

[40] B. Valeur, G. Weber, Resolution of the fluorescence excitation spectrum of indole into the 1La and 1Lb excitation bands, Photochem. Photobiol., 25 (1977) 441-444. http://doi.org/10.1111/j.1751-1097.1977.tb09168.x

Supplementary Material

Partition of antimicrobial *D-L-α*-Cyclic Peptides into bacterial model membranes

Bárbara Claro[a], Eva González-Freire[b], Juan R. Granja[b], Rebeca Garcia-Fandiño[a,b], Jana Gallová[c], Daniela Uhríková[c], Aleksander Fedorov[d], Ana Coutinho[d,e*], Margarida Bastos [a,*]

[a] CIQUP, Centro de Investigação em Química, Departamento de Química e Bioquímica, Faculdade de Ciências, Universidade do Porto, Porto, Portugal;

[b] Centro Singular de Investigación en Química Biolóxica e Materiais Moleculares (CiQUS), Departamento de Química Orgánica, Universidade de Santiago de Compostela, 15782 Santiago de Compostela, Spain

[c] Faculty of Pharmacy, Comenius University in Bratislava, 832 32 Bratislava, Slovak Republic

[d] Centro de Química -Física Molecular and Institute of Nanoscience and Nanotechnology, Instituto Superior Técnico, Universidade de Lisboa

Corresponding authors: Margarida Bastos (mbastos@fc.up.pt);

Ana Coutinho (ana.coutinho@tecnico.ulisboa.pt)

Table S1. Time-resolved fluorescence parameters (amplitudes, α_i, and fluorescence times, τ_i) for CPR, CPRT10 and CPRT14 in aqueous buffer and in the presence of 500 µM (outer leaflet) DMPG or DMPE:DMPG 1:1 large unilamellar vesicles at 38 °C.

Peptide	Medium	α_1	τ_1 (ns)	α_2	τ_2 (ns)	α_3	τ_3 (ns)	χ^2
CPR	buffer	0.23	0.32	0.61	1.2	0.16	2.8	1.126
	DMPG	0.29	0.51	0.46	1.5	0.25	3.6	1.135
	DMPE:DMPG (1:1)	0.19	0.35	0.59	1.2	0.21	3.1	0.898
CPRT10	buffer	0.29	0.35	0.59	1.3	0.12	3.1	1.101
	DMPG	0.25	0.48	0.39	1.6	0.37	3.7	1.027
	DMPE:DMPG (1:1)	0.22	0.70	0.47	2.1	0.31	4.0	1.003
CPRT14	buffer	0.26	0.30	0.58	1.2	0.16	2.9	1.081
	DMPG	0.22	0.34	0.42	1.5	0.36	3.9	1.308
	DMPE:DMPG (1:1)	0.22	0.49	0.45	1.8	0.33	3.8	1.062

VI. **"Study of Antimicrobial *D,L*-α-Cyclic Peptides by Small-Angle X-Ray Scattering: the membrane charge effect"**

Bárbara Claro, Juan R. Granja, Rebeca Garcia-Fandiño, Daniela Uhríková, Margarida Bastos

Study of Antimicrobial *D,L*-α-Cyclic Peptides by Small-Angle X-Ray Scattering: the membrane charge effect

Bárbara Claro[a], Juan R. Granja[b], Rebeca Garcia-Fandiño[a,b], Daniela Uhríková[c],

Margarida Bastos [a,*]

[a]CIQUP, Centro de Investigação em Química, Departamento de Química e Bioquímica, Faculdade de Ciências, Universidade do Porto, Porto, Portugal;
[b]Centro Singular de Investigación en Química Biolóxica e Materiais Moleculares (CiQUS), Departamento de Química Orgánica, Universidade de Santiago de Compostela, 15782 Santiago de Compostela, Spain
[c]Faculty of Pharmacy, Comenius University in Bratislava, 832 32 Bratislava, Slovak Republic

Corresponding authors: Margarida Bastos (mbastos@fc.up.pt)

Abstract

The present extremely high resistance to antibiotic turns the discovery of new antibiotic paradigms into a mandatory global health goal. Antimicrobial peptides (AMPs) represent a new approach to conventional therapeutics, as their main target is the pathogen membrane. Among these, antimicrobial *D,L*-α-cyclic peptides, with an even number of *D*- and *L*-amino acids have recently emerged. We used Small Angle X-ray diffraction (SAXS) to characterize structurally the interactions of a group of *D,L*-α-cyclic peptides with two different lipid model membranes [DMPE and DMPE:DMPG (1:3)], aiming at further understanding their mechanism of action. The effect of our five previously studied *D,L*-α-Cyclic peptides on DMPE(a highly prevalent lipid in bacterial membranes) model membranes was assessed, in gel and fluid phases. With the more promising peptides, with higher antimicrobial activity, we used also bacteria model membranes of DMPE:DMPG 3:1.

Our results show that all the peptides studied interact differently with both membrane systems, revealing that all factors are important in the differentiation – the peptide, the lipid membrane composition, the lipid phase and the lipid:peptide molar ratio.

As regarding the interactions with the lipid membrane bacterial model DMPE:DMPG 3:1, the results clearly show that the peptides with higher hydrophobic character (**CP1**, **CPRT10** and **CPRT14)** induce much larger structural changes, in line with their proven antimicrobial activity.

1. Introduction

Antimicrobial peptides (AMPs) are molecules that are present in the innate immune system of almost all living organisms, and that have been proposed as promising molecules to replace conventional antibiotics [1-3]. Finding new antibiotic paradigms is of major importance nowadays, due to a global emergence of multidrug-resistant bacteria, that led to an antibiotics' efficacy decay [4]. AMPs represent a new approach to conventional therapeutics, as their main target is the pathogen membrane and not a specific protein, lowering thus the rapid emergence of resistance [5-8]. Unfortunately, this could not yet be achieved due to several limitations, such as systemic toxicity and high dosing in order to maintain a sufficient concentration of drug.

Different strategies have been used to increase the antimicrobial properties and activity of AMPs against diverse pathogens, together with the decrease in their cytotoxicity toward host cells [6]. One recent proposed strategy is the use of cyclic peptides, that has shown to enhance peptide's activity [9-11]. Within this line, the use of antimicrobial *D*,*L*-α-cyclic peptides (*D*,*L*-α-CPs), with an even number of alternating *D*- and *L*-amino acids, has experimented a increasing interest [10, 12-16]. *D*,*L*-α-CPs are known to self-assemble under appropriate conditions (like in presence of a membrane[13]), by intermolecular hydrogen bonds between the peptide bonds (proton (N-H) and carbonyl (C=O)). These peptides adopt flat-ring-shape conformations with the amide functions extended perpendicularly to the plane of the backbone cyclic structure. This assembling leads to tubular β-sheet structures, that are the supramolecular active structures, and have been named self-assembled cyclic peptide nanotubes (SCPNs). These *D*,*L*-α-CPs can be tunned to act as antimicrobial peptides by varying the number and/or the type of amino acids present, changing the solubility, diameter, and the outer properties of the nanotube [10, 12]. Further to these aspects, the presence of *D*-amino acids in the CPs' structure it is also metabolically an important factor, since it helps to increase their resistance against protease degradation, which alongside with their

robust secondary structure, makes these CPs very promising antimicrobial candidates [12, 15].

Different mechanisms of action have been proposed for different AMPs [5, 17, 18]. As regarding *D,L*-α-CPs, although their mechanism is not clearly established [10, 19, 20], the available information suggests that they tend to follow mechanisms that reply on same basis as conventional AMPs. Thus, the action is triggered by electrostatic interaction, where the cationic residues present in the peptides interact with the anionic bacterial membrane (pathogens have a predominance of lipids with negatively charged headgroups in the outer leaflet). Latter, the hydrophobic groups promote the CP's insertion into the membrane core [13]. As a result, accumulation of the peptide at the membrane surface occurs, and after a threshold value a structure rearrangement occurs, leading to segregation / permeabilization, pore formation or aggregation, membrane stacking or membrane micellization [21-25]. In the case of the *D,L*-α-CPs, it has been proposed that nanotubes are the active component whose formation is triggered by hydrogen bond formation strengthened by the lipidic media.

X-ray diffraction (SAXS) is a powerful experimental technique in lipid membrane studies, as structural parameters of the various lamellar, hexagonal or cubic phases can be derived from SAXS measurements in appropriate conditions, as well as their changes upon interaction with other molecules [42]. This can elucidate the structural changes in membranes upon contact with antimicrobial peptides, contributing thus to the unravelling of molecular mechanisms responsible for the bacterial killing activity [26, 27].This technique is very useful in biological studies, since it can be performed under near-physiological conditions, varying parameters like pH, ionic strength, concentration of additives, temperature, and providing detailed information on structure and function of peptides and proteins [24, 28-30], as well as on the structure of hydrated membranes alone and when interacting with peptides and proteins [24, 31-34]. Alongside with SAXS, wide angle x-ray scattering (WAXS) can also be used to examine and characterize the hydrocarbon chain packing in lipid assemblies, thus providing a detailed information of their supramolecular and local structure [35].

In present work, we studied a group of *D,L*-α-CPs (**CP1**, **CP2**, **CPR**, **CPRT10** and **CPRT14,** Table 1 and Fig. 1), previously reported by our group as potential antimicrobial peptides [19, 20, 36, 37], with the aim to characterize their influence on the structure of selected lipid model membranes, helping thus the unravelling of their mechanism of action.

CP1 is an original Ghadiri's peptide [10] of known antimicrobial activity, used as template to create **CP2,** designed to improve the solubility in aqueous solution [19]. **CP1** has an ideal amphipathic structure, characteristic of the best AMPs, containing on

one side basic residues to promote affinity for the negatively charged bacterial membranes (hydrophilic part), and another part composed of hydrophobic residues (of which three tryptophans), to promote insertion into the membrane core (hydrophobic part). **CP2** has a reduced hydrophobic content (only one tryptophan), that combined with three charged lysines and polar non-charged residues led to an increased solubility. The peptides **CPR**, **CPRT10** and **CPRT14** are second generation, derived from **CP2**, mutating a lysine in **CP2** by an arginine in **CPR**. Finally, **CPRT10** and **CPRT14** were obtained from **CPR** by attaching a 10 and a 14 hydrocarbon tail, respectively, to the propargylglycine group (Pg) structure in **CPR**. All the peptides were studied in presence of multilamellar vesicles (MLVs) of the zwitterionic lipid DMPE (1,2-dimyristoyl-sn-glycero-3-phosphoethanolamine), highly prevalent in bacterial membranes. Thereafter we chose the second-generation peptides (**CPR**, **CPRT10** and **CPRT14**) for further study, because of their improved antimicrobial activity, especially against Gram-positive bacteria [12]. We did then use oligolamellar vesicles (OLVs) of mixtures of DMPE with DMPG (1,2-dimyristoyl-sn-glycero-3-phospho-(1'-rac-glycerol)), at a 3:1 molar ratio.

Our results show that the five peptides interact differently with both membrane systems, showing that all factors are important in the differentiation – the peptide, the lipid membrane composition, the lipid phase and the lipid:peptide (L:P) molar ratio.

Original CP

2nd Generation of CPs
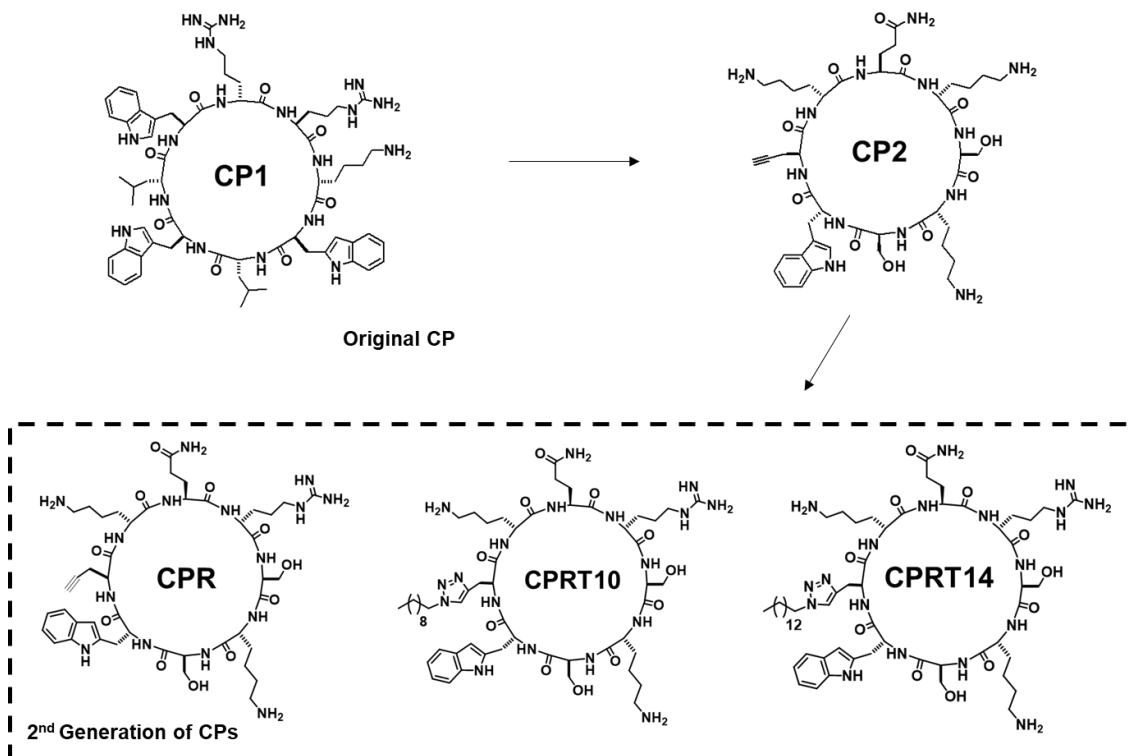
Fig. 1. Cyclic Peptides Structures used in this study. **CP1** is the original peptide from Ghadiri's group [10], **CP2** derived from this first peptide (changes described in then text) and was then used as template for the second generation peptides, **CPR**, **CPRT10** and **CPRT14**.

2.   Materials and Methods

2.1.   Peptides

The peptide's synthesis, purification and characterization were previously described [12, 19]. The amino acid composition of the used peptides can be found in Table 1.

Table 1 - *D,L*-α-Cyclic Peptides used. Pg denotes propargylglycine group, X that denotes (*S*)-2-amino-3-(1λ^2,2,3-triazol-4-yl)propanoic acid to which a hydrocarbon tail is attached in the case of **CPRT10** and **CPRT14.** The underline residues are *D* amino acids.

NAME OF PEPTIDE	STRUCTURE
CP1	*c*-[RRKWLWLW]
CP2	*c*-[KSKSWPgKQ]
CPR	*c*-[RSKSWPgKQ]
CPRT10	*c*-[RSKSWX^{C10}KQ]
CPRT14	*c*-[RSKSWX^{C14}KQ]

2.2.   Preparation and Characterization of Liposomes

DMPE powder rigorously weighted was directly hydrated with buffer (HEPES (10 mM HEPES, 150 mM NaCl, 0.02% NaN$_3$, 1 mM EDTA, pH 7.45), all purchased from Sigma-Aldrich, Germany), pH 7.45), since it is a single lipid that can easily form multilamellar structures using this procedure.

Mixtures of DMPE and DMPG (Avanti Polar Lipids, Alabama, USA) at a 3:1 molar ratio were weighted and dissolved in an azeotropic mixture of chloroform/methanol (87.4:12.6 %(v/v)). A lipid film was obtained by evaporating the chloroform/methanol under vacuum at a rotary evaporator at 70 °C and then kept overnight under high vacuum (< 10 mbar) to remove any trace of the organic solvents. The lipid film was then hydrated with the same buffer, at temperature ~60 °C (mixture in fluid phase). DMPE and DMPE:DMPG (3:1) suspensions , went through several cycles of vortex/incubation, at a temperature above own T_m, and then frozen in liquid nitrogen and thawed above respective T_m, repeating the sequence 5 times. The final phospholipid concentration was determined in the end using a modified version of the

Bartlett phosphate assay [38]. In the case of **CP1,** 0.7% of DMSO was added to the buffer due to its low solubility in pure aqueous media**,** and the same buffer was used to prepare the lipid system, using the same preparation procedure.

The average particle sizes were measured by dynamic light scattering (DLS) after preparation on a Malvern Zetasizer Nano ZS from Malvern Instruments (Malvern, UK). The measurements were performed above the transition temperature of each system (T_m) at a total lipid concentration of 0.1 mM, using a He-Ne laser (wavelength 633 nm) as a source of incident light, and operating at a scattering angle of 173°.

Mixtures of CPs and lipids were prepared three days before the measurements. The CPs solution (in the same buffer as the prepared liposomes) was in each case added to the lipid suspension, at the desired lipid-to-peptide (L:P) ratio, and the samples were then incubated for 30 min above the lipid or lipid mixture's T_m. After this the samples were transfered into glass capillaries (Spezialglas Markröhrchen 1.5 mm capillaries; Glass Technik 37 & Konstruktion – Müller & Müller OHG, Germany), and centrifuged for 2 min at 2000 g. This step was carefully repeated until we had a good amount of sample mixture at the bottom and a significant amount of supernatant in the capillaries, to guarantee that all samples were studied at high water contents. Lastly, the capillaries were sealed with a melted commercial wax.

2.3.   SAXS and WAXS Measurements

SAXS and WAXS experiments were performed at the BL11 - NCD-SWEET beamline of the ALBA synchrotron (Cerdanyola del Vallès, Spain) using linearly polarized radiation with a wavelength 1 Å. CCD Quantum 210r camera was supplied by ADSC for SAXS detection. The WAXS detector was the LX255HS, which was equipped with three cooled CCD modules from Rayonix having a dynamic range of 16 bits. The raw data were normalized against the incident beam intensity. The q range was calibrated using silver behenate (AgBh) for SAXS and comium oxide (Cr_2O_3) for WAXS. Scattering patterns were evaluated according to the intensity of the incident beam following an exponential model. SAXS diffraction maxima were derived by fitting each peak with a Lorentzian curve and a linear background. The capillary samples were placed vertically and thermalized before being exposed to the radiation. Linkam® TMS600 heating stage was used for the measurements. SAXS/WAXS patterns were taken with different temperature programs, depending on lipid system:

i) DMPE, scan from 30 °C to 70 °C at a heating rate of 1 °C/min, with a recorded frame of every minute, with 0.4 s exposure. Temperature scans were performed at a scan rate 1 °C/min;

ii) DMPE:CPs, 4 frames each, with 2 s exposure, at 30°, 40°, 45° and 55°C;

iii) DMPE:DMPG (3:1) and DMPE:DMPG (3:1):CPs, 6 frames each with 2 s exposure, at 20°C, 30°, 37°C, 40°, 45° and 55°C.

All samples underwent through an equilibration period of ~30 min before each measurement in a water bath at a temperature above the respective T_m, and a three-minute equilibration time before exposure to the radiation.

2.4. Results and discussion

DMPE membranes

Typical SAXS patterns for pure DMPE at selected temperatures in the gel and fluid phase (T_m = 50.3 °C, as determined by us in same buffer composition [18]), are plotted in Fig. 1. All patterns show a system with long-range order, characteristic of well-organized DMPE multilamellar vesicles. The repeat distance, d, derived from the position of peak's maxima, is a sum of the lipid bilayer thickness (d_L) and the thickness of the water layer (d_w) between bilayers. From analysis of peak positions in SAXS we retrieved d_1= 5.62±0.01 nm at 30 °C and d_1= 4.89±0.01 nm at 55 °C (Table 2), in very good agreement of the values reported for DMPE by Ortiz *et al.* [39] (d_1= 5.6 nm at 25 °C and d_1= 4.8 nm at 55 °C). The repeat distance values obtained for DMPE in the buffer containing 0.7% of DMSO, which was used with the peptide **CP1**, were very similar to the ones obtained in its absence, namely d_1= 5.62±0.01 nm at 30 °C and d_1= 4.8±0.3 nm at 55 °C.
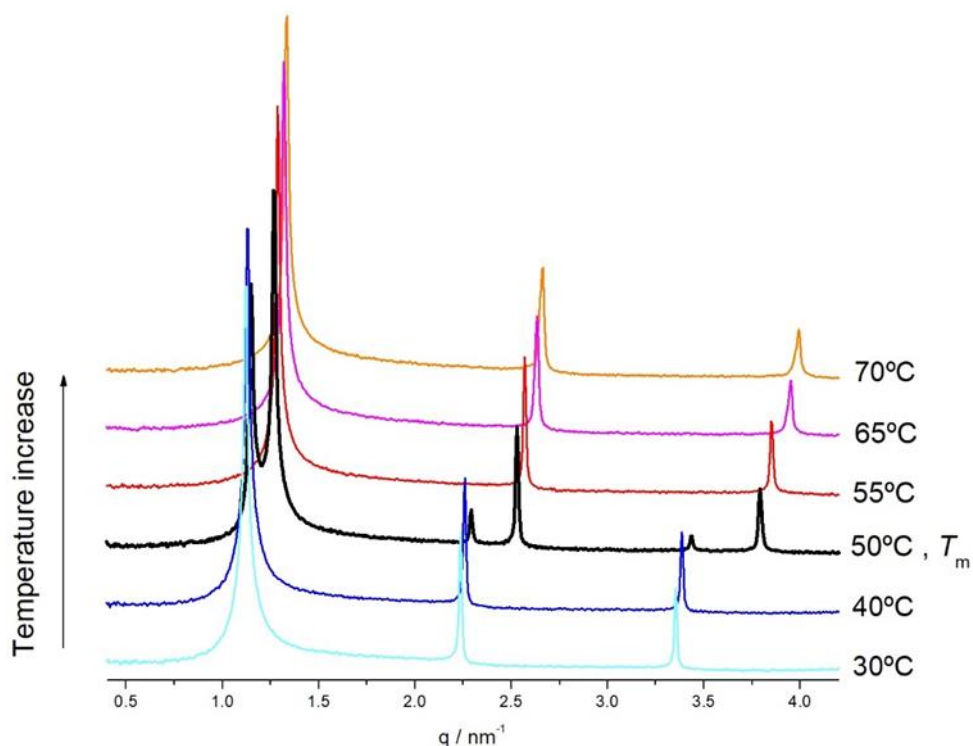
Fig. 2. SAXS patterns of DMPE multilamellar vesicles at selected temperatures in gel and fluid phases. The transition temperature at ~50 °C is also clear here from the respective pattern.

To obtain information about the packing of the DMPE acyl chains in both phases, we also made measurements in the wide-angle region (WAXS). In Fig. 3 are plotted the WAX patterns obtained at the same chosen temperatures. The patterns as a function of temperature show order-disorder characteristic of the lipid's acyl chains in a gel and liquid-crystalline state, respectively. Below the phase transition (30 °C, Fig. 2), pure DMPE shows a single, sharp symmetric peak at $q \sim 15.02$ nm^{-1}, characteristic for lipid's acyl chains packed in a hexagonal lattice, with the direction of the chains normal to the membrane surface, characteristic of an untitled gel phase (*L*β) [40]. This value is in perfect agreement with the one we found in a previous study for another PE system [24], where we got for POPE a WAX peak maximum at $q\sim15.76$ nm^{-1}. These values correspond to an average separation of the hydrocarbon chains of ~ 0.4 nm [23]. Above the phase transition (55 °C, Fig. 2) we can see a very broad component centered at $q \sim 14$ nm^{-1}, characteristic for lipid's acyl chains in a fluid, liquid crystalline state.
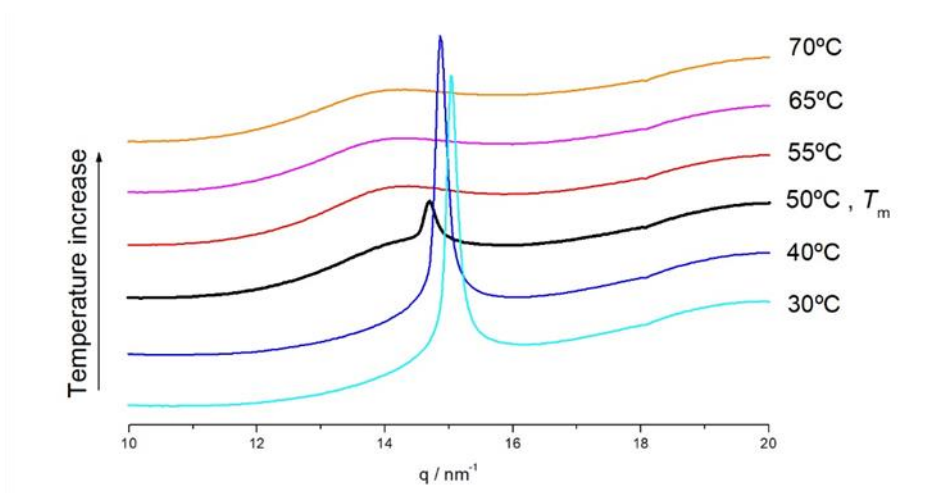
Fig. 3. WAXS patterns of DMPE multilamellar vesicles at the same selected temperatures as shown for SAXS in Fig. 2.

After the SAXS and WAXS characterization of the DMPE liposomes alone, the effect of the cyclic antimicrobial peptide's candidates (5 peptides, described in Table 1 and Fig. 1) was tested on this lipid system, at different L:P ratios. Examples of the obtained SAXS patterns for mixture of each peptide with DMPE at the highest studied L:P ratio in each case can be seen in Fig. 4 (30 °C, gel phase) and Fig. 5 (55 °C, fluid phase).
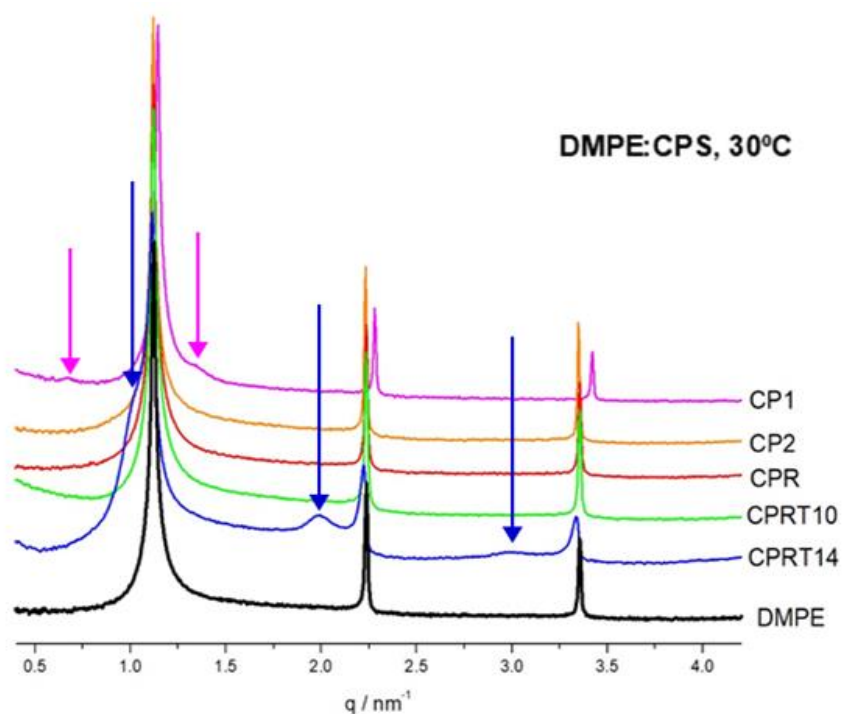
Fig. 4– SAXS patterns of DMPE and its mixtures with the five studied CPs at the highest L:P ratio for each one, at 30ºC (gel phase). The arrows show the reflections of the additional lamellar phase (magenta for **CP1** and blue for **CPRT14**).

As can be seen in Fig. 3, in the gel state **CPRT14** has a significant effect on the structure of DMPE vesicles, presenting an onset of an additional lamellar phase. We determined its repeat distance, d_2 = 6.3±0.2 nm at both L:P ratios (Table 2). We detected also a slight increase in d_1, giving values 5.66 nm for L:P 24:1 and 5.70 nm for 15:1.. In the case of **CP1**, a small shift to the right in all reflections is observed, that can be due to the presence of DMSO, as well as the appearance of a new lamellar phase, although with less intense reflections as compared to **CPRT14**, but resulting in a much larger increase in repeat distance, to 9.3 nm (Table 2). This increase is easy to rationalize, as DMPE is a zwitterionic lipid, with a surface charge close to zero at the studied pH, and thus the partition of positively charged peptides to the lipid membrane should increase the surface charge that will became positive, and consequently separate the bilayers, with increase in the repeat distance, as observed for these two peptides. The coexistence of two lamellar phases suggests that the distribution of the two peptides is not homogeneous in the membrane, with parts rich in the peptides, with significantly higher repeat distances, whereas other parts of the membrane have a low peptide content and thus keeping repeat distances close to the ones observed for DMPE. As regarding the other peptides, **CP2**, **CPR** and **CPRT10**, they do not affect the lamellar phase of DMPE in gel phase (Fig. 4 and Table 2).

Table 2. Repeat distances retrieved for pure DMPE and its mixtures with the five studied peptides, at different molar ratios (L:P) and at temperatures 30 ºC (gel phase) and 55 ºC (fluid phase).

	CP	L:P	30 ºC		55 ºC
			d_1/ nm	d_2/ nm	d_1/ nm
DMPE	-	1:0	**5.62±0.01**	-	**4.89±0.01**
	CP1	25:1	5.51±0.01	9.3±0.2	4.76±0.01
		19:1	5.47±0.01	9.3±0.4	4.72±0.01
	CP2	19:1	5.63±0.01	-	4.89±0.01
	CPR	25:1	5.62±0.01	-	4.89±0.01
	CPRT10	18:1	5.62±0.01	-	4.92±0.01
		11:1	5.62±0.01	-	4.92±0.01
	CPRT14	24:1	5.66±0.01	6.3±0.2	4.96±0.01
		15:1	5.70±0.05	6.3±0.2	5.0±0.1

Considering now the fluid phase, we can see in Fig. 5 and Table 2 that we observe in all cases only one lamellar phase, for all peptides and L:P ratios. Taking a close look at the values presented in Table 2, we can see that, as expected, there are no differences in the repeat distances in the presence of **CP2** and **CPR**. The peptides **CP1**, **CPRT14** and **CPRT10** affected the lamellar packing of DMPE, however the changes in the repeat distances do not exceed ± 0.2 nm.
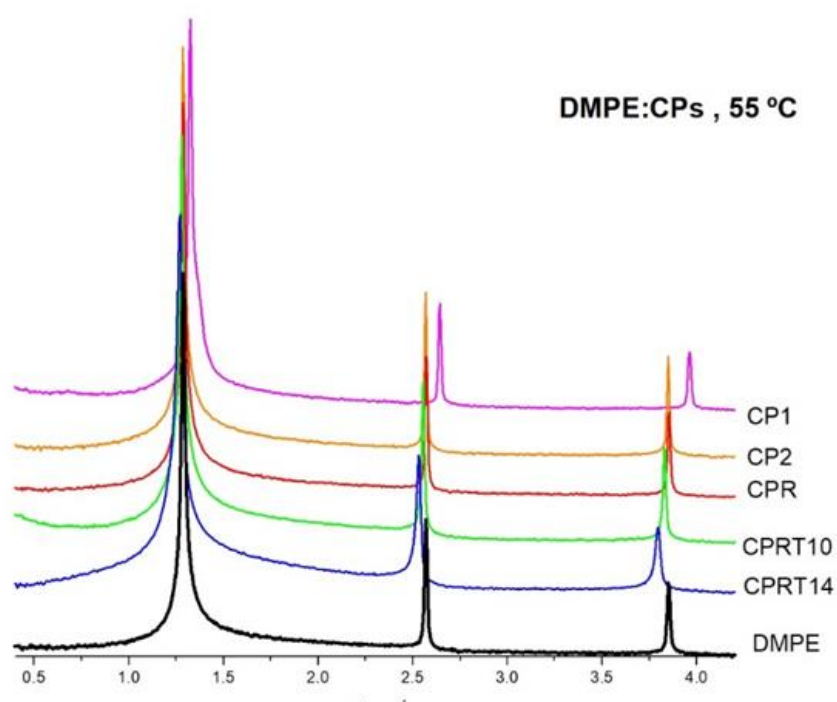
Fig. 5 – SAXS patterns of DMPE its mixtures with the five studied CPs for the highest L:P ratio for each one, at 55ºC (fluid phase).

The direction and amount of change in repeat distance observed for each peptide is now analyzed in detail. Starting with **CP1** and comparing the distance with the one observed in the fluid phase in the presence of DMSO, d_1= 4.8±0.3 nm at 55 ºC, we observe for both L:P ratios values that are the same, within uncertainty. Although we would expect as said an increase in d, this constancy can arise if the peptide induces a packing effect, as it has 3 Trp, and thus it is expected to have a deeper insertion in the membrane core, that counteract the increase in distance due to charging up the membrane surface due to peptide partition. For **CPRT10** and **CPRT14**, the observed behavior is the expected one – a small increase in repeat distance, in the case of

CPRT10 similar for both L:P ratios, and in the case of **CPRT14** even slightly higher for the highest L:P ratio.

Finally, briefly considering the WAXS patterns for these DMPE/CP mixtures, we can see in Fig. 6 that overall, the pattern is typical for a gel L_β phase with acyl chains oriented perpendicularly to the plane of the bilayer and packed in a hexagonal lattice, as observed for DMPE alone. Nevertheless, we can also see that **CP1** and **CPRT14** change slightly the position of the maxima of the WAX diffraction peak, in both cases towards lower q values, thus suggesting that only these two peptides change to some extent the packing of the phosphatidylethanolamine in gel phase.
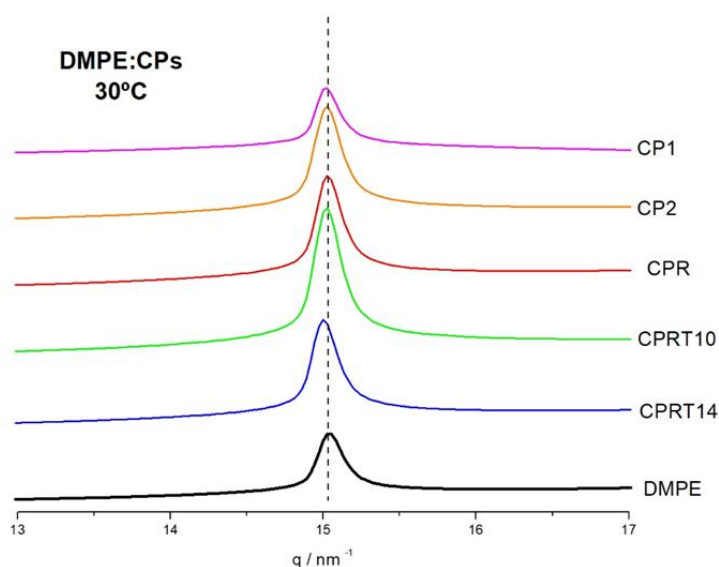
Fig. 6. WAXS patterns of DMPE and DMPE mixed with the different CPs for the highest L:P ratio in each case, at 30 ºC (gel L_β phase).

Overall, all these results are in full agreement with our previous studies, where we showed that only **CP1** [19] and **CPRT14** [37] interact significantly with DMPE multilamellar membranes.

DMPE:DMPG (3:1) membrane system

As described in the introduction, we chose the second generation peptides (**CPR**, **CPRT10** and **CPRT14**) for further study, because of their improved antimicrobial activity, especially against Gram-positive bacteria [12]. With this aim, we used the mixture of DMPE with DMPG at a 3:1 molar ratio as a model membrane. The mixture forms oligolamellar vesicles (OLVs), with size's distribution between 76 and 1000 nm, and a polydispersity index (PDI) of 0.9.

Starting with the pure lipid system, SAXS patterns at different chosen temperatures can be found in Fig. 7
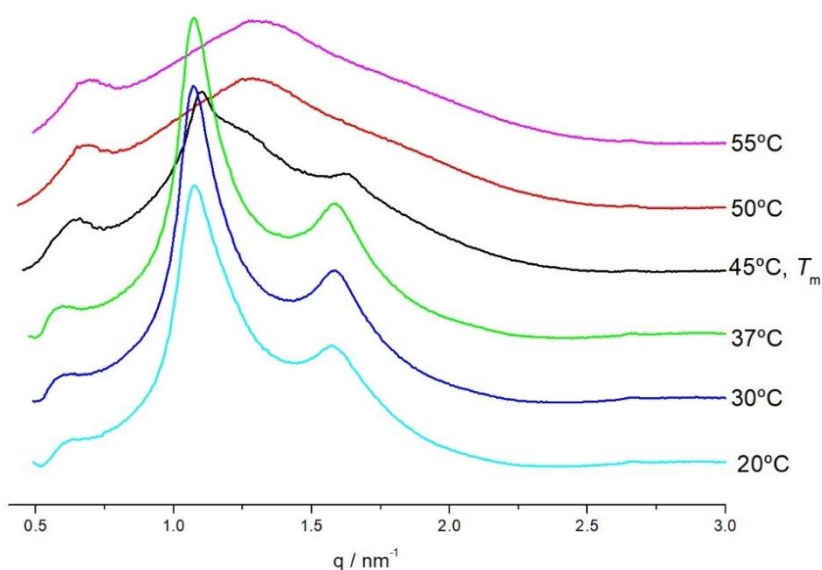
Fig. 7. SAXS patterns of DMPE:DMPG (3:1) (OLVs) at selected temperatures in gel and fluid phases. The transition temperature at 45 ℃ is clearly seen in the respective pattern.

Above the phase transition (T_m= 45 ℃), in liquid crystalline phase L_α, we observe a broad peak with two non-well resolved maxima (Fig. 7). This pattern reflects a system with poor long-range order, as expected for OLV vesicles with a negatively charged surface due to the presence of DMPG. The repeat distance was calculated as d = 10.4 ± 0.3 nm at 55 ℃. When compared to the value above for DMPE at the same temperature, 4.89 ± 0.01 nm, we see that the DMPE:DMPG (3:1) lamellar system swells, due to negative surface charge imposed by DMPG. In fact, increasing the water content between the lamellae with consequent higher fluctuations gives rise to further disorder in relative positions of the unit cells, which translates into a broadening of the diffraction peaks.

At temperatures below T_m, the system is in gel L_β phase, and indeed the peaks are less broad and better resolved. The peaks at q ~ 0.643 nm^{-1}, 1.074 nm^{-1} and 1.590 nm^{-1} were identified as a superposition of two lamellar phases, with repeat distances 10.6 ± 0.3 and 11.8 ± 0.4 nm. Comparing with the value obtained for pure DMPE at the same temperature, 5.62 ± 0.01 nm, indeed we see a much larger distance (almost twice), due to the negative surface charge imposed by the presence of DMPG. The existence of two lamellar phases in a gel state of the mixture can be rationalized as the system DMPE:DMPG at pH 7, 100 mM NaCl, was shown to present deviations from ideal

mixing, particularly at DMPG contents < 50% [41]. The authors further state that DMPEDMPG lipid pair formation is favored in both phases but is more pronounced in the gel phase. Therefore, as we only have 25% DMPG, we can assume that the system is not fully homogeneous in gel phase, having parts that have a higher prevalence of DMPE-DMPG pairs, leading to a higher repeat distance due to charge (11.8 ± 0.4 nm) whereas in other parts DMPE is more predominant, and thus the distance is somewhat smaller (10.6 ± 0.3 nm).

Considering now the differences observed upon CP's addition, the obtained SAXS patterns of pure DMPE:DMPG (3:1) and its mixtures with the three peptides **CPR**, **CPRT10** and **CPRT14** at the highest L:P ratio, can be seen in Fig. 8 **A** for the gel phase (30 ºC) and in Fig. 8 **B** in the fluid phase (55 ºC). All repeat distances retrieved at both temperatures and studied L:P ratios can be found in Table 3.
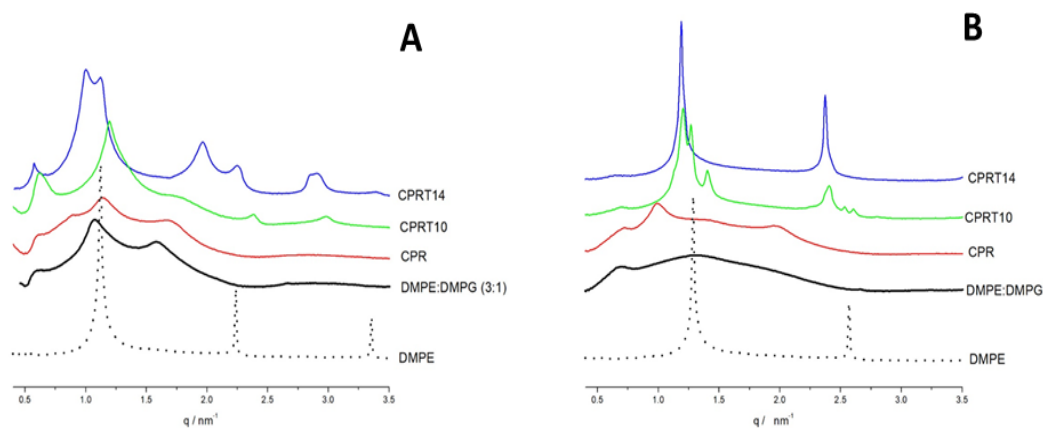
Fig 8. SAXS patterns of pure DMPE:DMPG (3:1) and its mixtures with **CPR**, **CPRT10** and **CPRT14** at the highest studied L:P ratio: **A** - at 30ºC (gel phase) and **B** - at 55ºC (fluid phase). The diffractogram for DMPE at the same temperatures is also represented (dashed lines).

Starting with the results in the gel phase, the first aspect that is apparent from Table 3 is that for all peptides we continue to see the coexistence of two lamellar phases in the gel state. We can further see that one of them has a repeat distance equal (or very close) to the smallest value found for the pure lipid system (10.6 ± 0.3 nm) whereas the other have repeat distances significantly smaller than the one found in the pure lipid system (11.8 ± 0.4 nm). Considering what we described above as our interpretation of the two coexisting phases in DMPE:DMPG (3:1) in gel phase, namely that the part with higher repeat distance would have a higher prevalence of DMPE-DMPG pairs, and the other would be richer in DMPE, the results observed in the presence of the peptides make perfect sense – since the peptides are positively charged, they will interact

preferentially with the negatively charged DMPG, so they will affect mainly the parts of the membranes richer in DMPE-DMPG pairs, and due to charge compensation, the repeat distances will drop significantly – from 11.8 ± 0.4 nm in DMPE:DMPG (3:1) to 7.4 ± 0.1 nm for **CPR**, 5.27 ± 0.04 nm for **CPRT10** and 6.5 ± 0.1 nm for **CPRT14**. Indeed, the decrease in repeat distance follows the sequence **CPR** > **CPRT10** ≈ **CPRT14**, as could be expected from our previous results on their mixed membrane interactions [36, 37].

It should be noted that in the case of **CPRT10** and **CPRT14** the peaks are better defined as compared to the pure lipid system, showing that the peptides induce some ordering in the lipid system. Further, it is clear from the plot in Fig. 8 **A** that the largest difference is found for **CPRT14**, where the diffractogram deviates more significantly from the one for the pure lipid system. For this peptide the part with lower repeat distance is also affected, becoming larger (11.21± 0.08 nm) than in the pure lipid system. Again, this is in line with what we reported above, and found previously by DSC [37], *i.e.*, that this peptide interacts with DMPE, thus charging up positively this part of the membrane system, and as a result increasing this repeat distance.

Table 3. Repeat distances retrieved for pure DMPE:DMPG (3:1) and its mixtures with the three second generation peptides (**CPR**, **CPRT10** and **CPRT14)**, at different molar ratios (L:P) and at temperatures 30 ºC (gel phase) and 55 ºC (fluid phase).

	CP	L:P	30 ºC		55 ºC		
			d_1/ nm	d_2/ nm	d_1/ nm	d_2/ nm	d_3/ nm
DMPE:DMPG 3:1	-	-	**10.6±0.3**	**11.8±0.4**	**10.4±0.3**	-	-
	CPR	25:1	10.7±0.4	7.4±0.1	8.75±0.04	6.40±0.03	-
		16:1	10.5±0.3	7.27±0.03	9.0±0.2	6.16±0.01	-
	CPRT10	18:1	10.6±0.1	5.27±0.04	9.89±0.04	5.23±0.03	4.76±0.05
	CPRT14	24:1	11.21±0.08	6.5±0.1	5.30±0.02	-	-
		15:1	11.18±0.01	6.33±0.03	5.29±0.02	-	-

As regarding the fluid phase, a curious and more complex situation appears – from one lamellar phase in the pure lipid system, now we retrieve two lamellar phases in the presence of **CPR**, three when **CPRT10** is added, and only one in the case of **CPRT14** (Table 3). From the patterns in Fig 8 **B**, it is clear that the peptides induce an increase in order in the lipid system in the fluid phase, where the rather diffuse and broad peaks observed for DMPE:DMPG (3:1) are now sharper. It is well known that there is always a better interaction between added peptides and the lipid membrane system in the fluid

phase, and thus this ordering becomes apparent. For **CPR,** we have thus two phases, both with smaller repeat distances as compared to the pure lipid, reflecting the charge compensation that results from the presence of the peptide. The fact that we have two phases must reflect that the sample is not fully homogeneous, with parts of the membrane richer in peptide (smaller *d*). In the case of **CPRT10**, the situation is even more complex, as three phases appear. The first two are rather similar to the ones observed to **CPR**, and thus the same interpretation applies. As for the third one, it is worth noting that the retrieved distance, 4.76±0.05 nm, is very close to the one found for DMPE 4.89 ± 0.01 nm. This peptide has a high partition to negatively charged membranes [36], and thus our view is that it can very successfully segregate all DMPG, and thus originating a part of the membrane that is totally depleted in DMPG, showing therefore the repeat distance of DMPE. Finally in the case of **CPRT14**, curiously we only have one phase at 55 °C, as for the pure lipid system, but with a repeat distance that is almost half. If we look at the respective diffractogram in Fig. 8 **B**, as well as to the one for DMPE also represented there, we can observe that the reflections are almost as sharp as the ones pertaining DMPE and appear at close *q* values, although shifted to the right. The retrieved distances, 5.30 ± 0.02 nm for L:P 24:1 or 5.29 ± 0.02 nm for L:P 15:1, are the same within uncertainty, and only somewhat larger than the one for pure DMPE at this temperature. We believe that this reflects the very destructive effect of this peptide in the membrane, where most likely it binds to DMPG rich patches, leading to aggregation, possibly in lipid/peptide aggregates with no long-range order, leaving the remaining membrane almost only formed by DMPE. The possible membrane micellization can not be shown here, as we did not extend our SAXS measurements to the low *q* range where the cubic phases would appear.

3.   Conclusions

Using Small-Angle X- Ray Scattering (SAXS) and Wide-Angle X- Ray Scattering (WAXS), the interaction between different *D,L*-α-cyclic peptides (**CP1, CP2, CPR, CPRT10 and CPRT14**) and two membrane models [DMPE and DMPE:DMPG (3:1)] was characterized.

When the peptides are added to the DMPE multilamellar system, only the two more hydrophobic peptides, **CP1** and **CPRT14,** changed the repeat distances, and induced the appearance of a second lamellar phase, at temperature below T_m, in agreement with our previous findings that these are the only peptides that interact with DMPE. This increase in repeat distance reflects the positive membrane surface charge resulting from peptide partition, having as consequence the bilayer's separation. The

repeat distances in fluid lamellar phase L_α were the same as for pure DMPE, for all peptides.

As regarding the mixed system DMPE:DMPG (3:1), we have the typical behavior of system with poor long-range order is observed in the absence of peptides, as expected for OLV vesicles with a negatively charged surface due to the presence of DMPG. When compared to DMPE, we observed that the system swells, due to negative surface charge imposed by DMPG.

At odds with the fluid phase, we identified the presence of two lamellar phases below T_m, with repeat distances that are about twice the one retrieved for pure DMPE at the same temperature. The presence of two lamellar phase in this system can be rationalized as due to the reported preference for DMPE-DMPG lipid pair formation, that is more prevalent in the gel phase.

When the peptides are added to this lipid system, two lamellar phases are still observed for the three peptides in gel phase - one with a repeat distance equal (or very close) to the smallest value found for the pure lipid system and the other with a smaller repeat distance. Since the peptides are positively charged, they will interact preferentially with the negatively charged DMPG, affect thus mainly the parts of the membranes richer in DMPE-DMPG pairs. Due to charge compensation, the repeat distances dropped significantly.

As regarding the fluid phase, the situation is more complex, and the three studied systems are now significantly different. We identified one lamellar phase in the pure DMPE:DMPG (3:1) lipid system, two lamellar phases in the presence of **CPR**, three with **CPRT10** and only one in the case of **CPRT14.** These differences could be rationalized as reflecting the different affinity of the peptides to the negatively charged membranes.

Finally, as regarding the peptide's possible antimicrobial mechanism of action, our structural results suggest that the active peptides **CPRT10** and **CPRT14** act by membrane segregation, due to their DMPG preference, that eventually impairs membrane function (**CPRT10**) or leads to membrane destruction, with possible membrane micellization (**CPRT14**).

References

[1] M. Magana, M. Pushpanathan, A.L. Santos, L. Leanse, M. Fernandez, A. Ioannidis, M.A. Giulianotti, Y. Apidianakis, S. Bradfute, A.L. Ferguson, A. Cherkasov, M.N. Seleem, C. Pinilla, C. de la Fuente-Nunez, T. Lazaridis, T. Dai, R.A. Houghten, R.E.W. Hancock, G.P. Tegos, The value of antimicrobial peptides in the age of resistance, Lancet. Infect. Dis., 20 (2020) e216-e230.

[2] Y. Huan, Q. Kong, H. Mou, H. Yi, Antimicrobial Peptides: Classification, Design, Application and Research Progress in Multiple Fields, Front. Microbiol., 11 (2020).

[3] C. de la Fuente-Núñez, O.N. Silva, T.K. Lu, O.L. Franco, Antimicrobial peptides: Role in human disease and potential as immunotherapies, Pharmacol. Ther., 178 (2017) 132-140.

[4] M. Mahlapuu, J. Håkansson, L. Ringstad, C. Björn, Antimicrobial Peptides: An Emerging Category of Therapeutic Agents, Front. Cell. Infect. Microbiol., 6 (2016).

[5] C.D. Fjell, J.A. Hiss, R.E.W. Hancock, G. Schneider, Designing antimicrobial peptides: form follows function, Nat. Rev. Drug Discov., 11 (2011) 37-51.

[6] E.F. Haney, R.E. Hancock, Peptide design for antimicrobial and immunomodulatory applications, Biopolymers, 100 (2013) 572-583.

[7] A.T.Y. Yeung, S.L. Gellatly, R.E.W. Hancock, Multifunctional cationic host defence peptides and their clinical applications, Cell. Mol. Life. Sci., 68 (2011) 2161-2176.

[8] R.E.W. Hancock, H.-G. Sahl, Antimicrobial and host-defense peptides as new anti-infective therapeutic strategies, Nat. Biotechnol., 24 (2006) 1551-1557.

[9] C. Appelt, A. Wessolowski, M. Dathe, P. Schmieder, Structures of cyclic, antimicrobial peptides in a membrane-mimicking environment define requirements for activity, J. Pept. Sci., 14 (2008) 524-527.

[10] S. Fernandez-Lopez, H.-S. Kim, E.C. Choi, M. Delgado, J.R. Granja, A. Khasanov, K. Kraehenbuehl, G. Long, D.A. Weinberger, K.M. Wilcoxen, M.R. Ghadiri, Antibacterial agents based on the cyclic d,l-α-peptide architecture, Nature, 412 (2001) 452-455.

[11] M. Dathe, H. Nikolenko, J. Klose, M. Bienert, Cyclization increases the antimicrobial activity and selectivity of arginine-and tryptophan-containing hexapeptides, Biochemistry, 43 (2004) 9140-9150.

[12] E. González-Freire, F. Novelli, A. Pérez-Estévez, R. Seoane, M. Amorín, J.R. Granja, Double orthogonal click reactions for the development of antimicrobial peptide nanotubes, Eur. J., 27 (2021) 3029 –3038..

[13] H.S. Kim, J.D. Hartgerink, M.R. Ghadiri, Oriented Self-Assembly of Cyclic Peptide Nanotubes in Lipid Membranes, J. Am. Chem. Soc., 120 (1998) 4417-4424.

[14] M.W. Lee, J. de Anda, C. Kroll, C. Bieniossek, K. Bradley, K.E. Amrein, G.C.L. Wong, How do cyclic antibiotics with activity against Gram-negative bacteria permeate membranes? A machine learning informed experimental study, Biochim. Biophys. Acta, Biomembr., 1862 (2020) 183302.

[15] R.-V. Nuria, H.L. Ozores, G. Arcadio, G.-F. Eva, F. Alberto, P. Michele, M.P. Juan, O. Juan, M. Javier, G.-F. Rebeca, A. Manuel, R.G. Juan, Membrane-Targeted Self-Assembling Cyclic Peptide Nanotubes, Curr. Top. Med. Chem. , 14 (2014) 2647-2661.

[16] M.R. Ghadiri, J.R. Granja, R.A. Milligan, D.E. McRee, N. Khazanovich, Self-assembling organic nanotubes based on a cyclic peptide architecture, Nature, 366 (1993) 324-327.

[17] L.A. Calderon, A.M. Soares, R.G. Stábeli, Anuran Antimicrobial Peptides: an alternative for the development of nanotechnological based therapies for multi-drug-resistant infections, Signpost Open J Biochem Biotech, 1 (2012) 1-11.

[18] W.C. Wimley, K. Hristova, Antimicrobial peptides: successes, challenges and unanswered questions, J. Membr. Biol. , 239 (2011) 27-34.

[19] B. Claro, E. González-Freire, M. Calvelo, L.J. Bessa, E. Goormaghtigh, M. Amorín, J.R. Granja, R. Garcia-Fandiño, M. Bastos, Membrane targeting antimicrobial cyclic peptide nanotubes – an experimental and computational study, Colloids Surf. B, (2020) 111349.

[20] B. Claro, E. Goormaghtigh, M. Bastos, Attenuated total reflection Fourier transform infrared spectroscopy: a tool to characterize antimicrobial cyclic peptide/membrane interactions, Eur. Biophys. J., S.I. dedicated to COST Action CA15126, MOBIEU: Between atom and cell, 50 (2021), 629–639.

[21] M. Bastos, T. Silva, V. Teixeira, K. Nazmi, J.G. Bolscher, S.S. Funari, D. Uhrikova, Lactoferrin-derived antimicrobial peptide induces a micellar cubic phase in a model membrane system, Biophys J, 101 (2011) L20-22.

[22] K.A. Brogden, Antimicrobial peptides: pore formers or metabolic inhibitors in bacteria?, Nat. Rev. Microbiol., 3 (2005) 238-250.

[23] T. Silva, R. Adão, K. Nazmi, J.G.M. Bolscher, S.S. Funari, D. Uhríková, M. Bastos, Structural diversity and mode of action on lipid membranes of three lactoferrin candidacidal peptides, Biochim. Biophys. Acta, Biomembr., 1828 (2013) 1329-1339.

[24] T. Silva, B. Claro, B.F.B. Silva, N. Vale, P. Gomes, M.S. Gomes, S.S. Funari, J. Teixeira, D. Uhríková, M. Bastos, Unravelling a Mechanism of Action for a Cecropin A-Melittin Hybrid

Antimicrobial Peptide: The Induced Formation of Multilamellar Lipid Stacks, Langmuir, 34 (2018) 2158-2170.

[25] V. Teixeira, M.J. Feio, M. Bastos, Role of lipids in the interaction of antimicrobial peptides with membranes, Prog. Lipid Res., 51 (2012) 149-177.

[26] A. Mishra, K.P. Tai, N.W. Schmidt, A.J. Ouellette, G.C. Wong, Small-angle X-ray scattering studies of peptide-lipid interactions using the mouse paneth cell α-defensin cryptdin-4, Methods Enzymol., 492 (2011) 127-149.

[27] G. Pabst, N. Kučerka, M.P. Nieh, M.C. Rheinstädter, J. Katsaras, Applications of neutron and X-ray scattering to the study of biologically relevant model membranes, Chem. Phys. Lipids, 163 (2010) 460-479.

[28] S. Danner, G. Pabst, K. Lohner, A. Hickel, Structure and Thermotropic Behavior of the Staphylococcus aureus Lipid Lysyl-Dipalmitoylphosphatidylglycerol, Biophys. J., 94 (2008) 2150-2159.

[29] P. Heftberger, B. Kollmitzer, F.A. Heberle, J. Pan, M. Rappolt, H. Amenitsch, N. Kučerka, J. Katsaras, G. Pabst, Global small-angle X-ray scattering data analysis for multilamellar vesicles: the evolution of the scattering density profile model, J Appl Crystallogr, 47 (2014) 173-180.

[30] X. Fang, J. Wang, I.P. O'Carroll, M. Mitchell, X. Zuo, Y. Wang, P. Yu, Y. Liu, J.W. Rausch, M.A. Dyba, An unusual topological structure of the HIV-1 Rev response element, Cell, 155 (2013) 594-605.

[31] C. Dargel, R. Geisler, Y. Hannappel, I. Kemker, N. Sewald, T. Hellweg, Self-Assembly of the Bio-Surfactant Aescin in Solution: A Small-Angle X-ray Scattering and Fluorescence Study, Colloids Interfaces, 3 (2019) 47.

[32] J. Karlovská, K. Lohner, G. Degovics, I. Lacko, F. Devínsky, P. Balgavý, Effects of non-ionic surfactants N-alkyl-N,N-dimethylamine-N-oxides on the structure of a phospholipid bilayer: small-angle X-ray diffraction study, Chem. Phys. Lipids, 129 (2004) 31-41.

[33] R.N.A.H. Lewis, D. Zweytick, G. Pabst, K. Lohner, R.N. McElhaney, Calorimetric, X-Ray Diffraction, and Spectroscopic Studies of the Thermotropic Phase Behavior and Organization of Tetramyristoyl Cardiolipin Membranes, Biophys. J., 92 (2007) 3166-3177.

[34] H. Mendil-Jakani, I. Zamanillo Lopez, P.M. Legrand, V.H. Mareau, L. Gonon, A new interpretation of SAXS peaks in sulfonated poly(ether ether ketone) (sPEEK) membranes for fuel cells, Phys. Chem. Chem. Phys., 16 (2014) 11243-11250.

[35] T.T. Mills, S. Tristram-Nagle, F.A. Heberle, N.F. Morales, J. Zhao, J. Wu, G.E.S. Toombes, J.F. Nagle, G.W. Feigenson, Liquid-Liquid Domains in Bilayers Detected by Wide Angle X-Ray Scattering, Biophysical Journal, 95 (2008) 682-690.

[36] B. Claro, E. González-Freire, J.R. Granja, R. Garcia-Fandiño, J. Gallová, D. Uhríková, A. Fedorov, A. Coutinho, M. Bastos, Partition of antimicrobial D-L-α-Cyclic Peptides into bacterial model membranes Biochim. Biophys. Acta, Biomembr. (submitted, 2021).

[37] B. Claro, A. Peón, E. González-Freire, E. Goormaghtigh, M. Amorín, J.R. Granja, R. Garcia-Fandiño, M. Bastos, Macromolecular assembly and membrane activity of antimicrobial D,L-α-Cyclic peptides, Colloids Surf., B, (submitted, 2021).

[38] G.R. Bartlett, Phosphorus assay in column chromatography, J. Biol. chem., 234 (1959) 466-468.

[39] A. Ortiz, J.A. Teruel, M.J. Espuny, A. Marqués, Á. Manresa, F.J. Aranda, Interactions of a Rhodococcus sp. biosurfactant trehalose lipid with phosphatidylethanolamine membranes, Biochim. Biophys. Acta, Biomembr., 1778 (2008) 2806-2813.

[40] J.M. Seddon, K. Harlos, D. Marsh, Metastability and polymorphism in the gel and fluid bilayer phases of dilauroylphosphatidylethanolamine. Two crystalline forms in excess water, J Biol Chem, 258 (1983) 3850-3854.

[41] P. Garidel, C. Johann, A. Blume, The calculation of heat capacity curves and phase diagrams based on regular solution theory, J. Therm. Anal. Calorim., 82 (2005) 447-455.

[42] J. F.Nagle, S. Tristram-Nagle, Structure of lipid bilayers. , Biochim. Biophys. Acta, Biomembr., 1469 (2000), 159–195.

VII. **"A multi-laboratory benchmark study of isothermal titration calorimetry (ITC) using Ca^{2+} and Mg^{2+} binding to EDTA"**

Adrian Velazquez-Campoy, Bárbara Claro, Olga Abian, Jonas Höring, Louis Bourlon, Rafael Claveria-Gimeno, Eric Ennifar, Patrick England, Jonathan Brad Chaires, Di Wu, Grzegorz Piszczek, Chad Brautigam, Shih-Chia Tso, Huaying Zhao, Peter Schuck, Sandro Keller, Margarida Bastos **(2021),** *European Biophysics Journal*, 50, 429-451.

ORIGINAL ARTICLE

A multi-laboratory benchmark study of isothermal titration calorimetry (ITC) using Ca^{2+} and Mg^{2+} binding to EDTA

Adrian Velazquez-Campoy[1,2,3,4] · Bárbara Claro[5] · Olga Abian[1,2,3,6] · Jonas Höring[7] · Louis Bourlon[8] ·
Rafael Claveria-Gimeno[1,2,6] · Eric Ennifar[9] · Patrick England[8] · Jonathan Brad Chaires[10] · Di Wu[11] ·
Grzegorz Piszczek[11] · Chad Brautigam[12] · Shih-Chia Tso[13] · Huaying Zhao[14] · Peter Schuck[14] ·
Sandro Keller[15,16,17] · Margarida Bastos[5]

Abstract

A small-scale ITC benchmarking study was performed involving 9 biophysics laboratories/facilities, to evaluate inter-laboratory and intra-laboratory basal levels of uncertainty. Our prime goal was to assess a number of important factors that can influence both the data gathered by this technique and the thermodynamic parameter values derived therefrom. In its first part, the study involved 5 laboratories and 13 different instruments, working with centrally prepared samples and the same experimental protocol. The second part involved 4 additional laboratories and 6 more instruments, where the users prepared their own samples according to provided instructions and did the experiments following the same protocol as in the first part. The study design comprised: (1) selecting a minimal set of laboratories; (2) providing very stable samples; (3) providing samples not requiring preparation or manipulation; and (4) providing a well-defined and detailed experimental protocol. Thus, we were able to assess: (i) the variability due to instrument and data analysis performed by each user on centrally prepared samples; (ii) the comparability of data retrieved when using 4 different software packages to analyze the same data, besides the data analysis carried out by the different users on their own experimental results; and (iii) the variability due to local sample preparation (second part of the study). Individual values, as well as averages and standard deviations for the binding parameters for EDTA-cation interaction, were used as metrics for comparing the equilibrium association constant ($\log K$), enthalpy of interaction (ΔH), and the so-called "stoichiometry" (n), a concentration-correction factor.

Introduction

Science is based on the progressive advance of knowledge and its application. The overall process encompasses collecting evidence and applying inductive reasoning to establishing hypotheses, leading to refuting or confirming these hypotheses through controlled, goal-defined

Special Issue: COST Action CA15126, MOBIEU: Between atom and cell.

✉ Adrian Velazquez-Campoy
adrianvc@unizar.es

✉ Margarida Bastos
mbastos@fc.up.pt

Extended author information available on the last page of the article

experimentation. Careful experimental design, execution and analysis are key elements for the appropriate and trustworthy implementation of the scientific method. Usefulness and relevance of experimental data depend on the expected impact of the scientific or technical objectives, but they ultimately rely on the quality and reliability of those experimental data.

Currently, there is a dramatic confidence crisis in scientific research, affecting mainly biologically oriented research (with a strong focus in biomedical research), reflected in numbers of retracted articles and research misconduct continuously increasing. The lack of reproducibility is a matter of severe concern among researchers from academia and industry (Baker 2016; Begley and Ellis 2012; Ioannidis 2016; Mobley et al. 2013; Prinz et al. 2011), but there is still an ongoing debate on the criteria that should be used to

define reproducibility. Depending on the system under study, the variability sources affecting the ability to reproduce the experimental data may be more numerous and detrimental for the outcome of the research activity, and very often they remain elusive to the experimenter. Thus, assays performed in vivo or in cells may be trickier and more susceptible to the experimental conditions and they may be more dependent on an appropriate characterization of the system under study. Still, in vitro biophysical studies involving purified biological macromolecules are affected by their labile and heterogeneous nature, the increasing sophistication of the instrumental techniques, the complexity of the models used to represent and build operational schemes of the system under study, and last, but not least, the very often demanding data analysis used.

Undoubtedly good data can only be obtained with precise, accurately calibrated, and well-maintained instrumentation. Experimental techniques are constantly evolving and improving thanks to new technological developments, driven by new applications and new systems under study that push the search for wider boundaries and increased sensitivity, accuracy and applicability. Instrument performance can be assessed by selecting appropriate standards and the use of appropriate metrics for comparing precision and accuracy, and also to evaluate inter-experiment variability. To this goal, benchmark studies, involving a multifactorial comparison of experimental procedures or instrumentation, provide invaluable information on the variability associated with instruments, samples, procedures, and users. Precision and accuracy may depend on the instrument and the system under study, but also on the user skills and training, as well as on the experimental protocol and the data analysis methodology. Parsing experimental variability into its different sources is instrumental for a correct process performance assessment.

While decades ago isothermal titration calorimetry (ITC) was considered an obscure technique mostly used by calorimetry specialists, in many cases the designers of the instruments (Bastos 2016), nowadays it has become a gold-standard for studying intermolecular interactions in solution, with a strong emphasis in biological interactions (Chaires 2008; Chaires et al. 2015; Freire 2001; Freire et al. 1990; Perozzo et al. 2004; Velazquez-Campoy and Freire 2005, 2006). ITC is at present widely employed in academic and industry laboratories thanks to the availability of high-sensitivity commercial instruments that allow the determination of binding affinity (through the association constant or the Gibbs energy of interaction), the binding enthalpy, and in some cases the binding stoichiometry for a given biomolecular interaction. Numerous advantages of ITC (e.g., interaction monitored in solution, no requirement for labelling reactants, high-content information in a single experiment, non-destructive assay, possibility of employing

optically active solutions, wide practical window for affinity determination from submillimolar to nanomolar, i.e., K_d from 100 µM to 1 nM) usually counterbalance its disadvantages (e.g., time consuming and low throughput, sample consuming, difficult modeling and intricate data analysis). Extensions of the standard protocol allow the determination of much lower/higher affinities (e.g., displacement titration with competitive ligands).

In a previous ITC benchmark study, interlaboratory variability was assessed by quantifying the binding affinity and enthalpy for carbonic anhydrase II (CAII) interacting with 4-carboxybenzenesulfonamide (CBS) in fourteen ITC instruments (Myszka et al. 2003). This study provided valuable information: (i) experimental results agreed with biosensor determinations; and (ii) reasonable experimental variability was observed (coefficients of variation of 2%, 24% and 16% for K_d, ΔH and n, respectively) given the delicate nature of the sample, as well as the experimental design autonomy and individual sample manipulation for each participant. In that study, participants prepared and manipulated samples (reconstitution from lyophilized material and dialysis, determination of extinction coefficients), designed and executed their preferred ITC experimental protocol according to the information provided by the study coordinators, and analyzed the data following their usual software and methodology. Nevertheless, although this operational procedure reflects real work in a biophysical laboratory, it does not allow to assess and estimate the significance of individual variability sources. In addition, as pointed out previously (Chodera and Mobley 2013; Tellinghuisen and Chodera 2011), errors in ITC might be underreported for several reasons. Titrant concentration is one of the main sources of error since it is usually assumed to be known exactly (titrant is the reactant located in the injection syringe, while titrand is the reactant located in the calorimetric cell). In addition, reported errors are often those corresponding to the fitting procedure or derived from repeated measurements using the same stock solutions. Furthermore, a comprehensive analysis suggested the estimated parameters are very sensitive to the way the background injection heat is accounted for (the so-called "dilution heat").

Standards are used for calibration and to provide reference values in analytical procedures. A primary standard is defined as a reagent that has high stability and low hygroscopicity, can be obtained with high purity, and its solutions can be prepared with a concentration that remains constant for a long period of time; if possible, it should have low or no toxicity, and a wide availability. Although several standards for ITC were proposed previously (Adão et al. 2012; Baranauskienė et al. 2009; Wadsö and Goldberg 2001), the binding of Ca^{2+} to EDTA has become a common standard, not the least because manufacturers of ITC microcalorimeters started to propose

this reaction, in some cases providing samples (solutions already prepared) for users. Recently, EDTA–Ca^{2+} interaction was thoroughly tested to prove it useful as a standard reaction test for ITC (Ràfols et al. 2016). The uncertainties in the parameters were rather low, but that study only involved two VP-ITC calorimeters. In this study we chose two EDTA reactions, EDTA–Ca^{2+} (exothermic) and EDTA–Mg^{2+} (endothermic), studied at 298.15 K. Because the interaction of EDTA with metal cations is highly dependent on pH, the experimental conditions were selected to avoid a too high or too low binding affinity, and concentrations were set for an appropriate signal-to-noise ratio.

Regarding the metrics chosen for a benchmark study, one has to consider that they should be readily measured or calculated from the measurements and thereafter used to describe the variability and compare instrument and process performance. In this ITC benchmark study, individual values, as well as averages and standard deviations for the binding parameters for the EDTA–cation interaction were used as metrics for comparison: association equilibrium constant ($\log K$, dimensionless, but based on concentration equilibrium constants and assuming a standard state concentration of 1 mol L^{-1}), enthalpy of interaction (ΔH, in kJ mol^{-1}), and stoichiometry (n). When handling equilibrium constants, neither arithmetic averages nor arithmetic standard deviations should be calculated, as asymmetric profile likelihood confidence intervals offer a better representation of the variability of this estimated parameter (Paketurytė et al. 2020). Nevertheless, to use metrics with which most users are familiar, $\log K$ (decimal logarithm of the dimensionless equilibrium constant) instead of K values were considered, as: (i) $\log K$ is proportional to the standard Gibbs energy of interaction ($\Delta G^o = -RT \ln K = -2.3026 \, RT \log K$), and arithmetic averages and standard deviations can be calculated for this parameter; and (ii) the standard deviation of $\log K$ provides a direct estimation of the relative error in K ($\Delta \log K \approx 0.434 \Delta K/K$). ITC allows the assessment of the binding stoichiometry through the parameter n, if the concentrations are well known. In addition, because the binding stoichiometry is very often implicit in the binding model chosen by the user for data analysis, the parameter n reflects then possible uncertainties in the concentrations of titrant and titrand. In practice, considering that the parameter n always appears multiplying the concentration of titrand in the calorimetric cell, n is more correctly interpreted as a correction factor for titrand concentration (e.g., fraction of active titrand, or corrective factor for errors due to sample manipulation and/or incorrect concentration). We would like to stress that in different softwares the user can choose whether the correction factor/competent fraction n (or its complementary, the reactant incompetent fraction) is to be applied to the titrant (in the syringe) or to the titrand (in the cell). Therefore,

when reporting results, the choice made by the user when performing the calculations should always be stated.

Thus, in summary, in the ITC benchmark study here reported, we tried to evaluate inter-laboratory (individual determinations and pooled determinations summarized with averages and standard deviations) and intra-laboratory (individual determinations) basal levels of uncertainty from instruments by: (1) selecting a minimal set of laboratories with ample experience in ITC; (2) providing a sample with no degradation propensity or solubility problems; (3) providing a common sample not requiring any preparation or manipulation by the participants prior to their use; (4) providing a fixed experimental protocol; (5) and, besides the data analysis carried out by the different users on their own experimental results, performing a complete data analysis of all data using four different software packages (Origin 7.0 with user-defined routines, AFFINImeter, NITPIC-SEDPHAT, and PEAQ-ITC), to reduce data analysis variability and compare those different software packages. Finally, the importance of independent sample preparation was assessed in a second round of the benchmarking study.

Materials and methods

The samples were centrally prepared by M.B. To prepare the stock solutions, the procedure was the following:

1. The content of an EDTA ampoule FIXANAL from Fluka/Sigma-Aldrich was quantitatively diluted in a volumetric flask to prepare 1 dm^3 of solution of concentration 0.1000 mol dm^{-3}. The solution was immediately passed to a plastic bottle, as EDTA cannot be stored in glass containers, as it leaches metal ions from soft glass containers;
2. The Ca^{2+} and Mg^{2+} solutions were prepared from $Ca(NO_3)_2 \cdot 4H_2O$ for analysis (99–102%) from Merck and $Mg(NO_3)_2 \cdot 6H_2O$ for analysis (99–102%) from Merck, both used as received. In both cases, the appropriate amount of solid to prepare a 0.1 mol dm^{-3} solution was weighed, transferred to a volumetric flask, and rigorously diluted with water;
3. Finally, the precise concentrations of Ca^{2+} and Mg^{2+} were thereafter determined analytically, by volumetric titration with standard EDTA, using Eriochrome Black T as indicator (Kolthoff and Elving 1959).

Thereafter each stock solution was then diluted to the desired final concentrations with the respective buffer as indicated in the protocol (no additional pipetting was required). Because of the high concentration of stock solutions, the dilution of buffer components in the final solution is negligible. The amounts needed for each lab were

transferred to appropriate containers, all duly labeled as shown in Supplementary Material (S1), and sent by Express mail to the other four laboratories participating in the first phase of this study, together with detailed procedural instructions, also described in Supplementary Material (S2).

Setup of the benchmark study

Two suitable test reactions were chosen, the binding of Ca^{2+} or Mg^{2+} to EDTA (see Fig. 1), in different buffer conditions chosen to provide moderate K values for the association. The Ca^{2+}/EDTA association was studied in 10 mM MES buffer, pH 5.60 and the Mg^{2+}/EDTA in 10 mM HEPES, 100 mM NaCl, pH 7.40, and studied at 298.15 K. In each case EDTA was prepared in the same corresponding buffer.

First round of the benchmark study—workflow and data analysis

All solutions prepared centrally, were sent to the 5 participating labs, located in Spain (Adrián Velázquez-Campoy, University of Zaragoza), Portugal (Margarida Bastos, University of Porto), France (Eric Ennifar, Université de Strasbourg and Patrick England, Institut Pasteur), and Germany (Sandro Keller, Technische Universität Kaiserslautern (TUK)). The samples were accompanied by a detailed protocol describing the setup of the experiments (see Supplementary Material S2). With the intent to broaden the instruments used in the study, representatives of TA Instruments (New Castle, U.S.A) (manufacturer of Nano ITC and Affinity ITC) were contacted to take part in the study, but they declined due to lack of time and resources to participate. Thus, only instruments from MicroCal/Malvern-Panalytical (Malvern, U.K.) were finally part of this benchmark study, and the instruments involved were 6 VP-ITC, 3 PEAQ-ITC, 3 iTC200, and 1 Auto-iTC200, distributed in the participating labs that are here randomly labeled as L1-L5, and the instrument distribution is detailed below and in table S1 (Supplementary Material):

L1—two VP-ITC and one Auto-iTC200.
L2—one VP-ITC and one PEAQ-ITC.

L3—one iTC200 and two PEAQ-ITC.
L4—one VP-ITC and one iTC200.
L5—one VP-ITC and one iTC200.

The participants were asked to analyze their results as they usually do, sending the obtained raw data and calculated thermodynamic parameters to M.B. All results were subsequently analyzed independently using four different data treatment programs:

•Origin (with user-defined functions), by Adrián Velázquez-Campoy.

•AFFINImeter, by Margarida Bastos.

•NITPIC + SEDPHAT, by Jonas Höring (laboratory of Sandro Keller).

•PEAQ-ITC software, by Eric Ennifar.

Second round of benchmarking—workflow and data analysis

After this, a second group of four selected laboratories, with a large experience in ITC, performed the same experiments, using the same experimental protocol, but preparing their own samples—Chad Brautigam/Shih-Chia Tso (VP-ITC and iTC200) at UT Southwestern Medical Center, USA, Grzegorz Piszczek (VP-ITC and iTC200) and Peter Schuck/Huaying Zhao (VP-ITC) at NIH, USA, and Jonathan B. Chaires (VP-ITC) at University of Louisville, USA (labelled radomly as L6-L9). This allowed us to assess the importance of independent sample preparation.

Results and discussion

Examples of the curves obtained for the two chosen binding reactions can be seen in Fig. 2, plotted in Origin, for the three instruments: VP-ITC, Auto-iTC200, and PEAQ-ITC. Although the thermogram profile is usually similar to the binding isotherm shape, some dissimilarities may arise. The geometry and size of the cell and the stirring efficiency (stirring speed and ratio between injection volume and cell volume) influences the instrumental time constant for heat evacuation, which determines

Fig. 1 Chemical reaction studied here, where M^{2+} was either Ca^{2+} in 10 mM MES buffer, pH 5.60 or Mg^{2+} in 10 mM HEPES, 100 mM NaCl, pH 7.40. EDTA was prepared in each case in the respective buffer
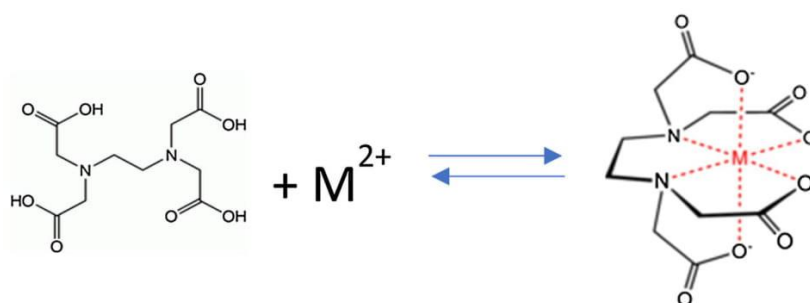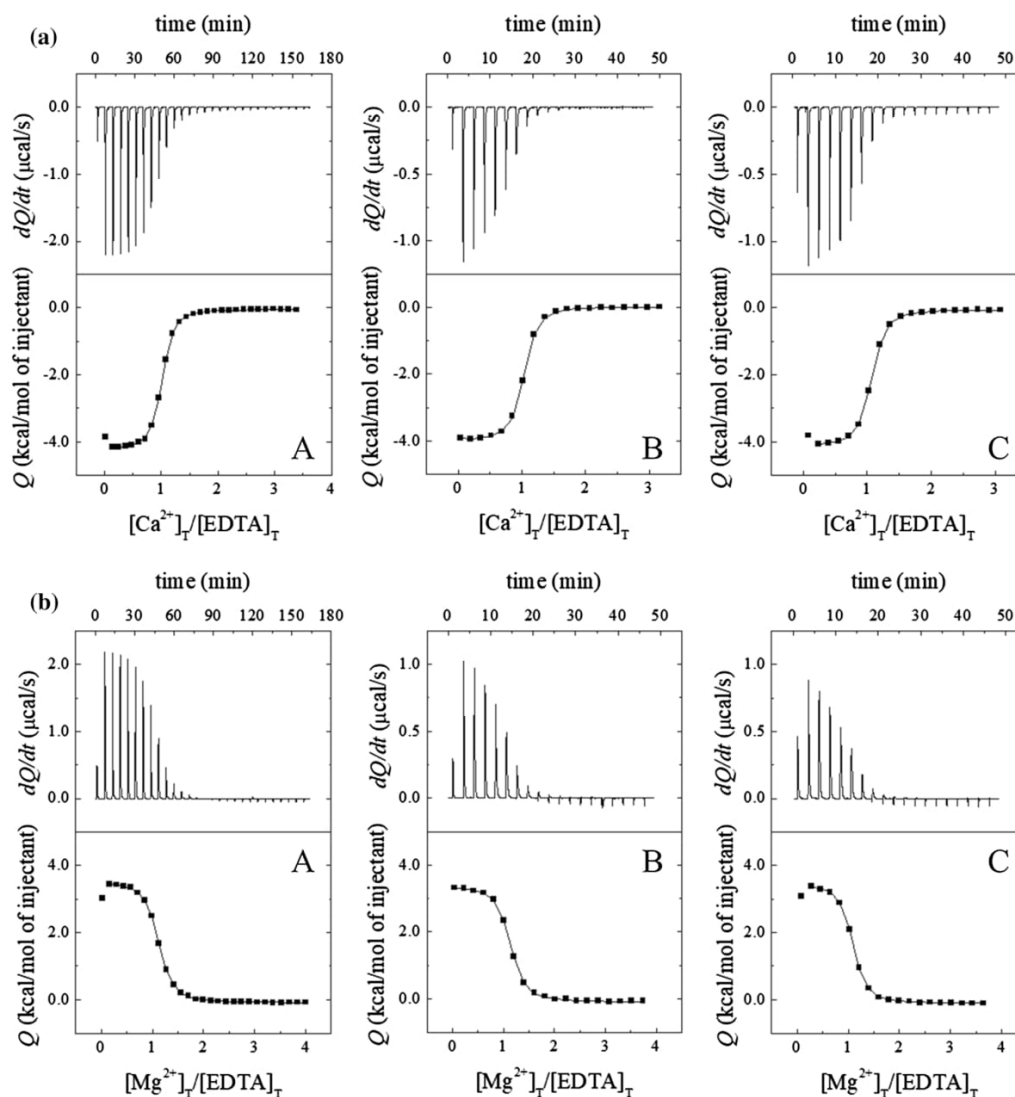
Fig. 2 Typical titrations obtained for **a** EDTA-Ca^{2+} and **b** EDTA-Mg^{2+} interactions with **a** high-volume VP-ITC, and **b**, **c** low-volume Auto-iTC200 and PEAQ-ITC titration calorimeters, plotted with Origin. Upper plots show the baseline-subtracted thermogram (thermal power required to maintain a temperature difference between a sample and reference cells as close to zero as possible, as a function of time) and lower plots show the binding isotherm (titrant-normalized heat effects per injection as a function of the molar ratio of the two reactants), with the *black line* representing the fit to the isotherm data, yielding the parameters log*K*, ΔH, and *n*

the maximal deflection (height) and width of the peaks. In addition, it is known that approaching the inflection point the peaks become broader and, therefore, the heights become smaller than expected (Dumas 2016). Thus, the thermogram profiles from VP-ITC closely resemble the binding isotherms, but the thermogram profiles from iTC200 and PEAQ-ITC are somewhat different from the binding isotherms. Further to this, the number of constant peaks is not that different, but the difference arises from

the different [M^{2+}]/[EDTA] after each injection, which results from the difference in volumes of the large cell instrument (VP-ITC) and the small cell ones (ITC200 and PEAQ-ITC), particularly considering that the same concentrations are used for the metals and EDTA in the two types of instruments. That is also another reason for the fact that in ITC200 and PEAQ-ITC there is a rapid decrease of the peaks intensity at the beginning of the

titration and yet a plateau phase still exists at the beginning of the isotherm.

Data analyzed by each participant laboratory

As stated in the methodology above, each participating lab was asked to process their data as they usually do and send the results together with the raw data. The thermodynamic parameters so retrieved can be found in Tables 1, 2 and are represented as bar plots in Figs. 3, 4. Averages and standard deviations were calculated using standard equations. The overall average and standard deviation from all values are shown in Table 3.

Values for the standard deviations were rounded-off following common practice when reporting the experimental error. For better comparison, values with more figures than the significant ones are shown in parenthesis after the correctly reported uncertainty.

Regarding the association constant, we can see from the $\log K$ values in Tables 1, 2 and the first plot in Figs. 3, 4 that for both binding reactions all, except L5-1 for Ca^{2+}, individual average values agreed in almost all cases within combined uncertainty with the overall average value (Table 3). Nevertheless, some values stand out as presenting quite high uncertainties—L3-1 and L3-3 (iTC2000 and PEAQITC, respectively), and L4-1 (VP-ITC) and L4-2 (iTC2000).

Table 1 Estimated parameters for the association constant (K), interaction enthalpy (ΔH) and stoichiometry (or binding competent fraction, n) for the EDTA–Ca^{2+} interaction in the calorimeters included in the first round of this benchmark study

Location	Instrument	N	$\log K$	sd-$\log K$	ΔH kJ mol^{-1}	sd-ΔH kJ mol^{-1}	n	sd-n
L1	L1-1 VP-ITC1	3	5.97	0.02	−17.5	0.1	0.977	0.008
	L1-2 VP-ITC2	3	5.98	0.02	−17.9	0.1	0.94	0.02
	L1-3 Auto-iTC200	5	5.98	0.02	−16.9	0.1	0.962	0.006
L2	L2-1 VP-ITC	5	5.92	0.01	−17.5	0.2	0.96	0.01
	L2-2 PEAQ-ITC	3	6.01	0.02	−16.9	0.3	0.99	0.04
L3	L3-1 iTC200	5	6.00	0.06	−18.0	0.4	0.83	0.03
	L3-2 PEAQ-ITC1	3	6.00	0.02	−18.02	0.06	0.91	0.02
	L3-3 PEAQ-ITC2	3	6.01	0.05	−17	2	0.9	0.1
L4	L4-1 VP-ITC	4	5.94	0.07	−17.7	0.08	0.9	0.1
	L4-2 iTC200	4	5.90	0.08	−16.9	0.5	0.88	0.04
L5	L5-1 VP-ITC	7	5.89	0.02	−17.6	0.2	0.95	0.02
	L5-2 iTC200	4	5.96	0.04	−17.5	0.3	0.84	0.06

Best estimates were obtained by non-linear least squares regression data analysis, as reported by each user from labs L1–L5. The programs used for data treatment in each case were: *L1* Origin with user-defined routines; *L2* PEAQ-ITC; *L3* PEAQ-ITC; *L4* NITPIC-Origin; and *L5* NITPIC/SEDPHAT

N number of assay replicates; *sd* standard deviation

Table 2 Estimated parameter values for the association constant (K), interaction enthalpy (ΔH), and "stoichiometry" (or binding-competent fraction, n) for the EDTA–Mg^{2+} interaction in the calorimeters included in the first round of this benchmark study

Location	Instrument	N	$\log K$	sd-$\log K$	ΔH kJ mol^{-1}	sd-ΔH kJ mol^{-1}	n	sd-n
L1	L1-1 VP-ITC1	3	5.76	0.04	15.3	0.1	1.07	0.02
	L1-2 VP-ITC2	3	5.80	0.02	15.60	0.06	1.032	0.006
	L1-3 Auto-iTC200	5	5.76	0.02	14.6	0.1	1.058	0.006
L2	L2-1 VP-ITC	5	5.78	0.03	15.1	0.2	1.01	0.02
	L2-2 PEAQ-ITC	3	5.84	0.06	14.8	0.1	1.00	0.02
L3	L3-1 iTC200	4	5.68	0.05	15.1	0.1	0.98	0.04
	L3-2 PEAQ-ITC1	6	5.73	0.06	15.2	0.1	0.90	0.08
	L3-3 PEAQ-ITC2	4	5.70	0.04	15.2	0.3	0.96	0.06
L4	L4-1 VP-ITC	4	5.79	0.02	15.3	0.3	1.01	0.05
	L4-2 iTC200	4	5.78	0.02	15.0	0.2	0.94	0.04
L5	L5-1 VP-ITC	7	5.71	0.02	15.1	0.2	1.00	0.03
	L5-2 iTC200	4	5.68	0.06	14.2	0.3	0.94	0.02

Best estimates were obtained by non-linear least squares regression data analysis, as reported by each user from labs L1–L5. The programs used for data treatment in each case were: *L1* origin with user-defined routines; *L2* PEAQ-ITC; *L3* PEAQ-ITC; *L4* Origin; and *L5* NITPIC/SEDPHAT

N number of assay replicates; *sd* standard deviation
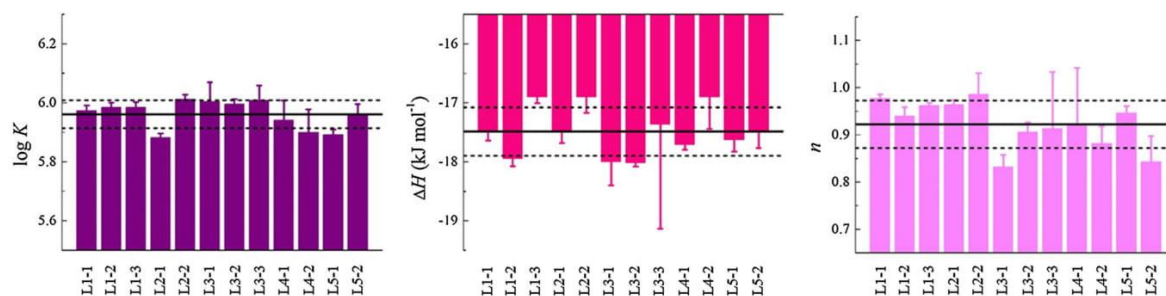
Fig. 3 Average values for binding affinity (log$K$), binding enthalpy (ΔH) and binding stoichiometry (n) for the EDTA–Ca^{2+} interaction measured and analyzed by each laboratory L1–L5. The error bars reflect the standard deviations for the measured parameters. The LX-Y code indicates the laboratory and the instrument employed according to Table 1. The continuous line is the global average of all measured values and the *dotted lines* indicate the limits for the corresponding standard deviations (Table 3)
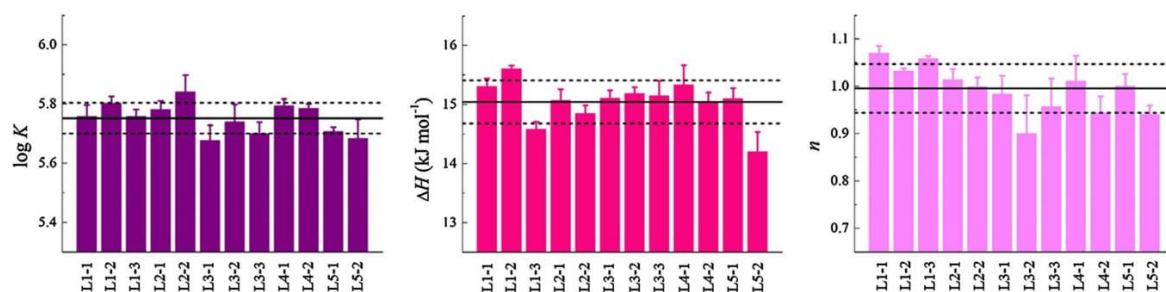
Fig. 4 Average values for binding affinity (log$K$), binding enthalpy (ΔH) and binding stoichiometry (n) for the EDTA–Mg^{2+} interaction measured and analyzed by each laboratory L1–L5. The error bars reflect the standard deviations for the measured parameters. The LX-Y code indicates the laboratory and the instrument employed according to Table 2. The continuous line is the global average of all measured values and the *dotted lines* indicate limits for the corresponding standard deviations (Table 3)

Table 3 Estimated parameter values for the association constant (K), interaction enthalpy (ΔH), and "stoichiometry" (or binding-competent fraction, n) for the interaction of Ca^{2+}/EDTA (MES 10 mM, pH 5.60) and Mg^{2+}/EDTA (HEPES 10 mM, pH 7.40, NaCl 100 mM) from global average and standard deviation of all results obtained and analyzed in the facilities included in the first round of this benchmark study (common sample) as reported by the users

Ligand	log$K$	sd-log$K$	ΔH kJ mol^{-1}	sd-ΔH kJ mol^{-1}	n	sd-n
Ca^{2+}	5.97	0.05 (0.0471)	−17.5	0.4 (0.411)	0.92	0.05 (0.0504)
Mg^{2+}	5.75	0.05 (0.0518)	15.0	0.4 (0.366)	0.99	0.05 (0.0515)

sd standard deviation

Except for the value for VP-ITC (L4-1), that typically present low uncertainties, the other cases are iTC200 (usually high uncertainties, see plots in the end of the discussion) and the PEAQ-ITC L3-3, that always presents high dispersion. Thus, this points to a possible problem in L3-3, and also possibly in L4-1, although less significant. Thus, for this property, the user and instrument variability are not reflected in very significant differences in the retrieved thermodynamic association constant, that shows an uncertainty of 0.04–0.05 for log$K$ (0.7–0.9% in log$K$ or 2% in K) in the global average values reported in Table 3. As for the binding enthalpy ΔH of the EDTA–Ca^{2+} interaction, all, except L1-3, also agreed within combined uncertainty with the global average value (Table 3), but again the uncertainty for L3-3 is very large. For the EDTA–Mg^{2+} interaction, only L1-2 and L5-2 did not agree with the combined uncertainty with the global average binding enthalpy (Table 3). It remains difficult to explain why L3-3 presents so high dispersion in the Ca/EDTA but not in the Mg/EDTA system. Overall, the uncertainties in this parameter are low (except for L3-3 in the EDTA-Ca^{2+} (even considering that the number of repeats per instrument and Lab was often small)), leading to an uncertainty

of 0.4 kJ/mol (2–3% in ΔH) in the global average values reported in Table 3. Finally, regarding the *n* value, in the case of EDTA–Ca^{2+}, only L3-1 did not agree within the combined uncertainty of 0.05 (5%), but the uncertainties for L3-3 and L4-1 are large, whereas for EDTA–Mg^{2+}, no outlier was found (although L1-1 is on the limit of agreement).

So, overall, we can say that our study shows that when the same sample is used, although outliers exist, both depending on instrument and on lab, most results produced by all instruments in the various laboratories involved in first-round agree within the combined uncertainty. There is a tendency for iTC200 to produce data with the highest uncertainties, and VP-ITC with the lowest ones (in fact, for two instruments with similar absolute heat sensitivity, the larger the cell volume, the better the specific sensitivity and the smaller the detectable change in the macromolecule concentration (Velázquez-Campoy et al. 2000)). That comparison is detailed below, at the end of the Results and Discussion section. Still, to judge the reported uncertainties, it must be born in mind that a $+0.5$ difference in $\log K$ corresponds to a threefold difference in the association constant K (roughly, $+3$ kJ mol^{-1} difference for ΔG at 298.15 K), and a difference of $+0.1$ in $\log K$ corresponds to a 1.3-fold difference in the association constant K (roughly, $+0.6$ kJ mol^{-1} difference for ΔG at 298.15 K).

Data analyzed by four different softwares

As explained above in Materials and methods section, all results were analyzed independently by four of us, using different data treatment programs. For easy reference in the following, we will use the following notation:

Soft 1—Origin (with user-defined (AVC) functions).
Soft 2—AFFINImeter.
Soft 3—NITPIC + SEDPHAT.
Soft 4—PEAQ-ITC.

Some examples of the layouts obtained with Origin were shown in Fig. 2, and examples for the other 3 softwares can be seen in Fig. 5.

Although sharing many common features, several aspects differ in the way data is treated in these four programs, and they deserve mention here. These programs treat the integration baseline differently, and that might have an important reflection in the retrieved results. In the cases of Origin and PEAQ-ITC, the analysis software generates automatically the baseline and the range over which to integrate the injection peaks. If needed/wanted, the baseline and integration range can be adjusted manually by the user, for each individual peak (as described in the respective software instruction manual). In the case of AFFINImeter (Piñeiro et al. 2019), the software automatically generates a baseline for each injection, which is subtracted from the raw signal. The individual baselines are obtained by fitting a smooth function joining the first point of the signal injection to
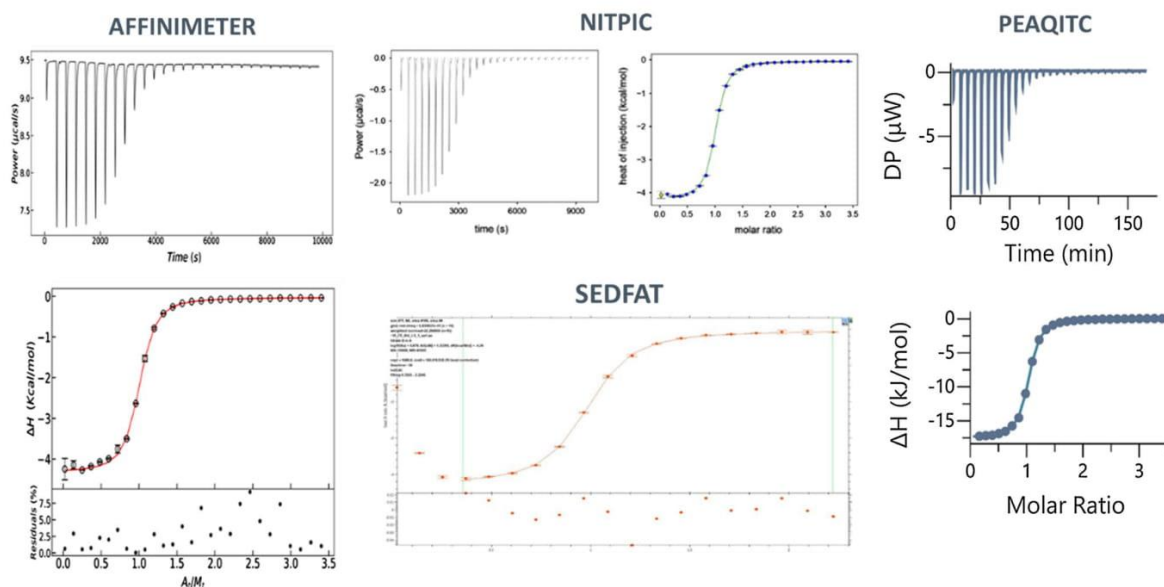

Fig. 5 Typical plots obtained for an EDTA–Ca^{2+} titration, as derived from Soft 2 (AFFINImeter), Soft 3 (NITPIC/SEDPHAT) and Soft 4 (PEAQ-ITC) with a high-volume VP-ITC. Upper plots show the thermogram and lower ones the binding isotherm along with the fit line. Typical plots obtained with Soft 1 (Origin with user-defined functions) were shown in Fig. 2

the trend of the last part of the signal, i.e., excluding the perturbed region, using a linear combination of orthogonal functions (Legendre polynomials of first, second and third order). Finally, in the case of NITPIC (Keller et al. 2012; Scheuermann and Brautigam 2015), an automated peak assignment based on peak-shape analysis via singular value decomposition (SVD) in combination with detailed least-squares modeling of local pre- and post-injection baselines is performed. The program developed an approach for automatic peak integration of ITC thermograms, based on statistical principles and exploiting the specific data structure of ITC thermograms. On the basis of the expected properties of local continuity in the baseline, the program does a detailed modeling of the pre- and post-injection baselines, estimates consensus baselines spanning each injection, and their confidence limits are determined for all peaks. In both AFFINImeter and NITPIC the user can change integration limits, and the baseline is recalculated by the software. Overall, Origin and PEAQ-ITC offer the possibility of user intervention when integrating the heat effects, which may be beneficial or prejudicial depending on the user proficiency in calorimetric data analysis.

As regarding the approach to the n value—usually reporting the stoichiometry, but also functioning operationally as a correction factor for titrand (or titrant) concentration, since the stoichiometry is often implicit in the model, both the commercial Origin (and consequently PEAQ-ITC) as well as the version with user-defined routines use a "renormalizing" factor n that multiplies the concentration of titrand in the cell every time that concentration appears in the binding equilibrium equations. The concentrations of titrant in syringe and titrand in the cell are fixed during the fitting, and thus n may absorb any uncertainties in both titrand and titrant concentrations. Usually, the titrant concentration is considered to be well-known, and thus the n value is interpreted as a correction to the titrand concentration. In general, a correction factor n for the titrand concentration can also be interpreted as a correction factor $1/n$ for the titrant concentration. Indeed, changing the titrant concentration alter the heats (as Q is measured and then divided by the molar amount of injectant, thus depending on titrant concentration) as well as the molar ratio, while changes in the titrand concentration only affect the molar ratio. This has already been discussed in the literature, showing that an error of 10% in the titrant concentration will lead directly to 10% errors in K and ΔH (Tellinghuisen 2005; Tellinghuisen and Chodera 2011). In AFFINImeter (Piñeiro et al. 2019), the user has the choice between three different "n" values which are called r_M, r_A and r_B. Each of these r values represent factors to correct the concentration of the main compound in the sample cell, M, the main compound in the syringe, A, and in the case of mixtures the secondary compound that can be in the cell, in the syringe or in both places, B. AFFINImeter

also allows introducing mathematical restrictions between these or/and other parameters. In SEDPHAT (Brautigam et al. 2016; Zhao et al. 2015), concentration errors can be accounted for as 'incompetent fractions' (for example, fractions of unfolded protein) of either the component in the cell or in the syringe or alternatively, directly as a concentration correction factor of either component. The difference is practical in that incompetent fractions cannot be negative, therefore imposing lower limits on concentration errors. Both approaches permit straightforward global modeling and multi-method modeling since the reaction order is directly fixed by the reaction scheme defined by the user. It is usually used to correct for the titrand concentration, providing results then comparable to the n values obtained in Origin, PEAQ-ITC or AFFINImeter r_M, with $n = 1 -$ 'incompetent fraction', or to a concentration factor of magnitude $(n - 1)$ for the component in the syringe. Therefore, in all cases care must be taken to explicitly state the approach used, i.e., which concentration is being corrected for. In the results here reported, the competent fraction always refers to the titrand.

Finally, as regarding the heat of dilution, all softwares here used to consider the heat of dilution as a fitting parameter, that can thus be obtained together with K, ΔH and n (please note that the commercial Origin software does not fit for the dilution heat, only the version here used can do that, due to user-defined fitting routines). Further, all softwares permit the use of custom dilution experiments.

The results obtained for all data treated with Soft 1–4 can be found in Tables 4, 5, 6, 7 for EDTA–Ca^{2+} and in Tables 8, 9, 10, 11 for EDTA–Mg^{2+}. In all cases, averages and standard deviations were calculated using standard equations.

To facilitate the visual comparison of the obtained values, we produced the plots shown in Figs. 6, 7, where one can see the dispersion of the experimental individual values obtained with each instrument from each participating lab assess the potential correlation between affinity (K) and enthalpy (ΔH), and the influence of the software package used for data analysis. In Figures S1 and S2 (Supplementary Material) similar plots are shown, but using averages and standard deviations instead of individual values. In this way, one can more easily observe the dispersion of values obtained with each instrument in each laboratory.

Several aspects are clearly apparent from Figs. 6, 7: (i) overall we can say that there is no significant difference between the 4 used software packages; (ii) although there is some dispersion (even some outliers) between the values obtained in different laboratories and with different instruments, there is no clear trend that could lead to a distinction of instrument performance; (iii) the potential and expected correlation between affinity (K) and enthalpy (ΔH) is, in general, not observed with these data.

Table 4 Estimated parameter values for the association constant (K), interaction enthalpy (ΔH), and "stoichiometry" (or binding-competent fraction, n) for the EDTA–Ca^{2+} interaction in the calorimeters included in the first round of this benchmark study

Location	Instrument	N	log$K$	sd-log$K$	ΔH kJ mol^{-1}	sd-ΔH kJ mol^{-1}	n	sd-n
L1	L1-1 VP-ITC1	3	5.97	0.02	−17.5	0.1	0.977	0.008
	L1-2 VP-ITC2	3	5.98	0.02	−17.9	0.1	0.94	0.02
	L1-3 Auto-iTC200	5	5.98	0.02	−16.9	0.1	0.962	0.006
L2	L2-1 VP-ITC	5	5.90	0.02	−17.5	0.1	0.96	0.01
	L2-2 PEAQ-ITC	3	5.97	0.02	−17.2	0.1	0.98	0.04
L3	L3-1 iTC200	5	6.00	0.04	−18.2	0.2	0.81	0.05
	L3-2 PEAQ-ITC1	3	5.99	0.02	−18.2	0.3	0.91	0.02
	L3-3 PEAQ-ITC2	3	5.99	0.07	−18	2	0.9	0.1
L4	L4-1 VP-ITC	4	5.95	0.06	−17.8	0.1	0.9	0.1
	L4-2 iTC200	4	5.94	0.04	−17.1	0.6	0.90	0.05
L5	L5-1 VP-ITC	7	5.92	0.02	−17.85	0.08	0.95	0.01
	L5-2 iTC200	4	5.99	0.06	−17.5	0.3	0.87	0.02

Best estimates were obtained by non-linear least squares regression data analysis using the Origin 7.0 software with user-defined fitting routines (Soft 1)

N number of assay replicates, *sd* standard deviation

Table 5 Estimated parameter values for the association constant (K), interaction enthalpy (ΔH), and "stoichiometry" (or binding-competent fraction, n) for the EDTA–Ca^{2+} interaction in the calorimeters included in the first round of this benchmark study

Location	Instrument	N	log$K$	sd-log$K$	ΔH kJ mol^{-1}	sd-ΔH kJ mol^{-1}	n	sd-n
L1	L1-1 VP-ITC1	3	5.94	0.02	−17.9	0.2	0.97	0.01
	L1-2 VP-ITC2	3	5.95	0.03	−18.0	0.2	0.93	0.02
	L1-3 Auto-iTC200	5	5.97	0.01	−16.96	0.03	0.954	0.007
L2	L2-1 VP-ITC	5	5.92	0.01	−17.2	0.2	0.96	0.01
	L2-2 PEAQ-ITC	3	6.01	0.02	−16.9	0.3	0.99	0.04
L3	L3-1 iTC200	5	5.99	0.09	−18.4	0.5	0.92	0.01
	L3-2 PEAQ-ITC1	3	5.99	0.08	−18.3	0.4	0.91	0.02
	L3-3 PEAQ-ITC2	3	6.04	0.04	−18	2	0.9	0.1
L4	L4-1 VP-ITC	4	5.93	0.09	−17.9	0.2	0.9	0.1
	L4-2 iTC200	4	5.97	0.08	−17.0	0.6	0.89	0.04
L5	L5-1 VP-ITC	7	5.89	0.04	−16	1	0.93	0.02
	L5-2 iTC200	4	5.96	0.08	−17.7	0.3	0.86	0.03

Best estimates were obtained by non-linear least squares regression data analysis using the AFFINImeter software (Soft 2)

N number of assay replicates, *sd* standard deviation

In Fig. 8, a further comparison is presented, as we plot the parameter n *vs* the enthalpy, ΔH, to check for the potential correlation between these two parameters, that is reasonable to expect (Chodera and Mobley 2013; Tellinghuisen and Chodera 2011). The data is plotted for both EDTA–Ca^{2+} and EDTA–Mg^{2+}, as analyzed individually by the users (above) and centrally by Soft 1 (Origin (with user-defined functions). In general, by eye we could suspect a weak correlation for Ca^{2+}/EDTA, whereas no correlation is apparent for EDTA–Mg^{2+}. To test the possibility of correlations more thoroughly, we did several linear fittings from data in plots of ΔH vs log$K$, using the values as analyzed from each laboratory. A very wide range for R values was found, both positive and negative, as with a small number of data (replicates for labs are between three and seven, but usually

four) it is easy to get correlations, that cannot be meaningful. Therefore, we did the fit with all data, and the R value is almost zero. We also assessed n vs log$K$, and n vs ΔH, with R values less than 0.5. Thus overall, we conclude that there is no significant correlation between the parameters. Indeed, this study represents a particular experimental situation, dealing with simple chemical compounds, under very controlled set-up, which makes this lack of a strong correlation understandable. With more complex and bio-related systems, and including several replicates from different stock solutions, a stronger correlation is expected and often found.

Overall, the assembled data are robust, reproducible, and slightly dependent on the instrument (indeed the larger volume VP-ITC produces data with somewhat smaller uncertainty, as expected) and hardly dependent on the software

Table 6 Estimated parameter values for the association constant (K), interaction enthalpy (ΔH), and "stoichiometry" (or binding-competent fraction, n) for the EDTA–Ca^{2+} interaction in the calorimeters included in the first round of this benchmark study

Location	Instrument	N	log$K$	sd-log$K$	ΔH kJ mol^{-1}	sd-ΔH kJ mol^{-1}	n	sd-n
L1	L1-1 VP-ITC1	3	5.94	0.01	−17.6	0.1	0.973	0.008
	L1-2 VP-ITC2	3	5.96	0.01	−18.0	0.1	0.94	0.02
	L1-3 Auto-iTC200	5	5.97	0.02	−16.82	0.06	0.96	0.01
L2	L2-1 VP-ITC	5	5.89	0.01	−17.43	0.09	0.96	0.01
	L2-2 PEAQ-ITC	3	5.98	0.01	−17.0	0.1	0.98	0.04
L3	L3-1 iTC200	5	5.91	0.04	−18.2	0.3	0.81	0.02
	L3-2 PEAQ-ITC1	3	6.02	0.03	−18.1	0.2	0.917	0.008
	L3-3 PEAQ-ITC2	3	6.00	0.05	−17	2	0.9	0.1
L4	L4-1 VP-ITC	4	5.94	0.05	−17.7	0.1	0.9	0.1
	L4-2 iTC200	4	5.90	0.08	−16.9	0.5	0.88	0.04
L5	L5-1 VP-ITC	7	5.89	0.02	−17.6	0.2	0.95	0.01
	L5-2 iTC200	4	5.96	0.04	−17.5	0.3	0.84	0.06

Best estimates were obtained by non-linear least squares regression data analysis using the NITPIC-SED-PHAT software (Soft 3)

N: number of assay replicates, *sd* standard deviation

Table 7 Estimated parameter values for the association constant (K), interaction enthalpy (ΔH), and "stoichiometry" (or binding-competent fraction, n) for the EDTA-Ca^{2+} interaction in the calorimeters included in the first round of this benchmark study

Location	Instrument	N	log$K$	sd-log$K$	ΔH kJ mol^{-1}	sd-ΔH kJ mol^{-1}	n	sd-n
L1	L1-1 VP-ITC1	3	5.97	0.02	−17.5	0.1	0.978	0.008
	L1-2 VP-ITC2	3	5.983	0.008	−17.9	0.1	0.94	0.02
	L1-3 Auto-iTC200	5	5.97	0.02	−16.81	0.09	0.966	0.009
L2	L2-1 VP-ITC	5	5.89	0.01	−17.5	0.1	0.96	0.01
	L2-2 PEAQ-ITC	3	6.034	0.005	−16.9	0.3	0.99	0.04
L3	L3-1 iTC200	5	6.00	0.06	−18.0	0.4	0.83	0.03
	L3-2 PEAQ-ITC1	3	6.00	0.02	−18.02	0.06	0.91	0.02
	L3-3 PEAQ-ITC2	3	6.01	0.05	−17	2	0.9	0.1
L4	L4-1 VP-ITC	4	5.98	0.03	−16.8	0.4	0.90	0.06
	L4-2 iTC200	4	5.98	0.05	−17.5	0.2	0.9	0.1
L5	L5-1 VP-ITC	7	5.93	0.02	−17.8	0.1	0.95	0.01
	L5-2 iTC200	4	5.99	0.04	−17.4	0.2	0.88	0.02

Best estimates were obtained by non-linear least squares regression data analysis using the PEAQ-ITC software (Soft 4)

N number of assay replicates, *sd* standard deviation

used. Therefore, these data can lead to trustworthy thermodynamic data that enables future use of these complex-formation reactions as test reactions for the performance of instrument and users. As such, a table similar to Table 3 was constructed (Table 12), with the global average and standard deviations of all results obtained in the first round of this benchmark study (common sample), with the thermodynamic parameters association constant (log$K$), interaction enthalpy (ΔH) and stoichiometry (or binding competent fraction, n) for the interaction of Ca^{2+}/EDTA and Mg^{2+}/EDTA now taken from the treatment of all pooled results obtained with the four different softwares (Soft 1–4). It can be seen in Table 12 that the average values do not change significantly, showing that the four softwares used do not lead, in this case, to significantly different values, as referred

to above. It should be noted that indeed the standard deviations are here much lower, as the number of values now is four times larger; thus, the decrease in standard deviation is indeed artificial, as the results are based on the same number of original independent experiments. As these results are more homogeneous, because all data from each reaction is calculated by the same person in each software, we use these values in our comparisons and discussion hereafter. Nevertheless, for future use by the community as reference values for these two test reactions, readers should consider the values in Table 3, as they report a realistic data dispersion, more meaningful for comparisons with values retrieved by regular users.

The results here obtained are in excellent agreement with values reported at 298 K and similar experimental conditions

Table 8 Estimated parameter values for the association constant (K), interaction enthalpy (ΔH), and "stoichiometry" (or binding-competent fraction, n) for the EDTA–Mg^{2+} interaction in the calorimeters included in the first round of this benchmark study

Location	Instrument	N	log$K$	sd-log$K$	ΔH kJ mol^{-1}	sd-ΔH kJ mol^{-1}	n	sd-n
L1	L1-1 VP-ITC1	3	5.76	0.04	15.3	0.1	1.07	0.02
	L1-2 VP-ITC2	3	5.80	0.02	15.60	0.06	1.032	0.006
	L1-3 Auto-iTC200	5	5.76	0.02	14.6	0.1	1.058	0.006
L2	L2-1 VP-ITC	5	5.82	0.02	14.8	0.2	1.01	0.02
	L2-2 PEAQ-ITC	3	5.80	0.02	15.08	0.09	1.00	0.02
L3	L3-1 iTC200	4	5.67	0.09	15.4	0.3	0.97	0.04
	L3-2 PEAQ-ITC1	6	5.75	0.04	15.4	0.3	0.91	0.08
	L3-3 PEAQ-ITC2	4	5.73	0.04	15.2	0.2	0.95	0.04
L4	L4-1 VP-ITC	4	5.77	0.02	15.5	0.3	1.03	0.06
	L4-2 iTC200	4	5.75	0.02	15.4	0.2	0.98	0.04
L5	L5-1 VP-ITC	7	5.71	0.02	15.4	0.1	1.01	0.03
	L5-2 iTC200	4	5.73	0.02	14.8	0.4	0.98	0.03

Best estimates were obtained by non-linear least squares regression data analysis using the Origin 7.0 software with user-defined fitting routines (Soft 1)

N number of assay replicates, *sd* standard deviation

Table 9 Estimated parameter values for the association constant (K), interaction enthalpy (ΔH), and "stoichiometry" (or binding-competent fraction, n) for the EDTA–Mg^{2+} interaction in the calorimeters included in the first round of this benchmark study

Location	Instrument	N	log$K$	sd-log$K$	ΔH kJ mol^{-1}	sd-ΔH kJ mol^{-1}	n	sd-n
L1	L1-1 VP-ITC1	3	5.77	0.09	15.5	0.1	1.07	0.01
	L1-2 VP-ITC2	3	5.78	0.04	16.0	0.5	1.021	0.009
	L1-3 Auto-iTC200	5	5.76	0.04	14.64	0.08	1.046	0.008
L2	L2-1 VP-ITC	5	5.78	0.03	15.1	0.2	1.01	0.02
	L2-2 PEAQ-ITC	3	5.84	0.06	14.4	0.1	1.00	0.02
L3	L3-1 iTC200	4	5.6	0.2	15.6	0.7	0.91	0.02
	L3-2 PEAQ-ITC1	6	5.82	0.08	15.2	0.2	0.90	0.08
	L3-3 PEAQ-ITC2	4	5.75	0.07	15.3	0.1	0.94	0.06
L4	L4-1 VP-ITC	4	5.74	0.02	15.8	0.4	1.02	0.06
	L4-2 iTC200	4	5.77	0.06	15.2	0.2	0.96	0.03
L5	L5-1 VP-ITC	7	5.67	0.04	14	1	0.97	0.02
	iTC200	4	5.68	0.06	14.5	0.4	0.94	0.02

Best estimates were obtained by non-linear least squares regression data analysis using the AFFINImeter software (Soft 2)

N number of assay replicates; *sd* standard deviation

for Ca^{2+}/EDTA, also in MES 10 mM, pH 5.6 (Claveria-Gimeno et al. 2019) where the authors obtained log$K = 5.23$ (12% difference) and $\Delta H = -17.1 \pm 0.4$ kJ mol^{-1} (2% difference). For Mg^{2+}/EDTA, another work (Vega et al. 2015) reports values for similar (but not equal conditions), namely 10 mM MOPS, 100 mM NaCl, pH 7.0, as log$K = 5.18$ (10% difference) and $\Delta H = +13.0 \pm 0.8$ kJ mol^{-1} (14% difference). These last results stress the influence of buffer conditions on the interaction parameters.

Second round of benchmarking

Four additional laboratories (L6–L9) participated in the second round of this benchmark study, using the instruments and data treatment programs listed in Table S1. For these

experiments, as described above in Materials and Methods, they prepared their own samples, according to the instructions provided, to be similar to the preparations made for the first round, except that the concentrations of Ca^{2+} and Mg^{2+} were just inferred from the amount of powder weighed, without analytical determination. It should be noted that labs L7 and L8 shared the same sample preparation.

The results obtained, as analyzed by the same laboratories performing the experiments, can be seen in Table 13 (for EDTA–Ca^{2+}) and 14 (EDTA–Mg^{2+}). As labs L6–L8 used NITPIC/SEDPHAT to globally analyze all experiments performed in a given instrument (thermogram integrated in NITPIC and the resulting isotherm transferred to SEDPHAT for binding analysis), the uncertainty results were provided

Table 10 Estimated parameter values for the association constant (K), interaction enthalpy (ΔH), and "stoichiometry" (or binding-competent fraction, n) for the EDTA–Mg^{2+} interaction in the calorimeters included in the first round of this benchmark study

Location	Instrument	N	$\log K$	sd-$\log K$	ΔH kJ mol^{-1}	sd-ΔH kJ mol^{-1}	n	sd-n
L1	L1-1 VP-ITC1	3	5.75	0.04	15.2	0.2	1.07	0.01
	L1-2 VP-ITC2	3	5.78	0.03	15.45	0.07	1.022	0.005
	L1-3 Auto-iTC200	5	5.74	0.02	14.43	0.05	1.040	0.009
L2	L2-1 VP-ITC	5	5.80	0.03	14.8	0.1	1.01	0.03
	L2-2 PEAQ-ITC	3	5.81	0.03	14.8	0.1	1.00	0.03
L3	L3-1 iTC200	4	5.6	0.1	15.4	0.2	0.92	0.01
	L3-2 PEAQ-ITC1	6	5.74	0.06	15.1	0.2	0.90	0.08
	L3-3 PEAQ-ITC2	4	5.74	0.04	14.9	0.1	0.96	0.04
L4	L4-1 VP-ITC	4	5.76	0.01	15.5	0.3	1.03	0.06
	L4-2 iTC200	4	5.76	0.01	15.0	02	0.96	0.04
L5	L5-1 VP-ITC	7	5.71	0.02	15.1	0.2	1.00	0.03
	L5-2 iTC200	4	5.68	0.06	14.2	0.3	0.94	0.02

Best estimates were obtained by non-linear least squares regression data analysis using the NITPIC-SED-PHAT software (Soft 3)

N number of assay replicates, *sd* standard deviation

Table 11 Estimated parameter values for the association constant (K), interaction enthalpy (ΔH), and "stoichiometry" (or binding-competent fraction, n) for the EDTA–Mg^{2+} interaction in the calorimeters included in the first round of this benchmark study

Location	Instrument	N	$\log K$	sd-$\log K$	ΔH kJ mol^{-1}	sd-ΔH kJ mol^{-1}	n	sd-n
L1	L1-1 VP-ITC1	3	5.76	0.04	15.2	0.2	1.07	0.02
	L1-2 VP-ITC2	3	5.80	0.02	15.5	0.1	1.030	0.001
	L1-3 Auto-iTC200	5	5.77	0.01	14.45	0.04	1.060	0.007
L2	L2-1 VP-ITC	5	5.82	0.03	14.7	0.2	1.01	0.02
	L2-2 PEAQ-ITC	3	5.875	0.005	14.6	0.2	0.99	0.02
L3	L3-1 iTC200	4	5.68	0.05	15.1	0.1	0.98	0.04
	L3-2 PEAQ-ITC1	6	5.74	0.06	15.2	0.1	0.90	0.08
	L3-3 PEAQ-ITC2	4	5.70	0.04	15.2	0.3	0.96	0.06
L4	L4-1 VP-ITC	4	5.78	0.03	15.4	0.3	1.03	0.06
	L4-2 iTC200	4	5.79	0.01	15.0	0.2	0.97	0.04
L5	L5-1 VP-ITC	7	5.71	0.03	15.3	0.2	1.01	0.04
	L5-2 iTC200	4	5.70	0.09	14.3	0.3	0.96	0.01

Best estimates were obtained by non-linear least squares regression data analysis using the PEAQ-ITC software (Soft 4)

N number of assay replicates, *sd* standard deviation

using the 95% confidence interval ($\pm \Delta CI95$ in Table 13), that SEDPHAT provides using a post-hoc procedure.

To allow comparison between these new sets of results, both among themselves and with the results obtained in the first round, we show in Tables 13, 14 the results obtained in laboratories L1 and L5 (from the first round) together with the results for the new labs L6–9, for EDTA–Ca^{2+} and EDTA–Mg^{2+}, respectively (plotted in Figs. 9, 10). These two labs were chosen as L5 did use the same software to analyze their data, and L1 and L5 also analyzed globally the experiments for each instrument and provided the uncertainty using the CI95.

Several points are apparent from Table 13 and Fig. 9, for the EDTA–Ca^{2+} experiments: (i) the values for the three parameters from the two labs that used the same samples (L7 and L8) are in closer agreement (although the ΔH for L7-2 is rather low and outside combined uncertainties) than the parameters from those labs that used different samples; (ii) as compared to the values obtained in round 1 (L1, L5), the ΔH values from L6 are significantly smaller (in absolute value), those from L7 and L8 are in rather good agreement, whereas the value for L9 is significantly higher (in absolute value); (iii) the values for log K from L6 and L9 are significantly lower than the ones from L7 and L8, and lower (L6 and L9) and higher (L7, L8) from the one obtained in L1 and L5 (outside combined uncertainties); (iv) curiously, the values for ΔH for L7 and L8 (same samples) do not agree with each other within combined uncertainty, as do log$K$ and n. Finally, regarding the n values now retrieved, they are roughly all in good agreement. Thus, although it seemed at
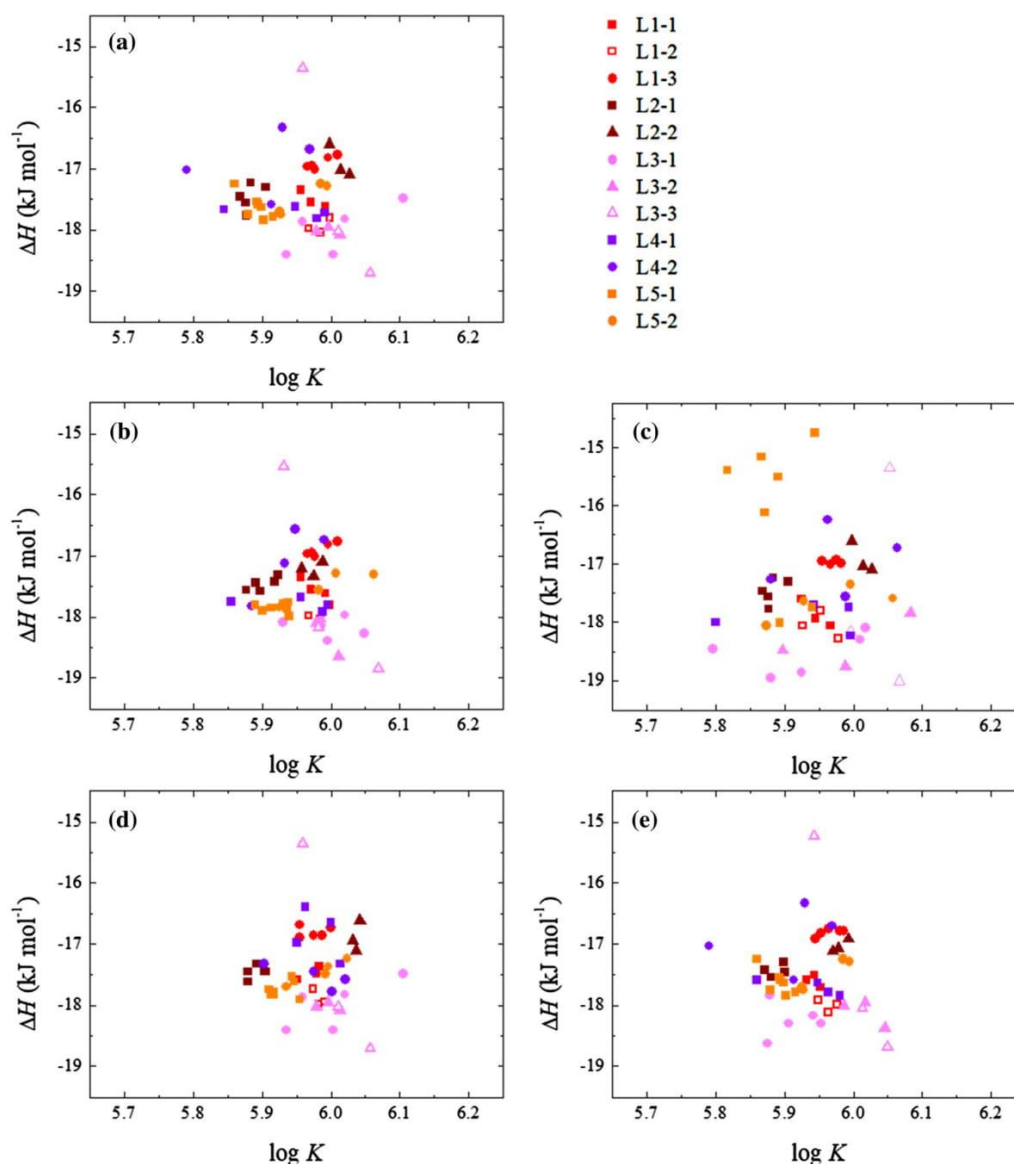
Fig. 6 Individual values for binding affinity ($\log K$) and binding enthalpy (ΔH) for the EDTA–Ca^{2+} interaction measured in each laboratory and analyzed **a** by each laboratory L1–L5, or centrally **b** by Soft 1 (Origin with user-defined functions), **c** by Soft 2 (AFFINImeter), **d** by Soft 3 (NITPIC + SEDPHAT), and **e** by Soft 4 (PEAQ-ITC). The LX-Y code indicates the laboratory and the instruments employed according to Table S1

first sight that sample preparation was the more important discriminating factor, our data do not fully support this view. Significant differences in ΔH could be due to a calibration problem, and this is one of the advantages of using a test reaction—if all other factors are correct, it would point to a calibration issue, and the company should be called for electrical calibration of the instrument (in these ITC instruments the parameters related to calibration, i.e., transformation of signal into heat value, cannot be changed by the user). In the present case, that could be the case for L7-2, whereas the significant outlier from L6 points to a problem in sample preparation, as it would be unlikely that both instruments from this laboratory had the same calibration problem at the same time.

Turning now to the EDTA–Mg^{2+} experiments (Table 14, Fig. 10), we face a different situation: a
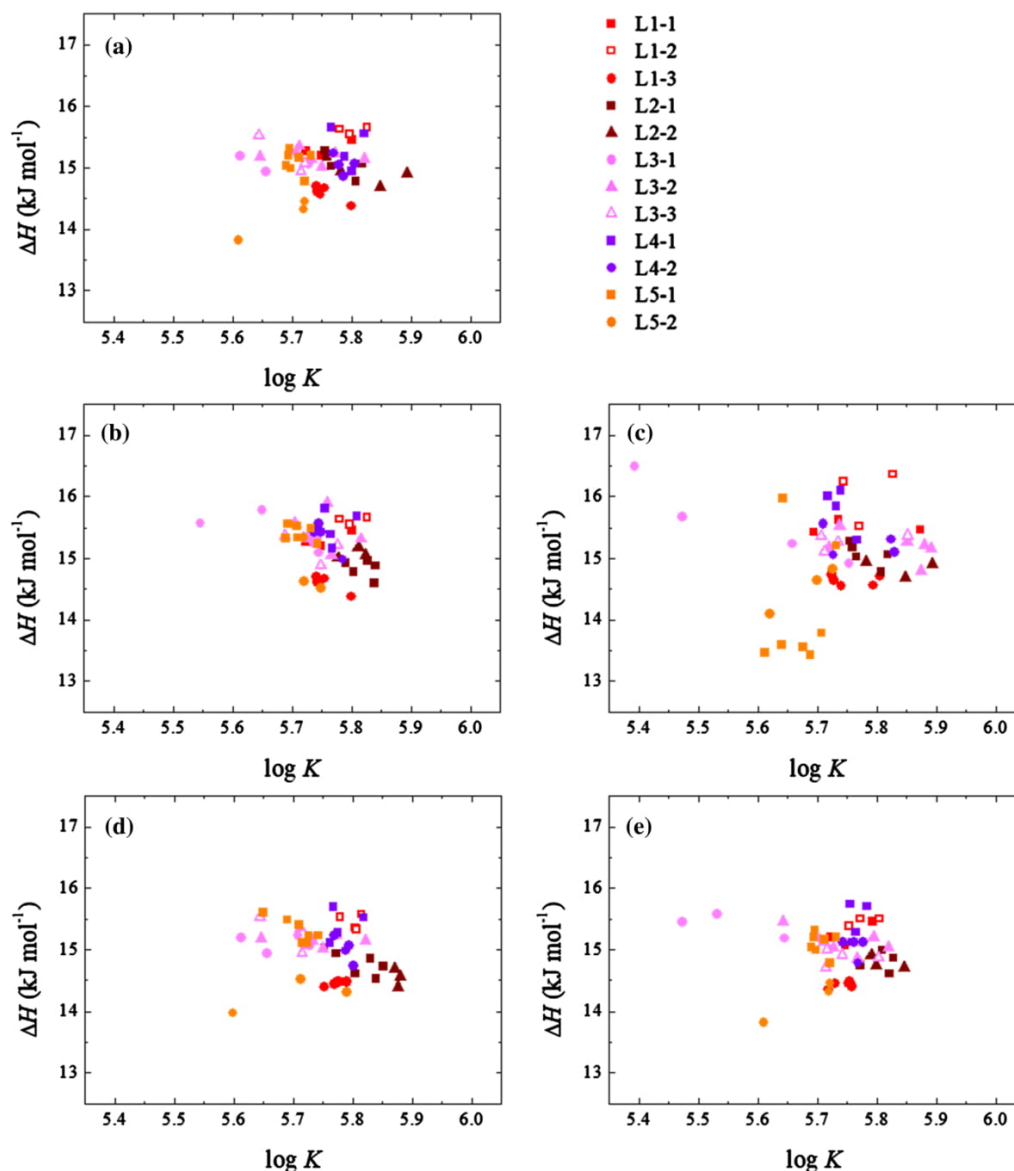
Fig. 7 Individual values for binding affinity (log$K$) and binding enthalpy (ΔH) for the EDTA-Mg^{2+} interaction measured in each laboratory and analyzed **a** by each laboratory L1–L5, **b** by Soft 1 (Origin with user-defined functions), **c** by Soft 2 (AFFINImeter), **d** by Soft 3 (NITPIC + SEDPHAT), and **e** by Soft 4 (PEAQ-ITC). The LX-Y code indicates the laboratory and the instrument employed according to Table S1

reasonable agreement is found between all log$K$ values (including between benchmark rounds), but the values for ΔH are in rather good agreement for L6, are significantly larger for Labs L7 and L8, and even further away for L9, as compared to the results obtained in the first round. Considering that the n values show a good agreement between all labs (L1, L5 and L6–8, except for L9—too low, outlier),

this would point to either a calibration problem or an error in the Mg concentration for L9. It should be stressed that both Ca and Mg salts to be used must either be from freshly opened bottles or conveniently conditioned to guarantee that the hydration water taken into account in molar mass corresponds to the real one. Conversely, the actual correct concentration can be assessed after preparation,

314 | FCUP
Characterization of the Self-Assembling of antimicrobial *D,L-* α Cyclic
Peptides at Bacterial Model Membranes

European Biophysics Journal

Table 14 Estimated parameter values for the association constant, interaction enthalpy, and "stoichiometry" (or binding-competent fraction) for the interaction of Mg^{2+} with EDTA in the calorimeters included in this benchmark study

Location	Instrument	N	logK	−ΔCI95 +ΔCI95	ΔH kJ mol⁻¹	−ΔCI95 +ΔCI95 kJ mol⁻¹	n	−ΔCI95 +ΔCI95
L1	L1-1 VP-ITC1	3	5.76	−0.021 0.021	15.31	−0.08 0.08	1.055	−0.005 0.006
	L1-2 VP-ITC2	3	5.80	−0.010 0.010	15.60	−0.04 0.04	1.024	−0.002 0.003
	L1-3 Auto-iTC200	5	5.76	−0.017 0.017	14.57	−0.07 0.06	1.060	−0.006 0.006
L5	L5-1 VP-ITC	7	5.71	−0.042 0.044	15.0	−0.14 0.18	1.00	−0.023 0.023
	L5-2 iTC200	4	5.7	−0.114 0.120	14.1	−0.42 0.47	0.94	−0.021 0.021
L6	L6-1 VP-ITC	3	5.71	−0.03 0.03	15.9	−0.18 0.19	1.022	−0.006 0.006
	L6-2 iTC200	5	5.75	−0.04 0.05	15.8	−0.19 0.20	1.035	−0.007 0.006
L7	L7-1 VP-ITC	5	5.86	−0.05 0.05	18.4	−0.21 0.25	0.99	−0.010 0.010
	L7-2 iTC200	6	5.89	−0.07 0.07	17.2	−0.29 0.33	0.95	−0.009 0.008
L8	VP-ITC	4	5.86	−0.03 0.03	19.0	−0.17 0.17	0.931	−0.004 0.004
L9*	VP-ITC	5	5.91	−0.029 0.029	22.2	−0.76 0.76	0.74	−0.031 0.031

Best estimates were obtained by global non-linear least squares regression data analysis of all experiments performed in a given instrument. Profile likelihood asymmetric confidence intervals (95%) are shown

N number of assay replicates, confidence interval: $[-\Delta CI95, +\Delta CI95]$

*Lab 9 did not send the results as average and CI95. To be comparable with the other four sets of data from the other labs, the limits for the parametric symmetric confidence interval at 95% are $\pm t_{N-1}(0.025) \times sd/\sqrt{N}$, which for $N=5$ is similar to $\pm sd$, the standard deviation

**As the 95% profile likelihood confidence intervals are not symmetric, we did correct the number of significant figures of each parameter according to its uncertainty, but let one extra figure in the values of upper and lower CI limits, to underline this asymmetry
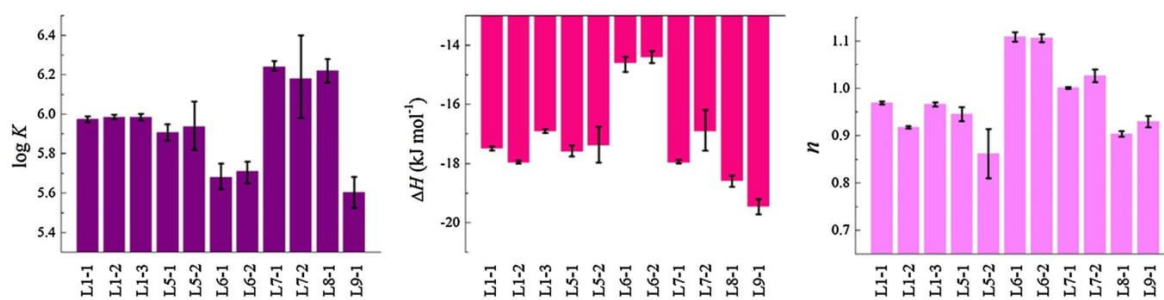

Fig. 9 Average values for the binding affinity (log*K*), binding enthalpy (ΔH), and binding "stoichiometry" (or binding-competent fraction, *n*) for the EDTA–Ca^{2+} interaction measured and analyzed by each laboratory L1, L5 and L6–L9. The error bars reflect the confidence intervals (95%) for the measured parameters. The LX-Y code indicates the laboratory and the instrument employed according to Table S1
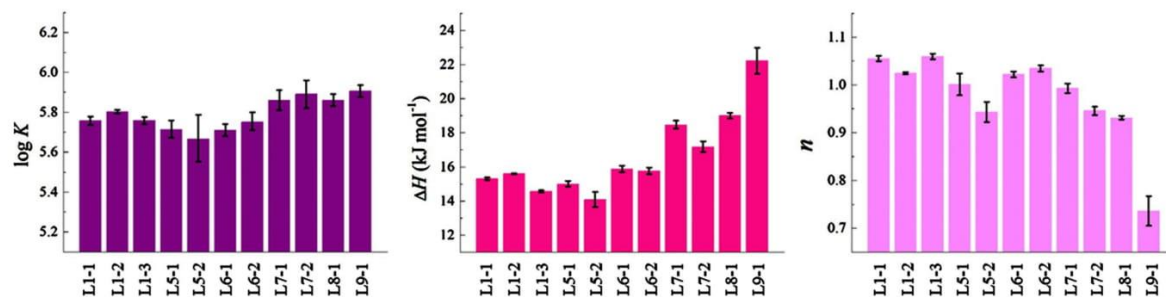
Fig. 10 Average values for the binding affinity (log$K$), binding enthalpy (ΔH), and binding "stoichiometry" (or binding-competent fraction, n) for the EDTA–Mg^{2+} interaction measured and analyzed by each laboratory L1, L5 and L6–L9. The error bars reflect the con-fidence intervals (95%) for the measured parameters. The LX-Y code indicates the laboratory and the instrument employed according to Table S1
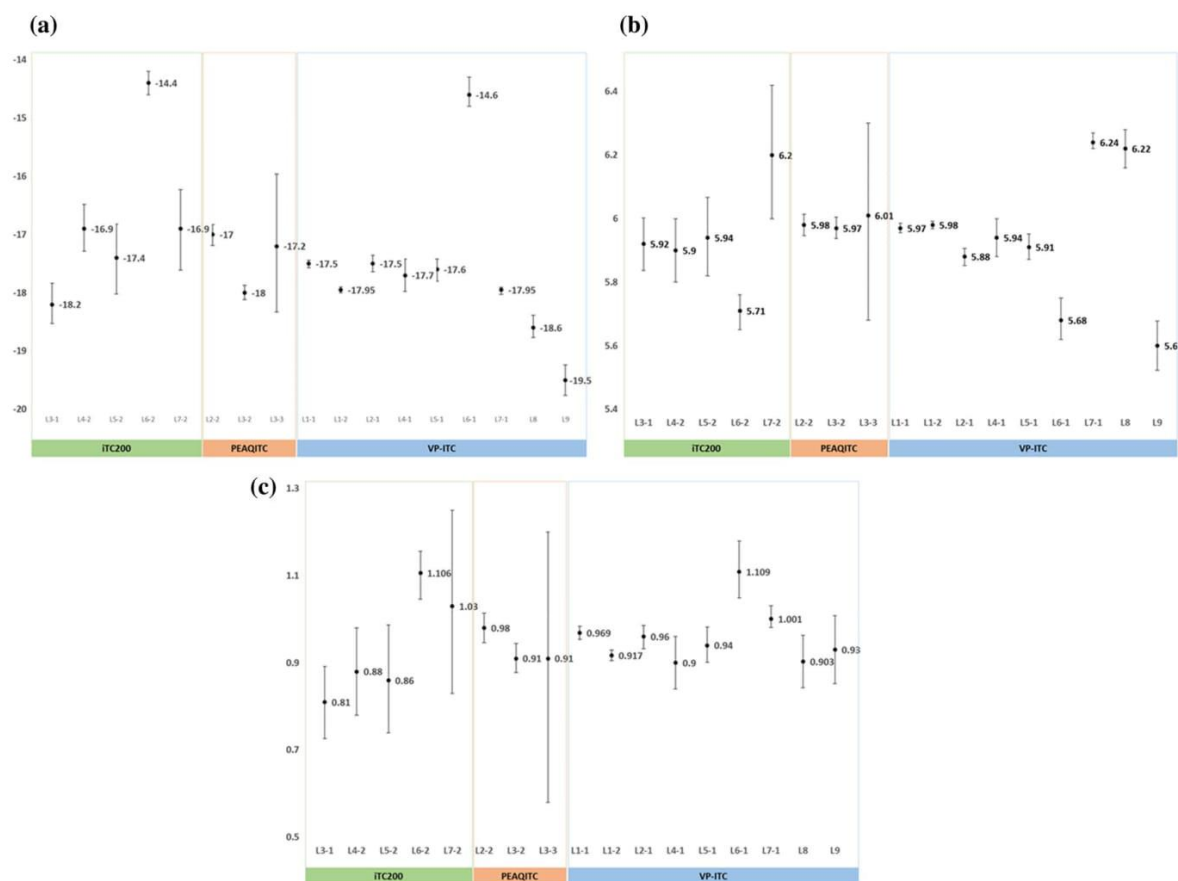

Fig. 11 Values for the parameters ΔH (**a**), K (**b**), and n (**c**) for the reaction Ca^{2+}/EDTA as obtained in all laboratories involved, grouped by instrument. The error bars represent the uncertainty here expressed as the CI95

smaller than those determined from the CAII-AZM and CAII-CBS studies, and comparable to the uncertainties potentially achievable given the high sensitivity of modern calorimeters. In addition, many of these values are considerably better than those indicated by the calorimeter manufacturer in their test kit based on the EDTA–Ca interaction (5% for n, 10% for K, and 10% for ΔH), and similar or better compared to a small study with just two VP-ITC instruments (5% for n, 5% for K, and 0.3 kJ/mol for ΔH) (Ràfols et al. 2016).

Indeed, the systems chosen produced highly reproducible results, not particularly dependent on any of the assessed variables. As such, this reinforces our proposal for both these ligand-binding reactions being used as test reactions for instrument and user performance. The thermodynamic parameters provided in Table 3 can thus be taken as reference values for the use of these test reactions for assessment of instrument and user performance, under the experimental conditions here detailed—for $Ca^{2+}/EDTA$, log $K = 5.97 \pm 0.04$, or $K_a = (9.3 \pm 0.9) \times 10^5$, $\Delta H = -17.5 \pm 0.4$ kJ mol^{-1} and $n = 0.92 \pm 0.05$, whereas for $Mg^{2+}/EDTA$ log $K = 5.75 \pm 0.05$, or $K_a = (5.6 \pm 0.6) \times 10^5$, $\Delta H = +15.0 \pm 0.4$ kJ mol^{-1} and $n = 0.99 \pm 0.05$.

In principle, if the values for the interaction parameters obtained in a series of experiments lie far outside from the reported ranges, that could be due to a combination of three factors: instrument problem, sample problem, and protocol (experiment plus data analysis) problem. In that case, the user should employ fresh calibrated solutions (either provided by the calorimeter manufacturer or by chemicals distributors) in order to rule out a sample problem. If by doing this, and checking if the instrument is thoroughly cleaned, the experiment is performed following standard settings, and the data analysis is done properly, interaction parameters still fall outside the expected ranges, this should be considered as an indication of an instrument problem. Some actions can be done by the user (e.g., change the injection syringe or perform an electrical calibration), but a thorough revision of the instrument might require the assistance of the technical service.

Different software packages offer different possibilities—in all cases the integration is done automatically with little or no intervention from the user, and thereafter the user can correct or adjust different items depending on the program used—e.g., integration limits (AFFINImeter), baseline type, injection and baseline parameters, polynomial fitting parameters, etc. (NITPIC), the baseline and the integration range (e.g., Origin and PEAQ-ITC). This implies that although the binding equations are identical in all softwares, these factors generate differences in the retrieved parameters, as the data analysis results will strongly depend on the integration, together with the way handling of the background injection heat is performed. In addition, AFFINImeter and SEDPHAT provide the user with a variety of interaction models and experimental protocols for data analysis, while Origin and PEAQ-ITC are less versatile unless the user has sufficient proficiency in ITC data analysis and user-defined fitting routines.

References

Adão R, Bai G, Loh W, Bastos M (2012) Chemical calibration of isothermal titration calorimeters: an evaluation of the dilution of propan-1-ol into water as a test reaction using different calorimeters, concentrations, and temperatures. J ChemThermodyn 52:57–63. https://doi.org/10.1016/j.jct.2011.12.018

Baker M (2016) Reproducibility: seek out stronger science. Nature 537:703–704. https://doi.org/10.1038/nj7622-703a

Baranauskienė L, Petrikaitė V, Matulienė J, Matulis D (2009) Titration calorimetry standards and the precision of isothermal titration calorimetry data. Int J MolSci 10:2752–2762

Bastos M (2016) Biocalorimetry: foundations and contemporary approaches, 1st edn. CRC Press. https://doi.org/10.1201/b20161

Begley CG, Ellis LM (2012) Raise standards for preclinical cancer research. Nature 483:531–533. https://doi.org/10.1038/483531a

Brautigam CA, Zhao H, Vargas C, Keller S, Schuck P (2016) Integration and global analysis of isothermal titration calorimetry data for studying macromolecular interactions. Nat Protoc 11:882–894. https://doi.org/10.1038/nprot.2016.044. http://www.nature.com/nprot/journal/v11/n5/abs/nprot.2016.044.html#supplementary-information

Chaires JB (2008) Calorimetry and thermodynamics in drug design. Annu Rev Biophys 37:135–151. https://doi.org/10.1146/annurev.biophys.36.040306.132812

Chaires JB, Hansen LD, Keller S, Brautigam CA, Zhao H, Schuck P (2015) Biocalorimetry. Methods 76:1–2. https://doi.org/10.1016/j.ymeth.2015.02.001

Chodera JD, Mobley DL (2013) Entropy-enthalpy compensation: role and ramifications in biomolecular ligand recognition and design. Annu Rev Biophys 42:121–142. https://doi.org/10.1146/annurev-biophys-083012-130318

Claveria-Gimeno R, Vega S, Abian O, Velazquez-Campoy A (2019) Tinkering with binding polynomials in isothermal titration calorimetry. Methods MolBiol 1964:185–213. https://doi.org/10.1007/978-1-4939-9179-2_14

Dumas P (2016) Joining thermodynamics and kinetics by kinITC. In: Bastos M (ed) Biocalorimetry: foundations and contemporary approaches. CRC Press, Taylor & Francis, p 20

Freire E (2001) The thermodynamic linkage between protein structure, stability, and function. Methods MolBiol 168:37–68

Freire E, Mayorga OL, Straume M (1990) Isothermal titration calorimetry. Anal Chem 62:950A-958A

Hansen LD, Quinn C (2019) Obtaining precise and accurate results by ITC. EurBiophys J 48:825–835. https://doi.org/10.1007/s00249-019-01399-8

Hansen LD, Fellingham GW, Russell DJ (2011) Simultaneous determination of equilibrium constants and enthalpy changes by titration calorimetry: methods, instruments, and uncertainties. Anal Biochem 409:220–229. https://doi.org/10.1016/j.ab.2010.11.002

Ioannidis JP (2016) Why most clinical research is not useful. PLoS Med 13:e1002049. https://doi.org/10.1371/journal.pmed.1002049

Kantonen SA, Henriksen NM, Gilson MK (2017) Evaluation and minimization of uncertainty in ITC binding measurements: heat error, concentration error, saturation, and stoichiometry. BiochimBiophysActa Gen Subj 1861:485–498. https://doi.org/10.1016/j.bbagen.2016.09.002

Keller S, Vargas C, Zhao H, Piszczek G, Brautigam CA, Schuck P (2012) High-precision isothermal titration calorimetry with automated peak-shape analysis. Anal Chem 84:5066–5073. https://doi.org/10.1021/ac3007522

Kolthoff IM, Elving PJ (1959) Treatise on analytical chemistry. InterscienceEncyclopedia, New York

Mobley A, Linder SK, Braeuer R, Ellis LM, Zwelling L (2013) A survey on data reproducibility in cancer research provides insights into our limited ability to translate findings from the laboratory to the clinic. PLoS One 8:e63221. https://doi.org/10.1371/journal.pone.0063221

Myszka DG et al (2003) The ABRF-MIRG'02 study: assembly state, thermodynamic, and kinetic analysis of an enzyme/inhibitor interaction. J Biomol Tech 14:247–269

Paketuryte V, Linkuviene V, Krainer G, Chen WY, Matulis D (2019) Repeatability, precision, and accuracy of the enthalpies and Gibbs energies of a protein-ligand binding reaction measured by isothermal titration calorimetry. EurBiophys J 48:139–152. https://doi.org/10.1007/s00249-018-1341-z

Paketurytė V et al (2020) Uncertainty of a protein-ligand binding constant: asymmetric confidence interval versus standard error. Biophys. J, Eur

Perozzo R, Folkers G, Scapozza L (2004) Thermodynamics of protein-ligand interactions: history, presence, and future aspects. J Recept Signal Transduct Res 24:1–52. https://doi.org/10.1081/rrs-120037896

Piñeiro Á et al (2019) AFFINImeter: a software to analyze molecular recognition processes from experimental data. Anal Biochem 577:117–134. https://doi.org/10.1016/j.ab.2019.02.031

Prinz F, Schlange T, Asadullah K (2011) Believe it or not: how much can we rely on published data on potential drug targets? Nat Rev Drug Discovery 10:712–712. https://doi.org/10.1038/nrd3439-c1

Ràfols C, Bosch E, Barbas R, Prohens R (2016) The Ca2+–EDTA chelation as standard reaction to validate Isothermal Titration Calorimeter measurements (ITC). Talanta 154:354–359. https://doi.org/10.1016/j.talanta.2016.03.075

Scheuermann TH, Brautigam CA (2015) High-precision, automated integration of multiple isothermal titration calorimetric thermograms: new features of NITPIC. Methods 76:87–98. https://doi.org/10.1016/j.ymeth.2014.11.024

Tellinghuisen J (2005) Optimizing experimental parameters in isothermal titration calorimetry. J Phys Chem B 109:20027–20035. https://doi.org/10.1021/jp053550y

Tellinghuisen J (2012) Designing isothermal titration calorimetry experiments for the study of 1:1 binding: problems with the "standard protocol." Anal Biochem 424:211–220. https://doi.org/10.1016/j.ab.2011.12.035

Tellinghuisen J (2016) Optimizing isothermal titration calorimetry protocols for the study of 1:1 binding: keeping it simple. BiochimBiophysActa 1860:861–867. https://doi.org/10.1016/j.bbagen.2015.10.011

Tellinghuisen J (2018) Critique of methods for estimating heats in isothermal titration calorimetry. Anal Biochem 563:79–86. https://doi.org/10.1016/j.ab.2018.08.015

Tellinghuisen J, Chodera JD (2011) Systematic errors in isothermal titration calorimetry: concentrations and baselines. Anal Biochem 414:297–299. https://doi.org/10.1016/j.ab.2011.03.024

Vega S, Abian O, Velazquez-Campoy A (2015) A unified framework based on the binding polynomial for characterizing biological systems by isothermal titration calorimetry. Methods 76:99–115. https://doi.org/10.1016/j.ymeth.2014.09.010

Velázquez-Campoy A, López-Mayorga O, Cabrerizo-Vílchez MA (2000) Development of an isothermal titration microcalorimetric system with digital control and dynamic power Peltier compensation. I. Description and basic performance. Rev SciInstrum 71:1824–1831. https://doi.org/10.1063/1.1150543

Velazquez-Campoy A (2015) Geometric features of the Wiseman isotherm in isothermal titration calorimetry. J Therm Anal Calorim 122:1477–1483. https://doi.org/10.1007/s10973-015-4775-x

Velazquez-Campoy A, Freire E (2005) ITC in the post-genomic era...? Priceless BiophysChem 115:115–124. https://doi.org/10.1016/j.bpc.2004.12.015

Velazquez-Campoy A, Freire E (2006) Isothermal titration calorimetry to determine association constants for high-affinity ligands. Nat Protocols 1:186–191

Wadsö I, Goldberg RN (2001) Standards in isothermal microcalorimetry (IUPAC Technical report). Pure ApplChem 73:1625–1639

Zhao H, Piszczek G, Schuck P (2015) SEDPHAT—a platform for global ITC analysis and global multi-method analysis of molecular interactions. Methods (San Diego, Calif) 76:137–148. https://doi.org/10.1016/j.ymeth.2014.11.012

Authors and Affiliations

Adrian Velazquez-Campoy[1,2,3,4] · **Bárbara Claro**[5] · **Olga Abian**[1,2,3,6] · **Jonas Höring**[7] · **Louis Bourlon**[8] · **Rafael Claveria-Gimeno**[1,2,6] · **Eric Ennifar**[9] · **Patrick England**[8] · **Jonathan Brad Chaires**[10] · **Di Wu**[11] · **Grzegorz Piszczek**[11] · **Chad Brautigam**[12] · **Shih-Chia Tso**[13] · **Huaying Zhao**[14] · **Peter Schuck**[14] · **Sandro Keller**[15,16,17] · **Margarida Bastos**[5]

1   Institute of Biocomputation and Physics of Complex Systems (BIFI), Joint Units IQFR-CSIC-BIFI, and GBsC-CSIC-BIFI, Department of Biochemistry and Molecular and Cell Biology, Universidad de Zaragoza, Zaragoza, Spain

2   Aragon Institute for Health Research (IIS Aragon), Zaragoza, Spain

3   Centro de Investigación Biomédica en Red en El Área Temática de Enfermedades Hepáticas y Digestivas (CIBERehd), Madrid, Spain

4   Fundacion ARAID, Government of Aragon, Zaragoza, Spain

5   CIQUP, Department of Chemistry and Biochemistry, Faculty of Sciences, University of Porto, Porto, Portugal

6   Aragon Health Sciences Institute (IACS), Zaragoza, Spain

7   Molecular Biophysics, Technische Universität Kaiserslautern (TUK), Erwin-Schrödinger-Str. 13, 67663 Kaiserslautern, Germany

8   Plate-Forme de Biophysique Moléculaire, Institut Pasteur, Paris, France

9   Architecture Et Réactivité de L'ARN, CNRS UPR 9002, Institut de Biologie Moléculaire et Cellulaire, Université de Strasbourg, 67000 Strasbourg, France

10   James Graham Brown Cancer Center, University of Louisville, Louisville, KY 20202, USA

11   Biophysics Core Facility, National Heart, Lung, and Blood Institute, National Institutes of Health, Bethesda, MD 20892, USA

12   Departments of Biophysics and Microbiology, UT Southwestern Medical Center, Dallas, TX, USA

13   Department of Biophysics, UT Southwestern Medical Center, Dallas, TX, USA

14   Dynamics of Macromolecular Assembly Section, Laboratory of Cellular Imaging and Macromolecular Biophysics, National Institute of Biomedical Imaging and Bioengineering, National Institutes of Health, Bethesda, MD 20892, USA

15   Biophysics, Institute of Molecular Biosciences (IMB), NAWI Graz, University of Graz, Humboldtstr. 50/III, 8010 Graz, Austria

16   Field of Excellence BioHealth, University of Graz, Graz, Austria

17   BioTechMed-Graz, Graz, Austria

Supplementary Material

A multi-laboratory benchmark study of isothermal titration calorimetry (ITC) using Ca^{2+} and Mg^{2+} binding to EDTA

Adrian Velazquez-Campoy[1,2,3,4], Bárbara Claro[5], Olga Abian[1,2,3,6], Jonas Höring[7], Louis Bourlon[8], Rafael Claveria-Gimeno[1,2,6], Eric Ennifar[9], Patrick England[8], Jonathan Brad Chaires[10], Di Wu[11], Grzegorz Piszczek[11], Chad Brautigam[12], Shih-Chia Tso[13], Huaying Zhao[14], Peter Schuck[14], Sandro Keller[15,16,17], Margarida Bastos[5]

[1] Institute of Biocomputation and Physics of Complex Systems (BIFI), Joint Units IQFR-CSIC-BIFI, and GBsC-CSIC-BIFI, and Department of Biochemistry and Molecular and Cell Biology, Universidad de Zaragoza, Zaragoza, Spain
[2] Aragon Institute for Health Research (IIS Aragon), Zaragoza, Spain
[3] Centro de Investigación Biomédica en Red en el Área Temática de Enfermedades Hepáticas y Digestivas (CIBERehd), Madrid, Spain
[4] Fundacion ARAID, Government of Aragon, Zaragoza, Spain
[5] CIQUP, Department of Chemistry and Biochemistry, Faculty of sciences, University of Porto, Portugal
[6] Aragon Health Sciences Institute (IACS), Zaragoza, Spain
[7] Molecular Biophysics, Technische Universität Kaiserslautern (TUK), Erwin-Schrödinger-Str. 13, 67663 Kaiserslautern, Germany
[8] Plate-forme de Biophysique Moléculaire, Institut Pasteur, Paris, France
[9] Architecture et Réactivité de l'ARN, CNRS UPR 9002, Institut de Biologie Moléculaire et Cellulaire, Université de Strasbourg, 67 000 Strasbourg, France
[10s] James Graham Brown Cancer Center, University of Louisville, Louisville, KY, 20202 USA
[11] Biophysics Core Facility, National Heart, Lung, and Blood Institute, National Institutes of Health, Bethesda, MD, 20892, USA
[12] Departments of Biophysics and Microbiology, UT Southwestern Medical Center, Dallas, TX, USA
[13] Department of Biophysics, UT Southwestern Medical Center, Dallas, TX, USA
[14] Dynamics of Macromolecular Assembly Section, Laboratory of Cellular Imaging and Macromolecular Biophysics, National Institute of Biomedical Imaging and Bioengineering, National Institutes of Health, Bethesda, MD 20892, USA
[15] Biophysics, Institute of Molecular Biosciences (IMB), NAWI Graz, University of Graz, Humboldtstr. 50/III, 8010 Graz, Austria
[16] Field of Excellence BioHealth, University of Graz, Graz, Austria
[17] BioTechMed-Graz, Graz, Austria
Corresponding authors: mbastos@fc.up.pt, adrianvc@unizar.es

Corresponding authors: mbastos@fc.up.pt, adrianvc@unizar.es

S1. Samples sent to the 5 Labs participating in the first round of the benchmark study (labeled L1-L5 in the text)

Each of the 5 initial participating Labs received the samples as detailed in the table below, with each sample labeled as also shown.

Ca, Mg and EDTA samples sent to the 5 Labs participating in the first round of the benchmark study

	Volume for VPITC										Volume for 200 μL instruments					
	Ca²⁺ in MES	EDTA in MES	MES Buffer	Mg²⁺ in HEPES	EDTA in HEPES	Hepes Buffer		Ca²⁺ in MES	EDTA in MES	MES Buffer		Ca²⁺ in MES	EDTA in MES	MES Buffer	Mg²⁺ in HEPES	EDTA in HEPES	Hepes Buffer
	7.5	30	15	7.5	30	15		12	35	20		4	4.5	20	4	4.5	5

Lab	Instuments		Ca²⁺ in MES	EDTA in MES	MES Buffer	Mg²⁺ in HEPES	EDTA in HEPES	Hepes Buffer	Ca²⁺ in MES	Mg²⁺ in HEPES	EDTA in MES	EDTA in HEPES	Hepes Buffer
L1	VP-ITC	AutoITC200	12	35	20	12	35	20	12	35	20		
L2	VP-ITC	PEAQ-ITC	12	35	20	12	35	20					
L3	VP-ITC	ITC200	PEAQ-ITC	16	39	25	16	39	25				
L4	VP-ITC	ITC200		12	35	20	12	35	20				
L5	VP-ITC	ITC200		12	35	20	12	35	20				

[Ca²⁺] = 1600 μM
10 mM MES, pH=5.60

[Mg²⁺] = 1890 μM
10 mM Hepes, 100 mM NaCl,
pH=7.40

[EDTA] = 100 μM
10 mM MES, pH=5.60

[EDTA] = 100 μM
10 mM Hepes, 100 mM NaCl,
pH=7.40

Buffer
10 mM MES, pH=5.60

Buffer
10 mM Hepes, 100 mM NaCl,
pH=7.40

S2. Protocol to be followed in the experiments

The following protocol was sent to all participant Labs

COST ARBRE-MOBIEU

ITC benchmarking

Test reactions –   Binding of Ca^{2+} or Mg^{2+} to EDTA

Buffer for Ca^{2+} experiments – 10 mM MES, pH 5.60

Buffer for Mg^{2+} experiments– 10 mM HEPES, 100 mM NaCl, pH

7.40

1. Titration of Ca^{2+} into EDTA

Sample concentrations: Syringe: Ca^{2+} 1600 ☐M

Cell: EDTA 100.0 ☐M

2. Titration of Mg^{2+} into EDTA

Sample concentrations: Syringe: Mg^{2+} 1890 ☐M

Cell: EDTA 100.0 ☐M

Instrument settings:

Number of injections:	28 in VP-ITC
	19 for PEAQ-ITC, iTC200, Auto-iTC200
Vol. 1st injection:	2 µL in VP-ITC
	0.4 µL in PEAQ-ITC, iTC200, Auto-iTC200
Vol. following injections:	10 µL in VP-ITC
	2 µL in PEAQ-ITC, iTC200, Auto-iTC200
Temperature:	25 °C
Reference power:	10 µcal/s
Feedback:	high
Stirring speed:	351 rpm in VP-ITC
	750 rpm in PEAQ-ITC, iTC200, Auto-iTC200
Spacing:	350 s in VP-ITC
	150 s in PEAQ-ITC, iTC200, Auto-iTC200
Initial delay:	150 s in VPITC
	60 s in PEAQ-ITC, iTC200, Auto-iTC200
Filter period:	2 s

Sample cell pre-rinsed (twice) and soaked (once for 5 min) with EDTA

Notes:

1. Each experiment (Ca^{2+} with EDTA and Mg^{2+} with EDTA) should be performed <u>at least 3 times, and if possible 5 times.</u> The amounts of samples sent is enough for 5 experiments in the conditions above. Thus, I trust it will be possible for each participant to obtain at least 3 good titrations for each reaction.

2. I found that even with good washing procedures it is sometimes hard to get rid of the Ca^{2+} in the syringe, which will translate into obtaining exothermic heat of dilution for Mg^{2+} if you do the Ca^{2+} experiments first, as Ca is a stronger ligand and has an exothermic dilution heat. So, I would suggest doing first the (Mg^{2+} + EDTA), and after the (Ca^{2+} + EDTA) titrations.

3. Each participant should after the experiments
   a. analyze their data as they usually do
   b. send the raw data as well as the analyzed data and results to Margarida Bastos, Eric Ennifar, Adrian Velázquez-Campoy and Sandro Keller:

   Margarida Bastos   mbastos@fc.up.pt
   Eric Ennifar   e.ennifar@unistra.fr
   Adrian Velazquez-Campoy adrianvc@unizar.es
   Sandro Keller   sandro.keller@biologie.uni-kl.de

Table S1. ITC instruments and software used by each participating Lab in the benchmark study.

| Location	Code	Instrument	Software for data analysis
	L1-1	VP-ITC1	
L1	L1-2	VP-ITC2	Origin with user-defined functions
	L1-3	Auto-iTC200	
L2	L2-1	VP-ITC	PEAQ-ITC
	L2-2	PEAQ-ITC	
	L3-1	iTC200	
L3	L3-2	PEAQ-ITC1	PEAQ-ITC
	L3-3	PEAQ-ITC2	
L4	L4-1	VP-ITC	Standard Origin (Mg)/NITPIC (Ca)
	L4-2	iTC200	
L5	L5-1	VP-ITC	NITPIC-SEDPHAT
	L5-2	iTC200	
L6	L6-1	VP-ITC	NITPIC-SEDPHAT
	L6-2	iTC200	
L7	L7-1	VP-ITC	NITPIC-SEDPHAT
	L7-2	iTC200	
L8	L8-1	VP-ITC	NITPIC-SEDPHAT
L9	L9-1	VP-ITC	Standard Origin
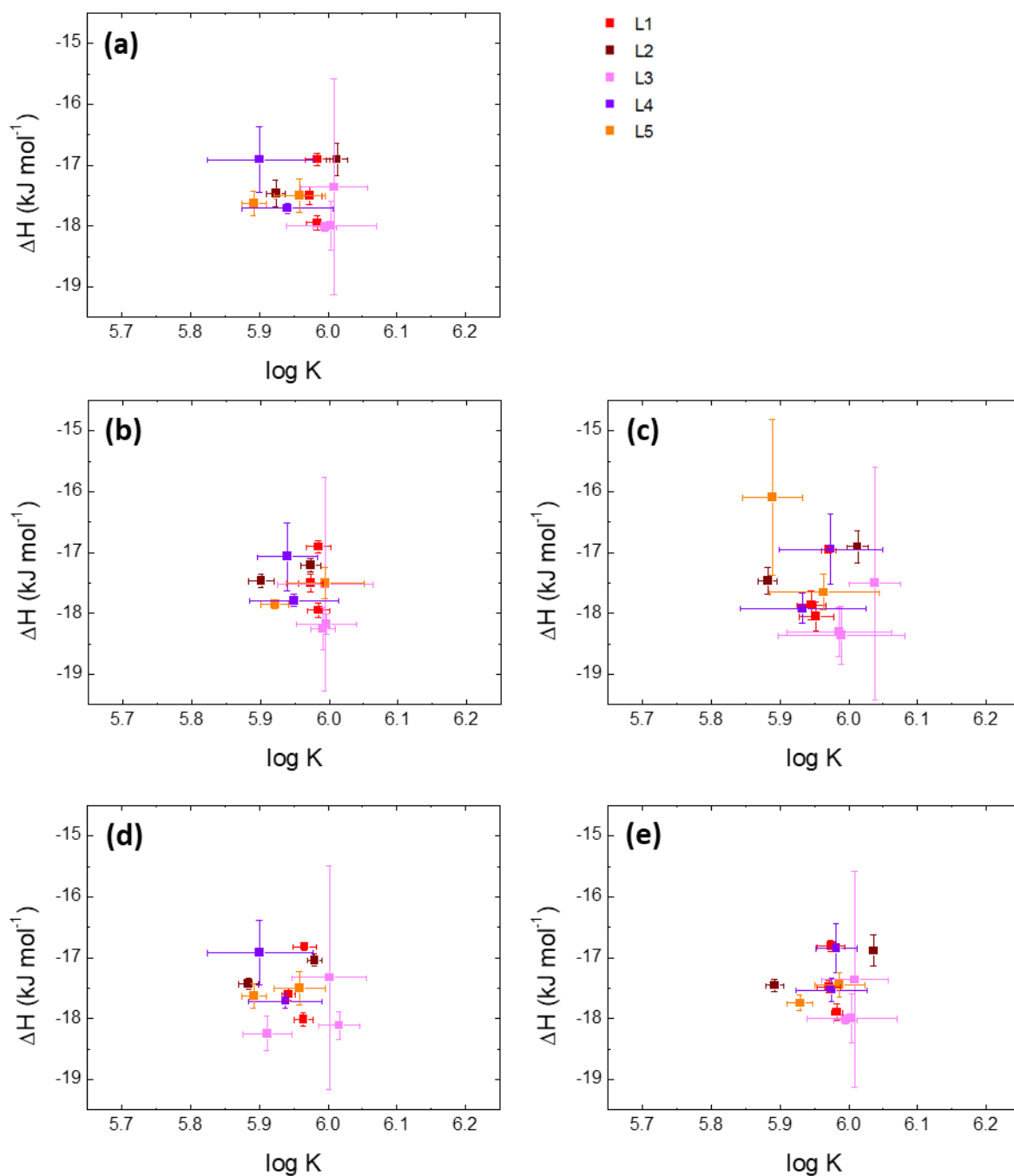
Figure S1. Average values for binding affinity (log$K$) and binding enthalpy (ΔH) for the EDTA-Ca^{2+} interaction measured in each laboratory, and analyzed by each laboratory in their usual way: (a) analyzed by L1; (b) analyzed by L2; (c) analyzed by L3; (d) analyzed by L4 and (e) analyzed by L5. Error bars indicate the standard deviations. The LX color code indicates the laboratory in which the experiments were performed according to Table S1.
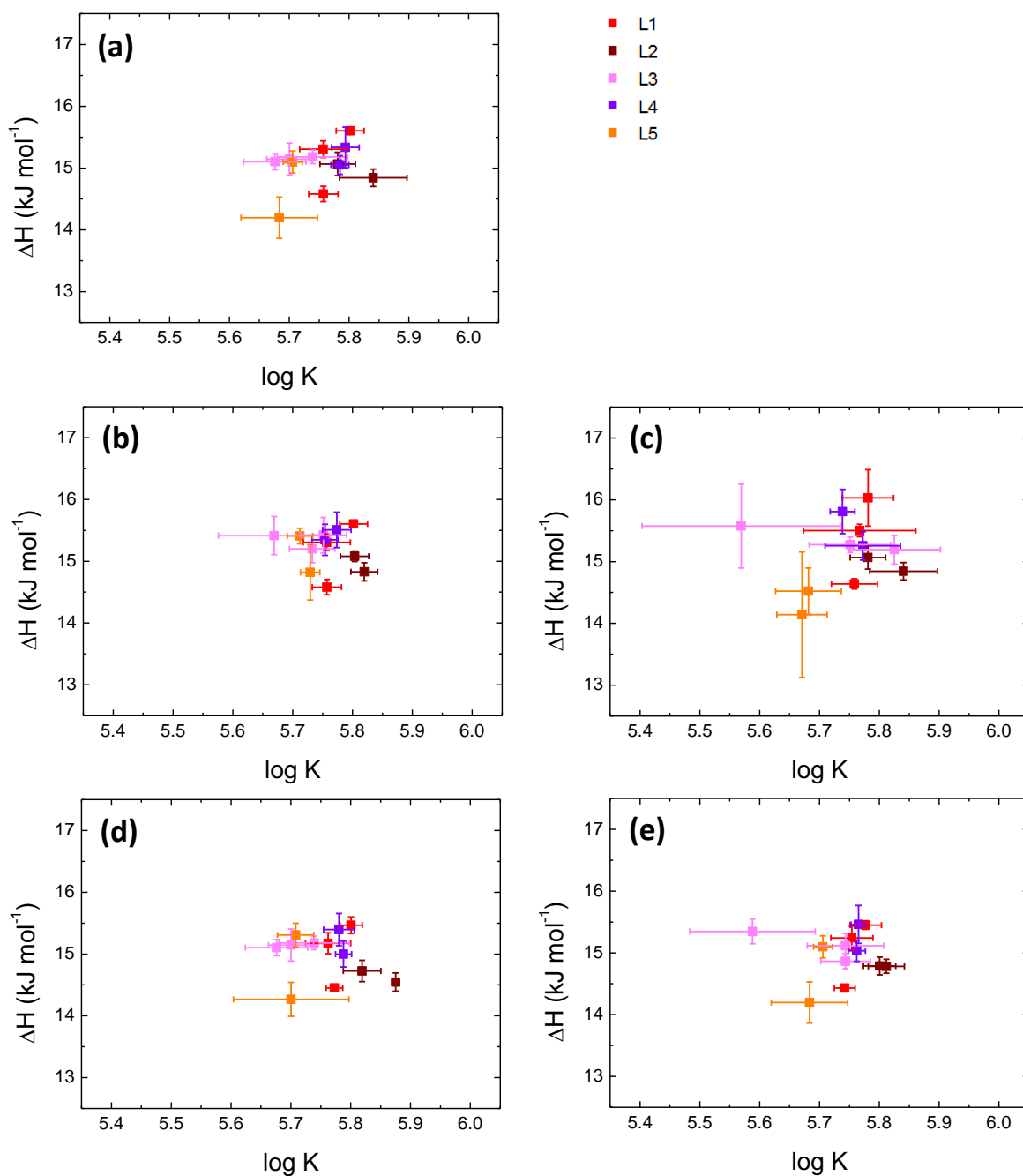
Figure S2. Average values for binding affinity (log$K$) and binding enthalpy (ΔH) for the EDTA-Mg^{2+} interaction measured in each laboratory, and analyzed by each laboratory in their usual way: (a) analyzed by L1; (b) analyzed by L2; (c) analyzed by L3; (d) analyzed by L4 and (e) analyzed by L5. Error bars indicate the standard deviations. The LX color code indicates the laboratory in which the experiments were performed according to Table S1.
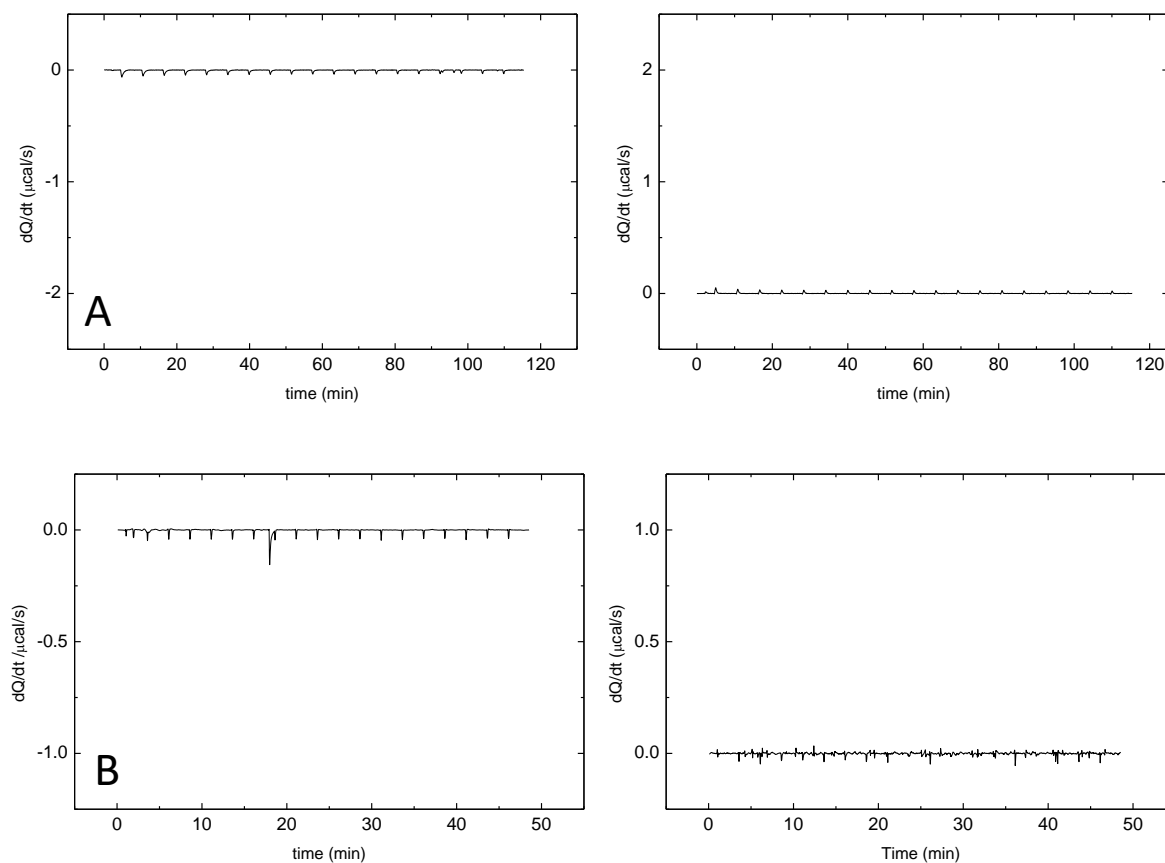
Figure S3. Typical control experiments corresponding to the injection of titrant into buffer in order to observe potential unspecific titrant-related phenomena or mismatches between solutions. Experiments were done in a (A) PEAQ-ITC and a (B) VP-ITC, by injecting (left) calcium solution and (right) magnesium solution at the same concentration as that employed in the EDTA-cation titration. Plots have been drawn using the same scales as those in the EDTA-cation experiments.
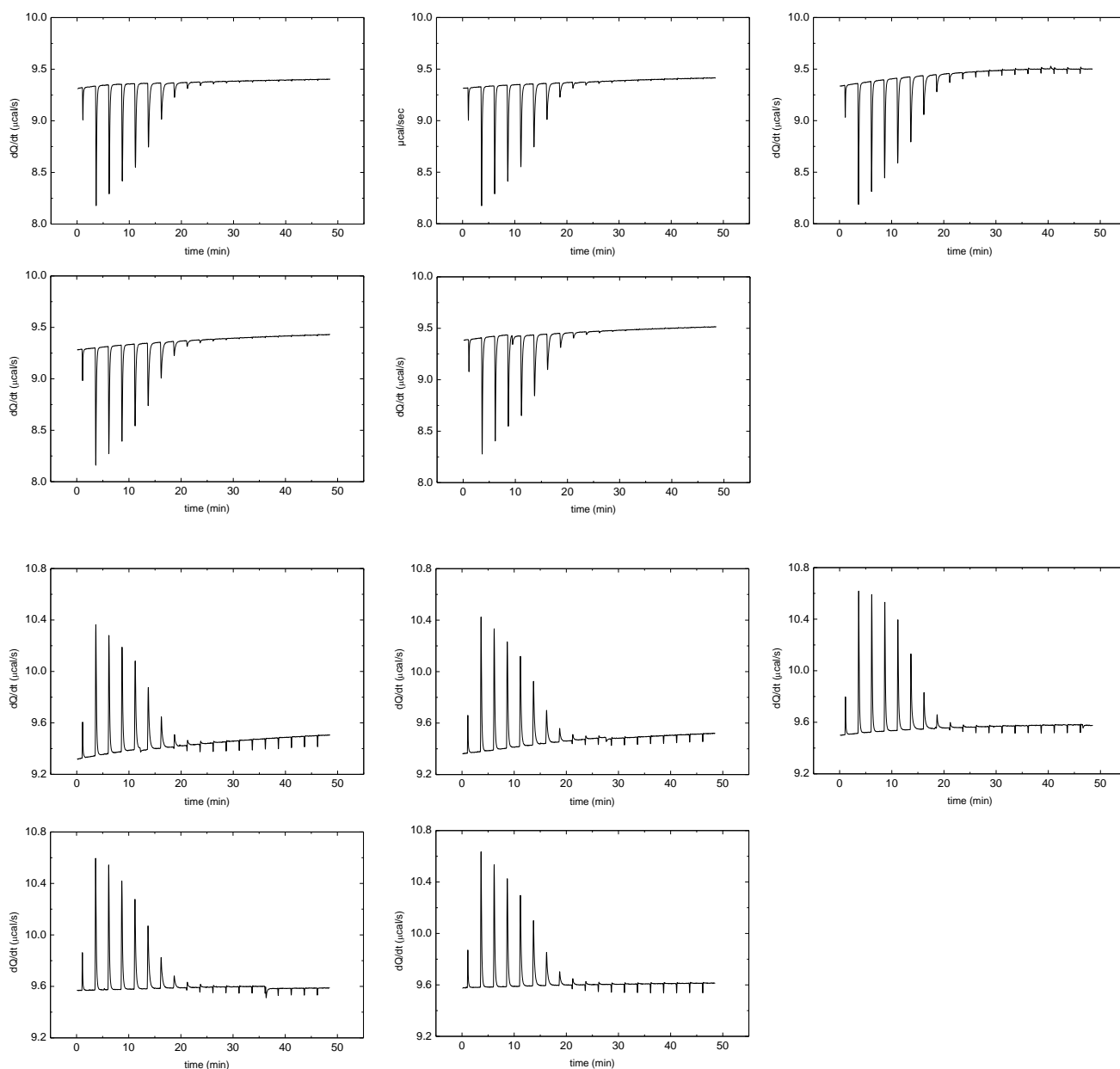
Figure S4. Full set of calorimetric titrations (5 experiments) performed in an Auto-iTC200 corresponding to EDTA-Ca^{2+} (upper plots with negative deflections due to the exothermic nature of the interaction) and EDTA-Mg^{2+} interaction (lower plots with positive deflections due to the endothermic nature of the interaction). The raw thermograms with no baseline correction are shown.

Figure S5. Full set of calorimetric titrations performed in two VP-ITCs (two instruments x 3 titrations) corresponding to EDTA-Ca^{2+} (plots with negative deflections due to the exothermic nature of the interaction) and EDTA-Mg^{2+} interaction (plots with positive deflections due to the endothermic nature of the interaction). The raw thermograms with no baseline correction are shown.
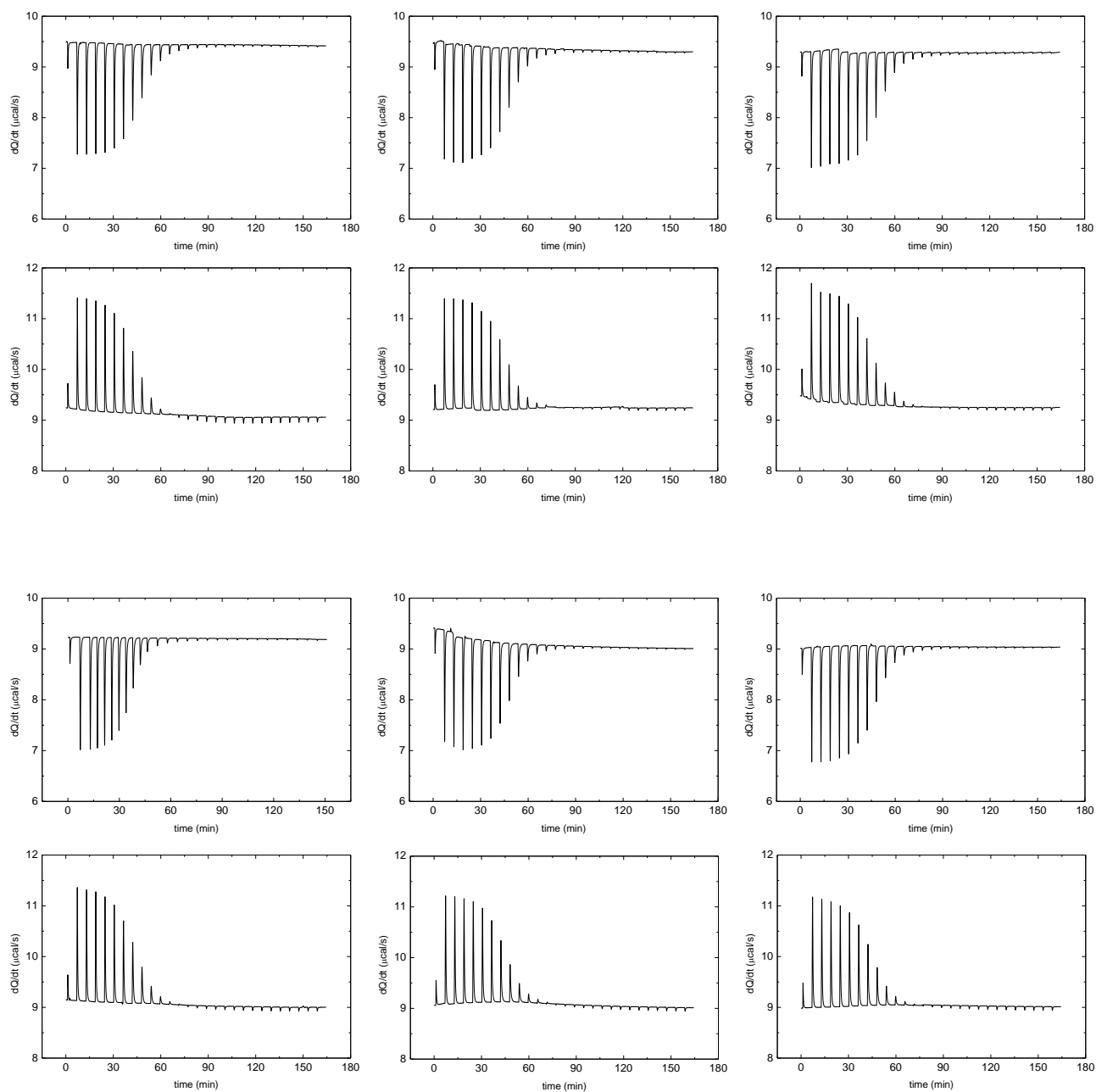
PART IV

Final Remarks
and Future
Perspectives

Final Remarks

The use of different biophysical experimental techniques (DSC, Fluorescence, SAXS and ATR-FTIR) together with the in silico approach by using CG-MD simulations, allow the study of the interactions of different antimicrobial *D,L*-α-cyclic peptides with bacterial lipid model membranes. This approach aimed ultimately at understanding the *D,L*-α-cyclic peptides' mechanisms of action.

The five CPs here studied, included a **first generation** (**CP1** and **CP2**) and a **second generation** (**CPR**, **CPRT10** and **CPRT14**) with improved antimicrobial activity. As lipid model membranes DMPG and DMPE:DMPG mixtures of varying negative charge content were used. To check the importance of peptide concentration, different lipid:peptide ratios were used.

We observed by DSC that the electrostatic interaction was the main driving force. In the case of first-generation peptides, the interaction was overall stronger for **CP1** than **CP2,** due to the hydrophobic component of the interaction**.** As regarding second generation, the peptides with tail, **CPRT10** and **CPRT14**, have a much stronger membrane interactions, again due mainly to the hydrophobic component. CG-MD confirmed the importance of electrostatics, as the main peptide-lipid contacts occur with negatively charged lipids These interactions were moderated when the zwitterionic DMPE was added to DMPG. Lipid segregation was observed in both peptide generations. Remarkably, **CP1** de-mixed significantly the two lipid components of the system with 10% of negative charge (DMPE:DMPG (1:9)), and in the case of the second generation peptides, **CPRT14** was able to micellize the DMPG membrane at the highest L:P content. These two peptides were the only ones to have an interaction with DMPE, although mild.

CG-MD simulations allows us to visualize the *D,L*-α-CPs/membrane interactions. For **CP1** and **CP2** simulations were performed with peptides constrained as nanotubes. The CG-MD for the **second generation**, were performed starting with the peptides non assembled in solution and following their assembly in the presence of the membrane. Our results show that the supramolecular structures adopted by the three peptides are different, namely short nanotubes in the case of **CPR**, and mainly micellar-type aggregates in the case of **CPRT10** and **CPRT14.**

ATR-FTIR shows that in the presence of membranes the peptides assemble mainly as nanotubes with β-sheet structure, but the presence of other type of aggregated structures (seen in amide I band peaks) was also seen. The use of

polarized light allowed us to observe that the peptides lie parallel to the membrane surface.

Fluorescence measurements were performed for the **second generation** peptides, to quantify their partition to membranes of DMPG and DMPE:DMPG(1:1). The results shown that **CPR** has a significantly lower partition than **CPRT10** and **CPRT14**, particularly to DMPE:DMPG (1:1), in line with the DSC conclusions. The introduction of a hydrocarbon tail in **CPRT10** and **CPRT14** proved to significantly increase the partition (importance of the hydrophobic component of the interaction), and further showed that the length of the tail becomes more important than the negative charge content of the membrane, as similar values were obtained for each peptide in both membrane systems, whereas they were about one order of magnitude higher for **CPRT14** in both systems. The membrane destruction was clear in the leakage studies, where a faster and much more complete leakage was observed for the peptides with tail.

The SAXS and WAXS results showed that only **CP1** and **CPRT14** interacted significantly with DMPE, in perfect agreement with the DSC results. These peptides were able to create a second lamellar phase in gel state of DMPE, with higher repeat distance, as a result of charging up the membrane. As regarding the interactions of the second generation peptides with the bacterial model membrane DMPE:DMPG (3:1), the SAXS results showed that **CPRT10** and **CPRT14** had a much stronger interaction in gel and fluid phases, in line with the DSC, CG-MD and fluorescence results. Further, the observed significant interaction in fluid phase is in line with their proven antimicrobial activity.

Finally, as regarding the peptide's possible antimicrobial mechanism of action, our structural and CG-MD results suggest that the active peptides **CPRT10** and **CPRT14** act by membrane segregation, due to their DMPG preference, that eventually impairs membrane function (**CPRT10**) or leads to membrane destruction, with possible membrane micellization (**CPRT14**).

Future Perspectives

The research work developed left some open questions that may be seen as research opportunities to develop new and improved antimicrobial cyclic peptides.

The size of the nanotubes still remains elusive, since we could get some results from CG-MD, but experimentally we could only show that they exist (ATR-FTIR), but not assess they size. Thus, techniques such as TEM could be used in the future to try to have information on this.

It would be also very interesting to further characterize the position of the amino acid residues in the membrane, using solid state NMR and atomistic MD simulations. The solid-state NMR studies were already started, but there was not possible to conclude them within the timeframe of this thesis. Another interesting approach would be the use of more realistic membranes, such as bacterial extracts, to perform studies by DSC and Fluorescence spectroscopy.

Considering the differences between **CP2** and **CPR** (one Lys substituted by Arg in **CPR**), new studies focusing the role of these residues in antimicrobial action should be performed.

Another direction of research would be the use of biofilms, to assess the effect of these peptides. Biofilms are a serious health concern, that contributes to persistent chronic infections due to their ability to tolerate antibiotics, host defense systems and other external stress factors.

Hopefully, from the results here and these prospective studies, new and improved antimicrobial peptide will be discovered.